Structural and biochemical characterization of gephyrin and various gephyrin-ligand complexes

Strukturelle und biochemische Charakterisierung von Gephyrin und verschiedenen Gephyrin-Liganden-Komplexen

Doctoral thesis for a doctoral degree
at the Graduate School of Life Sciences,
Julius-Maximilians-Universität Würzburg,
Section Biomedicine

Submitted by
Bodo Sander
from
Frankfurt am Main

Würzburg, 30th of May 2014

Dedicated to my dear Gudrun

Submitted on: ……..

Office stamp

Members of the *Promotionskomitee*:

Chairperson:	Thomas Dandekar
Primary Supervisor:	Hermann Schindelin
Supervisor (Second):	Thomas Müller
Supervisor (Third):	Thomas Raabe

Date of Public Defense: ……..

Date of Receipt of Certificates: ……..

TABLE OF CONTENTS

AFFIDAVIT/EIDESSTATTLICHE ERKLÄRUNG

Affidavit

I hereby declare that my thesis entitled

"Structural and biochemical characterization of gephyrin and various gephyrin-ligand complexes"

is the result of my own work. I did not receive any help or support from commercial consultants. All sources and/or materials applied are listed and specified in the thesis.

Furthermore, I confirm that this thesis has not yet been submitted as part of another examination process neither in identical nor in similar form.

Place, Date Signature

Eidesstattliche Erklärung

Hiermit erkläre ich an Eides statt, die Dissertation mit dem Titel

"Strukturelle und biochemische Charakterisierung von Gephyrin und verschiedenen Gephyrin-Liganden-Komplexen"

eigenständig, d.h. insbesondere selbständig und ohne Hilfe eines kommerziellen Promotionsberaters angefertigt und keine anderen als die von mir angegebenen Quellen und Hilfsmittel verwendet zu haben.

Ich erkläre außerdem, dass die Dissertation weder in gleicher noch in ähnlicher Form bereits in einem anderen Prüfungsverfahren vorgelegen hat.

Ort, Datum Unterschrift

ACKNOWLEDGEMENTS

As a matter of fact, this work would not have been possible without the support of others, so many that I'm afraid that I forget anyone. To all those, I express my apologies. Nevertheless, there is still a long list of people I remember.

First of all, I would like to thank my primary supervisor Prof. Hermann Schindelin who gave me the opportunity to work on these three exciting projects. I thank him for all the significant scientific input and his aid, which was not limited to scientific issues. My thanks also go to my two other supervisors Prof. Thomas Raabe and Prof. Thomas Müller for their support. In addition I would like to thank Prof. Hermann Schindelin and Prof. Thomas Müller also for acting as reviewers of this thesis. For financial support I would like to thank the SFB 487 as well as the BioMedTec International Graduate School of Science (BIGSS).

I would also like to take the opportunity to express my gratitude to all current and past members of the Schindelin and Kisker labs. This would be a long list, and therefore I decided to focus on people, who gave direct input to this work.

Dr. Daniela Schneeberger considerably facilitated especially the first year of my thesis, helping me to find my way in the lab. But also in the final stages she helped me by providing collybistin DNA constructs as well as purified collybistin. I am also thankful for all the vivid discussions we had. Likewise, I would like to thank Dr. Petra Hänzelmann who always shared her enormous wealth of experience and gave invaluable input. I am also thankful for fruitful discussions with Dr. Jochen Kuper, Dr. Florian Sauer, Dr. Hans Maric, Carolyn Delto and Dr. Antje Schäfer. I profited from the knowledge of Dr. Antje Schäfer, Dr. Maria Hirschbeck and Dr. Jochen Kuper during the beamline trips to Berlin and Grenoble. Kristina Keller, a former diploma student in the lab, worked carefully and with great endurance on two gephyrin projects, and her results were the basis for the phosphomimic project. I would like to thank Dr. Melissa Graewart (EMBL Hamburg) for performing low-angle light scattering experiments for me and Dr. Armin Welker for his efforts to synthesize an ATP analogue for crosslinking purposes. Florian Rohleder provided the *Chaetomium thermophilum* PCNA plasmid, helping me to generate a positive control in the context of the Geph-DYNLL1 project. I am also grateful for contributions of Dr. Eunyoung Lee and Dr. Eun-Young Kim, which paved the way for the presented work.

Dr. Bernhard Fröhlich und Christian Weinberger I would like to acknowledge for their steady and spontaneous helpfulness concerning IT issues. Without their help I could not have performed all the SAXS analysis in the required scale.

I appreciated Prof. Nils Brose's and Dr. Tolga Soykan's (both MPI für experimentelle Medizin, Göttingen) open and hence helpful handling of unpublished data and many enlightening discussions.

As I had no expertise in SAXS and AFM data analysis I owe a great debt to all the people who contributed to the manuscript. Dr. Alexander Shkumatov and Giancarlo Tria introduced me to and provided help during the SAXS measurements in Hamburg but were also helpful in the course of the data analysis. Dr. Jörg Günter Grossmann (University of Liverpool) who had carried out initial SAXS analyses of gephyrin at Daresbury put a lot of efforts into the project and provided significant input and helpful insights into SAXS data analysis. Giancarlo Tria improved the ensemble optimization method, thereby enabling me to carry out meaningful SAXS analyses of gephyrin constructs at all. Dr. Alexey Kikhney I would like to thank for helpful discussions on the SAXS data of the gephyrin-DYNLL complex (2011 and 2012). Coming back to Würzburg, I would like point out that I am indebted to Dr. Ingrid Tessmer who carried out the AFM measurements and taught me AFM data analysis. Her help was not restricted to the mere help in technical questions, but also included enlightening disccusions. Furthermore I would like to thank all authors for critical reading, which helped to improve the quality of the manuscript: Dr. Alex Shkumatov, Giancarlo Tria and Prof. Dmitri Svergun (all from the EMBL in Hamburg), Dr. Jörg-Günter Grossmann (University of Liverpool), Dr. Ingrid Tessmer and Prof. Hermann Schindelin.

Last but certainly not least I would express my cordial gratitude to my girlfriend Gudrun Michels and my family. Their continuous and unconditional support during all these years cannot be sufficiently appreciated.

SUMMARY

Efficient synaptic neurotransmission requires the exact apposition of presynaptic terminals and matching neurotransmitter receptor clusters on the postsynaptic side. The receptors are embedded in the postsynaptic density, which also contains scaffolding and regulatory proteins that ensure high local receptor concentrations. At inhibitory synapses the cytosolic scaffolding protein gephyrin assumes an essential organizing role within the postsynaptic density by the formation of self-oligomers which provide a high density of binding sites for certain γ-amino butyric acid type A ($GABA_A$) and the large majority of glycine receptors (GlyR). Gephyrin contains two oligomerization domains: In isolation, the 20 kDa N-terminal G domain (GephG) and the 46 kDa E domain (GephE) trimerize and dimerize, respectively. In the full-length protein the domains are interconnected by a central ~150 amino acid linker, and only GephG trimerization is utilized, whereas GephE dimerization is prevented, thus suggesting the need for a trigger to release GephE autoinhibition, which would pave the way for the formation of higher oligomers and for efficient receptor clustering. The structural basis for this GephE autoinhibition has remained elusive so far, but the linker was reported to be sufficient for autoinhibition. This work dealt with the biochemical and structural characterization of apo-gephyrin and gephyrin in complexes with ligands which are known to promote the formation of synaptic gephyrin clusters (collybistin and neuroligin 2) and reorganize them (dynein light chain 1).

For full-length gephyrin no structural information has been available so far. Atomic force microscopy (AFM) and small-angle X-ray scattering (SAXS) analyses described in this thesis disclosed that the gephyrin trimer forms a highly flexible assembly, which, due to the long linker, can switch between compact and extended conformational states in solution, with a preference for compact states. This partial compaction and potentially GephE autoinhibition are achieved by interactions of parts of the linker with the G and E domains, as suggested by circular dichroism spectroscopy. However, the linker on its own cannot account for GephE blockage, as size exclusion chromatography experiments coupled with multi angle light scattering detection (SEC-MALS) and SAXS analyses revealed that a gephyrin variant only encompassing the linker and GephE (GephLE) forms dimers and not monomers as suggested by an earlier study. The oligomeric state of GephLE and the observation that several gephyrin variants, in which linker segments of varying length were deleted, predominantly formed trimers, suggested the presence of a linker independent mechanism of GephE dimerization blockade. Taken together, the data indicated that linker-dependent and linker-independent mechanisms mediate gephyrin autoinhibition.

In the second project gephyrin's interaction with DYNLL1 (**Dyn**ein **L**C8 **L**ight Chain **1**) was characterized. DYNLL1 is a 25 kDa dimer incorporated into the dynein motor and provides two binding sites, each of which can accommodate an octapeptide derived from gephyrin's linker region

(referred to as $Geph_{DB}$). Originally, DYNLL1 was regarded as a cargo adaptor, linking gephyrin-GlyR complexes to the dynein motor, thus driving their retrograde transport and leading to a decrease of synaptic gephyrin-GlyR complexes.

Building on these studies, this thesis assessed the cargo hypothesis as well as the so far unclear stoichiometry of the gephyrin-DYNLL1 complex. The cargo scenario would require ternary complex formation between gephyrin, DYNLL1 and the dynein intermediate chain (DIC) of the dynein motor. However, such a complex could not be detected by analytical size exclusion chromatography (aSEC) experiments – presumably because gephyrin and DIC competed for a common binding site in DYNLL1. This finding was consistent with a single DYNLL1 dimer capturing two linker segments of a single gephyrin trimer as suggested by a 26 kDa mass increase of the gephyrin species in the presence of DYNLL1 in SEC-MALS experiments. aSEC experiments at even higher concentrations (~20 µM gephyrin and ~80 µM DYNLL1) indicated that the affinity of $Geph_{DB}$ was significantly impaired in the context of full-length gephyrin but also in a variant that bears only GephG and the first 39 residues of the linker (GephGL220). Presumably due to avidity effects two linkers stably associated with a single DYNLL1 dimer, whereas the third DYNLL1 binding motif remained predominantly unoccupied unless high concentrations of GephGL220 (50 µM) and DYNLL1 (200 µM) were used. These findings indicate that an interplay between GephG and the N-terminal linker segment mediates the attenuation of $Geph_{DB}$ affinity towards DYNLL1 and that preventing DYNLL1 from the induction of higher gephyrin oligomers is either advantageous for DYNLL1-mediated reorganization of gephyrin-GlyR clusters or that DYNLL1 exerts possibly two (concentration-dependent) actions on gephyrin.

The gephyrin-collybistin-neuroligin 2 complex was the subject of the third project. Previously, collybistin and gephyrin were observed to mutually trigger their translocation to the postsynaptic membrane, where the disordered cytoplasmic tail of the postsynaptic cell adhesion molecule NL2 ($NL2_{cyt}$) causes the anchoring of collybistin 2 (CB2) by binding to its SH3 domain, thereby releasing SH3 domain mediated autoinhibiton of CB2 binding to the membrane phospholipid phosphatidylinositol-3-phosphate. Critical for this event is the binding of gephyrin to both CB2 and NL2, presumably via GephE.

Following up on these previous studies biochemical data presented in this thesis confirm the formation of the ternary complex. Unexpectedly, analyses by means of native polyacrylamide gel electrophoresis pointed to: (1) The existence of a complex containing $NL2_{cyt}$ and CB2 lacking the SH3 domain and consequently an additional NL2 binding site in CB2. (2) Attenuated gephyrin-collybistin complex formation in the presence of the SH3 domain. (3) A requirement for high $NL2_{cyt}$ concentrations (> 30 µM) during the formation of the ternary complex. This might allow for the regulation by other factors such as additional binding partners or posttranslational modifications.

Although of preliminary character, these results provide a starting point for future studies, which will hopefully elucidate the interplay between gephyrin, collybistin, NL2 and certain $GABA_A$ receptors.

ZUSAMMENFASSUNG

Eine effiziente synaptische Neurotransmission macht es erforderlich, dass sich presynaptische Nervenenden und die Schar (*engl.* Cluster) der dazugehörigen Neurotransmitterrezeptoren auf der postsynaptischen Seite exakt gegenüberliegen. Die Rezeptoren sind in der postsynaptischen Dichte eingebettet, die auch Gerüstproteine und regulatorische Proteine enthält, die hohe lokale Rezeptor-Konzentrationen gewährleisten. An inhibitorischen Synapsen übernimmt das cytosolische Gerüstprotein Gephyrin eine essentielle Rolle in der postsynaptischen Dichte durch die Bildung von Homo-Oligomeren, die für eine hohe Dichte an Bindungsstellen für bestimmte γ-Aminobuttersäure Typ A- ($GABA_A$)- und die große Mehrheit der Glyzin-Rezeptoren (GlyR) sorgen. Gephyrin enthält zwei Oligomerisierungsdomänen: In isolierter Form bildet die N-terminale 20 kDa große G-Domäne (GephG) und die C-terminale 46 kDa große E-Domäne (GephE) Trimere beziehungsweise Dimere. Im Volllängenprotein sind die Domänen durch einen zentrale ~150 Aminosäure lange Region (auch Linker genannt) verknüpft, und nur von der GephG-Trimerisiung wird Gebrauch gemacht, wohingegen die GephE-Dimerisierung unterbunden ist, was nahelegt, dass ein Auslöser benötigt wird, der die Autoinhibierung von GephE aufhebt und dadurch den Weg zur Bildung höherer Oligomere ebnet. Die strukturelle Basis für die GephE- Autoinhibierung ist bislang nicht bekannt, aber eine veröffentlichte Studie kam zu dem Schluss, dass der Linker ausreicht, um die GephE-Dimerisierung zu inhibieren. Diese Arbeit beinhaltet die biochemische und strukturelle Charakterisierung von apo-Gephyrin und Gephyrin in Komplexen mit Liganden, von denen bekannt ist, dass sie entweder die Bildung von synaptischen Gephyrin-Selbstoligomeren begünstigen (Collybistin und Neuroligin 2) oder die Gephyrin-Selbstoligomere reorganisieren (Dynein leichte Kette 1).

Für Volllängen-Gephyrin gab es bislang keine strukturellen Informationen. Rasterkraftmikroskopie (*engl.* AFM)- und Röntgenkleinwinkelbeugungs (*engl.* SAXS)-Analysen, die in dieser Arbeit beschrieben sind, deckten auf, dass das Gephyrin-Trimer eine hoch flexible Einheit ist, die – durch den langen Linker – zwischen kompakten und extendierten Zuständen hin- und herwechselt, mit einer leichten Präferenz für kompakte Zustände. Spektroskopische Messungen des zirkulären Dichroismus legten nahe, dass die partielle Kompaktierung und möglicherweise auch die GephE-Autoinhibition durch Interaktionen von Teilen des Linkers mit den G- und E-Domänen erreicht werden. Aber der Linker alleine kann nicht für die GephE-Blockade verantwortlich zeichnen, weil Größenausschluss-Chromatographie-Experimente gekoppelt mit Multiwinkel-Lichtstreudetektion (englische Abkürzung SEC-MALS) offenlegten, dass eine Gephyrin-Variante, die nur den Linker und GephE umfasst (GephLE), Dimere und keine Monomere ausbildet, wie in einer früheren Studie postuliert wurde. Der oligomere Zustand von GephLE und die Beobachtung, dass alle Gephyrin-Varianten, in denen Linker-Segmente verschiedener Länge deletiert wurden, überwiegend Trimere

bildeten, legen nahe, dass ein Linker-unabhängiger Mechanismus für die GephE-Dimerisierungsblockade existiert. Zusammengenommen deuten die Daten darauf hin, dass Linker-abhängige und -unabhängige Mechanismen die GephE-Autoinhibtion vermitteln.

Im zweiten Projekt wurde die Interaktion von Gephyrin mit DYNLL1 (**Dyn**ein **L**C8 **L**ight Chain **1**) charakterisiert. DYNLL1 is ein 25 kDa-Dimer, das im Dynein-Motor integriert ist, und bietet zwei Bindestellen, die beide ein von der Gephyrin-Linker-Region abgeleitetes Oktapeptid (im Weiteren $Geph_{DB}$) aufnehmen können. Ursprünglich wurde DYNLL1 als ein Ladungsadapter betrachtet, der Gephyrin-GlyR-Komplexe mit dem Dynein-Motor verknüpft und dadurch ihren retrograden Transport vorantreibt und somit zu einer Abnahme synaptischer Gephyrin-GlyR-Komplexe führt.

Auf diesen Studien aufbauend, wurde in dieser Arbeit die Ladungsadapter-Hypothese analysiert ebenso wie die bislang unklare Stöchiometrie des Gephyrin-DYNLL1-Komplexes. Das Ladungsadapter-Szenario würde einen ternären Komplex aus Gephyrin, DYNLL1 und der mittleren Dynein-Kette (englische Abkürzung DIC) voraussetzen. Ein solcher Komplex konnte mittels analytischer Größenausschlusschromatographie (englische Abkürzung aSEC) nicht detektiert werden – vermutlich, weil Gephyrin und DIC um eine gemeinsame Bindungsstelle in DYNLL1 konkurrierten. Dieser Befund war konsistent mit einem Modell, in dem ein einzelnes DYNLL1-Dimer zwei Linker eines (einzelnen) Gephyrin-Trimers bindet, wie es auch durch eine 26 kDa-Massen-Zunahme der Gephyrin-Spezies in der Anwesenheit von DYNLL1 in SEC-MALS-Experimenten nahegelegt wurde. aSEC-Experimente auch bei hohen Konzentrationen (~20 µM Gephyrin und ~80 µM DYNLL1) deuteten darauf hin, dass die Affinität von $Geph_{DB}$ im Kontext von Volllängen-Gephyrin signifikant beeinträchtigt war, aber auch bei einer Gephyrin-Variante, die nur GephG und die ersten 39 Reste des Linkers entielt (GephGL220). Voraussichtlich aufgrund von Aviditätseffekten banden zwei Linker stabil an ein einzelnes DYNLL1-Dimer, wohingegen das dritte DYNLL1-Bindungsmotiv unbesetzt blieb, so lange nicht hohe Konzentrationen an GephGL220 (50 µM) und DYNLL1 (200 µM) eingesetzt wurden. Diese Ergebnisse deuteten an, dass ein Zusammenspiel von GephG und dem N-terminalen Linker-Segment die Abschwächung der $Geph_{DB}$-Affinität zu DYNLL1 vermittelt und dass die Verhinderung der Induktion höherer Oligomere durch DYNLL1 entweder vorteilhaft für die Reorganization von Gephyrin-GlyR-Clustern ist oder dass DYNLL1 zwei (konzentrationsabhängige) Wirkungen auf Gephyrin ausübt.

Der Gephyrin-Collybistin-Neuroligin 2-Komplex war Gegenstand des dritten Projektes. Im Vorfeld dieser Arbeit wurde festgestellt, dass Collybistin und Gephyrin gegenseitig ihre Translokation zur postsynaptischen Membran einleiten, wo der ungeordnete, cytosolische Anteil des postsynaptischen Zelladhäsionsmembranmoleküls Neuroligin 2 ($NL2_{cyt}$) die Verankerung von Collybistin 2 (CB2) durch das Binden an seine “src homology 3”-Domäne (SH3-Domäne) bewirkt und dadurch die SH3-Domänen-vermittelte Autoinhibition der CB2-Bindung an das Membran-Phospholipid

Phosphatidylinositol-3-phosphat aufhebt. Entscheidend für dieses Ereignis ist, dass Gephyrin sowohl an CB als auch an $NL2_{cyt}$ bindet, vermutlich vermittelt durch GephE.

In einer Fortsetzung dieser früheren Studien bestätigen biochemische Daten in dieser Arbeit die Bildung des ternären Komplexes. Unerwarteterweise deuteten Analysen mittels nativer Polyacrylamidgelektrophorese auf: (1) Die Existenz eines Komplexes aus $NL2_{cyt}$ und CB2 ohne SH3-Domäne und damit auf eine zusätzliche NL2-Bindungsstelle in CB2. (2) Abgeschwächte Gephyrin-Collybistin-Komplexbildung in der Anwesenheit der SH3-Domäne. (3) Hohe NL2-Konzentrationen (>30 µM) als Voraussetzung für die Bildung des ternären Komplexes. Dies könnte die Regulation durch andere Faktoren wie zusätzliche Bindungspartner oder posttranslationale Modifikationen ermöglichen. Wenngleich die Ergebnisse von vorläufigem Charakter sind, stellen sie einen Startpunkt für künftige Arbeiten dar, welche hoffentlich das Zusammenspiel von Gephyrin, Collybistin, NL2 und bestimmten $GABA_A$-Rezeptoren weiter aufklären werden.

I. MAIN INTRODUCTION

Neurons represent the principal basic units of the nervous system, which is composed of the central nervous system (CNS) and the peripheral nervous system (PNS). Brain and spinal cord neurons constitute the CNS, and the remaining neurons connect the periphery with the CNS and are referred to as the PNS. Peripheral nerves transmit information to the CNS, where the information is integrated and processed and transmitted to the PNS again. This exchange is involved in virtually all body functions and endows an organism with control of internal organs, perception of stimuli and appropriate reactions to the latter. In light of the many diverse functions it appears plausible why the brain is the most complex organ in the human body, and this is reflected in the huge numbers of neurons (Purves *et al.*, 2004). A relatively recent rough estimate, which relied on earlier work in the period from 1953 to 1975, assumed that the human brain on its own contains 86 billion neurons (Williams & Herrup, 1988).

Neurons are polarized cells, in which two kinds of more or less ramified protrusions point away from the central cell body – namely axons and dendrites. The majority of neurons are connected via chemical synapses. Chemical synapses in the CNS connect a presynaptic axon ending (also referred to as “bouton”) with a postsynaptic dendrite, separated by the synaptic cleft, a narrow gap in the extracellular space (Purves *et al.*, 2004). In chemical signal transmission vesicles fuse with the plasma membrane of the presynaptic terminal and release their content, the neurotransmitters, into the synaptic cleft (Sudhof, 2013). There the neurotransmitters bind to the extracellular part of ligand-gated ion channels, which are embedded in the postsynaptic cell membrane. Binding results in a conformational change which leads to an opening of the channel and triggers ion influx or efflux in response to the respective ion concentrations in the cytosol and the synaptic cleft. Ion influx is observed if the extracellular ion concentration exceeds the cytosolic concentration, and, *vice versa*, an efflux occurs if the intracellular concentration is higher than the extracellular concentration. These fluxes result in local changes of the membrane potential, eliciting inhibitory postsynaptic potentials (IPSPs) or excitatory postsynaptic potentials (EPSPs), depending on the membrane potential and the receptor reversal potential. PSPs are summed up at the axon initial segment (AIS), and, if a threshold potential is exceeded, the neuron generates an action potential, which is propagated along the axon to the presynaptic terminal of the postsynaptic neuron and will increase the propensity of vesicle release at the next synapse. Synapses which exert EPSPs and IPSPs at the postsynaptic cell, are called excitatory and inhibitory synapses, respectively (Purves *et al.*, 2004).

In addition to the vast number of neurons other factors contribute to the complexity of the system which is required to fulfil a large variety of tasks. Only a few of them are mentioned here: Neurons are highly interconnected and organised in specific circuits and can regulate their propensity for neurotransmitter release. In these circuits a single neuron can target not just a single neuron but

several neurons, and also the target location can vary. Depending on the task and the developmental stage, synapses can be rather transient or rather stable, hence a neuron can be targeted by predominantly excitatory synapses in one stage and then by inhibitory ones at another (Purves *et al.*, 2004). The following introduction will focus on inhibitory synapses in mammals.

I.A. Inhibitory Neurotransmission

The vast majority (~90%) of synapses are excitatory (Heller *et al.*, 2012), where the tetrameric ionotropic glutamate receptors, namely the NMDA (N-Methyl-D-aspartic acid), AMPA (α-amino-3-hydroxy-5-methyl-4-isoxazolepropionic acid) and kainate receptors, enhance the permeability for Na^+, K^+ and the second messenger Ca^{2+}, whose influx generally leads to depolarizing EPSPs (Ozawa *et al.*, 1998). At these synapses the presynaptic axon targets so-called dendritic spines, which are small button-like protrusions (Harris & Kater, 1994) with properties of a micro-compartment (Bloodgood & Sabatini, 2005, Sheng & Hoogenraad, 2007) (Fig. 1). At inhibitory synapses γ-aminobutyric acid (GABA) and glycine are the principal neurotransmitters and bind to receptors of the family of pentameric Cys-loop receptors, namely $GABA_A$ and glycine receptors, which allow Cl^- to enter the cell, typically eliciting a hyperpolarizing IPSP.

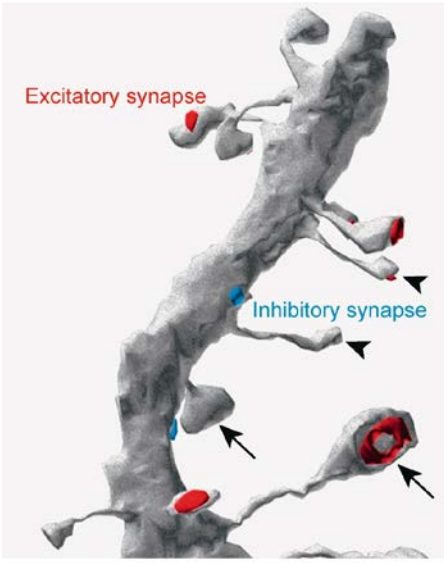

Sheng M, Hoogenraad CC. 2007. Annu. Rev. Biochem. 76:823–47

Figure 1 The different organization of postsynaptic sites at inhibitory and excitatory synapses. This image is taken from Sheng & Hoogenraad (2007) and displays an EM reconstruction of a dendritic segment from the CA1 region of the hippocampus. While inhibitory synapses are located at the dendritic shaft, excitatory synapses protrude from the shaft to form dendritic spines. Inhibitory and excitatory PSDs are shown in blue and in red, respectively. The latter PSDs can form thin spines (*arrowheads*) and mushroom spines (*arrows*).

Inhibitory neurons are – with a few exceptions (Bagnall *et al.*, 2009, Jinno *et al.*, 2007) – rather small and act rather locally (and are referred to as interneurons), whereas most neurons connecting different brain regions are excitatory (referred to as projection neurons). The original view on synaptic inhibition focussed on its counterbalancing properties on excitatory neurons. Indeed, a balance of excitation and inhibition (referred to as E/I balance) is required for the maintenance of proper functioning of the nervous system, as illustrated by diseases, where this balance is disturbed, e.g. epilepsy, sleep and psychiatric disorders and motoric syndromes (Birke & Draguhn, 2010). Beyond that inhibitory neurons can be electrically coupled to synchronize

their inhibition on a multitude of targets, giving rise to network oscillations in local circuits (Birke & Draguhn, 2010).

Hence, although less abundant and usually smaller in size than their excitatory counterparts, inhibitory neurons can infer a so far only partially disclosed complexity in neuronal circuits, and accordingly inhibitory neurotransmission should not simply be regarded as assistant of excitatory neurotransmission (Birke & Draguhn, 2010). Indeed inhibitory neurons make use of additional instruments which complicate a straightforward deciphering of neuronal circuits.

Interneurons can project to various sites on the target neuron, covering the surface area from dendrites to the presynaptic boutons (Draguhn *et al.*, 2008, Freund & Katona, 2007, Kullmann *et al.*, 2005), of which dendrites and the cell body are the most extensively studied targets: While inhibition at dendrites rather seems to be local and regulates excitatory input, perisomatic inhibition is far more effective in regulating the output of the postsynaptic cell (Freund & Katona, 2007). Yet even the same target compartment can receive input from various types of interneurons, and around 20 different inhibitory interneuron types have been described so far, which are presumably adjusted to various purposes (Kepecs & Fishell, 2014).

Receptors are not restricted to synaptic sites, they are also found – in a more dispersed form – at extrasynaptic sites where they mediate tonic inhibition which is distinguished from phasic inhibition at synaptic sites. These extrasynaptic receptor populations display a subunit composition different from that of synaptic receptors and exhibit a higher transmitter affinity so that they can detect comparatively small ambient concentrations of neurotransmitters of glial origin (Lee *et al.*, 2010) or resulting from release or transmitter spillover after synaptic transmission (Brickley & Mody, 2012, Takazawa & MacDermott, 2010). Not surprisingly, ambient neurotransmitter concentrations can also be regulated, for example by glycine transporter 1 (GlyT1) expressed on glia cells (Zhang *et al.*, 2008). Tonic inhibition appears to reduce neuron excitability less precisely which, however, does not mean that it does not fulfil important functions, and, indeed, tonic inhibition has been implicated in learning and memory (Mohler, 2009). One should also mention that tonic transmission is not restricted to inhibitory neurons but is also used in the context of excitatory transmission (Cavelier *et al.*, 2005).

Intriguingly, GABAergic and glycinergic synapses can even be excitatory. Before birth the importer of $Na^+/K^+/Cl^-$ (NKCC1) is up-regulated, and this leads to an increase in cytosolic Cl^- concentrations. Hence, channel opening results in depolarization instead of hyperolarization (Ben-Ari, 2002). The upregulation of the K^+/Cl^- exporter KCC2 along with a downregulation of NKCC1 renders GABA- and glycinergic synapses inhibitory (Birke & Draguhn, 2010, Blaesse *et al.*, 2009).

I.A.1. The Cys-loop glycine and $GABA_A$ receptors

The neurotransmitter receptors are obviously the most important components of PSDs. $GABA_A$ and glycine receptors belong to the family of Cys-loop receptors, that also comprise nicotinic acetylcholine (nAChRs) and serotonin type 3 ($5\text{-}HT_3R$) receptors as well as the zinc activated channels (ZACs) (Davies *et al.*, 2003). They are also referred to as pentameric ligand-gated ion channels (pLGICs), because they assemble into pseudosymmetric (hetero-)pentameric channels. They share a common architecture and each subunit contains four transmembrane helices (M1-M4), which are flanked by a relatively large N-terminal domain and a short extracellular C-terminus on the extracellular side and a large intracellular loop between helices M3 and M4 (M3-M4 loop). The N-terminal domain harbours also the Cys-loop, a conserved 15-residue stretch enclosed by a disulfide bridge (Thompson *et al.*, 2010). However, this loop does not seem to be essential for the proper functioning of all receptors of this family (Bocquet *et al.*, 2007).

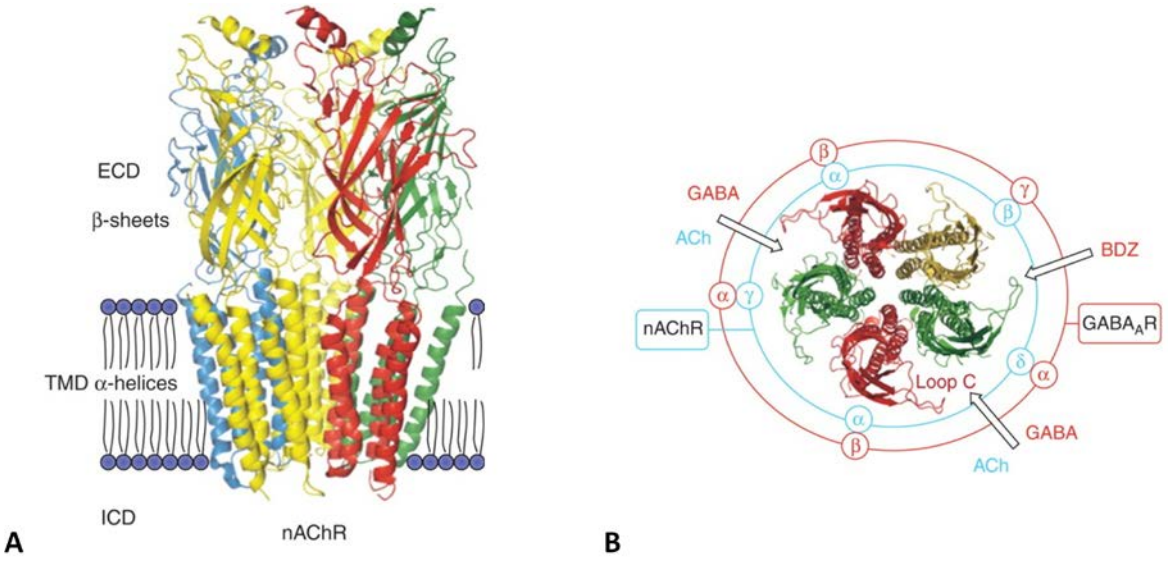

Figure 2 Organization of pLGICs. Figures were adapted and modified from (Smart & Paoletti, 2012) with the permission of the Cold Spring Harbor Laboratory Press (Cold Spring Harb Perspect Biol 2012;4:a009662). (A) *Torpedo marmorata* nAChR (PDB code: 2BG9) (Unwin, 2005). Intracellular helices preceding M4 are not shown. (B) View of a Cys-loop receptor from the synaptic side to exemplify the subunit composition of nAChR and the prevalent $GABA_AR$. Binding sites for GABA and benzodiazepines (BDZ) are indicated by the arrows.

Up to now no crystal structures of complete mammalian Cys-loop receptors are available at a resolution that allows for the assignment of individual amino acid side chains. Nevertheless, for the nAChR from *Torpedo marmorata* information up to 4 Å is available (Unwin, 2005) (Fig. 2A). Higher resolution structures for acetylcholine binding protein (AChBP) pentamers, which share ~25% sequence identity with the extracellular domain of the nAChR (Brejc *et al.*, 2001, Celie *et al.*, 2004) enhanced the understanding of Cys-loop receptors, and their relevance was underscored by their structural similarity with the structure of the extracellular domain of an nAChrR monomer (Dellisanti

et al., 2007). These structures were also similar to those of prokaryotic LGICs (Bocquet *et al.*, 2009, Hilf & Dutzler, 2008) and the homopentameric *Caenorhabditis elegans* glutamate-gated chloride channel α (GluCl) (Hibbs & Gouaux, 2011). Recently, a crystal structure of an AChBP chimera containing the ligand binding motif of the 5-HT3R revealed the assembly of a mammalian ligand binding domain pentamer (Kesters *et al.*, 2013). These models can be used for more refined implications about the functioning of LGICs, e.g. the process of ligand gating (Calimet *et al.*, 2013).

Typically pLGICs contain different subunits, and their composition can give rise to differences in ligand binding and ion gating. The ligand binding site resides in the N-terminal domain, but beyond that pLGICs provide binding sites for allosteric modulators such as ions, alcohols, anaesthetics and other organic and inorganic compounds in the N-terminal domain but also the transmembrane helices. The actual channel is built up by the M2 helices. Together with charged rings at either channel end M2 was reported to contribute to ion selectivity (Thompson & Lummis, 2003). The "intracellular domain" mainly consists of the intracellular M3-M4 loop (~100-270 residues), which provides binding sites for cytosolic proteins that promote LGIC clustering, assembly and transport.

I.A.1.1 Glycine receptors

Glycinergic synapses are rather enriched in caudal brain regions, the brain stem and the spinal cord and are involved in locomotor behaviour, respiration as well as audition and vision (Baer *et al.*, 2009, Legendre, 2001). Consistent with GlyR location at these sites dysregulated glycinergic transmission has been shown to be implicated in diseases like hyperekplexia (also referred to as startle disease) (Harvey et al., 2008) and tinnitus (Wang et al., 2011).

There are five genes encoding for GlyR subunits: GlyRα1-4 (48 kDa) and GlyRβ (58 kDa). GlyRs seem to assemble predominantly into GlyR$\alpha 1_2$-GlyRβ_3 pentamers (Dutertre *et al.*, 2012, Grudzinska *et al.*, 2005), which upon glycine binding change their permeability for Cl^-. Both subunits contribute to glycine binding via inter-subunit binding grooves (Dutertre *et al.*, 2012). Alternative splicing (Betz & Laube, 2006, Oertel *et al.*, 2007) as well as mRNA editing (Meier *et al.*, 2005) influence ligand binding (Meier *et al.*, 2005) and receptor localization (Melzer *et al.*, 2010).

Beyond glycine taurine and β-alanine can act as GlyR agonists, whereas strychnine exhibits an antagonistic effect (Legendre, 2001). Furthermore, GlyRs are subject to allosteric modulation by endocannabinoids (Lozovaya *et al.*, 2011), neurosteroids (Maksay *et al.*, 2001), anesthetics (Bertaccini *et al.*, 2010, Chau, 2010), ethanol (McCracken *et al.*, 2010, McCracken *et al.*, 2013, Welsh *et al.*, 2009) as well as Zn^{2+} (Miller *et al.*, 2008) and tropeines (Maksay *et al.*, 2008), which bind to the transmembrane helices and/or the ligand binding domain. Notably, also glutamate, the predominant neurotransmitter at excitatory synapses, was observed to potentiate GlyR responses, possibly providing a link between excitatory and inhibitory transmission (Liu *et al.*, 2010).

GlyRs can interact with cytosolic proteins via their TM3-4 loops: GlyRα1 and GlyRα3 subunits can bind to karyopherins α3 and α4 which have been implicated in nuclear transport (Melzer *et al.*, 2010). Also the GlyR β subunit can interact with several proteins involved in transport processes: Recently syndapin I (SdpI) and two splice variants of SdpII were reported to interact with the TM3-4 loop via their SH3 domain, thereby enhancing GlyR clustering (del Pino *et al.*, 2014). Furthermore Vps-35 (Vacuolar protein sorting-35) and neurobeachin (del Pino *et al.*, 2011) bind to the β subunit. The latter has also been shown to drive postsynaptic accumulation of $GABA_A$, NMDA, AMPA and kainate receptors (Nair *et al.*, 2013). Most importantly, the GlyR β subunit (but not the α subunits (Kirsch *et al.*, 1995)) interacts with gephyrin (Meyer *et al.*, 1995). The affinity of this interaction is so tight that gephyrin was highly enriched in native GlyR preparations and therefore initially regarded as a GlyR subunit (Betz *et al.*, 1991). Antisense oligonucleotide mediated depletion of gephyrin in spinal neurons significantly affected GlyR clustering (Kirsch *et al.*, 1993).

I.A.1.2 $GABA_A$ receptors

$GABA_A$ receptors are the prevalent LGICs at inhibitory synapses in most brain regions. In these receptors GABA binding induces a higher permeability for Cl^- but also HCO_3^- (Birke & Draguhn, 2010). Metabotropic $GABA_B$ receptors are involved in neuronal processes as well, but are described elsewhere as they are not relevant for this work (Ulrich & Bettler, 2007). Dysregulated GABAergic transmission via ionotropic receptors has been shown to be involved in several neurological diseases such as epilepsy, anxiety, mood disorders, mental disorders and schizophrenia (Marin, 2012).

$GABA_AR$ subunits can be subdivided into eight classes, some of which comprise several members: α(1-6), β(1-3), y(1-3), δ, ε, $\rho(1-3)$ (previously referred to as $GABA_C$ receptors), θ, π. Alternative splicing was documented for several of them (Mehta & Ticku, 1999). Of the plethora of theoretically possible configurations only a subset has been experimentally verified (Olsen & Sieghart, 2008); it is assumed that most receptors are composed of two α-, two β- and one γ-subunit(s) (Fig. 2B), where two different α- or β-subunits can be incorporated (Balic *et al.*, 2009). Sometimes the y-subunit is replaced by δ- or ε-subunits (Jones & Henderson, 2007). Subunit composition can significantly vary with the localization of the receptor. This is valid on the cellular and even on the subcellular level. $\alpha_{1/2/3}/\beta/\gamma_2$ receptors localize to postsynaptic sites, whereas $\alpha_{4/5/6}/\beta/\gamma_2$ and $\alpha_{4/5/6}/\beta/\delta$ receptors rather reside at extrasynaptic sites (Brickley & Mody, 2012), contributing to tonic inhibition (section I.A).

Like other pGLIC family members $GABA_A$ receptors are also subject to allosteric modulation by a spectrum of ligands, which partially overlaps with that of GlyR modulators: Amongst others, Zn^{2+} (Hosie *et al.*, 2003), anesthetics (Korpi *et al.*, 2002), ethanol (Kumar *et al.*, 2009), endozepines (Christian *et al.*, 2013) and neurosteroids (Carver & Reddy, 2013) can modify the receptor response. Presumably the most prominent allosteric modulators are benzodiazepines. They alter the affinity of

$GABA_A$ receptors to GABA by binding to the interface between the α and γ2 subunits (Rudolph & Knoflach, 2011). In knock-out mice, in which a crucial determinant of diazepam binding in individual α subunits was affected, the various effects of diazepam could be dissected and α subunits could be linked to certain diazepam effects. These results also provide a rational basis for more selective drugs (Rudolph & Knoflach, 2011) (Table 1).

	$\alpha_1/\beta/\gamma_2$	$\alpha_2/\beta/\gamma_2$	$\alpha_3/\beta/\gamma_2$	$\alpha_5/\beta/\gamma_2$
sedation	x			
addiction	x			
anterograde amnesia	x			
anticonvulsant activity	x			
anxiolysis		x		
antihyperalgesia		x	x	
antidepressant activity		x		
cognitive impairment		x		x
myorelaxation		x	x	x
sensorimotor gating			x	x

Table 1 Different α subunits are involved in different circuits of the brain, giving rise to various body functions. The table is based on Fig. 1 in (Rudolph & Knoflach, 2011) and summarizes the contributions of differentially assembled receptors to the spectrum of responses to diazepam treatment.

Via their TM3-4 loops $GABA_A$ receptors can bind to several trafficking proteins (Luscher *et al.*, 2011), of which only two are mentioned here: The multi-domain protein muskelin unites in a unique manner the regulation of microtubule- and actin-dependent transport of $GABA_A$Rs containing the α1 subunit (Heisler *et al.*, 2011). Neurobeachin, also a binding partner for the GlyR β subunit (del Pino *et al.*, 2014), was shown to drive postsynaptic accumulation of $GABA_A$, NMDA, AMPA and kainate receptors (Nair *et al.*, 2013).

The TM3-4 loops of $GABA_A$R subunits α1, α3, β2, β3 and to a lower extent also α2 mediate $GABA_A$R enrichment at synapses by direct interactions with gephyrin (Kirsch *et al.*, 1995, Kowalczyk *et al.*, 2013, Maric *et al.*, 2011, Mukherjee *et al.*, 2011, Tretter *et al.*, 2008, Tretter *et al.*, 2011). The gephyrin-$GABA_A$R interaction was suggested by colocalization studies quite early (Kirsch *et al.*, 1995, Sassoe-Pognetto *et al.*, 1995), but it took more than 10 years until the first biochemical studies allowed for binding site mapping (Tretter *et al.*, 2008) – in part this was due to lower affinities in comparison with the GlyR β subunit-gephyrin interaction and due to the detergent-sensitivity of the complex (Tretter *et al.*, 2008).

I.B. Receptor clustering at inhibitory synapses

For fast neurotransmission ionotropic receptors need not only be present in the postsynaptic membrane but mechanisms must exist which achieve high local concentrations and reduced diffusion of these receptors. In fact, synapses provide the framework which ensures fast synaptic (phasic) transmission and require an appropriate alignment of presynaptic boutons with the postsynaptic density. Central components of postsynaptic densities are scaffolding proteins which

can self-associate and simultaneously bind the receptors. Several examples are known, and at inhibitory synapses the protein gephyrin carries out this role (Colledge & Froehner, 1998).

Electron micrographs revealed that excitatory and inhibitory synapses can also be distinguished by their distinct morphology: Excitatory synapses are asymmetric in that the postsynaptic membrane appears thicker than the presynaptic membrane, while at inhibitory synapses both membranes seem to be of comparable thickness. The asymmetric distribution of electron-dense material at excitatory synapses can be attributed to a huge postsynaptic density harbouring receptors, which are surrounded by additional ion channels, G-protein coupled receptors, receptor tyrosine kinases, cell adhesion molecules as well as signalling (Sheng & Hoogenraad, 2007) and scaffolding proteins. This protein matrix is obviously involved in signalling processes but also in the anchoring of glutamate receptors which are so enriched that they are referred to as clusters (Craig *et al.*, 1994). These clusters are stabilized by scaffolding proteins, of which PSD-95 seems to play the pivotal role.

The comparatively thin PSD at inhibitory synapses is less well understood. In addition remarkable interneuron diversity mirrored by heterogeneous receptor subunit compositions certainly complicated the investigation of these synapses (Kepecs & Fishell, 2014). Heterogeneity does not seem to be restricted to the receptors, and proteins important for receptor clustering at one synapse type might be dispensable for another (Knuesel *et al.*, 1999, Panzanelli *et al.*, 2005, Papadopoulos *et al.*, 2007). However, at a considerable fraction of inhibitory synapses gephyrin turned out to be the central scaffolding protein.

Gephyrin does not only interact with the receptors but also with cell adhesion molecules, signalling molecules, proteins implicated in cytoskeleton organization and motor protein complexes, all of which contribute in some way or another to the anchoring of the receptors and consequently to synaptic strength, which increases with the number of functional receptors. The term “synaptic plasticity” refers to the temporal change in synaptic strength. For instance during development there is a critical period of plasticity, which correlates with the degree of maturation of cortical GABAergic neurons (Chen & Nedivi, 2013). Disturbances in the molecular composition of synapses confer to disturbed plasticity and neurological disorders (Baroncelli *et al.*, 2011).

I.C. Receptor clustering at inhibitory synapses by gephyrin

Gephyrin was originally identified as a protein which simultaneously binds to glycine receptors and tubulin at postsynaptic densities. Hence, it was named gephyrin (greek: γεπηψρα for bridge). Over time it turned out that gephyrin is also crucially involved in the clustering of $GABA_A$ receptors. Yet beyond this gephyrin fulfils another function: It catalyses the two final steps of molybdenum cofactor (Moco) biosynthesis (Schwarz *et al.*, 2009). These two functionalities render gephyrin a moonlighting protein (Copley, 2003).

Both functions turned out to be essential (Feng *et al.*, 1998). A lack of Moco results in compromised activity of Moco-dependent enzymes (Reiss & Hahnewald, 2011) and consequently in severe neurodegeneration and often leads to early-childhood death. Mice, in which Moco biosynthesis had been affected, survived for 1 to 11 days, while their GlyR clustering was not affected (Lee *et al.*, 2002). In contrast, gephyrin knock-out mice die within the first few hours with symptoms like hyperexcitability that were attributed to both defects in neurotransmission at inhibitory synapses and Moco biosynthesis (Feng *et al.*, 1998). The need for both functions was underscored by further knock-out experiments: In gephyrin-deficient mice, whose Moco biosynthesis was partially rescued by the transgenic expression of a CNX1 (the plant orthologue of gephyrin, see next section), the life span was not altered, presumably as a consequence of the still disturbed receptor clustering (Grosskreutz *et al.*, 2003). In the following section important aspects of both functions will be presented based on the domain architecture which is described beforehand.

I.C.1. Domain architecture of gephyrin

Gephyrin possesses a 20 kDa N-terminal G domain (GephG) and a 46 kDa C-terminal E domain (GephE). These domains are connected by a linker of ~150 amino acids depending on the splice variant (see section I.C.2.1). The bacterial counterparts of the two terminal domains – called Mo**g**A and Mo**e**A, respectively – exist as separate enzymes and catalyse the last two steps during Moco biosynthesis (Mendel, 2013), as it was suggested by gephyrin knock-out mice analysis (Feng *et al.*, 1998) and confirmed later on (Stallmeyer *et al.*, 1999). Obviously, the conjunction of MogA and MoeA was advantageous, as it occurred in two independent ways during evolution: While in mammals GephG precedes GephE in the primary sequence, in plants the domain organization is inverted and CNX1E (corresponding to GephE) precedes CNX1G (Fig. 3A). At least in the case of gephyrin domain fusion was shown to confer to substrate channeling in Moco biosynthesis (Belaidi & Schwarz, 2012).

The crystal structures of gephyrin's isolated domains could be solved and revealed – in agreement with the bacterial enzymes – trimerization of GephG (Schwarz *et al.*, 2001, Sola *et al.*, 2001) and dimerization of GephE (Kim *et al.*, 2006, Sola *et al.*, 2004). A simultaneous utilization of both oligomer interfaces was postulated to give rise to a so-called hexagonal lattice (Kneussel & Betz, 2000, Xiang *et al.*, 2001) (Fig. 3C). This idea was supported by further studies, in which interference with either interface in neurons disrupted gephyrin clusters (Saiyed *et al.*, 2007) and led to a dispersal of GlyRs and $GABA_A$Rs (Calamai *et al.*, 2009, Lardi-Studler *et al.*, 2007). The receptor-gephyrin dependence at postsynaptic sites is the result of the receptor association with the gephyrin clusters, which offer a high density of receptor binding sites (sections I.C.4 & I.C.5). Hence, gephyrin has been regarded as a trap for GlyRs and $GABA_A$Rs. Although the direct visualization of the proposed hexagonal lattice has

not been provided so far, this hypothesis is still attractive. Further information on gephyrin and the gephyrin-receptor interactions are given in sections III.A.1 and I.C.5, respectively.

I.C.2. Heterogeneity of gephyrin

The long linker of gephyrin could possibly increase its heterogeneity, and two important mechanisms in this context are alternative splicing and posttranslational modifications.

I.C.2.1 Alternative splicing

The gephyrin gene consists of 29 exons, of which 10 have been shown to be subject to alternative splicing. In particular, one variant is generated which is thought to limit gephyrin cluster size (Bedet *et al.*, 2006). In this variant splice cassette G2, a 13 residue stretch, is inserted into GephG which is predicted to interfere with GephG trimerization, thereby compromising gephyrin clustering at inhibitory synapses as well as its enzymatic activity during Moco biosynthesis (Smolinsky *et al.*, 2008).

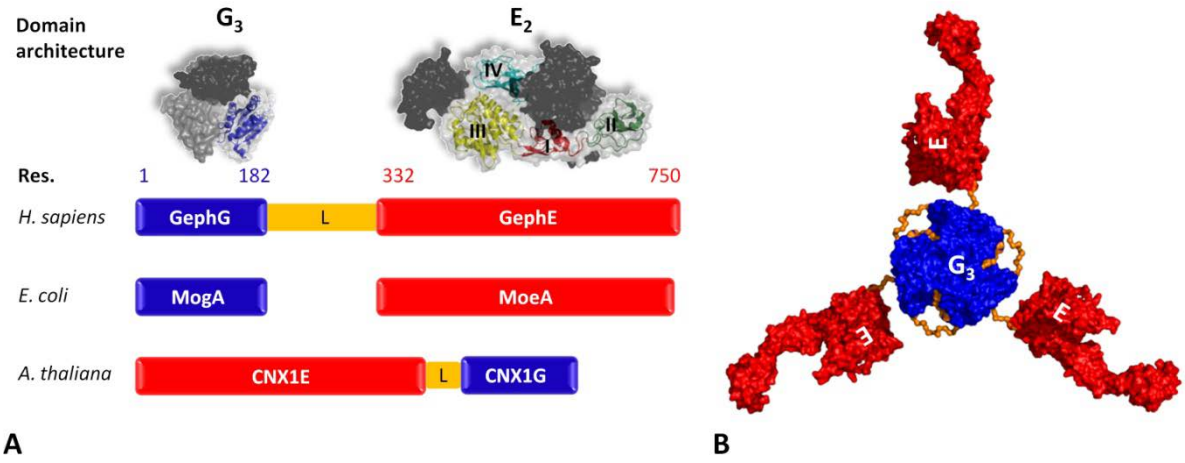

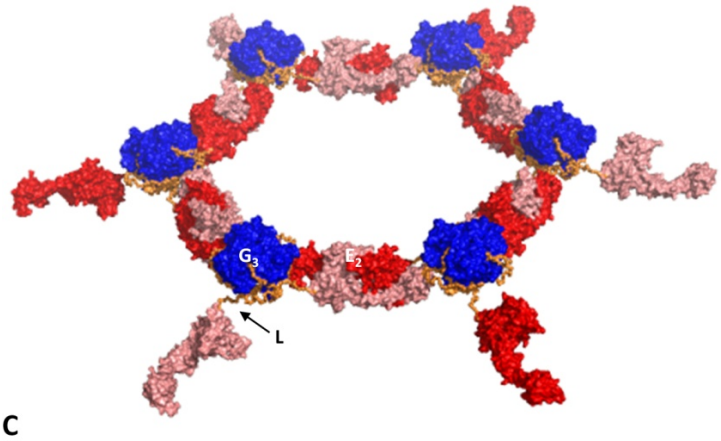

Figure 3 Domain architecture of gephyrin. (A) GephG and its orthologues MogA and CNX1G trimerize (G_3) in their isolated forms, while isolated GephE and the respective orthologues dimerize (E_2). In *E. coli* GephG and GephE are separate entities, in the plant *Arabidopsis thaliana* orthologous G and E domains are inverted with respect to gephyrin and connected by a significantly shorter linker. (B) Gephyrin overexpressed in *E. coli* is predominantly trimeric, indicating the use of G_3 but not of E_2. (C) Several trimers as depicted in (B) could theoretically be assembled into a hexagonal scaffold. For better legibility GephE domains of adjacent trimers are coloured differently (one in salmon, one in red). The models in (B) and (C) are hypothetical.

The long interdomain linker contains two splice sites, at which cassettes C3 and C4 can be inserted (Fig. 4). These two splice sites (along with splice cassette G2 inserted in GephG, see section I.C.2.1) are the ones that have been investigated most extensively so far: Gephyrin containing the C3 cassette, which was shown to be used in glia (Smolinsky *et al.*, 2008), liver (Paarmann *et al.*, 2006), and kidney (Ramming *et al.*, 2000), displayed a weaker affinity towards the glycine receptor and an attenuated tendency to form higher oligomers after expression in SF9 cells, when compared with gephyrin containing cassette C4c and gephyrin without a splice cassette (Herweg & Schwarz, 2012). Last but not least, in neurons C3 is excluded from gephyrin transcripts by the NOVA proteins, which regulate pre-mRNA splicing (Ule *et al.*, 2003). Hence, gephyrin variants containing splice cassette C3, which is also incorporated in the majority of gephyrin molecules in liver (Nawrotzki *et al.*, 2012), are thought to be primarily involved in Moco biosynthesis.

On the contrary, splice cassettes of the C4 type are present in neurons, with cassettes C4c and C4d being more abundant than cassette C4a although this difference was not statistically significant due to the small number of experiments (Paarmann *et al.*, 2006). It could be shown that C4c did not affect GlyR binding (Herweg & Schwarz, 2012) and that the insertion of several C4 cassettes did not impair Moco biosynthesis (Smolinsky *et al.*, 2008). The gephyrin variant used in this work was splice variant P2, which contains only the C4c cassette (14 residues).

I.C.2.2 Gephyrin phosphorylation

Gephyrin is a phosphoprotein, and the linker harbours several phosphorylation sites with 32 having been identified as of April 2014 (Bausen *et al.*, 2010, Charrier *et al.*, 2010, Herweg & Schwarz, 2012, Huttlin *et al.*, 2010, Kuhse *et al.*, 2012, Langosch *et al.*, 1992, Rui *et al.*, 2013, Tyagarajan *et al.*, 2011b, Tyagarajan *et al.*, 2013, Zita *et al.*, 2007) (Fig. 4). Of these, only a few phosphorylations and the corresponding kinases were characterized with regard to the clustering properties of gephyrin (Zacchi *et al.*, 2014).

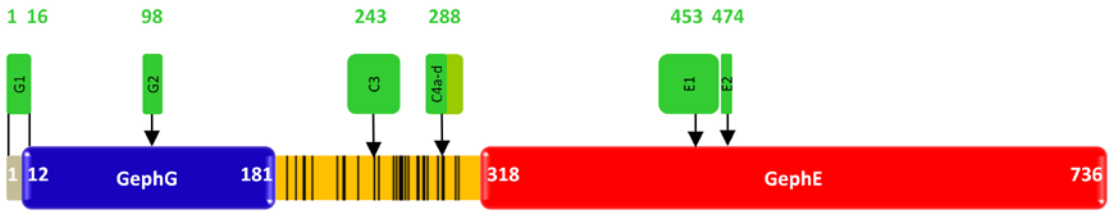

Figure 4 The localization of splice cassettes and phosphorylation sites in gephyrin. The numbering refers to splice variant Geph P1 (residues 1 to 736) which does not contain alternatively splice cassettes. Constitutively spliced exons are not displayed. Splice cassettes C3 (36 residue insert in *Rattus norvegicus*) and C4a-d (14-24 residue inserts) in the linker, which are incorporated at residues 243 and 288, and G2 in GephG are the most important splice cassettes. The linker is shown in yellow, phosphorylation sites are indicated by black stripes and are dispersed all over the linker.

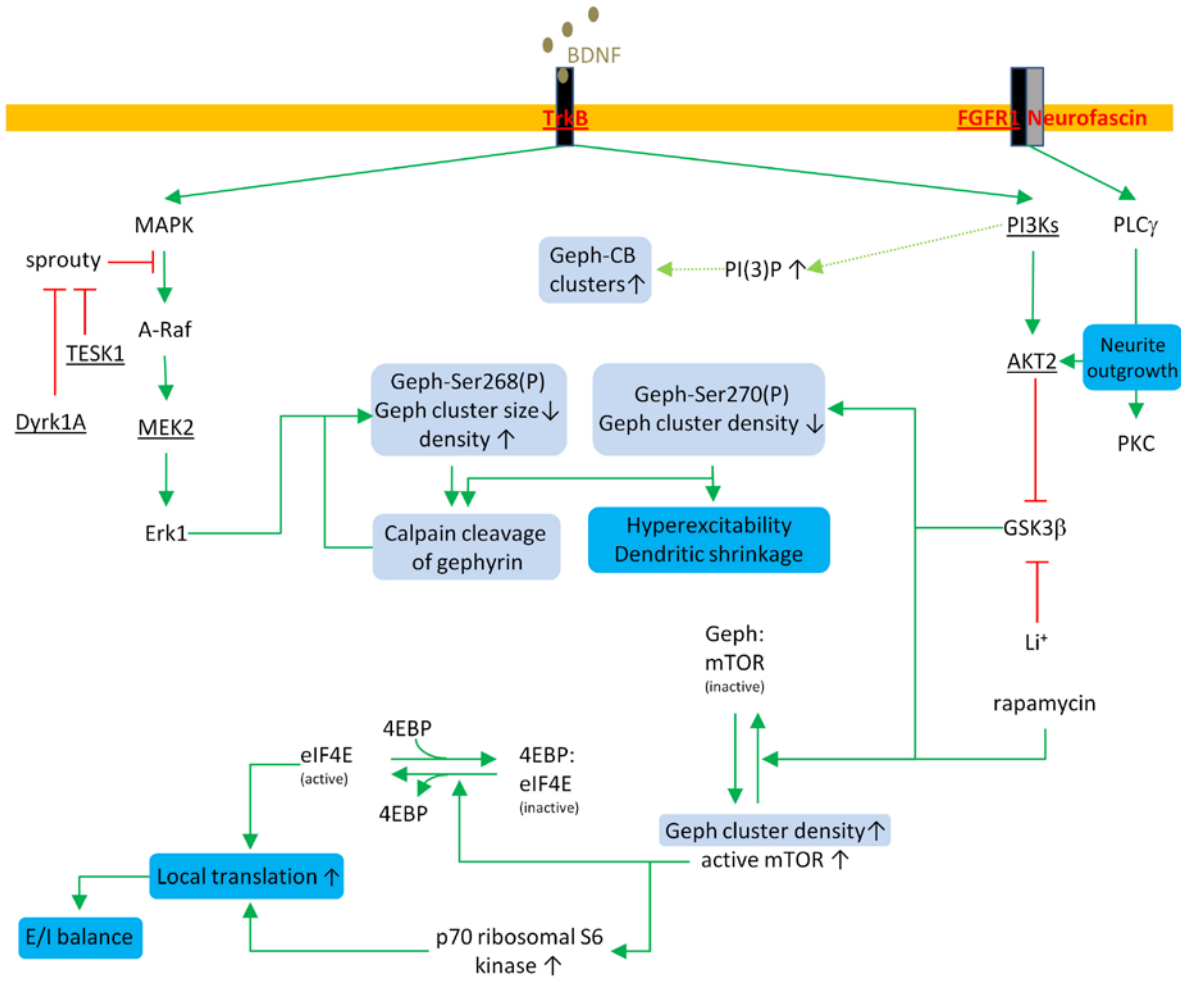

Figure 5 Signalling pathways with impact on gephyrin phosphorylation at Ser268 and Ser270. This scheme is in part adapted from (Wuchter *et al.*, 2012) and was further extended based on findings from (Kriebel *et al.*, 2011, Rui *et al.*, 2013, Tyagarajan *et al.*, 2011b, Tyagarajan *et al.*, 2013). Green arrows and red lines indicate activation and inhibition of downstream effectors, respectively. Light green arrows mark possible links to gephyrin-collybistin (CB) clustering (I.D.3), for which a definite proof is still missing. Underscored signalling components were identified in the mentioned kinome-wide siRNA screen (Kriebel *et al.*, 2011). GSK3β is one of the major branch points, favouring gephyrin-mTOR complexes (Geph:mTOR), regulating gephyrin cluster density and dendritic shrinkage. Whether Ser270 phosophorylation is important in mTOR inactivation has not been elucidated yet. Further details are given in the main text. Downstream signalling of active mTOR is described in section I.D.5. Disinhibited local translation leads to NL1 overexpression and overshooting E/I balance, paving the way for autism-like behaviour (Gkogkas *et al.*, 2013).

In the last few years especially BDNF (brain derived neurotrophic factor) signalling via its receptor TrkB (tropomyosin-related kinase B) was investigated with respect to GABAergic transmission. The consequences of BDNF signalling on $GABA_ARs$ and gephyrin depended on the cell type, the developmental status, and the duration of BDNF exposure (Mou *et al.*, 2013). For example, 20 minutes of BDNF signalling led to rapid gephyrin degradation, whereas a BDNF exposure of four hours resulted in increased gephyrin levels (Mou *et al.*, 2013).

Given the large body of evidence that synaptic $GABA_A$Rs and gephyrin levels are subject of BDNF-dependent regulation, it was no surprise, when a kinome-wide siRNA screen revealed 12 candidate kinases implicated in gephyrin clustering (Wuchter *et al.*, 2012) (Fig. 5), of which several are involved in BDNF signalling. Hence, the receptor tyrosine kinase TrkB-related pathway was investigated in more detail. Two branches of the TrkB pathway converge in the regulation of the gephyrin-mTOR complex stability: mTOR, a protein involved in local protein synthesis (section I.D.5), is activated via phosphatidylinositide 3-kinases/protein kinase B (PI3K/PKB) and mitogen-activated protein kinase (MAPK) signalling, at the same time glycogen synthase kinase 3β (GSK3β), which phosphorylates mTOR and renders it in an inactive state, is inactivated by Ser9 phosphorylation via AKT (Fig. 5). These two events result in the dissociation of the gephyrin-mTOR complex, which in turn leads to enhanced gephyrin clustering and enhanced mTOR activity, exerting its effects via stimulating local protein synthesis (Wuchter *et al.*, 2012). Similar events may be triggered by the fibroblast growth factor receptor 1 upon association with the homophilic CAM neurofascin (Kriebel *et al.*, 2011) – albeit via the phopholipase Cγ/PKB (PLCγ/PKB) pathway (Kriebel *et al.*, 2011) (Fig. 5).

Further studies investigated gephyrin phosphorylation on the residue-level, with the linker region encompassing residues ~265 to ~280 being investigated in several publications. For instance, phosphorylation of Ser268 and Ser270 by ERK kinases and GSK3β, respectively, was shown to reduce gephyrin cluster size and density at GABAergic synapses, respectively (Rui *et al.*, 2013, Tyagarajan *et al.*, 2011b, Tyagarajan *et al.*, 2013). As for the latter residue, collybistin (see section I.D.3) seems to trigger Ser270 phosphorylation by Cdk kinases, but in contrast to other studies (Rui *et al.*, 2013, Tyagarajan *et al.*, 2011b, Tyagarajan *et al.*, 2013), attenuation of Ser270 phophorylation had no impact on gephyrin clustering (Kuhse *et al.*, 2012). Yet another group analysed the impact of Ser270 phosphorylation on dendritic branching. Higher phosphorylation levels of Ser270 led to dendritic shrinkage as a consequence of reduced $GABA_A$R clustering and the resulting overshooting hyperexcitability (Rui *et al.*, 2013), providing a potential link of gephyrin phosphorylation to disorders characterized by dendrite atrophies, such as Alzheimer's disease, schizophrenia and mental retardation (Kulkarni & Firestein, 2012). GSK3β inactivation upon BDNF signalling via TrkB receptors resulted in increased branching (Rui *et al.*, 2013). Other gephyrin residues in the mentioned phosphorylation site cluster (residues 265-280) were Thr276 and Ser277, whose replacement by alanines in GFP-gephyrin expressed in hippocampal neurons led to a gephyrin redistribution from postsynaptic densities to the cytoplasm (Kuhse *et al.*, 2012).

Another interesting phosphosite cluster is located in the N-terminal proline-rich linker region. Here, residues 188, 194 and 200 have been reported to be recognised by the peptidyl-prolyl-cis-trans-isomerase PIN1 (peptidyl-prolyl Isomerase NIMA interacting protein 1, where NIMA stands for Never In Mitosis A) (Liou *et al.*, 2011), which triggers a conformational change in gephyrin, resulting

in a higher affinity to the GlyR (Zita *et al.*, 2007). Rapamycin-mediated inhibition of mTOR1 (mammalian target of Rapamycin 1) in hepatocytes, led to a 12-fold increased phosphorylation level at Ser200 in liver (Demirkan *et al.*, 2011).

β_1-integrin was shown to elicit a signal cascade via PKC and CamKII that resulted in increased synaptic strength. *In vitro* kinase assays revealed that CamKIIα/CamKIIβ phosphorylated gephyrin at a solvent exposed loop of GephG (more specifically Ser47) and especially the C-terminal part of the linker (Ser280, Ser283, Ser286, Ser303, Ser305 and Ser17 of splice cassette C4a). β_3-integrin signalling led to a decrease in synaptic strength (Charrier *et al.*, 2010).

Protein phosphatase 1 was shown to increase gephyrin cluster size independent of residues 188 and 194 in the proline rich region of gephyrin's linker (Bausen *et al.*, 2010). Beyond that, gephyrin was reported to be proteolytically cleaved by calpain-1 upon phosphorylation (Tyagarajan *et al.*, 2013), palmitoylated (Kang *et al.*, 2008), acetylated (Tyagarajan *et al.*, 2013) and ubiquitinylated (Tyagarajan *et al.*, 2012). Although the majority of posttranslational modifications has been poorly understood so far, their sheer number and the so far published results suggest important roles in gephyrin functionality.

I.C.3. Gephyrin's role in Moco biosynthesis

As mentioned above, gephyrin also

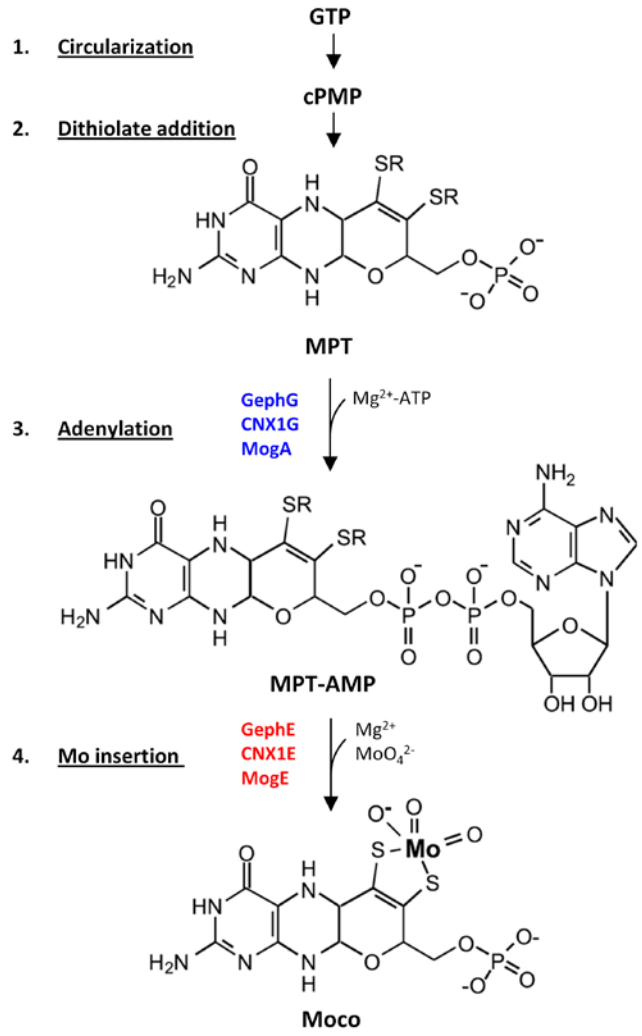

Figure 6 Moco biosynthesis in eukaryotes. The scheme is adopted and modified from (Mendel, 2013). This research was originally published in the Journal of Biochemistry. Mendel, R. R. (2013). The molybdenum cofactor. J Biol Chem 288, 13165-13172 © the American Society for Biochemistry and Molecular Biology. Gephyrin catalyses steps 3 and 4. GephG adenylates MPT in the presence of Mg^{2+}, and the resulting product MPT-AMP is transferred to GephE. Here it is deadenylated, and molybdate (MoO_4^{2-}) is integrated via the dithiolates (SR). The corresponding *E. coli* enzymes and plant domains are also indicated in blue and in red, respectively. cPMP is the abbreviation for cyclic pyranopterin monophosphate.

fulfils a second task, namely the biosynthesis of the molybdenum cofactor (Moco), which comprises a tricyclic metal-binding pterin (MPT) and molybdenum (Schwarz *et al.*, 2009). The Moco constitutes the catalytic centre of all molybdenum-dependent enzymes except for the bacterial nitrogenase (Schwarz & Mendel, 2006). MPT confers two dithiolates to coordinate molybdenum and is involved in the positioning of molybdenum in the active site and the modulation of its oxidation state, which can vary between +IV to +VI, enabling enzymes to catalyse two-electron reduction–oxidation reactions (Holliday *et al.*, 2007).

Moco deficiency results in a complete loss of sulphite, xanthine and aldehyde oxidase activities. The disease pattern seems to be dominated by the loss of sulphite oxidase (SO), which catalyses the oxidation of sulphite to sulphate. In turn a loss of SO results in toxically high sulphite levels, which lead to the neurodegenerative symptoms and early childhood death (Schwarz *et al.*, 2009).

Four steps (Fig. 6) are required for the biosynthesis of Moco from its original substrate guanosine tripohosphate (GTP), and the last two steps are carried out by MogA and MoeA in bacteria, CNX1 in plants and gephyrin in humans (Mendel, 2013). In humans, GephG (MogA orthologue) adenylates MPT, and GephE (MoeA orthologue) catalyses the hydrolysis of MPT-AMP and the subsequent coordination of molybdenum by the dithiolate function of MPT.

I.C.4. Gephyrin-LGIC interactions

Gephyrin (more specifically GephE) interacts with the TM3-4 loops of the GlyR β subunit (Kim *et al.*, 2006, Kneussel *et al.*, 1999b, Meyer *et al.*, 1995, Schrader *et al.*, 2004), the $GABA_AR$ subunits α1, α2 and α3 (Maric *et al.*, 2011) as well as with β2 and β3 (Kowalczyk *et al.*, 2013). The linear core binding motif of GlyR β was uncovered quite early (Meyer *et al.*, 1995) and determinants of binding were obtained soon after (Kneussel *et al.*, 1999b). A crystal structure of GephE in complex with a GlyR β subunit derived peptide confirmed these previous analyses and revealed (along with ITC and colocalization studies) that the GlyR binding was driven primarily by hydrophobic interactions. Interestingly, the GlyR β peptide bound at the dimer interface (Fig. 7) and was therefore suggested to contribute to GephE dimer stability (Kim *et al.*, 2006).

On the other hand, despite several traits of evidence (Kirsch *et al.*, 1995, Kneussel *et al.*, 1999a) gephyrin-$GABA_A$ receptor interactions remained less well understood for quite some time, at least in part due to methodological burdens like the detergent sensitivity of the gephyrin-$GABA_AR$ interaction (Tretter *et al.*, 2008). Subsequent comparative biochemical analysis of GephE complexes containing the TM3-4 loops from $GABA_AR$ subunits α1, α2 and α3 (carried out by Dr. Hans Maric, a former lab member (Maric, 2012)) revealed that α3 exhibited the highest GephE affinity (K_D = 5 µM) followed by α1 (K_D = 17 µM) and α2, for which no reliable K_D could be obtained. These values were significantly higher than the K_D for the GephE-GlyR interaction, whose ITC-derived isotherms were fitted with a

two-site binding model, yielding K_D values of 0.14 ± 0.1 and 7.7 ± 0.1 µM (Maric *et al.*, 2011). Notably, the $GABA_AR$ subunit with the highest affinity displayed the most commonalities with the GlyR β subunit.

Truncation of the GlyR/$GABA_AR$ subunit TM3-4 loops down to the identified core binding motifs abrogated interactions of GephE with α1/α3 but not with GlyR β, raising the possibility that there are additional determinants that appear to be essential at least for α1 and α3. One of the key findings was that $GABA_A$ receptors and GlyRs share a common binding site and sequence comparisons disclosed gephyrin binding motifs in $GABA_AR$s which rely on two aromatic residues (alignment in Fig. 7). During the course of my work, the (former) lab members Dr. Hans Maric and Vikram Kasaragod obtained crystal structures of GephE in complex with $GABA_AR$ subunit α3-derived peptides, which corroborated the binding studies (Kasaragod, Maric et al., unplublished work).

$GABA_AR$ β subunits 2 and 3 can interact with gephyrin as well: The $GABA_AR$ β3 subunit was among

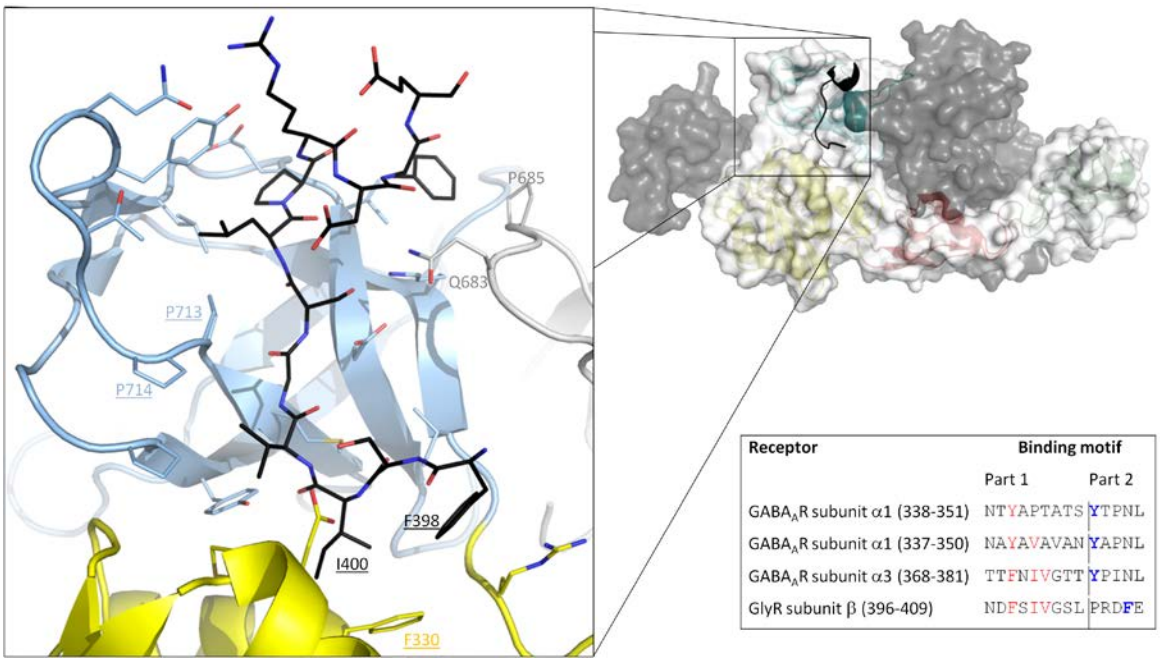

Figure 7 Gephyrin's interaction with GlyR/$GABA_AR$ TM3-4 intracellular loops. In the upper right the crystal structure of GephE in complex with a GlyR TM3-4 loop-derived peptide (PDB entry 2FTS, (Kim *et al.*, 2006)), which is shown in black. A close-up view of the binding site, in which the GlyR peptide and the GephE residues involved in the interaction are displayed in stick representation, reveals that mainly residues of GephE subdomain 4 (blue) and just a few residues of subdomain 3 (yellow) are involved. GlyR residues 398 and 400 bind to a hydrophobic pocket. Mutations of these residues as well as those at Phe330, Pro713, Pro713&Pro714 at least significantly affect complex formation. The sequence alignment of the GlyR β and $GABA_AR$ α1- α3 subunits revealed a moderate conservation of the residues in the first segment of the binding motif („Motif 1") – at least for $GABA_AR$ α3 and GlyR β subunits. Furthermore also the $GABA_AR$ counterparts of Phe330 of GlyR β are aromatic residues. In the second segment of the binding motifs ("Motif 2") $GABA_AR$ α3 does not share any commonalities with GlyR β but instead with $GABA_AR$ α1 and α2. The alignment was adapted and modified from (Maric, 2012).

the first subunits that was identified as a gephyrin binding partner (Kirsch *et al.*, 1995). A recent biochemical/cell biological study revealed that the β2 and β3 subunits directly interact with GephE in a manner analogous to the α subunits, but also for these subunits the affinity was clearly attenuated when compared to the GlyR β subunit (Kowalczyk *et al.*, 2013).

I.C.5. Hexagonal lattice

As mentioned above, gephyrin has been proposed to form a hexagonal lattice which traps receptors and immobilizes them in apposition to the presynatic terminals (Kneussel & Betz, 2000, Xiang *et al.*, 2001). The crystal structures of GephE with the intracellular receptor loops ((Kim *et al.*, 2006) & Kasaragod, Maric *et al.*, unpublished data) provide a rationale for the confinement of the receptors (Calamai *et al.*, 2009, Saiyed *et al.*, 2007). Over the last few years a multitude of publications had the gephyrin-receptor interactions as subject (initially with a focus on the gephyrin-GlyR interaction), and especially the application of single-particle tracking analyses proved useful in terms of characterization of the dynamics underlying receptor clustering (Dahan *et al.*, 2003, Meier *et al.*, 2001).

In line with the hexagonal scaffold hypothesis, SPT analyses proved that GlyRs exhibited longer dwell times at synaptic compared to extrasynaptic sites (Choquet & Triller, 2003, Dahan *et al.*, 2003). Later $GABA_A$Rs containing the α1 subunit were also shown to exhibit slightly longer dwell times when they encountered gephyrin clusters (Mukherjee *et al.*, 2011). A recent study suggested that gephyrin forms densely packed, rather planar structures just beneath the membrane (Specht *et al.*, 2013), as would be expected for the hexagonal scaffold.

Along this line, GlyR-gephyrin complex formation *per se* is not sufficient for clustering, as such complexes were also observed in cytosolic compartments and extrasynaptic membrane areas (Ehrensperger *et al.*, 2007, Maas *et al.*, 2006). These findings indicated that the mere interaction was not sufficient for clustering and that other factors contribute to receptor clustering (Ehrensperger *et al.*, 2007). Self-oligomerization of gephyrin was observed to be required for proper gephyrin clustering and receptor accumulation, as a disturbance of either GephG or GephE oligomerization resulted in reduced GlyR clustering (Calamai *et al.*, 2009, Saiyed *et al.*, 2007). Interestingly, the existence of additional factors was also suggested by the observation, that $GABA_A$R could be trapped at excitatory synapses and vice versa AMPA receptors at inhibitory synapses (Renner *et al.*, 2012). One such factor could be the cytoskeleton (see section I.D.2).

Heterogeneity in the composition of inhibitory synapses was also suggested by the observation of mixed GABAergic/glycinergic synapses. In an additional SPT analysis two populations of GlyRs were revealed, one of which was rather strongly associated with gephyrin scaffolds and another more dynamic GlyR population exhibiting shorter dwell times at synaptic clusters (Choquet & Triller, 2003,

Ehrensperger *et al.*, 2007). Previous estimates of stable and mobile GlyRs (Ehrensperger *et al.*, 2007) could be refined in a recent study that extended the SPT analyses, in that gephyrin clusters could be characterized as relatively shallow energy traps, with which only a small fraction of ~15% of the GlyRs exhibited more stable interactions (Masson *et al.*, 2014). Not only the receptors can be exchanged between synaptic and extrasynaptic sites but also gephyrin, as suggested by FRAP (fluorescence recovery after photobleaching) experiments in which recovery of synaptic gephyrin populations took tens of minutes (Vlachos *et al.*, 2013).

The mentioned extrasynaptic gephyrin-GlyR complexes need not necessarily comprise merely a single gephyrin trimer associated with a single receptor as extrasynaptic gephyrin-GlyR clusters were reported (Maas et al., 2006). They were observed to form mobile units, which migrated between active synapses (as defined by ongoing vesicle recycling) and were much smaller than their synaptic counterparts (by more than 50%). These migrating clusters were subject of dynein- and kinesin-mediated transport (described in section I.D.4), that is also regulated by AMPAR activity (Maas et al., 2009).

Further examples of receptor crosstalk (Shrivastava *et al.*, 2011) include blockage of potassium channels by 4-aminopyridine and NMDAR stimulation (presumably via the Ca^{2+} dependent phosphatase calcineurin), which both led to attenuated $GABA_AR$ and gephyrin clustering. Interestingly, these two channels triggered different signalling cascades for gephyrin cluster size decrease, implying that different mechanisms for cluster down-regulation exist (Niwa *et al.*, 2012). The findings that $GABA_AR$ clustering in spinal cord neurons and cluster disassembly during activity preceded gephyrin clustering and dispersal (Dumoulin *et al.*, 2000, Niwa *et al.*, 2012) was in line with several other examples which accounted for the existence of gephyrin-independent $GABA_AR$ clustering at synapses (Kneussel *et al.*, 2001, Levi *et al.*, 2004, Panzanelli *et al.*, 2011, Papadopoulos *et al.*, 2007). Vice versa, the absence of gephyrin clustering in selected regions in $GABA_AR$ knock-out mice can also be considered as a hint that $GABA_ARs$ contribute to gephyrin accumulation at PSDs (Essrich *et al.*, 1998, Kralic *et al.*, 2006, Panzanelli *et al.*, 2011, Studer *et al.*, 2006).

I.D. Gephyrin interaction partners

Taken together, these data suggested that gephyrin clusters at PSDs of inhibitory synapses can vary substantially, and this is, at least in part, related to the protein matrix around gephyrin-receptor clusters. Some important constituents of the glycinergic and GABAergic PSDs, which interact with gephyrin, are presented in the following sections (see also Fig. 8).

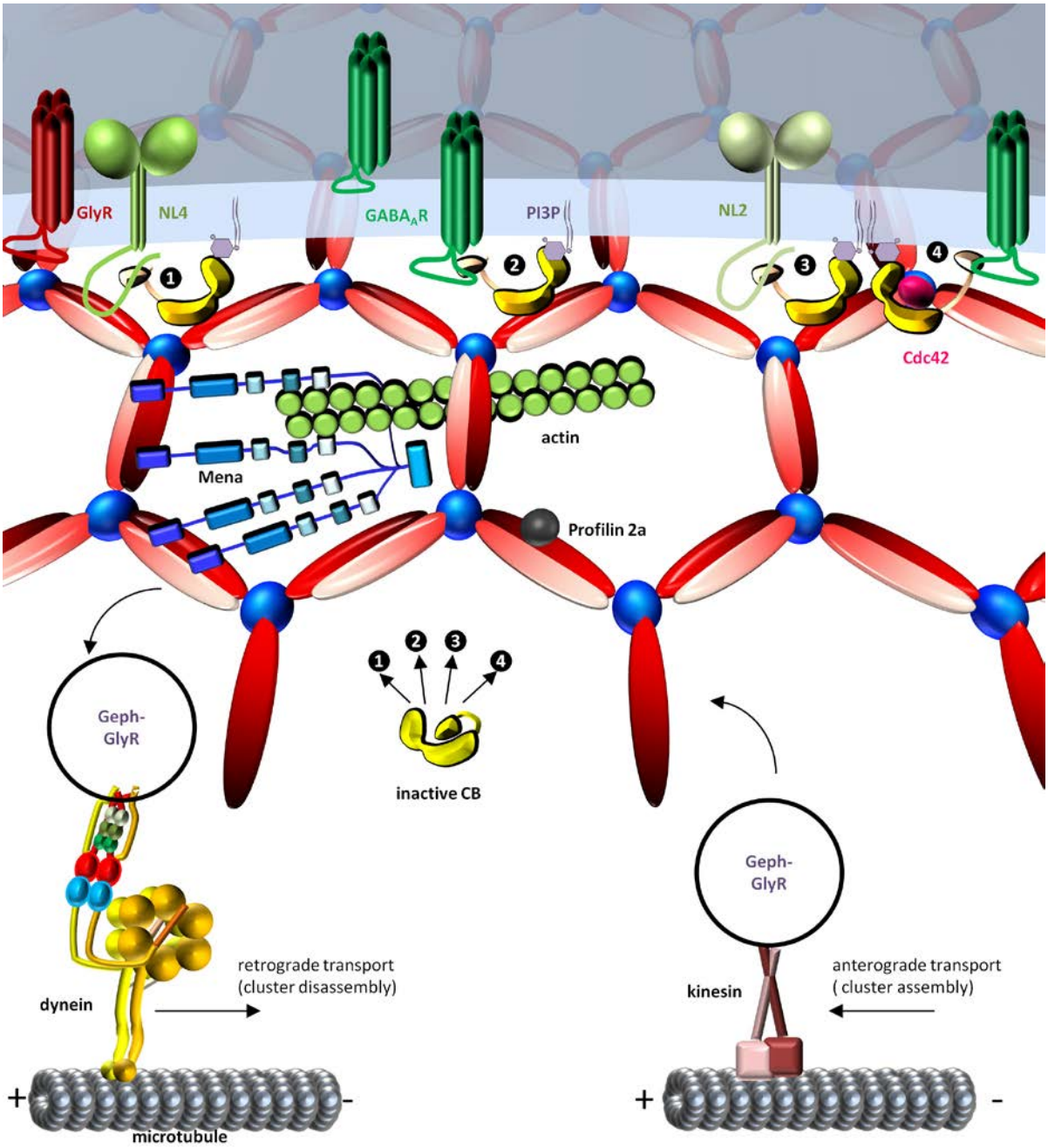

Figure 8 The role of gephyrin at the postsynaptic membrane of inhibitory synapses. Further details are given in the main text. Shown here are the interactions with pLGICs (I.C.4), with CAMs NL2 (at GABAergic synapses) and NL4 (at glycinergic synapses) (section I.D.1), with the actin cytoskeleton via Mena (section I.D.2), with signalling molecules (I.D.3) and trafficking proteins (I.D.4). Gephyrin-receptor clustering requires collybistin in the retina, in the basolateral amygdala and in the hippocampus. Four different pathways of collybistin activation (I.D.3) are displayed.

I.D.1. Cell adhesion molecules

Cell adhesion molecules (CAMs) are embedded in the pre- and postsynaptic membranes and mechanically link pre- and postsynaptic sites via interactions between their extracellular domains (Dalva *et al.*, 2007, Shen & Scheiffele, 2010, Yamagata *et al.*, 2003). In this respect CAMs were also shown to contribute to synapse formation: Axons with a certain set of presynaptic CAMs can select matching postsynaptic CAMs to establish a synaptic contact or *vice versa*. In addition, CAMs are critically involved in the maturation of the synapses as well: CAMs on both sides can recruit intracellular binding partners (Fig. 9) which e.g. mediate changes in the cytoskeleton (Biederer & Sudhof, 2001), vesicle release or the clustering of postsynaptic density components (Dean & Dresbach, 2006, Sun *et al.*, 2013, Yamagata *et al.*, 2003). However, under certain conditions CAMs can even trigger the down-regulation of synaptic strength, e.g. when their extracellular domains are separated from the remainder of the CAM (O'Connor *et al.*, 2009, Peixoto *et al.*, 2012, Suzuki *et al.*,

Presynaptic CAM	Postsynaptic CAM	Function	References
neurexins (Nrxs)	neuroligin 2 and 4 (NL2 and NL4)	Maturation and maintenance of GABAergeic and glycinergic synapses by NL2 and NL4, respectively	(Hoon *et al.*, 2009, Hoon *et al.*, 2011, Poulopoulos *et al.*, 2012)
presynaptic tyrosine phosphatase 6 (PTPδ)	slit and NTRK-like family protein 3 (slitrk3)	Differentiation, exclusively at inhibitory synapses	(Takahashi *et al.*, 2012)
Nrx/α-dystroglycan*	β-dystroglycan	Part of the dystroglycan complex which promotes $GABA_AR$ clustering	(Knuesel *et al.*, 1999, Panzanelli *et al.*, 2011)
immunoglobulin superfamily member 9b (IgSF9b)	IgSF9b	Posytsnaptic IgSF9b couples to NL2 via their common ligand synaptic scaffolding molecule (S-SCAM)	(Woo *et al.*, 2013)
plexin-B	semaphorin 4D	Promotes synapse assembly	(Kuzirian *et al.*, 2013, Paradis *et al.*, 2007, Raissi *et al.*, 2013)
α-Neurexin	calsyntenin-3	synaptogenesis	(Um *et al.*, 2014)
neuroplastin-65	neuroplastin-65	Stabilization/maintenance of synapses?, interacts with $GABA_AR$ α1, α2 & α5 subunits	(Herrera-Molina *et al.*, 2014, Sarto-Jackson *et al.*, 2012)
thrombospondin 1 (TSP1) and fibrinogen**	β-integrin	Regulation of synaptic dwell time of GlyRs and gephyrin	(Charrier *et al.*, 2010)
neurofascin	neurofascin	Stabilization of axo-axonic GABAergic synapses at the AIS, gephyrin clustering	(Burkarth *et al.*, 2007, Kriebel *et al.*, 2011, Kriebel *et al.*, 2012)

Table 2 Cell adhesion molecules (CAMs) at inhibitory synapses. CAM pairs marked in yellow were reported to be specific for inhibitory synapses. * α-dystroglycan is not a CAM but links Nrx and the CAM β-dystroglycan, which couples to NL2 via dystrophin, SynARFGEF and S-SCAM (Tyagarajan & Fritschy, 2014). **TSP1 and fibrinogen are components of the extracellular matrix.

2012).

I.D.1.1 The neuroligin-neurexin transsynaptic signalling complex

One of the most prominent heterophilic CAM pairs is the neurexin-neuroligin (Nrx-NL) axis (Missler *et al.*, 2012). Predominantly presynaptically localized neurexins (Berninghausen *et al.*, 2007, Taniguchi *et al.*, 2007) target postsynaptic neuroligins (Fig. 9). Both CAMs received a lot of attention over the last few years, at least in part because autism disorder spectrum disorders, Tourette's syndrome, learning disability, schizophrenia and Alzheimer's disease could be related to mutations in either Nrx or NL isoforms (Boucard *et al.*, 2005, Chih *et al.*, 2006, Jamain *et al.*, 2003, Laumonnier *et al.*, 2004, Lawson-Yuen *et al.*, 2008, Macarov *et al.*, 2007, Sindi *et al.*, 2014, Sun *et al.*, 2011a, Walsh *et al.*, 2008).

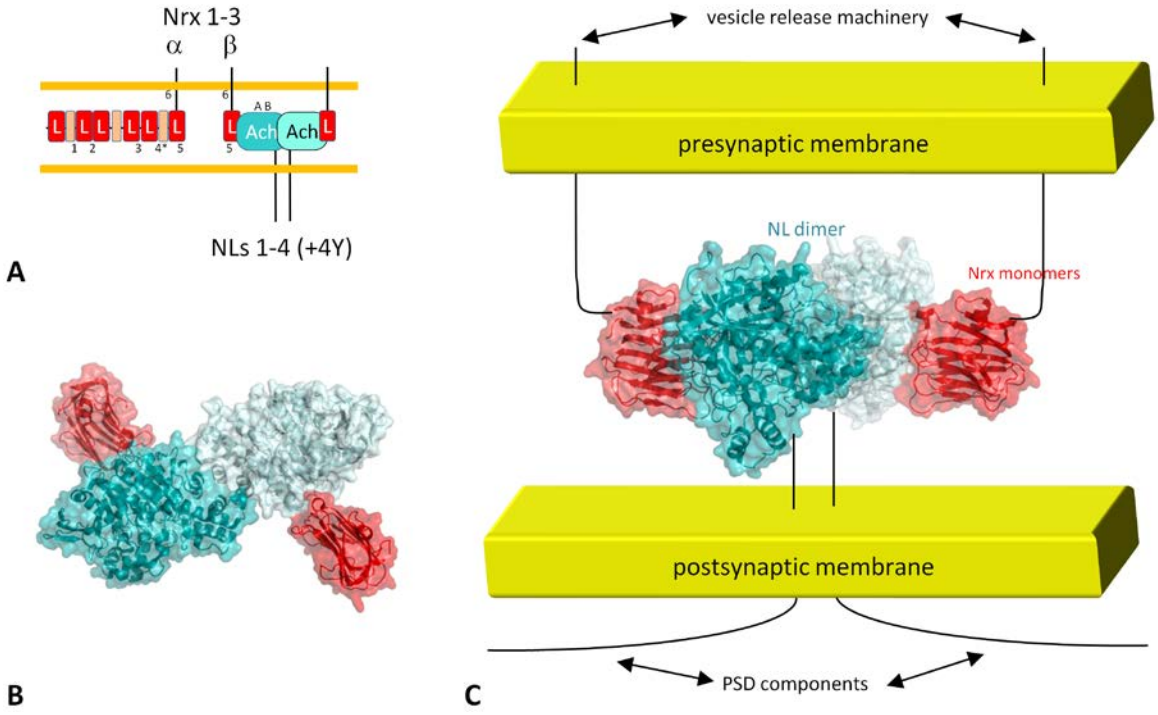

Figure 9 The Nrx-NL complex. (A) Domain organization of Nrxs and NLs. Each of the three Nrx genes possesses two promoters giving rise to isoforms α and β. L stands for LNS domain (specified in the main text), the salmon rectangles indicate the presence of three intercalated EGF-like domains. Numbers mark the splice sites in Nrxs, whereas A and B refer to splice sites in NLs. SS#4 (marked with a star) is only present in Nrxs 1&3. Note that the N-termini of both CAMs protrude into the synaptic cleft. β-Nrxs share the sixth LNS domain with α-Nrxs. (B) Crystal structure of the complex containing the dimeric acetylcholine-esterase homology domain of NL1 (cyan) and the LNS domain of Nrx1β (red), viewed along the twofold axis (Arac *et al.*, 2007). (C) Synthesis of (A) and (B). The C-terminal tails in the cytosol provide binding sites for pre- and postsynaptic machineries, respectively.

I.D.1.1.1 Neurexins

Three Neurexin (Nrx) genes encode for type I membrane proteins containing an extracellular region, a membrane segment and an intracellular region. For each gene two forms can be expressed, which vary only in their N-terminus: The extracellular region of Nrx-α is composed of six LNS (**L**aminin, **N**rx, **s**ex-hormone-binding globulin) domains and three interspersed EGF (**E**pidermal **G**rowth **F**actor)-like domains, while Nrx-β only features a single extracellular LNS domain (Tabuchi & Sudhof, 2002). This heterogeneity in combination with six (SS#1-6) and two splicing sites (SS#5-6) in α- and β-neurexins, respectively, can theoretically give rise to thousands of neurexin variants (Boucard *et al.*, 2005, Krueger *et al.*, 2012, Treutlein *et al.*, 2014) (Fig. 10). Alternative splicing of Nrx 3 can even generate a variant, which terminates after the extracellular domain (Ushkaryov & Sudhof, 1993).

I.D.1.1.2 Neuroligins

Neuroligins (NLs) are also type I membrane proteins. Four and five NLs are present in rodents and humans, respectively. The genes for NL3 and NL4 are found on the X chromosome, while the Y chromosome encodes for a fifth NL in primates, referred to as NL4Y (Missler *et al.*, 2012). NL1 is specifically localized to excitatory synapses (Song *et al.*, 1999), NL2 to GABAergic synapses (Varoqueaux *et al.*, 2004), whereas NLs 3 (Budreck & Scheiffele, 2007) and 4 can localize to both excitatory or inhibitory synapses (Krueger *et al.*, 2012). Neuroligins are made up from an extracellular acetylcholine esterase homology domain, followed by an extracellular glycosylation segment, a transmembrane domain and a cytosolic region (see also Fig. 80). NLs can also be alternatively spliced at two sites encoding for segments in the acetylcholine esterase homology domain (referred to as SSA & SSB) (Boucard et al., 2005, Ichtchenko et al., 1995, Ichtchenko et al., 1996).

In comparison to the actual acetylcholine esterase, extracellular domains of NLs have lost their catalytic activity (Comoletti *et al.*, 2003). While NL's extracellular domains dimerize, there is no evidence for oligomerization of Nrx since the available crystal structures of Nrx-NL complexes (Fig. 10) feature a NL dimer with two attached single LNS6 domains of Nrx (Arac *et al.*, 2007, Chen *et al.*, 2008, Leone *et al.*, 2010, Tanaka *et al.*, 2012).

I.D.1.2 Alternative splicing controls the neurexin-neuroligin assembly

Splice cassettes are only present in the extracellular domains of both proteins, which regulate extracellular Nrx-NL interactions and hence determine the fate of the corresponding synapse (Boucard *et al.*, 2005, Chih *et al.*, 2006, Fabrichny *et al.*, 2007). In this context splice site 4 (SS#4) of Nrxs and splice site B (SSB) of NLs deserve particular attention. The inclusion of SSB in NL1 decreases the number of potential Nrx binding partners, presumably because this insert is located at the edge

of the Nrx binding site (Chen *et al.*, 2008), *vice versa*, SS#4 in neurexin is close to the NL binding site (Arac *et al.*, 2007). NL2 never contains SSB and can bind to both α-Nrxs and β-Nrxs, irrespective of the presence of SS#4. A part of this "splicing code" is shown in Table 3. However, the evaluation of the affinities by SPR revealed a minor impact of SSB on the selectivity, as the affinities of NL1 to various neurexins differed in the low micromolar range by less than a factor of five (Koehnke *et al.*, 2010), suggesting that *in vivo* other factors contribute to the observed specificity. These findings also imply that NLs bind to several Nrx variants. This appears to be indeed of physiological relevance, as α-Nrxs undergo weaker interactions at nascent inhibitory synapses. Subsequently, β-Nrxs at the same synapses seem to mediate synapse validation upon neurotransmitter release (Fu & Huang, 2010).

NL/Nrx	α-Nrx (+SS#4)	α-Nrx (ΔSS#4)	β-Nrx (+SS#4)	β-Nrx (ΔSS#4)
NL1(+B)	-	-	-	+
NL1(ΔB)	-	+	+	+
NL2(ΔB)*	+	+	+	+

Table 3 Alternative splicing of NLs and Nrxs. Summarized here is the possibility of complex formation between the most prominent Nrx and NL splice variants. The table has been adapted from (Bang & Owczarek, 2013).

I.D.1.3 Neurexin-Neuroligin interactions are involved in the maturation of synapses

As pointed out above, CAMs can be principally considered as candidates for synapse formation. In the case of the NL-Nrx axis this assumption received support by observations that NLs, heterologously expressed in non-neuronal cells, possess the capability to induce formation of pre-synaptic zones in co-cultured neurons (Scheiffele *et al.*, 2000). *Vice versa*, in comparable experiments Nrxs induced the formation of post-synaptic density-like structures (Nam & Chen, 2005).

However, the involvement of NLs in synapse formation was contested by the study of a triple knockout mouse lacking NLs 1-3, which, in addition, did not express NL4 at detectable levels (Varoqueaux *et al.*, 2006). While these mice displayed a synapse number comparable to WT animals, and the ultrastructure of the synapses was not severely impaired, they died at birth due to respiratory failure as a consequence of impaired $GABA_A$ receptor recruitment to synapses in the brainstem (Varoqueaux *et al.*, 2006). In addition, NL1-3 knockout mice exhibited lower levels of proteins involved in the vesicle machinery at the presynaptic site (Varoqueaux *et al.*, 2006). Likewise, the analysis of mice lacking all α-neurexins did not result in reduced synapse formation, however, as for NLs, the vesicle release machinery was affected, leading to dysfunctional vesicle exocytosis (Missler *et al.*, 2003). The discrepancy between NL/Nrx-knockout mice analyses and the aforementioned *in vitro* co-culture assays could be resolved by the observation that the increase of synapse numbers upon overexpression of NL1 is presumably the consequence of NMDA receptor signalling, which led to the hypothesis that NLs are involved in synapse maturation rather than in synapse formation (Chubykin *et al.*, 2007).

A further study extended this view as two phases of synapse stabilization could be distinguished: In the first, NMDA receptor-independent phase contacting filopodia were stabilized, while the second phase required receptor activity and NL1's cytoplasmic tail (Chen *et al.*, 2010). The second phase led to a persistent synapse stabilization, which is presumably related to the involvement of NL1's cytosolic region. This was consistent with the observation that the extracellular domain of NL1 was sufficient to induce maturation in the presynaptic terminal, but that the cytoplasmic region was needed for persistent synapse stabilization (Wittenmayer *et al.*, 2009).

Beyond the so far mentioned roles in synapse validation, NL2 was even suggested to influence ion homeostasis: It is involved in regulating the expression of the postsynaptic potassium-chloride co-transporter KCC2 (Sun *et al.*, 2013), which is required to pump chloride ions out of the cell and consequently to maintain the chloride gradient, which renders the GABAergic reversal potential hyperpolarizing (Blaesse *et al.*, 2009). Knockdown of NL2 in cultured cortical neurons results in a depolarizing GABAergic reversal potential as a consequence of KCC2 loss (Sun *et al.*, 2013).

It should be noted, however, that the Nrx-NL axis can be regulated by other membrane proteins: For example, neurexins can bind to $GABA_A$ receptors (Zhang *et al.*, 2010). Vice versa, MDGA1 counteracts the Nrx-NL axis by competing with Nrx for a common binding site in NL2 (Lee *et al.*, 2013, Pettem *et al.*, 2013). In addition, NL1 action can be terminated by proteases which cleave off the extracellular domain (O'Connor *et al.*, 2009, Peixoto *et al.*, 2012, Suzuki *et al.*, 2012).

Taken together, these data strongly suggest that the trans-synaptic Nrx-NL axis is a key player in synapse maturation. The mode of action of Nrxs and NLs also involves their cytosolic tails, which offer a linkage to the presynaptic vesicle machinery and the postsynaptic density which anchors the neurotransmitter receptors (Dean & Dresbach, 2006, Krueger *et al.*, 2012, Sudhof, 2008). The cytoplasmic tails of NL2 and NL4 bind to gephyrin and collybistin (introduced in section I.D.3), and the gephyrin-collybistin-NL2 interaction is one of the subjects of this thesis and therefore introduced further in section III.C.1.

I.D.2. Cytoskeleton

The cytoskeleton plays an important role in the formation and organization of dendritic spines and hence is involved in synaptic plasticity at excitatory synapses (Shirao & Gonzalez-Billault, 2013). Although far less is known about the cytoskeleton at inhibitory synapses, similar roles have appeared plausible also at these specializations.

Gephyrin was reported to bind to microtubules with high affinity (Kirsch *et al.*, 1991), and a gephyrin linker segment, encoded by exon 14, displays high similarity to microtubule binding proteins MAP2 and tau (Ramming *et al.*, 2000). Important roles for the cytoskeleton were also supported by studies in which microtubule depolymerising agents were observed to reduce the

number of gephyrin clusters in spinal cord neurons (Kirsch & Betz, 1995, van Zundert *et al.*, 2004). In hippocampal neurons, however, microtubule disassembly did not affect gephyrin and $GABA_AR$ clusters (Allison *et al.*, 2000). The discrepancy between this and earlier studies was speculated to originate from different developmental stages, synapse type or the type of the receptor (Allison *et al.*, 2000). The influence of developmental changes in GlyR composition was analysed later on in spinal cord neurons: Here Gephyrin/GlyR clusters were affected by colchicines at immature rather than in mature glycinergic synapses, while GABAergic synapses were not influenced in any analysed developmental stage(van Zundert *et al.*, 2004). As microtubules were thought to be absent from synapses (Shirao & Gonzalez-Billault, 2013), the relevance of gephyrin-microtubule interactions was questioned. In the last few years however, evidence accumulated that argued for the presence of microtubules in dendritic spines, so that microtubule mediated anchoring of gephyrin appears to be a valid option (Shirao & Gonzalez-Billault, 2013).

Also actin filaments were shown to influence gephyrin and GlyR clustering (Charrier *et al.*, 2006). Actin deplomerization by cytochalasin D or latrunculin had no effect on cluster number but on cluster size (Kirsch & Betz, 1995). Later on it could be demonstrated that the gephyrin interaction with the microfilament system was mediated by ena/VASP (*enabled*/VAsodilator Stimulated Phosphoprotein) which binds to uncapped actin filaments (Bausen *et al.*, 2006). Actin dependence of gephyrin clustering appears to be restricted to the early stages of neuronal development (Bausen *et al.*, 2006).

In addition to Mena also profilin 2a, which promotes actin filament elongation, was identified as a binding partner of gephyrin (Giesemann *et al.*, 2003, Mammoto *et al.*, 1998, Murk *et al.*, 2012). However, the exact interplay of gephyrin, Mena (the neuronal form of ena/VASP) and profilin and its relevance for gephyrin clustering remains to be deciphered. Gephyrin competes with G-actin for the same binding site in profilin (Giesemann *et al.*, 2003). Disrupted profilin-G-actin interactions in the presence of gephyrin are expected to attenuate actin elongation, as profilin transfers oligomerization-competent G-actin to the actin-uncapping protein Mena, which in turn incorporates G-actin into a pre-existing F-actin filament ((Ferron *et al.*, 2007), see also Fig. 8, but also Fig 107).

The linkage of $GABA_AR$ $\alpha5$ subunit containing receptors to the cytoskeleton is mechanistically better understood: The protein radixin binds to the TM3-4 loop of the $\alpha5$ subunit (Loebrich *et al.*, 2006), gets activated by binding of the phospholipid PIP2 and phosphorylated, so that it can bind to filamentous actin. Notably this leads to extrasynaptic $GABA_A$ receptor clusters (Kneussel & Loebrich, 2007).

I.D.3. Signalling molecules

Over the years growing attention was directed at a new group of gephyrin binding partners – which based on previously published literature – appeared to be primarily implicated in the

organization of the postsynaptic cytoskeleton: Small GTPases and their regulators. Small GTPases are active upon GTP (guanosine-5'-triphosphate) binding, and their hydrolysis in the presence of GTPase activating proteins (GAPs) leads to their inactivation, *vice versa*, guanine nucleotide exchange factors (GEFs) remove GDP and replace it with GTP, thereby restoring the active state of the GTPase. For instance, the small GTPase Cdc42 (in its active state) is implicated in the control of the cytoskeleton with consequences for filopodia formation, neuron outgrowth and polarity as well as motility (Chen *et al.*, 2012). Via its effectors N-WASP and Arp2/3, Cdc42 can trigger actin filament elongation in dendritic spines (Irie & Yamaguchi, 2002).

While the originally assigned function was studied in more detail at excitatory synapses, at inhibitory synapses Cdc42 and its GEF collybistin were analysed for their role in gephyrin targeting to synapses. Gephyrin can interact with both proteins (Harvey *et al.*, 2004, Tyagarajan *et al.*, 2011a), but the interaction with collybistin is better understood. Although Cdc42 was also observed to trigger collybistin-gephyrin membrane targeting in non-neuronal cells (Mayer *et al.*, 2013), the study of a forebrain-specific Cdc42 knock-out did not reveal affected numbers of gephyrin and $GABA_AR$ γ2 subunit containing receptors in the hippocampus (Reddy-Alla *et al.*, 2010), suggesting that the GEF activity of collybistin and GTP hydrolysis of Cdc42 were dispensable. Conversely, analyses of collybistin-knockout mice revealed that collybistin triggers gephyrin targeting to GABAergic synapses in the hippocampus and the basolateral amygdala (Papadopoulos *et al.*, 2007) and consequently $GABA_AR$ clustering. Importantly, glycinergic transmission was not affected (Papadopoulos *et al.*, 2007). Notably, gephyrin-collybistin complexes require additional factors that drive their membrane anchoring presumably via the membrane phospholipid phosphatidylinositol-3-phosphate (PI(3)P) by activation of collybistin; the $GABA_AR$ α2 subunit (Saiepour *et al.*, 2010), the CAMs NL2 (Poulopoulos *et al.*, 2009) and NL4 (Hoon *et al.*, 2011), Cdc42 and the recently identified GTPase TC-10 (Mayer *et al.*, 2013) were described as such activators that consequently drive gephyrin and $GABA_AR$ clustering (with the exception of NL4, which is present at glycinergic synapses (Hoon *et al.*, 2011)). The gephyrin-collybistin-NL2 complex, which was shown to be implicated in perisomatic inhibition (Poulopoulos *et al.*, 2009), was one of the subjects of this work, and therefore more information will be provided in section III.C.1.

A GAP for the small GTPase Rac was also suggested to interact with gephyrin (Okada *et al.*, 2011). Coexpression of WRP (WAVE-associated Rac GAP, where WAVE stands for WASP family verprolin-homologous protein) led to an increased number of gephyrin clusters in cultured neurons, and this effect was dependent on the WRP SH3 domain. The SH3 domain binding epitope in gephyrin was mapped to residues 603 to 606 in GephE (Okada *et al.*, 2011). However, based on GephE crystal structures an interaction via SH3 domain-GephE appears questionable, as the putative WRP binding

is embedded in subdomain 3 and not freely accessible to SH3 domains which bind linear peptides. Thus, the observed effects on clustering might have been caused by other factors.

SynArfGEF acts as GEF for Arf6 and preferentially localizes to PSDs of perisomatic inhibitory synapses (Haenggi & Fritschy, 2006). SynArfGEF is an indirect link between the dystroglycan complex (Fukaya *et al.*, 2011) and NL2 (Sumita *et al.*, 2007) (see also Table 2), which represents an alternative $GABA_AR$ clustering pathway independent of gephyrin (Panzanelli *et al.*, 2011).

I.D.4. Trafficking proteins

As indicated above, proteins involved in the trafficking of receptors can coordinate the receptor insertion/removal in time and space (sections I.A.1 & I.C.5). Increased receptor numbers at synapses might be accomplished via the secretory pathway, via re-insertion after internalization or via recruitment from extrasynaptic membrane areas (Dumoulin *et al.*, 2009, Vithlani *et al.*, 2011). The long-range transport in axons is mediated by microtubule-based motors of the kinesin and dynein families, allows for an exchange of receptors (Hirokawa & Takemura, 2005) and paves the way for signalling endosomes being transported from the periphery to the cell body (Ibanez, 2007). GlyR and $GABA_AR$ trafficking was briefly introduced above and is the subject of several reviews (Dumoulin *et al.*, 2009, Luscher *et al.*, 2011, Vithlani *et al.*, 2011).

Often scaffolding proteins are associated with their ionotropic neuroreceptors during transport processes, and this principle also applies to the gephyrin-GlyR complex, which was not just identified at the membrane but also during passage of the receptor through the secretory pathway (Hanus *et al.*, 2004). Subsequently, the gephyrin-GlyR complex was also detected as a component of transport vesicles associated with the kinesin 5 (KIF5) and dynein motors, which mediate anterograde and retrograde transport, respectively (Maas *et al.*, 2006, Maas *et al.*, 2009). One interesting aspect of these studies was that the balance between anterograde and retrograde transport depended on neuronal activity. Kinesin-mediated anterograde transport was affected by the application of the GlyR-antagonist strychnine and by AMPAR stimulation (Maas *et al.*, 2009). A more detailed analysis of strychnine induced transport blockage revealed that polyglutamylation of microtubules (presumably as a consequence of AMPAR signalling) prevented anterograde gephyrin-GlyR cotransport but not kinesin-mediated transport *per se* (Maas *et al.*, 2009).

One component of the dynein motor, the dynein light chain 1 of the LC8 type (DYNLL1, actually DYNLL2 as well), directly interacts with gephyrin and was supposed to link gephyrin-GlyR complexes to the dynein motor. This hypothesis along with the biochemical characterization of the gephyrin-DYNLL1 was investigated in chapter III.B, where a more detailed introduction into the topic is given.

I.D.5. Local protein synthesis machinery

Synaptic plasticity requires quick adjustments of synaptic strength. Local protein synthesis allows for a rapid change in synapse composition by using mRNAs which were previously received from the cell body (Santos *et al.*, 2010). Gephyrin was shown to bind to RAFT1, a component of the mTOR1 and mTOR2 complexes (Sabatini *et al.*, 1999). mTOR1 (Wullschleger *et al.*, 2006) can phosphorylate the S6 kinase, which is involved in translation initiation (Fig. 5). mTOR1 also phosphorylates E4BP and thereby triggers its release from eIF4E, that can subsequently participate in local translation like the S6 kinase (Laplante & Sabatini, 2012). Gephyrin association with RAFT1 was reported to be required for mTOR downstream signalling (Sabatini *et al.*, 1999). Contrastingly, in a later study opposite effects of gephyrin association with mTOR were observed (Wuchter *et al.*, 2012) (see also section I.C.2.2). Another gephyrin binding partner participating in local protein synthesis is the eukaryotic initiation factor 3 (eIF3) (Sertie *et al.*, 2010), which prevents S6 kinase activity (Holz *et al.*, 2005) and which was found to be associated with collybistin as well (Sertie *et al.*, 2010).

I.D.6. Other gephyrin binding partners

Further gephyrin interaction partners have been identified, of which several do not fall into the listed categories and seem to play roles deviating from those initially assumed or for which only a single publication has been available. For instance, initially GABARAP was considered as a protein linking gephyrin to $GABA_A$Rs at the synapse. Indeed it can bind gephyrin and the $GABA_A$R γ2 subunit (Kneussel *et al.*, 2000, Wang *et al.*, 1999). However, gephyrin was dispensable for GABARAP localization, and in retina no significant GABARAP colocalization with gephyrin-GABAAR γ2 clusters was observed. Instead GABARAP displayed a cytosolic punctate distribution pointing to a role in $GABA_A$R trafficking (Kneussel *et al.*, 2000). However, the analysis of GABARAP knock-out mice revealed that GABARAP was dispensible for $GABA_A$R clustering (O'Sullivan *et al.*, 2005).

Another example is GRIP1 (glutamate receptor interacting proteins 1) which has been implicated in the transport of glutamate receptors, but was observed to directly interact with gephyrin in pulldown experiments, and its isoforms GRIP1c4-7 and GRIP1a/b colocalized with gephyrin at postsynaptic densities (Yu *et al.*, 2008). Beyond that GRIP1 can interact with GABARAP, however, detailed mechanistic studies on GRIP1 with respect to gephyrin clustering are still missing (Mohrluder *et al.*, 2009).

Hsc70 is a member of the 70 kDa heat shock proteins (Hsp70s) family, binds to gephyrin via GephG and was – based on single-particle tracking and colocalization studies – suggested to limit the extent of gephyrin clusters potentially by employing its chaperone activity or by facilitating gephyrin ubiquitylation, followed by degradation (Machado *et al.*, 2011).

I.E. Diseases related to dysfunctional gephyrin activity

It is not surprising that gephyrin is involved in a variety of diseases. Down-regulation of gephyrin functionality has been reported to be involved in hyperekplexia by affecting GlyR clustering (Davies *et al.*, 2010), in temporal lobe epilepsy (TLE) (Fang *et al.*, 2011, Forstera *et al.*, 2010, Thind *et al.*, 2010) and in idiopathic generalized epilepsy (IGE) (Dejanovic *et al.*, 2014) via dysfunctional $GABA_AR$ clustering, Alzheimer's disease (Agarwal *et al.*, 2008, Hales *et al.*, 2013) and, of course, Moco deficiency (Reiss & Hahnewald, 2011). In the stiff-man syndrome antibodies are raised against gephyrin (Butler *et al.*, 2000). In patients with TLE and IGE, deletions in GephG were detected, giving rise to gephyrin variants, which impaired proper gephyrin-receptor clustering in cultured neurons in a dominant-negative manner (Dejanovic *et al.*, 2014, Forstera *et al.*, 2010). Given the fact that gephyrin is an integral component of postsynaptic densities, it appears conceivable that it also plays so far undisclosed roles in GlyR- and $GABA_AR$-related disorders (see sections I.A.1.1 and I.A.1.2).

II. MATERIALS & METHODS

II.A. Materials

II.A.1. Equipment and instrumentation

Device	Specification/model	Company
Anion exchange chromatography column	MonoQ 10/100 GL	GE Healthcare
Autoclave	V-150	Systec
Balances	XS6002S Dual Range	Mettler Toledo
Balances	XS105 Dual Range	Mettler Toledo
Bottle for JLA 8.100 rotor	Bottle J-Lite 1000 mL	Beckmann Coulter
Calorimeter	Microcal VP-ITC	GE Healthcare
Calorimeter	Microcal iTC_{200}	GE Healthcare
Casting frame (for pouring single gels)	Mini-PROTEAN Casting Frame	Biorad
Casting gates for native agarose gel trays	Aluminium casting gates	Denville Scientific Inc.
Casting stand (for pouring single gels)	Mini-PROTEAN Tetra Cell Casting Module	Biorad
Cation exchange chromatography column	MonoS 10/100 GL	GE Healthcare
CD cuvette	QS-110	Hellma
CD spectropolarimeter	J-810	Jasco
Cell disruption system	Microfluidizer M-110P	Microfluidics
Cell disruption system	E615	Constant Systems Limited
Centrifuge	Avanti J-26 XP	Beckmann Coulter
Centrifuge	5417 R & 5810R	Eppendorf
Column bodies for affinity chromatography	Econo columns (1.5 x 15 cm or 2.5 x 20 cm)	Biorad
Combs for native agarose gels	15 cm wide combs for Vari-Gel™ Horizontal Maxi System	Denville Scientific Inc.
Crystallization robot	Analytic Honey Bee 963	Zinsser
Differential refractometer	Optilab T-rEX	Wyatt
DLS cuvette	105.205-Q5, 10 mm path length	Hellma
Electrophoresis gel imaging cabinet	Universal Hood II	Biorad
FPLC system	AEKTA purifier	GE Healthcare
Gel electophoresis chamber (NAGE)	Vari-Gel™ Horizontal Maxi System, complete 15 cm wide electrophoresis gel system	Denville Scientific Inc.
Gel electophoresis chamber (SDS-PAGE)	Mini-Protean® 3-cell	Biorad
Ice machine	Eismaschine 94774	Ziegra Eismaschinen
Illumination table	Leuchtplatte Größe 2E	Carl Roth
Liquid handling robot	Lissy	Zinsser Analytik
Loops for crystal mounting	CryoLoop	Hampton Research
Magnetic stirrer	MR 3002	Heidolph
MALS detector	Dawn 8^{+}	Wyatt

Microscope	SteREO Discovery.V12 or STEMI 2000	Zeiss
Microscope: Camera	AxioCam MRC	Zeiss
Microscope: Light source	KL 2500 LCD	Zeiss
PCR Cycler	Mastercylcer ep gradient S	Eppendorf
PCR Cycler	GeneAmp® PCR System 9700	Applied Biosystems
pH meter	BlueLine 14pH	Schott
Pipetboy	Pipetus®	Hirschmann Laborgeräte
Pipettes	Pipet lite	Rainin
Power supply (for gel electrophoresis chambers)	PowerPac Basic	Biorad
Rotor for Avanti J-26 XP	JA 25.50	Beckmann Coulter
Rotor for Avanti J-26 XP	JLA 8.100	Beckmann Coulter
Scanner	Odyssey	LI-COR
Shaker	LabTherm & LabTherm LT-X	Kühner
Shaker	ISF-1-W	Kühner
Shaker	ISF-1-X	Kühner
Spectrophotometer	Bio-Photometer	Eppendorf
Spectrophotometer	Nanodrop ND 1000	PEQLAB Biotechnologies
Stirrer	MR3002	Heidolph
Thermoblock	Rotilabo-Block Heater250	Carl Roth
Thermomixer	Comfort	Eppendorf
Tube for JA 25.50 rotor	Polypropylene bottle, screw-cap (29 x 104 mm, 50 mL)	Beckmann Coulter
Water bath	1092	GFL
X-ray cryosystem	X-Stream 2000	Rigaku
X-ray detector	R-AXIS HTC	Rigaku
X-ray generator	MicroMax-007HF	Rigaku
X-ray optics	VariMax HF	Osmic Inc.

Table 4 Equipment and instrumentation

II.A.2.Consumables

Material	Specification	Company
24-well plate	SuperClear	Crystalgen
96-well plate	ClearPlate Halfarea MB	Greiner
Chitin beads	S6651L	NEB
Cover slides	Circular, 22 mm diameter	Jena Bioscience
Dialysis cassettes	Slyde-A-Lyzer	Pierce Biotechnology
Nickel beads	Ni-IDA	Macherey & Nagel
Nickel beads	Ni-NTA agarose	Macherey & Nagel
Pipette tips	10 µl, 200 µl, 1000 µl	Rainin
Reaction tubes 15 / 50 mL	Greiner tube 15 / 50 mL	Greiner

Reaction tubes	0.2 mL /0.5 mL/ 1.5 mL/2 mL	Eppendorf
Disposable cuvettes	UVette®	Eppendorf
Syringe attachment filter	0.22 µm	Carl Roth
Tubing for dialysis	Dialysis Membrane MWCO 8,000, Spectra/Por®	SpectrumLabs.Com
Ultrafiltration units, MWCO 3-50 kDa, 0.5-20 mL	Vivaspin 0.5 – 20	Sartorius

Table 5 Consumables

II.A.3.Chemicals

Chemical	Supplier
2-Propanol (Isopropanol)	Carl Roth
Acrylamide	Sigma-Aldrich
Acetic acid (glacial)	Carl Roth
Ammonium carbonate	Fluka
Ammonium peroxodisulfate	Fluka
Ammonium sulfate	Carl Roth
Ampicillin (sodium salt)	Carl Roth
Benzaminidine hydrochloride	Calbiochem
β-Mercaptoethanol	Applichem
N,N'-methylenebisacrylamide	Carl Roth
Bis[sulfosuccinimidyl] suberate (abbreviation: BS^3)	Thermo Scientific Pierce
Bis[succinimidyl)penta(ethylene glycol) (abbreviation: $(PEG)_5$)	Thermo Scientific Pierce
Calcium chloride	Carl Roth
Chloramphenicol	Carl Roth
Coomassie Brilliant Blue R25	Carl Roth
Deoxy-ATP	New England Biolabs
Deoxy-CTP	New England Biolabs
Deoxy-GTP	New England Biolabs
Deoxy-TTP	New England Biolabs
Dimethylsulfoxide	Carl Roth
Dithiothreitol	Carl Roth
Ethanol (absolute)	Carl Roth
Ethanol (denatured)	Carl Roth
Formaldehyde	Carl Roth
Glycerol	AppliChem
Guanidinium chloride	Carl Roth
Hydrochloric acid	Carl Roth
Imidazole	Carl Roth
Kanamycine sulphate	Carl Roth
L-Glutathione (reduced)	AppliChem
Magnesium chloride	Carl Roth

MES	Sigma-Aldrich
Methanol	Carl Roth
Nickel sulfate	Carl Roth
Phenylmethylsulfonyl fluoride	Carl Roth
Polyethylene glycol 10,000	Fluka
Polyethylene glycol 3,000	Fluka
Polyethylene glycol 400	Fluka
Polyethylene glycol 5,000 monomethyl ether	Sigma-Aldrich
Potassium chloride	Carl Roth
Potassium hydroxide	Carl Roth
Potassium phosphate dibasic	Carl Roth
Potassium phosphate monobasic	Sigma-Aldrich
Potassium phosphate tribasic	Fluka
Silver nitrate	Sigma-Aldrich
Sodium acetate	Carl Roth
Sodium carbonate	Sigma-Aldrich
Sodium chloride	Carl Roth
Sodium dodecylsulfate	Carl Roth
Sodium hydroxide	Carl Roth
Sodium thiosulfate	Fluka
Trichloroacetic acid	Fluka
TRIS (2-Amino-2-hydroxymethyl-propane-1,3-diol)	Carl Roth
Tris(2-carboxyethyl)phosphine (referred to as TCEP)	Carl Roth
Urea	Carl Roth

Table 6 Chemicals

II.A.4.Crystallization screens

The following screens are commercially available, but were created with the in-house Lissy crystallization robot using the composition tables provided by the manufacturers. The resulting 96-deep-well-blocks with the mother liquors were used for the actual crystallization trials (see II.B.7.1.1).

Name	Company
Additive Screen	Hampton Research
Crystal Screen I + II	Hampton Research
Index Screen HT	Hampton Research
Nextal PEG Suite	Qiagen
Nucleix Suite	Qiagen
Protein Complex Screen	Qiagen
Wizard Screen 1	Emerald BioSystems
Wizard Screen 2	Emerald BioSystems

Table 7 Crystallization screens

II.A.5.Kits

Kit	Supplier
Quick Ligation Kit	New England Biolabs
Site-Directed Mutagenesis Kit	Stratagene
NucleoSpin Extract Kit	Macherey-Nagel
NucleoBond Plasmid Kit	Macherey-Nagel

Table 8 Kits

II.A.6.Purchased ladders & sample loading buffers

Ladder/dye/loading buffer	Supplier	Purpose
6x OrangeG loading dye with glycerol	Carl Roth	Loading dye, DNA & NAGE gels
GeneRuler 1 kbp	Thermo Scientific	DNA gels
GeneRuler 100 bp	Thermo Scientific	DNA gels
PageRuler prestained protein ladder	Thermo Scientific	SDS-PAGE gels
SyPro Orange protein gel stain 5,000x in DMSO	Invitrogen	Thermofluor

Table 9 Ladders & loading buffers.

II.A.7.Buffers & solutions

Unless otherwise stated, the pH of buffers was adjusted with 32% (w/v) sodium hydroxide or 37% (v/v) hydrochloric acid.

II.A.7.1 Buffers for protein purification and characterization

II.A.7.1.1 Buffers for cell lysis

LyBu 1	**LyBu 2**	**LyBu 3**	**LyBu 4**
100 mM Hepes pH 8	100 mM Tris pH 8.5	100 mM Hepes pH 8	100 mM Hepes pH 8
500 mM NaCl	500 mM NaCl	300 mM NaCl	500 mM NaCl
10 % Glycerol	1 mM EDTA	10 % Glycerol	10 % Glycerol
5 mM β-mercaptoethanol	5 mM β -mercaptoethanol	5 mM β -mercaptoethanol	2 mM β-mercaptoethanol
	0.1 % (w/v) Tween-20	10 mM EDTA	1 mM EDTA

Cell lysis is described in section II.B.3.1.

II.A.7.1.2 Buffers for nickel-affinity chromatography

Ni-1	**Ni-2**	**Ni-3**	**Ni-4**
50 mM Hepes pH 8	50 mM Hepes pH 8	50 mM Hepes pH 8	50 mM Hepes pH 8
500 mM NaCl	300 mM NaCl	250 mM NaCl	250 mM NaCl
5 mM β-mercaptoethanol	5 mM β-mercaptoethanol	5 mM β-mercaptoethanol	5 mM β-mercaptoethanol
10 mM imidazole	50 mM imidazole	250 mM imidazole	250 mM imidazole
			10 % glycerol

Ni-5

50 mM Hepes pH 8

100 mM NaCl

5 mM β-mercaptoethanol

250 mM imidazole

Nickel-affinity chromatography is described in section II.B.3.2.

II.A.7.1.3 Buffers for chitin-affinity chromatography

Chi C1

(wash)

50 mM Hepes pH 8

500 mM NaCl

5 mM β-mercaptoethanol

5 % glycerol

10 mM EDTA

Chi C2

(cleavage)

100 mM Hepes pH 8

150 mM NaCl

100 mM DTT

5 % glycerol

10 mM EDTA

Chi E1 (wash)

50 mM Hepes pH 8

500 mM NaCl

5 mM β-mercaptoethanol

1 mM EDTA

10 % glycerol

Chi E2 (cleavage)

20 mM Hepes pH 7

150 mM NaCl

5 mM β-mercaptoethanol

1 mM EDTA

10 % glycerol

Chi E3 (elution)

100 mM Hepes pH 8

150 mM NaCl

5 mM β-mercaptoethanol

1 mM EDTA

Chitin binding domain-affinity chromatography is described in section II.B.3.2.

II.A.7.1.4 Buffers for GST based-affinity chromatography

GST 1

50 mM Hepes pH 8

500 mM NaCl

10 % Glycerol

2 mM β-mercaptoethanol

1 mM EDTA

50 mM reduced glutathione

GST-based affinity chromatography is described in section II.B.3.2.

II.A.7.1.5 Buffers for His-tag, MBP-tag and GST-tag removal

ClBu NL

40 mM Tris pH 9.1

60 mM NaCl

1 mM β-mercaptoethanol

1 mM EDTA

ClBu MBP

20 mM HEPES pH 8

200 mM NaCl

1 mM β-mercaptoethanol

10 mM EDTA

10% Glycerol

ClBu SH3

20 mM HEPES pH 8

200 mM NaCl

0.5 mM β-mercaptoethanol

Tag removal is described in section II.B.3.3.

II.A.7.1.6 Buffers for ion exchange chromatography

MonoQ buffer A1	**MonoQ buffer A2**	**MonoQ buffer B1**	**MonoQ buffer B2**
20 mM Hepes pH 8	100 mM Tris pH 8.5	20 mM Hepes pH 8	20 mM Hepes pH 8
1 mM EDTA	2 M NaCl	10 mM EDTA	2 M NaCl
5 mM β-mercaptoethanol	1 mM EDTA	5 mM β-mercaptoethanol	10 mM EDTA
	5 mM β-mercaptoethanol	10 % Glycerol	5 mM β-mercaptoethanol
			10 % Glycerol

MonoS buffer A	**MonoS buffer B**
20 mM Pipes pH 6	20 mM Pipes pH 6
1 mM EDTA	2 M NaCl
5 mM β-mercaptoethanol	1 mM EDTA
	5 mM β-mercaptoethanol

Ion exchange chromatography is described in section II.B.3.4.

II.A.7.1.7 Buffers for size exclusion chromatography (SEC)

SEC-4	**SEC-5**	**SEC-6**
20 mM Hepes pH 8	20 mM Hepes pH 8	20 mM Hepes pH 8
150 mM NaCl	250 mM KCl	250 mM KCl
5 mM β-mercaptoethanol	5 mM β-mercaptoethanol	5 mM β-mercaptoethanol
1 mM EDTA	10 mM EDTA	10 mM EDTA
10 % Glycerol	10 % Glycerol	

SEC is described in section II.B.3.5.

II.A.7.1.8 Protein characterization/protein-protein interactions

SEC-1 buffer	**SEC-2 buffer**	**SEC-3 buffer**	**SEC-7 buffer**
20 mM Hepes pH 8	20 mM Hepes pH 8	20 mM Hepes pH 8	20 mM Hepes pH 7.6
250 mM NaCl	150 mM NaCl	150 mM NaCl	250 mM NaCl
5 mM β-mercaptoethanol	5 mM β-mercaptoethanol	5 mM β-mercaptoethanol	5 mM β-mercaptoethanol
1 mM EDTA	1 mM EDTA	1 mM EDTA	1 mM EDTA
		5 % glycerol	

The pH of SEC-7 buffer was 8.2 at 4°C (during dialysis) and 7.6 at 37°C, at which ITC experiments in chapter III.B were conducted.

II.A.7.2 Buffers and solutions for gel electrophoresis and related purposes

II.A.7.2.1 SDS-PAGE-gels

PAGE 10-18 % Separating gel	**PAGE 5 % Stacking Gel**	**5 x SDS-PAGE loading buffer**	**1 x Running buffer**
10-25% AA/BAA (29:1)	5-10% AA/BAA (37.5:1)	62.5 mM Tris pH 6.8	25 mM Tris
375 mM Tris pH 8.8	125 mM Tris pH 6.8	15 % (v/v) glycerol	192 mM glycine
0.1% SDS	0.1% SDS	4 % (w/v) SDS	0.1% SDS
0.25% APS	0.25% APS	4 % (v/v) β- mercaptoethanol	
0.05% TEMED	0.15% TEMED	0.15 % (w/v) Bromphenyl blue	

SDS-PAGE is described in II.B.4.1.

II.A.7.2.2 Native PAGE gels

The pH was adjusted with acetic acid.

Native PAGE gel	**Native PAGE Running buffer (=0.5x Tris/glycine)**
3.5 - 5 % acrylamide/bisacrylamide (80:1)	12.5 mM Tris pH 7.6-9
12.5 mM Tris pH 7.6-9	96 mM glycine
96 mM glycine	
H_2O ad 12.5 mL	
0.5 % APS	
0.1 % TEMED	

Native PAGE is described in II.B.5.3.

II.A.7.2.3 NAGE gels

The pH was adjusted with acetic acid. The following buffer was used for pouring the gels and electrophoresis:

0.5x Tris/glycine

12.5 mM Tris pH 7-9

96 mM glycine

NAGE is described in II.B.5.4.

II.A.7.2.4 DNA gels

The following buffer was used for pouring the gels and electrophoresis:

1 x TAE	**1 x TBE**
40 mM Tris	89 mM Tris
1 mM EDTA pH 8	2 mM EDTA pH 8
20 mM acetic acid	89 mM boric acid

II.A.7.2.5 Staining and destaining solutions (for PAGE & NAGE)

PAGE staining	**PAGE destaining**
40% methanol	50% ethanol
10% acetic acid	10% acetic acid
0.1% Coomassie Brilliant Blue R250	

II.A.7.2.6 Silver staining

Fixer	Sensitizer	Silver solution	Developer	Termination
50 % methanol	0.02% sodium thiosulfate	0.2% silver nitrate	6% sodium carbonate	1% acetic acid
10% acetic acid		0.75 µL/mL formaldehyde	0.5 µL/mL formaldehyde	

II.A.7.2.7 Western blot

Transfer buffer	TBS	Blocking medium
25 mM Tris	50 mM Tris/HCl pH 7.5	50 mM Tris/HCl pH 7.5
192 mM glycine	150 mM NaCl	150 mM NaCl
20 % MetOH		2.5 % (w/v) BSA
0.02 % SDS		

The Western blot protocol is given in II.B.4.2.

II.A.8.Peptides

Source Protein	Residues/sequence	biotinylated	Company
NL2-GB	768-783 PDYTLALRRAPDDVPL	Y	PANATecs (Tübingen, Germany)
NL2-GB+	762-790 LRPACPPDYTLALRRAPDDVPLLAPGALT	Y	PANATecs (Tübingen, Germany)
NL2-GB++	758-790 PAEALRPACPPDYTLALRRAPDDVPLLAPGALT	Y	PANATecs (Tübingen, Germany)
$Geph_{DB}$	203-214 KQTEDKGVQCEE	N	Genscript USA Inc. (Piscataway, New Jersey, USA)
$Geph_{DB+}$	190-214 PPPLSPPPTTSPHKQTEDKGVQCEE	Y	PANATecs (Tübingen, Germany)
$Geph_{DB2}$	258-272 RDTASLSTTPSESPR	N	Genscript USA Inc. (Piscataway, New Jersey, USA)

Table 10 Peptides

II.A.9.Medium, antibiotics & lac-operon inductor

LB (Lysogeny broth) medium for *E. coli* cultures (Lennox), antibiotics and the lac-operon inductor Isopropyl-β-1-thiogalactopyranoside (IPTG) were purchased from Carl Roth (Karlsruhe).

Antibiotics	Concentration
Ampicillin	100 µg/mL
Chloramphenicol	34 µg/mL
Kanamycin	50 µg/mL

Table 11 Antibiotics

II.A.10. *E. coli* strains

- DH5α (Invitrogen)

Genotype: F^- ϕ80*lac*ZΔM15 Δ(*lac*ZYA-*arg*F)U169 *rec*A1 *end*A1 *hsd*R17(r_k^-, m_k^+) *pho*A *sup*E44 *thi*-1 *gyr*A96 *rel*A1 λ^-

- BL21(DE3) (Invitrogen)

Genotype: *E. coli* B F^- *ompT hsdS*(r_B^- m_B^-) *dcm*$^+$ gal λ (DE3)

- BL21(DE3) RIL (Stratagene)

Geontype: *E. coli* B F^- *ompT hsdS*(r_B^- m_B^-) *dcm*$^+$ *Tet' gal* λ (DE3) endA Hte [cpn10 cpn60 $Gent^r$] [argU ileY leuW Str']

- BL21(DE3) Rosetta (Novagen)

E. coli B F^- *ompT hsdS*(r_B^- m_B^-) *dcm*$^+$ gal λ (DE3) pRARE (Cam^R)

II.A.11. Vectors

vector	Affinity tag	Solubility tag	Cleavage site	Company	Resin
pGEX4T-1	GST		thrombin	GE Healthcare	glutathione beads (GSTBind resin, Novagen)
pET28b	6xHis	-	thrombin	Novagen	Ni-IDA (Macherey Nagel)
pETM11	6xHis	-	TEV	EMBL	Ni-IDA (Macherey Nagel)
$pETM11^{nano}$	Nano	-	TEV	EMBL	Strep-tactin (IBA)
pETM30	6xHis	GST	TEV	EMBL	Ni-IDA (Macherey Nagel)
pETM41	6xHis	MBP	TEV	EMBL	Ni-IDA (Macherey Nagel)
pETM60	6xHis	NusA	TEV	EMBL	Ni-IDA (Macherey Nagel)
pTWIN1	Chitin binding domain	-	Intein (pH induced)	New England Biolabs	Chitin beads
pTYB12	Chitin binding domain	-	Intein (DTT induced)	New England Biolabs	Chitin beads

Table 12 Vectors

*$pETM11^{nano}$ was created using the pETM11 vector as a scaffold. The original 6xHis-tag was substituted for the following sequence: DVEAWLGAR. This Nano-tag was reported to bind to streptavidin with a higher affinity (K_D of 17 nM) than the Strep-tag II (K_D of 72 μM) (Lamla & Erdmann, 2004).

II.A.12. Expression constructs

Insert	Residues/mutations	vector	Expression/purification protocol	Source
GephWT	1-750	pET28b	1	Dr. Eun-Young Lee
Geph-S188A	1-750/S188A	pET28b	1	Bodo Sander
Geph-S188E	1-750/S188E	pET28b	1	Bodo Sander
Geph-S200E	1-750/S200E	pET28b	1	Bodo Sander
Geph-CL1	1-750/S188D&S194D&S200D	pET28b	1	Bodo Sander
Geph-CL2	1-750/T266E&S270E	pET28b	1	Bodo Sander
Geph-CL3	1-750/S280E/S283E/S286E	pET28b	1	Bodo Sander
Geph-S309E	1-750/S309E	pET28b	1	Bodo Sander
Geph-S319E	1-750/S1319E	pET28b	1	Bodo Sander
Geph-S333E	1-750/S333E	pET28b	1	Bodo Sander
GephΔ175-202	1-750/res. 175-202 deleted	pET28b	1	Bodo Sander
Geph-K67R	1-750/K67R	pET28b	1	Bodo Sander
Geph-K101R	1-750/K101R	pET28b	1	Bodo Sander
Geph-K67R&K101R	1-750/K67R&K101R	pET28b	1	Bodo Sander
Geph-EML3	1-202 (GephWT), 206-212 (VSRGTQT, derived from EML3), 213-750 (GephWT)	pET28b	1	Bodo Sander
GephG	1-181	pET28b	1	Bodo Sander
GephG-K67R&K101R	1-181/K67R&K101R	pET28b	1	Bodo Sander
GephG-K67R	1-181/K101R	pET28b	1	Bodo Sander
GephG-K101R	1-181/K67R	pET28b	1	Bodo Sander
GephGL202	1-202	pET28b	1	Bodo Sander
GephGL220	1-220	pET28b	1	Bodo Sander
GephGL253	1-253	pET16b	1	Dr. Florian Sauer
GephGL	1-331	pET28b	1	Bodo Sander
GephE	332-750	pTWIN1	2	Dr. Eun Young Kim
GephLE309	309-750	pET28b	1	Dr. Eun-Young Lee
GephLE208	208-750	pET28b	1	Dr. Eun-Young Lee
GephLE	182-750	pET28b	1	Bodo Sander
GephΔL	1-750/res. 186-331 deleted	pET28b	1	Bodo Sander
Geph-MLH1	1-750/res. 181-252 deleted	pET28b	1	Bodo Sander
Geph-MLH2	1-750/res. 253-331 deleted	pET28b	1	Bodo Sander
Geph-MLQ4	1-750/res. 253-302 deleted	pET28b	(1)	Bodo Sander
GephΔexon 14	1-750/res. 303-316 (=exon 14) deleted	pET28b	(1)	Bodo Sander
GephG$(GGS)_4$E	GephΔL+GGS tetra-repeat insert between res. 186 and 331	pET28b	1	Bodo Sander
$NL2_{cyt}$	700-836	pETM11	3	Bodo Sander
$NL2_{cyt}$-Y770A	700-836/Y770A	pETM11	3	Bodo Sander

$NL2_{cyt}$-Y770E	700-836/Y770E	pETM11	3	Bodo Sander
nano-$NL2_{cyt}$	700-836	$pETM11^{nano}$	3**	Bodo Sander
$NL2_{cyt}$-798term	700-798	pETM11	3	Bodo Sander
$NL2_{cyt}$-790term	700-789	pETM11	3	Bodo Sander
$NL2_{cyt}$-726-789	726-789	pETM11	3	Bodo Sander
$NL2_{cyt}$-735-789	735-789	pETM11	3	Bodo Sander
$NL2_{cyt}$-749-789	749-789	pETM11	3	Bodo Sander
$NL2_{cyt-}$CD8α	700-836/ res. 768-782 replaced by RPVVKSGDKPSLSAR (CD8α)	pETM11	3	Bodo Sander
$NL2_{cyt-}$CD8α -790term	700-790/ res. 768-782 replaced by RPVVKSGDKPSLSAR (CD8α)	pETM11	(3)	Bodo Sander
NusA-$NL2_{cyt}$	700-836	pETM60	3	Bodo Sander
$CB2_{SH3-}$-NL2	fusion of residues 700-836 ($NL2_{cyt}$) to C-terminus of $CB2_{SH3-}$	pETM41	5	Bodo Sander
GlyR-NL2	fusion of residues 700-836($NL2_{cyt}$) to C-terminus of MBP-GlyR (see below)	pETM41	*	Bodo Sander
CB-SH3	4-72 of murine $CB1_{SH3+}$, comprising exactly the same SH3 domain as *R. norvegicus* $CB2_{SH3+}$	pGEX4T-1	6	Dr. Tolga Soykan
$CB2_{SH3+}$	1-471	pETM11	****	Bodo Sander
$CB2_{SH3-}$	1-411	pETM11	****	Bodo Sander
$CB2_{SH3+}$ΔC15***	1-456	pTYB12	4	Dr. Daniela Schneeberger
$CB2_{SH3-}$	1-411	pTYB12	4	Dr. Song Xiang
$CB2_{SH3-}$ΔC15	1-396	pTYB12	4	Dr. Daniela Schneeberger
$CB2_{SH3+}$	1-471	pETM41	5	Bodo Sander
$CB2_{SH3+,}$ Δ3	1-468	pETM41	5	Bodo Sander
$CB2_{SH3+,}$ Δ7	1-464	pETM41	5	Bodo Sander
$CB2_{SH3-}$	1-411	pETM41	*	Bodo Sander
CB-PH-stalk	294-471	pETM41	5	Bodo Sander
$CB2_{SH3+}$	1-471	pETM30	5	Bodo Sander
$CB2_{SH3+}$	1-471	pETM60	*	Bodo Sander
DYNLL1-WT	1-89	pET28b	7	Dr. Eun-Young Lee
DYNLL1-H68A	1-89/H68A	pET28b	7	Dr. Eun-Young Lee
DYNLL1-S88E	1-89/S88E	pET28b	7	Dr. Eun-Young Lee
DYNLL1-WT	1-89	pETM11	7	Bodo Sander
ctPCNA	1-259	pETM11	used for cloning	Florian Rohleder
ctPCNA-DB	1-259/ GGGKQTEDKGVQCEE (extended $Geph_{DB}$ motif) inserted between residues 255&256	pETM11	3	Bodo Sander
NusA		pETM11	5	EMBL

MBP		pETM41	5	EMBL
MBP-DIC	161-172	pETM41	5	Bodo Sander
MBP-GlyR	401-448	pETM41	5	Bodo Sander
MBP-L	182-331 of Geph-WT	pETM41	5	Bodo Sander
MBP-L220	182-220	pETM41	5	Bodo Sander
MBP-(L252-331)	252-331 of Geph-WT	pETM41	5	Bodo Sander
MBP-L(303-331)	303-331 of Geph-WT	pETM41	5	Bodo Sander

Table 13 Expression constructs. The protein sequences were those of *Rattus norvegicus* with the exception of ctPCNA, which was derived from *Chaetomium thermophilum*. Gephyrin-derived sequences are coloured in light green and the numbering refers to the P2 splice variant of gephyrin (Appendix A). Likewise the plasmids derived from neuroligin 2 (NL2), collybistin (CB2) and dynein light chain 1 (DYNLL1) as well as maltose binding protein (MBP)- and NusA-fusion proteins are clustered and colour-coded, and their sequences are found in Appendix A as well. WT stands for wild-type, cyt stands for cytosolic, EML3 for echinoderm microtubule associated protein like 3, SH3 for src Homology 3 Domain (where src is an acronym for sarcoma), PH for pleckstrin homology domain, DIC for dynein intermediate chain, GlyR for glycine receptor (β subunit) and GST for glutathione S-transferase. Vectors, expression and purification protocols are specified in II.A.11 and II.B.2 and II.B.3, respectively. Bracketed expression/purification protocol numbers indicate that this construct was cloned but not expressed. However, based on the experiences with other mutants it is likely, that the bracketed protocol can be applied to this construct as well. For constructs marked with "*", which were cloned but not purified as well, no predictions are made. ** Note that a modified protocol 3 was used for this variant. *** Purified protein was a gift of Dr. Daniela Schneeberger. ****No overexpression was observed.

II.A.13. Enzymes

Enzyme	Source	Purpose
BamHI	New England Biolabs	Restriction enzyme digestion
Chymotrypsin	Sigma-Aldrich	Limited proteolysis
Desoxyribonuclease I	Invitrogen	DNA restriction, purification
DpnI	New England Biolabs	Restriction enzyme digestion
HindIII	New England Biolabs	Restriction enzyme digestion
*Nco*I	New England Biolabs	Restriction enzyme digestion
NdeI	New England Biolabs	Restriction enzyme digestion
NheI	New England Biolabs	Restriction enzyme digestion
Papain	Carl Roth	Limited proteolysis
Phusion DNA Polymerase	Finnzymes	PCR
Subtilisin	Carl Roth	Limited proteolysis
T4 DNA Ligase	Invitrogen	DNA ligation
Tobacco Etch Virus (TEV) protease	EMBL Hamburg	Tag cleavage
Thrombin	GE Healthcare	Tag cleavage
Trypsin	Sigma-Aldrich	Limited proteolysis

Table 14 Enzymes

II.A.14. Software, servers & databases

Software	Company/provider /references	Purpose
APBS	(Baker *et al.*, 2001, Dolinsky *et al.*, 2004)	Visualization of electrostatic potentials
ATSAS 2.5	(Petoukhov *et al.*, 2012)	SAXS data analysis
CCP4i package including amongst others POINTLESS, SCALA, TRUNCATE, REFMAC	http://www.ccp4.ac.uk/ccp4i_main.php	Analysis of crystallographic data
Dynamics®	Wyatt Technology Corporation	Analysis of DLS data
Geneious	http://www.geneious.com	Primer/sequence management
iTC200 software	Origin/GE Healthcare	ITC data acquisition & analysis
Microsoft EXCEL	Microsoft	General calculations
Microsoft Powerpoint	Microsoft	Generation of images
Microsoft WORD	Microsoft	Generation of documents
Mosflm	http://www.mrc-lmb.cam.ac.uk/harry/mosflm/	Integration of crystallographic data
Origin 8.0	OriginLab	Data analysis & representation
Origin 7 ITC	Origin/GE Healtchare	ITC data acquisition & analysis
PYMOL	DeLano Scientific LLC	Visualization of protein structures
Quantity One	Biorad	DNA gel analysis
Spectra Manager for J-810 spectropolarimeter	Jasco	CD data acquisition and analysis

Table 15 Software

Server	website	Purpose/references
blastp / blastn	http://blast.ncbi.nlm.nih.gov/	Sequence search (Shiryev *et al.*, 2007)
CONSURF	http://consurf.tau.ac.il/	Visualization of conservation among orthologues (Ashkenazy et al., 2010)
DALI	http://ekhidna.biocenter.helsinki.fi/dali_server/	Search for structural homologues (Holm et al., 2008)
PISA	http://www.ebi.ac.uk/pdbe/pisa/	Bioinformatic characterization of interfaces (Krissinel & Henrick, 2007)
propka	http://propka.ki.ku.dk/	Estimation of isoelectric points (Bas et al., 2008)
Protparam	http://web.expasy.org/protparam/	Calculation of molecular mass and extinction coefficients (Gasteiger et al., 2003)
PUBMED	http://www.ncbi.nlm.nih.gov/pubmed/	Literature search (Lu, 2011)
SAXS MoW	www.if.sc.usp.br/~saxs/	Molecular mass estimation using SAXS data (Fischer *et al.*, 2009)
TLSMD	http://skuld.bmsc.washington.edu/~tlsmd/	Determination of TLS groups (Painter & Merritt, 2006)
WebNMA analysis	http://apps.cbu.uib.no/webnma/home	Normal Mode Analysis (Hollup *et al.*, 2005)

Table 16 Servers

II.B. Methods

II.B.1. DNA propagation, analysis, purification and mutagenesis

II.B.1.1 Chemical transformation

Aliquots of 50 to 100 µL chemically competent *E. coli* DH5α (Stratagene) were incubated with 10-100 ng target DNA on ice for 30 to 45 minutes. Afterwards the cells were subjected to a 45 s-heat shock in a Thermomixer (Eppendorf). Subsequently, the cells were incubated on ice for two minutes, before 900 µL LB medium were added and the bacteria were shaken at 37°C at 200 rpm (Kuhner shaker) for 60 minutes. Afterwards the cells were centrifuged for 2 minutes at 1,000 g and resuspended in ~200 µL medium. The cell suspension was then applied to an LB-agar plate with the appropriate antibiotics and incubated overnight at 37 °C. Plates were only stored at 4°C when used for cloning purposes (for a maximum time of one week before they were discarded).

II.B.1.2 DNA analysis by gel electrophoresis and ultraviolet–visible spectroscopy

DNA quality and composition was assessed by DNA agarose gel electrophoresis. The gels contained 0.8% (w/v) NEEO ultra-quality agarose, 1x TAE buffer and either ethidium bromide or Midori Green Advance (Biozyme Scientific) (3 µL per 50 mL gel). DNA samples were mixed with 6 x DNA loading buffer (final concentration: 1x) and subjected to gel electrophoresis in 1x TAE buffer for 30 min at a voltage of 120 V. DNA fragments were visualized with the electrophoresis gel imaging cabinet Universal Hood II (Biorad) using a laser exciting the fluorescence of ethidium bromide or Midori Green which had intercalated in the respective DNA fragments. Their length was obtained by comparison with a DNA ladder (GeneRuler 100bp/1 kbp, Thermo Scientific). DNA concentrations were determined by ultraviolet-visible (UV-VIS) spectroscopy using a spectrophotometer (Nanodrop ND1000, PEQLAB) and assuming an extinction coefficient ε_{DNA}(260 nm) of 0.02 mL/µg·cm. Further descriptions on UV-VIS spectroscopy can be found in section II.B.4.4 .

II.B.1.3 Plasmid purification

Single colonies obtained after chemical transformation were transferred to LB-medium with the appropriate antibiotics. The cultures were shaken over night at 200 rpm at 37°C and finally centrifuged at 4,000 g for 5-10 min at 4°C before the DNA was obtained with the NucleoBond Plasmid Kit (Macherey-Nagel).

II.B.1.4 Cloning

Cloning was performed using the sticky end cohesion strategy (Cohen *et al.*, 1973). The sticky ends were generated by polymerase chain reaction (PCR) (Saiki *et al.*, 1985) of the target DNA fragment with appropriate primers containing overhangs that could be recognized by restriction

endonucleases later on. The target vector was digested with the same restriction enzymes, subsequently treated with calf intestinal alkaline phosphatase (New England Biolabs) to avoid re-ligation of the vector and purified using the NucleoSpin Extract Kit (Macherey Nagel). The PCR-amplified DNA was purified likewise to remove the restriction enzymes and added to the vector for sticky end cohesion followed by DNA ligation using the Quick Ligation protocol. The ligated DNA was used for chemical transformation as described in II.B.1.1.

II.B.1.5 Site-directed mutagenesis

Several constructs were available from predecessors, and variants constructed in this work were produced by site-directed mutagenesis (Table 13). Single point mutations were typically introduced using the QuikChange protocol: The target plasmid was amplified with two primers carrying the mutation of interest, one in the forward direction and the other in the reverse direction. The mismatch between primer and template was compensated by the surrounding bases. Usually, the mutation was in the middle of the primer, which was - apart from the mutation - constructed according to the general primer design rules. After amplification the original plasmid was digested with DpnI (New England Biolabs), which recognized methylated DNA, whereas the PCR amplificate was not targeted. Colonies obtained from chemical transformation were tested by sequencing.

If the QuikChange protocol failed, overlap mutagenesis was performed (Fig. 10) with primers designed for the QuikChange protocol. However, here the two primers (referred to as primers B and C) were not used simultaneously in one PCR. The respective second primers (referred to as A & D) carried sequences for either end plus restriction sites, via which the target gene was cloned into the vector. The resulting two PCR products (PCR 1 and PCR 2 in Fig. 10) were used as templates for a third PCR with the primers A & D to obtain the gene product carrying the mutation plus restriction

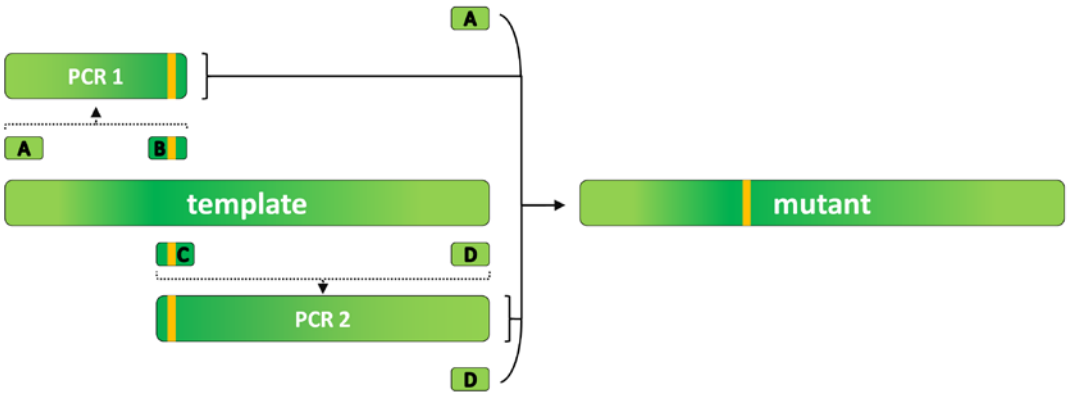

Figure 10 Overlap mutagenesis. Yellow coloured segments indicate the mutation site. Two preparatory PCRs (dotted lines) were performed with primers A & B and C & D, respectively, yielding PCR amplificates PCR 1 & 2, each carrying the mutation. The third (overlap) PCR was performed with PCR 1 and PCR 2 products and primers A & D, yielding the desired mutant.

sites ("mutant" in Fig. 10) with which it was cloned into the target vector as described in section II.B.1.4. Deletion or insertion variants were generated with overlap mutagenesis as well.

II.B.1.6 DNA gel extraction

For cloning purposes DNA fragments were separated by gel electrophoresis (section II.B.1.2), visualized by UV light and isolated with the NucleoSpin extraction kit (Macherey-Nagel) according to the manufacturer's manual. DNA was bound to spin columns, enriched, separated from disturbing contaminants and finally eluted in water.

II.B.2. Protein expression

The protein-encoding plasmid was transformed into BL21(DE3)RIL cells (Stratagene) as described in II.B.1.1 with one exception: $NL2_{cyt}$ expression using the pETM11/pETM11^{nano} vector (section II.A.11) was expressed in BL21(DE3) Rosetta cells (Novagen). A single colony from the resulting plates was transferred into a 500 mL flask containing 200 mL LB (plus the appropriate combination of antibiotics, see Tables 17 & 11), which was shaken over night at 37°C at 200 rpm (LabTherm & LabTherm LT-X shakers from Kühner). Then 25 mL of the overnight culture were used to inoculate 2.5 L LB medium in a 5 L flask (again containing the appropriate antibiotics). The cultures were shaken at 200 rpm (ISF-1-W and ISF-1-X shakers from Kühner) at 37°C until induction with IPTG after the OD_{600} reached values of 0.8 to 1. After induction the shaker temperature was decreased from 37°C to 15°C, with one exception: GephE expression was performed at 30°C. After 16-19 hours of expression cells were harvested by centrifugation in 1 L flasks (Bottle J-Lite 1,000 ml, Beckmann Coulter) for 8 minutes at 4°C and 6,000 g using an Avanti J-26 XP centrifuge (Beckmann Coulter). The resulting pellets were transferred to 50 mL Falcon™ tubes which were flash frozen in liquid nitrogen. Exact parameters like induction conditions and expression temperatures for the respective protein expressions are specified in Table 17. Differences in the treatment of pETM11- and pETM60 derived $NL2_{cyt}$ were restricted to the expression conditions, and the following purification steps were the same.

protocol	1 Gephyrin	2 GephE	3 NL2 (pETM60)	3* NL2 (pETM11)	4 Collybistin (intein)	5 Collybistin (MBP)	6 SH3	7 DYNLL1
cells	RIL	RIL	RIL	Rosetta	RIL	RIL	RIL	RIL
antibiotics	Kan/Cam	Amp/Cam	Kan/Cam	Kan/Cam	Amp/Cam	Amp/Cam	Amp/Cam	Kan/Cam

Table 17 Heterologous protein expression. Kanamycin (Kan), chloramphenicol (Cam) and ampicillin (Amp) were used at final concentrations of 50 µg/mL, 34 µg/mL and 100 µg/mL, respectively. *Nano-tagged $NL2_{cyt}$ was expressed like His-tagged $NL2_{cyt}$ using the pETM11 vector.

II.B.3. Protein purification

Principally, for apo-gephyrin, collybistin 1, collybistin 2 without SH3 domain, dynein light chain and PCNA established expression and purification protocols were available, and modifications were performed only at the purification level. The latter is true especially for apo-gephyrin, which had to be purified to a high level of homogeneity for SAXS and AFM analyses (section III.A.2.2 & Fig. 108). In principle, seven different purification protocols were used. The protocols were numbered and named after the longest protein variant which was purified with the respective protocol. Table 13 lists the protein variants used and also contains the number of the respective corresponding purification protocol. The buffers in Tables 18 to 23 are given in section II.A.7.1. All column materials were pre-equilibrated with the respective starting buffer. After each step the sample purity was checked by SDS-PAGE (II.B.4.1). All buffers were filtered using a bottle-top 0.2 µm filter. Buffers for ion exchange chromatography (II.B.3.4) and size exclusion chromatography (II.B.3.5) were used in the context of the AEKTA system (GE Healthcare) and were filtered and degassed.

II.B.3.1 Cell lysis & lysate clarification

In the first purification steps bacterial cells were lysed and centrifuged to get rid of the *E. coli* cell debris and insoluble protein. In all cases bacterial cells (obtained from 10 L culture) were resuspended in the 150-200 mL of the respective lysis buffer (plus the protease inhibitors listed in Table 18) and lysed twice with either the cell disruptor (Constant Systems Limited) or the fluidizer (Microfluidics) at a pressure of 1.5 kbar and 4°C. The lysate was cleared by centrifugation at 57,500 g at 4°C in a Beckmann JA 25.50 rotor for 45 min to 1 h or, alternatively, twice for 10 and 15 minutes at 57,500 g and 4°C. Note that His-tagged and Nano-tagged $NL2_{cyt}$ were treated in the same way.

protocol	1 Gephyrin	2 GephE	3 NL2	4 Collybistin (intein)	5 Collybistin (MBP)	6 SH3	7 DYNLL1
Lysis buffer	LyBu 1	LyBu 2	LyBu 1	LyBu 3	LyBu3	LyBu3	LyBu 1
Roche EDTA-free protease inhibitor cocktail tablets	3	2	2	2	2	-	1
Benzamidine [mg/mL]	0.75	0.75	0.75	0.75	0.75	-	0.75
PMSF [mg/mL]	0.375	0.375	0.375	0.375	0.375	-	0.375
Cell lysis cycles	2	2	2	2	2	2	2

Table 18 Protein purification – cell lysis. Constructs which were purified according to the protocols with the given numbers are found in Table 13. Buffers are listed in section II.A.7.1.

II.B.3.2 Affinity chromatography

Heterologously expressed proteins were separated from most of the host proteins in the second purification step, using affinity chromatography, during which tagged target proteins were enriched on the affinity matrix. Proteins containing the *Synechocystis species* DnaB intein (pTWIN1) or the *Saccharomyces cerevesiae* VMA intein/chitin binding domain (pTYB2 and pTYB12) were enriched via chitin beads, GST-tagged proteins via GST beads and His-tagged proteins via Ni-IDA beads (see also Table 12).

After clearance of the lysate (previous section), supernatants were incubated with the affinity matrices for 30 minutes or one hour (see table) and subsequently removed. Afterwards the beads were transferred to Econo columns (Biorad), washed and His-tagged proteins were eluted after 30 minutes incubation with elution buffer (Table 19), whereas target proteins carrying the chitin binding domain or a GST tag were released from their tags by on-column-cleavage (described in the next section II.B.3.3).

One protein, Nano-tagged $NL2_{cyt}$, is not listed in Table 19. It was enriched on Strep-tactin beads (purchased from iba) and extensively washed with LyBu 1 buffer. Unfortunately, the enriched protein was degraded to a 10 kDa protein (expected mass for the full-length protein: 17 kDa) and did not bind to GephE in preliminary binding experiments (data not shown).

protocol	1 Gephyrin	2 GephE	3 NL2	4 Collybistin (intein)	5 Collybistin (MBP)	6 SH3	7 DYNLL1
Temperature	4°C	4°C	4°C	4°C	4°C	4°C	4°C
Matrix	Ni-IDA	Chitin	Ni-IDA	Chitin	Ni-IDA	GSH	Ni-IDA
Bed volume [mL]	14	35	14	35	14	15	14
Incubation with the lysate [min]	30	60	30	60-90	30	120	30
Wash buffer 1 CV	LyBu 1 18	Chi-E1 60	LyBu 1 40-50	LyBu 3 10	LyBu 3 50	LyBu 3 50	LyBu 1 18
Wash buffer 2 CV	Ni-1 18	- -	- -	Chi-1 50	- -	- -	Ni-1 18
Wash buffer 3 CV	Ni-2 10	- -	- -	- -	- -	- -	- -
Elution buffer CV	Ni-3 8	- -	Ni-3 8	- -	Ni-4 8	- -	Ni-5 8

Table 19 Protein purification – affinity chromatography. Constructs which were purified according to the protocols with the given numbers are found in Table 13. Buffers are listed in section II.A.7.1. CV stands for column volumes.

MBP and NusA as well as several fusion protein variants in which the tag was not removed (Table 13, Table 21) were concentrated after elution and directly subjected to size exclusion chromatography (section II.B.3.5).

II.B.3.3 Tag removal

Principally, tags can interfere with the function of the target protein and were therefore often removed (Tables 20 & 21. CBD- and GST-tags were removed by an on-column-cleavage induced by a pH shift from pH 8 to pH 7 (protocol 2), by high concentrations of DTT (protocol 4) or by thrombin (protocol 6). His- and MBP-tag removal by proteolysis was carried out simultaneously with an over night dialysis against 2 litres of a buffer (4°C) that was at least similar to the starting buffer of the next purification step (protocols 3 & 5) (Table 20 & section II.A.7.1.5). The latter samples (protocol 3 & 5) were concentrated for 2 to 3 hours to achieve higher cleavage efficiency during dialysis. In proteins purified by means of protocols 3 and 5 tags were usually removed. Note that there were several exceptions from this rule (Table 21).

protocol	1 Gephyrin	2 GephE	3 NL2	4 Collybistin (intein)	5 Collybistin (MBP)	6 SH3	7 DYNLL1
Temperature	4°C	room temperature	4°C	4°C	4°C	room temperature	4°C
Dialysis (D) or on-column-cleavage (OCC)	-	OCC	D	OCC	D	OCC	-
Cleavage buffer	-	Chi-E2	ClBu-NL	Chi-C2	ClBu-MBP	ClBu-SH3	-
CV	-	5	-	5	-	-	-
Protease	-	-	TEV	-	TEV	Thrombin	-
Protease concentr.	-	-	0.3 µM	-	0.3 µM	1 U/mg	-
Incubation time [h]	-	72	16 -20	72	16 -20	24 h	-
Elution buffer	-	Chi-E3	-	Chi-C2		GST 1	-
CV	-	2	-	3		6	-

Table 20 Protein purification – tag removal. Constructs which were purified according to the protocols with the given numbers are found in Table 13. Buffers are listed in section II.A.7.1.5.

Protein	protocol	AIEX	Reasons for tag retention
MBP-DIC	5	N	signal enhancement
MBP-L220	5	N	signal enhancement
MBP-L(252-331)	5	N	signal enhancement, solubility
MBP-L(303-331)	5	N	signal enhancement, solubility
MBP-GlyR	5	N	signal enhancement
PCNA-DB	3	N	-
MBP-L	5	N	signal enhancement, solubility
NusA-NL2$_{cyt}$	3	N	signal enhancement, solubility

Table 21 Protein purification – tag removal (II). Constructs which were purified according to the protocols with the given numbers are found in Table 13. Buffers are listed in section II.A.7.1.5. Listed here are the proteins for which (according to protocols 3 and 5) tags should have been removed, however, tag removal was skipped either to enhance the solubility or to enhance the signal. For instance, the DIC peptide was small (< 2 kDa) and did not contain an aromatic residue and would have been difficult to detect in an aSEC experiment (II.B.5.5). Not only tag removal but also the anion exchange (AIEX) chromatography step was skipped. NusA-NL2$_{cyt}$ was normally purified according to protocol 3. Y stands for yes, N for no.

II.B.3.4 Ion exchange chromatography

Proteins or (different oligomeric states) with sufficiently different net charges could be separated from each other via anion or cation exchange chromatography (Jungbauer & Hahn, 2009). The choice of the matrix depended on the pI (isoelectric point) of the protein, either calculated by PROTPARAM or propka (see server list, Table 16). The pI is defined as the pH value at which the net charge of the protein is zero. Usually proteins are sufficiently negatively charged for binding to anion exchange chromatography columns, when their pI is 2 pH units below the pH of the binding buffer. Vice versa, when the protein pI exceeds the binding buffer pH by two pH units, it usually binds to the negatively charged cation exchange matrix. Once the proteins were bound, they could be eluted from the column by either an increase of the salt concentration or a change in the elution buffer pH.

Subsequent to the elution from the affinity chromatography column or to dialysis samples were diluted as indicated in Table 22 and either filtered with a 0.2 µM filter or centrifuged at 57,500 g for 15 minutes at 4°C. Buffers given in Table 22 were filtered and degassed. Ion exchange chromatography was conducted using pre-equlibrated MonoQ 10/100GL and MonoS 10/100GL columns (II.A.1) with an AEKTA purifier system (GE Healthcare). The injection rate was 2 ml/min and was adjusted if this speed could not be maintained due to increasing back pressure. Elution of the bound protein was performed using an increasing salt gradient. It should be noted that in the case of the gephyrin constructs, which were purified according to protocol 1, in addition to SDS-PAGE (II.B.4.1), native PAGE (II.B.5.3) was conducted to assess the sample composition in terms of the

oligomeric state (Fig. 18B). Unless otherwise stated only the trimeric fractions were further processed using protocol 1.

protocol	1 Gephyrin ****	2 GephE	3 NL2	4 Collybistin (intein)*	5 Collybistin (MBP)*	6 SH3	7 DYNLL1 *****
Temperature	4°C	4°C	4°C	4°C	4°C	-	4°C
Column	MonoQ 10/100 GL	MonoQ 10/100 GL	MonoQ 10/100 GL	MonoQ 10/100 GL	MonoQ 10/100 GL	-	MonoS 10/100 GL
Sample buffer***	1 x Ni-3 + 2 x MonoQ-A1	0.33 x Chi-E2 0.66 x Chi-E3 + 2 x MonoQ-A1	ClBu-NL	1 x Chi-C2 + 2 x MonoQ-C1	ClBu-MBP	-	1 x Ni-5 + 1x MonoS-A, adjusted to pH 6**
Buffer A	MonoQ-A1	MonoQ-A1	MonoQ-A1	MonoQ-C1	MonoQ-B1	-	MonoS-A
Buffer B	MonoQ-A2	MonoQ-A2	MonoQ-A2	MonoQ-C2	MonoQ-B2	-	MonoS-B
Sample injection/binding							
Starting buffer [%]	4	4	2.5	4	4	-	2.5
Flow rate [ml/min]	2	2	2	2	2	-	2
Elution							
Gradient I [%B]	4-10	4-7.5	2.5-100	4-100	4-100	-	2.5-20
CV	3	2	12.5	15	15	-	25
Flow rate	3	3	3	3	3	-	3
Gradient II [%B]	10-18	7.5-15	-	-	-	-	-
CV	35	25	-	-	-	-	-
Flow rate	3	3	-	-	-	-	-

Table 22 Protein purification – ion exchange chromatography Constructs which were purified according to the protocols with the given numbers are found in Table 13. Buffers are listed in section II.A.7.1.6. *These collybistin samples were subdivided into three aliquots, which were subjected to anion exchange chromatography successively. ** The pH was adjusted with HCl, with the same volume that has been required to shift the pH of a mixture of Ni-5 buffer and MonoS buffer A to a value of 6. *** The ratios were the result of protein dilution prior to ion exchange chromatography, which ensured binding to the columns. **** Gephyrin quality could be slightly improved with a modified multi-step gradient: 4-8.5% (over 3 CV), 8.5%-13% (35CV), 13%-18% (20 CV). However, the gradient given in the table was sufficient to ensure high protein quality. *****In most cases DYNLL1 purification was conducted without the ion exchange chromatography step. One exception, in which the MonoS step was included, was the batch that was used for the characterization of the gephyrin-DYNLL1 complex with SAXS (section III.B2.3).

II.B.3.5 Size exclusion chromatography (SEC)

The final polishing step was carried out with size exclusion chromatography which allows for the separation of components with a sufficient difference in hydrodynamic radius (R_H, also described in II.B.5.5). In short, proteins with a larger hydrodynamic radius enter the beads with a lower probability than proteins with a smaller hydrodynamic radius. Consequently, larger proteins display smaller elution volumes than smaller proteins.

Before the sample was applied to the SEC column (connected to an AEKTA purifier system, GE Healthcare), it was centrifuged for at least ten minutes at 25,000 g and at 4°C. SEC was conducted with a Superdex 200 XK26/60 column (column volume 330 mL) at 4°C and at a flow rate of 1 mL/min. One exception from this rule was the purification of higher oligomers of gephyrin (identified by native PAGE (II.B.5.3) after anion exchange chromatography, see also Fig. 18B) which were further purified with an analytical Superose 6 10/300GL column (volume: 24 mL) that was used at a flow rate of 0.5 mL/min and to which 500 µL sample aliquots were applied. The used buffers are given in Table 23. After SEC proteins were concentrated to final concentrations given in Table 23, frozen in liquid nitrogen and stored at -80°C.

protocol	1 Gephyrin	2 GephE	3 NL2*	4 Collybistin (intein)	5 Collybistin (MBP)	6 SH3	7 DYNLL1
Buffer	SEC-1	SEC-1	SEC-1	SEC-2	SEC-2	SEC-3	SEC-1
Final concentration [mg/mL]	10-16	10-15	10-12	8 ($CB2_{SH3-}$) 13 ($CB2_{SH3-}$ ΔC15)	5-6 (CB-PH-stalk) 1 ($CB2_{SH3+}$ variants)	1.3	15

Table 23 Protein purification – size exclusion chromatography. Constructs which were purified according to the protocols with the given numbers are found in Table 13. Buffers are listed in section II.A.7.1.6. * Note the remarks on $NL2_{cyt}$ concentration determination in section II.B.4.4.

II.B.4. Protein characterization

II.B.4.1 SDS-PAGE

Sodium dodecyl sulfate poly-acrylamide gel electrophoresis (SDS-PAGE) allowed for the analysis of sample constituents and was therefore an important tool during purifications (II.B.3) and in the analysis of analytical size exclusion chromatography experiments (II.B.5.5). In SDS-PAGE denatured proteins were loaded on a gel and exposed to an electric field. This led to a separation of the proteins by their molecular masses. To avoid that protein shape and charge influenced the migration behaviour, the detergent SDS was included, which formed large complexes with the proteins. Due to the anionic character of SDS the charges of protein-SDS complexes were proportional to the

molecular mass. The inclusion of reducing agents in the loading buffer reduced disulphide bonds (Lottspeich & Zorbas, 1998).

Solutions for this procedure are given in section IIA.1.7.2. Gels (thickness: 0.75 cm) were prepared in casting frames and casting stands purchased from Biorad and contained the appropriate percentage of acrylamide in the separating gel and 5% acrylamide in the stacking gel (section II.A.7.2.1). Protein samples were mixed with 5 x protein sample buffer at a ratio of 5:1 and boiled for five minutes at 95° C. Together with a molecular weight marker (PageRuler protein ladder, Fermentas) they were loaded on SDS-PAGE gels immersed in 1 x running buffer (section II.A.7.2.1) in a Mini-Protean® 3-cell electrophoresis chamber (Biorad). Electrophoresis was performed for typically 50-60 min at 200 V. Usually gels were stained in Coomassie R250 containing PAGE staining solution for 15 minutes at room temperature, destained in PAGE destaining solution (II.A.7.1.5) for 30 minutes and heated in water to get rid of high background signals. Gels were scanned using the Odyssey system (LI-COR).

With Coomassie R250 protein normally amounts as small as 100 ng can be detected, and hence this staining method was sufficient for the analysis of aSEC experiments and purifications. When higher sensitivity was required, gels were stained with silver as follows (solutions given in II.A.7.2.6): After 1 hour incubation in the fixer solution the protein gel was washed in 50% ethanol for three times (20 min each). Subsequently the gel was subjected to the sensitizer solution for one minute before it was washed for three times with water (20 seconds/cycle). A 20 minute incubation in silver nitrate solution was followed by three washing cycles with water (three times á 20 seconds), before the actual developing reaction took place. The length of the developing step was variable and depended on the protein amounts to be shown. When the protein bands reached the desired intensity, the reaction was terminated by the addition of 1% acetic acid. The latter solution was also used for storage purposes.

II.B.4.2 Western Blot

Proteins can be visualized by Western blots if antibodies are available (Lottspeich & Zorbas, 1998, Towbin *et al.*, 1979). In short, the protein bands of SDS-PAGE gels were transferred to a membrane, incubated with a (primary) antibody raised against the target epitope and then with a secondary antibody which recognizes the first antibody and is coupled with horse-radish peroxidase (HRP). Washing steps ensured that the HRP specifically localized to the epitope recognized by the primary antibody. The addition of the HRP substrate luminol resulted in its oxidation to 3-aminophtalate, resulting in chemiluminescence at 425 nm.

The composition of the Western blot buffers is given in II.A.7.2.7. A polyvinylidenfluoride (PVDF) membrane was immersed in methanol (1 minute), water (2 minutes) and SDS transfer buffer

(2 minutes). The electrophoretic protein transfer from the SDS-PAGE gel to the activated PVDF membrane was conducted with a Biorad tank system according to the manufacturer's manual at a current of 300 mA for one hour at 4°C. The following steps were performed at room temperature (except for the incubation with the primary antibody). The membrane was blocked for 1 hour in TBS containing 2.5% (w/v) BSA and was washed with TBS-T (containing TBS and 0.05% Tween-20). Incubation with the primary antibody was conducted over night and followed by two rinsing steps with TBS (5 minutes each), and two steps with TBS-T (5 minutes each). Then the membrane was incubated with the secondary antibody for one hour and washed in TBS-T (3 x 10 minutes), before chemiluminescence detection was performed according to the manufacturer's manual (Thermo Scientific).

Antibodies were used as follows:

Antibody	Epitope	Dilution	Company
primary			
Polyclonal rabbit antiserum against neuroligin 2	$NL2_{cyt}$	1 : 1,000	Synaptic Systems
Anti-His	His-tag	1 : 1,000	Cell Signalling
secondary			
HRP-conjugated goat anti-rabbit	Rabbit IgG	1 : 5,000	Cell Signalling

Table 24 Antibodies. All antibodies were dissolved in PBS for storage at -20°C and in blocking solution during blot incubation.

II.B.4.3 Limited proteolysis

Limited proteolysis (Hubbard, 1998) was used to probe for conformational differences between proteins of comparable molecular mass. All samples contained the same amount of protein and were in exactly the same buffer (in SEC-4 buffer(II.A.7.1.7), unless otherwise stated). The final protein concentration was typically 1 mg/mL and the volume a multiple of 6-10 µL. Proteases (at concentrations given in the figures in the Results section) were pipetted onto the lids of the reaction tubes and added to the target protein samples by centrifugation. For time-course experiments aliquots of 5-8 µL were taken per time point and mixed with pre-heated 95°C hot 5x SDS-PAGE loading buffer (II.A.7.2.1, final concentration: 1x) by centrifugation to terminate the reaction. Subsequently samples were boiled for five minutes at 95°C and analysed by SDS-PAGE.

II.B.4.4 Ultraviolet–visible spectroscopy

Ultraviolet-visible (UV-VIS) spectroscopy (Lottspeich & Zorbas, 1998) was used to determine protein concentrations. Peptide bonds and aromatic amino acids absorb light in the UV-VIS region, and the fraction of absorbed light depends on the wavelength and the amino acid composition. The protein concentration can be determined according to the Lambert-Beer Law:

$$A_{280} = \varepsilon \cdot c \cdot d \qquad \text{(equation 1)}$$

A_{280} is the absorbance at 280 nm, d the path length (determined by the instrument), c the concentration and ε the extinction coefficient. The latter coefficient depends on the number of aromatic amino acids, where tryptophans absorb more light than tyrosines or cystines and can be calculated using Protparam. With the known path length, extinction coefficient and the A_{280}, obtained with a nanodrop UV/Vis spectrophotometer (Peqlab), the concentration could be derived.

For $NL2_{cyt}$ I observed that the A_{260}/A_{280} ratio and the A_{340} were shifted to higher values at higher concentrations (possibly due to scattering of $NL2_{cyt}$ aggregates). For instance, at an A_{280}=5 the A_{260}/A_{280} ratio was higher than 1. Hence, the protein was diluted until $0.2 < A_{280} < 0.8$ (at $A_{260}/A_{280} \leq 0.7$), and the dilution factor was multiplied by the A_{280} value of the diluted sample to determine the actual protein concentration. This phenomenon was observed at a salt concentration of 150 mM NaCl, but appeared to be less pronounced at 250 mM NaCl.

II.B.4.5 Thermofluor

Thermal protein stability can be assessed with the thermofluor method (Cummings *et al.*, 2006). The protein of interest is incubated with a fluorophor (SYPRO Orange) that displays increased quantum yields when it binds to hydrophobic patches, an event that occurs with a higher probability when the protein becomes denatured. The variation of fluorescence as a function of temperature gives rise to step-like fluorescence curves, where the x-coordinates of the inflection points yields the melting temperatures, T_M. As the experimental setup allows to record melting curves for 96 conditions at once, this method was also used to screen for buffer conditions or additives that stabilized proteins.

Typically 20 µL of protein (final concentration: 0.5 - 1 mg/mL) were mixed with 1.25 x SYPRO Orange protein gel stain. These mixtures were analysed in a 96 PP-PCR-plate (Greiner Bio-One International AG), using a Real-Time PCR system (Stratagene Mx3005P). Starting at 25 °C, the temperature was increased by 1°C per minute until a temperature of 95 °C was reached. The obtained curves were analysed with an Excel sheet provided by the Structural Genomics Consortium (SGC) in Oxford. Unless otherwise stated the experiments were conducted with SEC-4 buffer.

II.B.4.6 Circular dichroism spectroscopy

Circular dichroism (CD) analysis can yield information about the structural integrity of a protein and can also be used for thermal stability assays (Kelly *et al.*, 2005). In CD spectroscopy samples are exposed to a mixture of right- and left-circularly polarized light. Amino acids (except for glycine) are chiral probes, and as such they differently absorb right and left-polarized light, depending on protein secondary structure elements/content (λ=[240 nm, 180 nm]) as well as on their tertiary structure

(λ=[320 nm, 260 nm]). In this work the focus was set on the characterization of secondary structure content. For α-helices, β-strands, turns and intrinsically disordered elements spectra are available, so that deconvolution of the CD spectrum can theoretically yield the contributions of the individual secondary structure elements. For instance, a CD spectrum minimum at 200 nm points to a significant contribution of disordered elements to the analysed protein.

Circular dichroism experiments were conducted with a JASCO J-810 spectropolarimeter. Far UV spectra from 260 nm to 190 nm were recorded at a scanning speed of 20 nm/min with a response time of 1 s and a band width of 2 nm. As buffer, certain ions and reducing agents impeded the collection of data at wavelength below 200 nm, the buffer of the protein samples was exchanged to 50 mM potassium phosphate with the aid of ultrafiltration units (Sartorius Vivaspin 500, Goettingen). The decrease in circular dichroism at 200 nm (band with = 2 nm) was measured repeatedly (n = 5) as a function of temperature (20°C < T < 95°C) to obtain melting curves at a heating rate of 1°C/min.

II.B.4.7 Dynamic light scattering

Dynamic light scattering (DLS) was used to determine the hydrodynamic radii of proteins (Frisken, 2001). Samples were irradiated by laser light. Larger particles diffused with lower speed than smaller ones, and these differences translated into different degrees of intensity fluctuations of the scattered light. The so obtained diffusion coefficient correlated inversely with the hydrodynamic radius of the protein.

DLS measurements were performed at least in triplicate with a DynaPro Titan DLS photometer (Wyatt Technology) at 10°C and with a quartz cuvette containing the protein in SEC-1 buffer (II.A.7.1.8) at a concentration of 1.5 mg/mL. Data analysis was performed with the Dynamics 6.7.3 software using the "PBS" scenario, in which parameters like the refractive index and the viscosity were preset. The polydispersity (a measure for sample heterogeneity) of each species reported in the Results section was below 20% (data not shown).

II.B.5. Interaction studies

Several techniques were used for complex analysis. With 1:1 binding models I refer to an interaction in which the individual components P and L are in equilibrium with the complex PL:

$$P + L \rightleftharpoons PL$$

The mass action law yields an approximation of the dissociation constant K_D

$$K_D = \frac{[P]\cdot[L]}{[PL]} \qquad \text{(equation 2)}$$

Here edged brackets indicate concentrations of the respective species. Considering that complex

formation results in a decrease of the initial concentrations of the individual components $[P]_T$ and $[L]_T$ by the [PL] yields:

$$K_D = \frac{([P]_T - [PL]) \cdot ([L]_T - [PL])}{[PL]} \quad \text{(equation 3)}$$

The rearrangement of equation 3 gives the complex concentration:

$$[PL] = \frac{[P]_T + [L]_T + K_D}{2} \pm \sqrt{\frac{([P]_T + [L]_T + K_D)^2}{4} - [P]_T \cdot [L]_T} \quad \text{(equation 4)}$$

II.B.5.1 Pulldown assays

In pulldown assays protein X is immobilized on beads (referred to as bait) and incubated with protein Y (called "prey"). Then the prey is removed and beads are repeatedly washed with buffer until unspecifically bound prey is removed. In case of binding the bait-coupled beads are expected to enrich the prey protein which should be absent from bait-free control beads. This method was primarily used for the analysis of the gephyrin-NL2 interaction. Similar experiments were also performed with the gephyrin-collybistin-NL2 complex, in which GST-collybistin variants were used as bait proteins (data not shown).

II.B.5.1.1 Ni-TED matrix

$NL2_{cyt}$ and the mentioned variants were heterologously expressed using the pETM11 vector (Table 17) and their purification was terminated prior to the elution step in affinity chromatography (II.B.3.2). Beads were transferred to a Falcon™ tube, where they were extensively washed to remove residual traces of imidazole, yielding a 1:1 mixture of beads with binding buffer. All steps described below were carried out with binding buffer. From this slurry 40 µL-aliquots were passed into 1.5 mL reaction tubes. Controls (without $NL2_{cyt}$ protein) were treated analogously. Prior to the addition of the prey protein excessive buffer was removed. The prey protein, GephE, was added to the beads in the amounts given in Table 25, and the mixtures were incubated for one hour at 4°C. The supernatant was analysed by SDS-PAGE, and the beads were washed with binding buffer as indicated in Table 25. The beads were supplemented with 20 µL SDS PAGE buffer and boiled for 5 minutes before they were subjected to an SDS-PAGE analysis (along with the saved supernatants).

V(beads)	20 µL	20 µL
c(prey)	30 µM	30 µM
V(prey)	20 µL	30 µL
Incubation time	60 min	60 min
Incubation temperature	4°C	4°C
Washing steps	1 x 800 µL	2 x 800 µL
Binding buffer	20 mM Hepes/Tris pH 8 250 mM/150 mM NaCl	20 mM Hepes/Tris pH 8 250 mM/150 mM NaCl
Figure	Fig. 86A	Fig. 86B

Table 25 $NL2_{cyt}$-GephE pulldowns using Ni-TED matrix. V and c stand for volume and concentration, respectively.

II.B.5.1.2 Strep-tactin matrix

Biotinylated peptides were used to saturate Strep-tactin beads. Saturation was followed by UV-VIS spectrometry conducted with 1.3 µl aliquots of the supernatant. After equilibrium was reached (~120 minutes), the beads were extensively washed with binding buffer and distributed to the reaction tubes. From now on the procedure was the same as for the Nickel-matrix based experiments described above. Deviations from the procedure are summarized in Table 26.

V(beads)	8 µL
c(prey)	20 µM
V(prey)	20 µL
Incubation time	60 min
Incubation temparature	4°C
Washing steps	3 x 200 µL
Binding buffer	20 mM Hepes pH 7.4 150 mM NaCl
Figure	Fig. 86C

Table 26 $NL2_{cyt}$-gephyrin pulldowns using Strep-tactin beads.

II.B.5.2 Crosslinking

Chemical crosslinking was used to obtain information on intra- and intermolecular interactions. In this work homobifunctional crosslinkers, primarily BS^3, were used, which contained a reactive NHS (N-hydroxy-succinamide) group at either end, separated by a 11 Å spacer arm. Primary amines and the NHS ester groups reacted in a nucleophilic substitution reaction which yielded protein-crosslinker adducts and NHS as leaving groups. Desired crosslinking adducts were those in which the NHS groups reacted with different proteins. Primary amines are present in side chains of lysyl-residues or at the N-terminus. However, also hydroxyl-containing amino acids were described to act as nucleophiles on NHS esters (Maedler *et al.*, 2009) .

If present in target samples, reducing agents and/or Tris buffer (containing primary amines) were removed by buffer exchange via ultrafiltration devices. Pre-formed gephyrin-NL2 complexes were mixed with 200 µM of BS^3 crosslinker. The reaction was terminated after 10 minutes at 4°C by the addition of Tris (pH 7.5) at a final concentration of 60 mM. Aggregates were removed by a centrifugation step (10 minutes, 25,000 g, 4°C), before samples were analysed by SDS-PAGE.

II.B.5.3 Native PAGE

Protein mixtures were typically incubated over night or at least for four hours. Native PAGE gels (II.A.7.2.2) were poured using casting frames and casting stands (Biorad) at least 3 hours prior to electrophoresis. Gels were pre-run without samples for at least 20 minutes. Immediately before electrophoresis, samples were mixed with Roti®-Load DNA-orange 1 buffer (Carl Roth) in a ratio of 5:1 and centrifuged for 5 minutes at >13,000 g at 4°C. Electrophoresis was performed at 4°C with a Mini-Protean® 3-cell electrophoresis chamber (Biorad), filled with 12.5 mM Tris pH 8-9, 96 mM glycine buffer. Electrophoresis was conducted for ~150 minutes (pH 8) or ~90 minutes (pH 9) at currents of 55 mA and 80 mA, respectively. Native PAGE was also conducted during the course of purifications with protocol 1 to distinguish between trimeric and higher oligomeric species of the respective gephyrin variant (II.B.3.4).

II.B.5.4 Native agarose gel electrophoresis

Protein mixtures were typically incubated over night or at least for four hours and then mixed with OrangeG dye (Carl Roth) in a 5:1 ratio. Samples were loaded on an 0.8% agarose (HEEO ultra quality agarose, Carl Roth) gel (thickness: 1.5 mm) which contained 0.5x Tris/glycine. The pH is given in the respective figure captions. Electrophoresis was carried out in a horizontal electrophoresis unit (Vari-Gel™ Horizontal Gel System, Denville Scientific) at 4°C and a current of 50 mA for 3-4 hours. Gels were stained for 20 minutes in PAGE staining solution and destained over night in PAGE destaining solution (II.A.7.1.5). Shaking NAGE gels over night was avoided.

II.B.5.5 Analytical size exclusion chromatography (aSEC)

SEC (described in II.B.3.5) was also applied to analyse complexes qualitatively. Complexes typically displayed higher hydrodynamic radii and therefore eluted earlier than the corresponding individual constituents. aSEC was conducted with either a Superdex 200 10/300GL, a Superdex 75 10/300GL or a Superdex 200 5/150GL column (GE Healthcare) equilibrated in SEC-1 or SEC-2 buffer (given in II.A.7.1.8). Proteins and protein mixtures, typically in a total volume of 105-110 µL (10/300GL columns) or 45 µL (5/150 GL column), were incubated for at least one hour at 4°C and centrifuged prior to aSEC to remove aggregates. For the sample injection 100 µL (10/300GL columns) or 40 µL (5/150GL column) were used. The experiments were conducted at 4°C and a flow rate of 0.5 mL/min (10/300GL columns) or 0.15 mL/min (5/150GL column). Complex formation was either detected in chromatograms, in which the absorbance at 280 nm and 260 nm were plotted as a function of time, or by SDS-PAGE analysis of selected fractions. aSEC was also performed for preparative purposes before SAXS measurements (II.B.6.2.1) or as a ensuing purification step for higher oligomers of

gephyrin (II.B.3.4 & III.A.2.2), which were obtained after anion exchange chromatography. In these cases 500 µL samples were applied to the column.

II.B.5.6 Size exclusion chromatography coupled with multi-angle-light scattering (SEC-MALS)

This approach was an extension of aSEC experiments. aSEC experiments could be used for mass determination only if the analysed particle adopted a spherical conformation. Gephyrin and most related variants predominantly adopted non-spherical conformations. Hence, masses of these variants could not be estimated by SEC experiment analysis. In SEC-MALS experiments (Wen, Arakawa, Philo, 1996) conducted in the course of this work, the shape did not affect the mass determination (Atkins & De Paula, 2011). In contrast to conventional aSEC experiments, protein elution was not only detected by changes in the A_{280} but also by light scattering (at multiple positions (angles) relative to the primary beam) and changes in the refractive index (differential RI or dRI). The intensity of scattered light, $I(\theta)_{scattered}$, was proportional to the concentration *c* and the molecular mass *M:*

$$I(\theta)_{scattered} \propto \left(\frac{dn}{dc}\right)^2 \cdot P(\theta) \cdot c \cdot M \qquad \text{(equation 5)}$$

The change in the protein's refractive index n as a function of protein concentration c (dn/dc) was assumed to be a constant for protein samples – 0.185 mL/g, according to the manufacturer's instructions and in good agreement with a mean dn/dc value of 0.19 mL/g obtained for all proteins predicted from the human genome (Zhao *et al.*, 2011). The form factor $\mathrm{P}(\theta)$ was set to a value of 1, as the analysed particles were more than 10 times smaller than the wavelength of the incident radiation (Atkins & De Paula, 2011). The concentration c was obtained by RI measurements with an Optilab T-rEX refractometer (Wyatt) and $\mathrm{I}(\theta)_{\mathrm{scattered}}$ at various angles using a Dawn 8^+ MALS detector (Wyatt) and as all other factors not shown in equation 5 were also known, the molecular mass M could be obtained by analysis with the ASTRA 6.1 software (Wyatt). SEC-MALS experiments were principally conducted like aSEC experiments. Pre-equilibrated Superose 6 10/300GL and Superdex 200 10/300GL columns were loaded with 100 µL of sample and used at flow rates of 0.5 mL/min. In contrast to conventional aSEC experiments eluting proteins were not fractionated, and the experiments were performed at room temperature.

II.B.5.7 Isothermal titration calorimetry

Isothermal titration calorimetry (ITC) experiments allowed for the thermodynamic analysis of protein-ligand interactions (Pierce *et al.*, 1999) and were conducted with either a Microcal VP-ITC or a Microcal ITC_{200} calorimeter (Microcal/GE Healthcare). In the sample cell the protein-ligand interaction took place, whereas the reference cell only contained buffer. Upon complex formation by

the stepwise addition of ligand to protein thermal changes were detected by the calorimeter. A feedback mechanism maintained identical temperatures in both cells ("isothermal"), and the required changes in the heating power were recorded as a function of time. The isotherm was obtained by derivation of the thermogram curve with respect to time. In addition the time scale was replaced by the "molar ratio", which indicated the molar excess of ligand over the protein in the cell.

The fitting of the isotherm with the Origin 7 ITC or the NITPIC software (Keller *et al.*, 2012) yielded the desired parameters: The stoichiometry of an interaction was given by the projection of the inflection point onto the x-axis. The enthalpy was the extrapolated intersection point with the y-axis. ΔG could be derived from the steepness of the curve and was related to the enthalpy (ΔH) and the entropy (ΔS) via the Gibbs-Helmholtz equation (red in equation 6), so that at a given temperature TΔS could be calculated. The K_D could be derived from ΔG (blue in equation 6, where R was the universal gas constant (8.314 J/K/mol).

$$\Delta G = \Delta H - T\Delta S = RT \cdot lnK_D \qquad \text{(equation 6)}$$

All experiments were analysed using a 1:1 binding model. For ITC experiments both components had to be in the same buffer, and this was achieved by means of dialysis at 4°C overnight, where the volume ratio between the sample and the dialysis buffer was >2,000. Samples were centrifuged after dialysis, and their concentrations were determined via UV-VIS spectroscopy (section II.B.4.4). Not only proteins were dialyzed but also the peptides (II.A.8). When a peptide did not contain an aromatic residues (e.g. in the case for DYNLL binding motifs of gephyrin), the dry weight of the peptide (provided by the supplier) was considered as reliable. ITC experiments were usually conducted at 25°C, unless otherwise stated. One exception was the characterization of the gephyrin-DYNLL 1 interaction: All experiments shown in chapter III.B were performed at 37 °C. The intervals between two injections were 270 seconds (VP-ITC) and 180 seconds (iTC200), and the data points resulting from the first injection was always discarded.

II.B.6. Structural studies

II.B.6.1 Atomic force microscopy

In this work atomic force microscopy (AFM) (Fotiadis *et al.*, 2002) was used for single molecule analysis. For this purpose the protein was immobilized on a mica surface, which was raster-scanned by a probe consisting of a cantilever and an oscillating tip. A feedback loop ensured that the probe amplitude was kept constant throughout the data acquisition. For this purpose the deflection of a laser beam (directed at the probe) was monitored. Changes in the laser deflection occurred when the tip approached – and briefly interacted with – the immobilized protein, because the resulting atomic forces led to a short decrease of the amplitude of the probe oscillation. These events triggered changes in the feedback loop that aimed to keep the interaction between the tip-surface interactions

constant and yielded a surface topography, which was analysed in terms of the molecular mass distribution and maximum interatomic distances (D_{max}). The following description of the experimental design was adopted from my manuscript including only minor changes (Sander *et al.*, 2013).

Image collection and flattening were carried out by Dr. Ingrid Tessmer. First, protein samples were diluted in SEC-1 buffer to a final concentration of 5 - 10 nM and immediately deposited onto freshly cleaved mica, rinsed with deionized water and dried in a gentle stream of nitrogen. Data acquisition was conducted on a molecular force probe MFP-3D-BIO atomic force microscope (Asylum Research) in oscillating mode using Olympus OMCL-AC240 silicon probes with spring constants of ~2 N/m and resonance frequencies of ~70 kHz. 2 µm × 2 µm images were captured at a scan rate of 0.5 Hz and a resolution of 1024 × 1024 pixels. AFM experiments of wild-type and mutant gephyrin (Geph-ΔL, see section III.A.2.4) were carried out in triplicate.

AFM images were flattened to 3rd order using the Igor Pro based MFP software (Asylum Research). Peak volumes were measured using ImageSXM (S. Barret, University of Liverpool) at the level of individual molecules. Gephyrin's unstructured linker region was often not resolved in the topographical AFM images due to its low height. Wherever connecting linker structures were not resolved, volumes of individual domains were summed up to obtain the total particle AFM volume (see for example the pool of AFM structures in Fig. 22A). Protein molecular masses were derived from the AFM volumes by comparison with a standard linear relationship obtained using calibration proteins (Roth *et al.*, 2012). The molecular mass was derived from the centre positions of Gaussian fits to the distributions of measured volumes (see Fig. 21A) using the software Origin. Error ranges were determined as the standard deviation given by the width of the Gaussian. Typically, molecular masses derived from AFM volume analysis are accurate to within 10% (Ratcliff & Erie, 2001). All particles with molecular mass consistent with a gephyrin trimer (or within one standard deviation, SD, from the Gaussian centre) were chosen for analysis of the maximum diameter (D_{max}).

Particle dimensions (D_{max} and peak heights, $h_{gephyrin}$) were measured using ImageSXM and corrected for AFM tip induced topography convolutions as previously described (Winzer *et al.*, 2012). Briefly, the widths of DNA fragments was measured with the same AFM probe used for imaging of the gephyrin samples, before and after gephyrin analysis. DNA sections were described by assuming a box shape with a width of 20 Å (the theoretical width of the DNA double helix) and height h_{DNA} as measured from the images using the section tool in the MFP software. DNA widths were measured using ImageJ. Comparison of the theoretical DNA width (D_{DNA} = 20 Å) and the measured width (W_{DNA}) provides the radius of curvature of the employed AFM tip (r_{tip}):

$$r_{tip} = \frac{(W_{DNA} - D_{DNA})^2}{8\, h_{DNA}} \qquad \text{(equation 7)}$$

r_{tip} was calculated by intrapolation from the DNA images for each gephyrin deposition, resulting in r_{tip} values of 6.6 nm, 7.7 nm and 11.1 nm for the wild-type protein and 5.1 nm, 5.3 nm and 5.5 nm for Geph-ΔL. Finally, the contribution from the AFM tip to particle dimensions in the AFM images can be calculated and subtracted using equation 2 to obtain estimates of the true D_{max} values ($D_{max,corrected}$):

$$D_{max,corrected} = D_{max,measured} - 2 \cdot \sqrt{2\,h_{gephyrin} \cdot r_{tip} - h_{gephyrin}^{2}} \qquad \text{(equation 8)}$$

All D_{max} values reported here have been corrected for AFM tip effects. For analysis, particles in the images were grouped according to the number of segments visible, from one segment for globular particles to four segments for highly extended molecular assemblies. Distributions of D_{max} data for the separate globular and extended species were Gaussian with $R^2 > 0.94$.

II.B.6.2 Small angle X-ray scattering

II.B.6.2.1 X-ray scattering

With small angle X-ray scattering (SAXS) biomolecules can be characterized in solution on the nm-scale, whereas crystallography can reveal atomic details. There are some similarities shared by both methods: In both approaches sample atoms are irradiated by an X-ray beam and act as sources of secondary waves, which possess the same frequency as the incident beam (elastic scattering). Secondary waves emitted by several atoms can interfere constructively or destructively, leading to the summation of amplitudes or their cancelling-out, respectively (illustrated in Fig. 11A).

In crystals the sample molecules are at fixed positions, allowing for inter-molecular scattering events. Conversely, molecules can freely rotate and translate during SAXS experiments, restricting scattering events in this approach to the intra-molecular level (Fig. 11B). These factors lead to a significantly higher resolution in X-ray crystallography. Nevertheless, SAXS allows for shape determination of molecules recalcitrant to crystallization (Koch *et al.*, 2003, Mertens & Svergun, 2010, Serdyuk *et al.*, 2007). The approach also turned out to be useful for the characterization of flexible assemblies (Bernado & Svergun, 2012), which are not easily amenable to crystallization. The four previously mentioned references give a good overview of SAXS (Bernado & Svergun, 2012, Koch *et al.*, 2003, Mertens & Svergun, 2010, Serdyuk *et al.*, 2007), and some of their key points are summarized in the following as well as in subchapters II.B.6.2.2 – II.B.6.2.7.

The consideration of atoms as secondary sources of electromagnetic waves, the description of waves by complex numbers and the concept of interference (Fig. 11A) help to incorporate the information on the spatial distribution of atoms in a Fourier transform:

$$F(s) = \sum_J f_J e^{irs} = \sum_J f_J e^{i\varphi} \qquad \text{(equation 9)}$$

Atom j is characterized by f_j, r and φ (the scattering amplitude, the position relative to the origin, and the phase difference, respectively). s is the scattering vector (its derivation is given in Fig. 2A), also referred to as momentum transfer 4π sin(θ)/λ, with 2θ being the scattering angle and λ the

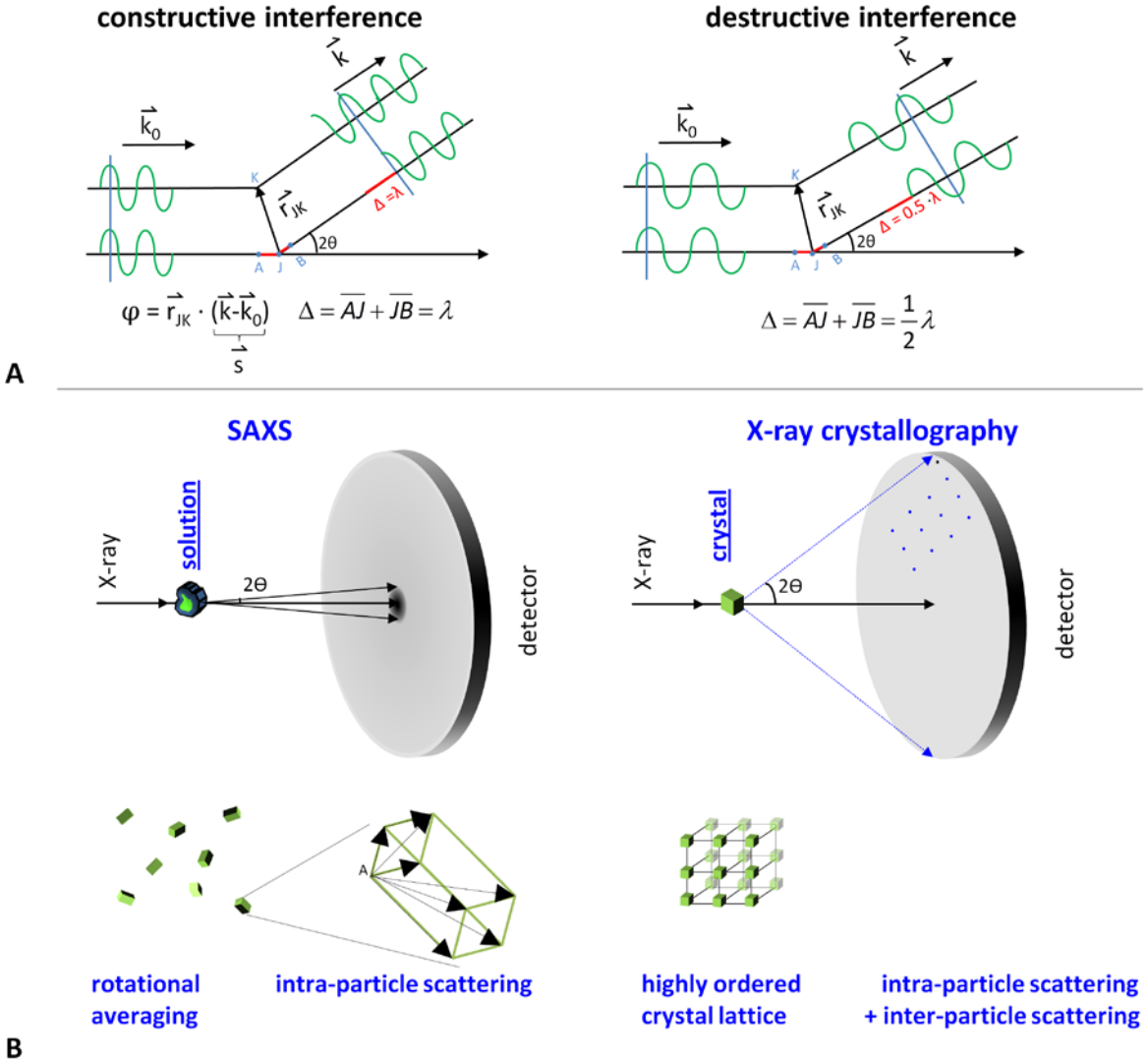

Figure 11 X-ray scattering. (A) An incident beam, represented as vector k_0 gets scattered at atoms J and K by the angle 2θ. In case of constructive interference the resulting secondary waves are in phase, because the path difference Δ (the delay between waves scattered by J and K) is equal to the wavelength λ (or more generally an integer multiple of λ, see also Fig. 13). The phase difference φ is 2π and equals the dot product of the distance vector r_{JK} and the scattering vector s (s=4π sin(θ)/λ). In case of destructive interference, the path difference Δ is (2n+1)·λ, where n is an integer. The addition of amplitudes results in cancellation. Note that 2θ and λ are different in the two scenarios. (B) Differences between SAXS (left-hand side) and X-ray crystallography (right-hand side). While in SAXS solutions give rise to radial scattering patterns, in crystallographic experiments ideally punctate scattering patterns are obtained. In SAXS inter-particle scattering is absent, and intra-particle scattering (indicated exemplarily by the arrows emanating from atom A) represents the primary source of information. Further details are given in the main text.

wavelength of the incident beam. Given the absence of inter-particle interference and the rotational averaging of N particles, the scattering intensity $I_N(s)$ can be described by the integral form of the Debye equation:

$$I_N(s) = \langle |F(s)|^2 \rangle = N \int \int (f_j - \rho^0 v_j)(f_k - \rho^0 v_k) \frac{\sin sr_{jk}}{sr_{jk}} dv_j dv_k \quad \text{(equation 10)}$$

Here, $\rho^0 v_J$ and $\rho^0 v_K$ are the solvent scattering intensities of atoms J and K and N the number of particles. Spherical averaging allowed to replace $e^{-i \cdot s \cdot r_{JK}}$ by $\frac{\sin sr_{JK}}{sr_{JK}}$ (Koch *et al.*, 2003, Serdyuk *et al.*, 2007) .

II.B.6.2.2 Data acquisition

In 2011 and 2012 synchrotron X-ray scattering data were collected at 10°C at the EMBL X33 beamline (DESY, Hamburg) (Roessle *et al.*, 2007) using a robotic sample changer (Round *et al.*, 2008) and a PILATUS 1M pixel detector (DECTRIS, Baden, Switzerland) at a sample-detector distance of 2.7 m and a wavelength of 1.54 Å. This set up covered a range of momentum transfer of 0.008 $Å^{-1} < s < 0.6$ $Å^{-1}$. In 2013 data were obtained at the EMBL P12 beamline (DESY, Hamburg) using a 2D photon counting Pilatus 2M pixel X-ray detector (Dectris) at a sample-detector distance of 3.1 m and a wavelength of 1.24 Å. This set up covered a range of momentum transfer of 0.006 $Å^{-1} < s < 0.33$ $Å^{-1}$.

Samples were prepared using aSEC columns (Superdex 200 10/300GL and Superose 6 10/300GL) (II.B.5.5) equilibrated in SEC-1 buffer, unless otherwise stated. Immediately before the SAXS experiments, samples were centrifuged for more than one hour at 4°C and more than 20,000 g. Then proteins were diluted as given in Table 27. In 2013 DTT at a final concentration of 1 mM was added immediately before data acquisition.

Protein	year	dilutions [mg/mL]						
		a	b	c	d	e	f	g
DYNLL1	2012	10	7	3	1.5			
DYNLL1	2013	7.5	3.8	2	1	0.5	0.3	
DYNLL1	2011	8	4	2	1			
Geph:dimerized β loop	2012	7	4	2	1			
Geph:DYNLL 1	2012	12	8	4	2			
Geph:DYNLL1	2013	10	7.5	5	2.5	1.5	1	0.5
Geph:DYNLL1	2011	8	4	2	1			
Geph-CL1	2012	10	8	4	2			
Geph-CL2	2012	12	7.5	3	1.5			
Geph-CL3	2012	12	7.5	3	1.5			
GephΔL	2012	8	4	2.5	1.3			
Geph-GL	2013	5	3.5	2	1	0.5		

Geph-GL220	2011	8	4	2	1			
GephGL220:DYNLL1	2012	7	3.5	2	1			
GephGL220:DYNLL1	2011	8	4	2	1			
Geph-GL253	2012	10	7	3	1.5			
Geph-LE	2013	9	6	3	1.5	1	0.5	
Geph-MLH1	2012	2	1.5	0.5				
Geph-MLH2	2012	6.5	4	3	1.5			
Geph-S309E	2012	10	5	2.5	1.3			
Geph-S333E	2012	12	7.5	3	1.5			
GephWT	2013	9	6	3	1.5	0.5	0.3	
GephWT	2011	8	4	2	1			
GephWT	2012	12	7.5	3	1.5			
GephWT (hexamer)	2012	10	8	4	2			
MBP-L	2013	9	6	3	1.5	1	0.5	
$NL2_{cyt}$	2013	9	6	3	1.5	1	0.5	

Table 27 Dilution series of proteins subjected to SAXS analysis. Complexes are indicated by a colon. The GlyR β-loop was dimerized by Hans Maric using a dibromobimane crosslinker (Maric, 2012). All gephyrin variants were analysed in their trimeric state, unless stated otherwise.

II.B.6.2.3 Data processing

The forward scattering I(0) and the radius of gyration (R_g) were calculated using the Guinier approximation and assuming that at very small angles ($s < 1.3/R_g$) the intensity was represented as

$$I(s) = I(0) \cdot e^{-\frac{sRg^2}{3}} \quad \text{(equation 11)}$$

The R_g is the mass weighted distance of each atom from the centre-of-mass of the particle and contains therefore information about the overall dimensions of a molecule:

$$R_g = \sqrt{\frac{\sum_i r_i^2 \cdot m_i}{\sum_i m_i}} \quad \text{(equation 12)}$$

Another approach to evaluate the overall dimensions was the calculation of the pair-distance distribution function P(r), which yielded estimates of the maximum particle dimension (D_{max}), I(0) and R_g. The P(r) function is the rearranged inverse Fourier transform of the Debye equation (equation 10) and was computed using GNOM (Svergun, 1992).

When a concentration dependence of the R_g was observed, PRIMUS (Konarev et al., 2003, Petoukhov et al., 2012) was used to extrapolate to theoretical infinite dilution. Alternatively, the small-angle data (0.008 $Å^{-1} < s < 0.12$ $Å^{-1}$) obtained at the lowest concentration were merged with data at the highest concentration (0.06 $Å^{-1} < s < 0.6$ $Å^{-1}$) or with the program ALMERGE (Franke *et al.*, 2012). Data exhibiting a clearly non-linear concentration dependence were not used for further

analysis, as non-linear concentration dependence can be a sign for complex dissociation (see also section III.B.2.3).

The molecular mass was derived from (1) the forward scattering was obtained by comparison with the I(0) of bovine serum albumin (Sigma-Aldrich), which has a molecular mass of 66.5 kDa (Mylonas & Svergun, 2007), (2) the excluded volume of the hydrated particle using the Porod invariant (Petoukhov *et al.*, 2012), (3) the excluded volumes of DAMMIN models (Svergun, 1999) without symmetry (Petoukhov *et al.*, 2012), (4) the volume of correlation (Rambo & Tainer, 2013) and (5) the SAXS MoW server (Fischer *et al.*, 2009). The molecular mass determination using the forward scattering was considered as the least reliable method because it was prone to erroneous concentrations.

II.B.6.2.4 The target function for modelling processes

Modelling involved the rearrangements of structural units of a given protein (dummy residues or domains of known structure), until its theoretical scattering pattern with intensities I_{model} for experimental s values (here referred to as s_n) displayed the lowest possible deviations from the experimentally derived scattering pattern with intensities I_{exp}. This condition was implemented in the target functions of all modelling programs used in this work which as discrepancy (χ^2):

$$\chi^2 = \frac{1}{N-1}\sum_{n=1}^{N}\left[\frac{\mu \cdot I_{model}(s_n) - I_{exp}(s_n))}{\sigma(s_{c)}}\right]^2 \qquad \text{(equation 13)}$$

Here, N is the number of experimental points, μ is a scaling factor and $\sigma(s_c)$ the experimental error (standard deviation derived from multiple expositions). Depending on the type of modelling further restraints were included, of which the most important are briefly summarized in the respective sections.

II.B.6.2.5 Ab initio modelling

Ab initio models using low resolution data in the range of 0.012 Å^{-1} < s_n < 0.17 Å^{-1} were created with DAMMIN (Svergun, 1999) and DAMMIF (Franke & Svergun, 2009). Using iterative procedures, both algorithms rearrange dummy residues (beads) within a search sphere with diameter D_{max} (obtained from the P(r) function), resulting in a scattering profile with the lowest possible discrepancy (χ^2) to the experimental data while keeping beads interconnected.

Alternative *ab initio* models were created with GASBOR (Svergun *et al.*, 2001) using an extended data range (0.012 Å^{-1} < s_j < 0.25 Å^{-1}). GASBOR requires the number of amino acids in the asymmetric unit and each bead summarizes one residue. Ten independent *ab initio* reconstructions were performed and then averaged using DAMAVER (Volkov & Svergun, 2003), which also provides a value

of normalized spatial discrepancy (NSD) representing a measure of similarity among different models. *Ab initio* models with the lowest average NSD value are shown in the figures.

II.B.6.2.6 (Combined) Rigid body/ab initio modelling

Combined *ab initio* and rigid body modelling was performed with BUNCH (Petoukhov & Svergun, 2005) by imposing threefold symmetry and using available high resolution structures of the individual domains (GephG (PDB code: 1JLJ) and GephE (PDB code: 2FTS)). The program BUNCH models the missing peptide segments as a chain of dummy residues that are separated by 3.8 Å to mimic a C_α chain. However, BUNCH can only be used for single chain modelling and thus is restricted to symmetric assemblies. Rigid body models without symmetry constraints (scenarios I & II, section III.A.2.5.2 & Fig. 25) were created with CORAL (Petoukhov *et al.*, 2012). As CORAL imposes a limit for the maximum linker length (99 residues) an alanine residue at position 263 (numbering includes the His-tag of the pET28 vector) was defined as accessory rigid body allowing the linker of 150 residues to be modelled as two linker segments of 59 and 90 residues, respectively. The modelling process is iterative and also aims to minimize χ^2 (equation 13). Ten models were generated for each scenario, this time using data in the range of 0.012 $Å^{-1} < s < 0.258$ $Å^{-1}$. After modelling the theoretical scattering profiles were computed with CRYSOL (Svergun *et al.*, 1995), fitting the experimental data within the interval 0.012 $Å^{-1} < s < 0.5$ $Å^{-1}$, using constant subtraction. Models with the lowest χ^2 value were taken as reference models and are presented in the figures. Rigid body modelling shown in this work was only conducted with GephWT.

II.B.6.2.7 Ensemble optimization method (EOM)

Flexibility was assessed with the ensemble-optimization method (Bernado *et al.*, 2007) (Fig. 12), which assumes the coexistence of a range of conformations in solution for which an average scattering intensity fits the experimental SAXS data. In the first step, an enhanced version of RANCH (Petoukhov et al, 2012) was used to create a pool of M=1,000,000 independent models (GephWT & GephΔL), 500,000 models (Geph-MLH1/2) and 250,000 models (GephGL variants, GephLE, MBPL and $NL2_{cyt}$) exhibiting either overall symmetry or no symmetry concerning the flexible parts and (if present) E domain. In this procedure residues belonging to flexible segments or the His-tags were modelled to adopt “native-like dihedral angles” instead of “random-coil dihedral angles” (defined by default in RANCH, see Appendix C). The theoretical scattering curve was then automatically computed for each model in the pool by CRYSOL (Svergun *et al.*, 1995). Afterwards, a genetic algorithm (GAJOE) selected ensembles of a varying number of conformers (from 2 to 20) by calculating the average theoretical profile and fitting it to the experimental SAXS data; again χ^2 was used as target function. The genetic algorithm was repeated 100 times (number of generations G =

M/500; number of ensembles C=M/1,000, see Fig. 12) and the ensemble with the lowest discrepancy was reported as the best solution out of 100 final ensembles.

Volume fractions of the corresponding models were confirmed by OLIGOMER (Konarev *et al.*, 2006). In order to distinguish between EOM models that show extended and compact conformations, two distributions, for R_g and D_{max}, respectively, were calculated using all the models belonging to the selected ensembles. Models with R_g and D_{max} values above the average values of the initial pools were classified as extended, and models with values below the average as compact.

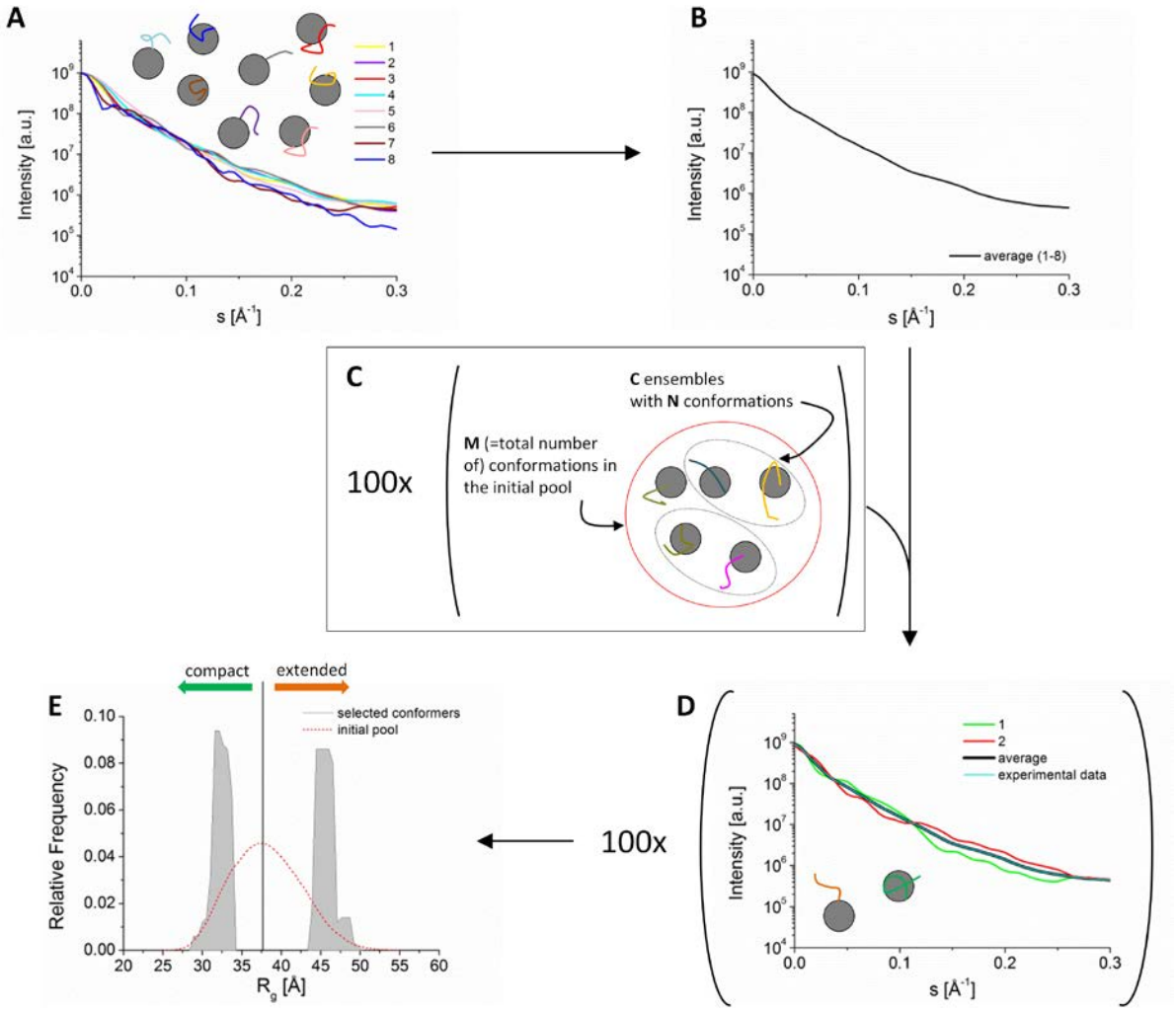

Figure 12 Principle of the ensemble optimization method (EOM). (A) Flexible proteins can be regarded as an ensemble of conformers. The scattering pattern of such a sample represents the average profile of all conformers (B). (C) In EOM first a large pool of M conformers is generated (using RANCH), of which C ensembles with N conformers are created (using the genetic algorithm GAJOE). The ensemble that (after G iterations) displays the best fit to the experimental data (D) is selected. This process is repeated for 100 times resulting in 100 ensembles. In E the R_g distributions of all M conformers ("initial pool") is compared to the corresponding distribution of all *selected* conformers. In this case extended and compact conformers equally contribute to the scattering profile. In this thesis always the enemble with the best fit to the data is displayed in the figures. Note that the chosen conformers represent just a rough approximation of the real situation (compare A & D).

II.B.6.2.8 Generation of scattering curves for test purposes

Some modelling programs were tested with respect to their reliability in the context of the complex gephyrin system containing a long linker, which could principally give rise to artificial models. As it was possible to create a scattering profile for any given conformer (using CRYSOL), one could test for example if the input scattering profile of a conformer with a certain feature resulted in the reconstruction of a model with the respective characteristic feature. If this feature was absent in the obtained model, a limitation of the modelling method was indicated. As unedited scattering profiles obtained with CRYSOL did neither contain experimental errors nor noise, these two parameters were imposed on the CRYSOL curves at levels similar to those of experimental scattering curves.

In a first step DAMMIN was used to fit the 2012 GephWT data, yielding excellent fits (Table 31). CRYSOL was used to recalculate the DAMMIN model scattering profile, yielding a curve with 256 data points equally distributed in a range of $0\ Å^{-1} < s < 0.5\ Å^{-1}$. The intensity differences between this idealized CRYSOL scattering curve and the experimental curve were then defined as “experimental noise”. Experimental errors were taken from the 2012 GephWT dataset, and errors in the small-angle region ($s < 0.01\ Å^{-1}$) were extrapolated. Real experimental errors and extrapolated errors are collectively referred to as “experimental errors” and indicated by quotation marks. These two parameters were added to the 256 data points of the CRYSOL curve generated from any tested conformer. Most of these tests concerned the reliability of *ab initio* modelling and EOM.

II.B.6.2.9 Calculation of R_g values for isolated linkers

EOM provided information on the compactness of assemblies. The common denominator of GephWT, GephGL and GephLE was the linker region. To obtain an additional measure of compactness, the radii of gyration of the isolated linkers of all conformers of the selected EOM ensembles were calculated using CRYSOL. For this purpose the GephG and GephE portions had to be deleted from the PDB files of the selected ensembles, and a PYTHON script was used for that (see Appendix B). The obtained values were weighted by the contribution of the respective conformers to the scattering pattern (as judged by the number of curves in the respective EOM log file).

II.B.7. Crystallography

X-ray crystallography can be used to determine structures of macromolecules with Å-accuracy. For this purpose crystals had to be obtained, which were used to diffract X-rays (see also section II.B.6.2 and Fig. 11). First crystallization is described, followed by data collection and analysis. As pointed out above, some key concepts are shared by SAXS and crystallography, and the reader is therefore also referred to the SAXS chapter II.B.6.2. As a matter of fact I can provide only a rough

overview of a few selected principles of crystallography. Further details are found in several books on this topic (Blow, 2002, Rupp, 2009, Sherwood & Cooper, 2011), which provided also the basis for the theoretical considerations given in the following.

II.B.7.1.1 Crystallization

The goal of crystallization was a single crystal, representing a highly ordered, regular array of macromolecules. Crystallization, as used in this work, relied on vapour diffusion. Proteins were mixed with the precipitant solution. As a consequence their concentrations decreased. However, the transfer of this small drop (2-6 µL) into a closed system containing 1 mL of the undiluted precipitant solution results in vapour diffusion and increasing concentrations of protein and precipitant in the drop. Depending on the condition the protein does not change its aggregate condition, forms aggregates or ideally crystals. The latter were provided starting points for the determination of a crystal structure. As crystallization conditions were unknown, high-throughput screening with the HoneyBee 963 crystallization robot (Genomic Solutions) and several crystallization screens (II.A.4) was performed. In a 96-well crystallization plate (Greiner Bio-One International AG) 0.3 µL protein and 0.3 µL precipitant solution were mixed and equilibrated against 40 µL of reservoir. At this stage vapour diffusion took place in the sitting drop setup, in which the protein-precipitant drop resided on a shelf. Crystallization plates were checked for crystals on a daily basis within the first week, afterwards every second to third day (within the first two to three weeks) and then on a weekly basis.

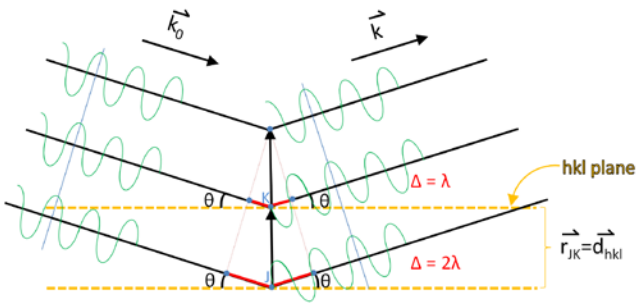

Figure 13 Bragg's law. Secondary waves emitted from atoms J and K (both are part of the same set of hkl planes) give rise to constructive interference (indicated by the arrows), as the path difference Δ equals an integer multiple of the wavelength λ of the incident beam. J and K are separated by d_{hkl}, the characteristic spacing between the hkl planes.

Promising conditions were chosen for follow-up refinement, in which vapour diffusion was achieved by the hanging drop method: The protein-precipitant solution was pipetted on a cover slide which was turned around and also served to seal the reservoir. Several parameters were changed with respect to the initial condition: Larger volumes were used. Mixtures of 1-3 µL protein solution and 1-3 µL precipitant solution were equilibrated against 1 mL reservoir. The experiments were conducted in a 24-well format, so two parameters of the original precipitant solution were changed (e.g. the pH and the precipitant concentration). Sometimes several drops containing protein at different concentrations were applied to the same cover slide. In addition parameters like the temperature, different protein

buffers etc. were varied (in separate experiments). Once single crystals were obtained, they were transferred to cryoloops which were immersed in the crystallization condition containing a cryoprotectant to avoid freezing damage during subsequent flash-freezing. In the case of the putative crystals of GephGL220-DYNLL1 and GephE-NL2$_{cyt,sh}$ glycerol was used as cryoprotectant at concentrations of 20% (v/v) and 33%, respectively. Crystals were stored in liquid nitrogen.

II.B.7.1.2 Data collection

During data collection flash-cooled crystals were irradiated by X-rays. Atoms emit a secondary wave which can constructively or destructively interfere with other secondary waves emitted by other atoms, leading to the summation of amplitudes or their cancelling-out, respectively (Fig. 11). Diffraction can be regarded as occurring on lattice planes, which are characterized by the Miller indices h, k, l and specific inter-plane distances d_{hkl} (Fig. 13). When these planes are in an appropriate orientation with respect to the primary beam, Bragg's law is satisfied and constructive interference is achieved (Fig. 13). To obtain sufficient information, the crystal has to be rotated, so that different planes are exposed to the primary beam and suffice Bragg's law:

$$n\lambda = 2d_{hkl}\, sin\theta \qquad \text{(equation 14)}$$

In equation 14 n is an integer, λ the wavelength of the primary beam and θ the angle that is made between the hkl plane and the incident beam (Fig. 13).

For initial characterization of single crystals in-house data collection was performed with a MicroMax-HF 007 generator (Rigaku) at a wavelength of 1.5418 Å and an R-AXIS HTC imaging plate detector. Two images were taken from crystals which were rotated by 0.5° during the 5-10 minutes long exposure interval, on at the initial position ("0°") and another one after rotation by 90°. Afterwards crystals were judged by resolution and mosaicity (a measure for the broadness of the spots correlating with crystal lattice disorder). For the most promising crystals of putative GephGL220-DYNLL1 and GephE-NL2$_{cyt,sh}$ complexes complete datasets were recorded at the synchrotron beamlines MX 14.1 (BESSY, Berlin) and ID29 (European Synchrotron Radiation Facility, Grenoble), respectively.

II.B.7.1.3 Data processing

Crystals are ideally composed of a regular three-dimensional array of unit cells which ideally possess the same content in exactly the same orientation. To derive the unit cell content, first the arrangement of the unit cells relative to each other was determined by indexing the datasets, which yielded the space group and the cell axes and angles as well as the orientation of the axes with respect to the primary beam and the mosaicity. Then pixels belonging to each reflection were integrated. Data procession was carried out with MOSFLM (Battye *et al.*, 2011). The space group was determined using POINTLESS (Evans, 2011), and equivalent reflections were scaled and merged with

SCALA (Evans, 2011). Initial data procession terminating after space group determination was also carried out to determine the data collection strategy (II.B.7.1.2).

Unfortunately, the measured intensities, which are proportional to the square of the structure factor amplitudes, are not sufficient to derive the unit cell content given by the electron density equation, which is related to equations 9 and 14:

$$\rho(x,y,z) = \frac{1}{V}\sum_h \sum_k \sum_l |F(hkl)|\, e^{i\cdot\varphi(hkl)-2\pi\cdot i(hx+ky+lz)} \qquad \text{(equation 15)}$$

$\rho(x,y,z)$ is the electron density, V is the volume of the cell, $|F(hkl)|$ the structure factor amplitude, φ the phase and x, y and z the coordinates in real space. However, the measured data do not contain information on the phases, which are essential for structure determination. TRUNCATE was used to convert intensities into structure factor amplitudes (Evans, 2011), but the loss of phases (also called the phase problem in crystallography) had to be overcome by a different approach presented in the next section.

II.B.7.1.4 Solution of the phase problem by molecular replacement

Principally, phases can be obtained using multiwavelength anomalous diffraction (MAD) or multiple isomorphous replacement (MIR) and its derivatives (SAD, SIR, MIRAS, SIRAS). However, as crystal structures of GephG and GephE were available, molecular replacement was used for phase determination. For this purpose the phase-independent Patterson function was calculated for both the search model (GephG or GephE) and the experimental data, and the corresponding maps were rearranged by translation and rotation until the maximum correlation between the maps was achieved. Molecular replacement was conducted with the programs MOLREP (Vagin & Teplyakov, 2010) and PHASER (McCoy *et al.*, 2007). The phase determination was successful for the data obtained from putative GephGL220-DYNL1 crystal, but electron density could only be assigned to GephG dataset (see Table 39). For the dataset on the putative GephE-NL2 complex no molecular replacement solution was found. So the following description applies only to the GephG dataset.

II.B.7.1.5 Refinement

Manual model building was performed with the program COOT (Emsley & Cowtan, 2004), with which the respective current model was displayed in stick representation and was superposed with electron density maps. COOT provided the tools to modify the model, e.g. by the addition and deletion of atoms/residues/molecules or the reorientation of side chains. This model was used as input for automated refinement with REFMAC (Murshudov *et al.*, 1997), in which stereochemical restraints from known high-resolution structures were included as e.g. bond lengths and angles. Non-crystallographic (NCS) restraints were used, as several copies of a component were present in the asymmetric unit cell. Another optional restraint was added by Translation/Libration/Screw (TLS)

refinement, in which all atoms of defined segments were assumed to exhibit similar flexibility. The rigid body segments, which were subject of TLS refinement, were determined with the TLSMD server (Painter & Merritt, 2006). The refinement aimed to reduce the R-factor, which is related to the difference between observed and calculated structure factor amplitudes, F_{obs} and F_{calc}, respectively:

$$R = \frac{\sum_{hkl}||F_{obs}(hkl)|-|F_{calc}(hkl)||}{\sum_{hkl}|F_{obs}(hkl)|} \quad \text{(equation 16)}$$

To minimize model bias, 5% of the reflections were reserved for a test set and not used for refinement as the other 95% (the working set). Also for the test set the R-factor was calculated, referred to as R_{free}, while the R factor of the working set was called R_{cryst}. The difference between R_{cryst} and R_{free} should be in the range from 5 to 10%. Another measure to improve structure quality was the weighting of the two terms concerning the reduction of the R factor and the mentioned restraints.

II.B.7.1.6 Structure validation

To assess the quality of the structure, several parameters beyond R_{cryst} and R_{free} can be used, some of which are presented here:

- R_{merge} was calculated in the context of data procession and was used to assess the reproducibility of multiple measurements of a given reflection (and its symmetry mates):

  $$R_{merge} = \frac{\sum_{hkl}\sum_{i=1}|I_i-\langle I\rangle|}{\sum_{hkl}\sum_{i=1} I_i} \quad \text{(equation 17)}$$

  I_i was the i^{th} measurement and $\langle I\rangle$ the weighted mean of all measurements of I. The use of this parameter is not undisputed, as R_{merge} increases with the number of observations, although higher redundancy is expected to increase the fidelity of the data (Diederichs & Karplus, 1997).
- $\langle I/\sigma(I)\rangle$ was likewise obtained after data procession and indicated the ratio of the average intensity and the corresponding standard deviation. Root mean square deviations (rmsds) in bond lengths (Å) and bond angles (°), should not exceed values of 0.01–0.02 Å and 2°, respectively.
- The peptide backbone of each residue can be described by the dihedral angles ϕ and ψ. The reference Ramachandran plot displays the probability of all ϕ/ψ pairs in a reference set of proteins. Regions with a high probability are called favoured, vice versa regions with minimum probability are considered as disallowed. The superposition of the reference Ramachandran plot and the Ramachandran plot of the final model reveals stereochemical abnormalities, which should not occur at a high frequency. Ramachandran statistics performed with RAMPAGE yielded the fraction of residues in the favoured, allowed, and disallowed regions of the Ramachandran diagram.

III. RESULTS & DISCUSSION

III.A. Gephyrin

III.A.1. Introduction

As mentioned above gephyrin has been assumed to self-assemble into a hexagonal lattice (sections I.C.1, I.C.5, Fig. 3). This introduction will focus on the properties of gephyrin which are already known to contribute/regulate its oligomeric state.

III.A.1.1 GephG

GephG is of globular shape and forms trimers via predominantly hydrophobic interfaces, in which three quarters of the contributing residues are hydrophobic (Schwarz *et al.*, 2001, Sola *et al.*, 2001) (Fig. 14A). For the *Arabidopsis thaliana* orthologue CNX1G, the crystal structure was solved in the presence of the MPT-AMP product (Kuper *et al.*, 2000), and GephG shares a very similar active site with CNX1G (Schwarz *et al.*, 2001), so that a superposition of both proteins results in a model of a GephG-MPT-AMP complex devoid of steric clashes (Fig. 14B). The insertion of the 13 residue-splice cassette G2 (previously referred to as C5 cassette) was shown to disturb trimerization (Bedet *et al.*, 2006) and consequently Moco biosynthesis as well as receptor clustering, which both rely on an intact trimerization (Bedet *et al.*, 2006, Calamai *et al.*, 2009, Smolinsky *et al.*, 2008) (Fig. 14B).

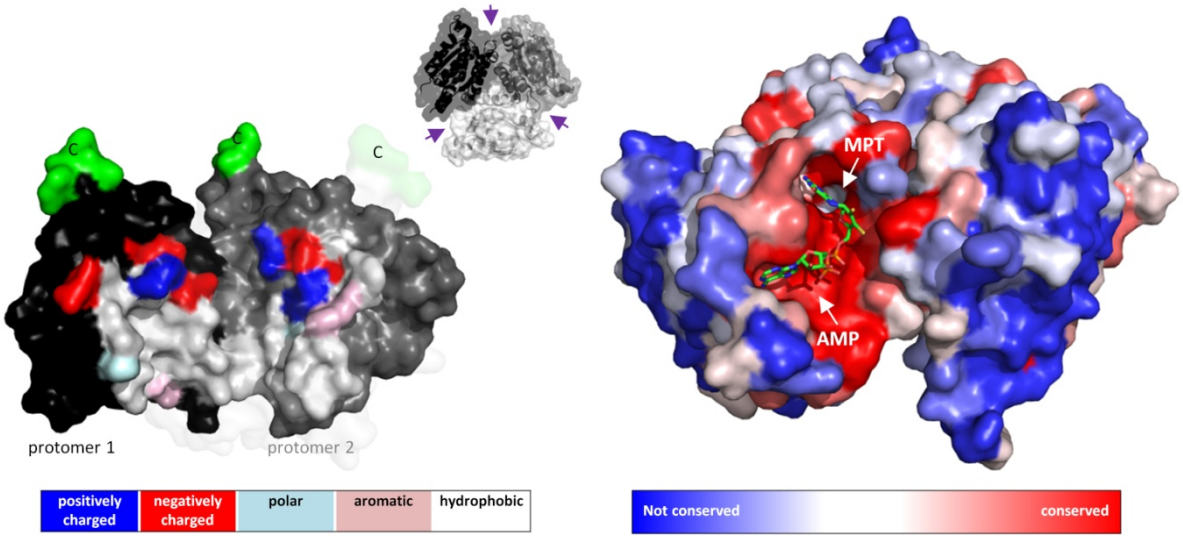

Figure 14 Structure of GephG. (A) GephG interface residues are largely hydrophobic. Protomer 3 from the upper pannel (top view) was removed in the side view, in which protomer 1 and 2 are coloured in black and grey, respectively. The C-termini are marked in green, and the colour code shown below highlights the character of the interface residues. The arrows in the upper pannel indicate the active site for the adenylation of MPT. (B) Residues involved in Moco biosynthesis are quite conserved while the other surface residues are not. The MPT-AMP stick model was obtained by the superposition of GephG (PDB code: 1JLJ) and CNX1G (PDB code: 1UUY). Note that this product does not sterically clash with GephG.

III.A.1.2 GephE

While GephG is of globular shape, GephE adopts an L-shaped elongated conformation. Two GephEs intercalate to form a dimer, at whose interface a common binding site for the GlyR β subunit and $GABA_AR$ subunits 1, 2 and 3 is provided (Fig. 15A, (Kim *et al.*, 2006)). The well conserved active site for Moco biosynthesis was mapped to another dimer interface, and indeed both protomers are required to catalyze the insertion of molybdenum into the pterin moeity (Nichols *et al.*, 2007) (Fig.

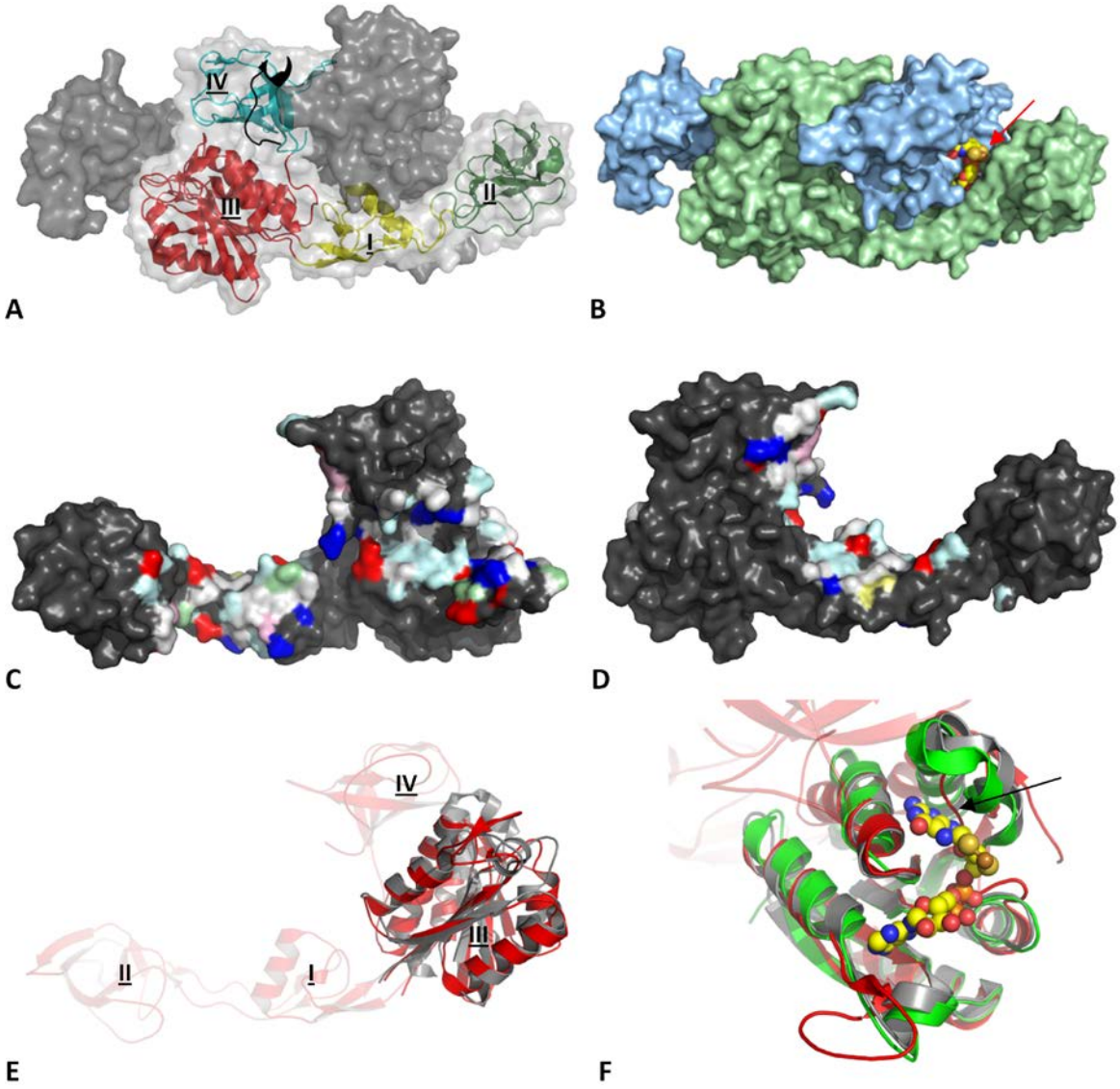

Figure 15 Structure of GephE. (A) GephE in its isolated form dimerizes. One protomer is highlighted by a grey, the other by a white surface representation. In the latter protomer the subdomains I-IV are marked. A GlyR β loop-derived peptide (black cartoon representation) binds to subdomains III and IV. (B) The active site for molybdenum insertion into the pterin moiety is marked with a red arrow. (C & D) The GephE dimer interface is non-continuous and contains a relatively high content of either charged or polar residues. The colour code is the same as in Fig. 14. (E) Superposition of GephG and subdomain III of GephE. (F) The superposition of CNX1G with the superposition of (E) underscores the high structural similarity of all three proteins. There is only one major difference in GephE, which leads to a sterical clash with MPT-AMP (marked by an arrow).

15B). One protomer can be divided into four subdomains (Kim *et al.*, 2006, Xiang *et al.*, 2001) (Fig. 15A). Subdomains 3 and 4 share a relatively large interface (~700 Å), so that they can be regarded as a relatively rigid entity. In comparison to this unit, subdomains 1 and 2 are small, and the hinge region between subdomains 1 and 2 was observed to contribute to flexibility, as mirrored by different orientations of subdomain 2 with respect to subdomains 1, 3 & 4 in several crystal structures (Nichols et al., 2007). In comparison to the GephG trimerization the contribution of hydrophobic residues to GephE dimerization is reduced to about one half (Fig. 15C&D). Despite the relatively high sequence similarity of GephE to the *E. coli* orthologue of 45%, the dimerization interface is not conserved (Sola *et al.*, 2004).

Notably, subdomain 3 shares a similar fold with GephG (Xiang *et al.*, 2001) (Fig. 15E) and was shown to harbour residues important for Moco biosynthesis (Nichols *et al.*, 2007). The superposition of CNX1-MPT-AMP with subdomain 3 of GephE leads to a GephE-MPT-AMP assembly (Nichols *et al.*, 2007) (Fig. 15E&F), which displays only a few steric clashes of one ring of the pterin moeity and GephE. However, the remainder of the cofactor matches well into the putative GephE active site, which contains residues that were shown to be crucial for catalysis of molybdenum insertion (Nichols *et al.*, 2007). The active site is not restricted to GephE subdomain 3 but also comprises significant patches of subdomain 2 of another GephE protomer.

III.A.1.3 GephL

While the structures for the terminal domains were solved, the structural features of the 136 to 196 residue-linker have remained elusive so far (Fritschy *et al.*, 2008, Nichols *et al.*, 2007, Tretter *et al.*, 2012). However, alternative splicing and phosphorylation have been investigated and are expected to give rise to a large heterogeneity of gephyrin, particularly in GephL. Their consequences are introduced above (section I.C.2).

III.A.1.4 Substrate channeling in Moco biosynthesis

Based on the structural similarity of GephG and subdomain 3 of GephE (Fig. 15E) a model was proposed in which the active site portions of GephE subdomain 2 and of GephG are in close proximity (Belaidi & Schwarz, 2012, Fritschy *et al.*, 2008). This model, in which three GephE monomers surround a trimeric GephG core can serve to explain the transfer of the GephG product MPT-AMP to the GephE (Belaidi & Schwarz, 2012, Fritschy *et al.*, 2008) (Fig. 16), however, as GephE dimerization could not occur without significant changes, this conformation could not catalyze the last step in Moco biosynthesis, as the active site of GephE, which requires two monomers (Nichols *et al.*, 2007) (Fig. 15B), could not be assembled in this conformation. In addition, this conformer would not be compatible with the proposed hexagonal scaffold.

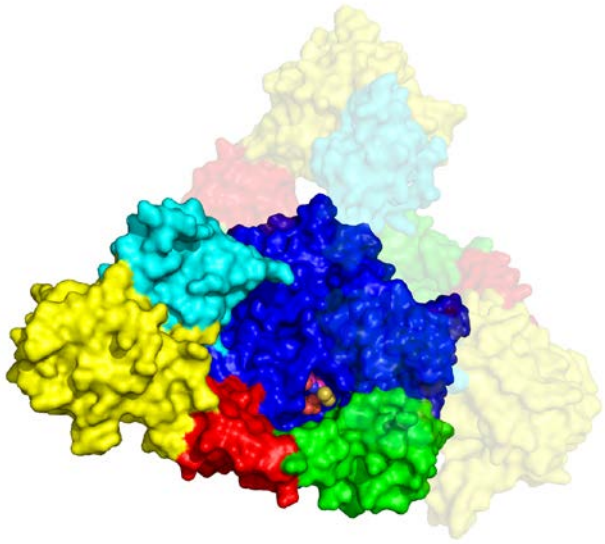

Figure 16 Proposed structural model for gephyrin trimers. GephG and subdomain 3 of one GephE protomers in the context of a GephE dimer were superposed as in Fig. 15E. The GephE protomer that superposed with GephG was then deleted. Especially, subdomain 2 (green) of GephE is in close proximity to the active site of GephG. Both the GlyR/$GABA_AR$ binding site and the putative collybistin site are solvent accessible (not shown). For the linkers no assumptions were made, hence they are not displayed (Belaidi & Schwarz, 2012, Fritschy *et al.*, 2008).

III.A.1.5 Gephyrin oligomers after overexpression or heterologous expression

The mentioned hexagonal lattice has never been observed directly. However, a recent single-molecule analysis in neurons pointed to a high density of gephyrin molecules at inhibitory synapses. Herein, a gephyrin density of 5,000 to 10,000 molecules per µm² was estimated. In addition in spinal cord neurons a 1:1 stoichiometry of gephyrin to the GlyR was determined, arguing for a close packing of gephyrin at the synapse as well (Specht *et al.*, 2013).

The hexagonal scaffold has appeared to be a logical consequence of the presence of two oligomerization domains in gephyrin. Later on, further studies corroborated this view: The absence of either terminal domain abrogated gephyrin clustering (Calamai *et al.*, 2009). Even when the domains were present, the mutation of three and four interface residues in GephE and GephG, respectively, which did not affect glycine receptor binding, led to gephyrin dispersal all over the neuronal somata and dendrites (Saiyed *et al.*, 2007).

Despite these findings, *E. coli*-derived gephyrin was found to be a trimer, arguing for an utilization of the trimeric GephG interface and against GephE dimerization (Schrader *et al.*, 2004, Sola *et al.*, 2004). Gephyrin expressed in *Xenopus laevis* ooycytes (Saiyed *et al.*, 2007) was predominantly organised in a ~640 kDa band, interpreted as a hexamer. SF9 cell-derived gephyrin was reported to form higher oligomers (hexamers, nonamers and even dodecamers) in contrast to *E. coli* derived gephyrin, and the authors attributed this difference to higher phosphorylation levels of gephyrin in SF9 cells (Herweg & Schwarz, 2012). In hepatocytes gephyrin catalyses Moco biosynthesis was shown to be part of a 600 kDa complex that is diffusively distributed in the cytoplasma. The 600 kDa complex roughly corresponds to a gephyrin hexamer but was also suggested to be a heterooligomer containing gephyrin and other Moco biosynthetic enzymes (Nawrotzki *et al.*, 2012).

Gephyrin on its own does not possess the capability to assemble into the proposed submembranous planar hexagonal lattice. For example, gephyrin expressed in HEK293 cells usually assembles into a few large cytoplasmic aggregates (Kirsch *et al.*, 1995), in contrast to hepatocytes (Nawrotzki *et al.*, 2012)) where it prevalently forms hexamers. It seems that these cannot only occur during heterologous expression, because they occur *in vivo* with endogenous gephyrin in the early stages of neuronal development (Colin *et al.*, 1996, Colin *et al.*, 1998, Papadopoulos *et al.*, 2008, Poulopoulos *et al.*, 2009, Sassoe-Pognetto & Wassle, 1997) or upon deletion of $GABA_A$ receptor subunits α1 and α3 (Kralic *et al.*, 2006, Studer *et al.*, 2006) as well. Notably, in HEK293 cells coexpressed GlyR β subunit containing receptors are not targeted to the plasma membrane in the presence of gephyrin and are instead recruited to the large gephyrin aggregates (Kirsch *et al.*, 1995), implying that plasma membrane localization requires neuron-specific factors. The formation of these large intracellular "blobs" relies on both intact GephG and GephE interfaces (Lardi-Studler *et al.*, 2007, Saiyed *et al.*, 2007). In addition, gephyrin blobs were shown to colocalize with the microtubule-organizing centre (MTOC). Interference with the dynein motor function by dynamitin overexpression led to a loss of colocalization with the MTOC, but the blobs persisted (Maas *et al.*, 2006). Therefore the exact composition of these blobs and the mechanisms that resolve these blobs remain to be deciphered. Nevertheless, several binding partners were shown to redistribute gephyrin from its intracellular aggregates to submembraneous compartments. Some of these binding partners are considered in later sections (sections III.B and III.C).

III.A.1.6 Aims

This chapter deals with the structural and biochemical characterization of trimeric *E. coli*-derived gephyrin. This trimeric state is considered to be autoinhibited in terms of impaired dimerization. The relative orientations of GephG-GephE to each other in the context of the full-length protein have remained elusive so far, but their arrangement might help to derive the mechanism(s) by which gephyrin is limited to its trimeric state and consequently how binding partners and posttranslational modifications (sections I.C.2.2, I.C.3.4 & I.D) might influence the oligomeric state, which is considered to be a critical property in terms of receptor clustering.

After an initial bioinformatic assessment of linker flexibility, preparatory steps towards gephyrin's characterization on the nm-scale were carried out. The latter analyses – conducted by means of atomic force microscopy and small-angle X-ray scattering - revealed an unexpectedly high degree of compaction. The ensuing efforts had the aim to identify segments, which are involved in this compaction and whose mutation/truncation potentially pave the way to higher oligomeric species. For this purpose potential interactions between the linker and the terminal domains were characterized, but also the hypothesis that GephG and GephE undergo complex formation was

tested. It should be mentioned that the characterization of apo-gephyrin by SAXS and AFM as well as the CD melting curves of holo-gephyrin, GephG and GephE have already been published (Sander *et al.*, 2013). These data are found in sections III.A.2.1, III.A.2.2, III.A.2.4, III.A.2.5 and III.A.6.2, and these chapters also contain published text.

III.A.2. Results

III.A.2.1 Secondary structure prediction

Gephyrin's susceptibility towards proteolytic digestion (Herweg & Schwarz, 2012) raises the question whether parts of the protein lack tertiary structure. Therefore, bioinformatic predictions of disorder and secondary structure were performed (Fig. 17). Six independent algorithms (Cole *et al.*, 2008, Kelley & Sternberg, 2009, Li *et al.*, 1999, Linding *et al.*, 2003, McGuffin *et al.*, 2000, Pollastri *et al.*, 2002, Ward *et al.*, 2004), which are part of the Phyre server, consistently predicted large parts of the linker to be unstructured (ranging from 56% to 100%). Notably the predicted degree of order/disorder was not evenly distributed in the linker region, and the following four regions of more or less equal length can be distinguished (the end of each segment is indicated by arrows in Fig. 17):

- The N-terminal 41-amino-acid segment of gephyrin's linker (residues 181-222) was predicted to contain a low secondary structure content of 26% ± 6% (obtained from the average sum of the α-helix and β-strand contents, predicted by the three algorithms PSIPRED, JNet and SSPro). However, this number might underestimate the real situation, as poly-proline helices are not considered by these algorithms. Two regions could potentially contain poly-proline helices (turquoise patches in Fig. 17), namely a proline-rich region (residues 187-201) and a cluster of charged residues (residues 213-222).

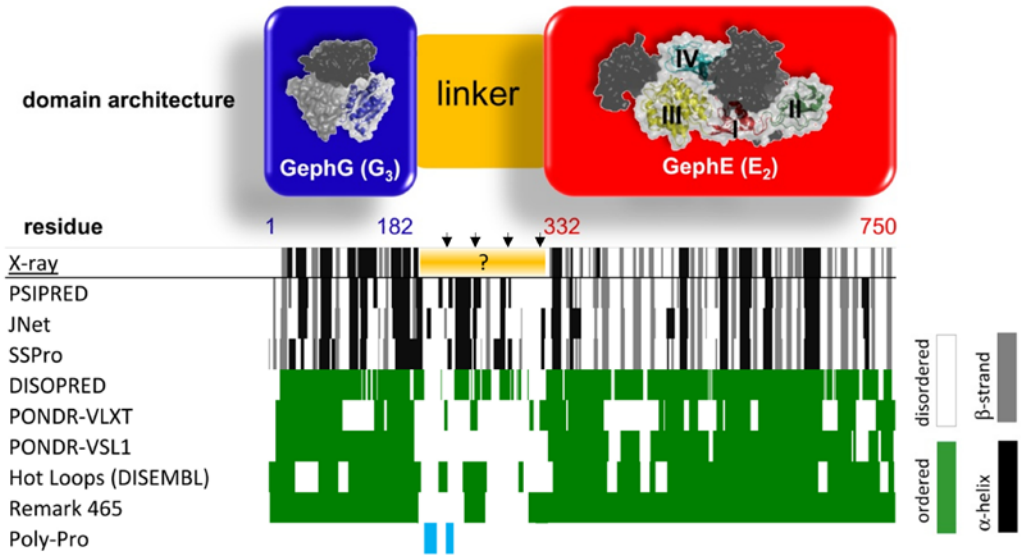

Figure 17 Domain architecture of gephyrin. Predictions of secondary structure and disordered regions. PSIPRED, JNet and SSpro predicted the secondary structure of the terminal domains, GephG and GephE, with 75-78% accuracy, as judged on the basis of the crystal structures ("X-ray"). The domain architecture is shown on top of the residue numbers. GephG forms trimers and GephE dimers with Roman numerals indicating the subdomain arrangement in one GephE monomer. Arrows (below the line with the residue numbers) indicate the subdivision of the linker into the four segments mentioned in the main text. Turquoise patches correspond to regions which potentially contain poly-proline helices.

- The N-terminal part is followed by a stretch of 27 residues (223-249), of which 85% ± 0% were predicted to be α-helical.
- For the remaining two 41 amino-acid-segments (residues 250-290 and residues 291-331) the secondary structure content decreased to values of 45% ± 16% and 11 % ± 10%, respectively.

These results suggested a predominantly disordered, flexible linker, which could potentially give rise to extended overall conformations, and could partly be explained by the fact that residues in the linker are biased towards a reduced content of hydrophobic, aromatic, bulky and order-promoting side chains, whereas an increased content of residues with a higher solvation potential as well as disorder-promoting residues is present (compared to GephG and GephE, Table 28) (Vacic *et al.*, 2007).

criterion	⇩/⇧	p-value	criterion	⇩/⇧	p-value
aromatic content	⇩	0.03610	high solvation poten. (J-T)	⇧	0.00014
hydrophobic (Eisenberg)	⇩	0.00021	frequent in coils (N)	⇧	0.02117
hydrophobic (K-D)	⇩	0.00411	disorder promoting (Dunker)	⇧	0.00003
high interface prop. (J-T)	⇩	0.00009	charged residues	*n. s.*	0.48956
frequent in β-strands (N)	⇩	0.00113	positively charged	*n. s.*	0.36198
bulky (Zimmerman)	⇩	0.00338	negatively charged	*n. s.*	0.95706
order promoting (Dunker)	⇩	0.00017	polar (Zimmerman)	*n. s.*	0.42658
large (Dawson)	⇩	0.02280	hydrophobic (F-P)	*n. s.*	0.10598
exposed (Janin)	⇧	0.00001	frequent in α-helices (N)	*n. s.*	0.44360
flexible (Vihinen)	⇧	0.01585	high linker propensity (G-H)	*n. s.*	0.88396

Table 28 Composition profiler analysis of gephyrin's linker region. This type of sequence analysis allows for a detection of a depletion (⇩) or an enrichment (⇧) of certain amino acid classes in the linker region versus a reference, which in this case was the rest of the protein, GephG and GephE. *n. s*. stands for *not significant (p-values > 0.05)*.

III.A.2.2 Holo-gephyrin purification

To clarify the impact of potential flexibility on the relative arrangement of globular protein domains, the complementary methods of AFM and SAXS were used in the course of this work. For both methods a high protein quality was desirable and was ensured using the already established three-step purification protocol (nickel affinity, anion exchange and size exclusion chromatography (SEC)) with some modifications, which mainly concerned the anion exchange chromatography step: The original salt gradient from 0 to 500 mM salt over 10 columns was replaced by a shallower gradient (35 column volumes) from 200 mM NaCl to 360 mM NaCl, preceded by a 3-5 column-volume-gradient from 80-200 mM NaCl. Whereas with the original protocol a single sharp peak was obtained (data not shown), the spreading of the gradient in the modified protocol resulted in most

cases in an asymmetric peak with at least one shoulder and allowed for a better separation of trimeric gephyrin from degradation products (pink in Fig. 18A&B) and higher oligomers (marked in red in Fig. 18A&B). Conservative pooling after anion exchange chromatography (Fig. 18A) was based on corresponding native gels (Fig. 18B) and resulted in low contributions of the two mentioned byproducts, so that after size exclusion chromatography a homogenous sample was obtained (Fig. 18C), which was suitable for protein characterization on the nm-scale.

Based on native PAGE with anion exchange chromatography fractions three major classes of species could be distinguished: First, putative higher oligomers, eluting at the highest salt concentration, which exhibited the smallest electrophoretic mobility, second, the putative trimeric species, with a slightly higher mobility; last, degradation products with the highest electrophoretic mobility, eluting at the lowest salt concentration. SEC purified higher oligomers (referred to as HO) exhibited a higher Stokes radius compared to the putative trimer pool (Fig. 19A). The corresponding

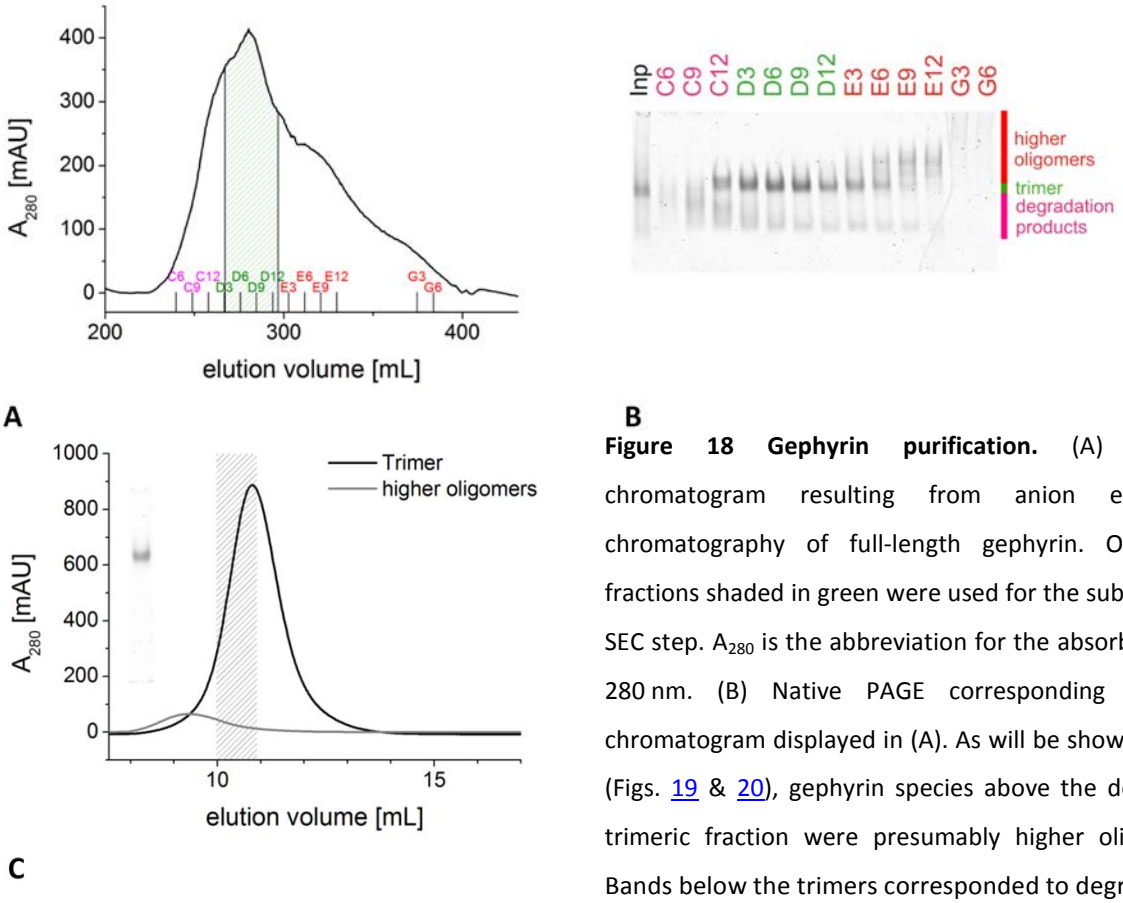

Figure 18 Gephyrin purification. (A) Typical chromatogram resulting from anion exchange chromatography of full-length gephyrin. Only the fractions shaded in green were used for the subsequent SEC step. A_{280} is the abbreviation for the absorbance at 280 nm. (B) Native PAGE corresponding to the chromatogram displayed in (A). As will be shown below (Figs. 19 & 20), gephyrin species above the dominant trimeric fraction were presumably higher oligomers. Bands below the trimers corresponded to degradation products. Conservative pooling led to a depletion of higher oligomers, as can be deduced from (C) which displays a typical chromatogram of the second, final SEC step (using SEC-1 buffer) carried out immediately prior to the SAXS and AFM experiments, for which only fractions were pooled that are marked by the grey shaded area. This representation also shows that conservative pooling almost completely eliminated residual higher oligomers, even if every tenth protein assembly would be a higher oligomer. The native PAGE gel (inset, left) confirmed sample homogeneity.

native gel revealed at least three species with a lower electrophoretic mobility than the putative trimeric fraction. Two fractions enriched in different putative higher oligomeric forms (marked blue and red in the inset of Fig. 19A), were used for re-chromatography, and, in fact, both species (referred to as higher oligomers 1 (HO1) and 2 (HO2)) again displayed a higher hydrodynamic radius than the trimer, but could be partially separated from each other (Fig. 19A). These results indicated that different forms of higher oligomers were obtained during the purification.

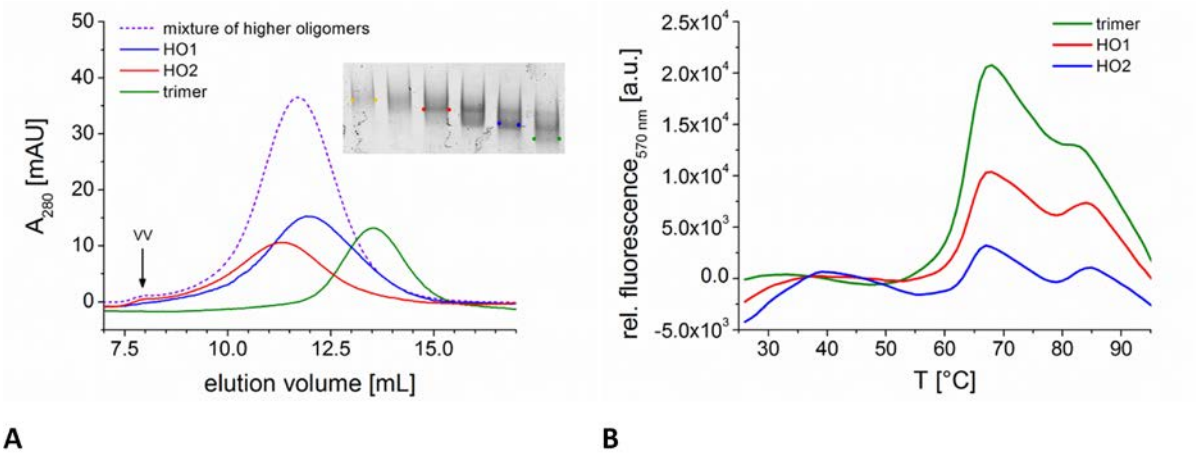

Figure 19 Gephyrin species with higher hydrodynamic radii were obtained during purification. (A) A mixture of higher oligomers was subjected to analytical SEC (aSEC) using a Superose 6 10/100 GL column (dotted curve) equilibrated in SEC-2 buffer. On the corresponding native gel (inset) at least three species other than the trimer could be distinguished (indicated by the points in the inset, whose colour code matches that of the chromatogram). HO1 and HO2 were obtained after re-chromatography of the blue and red marked fractions of the "mixture of higher oligomers" and eluted significantly earlier than trimeric gephyrin. The "mixture of higher oligomers" and HO2 formed aggregates, as indicated by the small peak eluting in the void volume (VV). Note that a separate gephyrin trimer pool was used for the experiment, with a higher purity than in the context of the "mixture of higher oligomers". (B) The trimer and the tested HO species exhibited similar thermal unfolding profiles in a Thermofluor experiment in SEC-4 buffer. Inflection points at ~63°C and ~81°C indicated unfolding of GephE and GephG, respectively (compare with Fig. 38A). Note, that HO2 exhibited an additional transition at ~35°C, and in this respect HO1 behaved like an intermediate between the trimer and HO2.

Although the CD spectrum of the mixture of higher oligomers purified by SEC did not significantly differ from that of the trimeric fractions (data not shown), HO1 and HO2 had a higher tendency to form aggregates, as exemplified by the fact, that pellets were obtained after long centrifugation steps (especially in the case of HO2). Consistent with this observation, a small peak in the void volume after re-chromatography was obtained for HO2. Thermofluor measurements revealed similar domain unfolding transitions for HO1 and HO2 in comparison with the trimer, however, with the difference of an additional unfolding process, which became especially apparent in HO2 (Fig. 19B). Which part(s) of gephyrin exactly unfold(s) at this step, remain(s) to be clarified.

III.A.2.3 Gephyrin characterization by light scattering

Initial dynamic light scattering (DLS) experiments were conducted to get hints at the size, shape and homogeneity of purified gephyrin, as given by the hydrodynamic radius R_H and the sample polydispersity, respectively. Both, the putative trimer and mixture of higher oligomers after SEC were aggregate-free, and the resulting polydispersity value of <20% implies sample homogeneity. As expected from the previous section, the mixture of higher oligomers (HO) exhibited a significantly larger Stokes radius (Table 29). The DLS-derived molecular masses given in Table 29 are shape-dependent, and hence SEC-MALS experiments (II.B.5.6) were carried out to overcome this limitation.

	$R_{H,DLS}$ [Å]	MM_{DLS} [kDa]	PD_{DLS} [%]	MM_{MALS} [kDa]	PD_{MALS}[%]
Geph WT	76±2	354±9	14.8±2.9	194±10	1.00±0.06
Geph HO	129±9	600±42	13.5±5.6	358±18	1.00±0.06

Table 29 Gephyrin characterization by DLS and MALS. $R_{H,DLS}$, hydrodynamic radius, determined by DLS; MM_{DLS}, molecular mass estimation based on the DLS-derived R_H; PD_{DLS}, polydispersity (DLS); MM_{MALS} and PD_{MALS}, MALS-derived molecular mass estimation and the sample polydispersity.

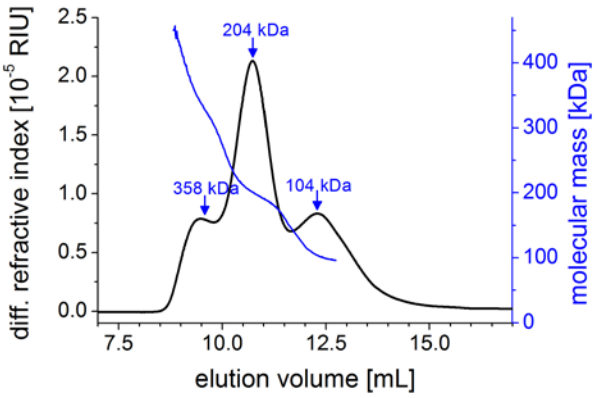

Figure 20 SEC-MALS with gephyrin. Chromatogram of gephyrin HO obtained after anion exchange chromatography, where protein elution from a Superose 6 10/300GL column (in SEC-2 buffer) is indicated by a change in the differential refractive index (left y-axis) and the corresponding mass distribution (right y-axis).

SEC-MALS experiments were first conducted with an anion exchange chromatography fraction containing higher oligomers (as in Fig. 18B), yielding masses of 358 kDa, 204 kDa and 104 kDa for the higher oligomers, the putative trimer and degradation products, respectively (Fig. 20). Due to the fact that different higher oligomers can hardly be separated without substantial sample loss, the focus of the following analysis was set on the characterization of putatively trimeric gephyrin (Fig. 18). Hence, further experiments were performed with SEC-purified putative trimer to achieve clarity in terms of the molecular mass. However, these samples yielded a molecular mass of 189 kDa, which is closer to the expected dimer mass of 167 kDa than to the trimer mass (250.5 kDa). A dynamic equilibrium between dimers and trimers was ruled out due to the constant mass distribution over the peaks of the putative trimer samples (Fig. 61C). Despite the small MALS-derived molecular mass, gephyrin will be – for structural reasons discussed below – considered to be a trimer.

III.A.2.4 AFM imaging detects flexibility in gephyrin

Atomic force microscopy (AFM) provides information on the single-molecule level (Lemaire *et al.*, 2006, Sacho *et al.*, 2008) and can also be used for the estimation of protein masses. Hence, AFM studies were conducted with gephyrin to evaluate the oligomeric state and its flexibility. Molecular mass analysis revealed a Gaussian distribution with a peak value corresponding to a molecular mass of 219 kDa ± 39 kDa (Fig. 21A, expected trimer mass = 250.5 kDa). Considering that linker segments were not always attached to the rest of the protein and hence were not resolved, one would expect the mass to be slightly underestimated. At the same time, the molecular mass of the sample particles was still significantly higher than that of a potential dimer (expected dimer mass = 167 kDa), confirming that the majority of gephyrin particles were trimeric, while only 1.9% ± 0.1% of the particles were consistent with a hexameric state.

The small species with masses < 40 kDa (Fig. 21A) did not represent degradation products of gephyrin. First, the contribution of this apparent species varied from deposition to deposition (between 3% and 29%). Second, control experiments confirmed that neither the full length protein, nor the E- or the G-domains of gephyrin are prone to degradation in AFM depositions (data not shown). This "peak" at approximately < 40 kDa is in fact not a dominant species but an exponentially decaying (likely instrumental) noise background (Ingrid Tessmer, personal communication).

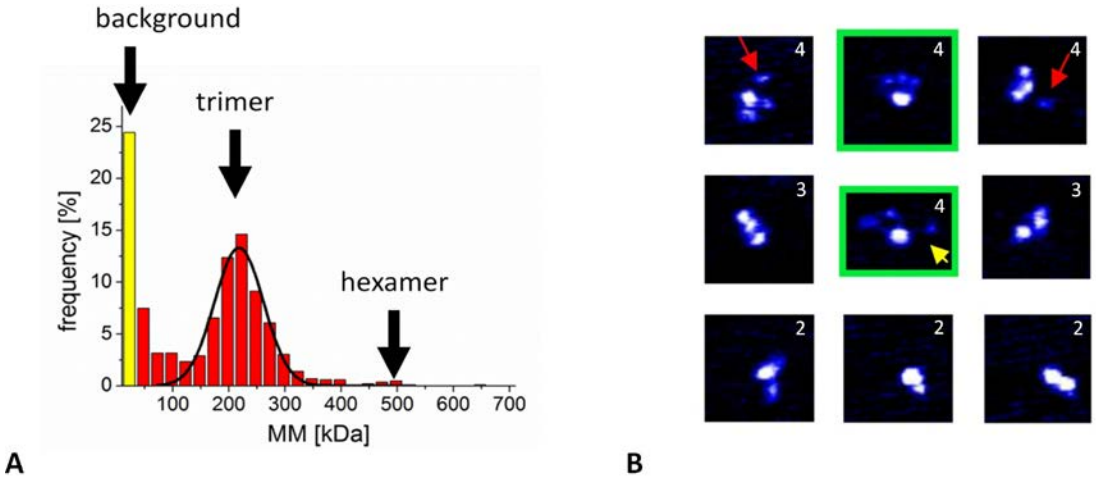

Figure 21 Gephyrin predominantly forms trimers with a high molecular plasticity. (A) The relative frequencies of all AFM depositions were averaged. In the images a significant fraction of the particles possessed an apparent molecular mass of < 40 kDa (indicated by the yellow bar), which most likely represents an experimentally induced background signal. (B) Typical examples for 1-, 2-, 3- and 4-segmented particles observed in AFM micrographs, where the number in the upper right corner indicates the number of segments. Red arrows mark small particles, which were considered to be part of the adjacent particles, if they were in close spatial proximity. This assumption was justified by the longest linkers that could be resolved (yellow arrow). The image excerpts highlighted with a green frame exemplify that the different appearance of the gephyrin particles were not simply a projection artifact, as these two particles were not congruent – no matter which rotations and/or translations were performed.

While gephyrin particles were homogenous in terms of molecular mass, they displayed highly diverse shapes, varying from compact to very extended assemblies (Figs. 21B & 22A), which most likely reflect different domain arrangements. This indicated a high level of plasticity in the molecules, which was also reflected in the broad AFM-derived D_{max} distribution, ranging from ~200 to ~500 Å (Fig. 22B). Particles were classified according to the number of segments they displayed (for examples see Figs. 21B & 22A), with the number of segments ranging from one to four: Globular particles consisting of only one segment made up 15.6% ± 4.0% of the sample, while 29.5% ± 1.3% contained 2, 37.2% ± 0.6% contained 3 and 17.8% ± 3.0% contained 4 segments. The large majority of multi-cluster particles (2 to 4 clusters) displayed a profile that was, in principle, consistent with asymmetric as well as symmetric models. Among the population with 4 clusters, more than 90%

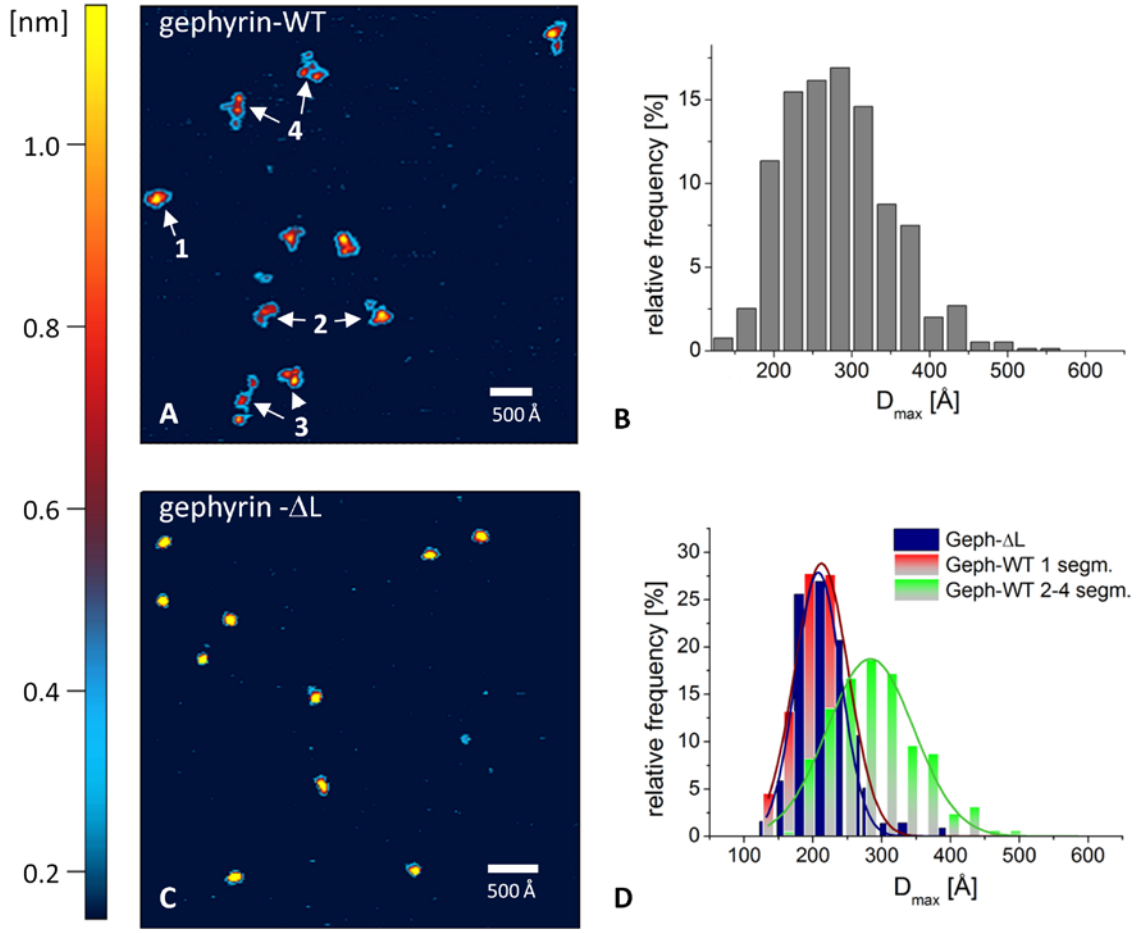

Figure 22 Comparative AFM analysis of gephyrin and Geph-ΔL. (A) AFM micrograph displaying the distinct classes of particles, containing one to four segments, as indicated in figure (1-4). The height scale is indicated by the colour bar on the left-hand side and applies to (A) and (C). (B) Size distribution of the trimeric fraction of wild-type gephyrin (n=413). (C) In contrast to gephyrin, Geph-ΔL displays a high level of homogeneity. (D) Separate size distributions of the compact and extended gephyrin populations (1 segment and 2-4 segments, respectively). The Geph-ΔL mutant showed a size distribution that strongly resembled that of compact full-length gephyrin.

were consistent with a quasi-symmetric assembly. Globular and extended conformers containing 2-4 clusters were analysed separately for particle size (Fig. 22D), resulting in D_{max} values of 212 Å and 283 Å, respectively.

To test whether it was the linker that mediated heterogeneity, a gephyrin construct missing the linker (Geph-ΔL, specifically residues 187-331 of the P2 splice variant, further analysis in section III.A.2.6.2) was investigated. The volume-derived molecular mass of 223.3 kDa ± 8.7 kDa was in line with Geph-ΔL forming a trimer (expected molecular mass = 203 kDa), implying that the GephG trimer interface was more stable then the GephE dimer interface. One can attribute the slightly larger volume-derived molecular mass for Geph-ΔL compared to full-length gephyrin to the fact that some parts of the linker were not resolved in the AFM analysis of full-length gephyrin, which was obviously not a problem in the linker-less variant. Since virtually all Geph-ΔL particles appeared globular in the AFM micrographs (Fig. 22C) and their D_{max} values (229 Å) were very similar to those observed for the globular fraction of full-length gephyrin (212 Å, Fig. 22D), one could conclude, that the linker mediated an equilibrium between very compact and extended states.

III.A.2.5 SAXS analysis of holo-gephyrin reveals its partial compaction

For AFM experiments gephyrin was analysed in the context of a dry mica surface. Complementary to this, a small angle X-ray scattering (SAXS) analysis in solution was carried out. The overall characterization of gephyrin was followed by two types of analysis, one considering gephyrin as a single conformer and one describing gephyrin as an ensemble of different conformers. Both approaches were also assessed in terms of their validity.

III.A.2.5.1 SAXS overall characterization

First, the molecular mass of gephyrin was derived. For this purpose the Porod volume (Porod, 1982) and the excluded particle volume (obtained with the program DAMMIN, (Petoukhov *et al.*, 2012)) were determined and divided by empirical constants (Table 30). The results were consistent with the trimeric state of gephyrin, as it was determined before (Schrader *et al.*, 2004, Sola *et al.*, 2004). Likewise, two further independent mass estimations were performed using the SAXS MoW server (Fischer *et al.*, 2009) and the volume of correlation calculation (Rambo & Tainer, 2013); both approaches also yielded masses that were comparable to an expected trimer mass of 250.5 kDa (Table 30).

Initial clues about the shape of gephyrin could be derived from the pair-distance distribution (Fig. 23A), the P(r) function, which represents a histogram of interatomic distances. The P(r) function clearly deviated from that of a compact assembly such as that of the catalase tetramer, which possesses a comparable molecular mass of 232 kDa (PDB code: 4BLC). The theoretical catalase

scattering pattern gives rise to a bell-shaped P(r) profile, while for gephyrin a tailing was observed with the curve intersecting with the x-axis at a maximum interatomic distance (D_{max}) of ~230 Å instead of 110 Å as in the case of the catalase (Fig. 23A). In agreement with this, the radius of gyration (R_g) of catalase (38 Å) was relatively small when compared to gephyrin with an R_g value of ~67 Å. Taken together, these parameters accounted for a rather elongated than for a quasi-globular shape of gephyrin.

At the same time several findings clearly indicated that the overall state of gephyrin was not entirely disordered. First, one may have expected an even larger D_{max} considering the 150 residue long linker, which theoretically could easily expand the GephG-GephE distance by 400 Å for each protomer (assuming C_α-C_α distances of 2.8 Å, as they can be encountered in β-strands). Second, the R_g/R_h ratio of 0.93 (as determined by SAXS (R_g) and DLS (R_h), respectively) corresponds to a relatively compact assembly. For comparison R_g/R_h ranges from ~1.5 for anisometric polymers to ~0.8 for a solid sphere (Rubinstein & Colby, 2003). Finally, the bell-shaped Kratky plot of gephyrin suggests that the protein was predominantly folded with a rather low contribution from random coils (Fig. 23B). A comparison of the Kratky plot to those computed for three conformers of different compactness suggested that the protein on average resembles an intermediate between a very compact and a slightly extended state (Fig. 23C). In fact, a peak broadening in Kratky plots similar to that of gephyrin was observed in simulated data of multidomain proteins connected by flexible linkers, which also displayed the tendency for a single peak in the Kratky plot that might point to a decoupling of movements of individual domains (Bernado, 2010), GephG and GephE in the case of gephyrin.

	R_g(Guinier) [Å]	R_g (P(r)) [Å]	D_{max} [Å]	Porod vol. [Å³]	MM_{Porod} [kDa]	MW_{DAMMIN} [kDa]	$MM_{SAXS-MOW}$ [kDa]	MM_{VC} [kDa]	$MM_{monomer}$ [kDa]
GephWT	62.5±2	66.7±2	240±45	369±50	231±45 (2.8)	232±45 (2.8)	226±23 (2.7)	238±21 (2.8)	251 (3)

Table 30 Overall characterization of full-length gephyrin by SAXS. Radii of gyration (R_g(Guinier) and R_g(P(r))) were either derived by the Guinier approximation or the P(r) function, respectively. The latter is referred to as real space R_g. The maximum interatomic distance D_{max} was obtained with the P(r) function as well. Molecular masses in kDa (MM) were derived by (1) division of the Porod volume in Å³ by a factor of 1.6 (MM_{Porod}), (2) division of the excluded volumes of DAMMIN models without symmetry (MM_{DAMMIN}), (3) by the SAXS-MOW webserver ($MM_{SAXS-MOW}$) and (4) by the volume of correlation invariant (VC), introduced by Rambo and Tainer (MM_{VC}). Values in brackets indicate the oligomeric state obtained by division of the experimental value by the molecular mass of the monomer ($MM_{monomer}$).

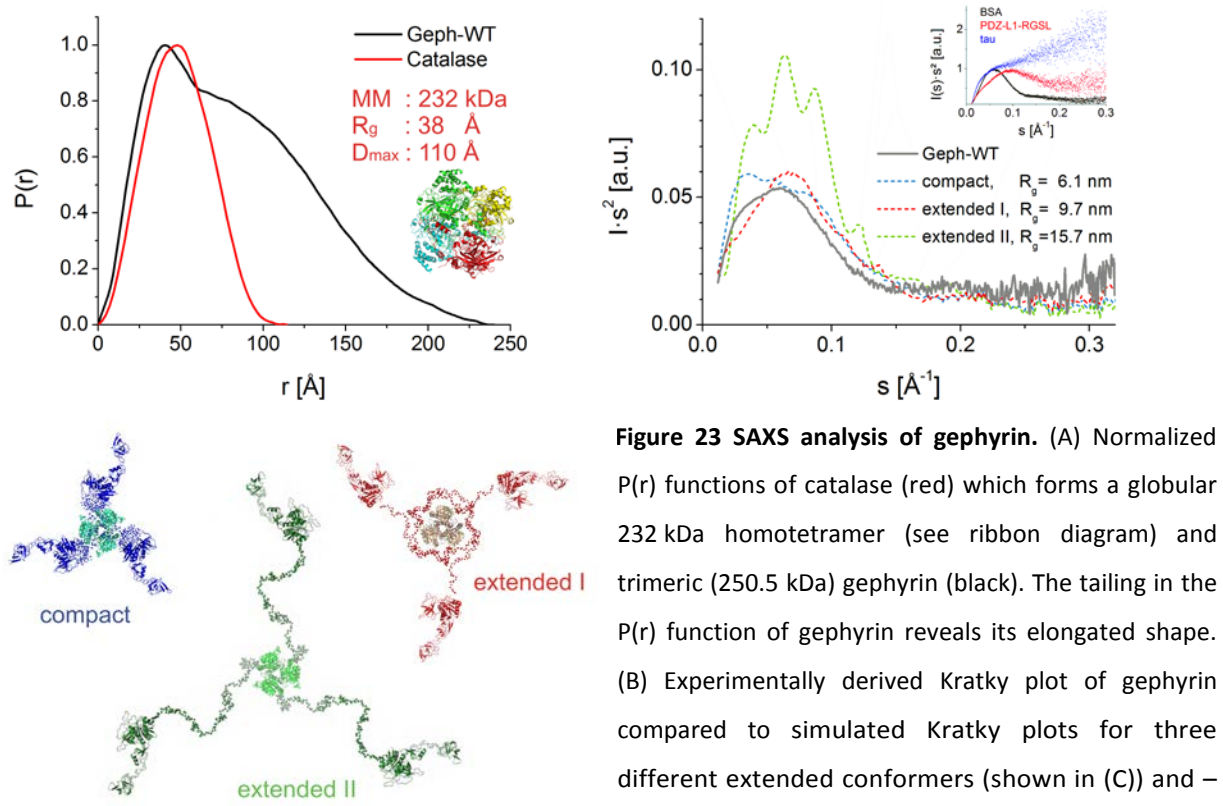

Figure 23 SAXS analysis of gephyrin. (A) Normalized P(r) functions of catalase (red) which forms a globular 232 kDa homotetramer (see ribbon diagram) and trimeric (250.5 kDa) gephyrin (black). The tailing in the P(r) function of gephyrin reveals its elongated shape. (B) Experimentally derived Kratky plot of gephyrin compared to simulated Kratky plots for three different extended conformers (shown in (C)) and – in the inset – with globular BSA, natively unfolded tau (Shkumatov *et al.*, 2011) and PDZ-L1-RGSL, a two-domain protein with a flexible linker representing 30% of the total protein (Bielnicki *et al.*, 2011) in a normalized representation.

III.A.2.5.2 Single conformation modelling is not a valid approach in the SAXS analysis of gephyrin

Overall protein shapes, built up by small spheres, representing dummy atoms, were calculated by *ab initio* modelling on the basis of the previously obtained P(r) function. Consistently, a*b initio* models created with DAMMIN, DAMMIF and GASBOR without symmetry constraints yielded rather elongated shapes. Also the application of threefold symmetry, potentially justified by the oligomeric state of the protein, did not lead to reliable and, in some cases, even ambiguous results (Fig. 24).

Since high-resolution structures were available for ~80% of the primary sequence, rigid body modelling (assuming a single conformer in the sample) was performed with the GephG and GephE crystal structures - initially using CORAL, assuming no symmetry except for the trimeric GephG which determines the oligomeric state of the full-length protein (Fig. 25). In accordance with the observed flexibility, however, rigid body modelling turned out to be problematic: First, rigid body models displayed a high normalized spatial discrepancy (NSD), which indicated a low reproducibility due to the fact that a single molecular conformation alone did not represent the experimental data adequately (Table 31), and second, no models could be obtained, which were at the same time biologically relevant and yielded good fits over the complete data range. The best fits could be

obtained with symmetric modelling using BUNCH, however, the obtained rigid triskelion was at variance with the sample heterogeneity observed by AFM (section III.A.2.4). These results indicated that rigid body modelling – assuming single fixed conformers – was not the method of choice to describe the scattering pattern of gephyrin.

Programme	asymmetric			symmetric*		
	χ	NSD	R_g [Å]	χ	NSD	R_g [Å]
***ab initio*: DAMMIN**	0.81	0.72±0.03	66.8	0.97	1.30±0.15	65.3
***ab initio*:DAMMIF**	0.85	0.76±0.03	66.9	1.55	1.37±0.22	66.9
***ab initio*:GASBOR**	1.36	1.98±0.06	67.2	1.80	1.63±0.27	64.6
RB: CORAL (asym. I)	1.46	2.47±0.03	80.6	n.a.		
RB: CORAL (asym. II)	2.27	2.32±0.08	79.8	n.a.		
RB: BUNCH (symmetric)	n.a.			1.50	1.52±0.17	66.9
EOM**	n.c.		80.8	0.80	n.c.	

Table 31 Quality of different SAXS models. n.c. not conducted; NSD normalized spatial discrepancy; asym. I/II rigid body modelling of asymmetric scenarios I or II, respectively. *Ab initio* and rigid body (RB) modelling assumed a single conformer, EOM a mixture of conformers (Fig. 12). *Symmetry refers to an overall threefold symmetry. **For EOM analysis a mixed pool of both symmetric and asymmetric linkers was created. Therefore, it was neither classified as purely symmetric nor purely asymmetric. It should be noted that the Guinier approximation for the EOM ensemble curve using the same resolution range as for the experimental data (compare with inset in Fig. 26B) yielded an R_g value of 65 Å.

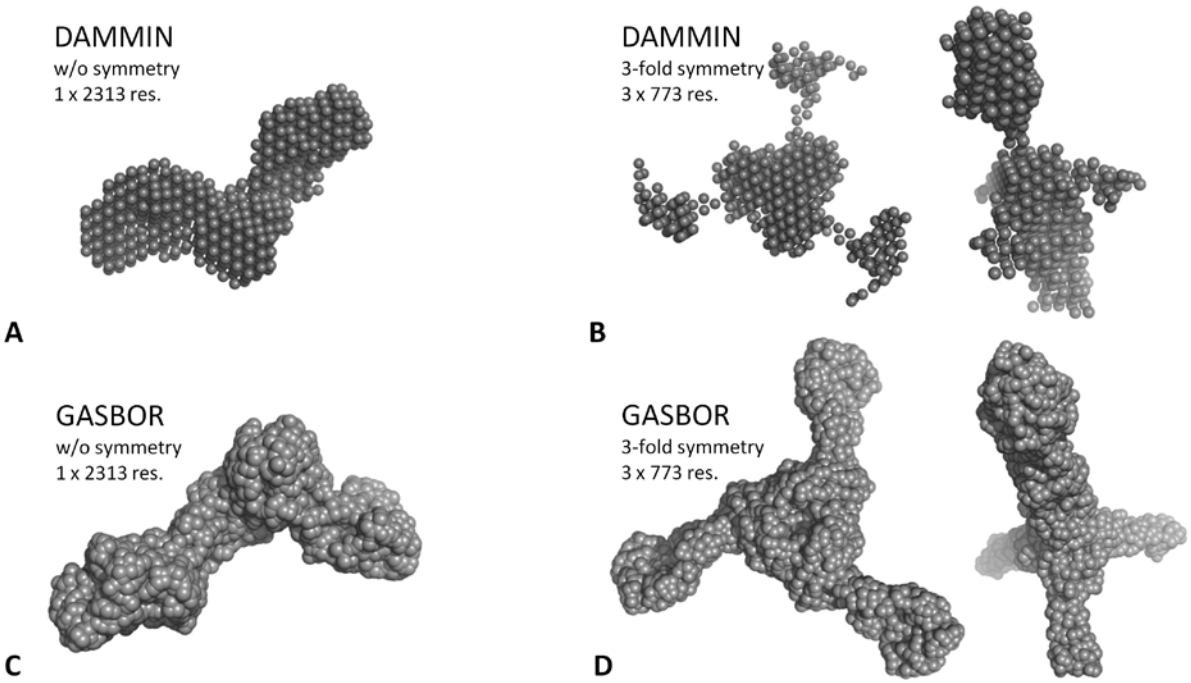

Figure 24 SAXS *ab initio* modelling. *Ab initio* models obtained with DAMMIN (A & B) and GASBOR (C & D). Elongated models were obtained with unconstrained modelling (A & C). The inclusion of a threefold symmetry constraint led to three-pronged star-like assemblies (B & D). It should be noted that rod-like structures as shown on the right-hand side in B were obtained to almost the same extent in DAMMIN (five of ten models) and DAMMIF (six of ten models, not shown), but not with GASBOR (D).

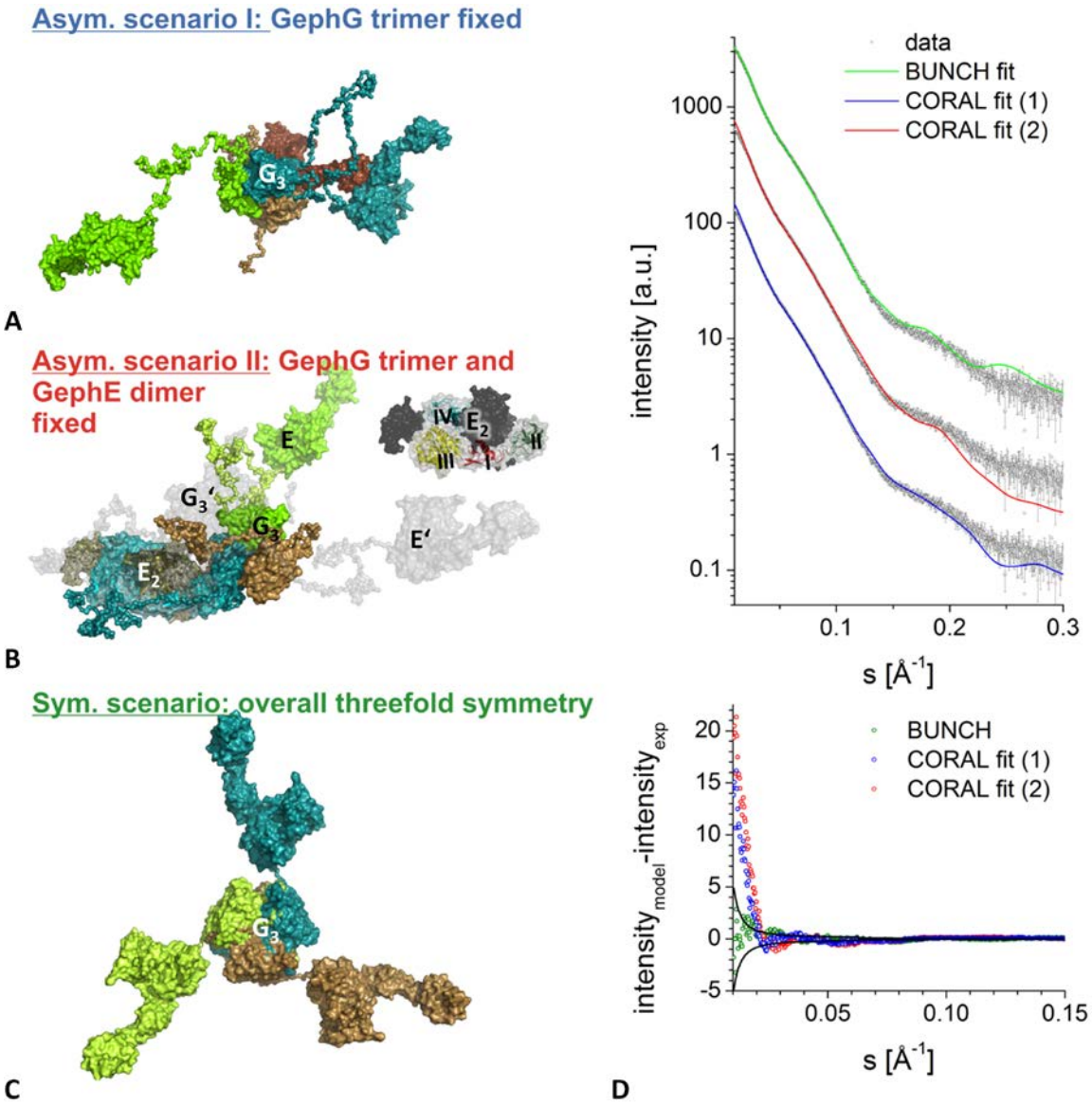

Figure 25 Rigid body models of gephyrin. The three protomers are displayed in brown, cyan and green. (A) Asymmetric models were obtained with the asymmetric scenario I (CORAL fit (1) in panel D), where only the GephG trimer interface (G_3, pdb code: 1JLJ) was fixed. Since in most of the models two GephEs were in close proximity, it was assumed in scenario II, that two GephEs undergo intratrimeric dimerization, with the dimer interface fixed (PDB code: 2FTS). For comparison the latter is shown with one protomer in dark grey and one in light grey with the arrangement of the subdomains. (B) For asymmetric scenario II (CORAL fit (2) in panel D) the high NSD of the solutions is exemplified by the superposition of the best, coloured solution with a grey conformer, for which the deviating domains are indicated by G3' and E'. (C) Symmetry was imposed to the models obtained with BUNCH. (BUNCH fit in panel D). (D) The fits corresponding to the displayed models displayed a good overall match to the experimental data, represented as grey spheres (upper panel), however, the residuals (lower panel) I_{model}-I_{exp} revealed that the symmetric BUNCH model is the only model which lies within the error ranges, as indicated by the black lines. In the upper panel the graphs for the symmetric scenario and the asymmetric CORAL scenario 2 was shifted along the y axis for better clarity.

III.A.2.5.3 Ensemble modelling of gephyrin

The ensemble optimization method (EOM, (Bernado *et al.*, 2007, Tria *et al.*, 2012)) allows one to analyse the scattering data in terms of ensembles of conformers and thus appears to be the best choice for the analysis of gephyrin. In short EOM was carried out as follows (Fig. 12): A large pool of conformers (half of them symmetric) was created. Then, a genetic algorithm selected sub-ensembles whose average theoretical scattering fit to the experimental SAXS data. Finally, the R_g histogram of the initial pool was compared to the corresponding histogram of 100 calculated ensembles (Fig. 26A), where models were classified as compact or extended according to their radius of gyration (see Fig. 26A and section II.B.6.2.7). A benchmark was performed to test which questions could be addressed with EOM.

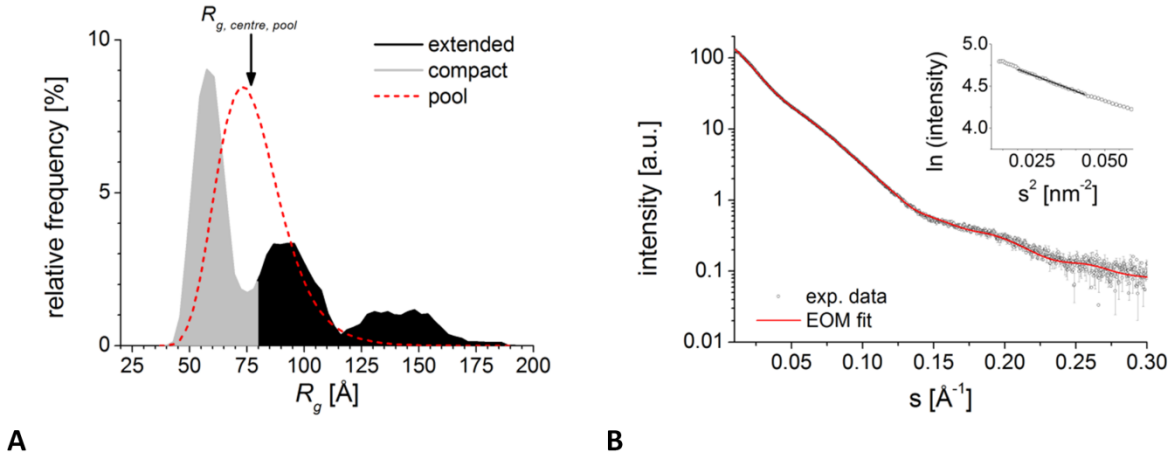

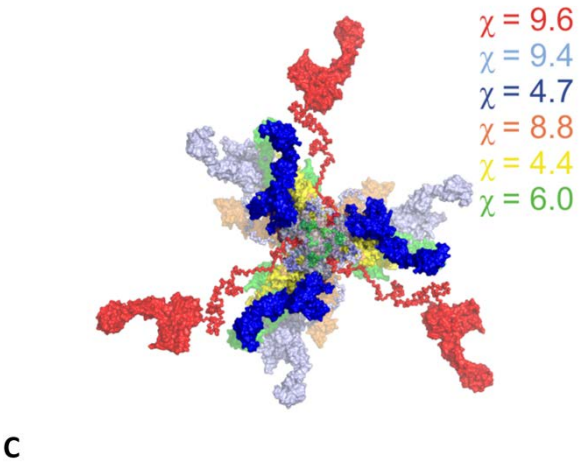

Figure 26 EOM analysis of gephyrin. (A) EOM R_g distribution of the initial random pool (red dashed line) and the selected ensemble (different grey shades) for full-length gephyrin. The broad distribution mirrors the conformational heterogeneity of the sample, however, there is a slight preference for compact states as indicated by the larger area under the curve for this fraction when compared to intermediate and extended conformers. (B) The simulated curve of the selected EOM ensemble is compared to the experimental curve (open circles and error bars). The Guinier plot in the inset revealed the structural integrity of the protein, with the line indicating the data points used for R_g and I(0) determination with GNOM. (C) EOM ensemble of the gephyrin trimer where different trimers were coloured differently. A higher degree of transparency for the orange and one of the light blue conformers indicates their smaller contribution to the total scattering. The individual conformers were also fit against the experimental data, and the obtained χ values are displayed in the corresponding colour. The χ value of the ensemble is 0.80.

III.A.2.5.3.1 Equilibrium of compact and extended gephyrin conformations

EOM analysis with optimized parameters (number of conformers and choice of the native-like dihedral angle library, see Appendix C for further details) reveals two interesting characteristics of gephyrin: First, almost the entire R_g range of the initial pool (red dashed line, Fig. 26A) was represented in the selected pool (grey-black distribution in Fig. 26A), which was indicative of a high degree of flexibility. Second, the R_g distribution for the selected ensemble displayed a clear maximum at R_g = 58 Å, followed by a shoulder at R_g = 93 Å and a third rather broad and not very pronounced maximum at R_g ~ 140 Å. The lack of a more prominent peak for the extended states indicated a higher heterogeneity of this population, which could be further subdivided into intermediate (peak at 93 Å) and elongated conformers (peak at 140 Å).

The ensemble with the best fit (χ = 0.80, Fig. 26B) contained six conformers (Fig. 26C) and their R_g values mirrored the peak positions of the R_g histogram, suggesting that the distribution was not significantly affected by ensembles with bad fits. Four conformers of this ensemble are compact (R_g values of 54-63 Å) and contribute 63% to the scattering, while the remaining contribution of 37% stemed from two extended conformers with R_g values of either 92 Å (intermediate) or 134 Å (elongated). A determination of the volume fractions with the program OLIGOMER was in line with the EOM results, also yielding a χ value of 0.80: The compact conformers contributed ~65% to the total scattering and the extended structures ~35%.

III.A.2.5.3.2 EOM benchmarking

In this section the validation of the EOM results is presented, with the intention to point out the limitations of the technique but also its strengths. Several aspects were evaluated. For most of these evaluations the scattering curves for certain scenarios were calculated (II.B.2.6.8). Then noise and errors were introduced (comparable to the levels of the experimental curve), and the resulting curve was used as input to EOM calculations .

The first issue is related to the criticism of one of the reviewers of our manuscript who raised doubts about the polymodal R_g distribution. This reviewer used the theoretical scattering pattern of a single conformer as input to the old version of EOM and obtained an artificial, polymodal R_g distribution, consistent with an ensemble of compact and extended states. To exclude that the newer version of EOM (2.0) employed in this study was prone to such artifacts, an EOM analysis was performed with the theoretical scattering patterns of the three conformers displayed in Fig. 23C, using a pool of only 20,000 conformers, which did not contain the original conformers. In none of the three cases was a pronounced polymodal character observed. The less smooth distribution for the rather unrealistic “extended II” conformer can be explained by the low occurrence of conformers with R_g > 147 Å in the original pool (only 9 of 20,000 conformers), hence bad fits with χ = 8.86 were

obtained) (Fig. 27A). One can therefore conclude that version 2.0 of EOM *per se* does not model data of single conformers as ensembles with multimodal R_g distributions.

The next validation step of EOM also concerned the polymodal R_g distribution: A recent study, which was again not conducted with the EOM 2.0 version, revealed that R_g distributions with an artificially polymodal character could be converted to monomodal distributions by an increase in the number of curves per ensemble (Boze *et al.*, 2010). It should be clarified here that the number of curves per ensemble (here denoted as n) is not equivalent to the number of conformers: For example, let us assume that two conformers contribute to a scattering profile, one accounting for

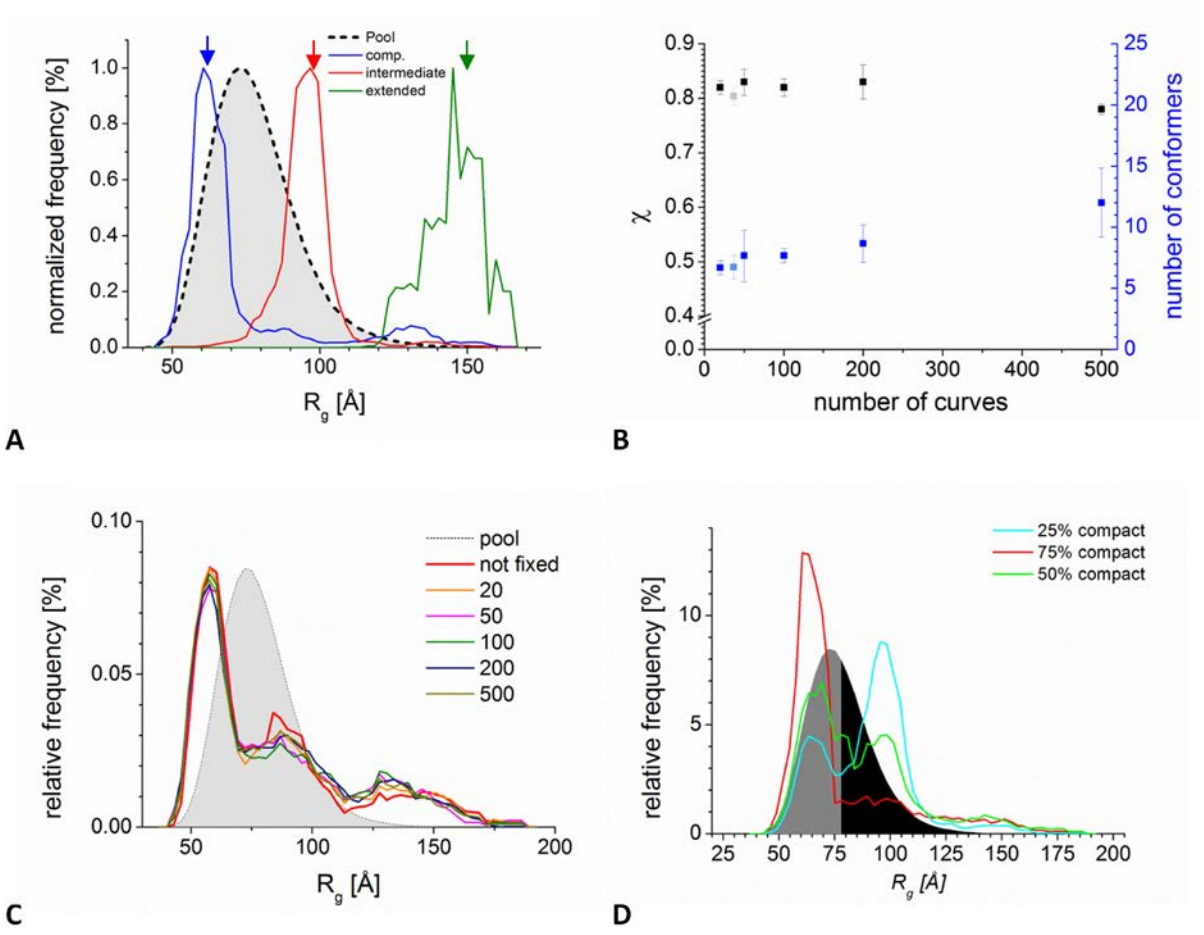

Figure 27 Validation of EOM results. (A) Theoretical curves of single conformers yielded ensembles with a monomodal Rg distribution. The peak positions were in good agreement with the R_g values of the original conformers, indicated by the arrows. (B) χ values and number of conformers as functions of the number of (fixed) curves. Pale blue and grey squares represent the experimentally derived ensemble (Fig. 26C). While the number of conformers slightly increased, χ was rather constant. (C) The R_g distributions were not affected by the higher numbers of curves per ensemble. In the "not fixed" mode EOM optimised the number of curves. (D) Theoretical curves of mixtures of compact and extended states were used as input for EOM, which could reproduce the ratio of compact and extended states, as judged by the areas under the curves. The grey and the black areas indicate the relative frequencies of compact and extended states in the initial pool, respectively. The initial pool was the same for all tested ratios.

one third of the scattering pattern and the other for two thirds. However, the number of curves would be three since the two conformers would contribute one and two curves, respectively. To test whether an increase in n leads to a loss of the polymodal character, EOM was repeated with a fixed number of conformers, ranging from 20 to 500. The results argued strongly against a significant impact of n on the EOM outcome (Fig. 27B): The increase in n led to an increased number of conformers, but just slightly better χ values, which are still absolutely comparable to the final ensemble presented above with 37 curves and 6 conformers. More importantly, the R_g profiles did not significantly differ, arguing against an artificially-induced polymodal R_g distribution (Fig. 27C).

The next EOM evaluation step dealt with the accuracy of the ratio of compact to extended states. For this purpose EOM calculations were conducted with theoretical scattering patterns of mixtures of the "compact" and "extended I" conformers shown in Fig. 23C, with ratios of 3:1, 1:1 and 1:3. The ratio of the peak heights was generally in line with the input ratios, albeit a bit shifted towards the more compact conformers, whereas the areas under the curves of the R_g distributions (72%, 53% and 30% contributed by the compact states for the 3:1, 1:1 and 1:3 ratios, respectively) were in slightly better agreement with the input ratios (Fig. 27D). As noise and error levels applied to the theoretical scattering curves were comparable to those of the experimental scattering data, and as the R_g values of the input conformers were comparable to those obtained from the peak positions of the R_g distributions (58 Å vs. expected R_g = 61 Å and 93 Å vs. expected R_g = 97 Å), one could conclude that the 2:1 ratio of compact to extended states obtained from the experimental data was quite accurate.

The next efforts focussed on whether the combination of SAXS and EOM was powerful enough to allow for the distinction between symmetric and asymmetric gephyrin (abbreviated as GephG_3E_2E, comparable to conformations of asymmetric scenario II, Fig. 25). The scattering curve of a theoretical GephG_3E_2E conformation (containing one intact GephG trimer interface and one intact GephE dimer interface (Fig. 28A) were used as input to EOM. The initial pool contained equal amounts of

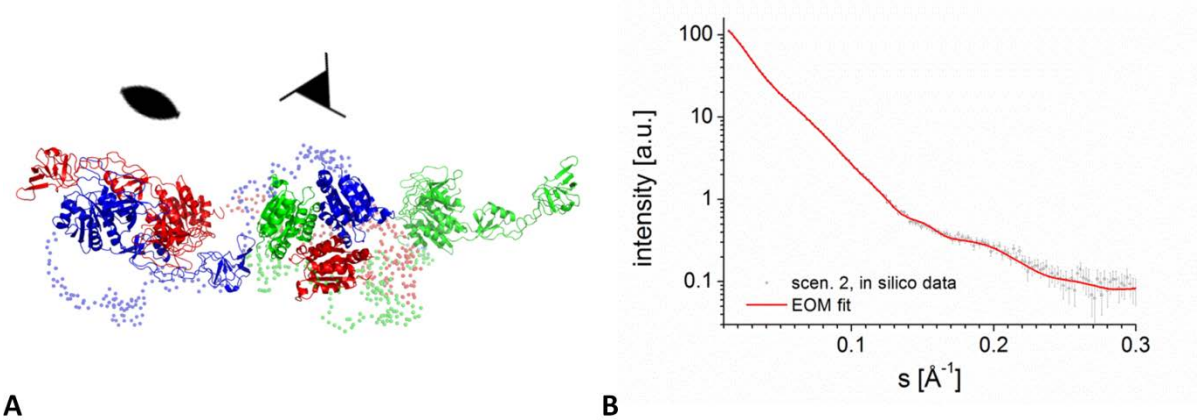

Figure 28 GephG_3E_2E conformations could not be recognized by EOM. (A) The GephG_3E_2E conformer used for the EOM benchmarking. (B) The fit of the selected ensemble displayed only slight deviations from the theoretical scattering curve of the used GephG_3E_2E conformer, yielding a χ value of 0.83.

symmetric and asymmetric conformers. One might have expected that a clearly elongated conformer as input would have resulted in predominantly asymmetric models. However, in all three runs – although very good fits were obtained (χ=0.83, Fig. 28B) – only symmetric models were selected (ensemble not shown). This implied that EOM, at least under the given conditions of resolution, noise and program parameters was of limited use for the distinction between symmetric and asymmetric assemblies.

Finally, EOM was also carried out with a pool containing dimers, with the GephE interface kept intact, to exclude that the SAXS analysis was biased by the assumption of the trimeric state. It turned out that EOM fits assuming dimers were clearly inferior to the analysis assuming trimers, scince the χ value of 1.49 for the dimer pool was considerably worse than the previously obtained value of 0.81 for the trimer pool. Major deviations from the experimental data were encountered in the small angle region (s<0.05 A) and in the range from 0.15 $Å^{-1}$ to 0.2 $Å^{-1}$ (Fig. 29A). While for the trimer scenario deviations were within the experimental error range (compare red and black lines in Fig. 29B), the experimental error ranges were clearly exceeded in the dimer scenario. Given the large number of conformers and the good fit for the trimeric scenario, dimers as a preponderant species in the sample could thus be excluded.

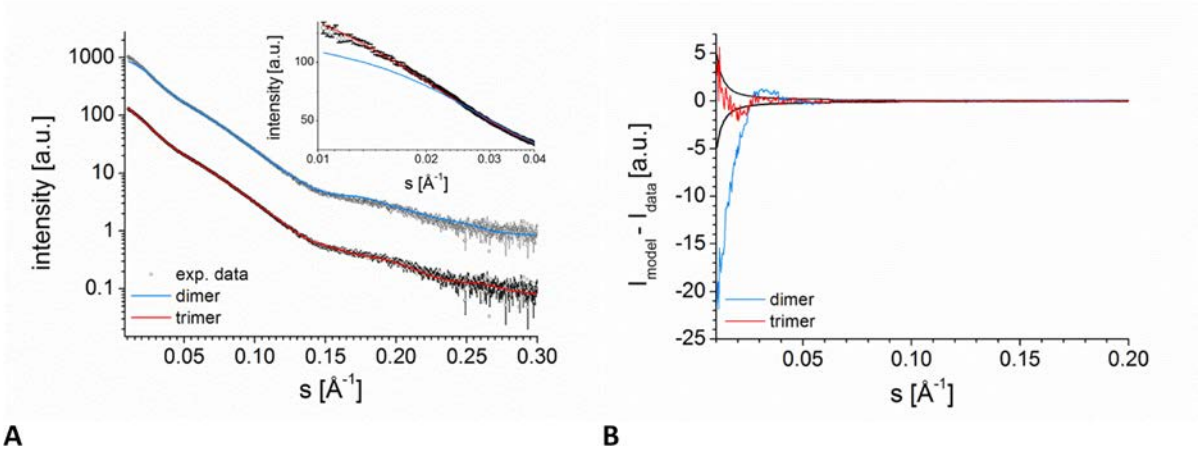

Figure 29 EOM fits with trimer pools are superior over those with dimer pools. (A) Experimental data (black circles) were fitted either with a pool of 950,000 trimers or 1,000,000 dimers. While the overall fit looked acceptable at first glance in both cases, the deviations for the dimer scenario in the small angle region (inset, magnified non-logarithmic I vs. lg(s) plot) were too high to justify the assumption of a dimeric state of gephyrin. (B) Accordingly, the graph of the differences between the theoretical scattering data of the respective ensemble (I_{model}) and the experimental data (I_{data}) clearly demonstrated significant differences for the dimer scenario in the small-angle region, which well exceeded the error levels indicated by the black curves.

III.A.2.6 Characterization of gephyrin linker mutants

Gephyrin's linker region presumably has a crucial impact on its conformation and has been suggested to be responsible for blocking GephE-mediated dimerization (Bedet *et al.*, 2006). Hence, the following section addresses the characterization of gephyrin's linker region with an emphasis on the identification of residues involved in blocking the GephE dimer interface. For this purpose either mutations or deletions were introduced. If these mutations favour GephE dimerization, a preference for higher oligomeric state should become evident. In the first part of the section the role of selected phosphorylation sites was analysed (Fig. 30), while the second part deals with mutants in which large linker segments were deleted.

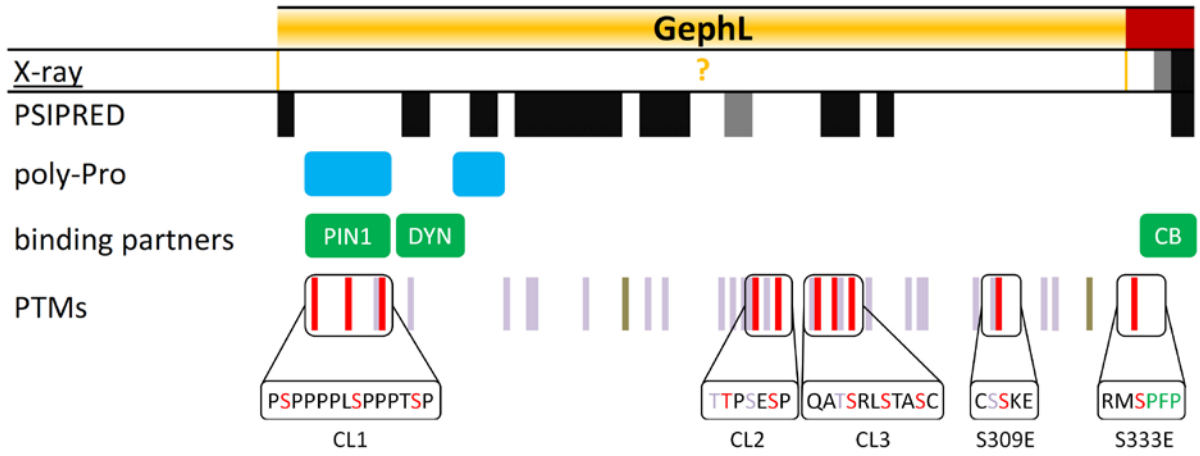

Figure 30 The Linker of gephyrin is a phosphorylation target. The linker and the very N-terminal end of GephE are displayed with the colour code for X-ray and PSIPRED secondary structure assignments (with the latter chosen as representative prediction algorithm) as in Fig. 17. Putative poly-proline helices are marked in light blue. The first putative poly-Pro region corresponds to the PIN1 binding motif, the second putative Poly-Pro helix does not contain a proline but instead a poly-glutamate stretch followed by two arginines. PTMs stand for post-translational modifications (found on www.phosphosite.org, April 2014), where red patches are residues that where replaced by phosphomimetic aspartates (CL1) or glutamates (CL2, CL3, S309, S333). Note that S333E directly precedes the CB binding site. Phosphosites not analysed in this thesis are marked in purple, while olive-green patches represent acetylation sites.

III.A.2.6.1 Phosphomimetic gephyrin mutants

Often phosphorylation sites are part of intrinsically disordered segments (Dunker *et al.*, 2002). This is also evident in gephyrin's linker: Thirty-two of the fourty serines or threonines in the linker region were already idenified as phosphorylation sites. One proteomic study revealed three phosphorylation clusters (CL1-3) (Fig. 30) which contained several phosphate groups within a single peptide of gephyrin (Huttlin *et al.*, 2010). To study their potential impact on gephyrin's overall structure, seryl- and threonyl-residues in the three identified phosphosite clusters as well as

individual residues in the second half of the linker and GephE were replaced with phosphomimetic residues (Fig. 30).

The mutants could be purified according to the same protocol as the wild-type protein resulting in similar yields and purities. None of the mutants displayed an obviously increased tendency to form higher oligomers compared to the wildtype protein, and hence all the following analyses were conducted with trimeric samples: aSEC experiments of the phosphomutants and the wildtype protein did not reveal significant differences in their hydrodynamic radius, which would point to a change in the oligomeric state of gephyrin. Likewise, thermal stability tests conducted with the Thermofluor assay did not point to significant alterations as well (data not shown). The SAXS studies were limited to an overall analysis: The R_g of the mutants (deduced from the Guinier approximation) varied between 63 Å and 65 Å (wildtype gepyrin: 63 Å, Table 31). Likewise, neither the scattering data (Fig. 31A) nor the comparison of the P(r) functions (data not shown) and the Kratky plots (Fig. 31B) disclosed significant conformational changes.

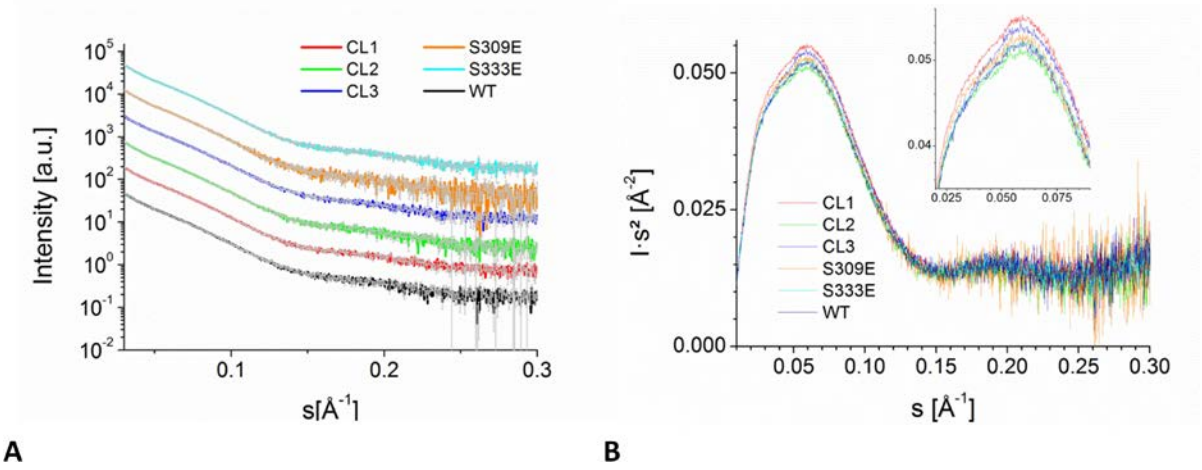

Figure 31 SAXS does not reveal significant conformational changes in the gephyrin phophomutants. While SAXS scattering curves (offset along the y-axis) in the I vs. s plot displayed similar profiles (A), the Kratky plot indicated gentle changes (B), which can be better recognized in the magnification (inset) and were most pronounced for CL1 and CL3.

Last, limited proteolysis was conducted to analyse potential conformational changes. Of all the mutants, only Geph-CL1 and CL3 displayed a proteolysis pattern, which could be clearly distinguished from the wildtype protein. Parts of the different proteolysis pattern for Geph-CL1 were already observed by a former diploma student, Kristina Keller (Keller, 2010): A major degradation product with an apparent mass of ~38 kDa was not observed in the wildtype protein, for which instead a ~33 kDa band was enriched (Fig. 32). Given that the apparent masses of GephG and GephE on an SDS-gel were ~24 kDa and 45 kDa, respectively, that left three possibilities: Degradation products between these two masses could be degraded GephE, a degraded GephGL fragment or even a product comprising parts of GephG and GephE together with the complete linker. Western blot

analysis using an anti-His antibody revealed that the huge majority of all bands below ~45 kDa were GL fragments, as above this mass the antibody recognized full-length gephyrin and yielded only weak signals for bands between 45 and 83 kDa (Fig. 33).

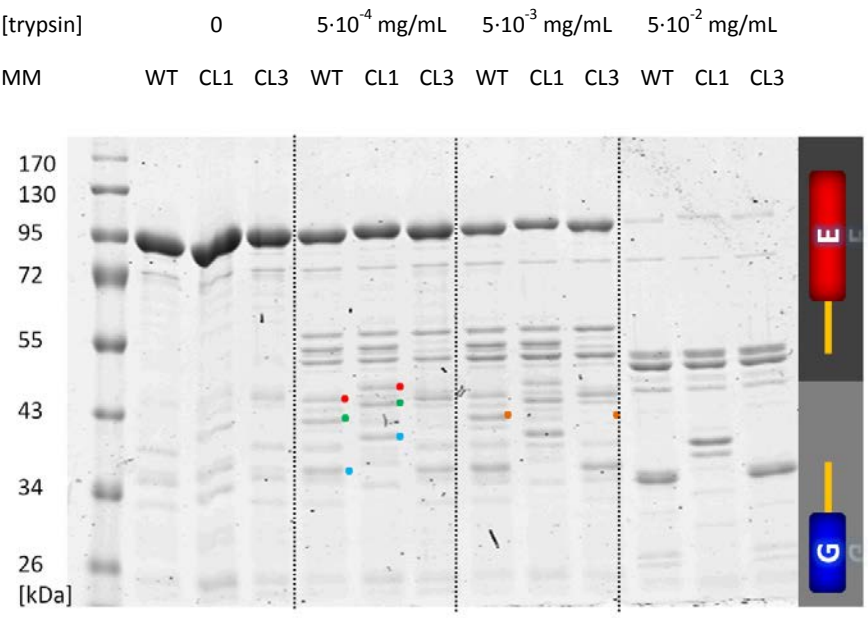

Figure 32 Limited proteolysis of gephyrin WT, CL1 and CL3. The three variants were trypsinated for one hour on ice at three different concentrations. As will be illustrated in Fig. 33, fragments with an apparent molecular mass below ~45 kDa are rather GL fragments, those exceeding 45 kDa rather correspond to GephE containing fragments.

The bands in question (33 kDa and 38 kDa) were recognized by the anti-His antibody which implies that the degradation products contained the N-terminal His-tag and differed in the linker by an extra segment with a mass of ~5 kDa. Further subtle differences could be observed, which also concerned the linker (red, green and blue points in Fig. 32). At least four (if not even six) bands appeared to be shifted to slightly higher molecular masses. It should be mentioned that incubation of Geph-CL1 with the prolyl-peptidyl-cis-trans isomerase PIN1, which was observed to bind to the poly-proline rich region (including the phosphorylation sites mimicked by the CL1 mutations) (Zita *et al.*,

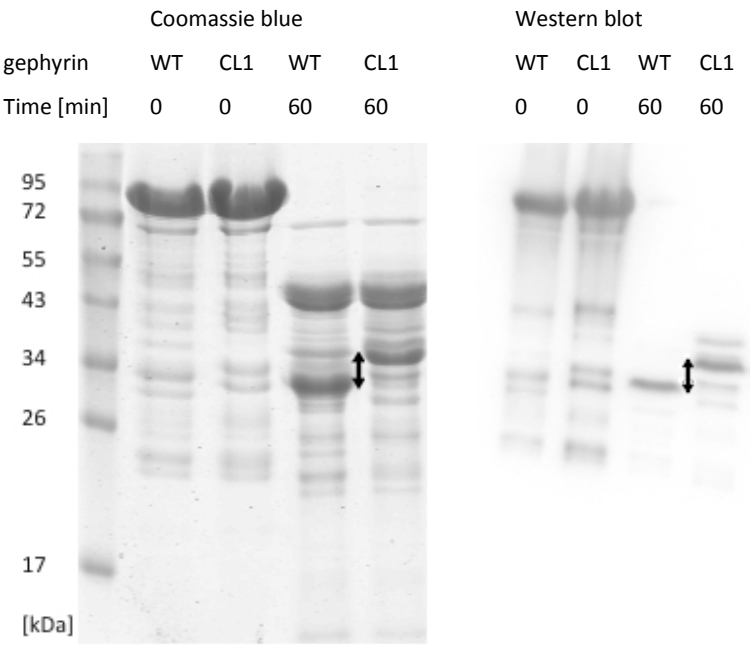

Figure 33 Limited proteolysis of gephyrin WT and Geph-CL1 revealed significant changes in the linker region. Gephyrin samples containing 1 mg/mL were digested for 0/60 minutes at room temperature with $5 \cdot 10^{-4}$ mg/mL trypsin. On the right-hand side a western blot is displayed for which an anti-His antibody was used. The double-headed arrows mark corresponding GephGL bands.

2007), did neither result in a change of the Stokes radius nor in significant changes in the limited proteolysis pattern (Keller, 2010). For Geph-CL3 changes with respect to GephWT were not that pronounced – at least at first glance: A GephWT degradation product at ~43 kDa could not be visualized in the CL3 variant (orange points in Fig. 32).

III.A.2.6.2 Analysis of gephyrin linker deletion mutants

In a different approach to identify determinants of the trimeric state, gephyrin variants were analysed, in which either the first or second half of the linker or almost the complete linker were deleted. The removal of a blocking linker segment could have potentially led to the formation of higher oligomers. Based on the secondary structure prediction (section III.A.2.1) and on the finding that limited proteolysis experiments resulted in an initially formed ~35 kDa His-tag containing fragment that was of virtually the same size as a construct comprising residues 1-253 (data not shown), Arg251 was arbitrarily defined as the last residue of the first linker half (Fig. 34).

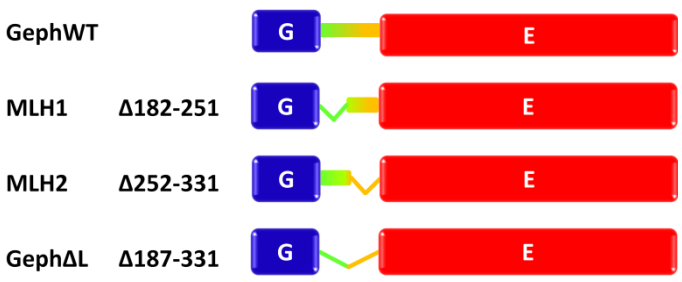

Figure 34 Overview of the gephyrin linker deletion mutants. Next to the abbreviations on the left-hand side (where MLH stands for missing linker half), the deleted range is given, indicated by a kink in the linker segment of the respective mutant (right-hand side). The linker spans the region between residues 182 and residues 331, implying that GephΔL still contains five residues of the N-terminal linker segment.

Linker deletion variants could be purified by the same purification protocol as the wild-type protein. In analogy to the full-length protein higher oligomers were also obtained for the linker variants and were separated from the putative trimeric fraction, which was still the preponderant species in all variants (Fig. 35). The trimeric linker variants did not form higher oligomers over time so that they can be regarded at least as kinetically stable. The assumption that also the linker deletion variants were trimeric was supported by the fact that after purification a prominent degradation product with an electrophoretic mobility similar to GephG was observed (apparent molecular mass: 24 kDa), presumably because GephG was incorporated in trimers with the respective linker deletion variant and can hence not be separated from the assembly (Fig. 36 and Fig. 39).

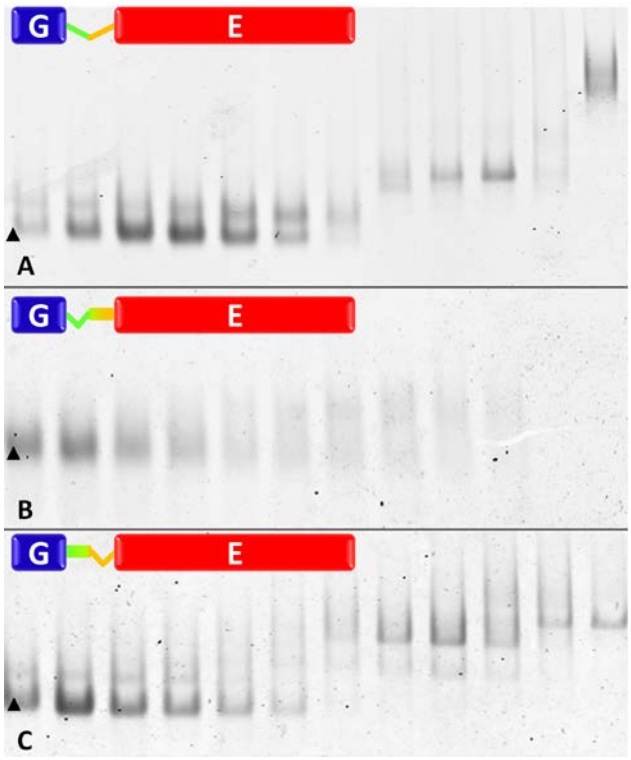

Figure 35 Native gels of linker deletion variants after anion exchange chromatography of the ΔL, MLH1 and MLH2 constructs (from top to bottom). (A) As for Geph-WT trimeric species are dominant and elute at lower salt concentrations (as indicated by the black triangles). Also in the case of MLH1 higher oligomers could have been detected, but presumably the lower resolution of the gel pretended the absence of several higher oligomeric species.

In a first step, the dimensions of the linker missing mutants were assessed in aSEC and DLS experiments and compared with those of full-length gephyrin. Not surprisingly, the aSEC chromatograms revealed the highest retention time (corresponding to a decreased hydrodynamic radius) for the variant without linker and the lowest retention time for the full-length protein (Fig. 37), and accordingly DLS results suggested the largest dimensions for the full-length protein and the most compact conformation for the variant which completely lacks the linker (Table 32). The most interesting finding was that both methods revealed significant differences between the two intermediates, MLH1 and MLH2, which possess virtually the same molecular masses. MLH2 was more extended than MLH1, as indicated by the higher DLS-derived hydrodynamic radius (6.9 nm vs. 6.3 nm) and the lower aSEC retention volume (11.0 mL vs. 11.3 mL) (Table 32).

SAXS results principally confirmed the trimeric state of the three deletion variants with deviations from the expected molecular mass of 13-23% (MLH1), 7-16% (MLH2) and 6-20% (ΔL) obtained by the different molecular mass determination methods (Table 32). In addition, the results from aSEC and DLS were confirmed: Compared to full-length gephyrin, deletion of the second half (MHL2) led to a slight decrease in the P(r)-derived maximal interatomic distance (D_{max}), from ~25 nm to ~23 nm, whereas deletion of the first half (MHL1) resulted in a D_{max} of only 18 nm, very close to the D_{max} value of 17.3 nm for GephΔL (Fig. 37B). R_g values were in accord with this order (Table 32). This

Figure 36 GephG was presumably the major degradation product of GephΔL. Compare the ~24 kDa band of the Geph ΔL sample (A) after anion exchange chromato-graphy with the GephG sample (B).

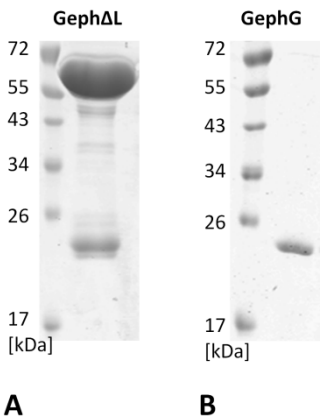

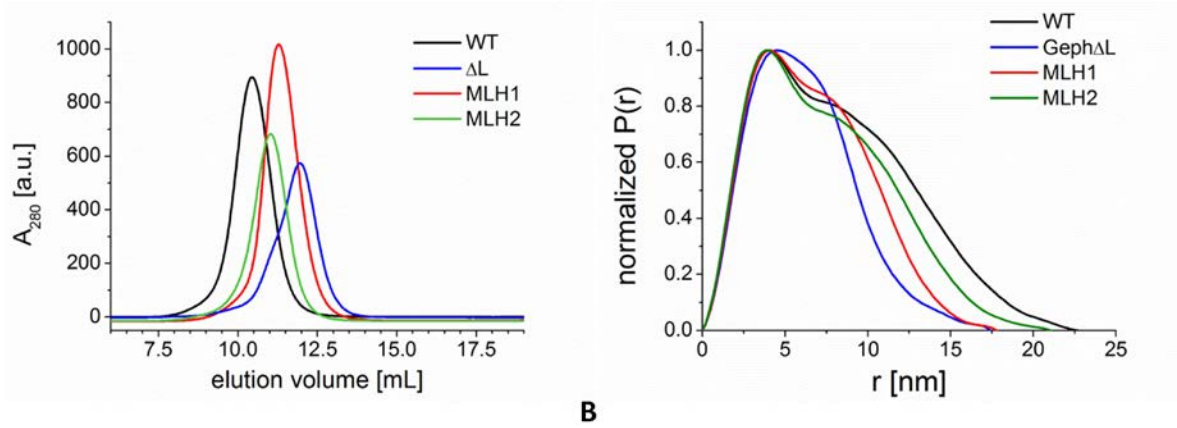

Figure 37 Dimension analysis of the linker deletion variants. (A) aSEC experiments revealed significantly different dimensions for MLH1 and MLH2 despite a negligible mass difference. (B) The SAXS data-derived P(r) functions of trimeric WT holo-gephyrin, MHL1/2 and ΔL argue for a higher degree of compaction in the MLH1 construct.

suggests that it is rather the first half of the linker (present in MLH2) than the second half of the linker that contributes to the extension of gephyrin. For unknown reasons, further SAXS analysis of the GephΔL and Geph-MLH1/2 data by ensemble modelling turned out not to be straightforward, yielding non-acceptable fits in the small-angle region, and the analysis was therefore put on hold (Appendix D).

	R_H [Å]	R_g(Guinier) [Å]	R_g (P(r)) [Å]	D_{max} [Å]	Porod vol. [Å³]	MM_{Porod} [kDa]	MW_{DAMMIN} [kDa]	$MM_{SAXS-MOW}$ [kDa]	MM_{VC} [kDa]	$MM_{monomer}$ [kDa]
MLH1	62±1	50±2	52±2	185±37	317±64	198±40 (2.6)	175±35 (2.3)	199±20 (2.6)	192.8±17 (2.5)	76
MLH2	69±0	57±2	57±2	220±44	337±67	210±42 (2.8)	189±38 (2.5)	209±21 (2.8)	194±18 (2.6)	75
ΔL	54±1	46±2	48±2	173±35	296±60	185±37 (2.7)	164±32 (2.4)	188±38 (2.8)	184±17 (2.7)	68

Table 32 Overall characterization of linker deletion variants by DLS and SAXS. R_H hydrodynamic radius derived from DLS analysis; *R_g(Guinier)* R_g based on Guinier approximation; *R_g(P(r))* R_g obtained by P(r) function; D_{max} maximum interatomic distance assessed with the P(r) function; molecular masses MM_{Porod}, MM_{DAMMIN}, MM_{VC}, $MM_{SAXS-MOW}$ were obtained by calculations of the Porod volume, the excluded volumes of DAMMIN models, the volume of correlation invariant and the SAXS-MOW webserver, respectively. Values in brackets indicate the oligomeric state obtained by division of the experimental value by the molecular mass of the monomer ($MM_{monomer}$).

Partial compaction of a presumably unstructured linker could arise from interactions with folded domains (Babu *et al.*, 2012), which would lead to differences in the thermal unfolding of the terminal domains in the context of the linker deletion variants. As already observed by Eunyoung Lee, a former PhD student in the lab, Thermofluor curves displayed two local maxima for constructs containing both terminal domains, one in the range of 60°C and one in the range of 80°C. The melting temperatures of 61°C and 80°C for isolated GephE and GephG, respectively, suggested that the lower T_M transition corresponded to GephE unfolding, whereas the transitions at higher T_M transitions indicated GephG destabilization (Fig. 38A). The degree of the latter can hardly be judged in Thermofluor curves, as GephE aggregation presumably gave rise to a signal decay, which interfered with the GephG signal increase. Thus, the focus was set on GephE (de-)stabilization in the different

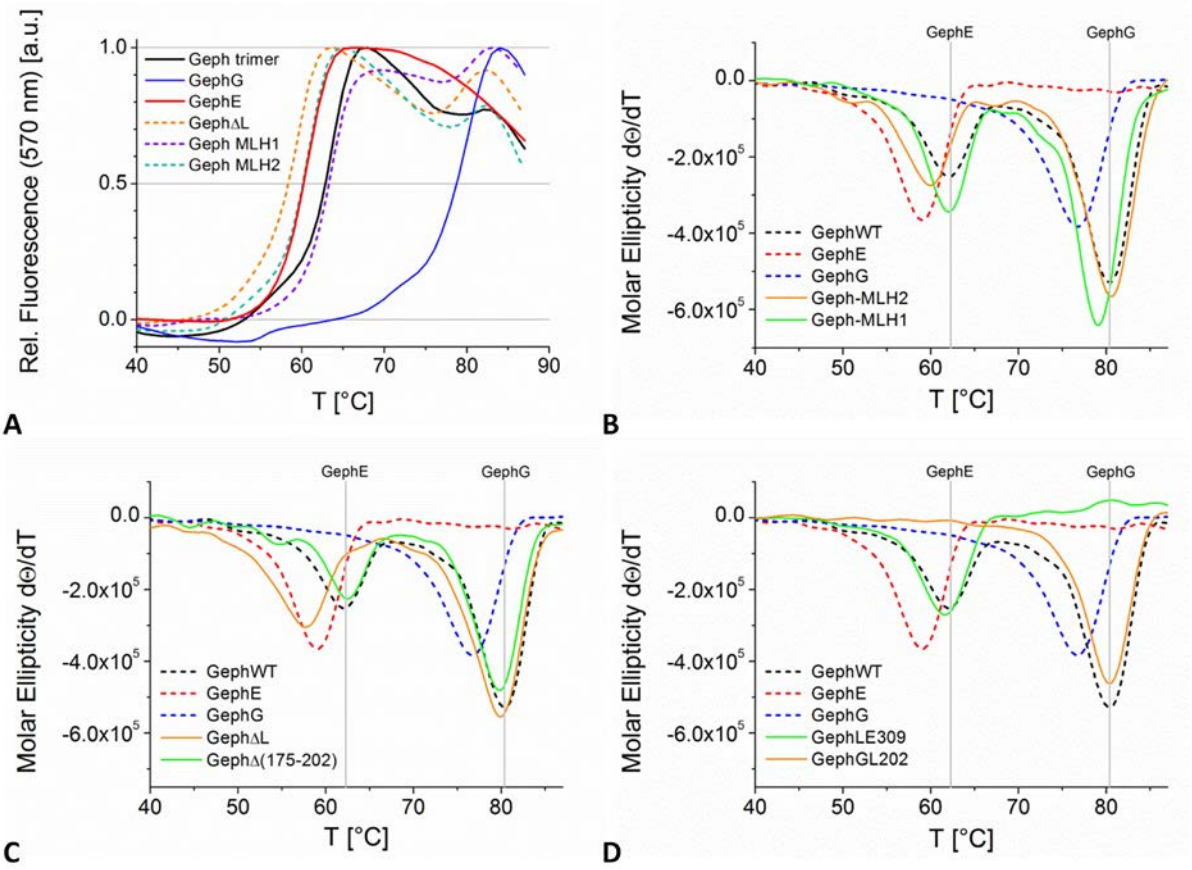

Figure 38 Thermostability analyses of various gephyrin variants. (A) Thermofluor melting curves of selected gephyrin variants. GephWT, GephG and GephE curves are shown in full lines, whereas the curves for the linker missing variants are displayed as dashed lines. (B) Deletion of either half of the linker led to a slight thermal destabilization of the respective adjacent domain (when compared to the full-length protein, whose melting temperatures were indicated by vertical lines). (C) Variants containing only the five N-terminal linker residues (GephΔL) and missing residues 175-202 (GephΔ(175-202)) both displayed no significant destabilization of the GephG interface. Note the destabilization of GephE in GephΔL to a higher extent than in GephE. (D) Adjacent linker segments of less than 25 residues were sufficient to increase the melting temperatures of the isolated domains to those of the full-length protein.

gephyrin variants. In comparison to isolated GephE, T_M values for GephE unfolding were higher for the full-length protein and Geph-MLH1, whereas no T_M shift was obtained for Geph-MLH2. Hence, a correlation between the degree of GephE stabilization and the presence of the second linker half could be observed. Interestingly, in the context of GephΔL GephE appeared to be even further destabilized (Fig. 38A).

Melting temperatures were also obtained by CD spectroscopy and were found to be generally consistent with the Thermofluor data in terms of stabilization (Table 33 & Fig. 38A). Beyond that, CD spectroscopy also allowed for a T_M analysis of the GephG transition, which revealed that GephG was stabilized as well in the context of the full-length protein (at least in the 50 mM potassium phosphate buffer, pH 8, used for CD experiments) but also in the linker deletion variants, including the GephΔL (missing residues 187-331) and the GephΔ(175-202) variants (Fig. 38C). Extensions of GephE and GephG by adjacent linker stretches of 23 residues (in GephLE309) and 21 residues (GL202), respectively, were sufficient to stabilize the terminal domains to the same extent as in the holo-protein (Fig. 38D).

	Thermofluor		CD	
	GephG	GephE	GephG	GephE
Geph-WT	81	63	80.4±0.2	62±0.3
GephG	80	n.a.	76.7±0.4	n.a.
GephE	n.a.	61	n.a.	58.9±0.1
GephGL	80	n.a.	n.d.	n.a.
GephGL202	n.d.	n.a.	80.4±0.2	n.a.
GephLE	n.a.	63	n.a.	n.d.
GephLE309	n.a.	n.d.	n.a.	61.6±0.2
Geph-ΔL	79.5	59.5	80.1±0.2	57.6±0.3
Geph-MLH1	80.5	63	79.2±0.3	62.1±0.1
Geph-MLH2	80.5	61	80.6±0.3	59.9±0.3

Table 33. Thermal stability of gephyrin and gephyrin deletion and truncation variants. The variants are listed on the left-hand side. The melting temperatures (in °C) of GephG and GephE interfaces were assessed by the Thermofluor method using SEC-4 buffer and the decrease in circular dichroism at 200 nm with increasing temperature in 50 mM potassium phosphate, pH 8. Values marked in red indicate a destabilization of the respective interface in comparison to the wild-type protein (underlined values). n.d.: not determined; n.a.: not available.

Linker-domain interactions might also become evident in limited proteolysis experiments with Geph-MLH1 and Geph-MLH2, which were found to be both trimers and comprised linker segments of comparable length. Two enzymes were used: Trypsin, which cleaves with a high specificity after basic residues, and subtilisin with a comparatively low specificity. The outcome was very similar for both proteases, indicating that there was no considerable bias due to the different amino acid compositions of the linker halves: The MHL1 construct displayed a delayed degradation for a linker segment adjacent to GephE (red box, Fig. 39), *vice versa*, in the MHL2 construct proteolysis was

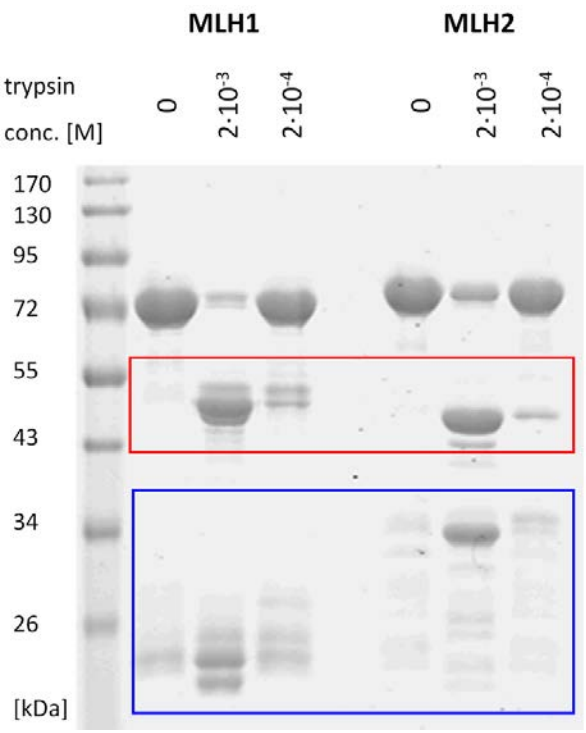

Figure 39 Comparative limited proteolysis of the MLH mutants. Based on western blot analysis (Fig. 33), fragments above ~45 kDa were identified as Linker-GephE segments and fragments between ~25 and ~45 kDa as GephG-linker segments. In MLH1 and MLH2 GephE-linker and GephG-linker fragments were stabilized (red and blue box), respectively.

retarded for a segment close to GephG (blue box, Fig. 39). These results suggested that the N-terminal part of the linker folded back onto GephG while the C-terminal linker segment interacted with GephE. As will be discussed below, further mapping of the stabilized segments, e.g. by mass spectrometry, was abandoned for reasons given in section III.A.4.6.

III.A.2.7 Analysis of the linker in different environments: MBP-linker, GephGL, GephLE

Results in the previous sections suggested an important role of the linker for the conformation and stabilization of the full-length protein. Hence, the following sections will focus on the characterization of linker compactness in different contexts, namely in

- the absence of a terminal domain (protein fusion of the maltose-binding protein (MBP) and the linker, chapter III.A.2.7.1), and
- the presence of either terminal domain (resulting in the constructs GephGL and GephLE, which are described in chapter III.A.2.7.2 and chapter III.A.2.7.4, respectively).

Between the GephGL and the GephLE chapters a small excursion is inserted, in which MBP-L variants and GephGL were utilized to probe potential linker-GephE interactions (chapter III.A.2.7.3).

III.A.2.7.1 MBP-Linker

As higher gephyrin oligomers had an increased tendency to form aggregates and Geph-ΔL on the other hand could be purified, expression and purification of the linker alone did not seem to be promising. Hence, it was decided to express the linker as a protein fusion with MBP (referred to as MBP-linker or MBP-L), as the MBP is well-known to even keep highly aggregation-prone proteins in solution (Sun *et al.*, 2011b).

The protein could be purified and concentrated up to 1 mM, for which – after centrifugation – very viscous, gel-like pseudo-pellets were obtained, which were reminiscent of a phase separation. Centrifugation of previously frozen protein (stored at -80°C for five months) for more than 3 hours to remove the gel-like aggregates resulted in concentrations of just 100 µM. These results implied, that the linker on its own was rather insoluble, even decreasing the solubility of the solubility tag MBP. Analytical SEC using a Superdex 200 10/300GL column revealed a huge increase in the hydrodynamic radius of MBP with the linker as fusion partner when compared to another MBP fusion protein (MBP-DIC), where DIC was a dodecapeptide derived from the intermediate chain of the dynein motor (see section III.B.2.14), resulting in a decrease in the elution volume by more than 2 mL.

	R_g(Guinier) [Å]	R_g(P(r)) [Å]	D_{max} [Å]	Porod vol. [Å³]	MM_{Porod} [kDa]	MW_{DAMMIN} [kDa]	$MM_{SAXS-MOW}$ [kDa]	MM_{VC} [kDa]	$MM_{monomer}$ [kDa]
MBP-L	45±4	54±4	235±45	149±30	93±20 (1.6)	88±20 (1.5)	97±20 (1.6)	78±8 (1.3)	61

Table 34 Overall characterization of the MBP-linker fusion protein by SAXS. *R_g(Guinier)* R_g based on Guinier approximation; *R_g(P(r))* R_g obtained by P(r) function; *D_{max}* maximum interatomic distance assessed with the P(r) function; molecular masses *MM_{Porod}*, *MM_{DAMMIN}*, *MM_{VC}*, *$MM_{SAXS-MOW}$* were obtained by calculations of the Porod volume, the excluded volumes of DAMMIN models, the volume of correlation invariant and the SAXS-MOW webserver, respectively. Values in brackets indicate the oligomeric state obtained by devision of the experimental value by the molecular mass of the monomer (*$MM_{monomer}$*).

SAXS experiments were carried out with protein (after two weeks of storage at -80°C) in a concentration range from 1 to 9 mg/mL (which corresponds to 18 to 163 µM). The curves obtained at the three highest concentrations could be superposed (not shown), however, only for the two highest concentrations the signal-to-noise ratio was sufficient to allow for further analysis. The R_g values (as determined by the Guinier approximation) varied between 43 and 47 Å. The Guinier plot displayed signs, which point to sample aggregation, especially for the two highest concentrations (6 and 9 mg/mL), rendering the value of the ensuing analysis questionable (Table 34). To minimize potential aggregation effects, the curve of the sample with the highest concentration was truncated and chosen for further analysis. EOM modelling did not yield fits of sufficient quality (χ = 1.5), especially in the small-angle region (Appendix E). Nevertheless, it appears as if MBP-L displayed a significantly increased R_g when compared to the theoretical R_g of MBP (MBP: 22 nm, MBP-L: ~45 nm,

Table 34). Preliminary MALS analysis of MBP-L, which was frozen in liquid nitrogen and stored for five months at -80°C, revealed a predominant population of aggregates and a minor fraction of one third with a molecular mass of ~200 kDa, which would be consistent with a MBP-L trimer (data not shown). For comparison the mass of the MBP-L monomer amounts to 61 kDa. Further analysis of MBP-L, which would need to be presumably conducted with a fresh protein preparation, will be performed after the thesis.

III.A.2.7.2 GephGL

While for the terminal domains the oligomerization interfaces are well-characterized, nothing is known about potential oligomerization interfaces in the linker region, which might regulate the oligomerization state of gephyrin as well. This hypothesis was fueled by studies of my predecessor Eunyoung Lee, who observed large hydrodynamic radii for various G-Linker constructs (Lee, 2009). Hence, several gephyrin constructs comprising GephG and linker segments of varying lengths were analysed with respect to their oligomeric state. Mutants (see Fig. 40) contained GephG plus the first quarter of the linker (GL220), the first half of the linker (GL253) or the complete linker (GL).

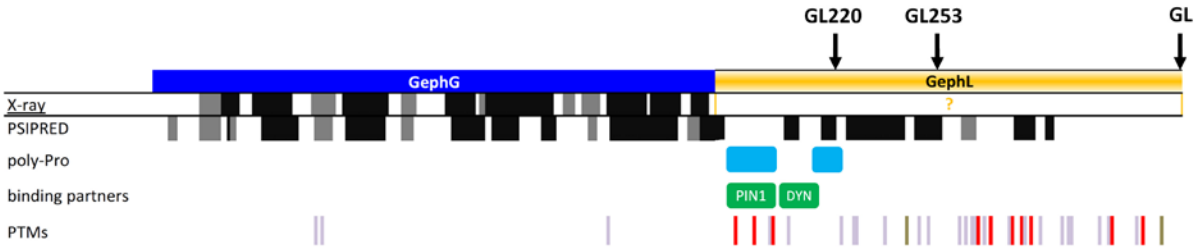

Figure 40 Organization of gephyrin G domain and the linker. Secondary structure assignment according to the X-ray structure (PDB code: 1JLJ) and the PSIPRED prediction are followed by the prediction of segments potentially adopting a poly-proline helix, binding motifs for interaction partners and post-translational modifications (PTMs) The colour code is the same as in Fig. 30, and the arrows on top as well as the numbers in the annotation indicate the last residues of the three GephGL constructs compared in this section.

For the purification of these constructs the same protocol could be applied as for full-length gephyrin. For all constructs (GL, GL253 and GL220) a multi-peak chromatogram was obtained during anion exchange chromatography, which resembled that of Geph-WT (exemplarily shown for the GephGL variant, Fig. 41). On SDS-PAGE gels after the anion exchange chromatography step an additional band at ~70-80 kDa became apparent for fractions that did not belong to the main peak, consistent with a copurified chaperone (Fig. 41A).

The chromatogram of the final preparative SEC step for GephGL unveiled a large hydrodynamic radius, reflected in an elution volume just slightly below that of full-length gephyrin. This result was

reproducible on an analytical SEC column, yielding a difference in the elution volumes of just 0.25 mL, when compared to the full-length protein (Fig. 41B).

As mentioned before, the relationship between mass and the elution volume in aSEC experiments is only valid for spherical proteins. Given that the linker is responsible for gephyrin's flexibility (chapter III.A.2.4), one should take into account that extended linkers in the context of trimers might have led to non-spherical shapes and hence to large hydrodynamic radii. This view is in line with MALS measurements of GephGL, which indicated a molecular mass of 106 kDa for GephGL, which was just slightly smaller than the expected 114 kDa for a trimer.

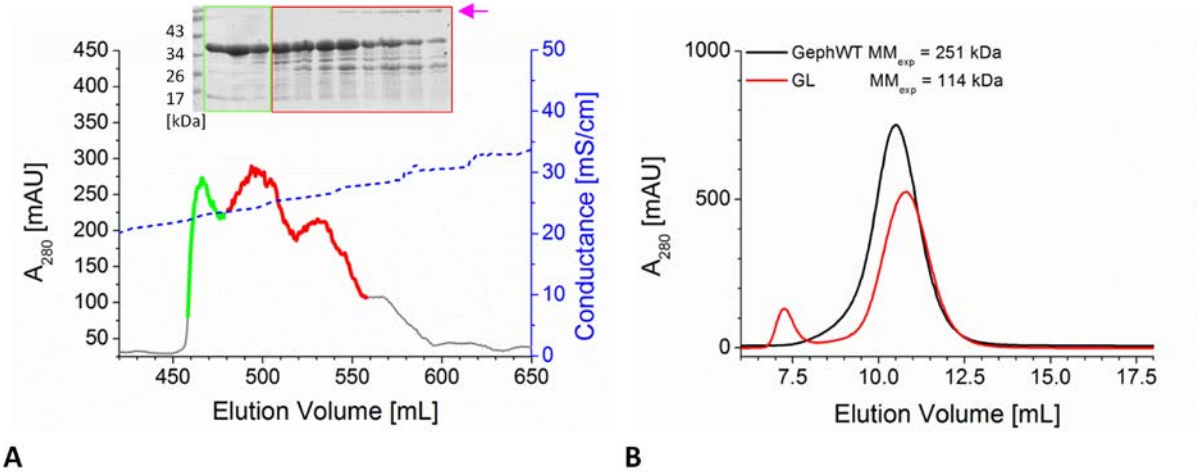

Figure 41 Purification of GephGL. (A) Anion exchange chromatography profile of GephGL. The inset displays a Coomassie stained SDS-gel of the corresponding fractions. Note the additional ~75 kDa band occurring at increasing salt concentrations. (B) SEC using a Superdex 200 10/300 GL column equilibrated in SEC-1 buffer. GephGL elutes just slightly later than GephWT, despite the fact that the respective expected trimer masses differed by a factor of more than two.

Hence, SAXS experiments were conducted to evaluate the oligomeric state of GephGL220, GephGL253 and GephGL but also to compare the linker dimensions with those of the linker in full-length gephyrin (Table 35 & Fig. 42). The R_g values of 38 Å (GL220), 45 Å (GL253) and 58 Å (GL) are significantly higher than the theoretical R_g of 24 Å, as determined for the crystal structure of GephG (PDB entry 1JLJ). P(r) functions, although more appropriate for proteins without conformational variability (Bernado, 2010), account for elongated conformations and revealed surprisingly small differences between GL220 and GL253 (Fig. 42A).

The molecular mass determination as deduced from the overall parameters suggested that all GephGL variants formed tetramers or pentamers (Table 35). These values should be taken with caution, as - not surprisingly - the excluded/Porod volumes of differently compact GL trimers varied with the R_g (Fig. 42B). This also implied that the molecular mass of several GephGL conformers – all forming trimers – varied with their compactness. This relationship was illustrated for the GephGL variant and revealed that the trimeric state was only obtained for very compact conformations, while

even just slightly extended conformers pretended falsely high (not low) molecular masses and consequently falsely high oligomeric states (Fig. 42B).

Hence, the parameters might be interpreted as a first hint that the GephGL variants formed extended trimers. To test this hypothesis, EOM was conducted with an initial pool containing only trimers, and indeed good fits could be obtained (Fig. 42C&D). Thus, one can conclude that extended linkers in gephyrin-GL give rise to the high values for the hydrodynamic radius and the SAXS-derived R_g of 58 Å (compared with 65 Å for full-length gephyrin) rather than a change in the oligomeric state.

In a next step, the R_g values for the isolated linkers of the final GephGL ensemble were weighted by the contribution of the corresponding model, yielding the R_g(Linker) of a theoretical average linker in the context of this variant (see Methods, section II.B.6.2.9). It turned out that that the R_g for the 16 kDa linker was 40.6 Å and hence in the same range as the R_g of 38 Å of the catalase tetramer, which possesses an almost 15-fold higher molecular mass of 232 kDa. The GephGL-linker R_g was also 1.5 times higher than the comparable R_g of gephyrin-WT linkers (28 Å), pointing to a considerable compaction of the linker in the context of full-length gephyrin, for which GephG on its own was not sufficient.

	R_g(Guinier) [Å]	R_g (P(r)) [Å]	D_{max} [Å]	Porod vol. [Å³]	MM_{Porod} [kDa]	MW_{DAMMIN} [kDa]	$MM_{SAXS-MOW}$ [kDa]	MM_{VC} [kDa]	MM_{MALS} [kDa]	$MM_{monomer}$ [kDa]
GephGL	58±3	66±2	260±52	284±56	178±36 (4.7)	159±32 (4.2)	167±17 (4.4)	129±13 (3.4)	106 (2.8)	38
GephGL253	42±2	46±2	162±32	187±38	117±23 (3.9)	108±22 (3.6)	121±24 (4.1)	106±11 (3.6)	n.d.	29.7
GephGL220	39±2	41±2	145±29	167±33	104±20 (3.9)	96±19 (3.6)	108±22 (4.1)	109±11 (4.1)	77 (2.9)	26.5

Table 35 Overall characterization of GephG-linker variants by SAXS. *R_g(Guinier)* R_g based on Guinier approximation; *R_g(P(r))* R_g obtained by P(r) function; *D_{max}* maximum interatomic distance assessed with the P(r) function; molecular masses *MM_{Porod}*, *MM_{DAMMIN}*, *MM_{VC}*, *$MM_{SAXS-MOW}$* were obtained by calculations of the Porod volume, the excluded volumes of DAMMIN models, the volume of correlation invariant and the SAXS-MOW webserver, respectively. Values in brackets indicate the oligomeric state obtained by devision of the experimental value by the molecular mass of the monomer (*$MM_{monomer}$*).

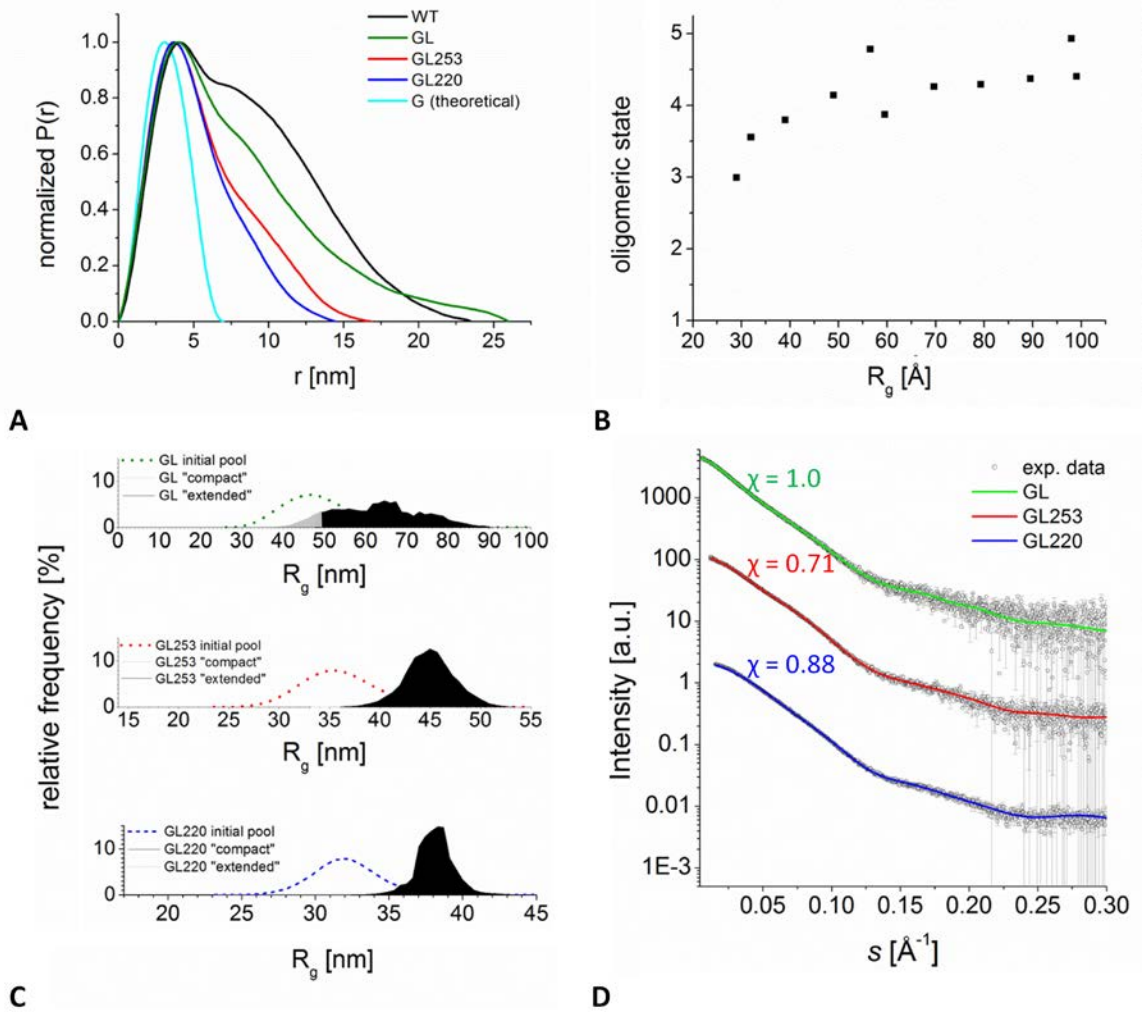

Figure 42 SAXS analysis of GephGL variants. (A) The normalized P(r) functions of the GephGL variants revealed their extended character (when compared with GephG and GephWT). Note the similar D_{max} values for GephWT and GephGL. (B) Molecular mass determination especially of GephGL was not straightforward, since the apparent oligomeric state increased as a function of R_g. For this graph, pseudo-experimental data for arbitrarily chosen GephGL conformers of the EOM-trimer pool with varying R_g values were generated (section II.B.6.2.8). Only for very compact conformers was the trimeric state correctly obtained. (C) EOM R_g distributions of the GephGL variants revealed a clear preference for extended states (black area under the curves), which was most pronounced for GephGL220 and less pronounced for GephGL. (D) EOM fits to the experimental data. The different curves were offset along the y-axis for clarity.

III.A.2.7.3 Approaches to probe the GephE-GephL interface

Based on the results of the previous sections, linker-GephE interactions were assumed to be a likely mechanism, which prevented dimerization of distinct gephyrin trimers. According to this hypothesis, an unmasked, monomeric GephE should be capable to bind to the linker. Monomeric GephE should be available in the context of the Geph-ΔL construct, since both inter- and intra-trimeric GephE dimerization are expected to be inhibited as outlined below:

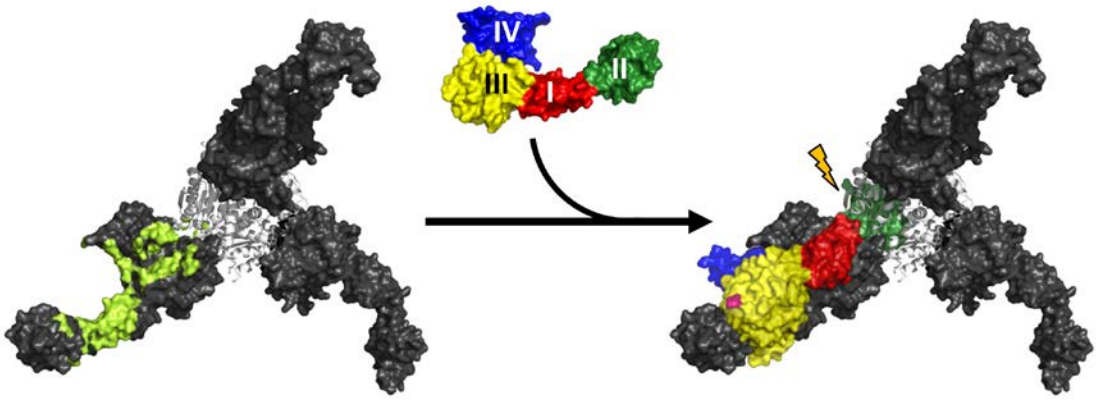

Figure 43 Hypothetical Geph-ΔL explaining why neiter inter- nor intra-trimeric dimerization are likely. Hpyothetical GephΔL conformer in which GephE monomers are coloured in dark grey extending away from the GephG trimer coloured in white. Geph-ΔL should offer three unmasked GephE interfaces, one of which is marked in lemon green on the left-hand side. Hypothetical binding of GephE coloured according to its subdomains as in Fig. 3 from a different trimer should not be possible in this configuration due to steric clashes of subdomain II of the incoming GephE (indicated by the flash on the right-hand side) with the GephG core. This panel also explains why intra-trimeric dimerization is not likely: The distance of ~80 Å between the GephG core and the N-terminus (coloured in magenta) of the second GephE subunit cannot be bridged by a five-residue-linker.

- Geph-ΔL trimer formed stable trimers (Fig. 47C). To form higher oligomers, GephE subdomain 2 of an approaching Geph-ΔL trimer would have to be inserted between GephE and GephG, which by and large is expected to be prevented (Fig. 43). Hence, one can assume that *inter-trimeric* GephE dimerization (Fig. 53) did not occur or was at least kinetically prevented.
- The linker connecting GephG and GephE, was only 5 residues long, and hence not long enough to allow for *intra-trimeric* GephE dimerization (Fig. 43).

The first-choice of binding partners for linker-accessible Geph-ΔL, which due to its absence of the linker should be able to interact with a linker provided in trans, were MBP-Linker constructs harbouring the second half of the linker, MBP-L(252-331), and the last fifth of the linker, MBP-L(303-331), as limited proteolysis and thermal unfolding assays pointed to interactions between the second half of the linker and GephE. As expected MBP-L(252-331) and MBP-L(303-331) could be obtained in acceptable amounts and purity. However, native PAGE analysis revealed no interactions of either MBP construct with Geph-ΔL (Fig. 44).

Hence, an alternative approach was chosen: MBP-L constructs were replaced by GephGL. This construct was expected to exert a higher affinity due to avidity effects (Kane, 2010), as now each binding partner offered three bindings sites. However, also this approach did not result in unambiguously positive results in nPAGE, aSEC and ITC – at least under the conditions tested (Fig.

45). Regarding the ITC experiment, there was a change from endothermic to rather exothermic heat signatures, however, this change did not provide a promising starting point for further experiments.

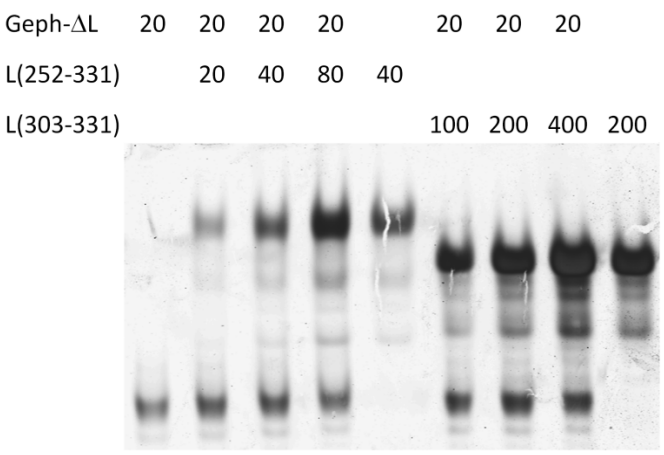

Figure 44 Native PAGE analysis of Geph-ΔL:Linker mixtures did not reveal linker interactions with either terminal domain. L(x-y) indicates the presence of a fusion protein of MBP with the linker comprising residues x to y. Concentrations are given in µM. Incubation was performed using SEC-4 buffer.

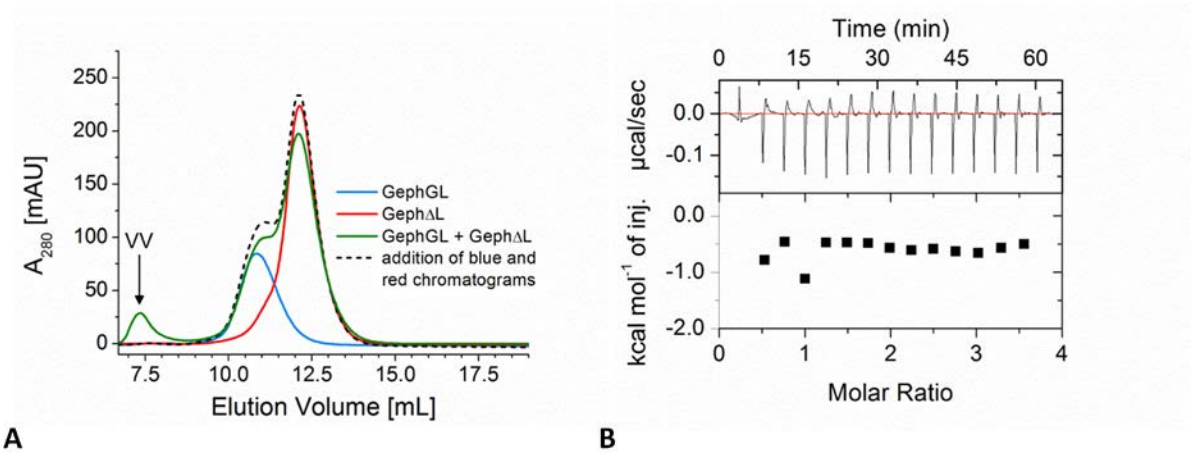

Figure 45 Geph-ΔL and GephGL do not form stable complexes. (A) Analytical SEC (conducted in SEC-2 buffer) of GephGL-GephΔL mixtures differed just slightly from the addition of the chromatograms of the individual components. VV stands for void volume. (B) A preliminary ITC experiment in SEC-2 buffer using 28 µM GephGL (cell) and 473 µM Geph-ΔL resulted in a curve with oscillations around -0.1 µcal/sec (upper panel).

III.A.2.7.4 GephLE: The linker on its own is not sufficient in preventing GephE dimerization

Presumably, the most suitable way to test interactions between the linker and GephE was the determination of the oligomeric state of Linker-GephE (referred to as GephLE, residues 182-750 of splice variant P2), as both putative binding partners are covalently linked as in the context of the full-

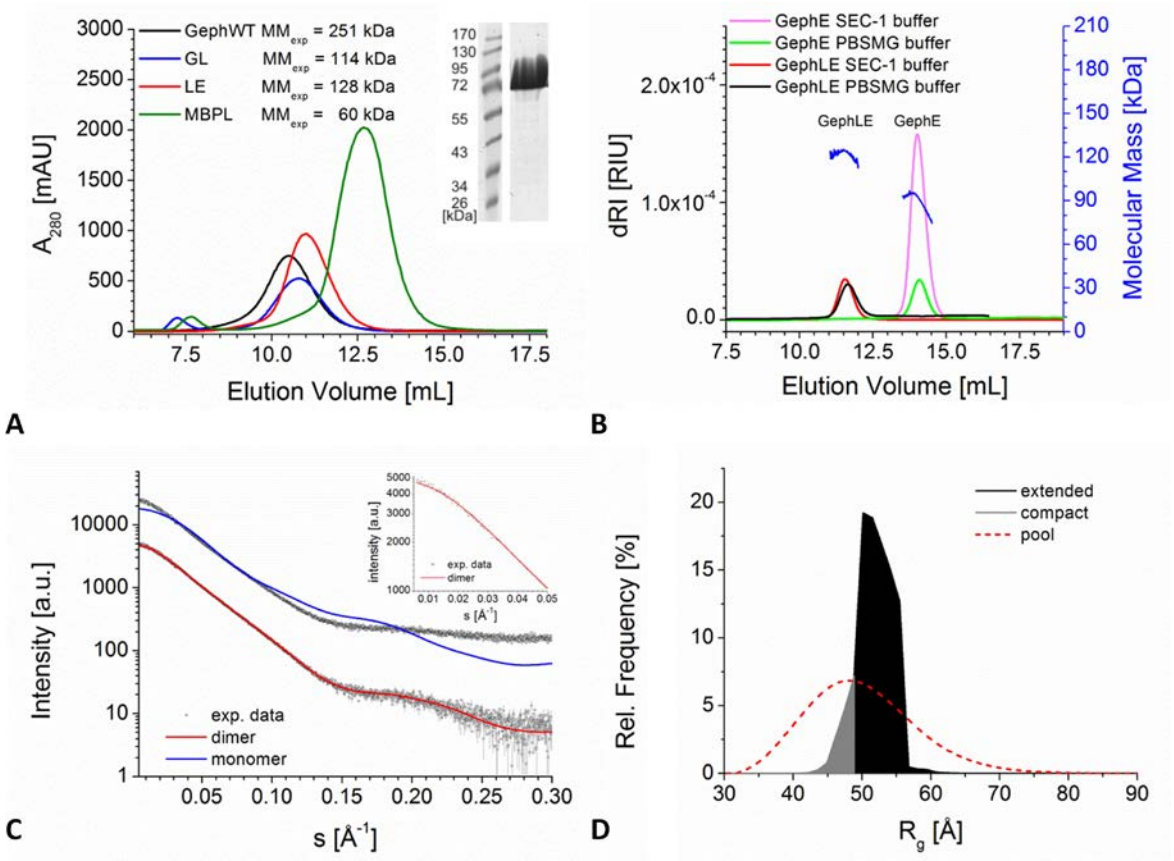

Figure 46 GephLE formed a dimer with a preference for extended states. (A) Comparative aSEC experiments with various linker-containing constructs revealed similar hydrodynamic radii for GephWT, GephGL and GephLE. In comparison to MBP-L the GephLE construct eluted significantly earlier despite similar molar monomer masses. The inset displays an excerpt of a Coomassie stained SDS-PAGE gel with GephLE after preparative SEC. (B) SEC-MALS experiments demonstrated that GephLE forms a dimer in SEC-1 buffer as well as the PBSMG buffer (described by Bedet et al., 2007). Blue curves indicate the masses of GephLE (124 kDa) and GephE (88 kDa), whereas the other curves are dRI (differential refractive index) plots. C) EOM analysis of GephLE pools containing either monomers (blue fit to the experimental data represented as small spheres) or dimers (red fit to the experimental data). For the monomeric scenario poor fits were obtained, suggesting that Geph-LE formed dimers. The inset displays the rather low signal-to noise ratio in the small-angle region. (D) The EOM R_g distribution for the dimer scenario revealed a preference for extended GephLE states.

length protein. Based on comparative aSEC experiments with a similar LE construct (containing an additional splice cassette in the linker, Fig. 52) and GephE it was proposed that the linker can interfere with GephE dimerization by folding back onto GephE (Bedet *et al.*, 2006).

A comparison of GephLE with the other linker containing variants presented above revealed that it has a rather large hydration radius (Fig. 46). In aSEC experiments GephLE eluted later than the full-length protein, but just slightly later than GephGL and clearly earlier than GephE and MBP-L (typically ~14 mL). Given the neglible differences in the monomer masses of GephLE and MBP-L (61.5 kDa and 60.4 kDa, respectively), these data were consistent with either a more pronounced linker compaction in the MBP-L construct (when compared to GephLE) or with a higher oligomeric state of GephLE, in which two or more linkers contributed to a large hydrodynamic radius.

SEC-MALS experiments under various conditions argued for the latter explanation – namely for the formation of dimers. In contrast to the observations of Bedet et al., GephLE eluted clearly earlier than GephE – in SEC-1 buffer as well as in the PBS buffer containing 20% glycerol that was used by Bedet et al. (2006). Only for the former condition a reliable molecular mass of 125 kDa (expected dimer mass: 128 kDa) could be determined. However, as for both proteins the hydrodynamic radius did not significantly differ under the conditions given, a considerable shift of GephLE to the monomeric state in PBSMG buffer was not very likely.

	R_g(Guinier) [Å]	R_g (P(r)) [Å]	D_{max} [Å]	Porod vol. [Å³]	MM_{Porod} [kDa]	MW_{DAMMIN} [kDa]	$MM_{SAXS-MOW}$ [kDa]	MM_{VC} [kDa]	$MM_{monomer}$ [kDa]
GephLE	5.3	56±2	225	291	182 (2.8)	159 (2.5)	174 (2.7)	150 (2.3)	64

Table 36 Overall characterization of GephLE by SAXS. *R_g(Guinier,)* R_g based on Guinier approximation; *R_g(P(r))* R_g obtained by P(r) function; *D_{max}*, maximum interatomic distance assessed with the P(r) function; molecular masses *MM_{Porod}*, *MM_{DAMMIN}*, *MM_{VC}*, *$MM_{SAXS-MOW}$* were obtained by calculations of the Porod volume, the excluded volumes of DAMMIN models, the volume of correlation invariant and the SAXS-MOW webserver, respectively. Values in brackets indicate the oligomeric state obtained by division of the experimental value by the molecular mass of the monomer (*$MM_{monomer}$*).

SAXS studies were carried out to further analyse the degree of linker compaction. Molecular mass estimations from the excluded volume, Porod volume, etc. turned to be inaccurate as already observed for GephGL, yielding for example a 2.7mer, which was apparently wrong (Table 36). Hence, the focus was shifted again on the ensemble modelling approach, as single conformation modelling was obviously misleading. SAXS experiments were consistent with GephLE dimer formation: Pools of 250,000 monomers and 250,000 dimers were created and used as input for subsequent EOM analyses. Three EOM modelling attempts with the monomer pool resulted in the selection of exactly the same ensemble, characterized by a poor χ value of 11.99. On the contrary, for the dimer scenario χ values of 1.85 were achieved with a decent fit. The latter value was acceptable with regard to the data noise present already in the small angle region (see inset Fig. 46A). The R_g distribution after EOM suggested a preference for extended states, however, not as pronounced as observed for the GephGL constructs. The average R_g value of the linker (determined in an analogous manner to the

one in section III.A.2.7.2) in the selected ensemble was 44.8 Å and thus comparable to the value obtained for GephGL, again pointing against the linker covering a significant portion of the GephE interface. Taken together, the data implied that the linker on its own was – at least under the tested conditions – not sufficient for preventing GephE dimerization in full-length gephyrin.

III.A.2.8 Assessing a potential GephG-GephE interaction

Since the linker on its own was not sufficient for blocking GephE dimerization, potential GephG-GephE interactions were tested. For this purpose an extended version of GephΔL was generated. In this variant, referred to as GephG$(GGS)_4$E, four GGS tripeptides were inserted between the five remaining residues of the linker and GephE of the GephΔL construct (Fig. 47A). In the absence of GephG-GephE interactions one would expect that the extension of the 5 amino-acid-linker of GephΔL by twelve additional residues would lead to a shift of the equilibrium from trimers to higher oligomers, potentially giving rise to a multitude of possible combinations (Fig. 47A). On the contrary, if GephG-GephE interactions were strong enough, GephE-GephE interactions should not occur, and trimers should be the only species being present (dark grey in Fig. 47A).

GephG$(GGS)_4$E was purified analogous to full-length gephyrin, and, as for the latter and the GephΔL variant, the chromatogram of the anion exchange chromatography step revealed sample heterogeneity (Fig. 47B), as suggested by the presence of two peaks. As for the other variants observed before, the peak at smaller salt concentrations contained the species with the highest electrophoretic mobility, and was therefore referred to as putative trimer fraction. As judged by anion exchange chromtagraphy profiles, pooling the fractions of the second peak resulted in a sample with a higher hydrodynamic radius than that of the predominant putative trimeric species. Therefore this pool was considered to contain “higher oligomers” (and is therefore referred to as HO or high R_H pool, Fig. 47B & C).

In a last step comparative SEC-MALS experiments were carried out with GephΔL and the two GephG$(GGS)_4$E pools. First, the comparison between the two GephG$(GGS)_4$E pools revealed the expected difference in terms of molecular weight: The mass derived from the centre of the higher oligomeric pool was 341 kDa, whereas the data analysis of the putative trimer pool revealed molecular masses half of that from the HO pool. Surprisingly, an equilibrium between a 174 kDa and a 156 kDa species was detected for the second pool (Fig. 47C). For GephΔL also an equilibrium between or a mixture of two species was obtained with masses close to those of the putative GephG$(GGS)_4$E trimer pool, namely 171 kDa and 155 kDa. For reasons discussed below, it appeared plausible to assume that GephΔL and GephG$(GGS)_4$E ~150-175 kDa species were indeed trimers (despite an expected trimer mass of 200 kDa), arguing for the presence of GephG-GephE interactions, as the absence of such interactions was expected to give rise to higher oligomers (Fig.

47A) in re-chromatography experiments as shown in Fig. 47C. Although higher oligomers obviously occurred, the putative trimers were therefore considered to be at least kinetically stable (Fig. 47B).

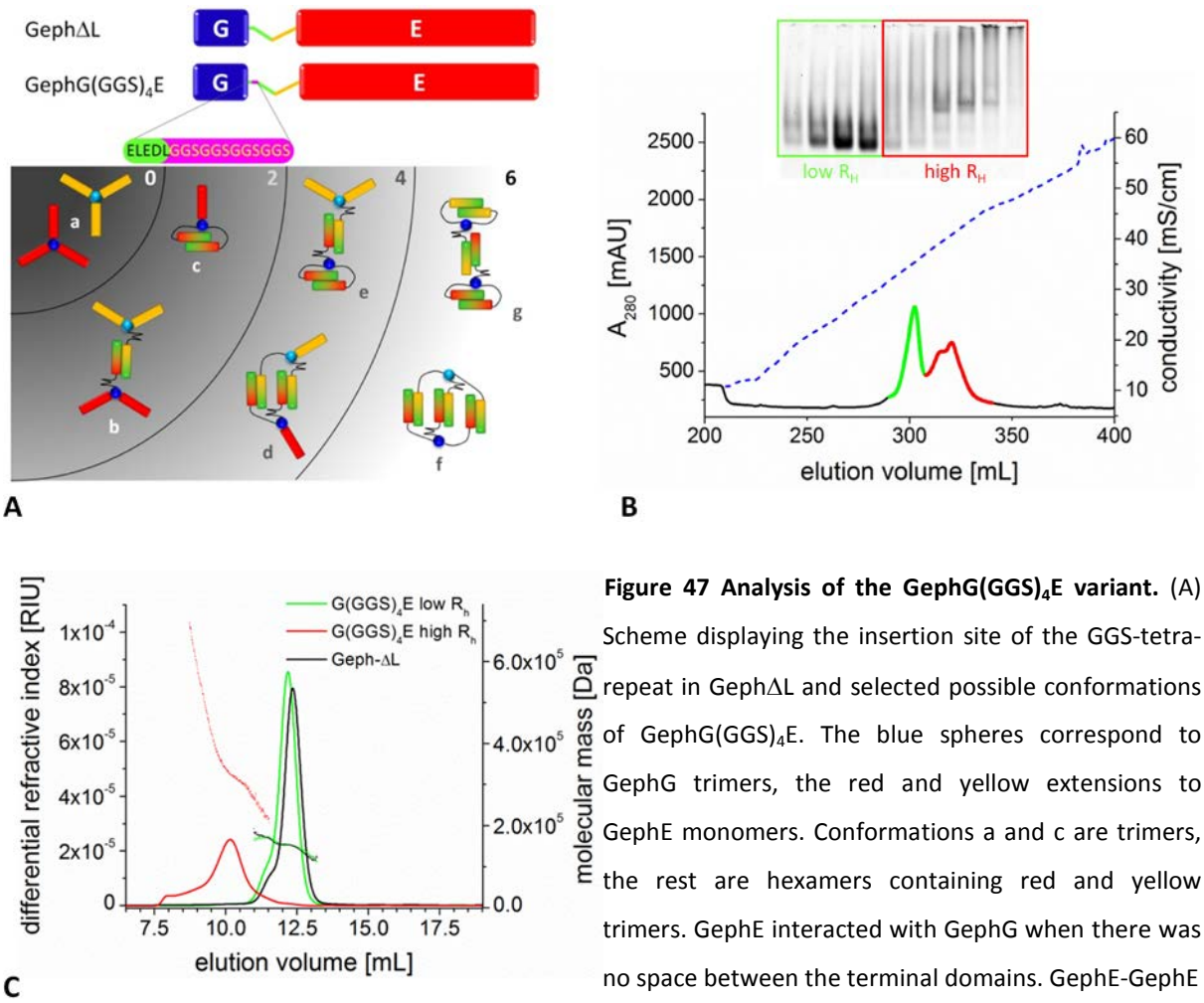

Figure 47 Analysis of the GephG(GGS)$_4$E variant. (A) Scheme displaying the insertion site of the GGS-tetra-repeat in GephΔL and selected possible conformations of GephG(GGS)$_4$E. The blue spheres correspond to GephG trimers, the red and yellow extensions to GephE monomers. Conformations a and c are trimers, the rest are hexamers containing red and yellow trimers. GephE interacted with GephG when there was no space between the terminal domains. GephE-GephE interactions (either inter-trimeric (conformer b) or intra-trimeric (see conformer c)) are indicated by green-coloured GephE extensions. Principally, higher oligomers than the hexamer were also possible and could occur via unpaired (hence non-green-coloured) GephEs. The grey-white gradient in the background indicates the shift from dominant GephG-GephE interactions (dark grey) to dominant GephE-GephE interactions (white). (B) Anion exchange chromatography of GephG(GGS)$_4$E allowed for the separation of various species which were separately subjected to SEC-MALS in (C). The analysis of two GephG(GGS)$_4$E pools (one with a "high" R_H, one with a lower R_H) in comparison with a trimeric GephΔL sample. The experiments were conducted in SEC-1 buffer.

As MogA-MoeA interactions were previously described (Magalon *et al.*, 2002), native gel and aSEC experiments with GephG-GephE mixtures were conducted to test for potential GephG-GephE interactions. However, neither approach yielded positive results. In native PAGE GephG-GephE mixtures exhibited electrophoretic mobility profiles very similar to the simple addition of the individual profiles, and no additional band pointing to a complex was detected (data not shown). The

outcome of the aSEC experiments was similar, even when 500 µL of a 125 µM GephG-125 µM GephE mixture was applied to the Superdex 200 10/300 GL column (Fig. 48).

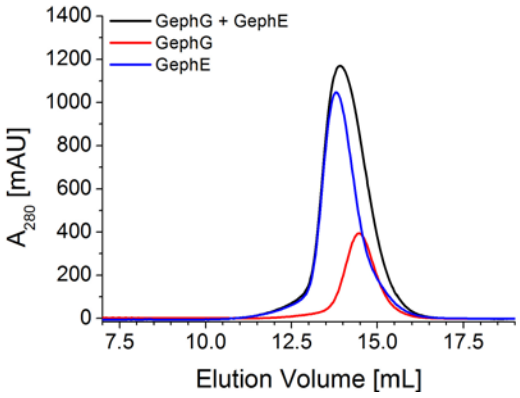

Figure 48 GephG and GephE did not exhibit a detectable affinity to each other in aSEC experiments. A Superdex 200 10/300GL was equilibrated in SEC-2 buffer (section II.A.7.1.8).

III.A.3. Discussion

Gephyrin is one of the key components of inhibitory postsynaptic densities (Fritschy *et al.*, 2008, Tretter *et al.*, 2012, Tyagarajan & Fritschy, 2014). It has been proposed that gephyrin exploits its two oligomerization interface to form a hexagonal scaffold, which would be endowed with a high density of glycine/$GABA_A$ receptor binding sites (Kneussel & Betz, 2000, Xiang *et al.*, 2001). The binding of the corresponding receptors to gephyrin clusters restricts their lateral mobility and ensures a proper apposition of the receptors to the presynaptic apparatus (Meier *et al.*, 2001, Mukherjee *et al.*, 2011). The formation of the scaffold appears to be a regulated process, as *E. coli*-derived gephyrin predominantly forms trimers (Herweg & Schwarz, 2012, Schrader *et al.*, 2004, Sola *et al.*, 2004). However, the exact mechanism(s) has (have) not been understood, primarily due to the lack of structural information on full-length gephyrin, for which no crystal structure could be obtained so far. It has been proposed that the prevalent trimeric state of recombinantly expressed gephyrin is related to the presence of the linker. These issues and findings defined the overall goals of the present work:

- To determine the relative arrangement of the terminal domains which are interconnected by a very long linker of 150 amino acids in the herein used P2 splice variant (specified in I.C.2.1 and Appendix A).
- To test whether heterologously expressed gephyrin can be converted from its predominantly trimeric state into higher oligomeric states by the introduction of selected point mutations or linker deletions. The identification of such mutants could have led to the identification of mechanisms, which keep gephyrin in its trimeric state.

It should be pointed out that significant parts of the discussion herein – specifically those concerning the characterization of trimeric wildtype gephyrin by SAXS and AFM – have already been published (Sander *et al.*, 2013).

III.A.3.1 Gephyrin predominantly forms trimers but also higher oligomers

The prevalent fraction of gephyrin was trimeric, but it turned out that gephyrin expressed in *E. coli* was even more heterogeneous with respect to its oligomeric state than initially thought, when the higher oligomeric fraction (Figs. 18C & 19A) was regarded as hexamer. The assumption of a hexamer appeared plausible, as the peak did not display a shoulder or indications of several species. However, based on native PAGE and aSEC experiments several distinct species with higher Stokes radii than that of the trimer were obtained, and these species could be hardly seperated (Fig. 19A). This finding is in contrast with the reported lack of higher oligomers after heterologous expression in *E. coli* (Herweg & Schwarz, 2012) but in line with a previous study, in which (also after heterologous expression in *E. coli*) also a minor fraction of gephyrin molecules was observed to exhibit higher

Stokes radii than the prevalent trimeric species (Schrader *et al.*, 2004). CD spectra of a mixture of species with higher Stokes radii were very similar to those obtained for trimeric gephyrin and, as the protein bound to MBP-GlyR in native gels (data not shown), one can conclude that these species were not just dysfunctional aggregates. Nevertheless, especially the species with larger hydrodynamic radii were more prone to aggregation than trimeric gephyrin. Remarkably the isolated linker, attached to the maltose binding protein, dramatically reduced the solubility of MBP down to 100 µM (section III.A.2.7.1). Usually MBP can be concentrated to at least 1 mM.

SAXS measurements of the mixture of higher oligomers (R_g ~ 100 Å, for comparison: R_g(trimer) = 65 Å, Table 30) were performed after thorough removal of potential aggregates immediately prior to the measurements (data not shown). Hence, the analysis revealed no obvious aggregation. However, modelling of this mixture of higher oligomers was not conclusive and was therefore abandoned. Whether these species represent different higher oligomeric states or not remains to be clarified. AFM might be a good choice to answer this question.

This work focused on the characterization of trimeric gephyrin, as this oligomer can be regarded as the autoinhibited form of gephyrin, where autoinhibtion refers to the fact that the trimer interface is utilized but not the dimer interface. MALS measurements caused some confusion on this view, as the derived molecular masses were closer to that of a dimer than to a trimer (Figs. 20 & 61C). However, experiments described in the literature and herein argue against dimers to be the prevalent species. Previously published crosslinking experiments pointed to trimeric gephyrin, which could only be converted to dimeric gephyrin after dialysis against a low salt buffer and a slightly acidic pH (Sola *et al.*, 2004), conditions which were not encountered during the MALS experiments.

In addition, SAXS data could only be analysed assuming gephyrin trimers, whereas the analysis failed for the dimer scenario (section III.A.2.5.3.2, Fig. 29). Notably, MALS measurements of GephΔL and GephG$(GGS)_4$E also yielded molecular masses too high for a dimer and too low for a trimer. Principally one might envision that degradation of Geph-WT, GephΔL and GephG$(GGS)_4$E affected the MALS analysis. However, this explanation would be inconsistent with the AFM-derived molecular masses. Second, the MALS-derived molecular masses for both GephΔL and GephWT were so small that, even if one assumes that the variants were directly degraded to GephG trimers, the GephG degradation product would contribute ~30% to the sample content, which is not in line with SDS-PAGE and native gel analysis of samples that were used for SAXS and AFM studies (Figs. 18, 44, 61A). From a structural point of view dimerization seems rather unlikely, as the exposure of two very hydrophobic interfaces of a GephG monomer (Fig. 14A) would have to be prevented by GephE, which does not provide two spatially aligned, sufficiently large hydrophobic interfaces (not shown), or by the linker, which is depleted of hydrophobic residues (Table 28).

Taken together, MALS seems to have also its limitations in the accuracy of mass determination. Which factors affected the analysis, remains to be clarified, but the hypothesis that an equilibrium between compact and extended states in full-length gephyrin led to an underestimation of the molecular mass, does not explain why molecular masses of GephΔL and GephG$(GGS)_4$E differed from the expected trimer mass to almost the same extent as the mass obtained for full-length gephyrin. Follow-up experiments, in which the assumed 150 kDa-170 kDa equilibrium can be manipulated, are required to understand the basis of this unexpected heterogeneity of GephΔL and GephG$(GGS)_4$E.

III.A.3.2 Gephyrin's linker mediates its conformational heterogeneity

The modified gephyrin purification protocol ensured a high purity by a shallow gradient in anion exchange chromatography, with which higher oligomers could be removed from the sample (section III.A.2.2). The purity of the protein used for shape analysis was checked by native PAGE and SDS-PAGE and was sufficient for SAXS and AFM analyses (Figs. 18C & 61A). These complementary approaches provided information on the protein in solution but also on the single-molecule level.

As bioinformatics suggested large parts of the linker to be intrinsically disordered (Fig. 17), the conformational variety observed with AFM was not a huge surprise (Fig. 21). Conformational heterogeneity was reflected by a broad D_{max} distribution (Fig. 22B) and by the observation of several classes of assemblies, ranging from globular particles with a single segment (species #1 in Fig. 22A) to those with different degrees of extended shapes (species #2-#4 in Fig. 22A): The D_{max} of the globular gephyrin species #1 was almost identical to that of GephΔL (Fig. 22D), while the most extended species displayed D_{max} values of more than 500 Å. Such heterogeneity was not observed for GephΔL, which displayed a narrow D_{max} distribution and more or less a single species instead of the four observed for full-length gephyrin (Fig. 22C). This demonstrated that it is the linker, which is responsible for the multitude of conformers.

In the course of this work it turned out that the apparent homogeneity of GephΔL might have partially resulted from the bad adherence of GephE to the AFM mica surface in SEC-1 buffer, as it was observed for dimeric GephE. Salt concentrations of 25 mM instead of 250 mM (as present in the SEC-1 buffer) ensured GephE deposition (Ingrid Tessmer, personal communication). Preliminary experiments, in which GephΔL was deposited in low salt buffer instead of the SEC-1 buffer, suggested that GephE deposition in the context of GephΔL was salt-dependent as well (data not shown), as the D_{max} values appeared to be higher in low salt buffer than in the SEC-1 buffer. Should a detailed analysis confirm the first impression, this would account for an enhanced deposition of GephE in the context of full-length gephyrin. AFM data of full-length gephyrin measured in low salt buffer should be quantitatively evaluated as well.

In line with the AFM data it turned out that conventional SAXS data analysis assuming a single conformation was inappropriate to describe the experimental data. For example, rigid body modelling yielded non-reproducible results (as indicated by NSD values significantly higher than 1 (Table 31, Fig. 25). The large NSD values indicate the presence of multiple conformations as previously described by Bernado (Bernado, 2010). Although the reproducibility was better for *ab initio* reconstructions (at least for asymmetric models NSD values smaller than 1 were achieved, Table 31), the extremely elongated *ab initio* conformers had to be taken with caution (Fig. 24), as AFM results suggested that gephyrin is a rather flat assembly with a higher heterogeneity. For flat assemblies like gephyrin *ab initio* reconstructions without symmetry restrictions normally fail (see test case 12 in Figure 4 of (Volkov *et al.*, 2003)). Such a flat assembly has not yet been described in practice with *ab initio* modelling, except for the analysis of the immunoglobulin M (Volkov *et al.*, 2003).

Also the analysis of the overall parameters pointed to structural heterogeneity: A single peak in the Kratky plot (Fig. 23B) and missing interdomain correlation peaks in the P(r) function (Fig. 23A), which is again similar to what was described earlier (Bernado, 2010). Hence, structural flexibility was further assessed with the advanced 2.0 version of EOM (Tria *et al.*, 2012). The resulting models were consistent with an elastic linker that allows trimeric gephyrin to switch between compact and very elongated conformations (Fig. 26C), as also suggested by the AFM analysis. Notably, the EOM-derived R_g distribution results suggest a slight preference for compact assemblies (Fig. 26A).

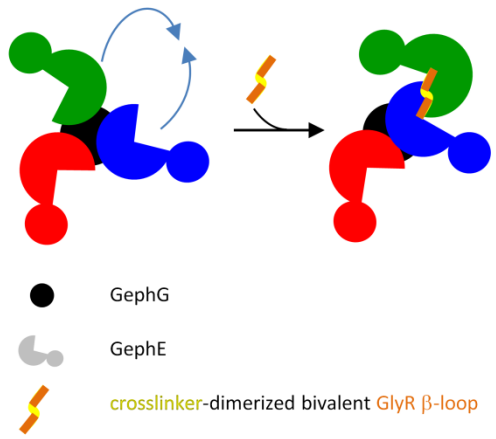

Figure 49 Rationale for the SAXS analysis of the gephyrin complex with a dimerized GlyR β-loop. If the average conformer of gephyrin in solution was symmetric, complex formation with a dimerized GlyR β-loop, which contains two binding epitopes for GephE, would lead to an asymmetric arrangement due to the short crosslinker bridging the two GlyR β-loop sequences.

The EOM approach was also tested in terms of the validity of certain conclusions, and the results suggest that the resulting mixture of compact and extended states was not an artefact (Fig. 27C) and that the dimensions of the resulting conformers as well as their contribution to the scattering pattern were correct with errors below 10% (Fig. 27D). Finally, the results also suggest that experimental noise and errors did not significantly affect the EOM analysis. However, it should be considered that SAXS is a low-resolution technique, hence the models in Fig. 26 rather serve as a rough estimate, and conclusions on the atomic level are not permitted (Bernado *et al.*, 2007). This means that exact mechanisms (e.g. of linker-GephE interactions) cannot be deduced. This was illustrated

for the $GephG_3E_2E$ conformation: Despite a clearly asymmetric input model, EOM-derived models were only symmetric (Fig. 28). Hence, SAXS data which were obtained for gephyrin in complex with a bivalent GlyR β-loop peptide (generated and kindly provided by Hans Maric), which is expected to introduce asymmetry in the gephyrin assembly (Fig. 49), could not be evaluated.

Nevertheless, the observed flexibility seemed to be characterized sufficiently well (Fig. 26) and might also explain the difficulties in separating higher gephyrin oligomers. For example, hexamers and nonamers can adopt many more extended states than trimers, but can also exist in very compact states as well, so that their average hydrodynamic radii could be very close to that of trimeric gephyrin, again underscoring the need for a purification protocol which allowed for minimization of the hexamer contribution to 2% at maximum (as suggested by the AFM analysis, Fig. 21A).

III.A.3.3 Gephyrin's linker interacts with the terminal domains

The partial compaction of trimeric gephyrin observed in AFM and SAXS could be explained by the fact that some parts of the linker are not flexible and seem to interact with both GephG and GephE. This conclusion was supported by an increased thermal stabilization of both terminal domains in the context of the full-length protein, as observed here with CD spectroscopy (Table 33) and earlier by differential scanning calorimetry (Herweg & Schwarz, 2012). Interactions with the linker and the terminal globular domains might explain at least in part why the radius of gyration was considerably smaller than would be expected for a gephyrin trimer with fully extended linkers where R_g values larger than 100 Å would be accessible.

However, based on CD results, linker segments are not expected to form extended interfaces with the terminal domains, as GephGL202 and GephLE309 were sufficient to induce higher melting temperatures in GephG and GephE, respectively, comparable to those obtained for the full-length protein (Table 33 & Fig. 38). This would be consistent with both domains being stabilized by segments of maximally 22 and 23 residues, respectively, leaving at least 105 residues, which could mediate the obvious flexibility of gephyrin. On the other hand, even the temperature increase rate of 1K/min might have been too low to resolve contributions of less stably attached linker segments. Therefore, CD melting experiments should be repeated at higher scan rates.

Thermofluor experiments supported the CD data and were in accordance with previous Thermofluor experiments conducted by Eun-Young Lee (Lee, 2009). Slight deviations in the melting temperatures obtained with CD and Thermofluor were possibly the result of the use of different buffers: 50 mM potassium phosphate in CD spectroscopy and SEC-4 buffer in the Thermofluor method. In the latter method the addition of 10% glycerol increased the thermal stability of both domains (data not shown).

III.A.3.4 The first half of the linker appears to be more extended than the second half

A high degree of linker compaction in the context of the full-length protein was also supported by the characterization of GephGL. This construct harboured the full linker but lacked GephE and displayed unexpectedly high R_g and R_H values close to that of full-length gephyrin (Table 35 & Fig. 41B). This was quite surprising given the monomer molecular masses of 35.6 kDa and 83.5 kDa of GephGL and full-length gephyrin, respectively, and raised the question whether GephGL simply forms a very extended trimer or whether the linker harbours an additional oligomerization interface. Such an interface was suggested before, when crosslinking experiments accounted for exon 14 as an additional dimer interface in the linker (Eguchi *et al.*, 2004). However, the latter hypothesis did not appear very likely, as MALS and SAXS measurements accounted for an extended GephGL trimer (Fig. 41B). Based on the latter experiments an estimation of the R_g of the linker (in the context of GephGL) was conducted, yielding a value of 41 Å, whereas the analogous calculation yielded an R_g of 28 Å for the linker in the context of the full-length gephyrin (section III.A.2.7.2).

For further characterization of the linker, gephyrin constructs were analysed in which either linker half was deleted. Although this approach failed to significantly shift the equilibrium of gephyrin trimers to higher oligomers (Figs. 35 & 37), the mutants provided valuable information: Both linker deletion variants displayed melting temperatures in agreement with either linker-GephE or linker-GephG interactions. If the first half of the linker was deleted, there was no effect on linker-GephE interactions, as the melting temperature for the GephE portion more or less equalled the T_M of the GephE portion in full-length gephyrin, whereas the deletion of the second linker half resulted in a decrease of GephE stability (Table 33 & Fig. 38). These results were consistent with the observation that GL202 and LE309 increased the thermal stabilities (with respect to the isolated domains) and suggested that adjacent linker regions interacted with (and stabilized) the respective domain (Table 33 & Fig. 38).

Comparative limited proteolysis experiments with MLH1 and MLH2 variants (Fig. 39) supported this idea, as in these experiments the terminal domains were also stabilized by adjacent linker segments. When these segments were missing, no stabilization of the corresponding domain could be observed, so that GephG attached linker segments were only protected from proteolysis in the Geph-MLH2 variant and GephE attached linker segments in Geph-MLH1. A mass spectrometry analysis would certainly not have been conclusive for the derivation of determinants of GephE masking, as even GephLE was not sufficient to prevent dimerization (Fig. 46).

To get a clue about the structural differences in the Geph-MLH variants, SAXS experiments were performed. Unfortunately SAXS data analysis in terms of EOM failed for unknown reasons. Using EOM the experimental data could only be fitted with significant discrepancies, especially in the small-angle region (where the ensemble fits displayed higher R_g values than the experimental data), so that

the results cannot be considered reliable (Appendix D). One possible explanation could be that GephE adopts conformations significantly different from that of the GephE monomer extracted from PDB entry 2FTS. WebNMA analysis (Hollup *et al.*, 2005) indeed reveals flexibility as it was observed for MoeA before (Nichols *et al.*, 2007), however, the R_g values of the obtained models did not significantly deviate from those obtained for the monomer (PDB entry 2FTS) (data not shown). Degradation of the proteins as an explanation for the bad fits was unlikely as well (Fig. 39). However, one could make use of the R_g values. The analysis was straightforward because of the similar Geph-MLH1 and Geph-MLH2 molecular masses, only deviating by less than one kDa. R_g comparisons revealed that Geph-MLH1 was more compact than Geph-MLH2, as indicated by the 7 Å higher R_g value of the Geph-MLH2 variant (Table 32). This is certainly not a dramatically high value, but the difference between Geph-MLH1 and Geph-ΔL (which contains a 5 residue-linker instead of a 67 residue-linker) was 8 Å and hence in the same range as the difference between the two Geph-MLH variants (containing 72 and 78 residues) (Table 32).

These results are consistent with the linker sequence analysis: In the first half of the linker there are several elements which can be presumed to adopt extended states or which were shown to be unstructured. Based on the available literature, the fifteen residue proline-rich stretch at the N-terminus of the linker region (residues 187-201) and the nine charged residues (EEEEEEKKD, residues 213-221) following the DYNLL binding motif might form extended poly-proline type II helices (Tiffany & Krimm, 1968). In addition, the dodecapeptide harbouring an extended DYNLL binding motif (residues 203-214) turned out to be disordered, as judged by CD experiments (Lee, 2009). Hence, the region between residues 187 and 221 might adopt prevalently extended conformations. However, as CD melting curves argue for a GephG association with (a) linker segment(s) in the region between 187 and 202, the linker might not completely protrude from GephG.

The only consistently predicted secondary structure element in the linker was a hydrophobic α-helix, in which the C3 splice site (I.C.2.1) is located. There might be interesting parallels to some protozoan dihydrofolate reductase-thymidylate synthases (O'Neil *et al.*, 2003): The two catalytic units are interconnected by a 69 residue-linker in the *T. gondii* variant, which was shown to form a swapped dimer, in which an interdomain linker helix contacted the respective other protomer. The α-helix was the only resolved structural element of the interdomain linker and was required for a proper positioning of the terminal domains (Sharma *et al.*, 2013). Something similar might apply to gephyrin. To explore this possibility, one might also include the predicted hydrophobic helix ($_{223}$GVASTEDSSSSHITAAALAAKIPDSII$_{249}$) in the GephΔL and GephG$(GGS)_4$E construct in future experiments.

For the second half of the linker no extended distinct segments can be distinguished in secondary structure predictions. However, based on these the third quarter appears to be more structured than

the linker segments adjacent to GephE, as especially the last quarter was devoid of predicted secondary structure. Presumably in this last quarter there is the interface for an interaction with GephE.

III.A.3.5 Phosphorylation

The most extensively explored posttranslational modification of gephyrin is phosphorylation. Until April 2014 32 phosphorylation sites (out of 40 serines, threonines and tyrosines in the linker region) could be detected (www.phosphosite.org). As phosphorylation sites are usually solvent exposed (Dunker *et al.*, 2002), this suggests that large parts of the linker are intrinsically disordered. On the other hand some phosphorylations (S188, S194, S200) have been demonstrated to regulate GlyR binding despite being separated from the GlyR binding site by 130 residues (Zita *et al.*, 2007), pointing to a less pronounced gap between GephE and the N-terminal region of the linker.

Several studies pointed to an important contribution of gephyrin phosphorylation to the stability of gephyrin clusters (Bausen *et al.*, 2010, Kuhse *et al.*, 2012, Rui *et al.*, 2013, Tyagarajan *et al.*, 2011b, Tyagarajan *et al.*, 2013, Zita *et al.*, 2007). In this work selected phosphomimetic gephyrin mutants were generated to assess potential shifts of the trimer equilibrium to higher oligomers. This approach was based on a detailed mass spectrometry based phophoproteomic study, which yielded several gephyrin-derived phosphopeptides, of which a significant portion contained multiple phosphorylations (up to three within one peptide) (Huttlin *et al.*, 2010). The phosphomimetic mutations were introduced into gephyrin at sites

- for which the effects of phosphorylation were characterized in cell biological studies (CL1 & CL2 (Tyagarajan *et al.*, 2011b, Zita *et al.*, 2007)). Phosphorylation of CL1 was required for the recognition by the peptidyl-prolyl-cis-trans isomerase PIN1 (Zita *et al.*, 2007), which was described to change the conformation of gephyrin, accompanied by an enhanced affinity for the glycine receptor, dephosphorylation of CL2 has been reported to lead to increased gephyrin cluster numbers (Tyagarajan *et al.*, 2011b).
- which are localized in the second half of the linker and which might mediate linker-GephE interactions that prevent GephE dimerization: S309E and CL3. The latter cluster and the β19-β20 loop of GephE involved in the dimer interface possess highly similar primary sequences. Most residues are at least of similar character, and mainly three methionines were exchanged to two alanines and a serine (Fig. 50). The β19-β20 loop binding portion of the other GephE (subdomain I) features a rather negatively charged surface. Should CL3 be involved in interactions with GephE (maybe acting in concert with other linker segments), phosphorylation of these residues as observed in (Huttlin *et al.*, 2010) might weaken a potential interaction of CL3 with GephE.

- which might regulate collybistin binding. Serine 333 immediately precedes the mapped collybistin binding site (334-PFPLTSMDKA-343) (Harvey *et al.*, 2004).

None of the mutants (Fig. 30) exhibited an obvious shift towards higher oligomers. Likewise, SAXS profiles did not significantly deviate from that of wildtype gephyrin, indicating no global changes in the conformations of the mutant proteins. In the case of the S333E mutant collybistin binding was not compromised (data not shown). It is clear that the replacement of phosphosites by their phosphomimetic counterparts might not be an appropriate substitution (Dephoure *et al.*, 2013). To overcome this problem, one could chose an alternative approach, namely an engineered *E. coli* strain, which can mediate cotranslational incorporation of phosphorylated amino acids into a target protein (Park *et al.*, 2011). This approach is currently established in the lab by Dr. Daniela Schneeberger.

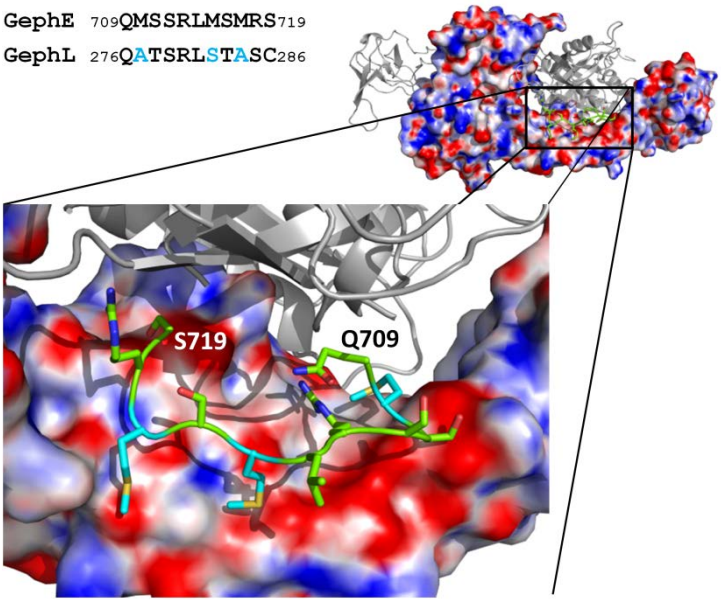

Figure 50 The location of the β19-β20 loop in GephE. Upper left: The β19-β20 loop (GephE) displays a high sequence similarity to CL3 (part of GephL). The methionine exchanges are highlighted in cyan in the alignment as well as the magnification of GephE. The charge distribution was obtained with APBS. Blue and red patches are positively and negatively charged surface areas, respectively.

Nevertheless, for two phosphomimetic mutants at least local changes became apparent in limited proteolysis experiments, namely for Geph-CL1 and Geph-CL3, of which the changes in Geph-CL1 were more pronounced (Fig. 32). Remarkably, neither my diploma student Kristina Keller (Keller, 2010) nor I could observe a change in the trypsination pattern of Geph-CL1 upon addition of the peptidyl-proly-cis-trans isomerase PIN1, although this was expected from the literature (Zita *et al.*, 2007). However, the differences between wildtype gephyrin and Geph-CL1 were reminiscent of the published differences between *E. coli*- and SF9 cell-derived gephyrin (Herweg & Schwarz, 2012) (Fig. 51). Maybe these findings are related to each other: *E. coli* and SF9 cells both express peptidyl-prolyl cis-trans isomerases (PPiases), which might recognize phosphorylated gephyrin in SF9 cells or the Geph-CL1 variant in *E. coli* (Alnemri *et al.*, 1994, Edwards *et al.*, 1997). This could explain why PIN1 addition after purification could not exert any effects in Geph-CL1 – maybe the desired change took already place in *E. coli*. At lower protease concentrations not only a single significant band shift of

Geph-CL1 with respect to wildtype gephyrin was observed (as in Fig. 33), but even multiple shifts (Fig. 32). One possibility was that an *E. coli* PPiase induced a conformational change, which in turn triggered a phosphorylation by an *E. coli* kinase, possibly in the second half of the linker (which would explain the multiple shifts above 34 kDa (Fig. 32), which was the apparent size of GephGL253 on an SDS-PAGE gel), that arrested the obtained Geph-CL1 conformation in a similar manner as was observed before for Cdc25 (Stukenberg & Kirschner, 2001). A treatment of Geph-CL1 with calf intestinal phosphatase did not reveal significant differences to an untreated sample so far (data not shown). However, Phos-tag gels (Kinoshita *et al.*, 2006) and/or mass spectrometric analyses are more sensitive and will reveal whether Geph-CL1 was phosphorylated. If this was the case, one could principally test whether similar changes occur in HEK293 cells or neurons and whether the mutation of the phosphorylation site to an alanine results in alterations in receptor clustering. The other possibility, namely that the multiple differences in proteolysis (Fig. 32) did not arise from phosphorylation, would not be less exciting, since residues at the N-terminus of the linker then would influence segments potentially 50 residues downstream of the phosphorylation site.

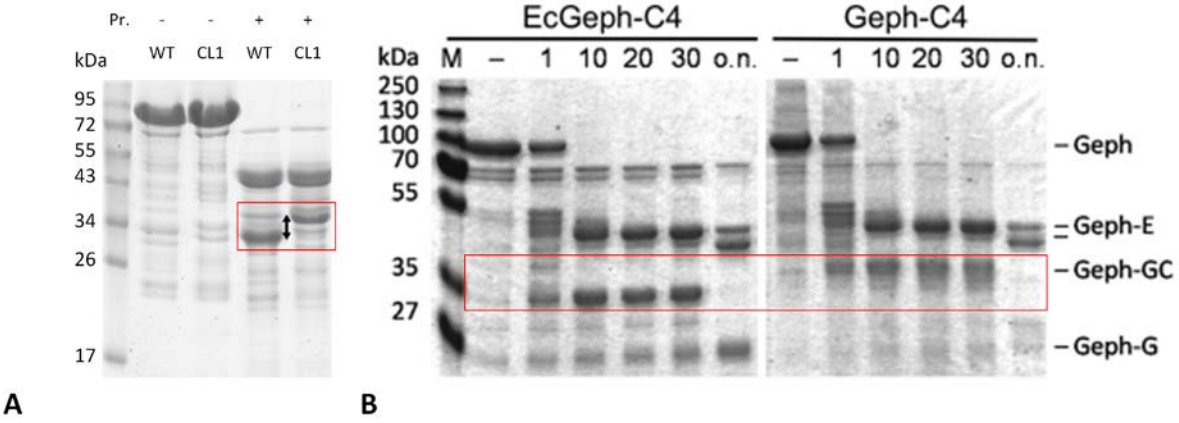

Figure 51 Limited proteolysis of Geph-P2 (WT vs. CL1 variant, *E. coli* derived vs. SF9 cell-derived). C4 indicates the presence of the C4c cassette, which is also used in the P2 splice variant in (A). Therefore WT in (A), EcGeph-C4 and Geph-C4 in (B) possessed identical primary sequences (except for the His-tags). (A) Excerpt from Fig. 33. Note the highlighted difference in the proteolysis patterns of GephWT and GephCL1, both derived from *E. coli* cells. *Pr.* stands for protease. (B) Excerpt from (Herweg & Schwarz, 2012). This research was originally published in the Journal of Biochemistry. Herweg, J. & Schwarz, G. (2012). Splice-specific glycine receptor binding, folding, and phosphorylation of the scaffolding protein gephyrin. J Biol Chem 287, 12645-12656 © the American Society for Biochemistry and Molecular Biology. Ec indicates that the protein was expressed in *E. coli*. Geph-C4 was obtained upon expression in SF9 cells. Samples were taken at different time points. The red-boxed differences are similar to those in (A).

Despite the lack of global conformational changes (Fig. 31) the phosphomimetic mutants should be tested for their binding capacity towards the gephyrin ligands available in the lab, also including PIN1 which could principally recognize one of the five other SP epitopes (although comparable experiments in the cellular context led to negative results (Zita *et al.*, 2007)).

III.A.3.6 Gephyrin's linker is not sufficient to prevent GephE dimerization

A previous study suggested that – in line with what has been discussed above – the linker is responsible for blocking GephE dimerization (Bedet *et al.*, 2006), thus explaining why GephE without the linker dimerized and full-length gephyrin predominantly formed trimers after expression in *E. coli*. Therefore, the subsequent experiments aimed to decipher the contribution of more defined linker segments or even individual residues, which mediate gephyrin autoinhibition. The GephΔL variant was expected to provide an unmasked GephE dimer interface (Fig. 43) and hence binding experiments with the isolated second linker half (fused to MBP) were conducted. These experiments did not point to interactions (Fig. 44), which could have been further analysed with selected point mutants or deletions. Likewise, GephGL, which could have potentially utilized avidity effects (promoting a more stable interaction than a single linker), did not bind to GephΔL at detectable levels in ITC, aSEC and native gels (Fig. 45 & data not shown).

Therefore the strategy was changed, and the focus was set on the analysis of the GephLE variant (section III.A.2.7.4). Given that the isolated linker and unmasked GephE could not undergo stable complex formation as long as these portions were separated, an analysis of the oligomeric state analysis of the GephLE construct, in which these portions were covalently linked, appeared to be more promising. The presence of GephLE monomers would have been an appropriate readout, which could have changed upon point mutations/deletions of important segments. In fact, in one publication GephLE was observed to exhibit a significantly smaller R_H than GephE despite its ~16 kDa higher molecular mass in aSEC experiments (Bedet *et al.*, 2006). Unfortunately, these results could not be reproduced herein (Fig. 46A & B): In aSEC experiments GephE displayed a significantly smaller R_H than GephLE and MALS experiments in SEC-1 buffer suggested a molecular mass consistent with a dimer, and the elution volumes of GephE and GephLE did not significantly change upon use of the same buffer described in (Bedet *et al.*, 2006) (Fig. 46B). Finally, SAXS measurements were not consistent with the monomeric state, and the resulting profiles could be satisfyingly fitted with an ensemble of (extended) dimers (Fig. 46C). The surprising differences between the results in this work and those in (Bedet *et al.*, 2006) can be explained by the use of different constructs, which harboured the C4c splice cassette (this work) or no splice cassette in the linker (Bedet *et al.*, 2006) or encompassed the 11 C-terminal residues resolved in the GephG crystal structures (Schwarz *et al.*, 2001, Sola *et al.*,

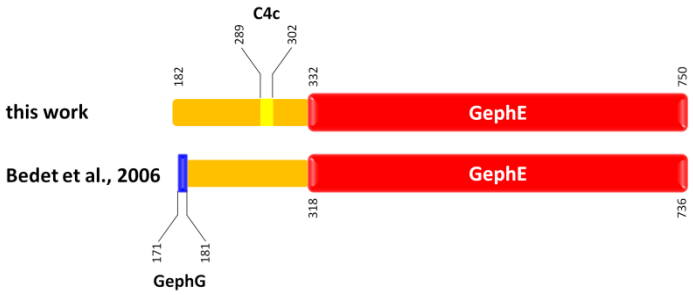

Figure 52 Different GephLE constructs used in (Bedet et al., 2006) and in this work.

2001) or not (Fig. 52). Either difference or a combination of both could account for the different oligomeric state. Hence, one could reassess the oligomeric state of the construct used in (Bedet *et al.*, 2006) and then delete either the C-terminus of GephG or add splice cassette C4c. Maybe this would help to pinpoint the mechanism of gephyrin autoinhibition.

One should also take into account splice cassette C3 (section I.C.2.1). The inclusion of this splice cassette was shown to reduce the propensity of gephyrin to form higher oligomers in comparison to gephyrin P1 and P2 splice variants lacking this cassette (Herweg & Schwarz, 2012). It might well be that a linker containing the C3 cassette forms a more stable complex with GephE and that the corresponding GephLE construct forms monomers, potentially serving as a good starting point to identify crucial linker segments preventing GephE dimerization also beyond the C3 cassette.

III.A.3.7 Do GephG-GephE interactions contribute to gephyrin autoinhibition?

Since at least the tested linker on its own was not sufficient to interfere with dimerization, GephG-GephE interactions were taken into account. This would be in line with previously described, albeit not further characterized MogA-MoeA interactions (Magalon *et al.*, 2002). This hypothesis was fostered by the prevalent trimeric oligomerization state of the Geph-MLH variants. Furthermore, CD melting curves suggested that not only GephG-linker variants displayed GephG stabilization (Table 33) but also the GephΔL variant, despite a lack of almost the complete linker except for the five N-terminal residues. One might have reasoned that these five residues were sufficient to mediate GephG stabilization, however, other linker deletion variants missing these five residues, namely MLH1 and GephΔ(175-202), also displayed T_M(GephG) values of 79-80°C compared to 80.4°C for full-length gephyrin and 76.7°C for GephG (Table 33), raising the possibility of GephG-GephE interactions. One might argue that the melting point of GephE in GephΔL was clearly reduced (T_M=57.6°C) with respect to GephE in the context of full-length gephyrin (T_M=62.0°C) and even GephE (T_M=58.9°C). On the other hand one should consider that a reliable T_M estimation of monomeric GephE has not been available. To derive such a value, one could analyse the GephE(G483R-R523E-A532R) mutant which was previously

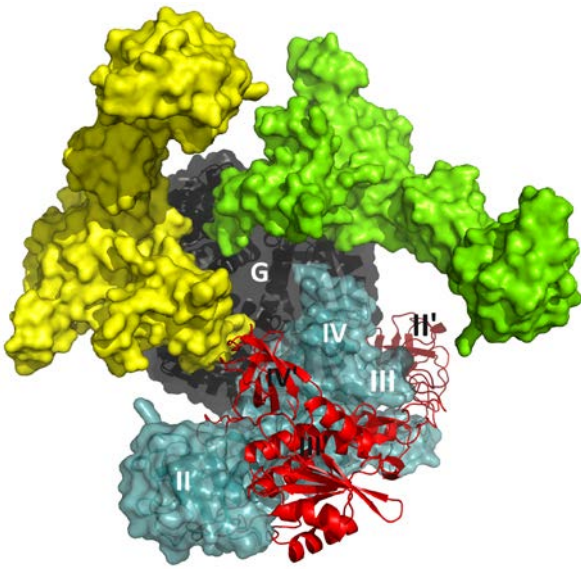

Figure 53 GephΔL *per se* is not dimerization incompetent. A GephΔL trimer, containing the GephG core (black) and three GephE monomers (cyan, yellow, green) is shown in a conformation, in which subdomain III ca be accessed by subdomain II' of an incoming GephE (red, ribbon representation).

shown (Saiyed *et al.*, 2007) to prevalently form dimers (of course only, if the far-UV CD spectra of GephE and the mutant are comparable).

A further (albeit indirect) hint at GephG-GephE interactions was obtained through the analysis of the GephG$(GGS)_4$E variant. While one could reason that intra-trimeric and inter-trimeric GephE dimerization was hindered by the short linker of just five amino acids in GephΔL, the addition of 12 residues of an unrelated linker sequence was expected to endow GephG$(GGS)_4$E with the capability to undergo at least intertrimeric GephE dimerization with a higher propensity than GephΔL (Fig. 43 & Fig. 47A). In contrast with this expectation, differences between GephΔL and GephG$(GGS)_4$E were marginal in SEC-MALS experiments. MALS results were not consistent with hexamers (for which masses of 400 kDa were expected) in the putative trimeric fraction. This was presumably not due to the linker being too short, as both GephΔL and GephG$(GGS)_4$E could form higher oligomers (Figs. 35 & 47C), presumably because GephE was not restricted to three-pronged star-like assemblies as assumed in Fig. 43. Therefore, subdomain III of GephE might have become available for inter-trimeric dimerization (Fig. 53). However, the predominant contribution was made by trimeric assemblies, accounting for an at least kinetically stable GephG$(GGS)_4$E trimer, which could only exist if dimerization was impeded in the absence of the gephyrin linker sequence (Fig. 47A). Therefore, another portion, namely GephG was expected to sterically interfere with dimerization.

One could extend these studies by using a longer linker than that in GephG$(GGS)_4$E, e.g. by, in the extreme case, an unrelated 136 residue linker (this is the linker length of splice variant P1). This would allow for conclusions on the contribution of the linker to gephyrin autoinhibition. However, one should also try to crystallize Geph-MLH1/2, GephΔL or GephG$(GGS)_4$E, as these structures might provide new insights not only into the gephyrin clustering function but also into the mechanism that governs the transfer of the rather unstable adenylated MPT intermediate (Kramer *et al.*, 1984) from the active site of GephG to that of GephE.

III.A.3.8 Are there candidate interfaces for GephG-GephE interactions?

The interaction between GephG and GephE must be rather weak, as aSEC and native PAGE experiments did not reveal complex formation under the given conditions (Fig. 48 and data not shown). The fact that even final concentrations in the range of 25 µM were not sufficient to obtain signs of complex formation, points to an affinity approaching the mM range (Fig. 48). Whether MPT or MPT-AMP might enhance GephG-GephE interactions is currently not known. The weak affinity precludes a simple biochemical characterization of the residues involved in the interaction.

As similar interactions were proposed also for the bacterial orthologues (Magalon *et al.*, 2002), residues involved in the transfer of MPT-AMP (the product of GephG and substrate of GephE) might be conserved and could be potentially identified in alignments. The selection of appropriate orthologues, however, does not appear to be straightforward. Chordate gephyrin orthologues are too closely related to derive a valid conclusion on this topic. A comparison with bacterial enzymes is presumably not the best alternative, as the fusion of GephG and GephE creates a scenario, which is completely different from that in *E. coli*, where the corresponding orthologues exist as separate enzymes. For example, the affinity of the *E. coli* enzymes to each other could be higher than for the separated mammalian counterparts - potentially due to an additional C-terminal loop which is specific for bacterial MogA orthologues and folds back onto the active site (Schwarz *et al.*, 2001). The linker in gephyrin, plants and fungi could compensate for a potentially weaker interaction between GephG and GephE (or CNX1G and CNX1E).

In plants and fungi gephyrin orthologues are not as conserved as in chordates. A CONSURF analysis of the fungi orthologues revealed that not only the active sites of GephG and GephE are highly conserved but also adjacent regions (Fig. 54). The conserved patches in GephG might serve as a docking site for the MPT synthase, which has to transfer MPT to GephG, but parts of these patches might be involved in the transfer from GephG to GephE as well.

In the previously proposed gephyrin model (presented in section III.A.1.4, Fig. 16) an MPT-AMP transfer between GephG and subdomain II was assumed (Belaidi & Schwarz, 2012, Fritschy *et al.*, 2008). One could, however, also envision an alternative arrangement, in which the MPT-AMP binding site of subdomain III of GephE and GephG are in close proximity (Fig. 55):

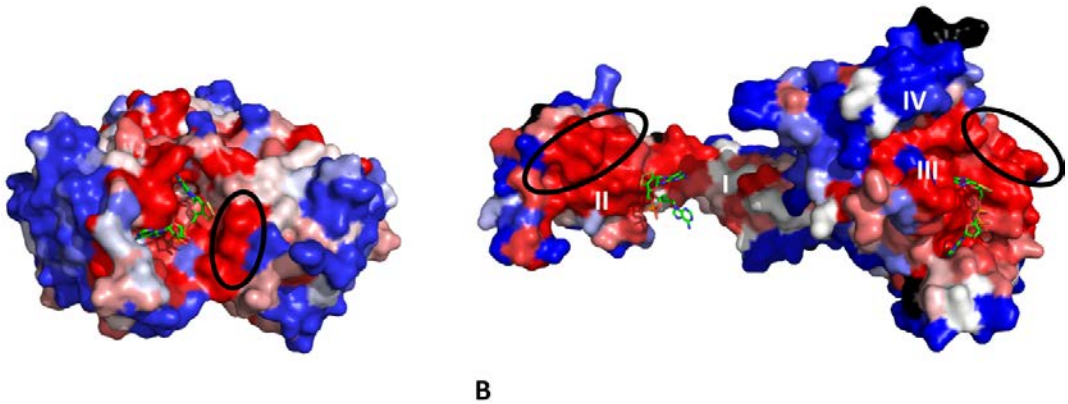

Figure 54 Residue conservation of 36 gephyrin orthologues in fungi, obtained with CONSURF. (A) GephG in complex with MPT-AMP obtained by superposition with PDB model 1UUY. (B) GephE complexed with two MPT-AMP molecules in stick representation. The other GephE protomer has been omitted for clarity. Note that in (A) and in (B) not only the MPT-AMP contacting residues are conserved but also surrounding patches, which is remarkable with respect to the fact, that in GephE these patches are even more conserved than the dimer interface in the centre. Black patches were considered as non-reliable predictions by CONSURF.

The GephG educt MPT has to be transferred from the MPT synthase to GephG. Surprisingly, in a recent study the affinity of *A. thaliana* MPT synthase to CNX1E was found to be more pronounced than to CNX1G, although the MPT conversion happens at CNX1G (Kaufholdt *et al.*, 2013). Should this also hold true for the gephyrin-MPT synthase interaction, a ternary complex of GephG, GephE and MPT synthase is conceivable, resulting in a presumably compact gephyrin conformation, in which also MPT adenylation by GephG takes place as well as the transfer of the resulting MPT-AMP to GephE. At this stage MPT-AMP is bound to an incomplete active site of subdomain III of GephE, which is only completed in the context of a GephE dimer (Xiang *et al.*, 2001). GephG-GephE interactions must therefore be broken, giving rise to another, more extended conformation (Fig. 55). It might well be that additional conformations are required, e.g. for the transfer of Moco, so that conformers like $GephG_3E_2E$ could exist (Fig. 28, not depicted in Fig. 55). Either way, structural plasticity is expected to pave the way for proper substrate channelling (Belaidi & Schwarz, 2012), which is required to protect the unstable MPT and MPT-AMP intermediates as well as the Moco product (Wuebbens & Rajagopalan, 1993).

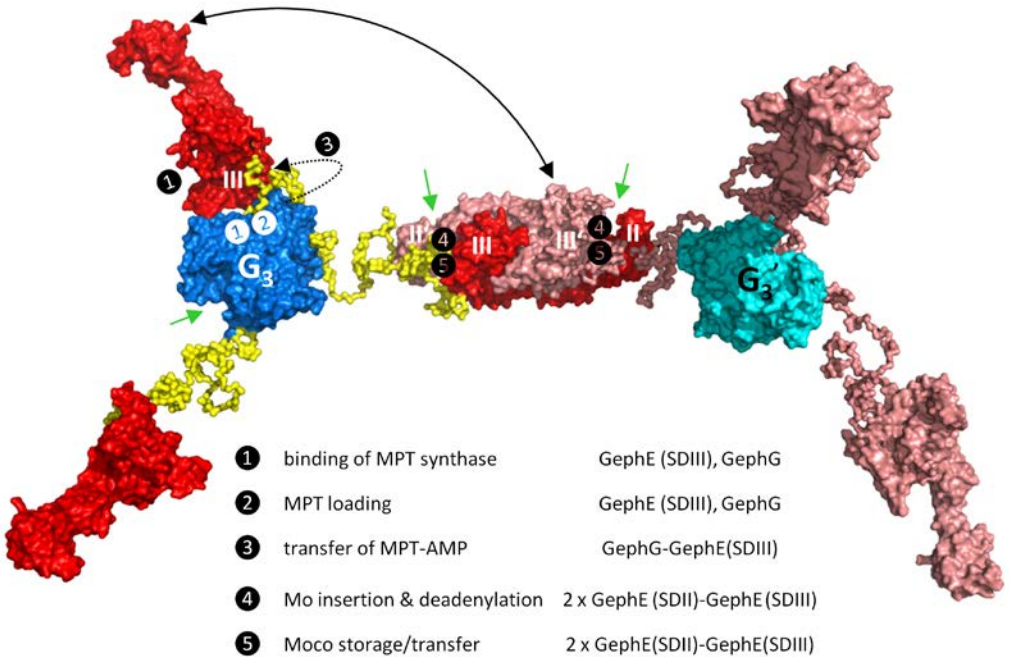

Figure 55 The putative role of gephyrin flexibility during Moco biosynthesis. Active sites in GephG (blue) and GephE (red, salmon) are marked with green arrows. Roman numerals refer to the subdomain architecture of GephE. Steps 1 to 3 might involve GephG and GephE subdomain III in a compact gephyrin conformation, while steps 4 and 5 take place at the bipartite GephE active site which requires a more extended conformation that allows for the interaction with another GephE, provided by another protomer of either the same or a different trimer. Only the latter scenario is depicted here. The table summarizes the respective steps to be taken for the conversion of MPT to Moco and where they are expected to take place.

Coming back to the negative binding results obtained with GephG-GephE mixtures: GephG-GephE subdomain III interactions could prevent dimerization for basically the same reason as given in Fig. 43: GephG and GephE subdomain II of an incoming dimer would sterically clash. Vice versa, GephE dimerization might prevent GephG from binding to subdomain III of GephE, and this might explain the negative results in GephG-GephE binding assays. Hence, one could test, whether GephG-GephE interactions are favoured in the absence of subdomain II. Comparable constructs have been used in previous studies (Nichols *et al.*, 2007, Smolinsky *et al.*, 2008). Alternatively, one could test the possibility of a GephE-subdomain II interaction with GephG, as this is required in the published model (Belaidi & Schwarz, 2012, Fritschy *et al.*, 2008).

III.A.3.9 A modified gephyrin model

As the linker in GephLE on its own could not prevent dimerization, it was clear that GephG was involved in preventing dimerization as well (at least in the P2 splice variant used here). The postulated GephG-GephE interaction (Fig. 56) could resolve this question and was compatible with compact states observed in SAXS and AFM. However, GephG-GephE interactions cannot be the only mechanism for preventing GephE dimerization, as in Moco biosynthesis at least two conformations are needed (Fig. 55) and as in both AFM and SAXS studies compact and extended states were observed. For the latter states GephG-GephE interactions are unrealistic (given D_{max} values of 500 Å), and additional, linker-dependent mechanisms are required, which in turn do not work in the absence of GephG.

One can propose a model that reconciles the equilibrium between compact and extended states, the trimeric oligomerization states and differential stabilization of Geph-MLH, GephΔL and GephG$(GGS)_4$E as well as the finding that GephLE did not dimerize (Fig. 56). This model does not take into account potential domain swapping, secondary structure elements (the putative α- and poly-proline helices) and the influence of ligands (protein or Moco intermediates). It also does not claim high fidelity with respect to GephE interacting segments or other linker conformations as well.

It is assumed that GephE dimerization in the compact state(s) and the extended state(s) is prevented by two different mechanisms. In the compact state (state C in Fig. 56) GephG-GephE interactions are involved, whereas in the extended state (state C in Fig. 56) a C-terminal linker segment (LinkerC) interacts with GephE and thereby masks the dimerization interface as suggested previously (Bedet et al. 2006). This extended state is metastable, so that the linker can detach from the dimer interface (state B). State B is short-lived, because the GephE dimer interface is more stable

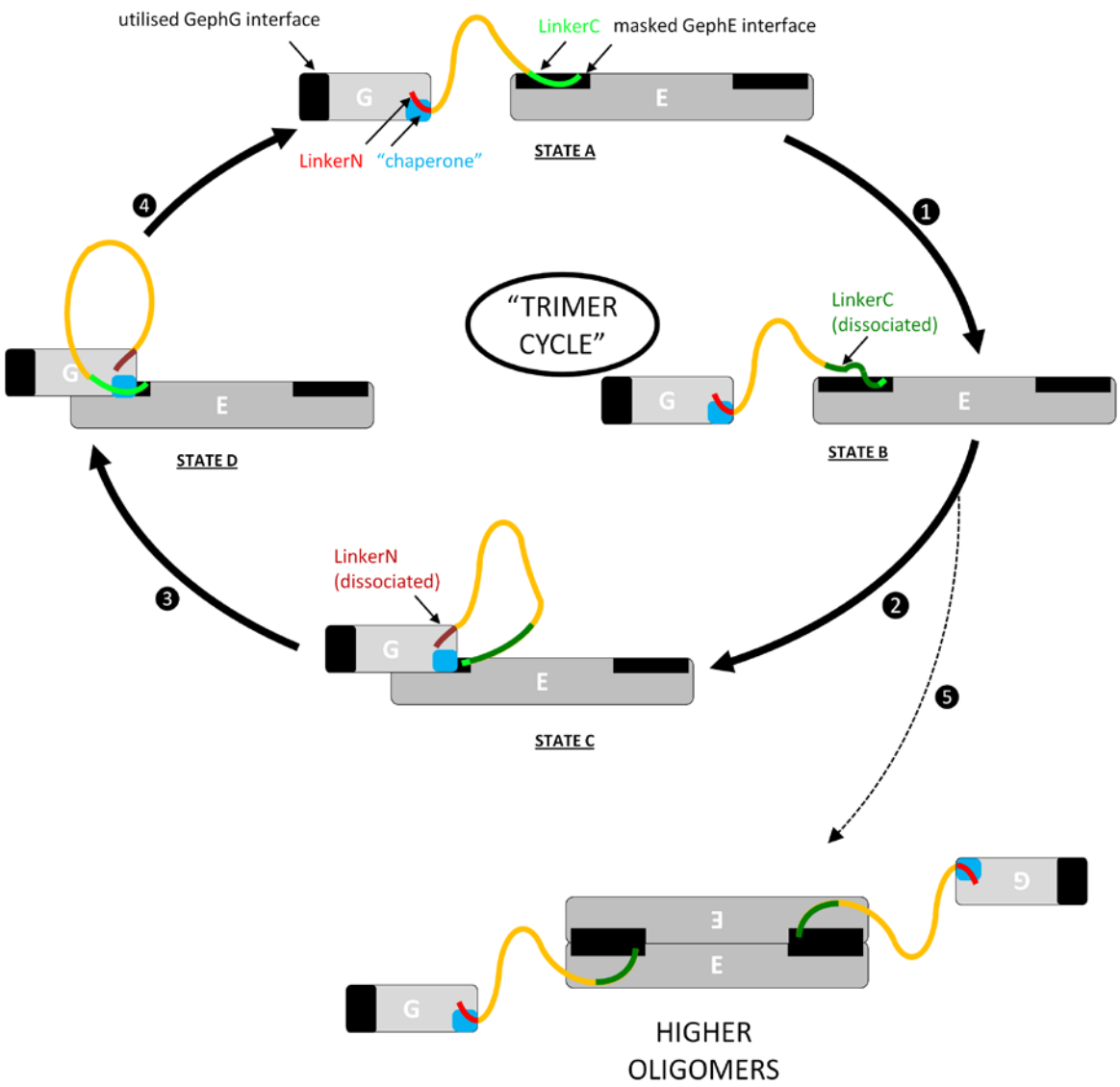

Figure 56 Model suggesting how GephE dimerization in the context of trimeric gephyrin is prevented. Basically an equilibrium between compact and extended states (referred to as states C and A, respectively) is assumed, in which dimerization is prevented by GephG-GephE interactions and linkerC-GephE interactions, respectively. Interactions between the linker and GephE are metastable (state A), so that some gephyrin trimers can form higher oligomers (❺). However, GephG-GephE interactions are preferred and pave the way for GephG chaperone activity (state D) which is required to regenerate LinkerC conformations that can block GephE dimerization.

in an occupied state. Hence, even a small fraction of gephyrin trimers can now use their dimer interfaces either within a trimeric assembly or in the context of a higher oligomer (❺ in Fig. 56). However, the majority of gephyrin assemblies will remain in the "trimer cycle" (❶-❹), because intramolecular GephG-GephE interactions will dominate over inter-assembly dimerization and drive gephyrin into the compact state C. GephG-GephE interactions and/or linker detachment from GephE will trigger the dissociation of an N-terminal linker segment from a GephG portion, that acts like a chaperone for the C-terminal linker segment (state D). The now properly "refolded" linker segment

LinkerC can now rebind to the GephE dimerization interface, so that LinkerN can occupy the GephG "chaperone" again (state A).

This model explains why all linker deletion variants failed to preferentially assemble into higher oligomers – because the linker independent GephG-GephE interaction serves as a backup mechanism to prevent inter-trimeric dimerization. This equilibrium could be altered by ligands (during Moco biosynthesis), binding partners, splice variants or by posttranslational modifications. Gephyrin's interactions with several binding partners, namely DYNLL1, NL2 and collybistin, are described in chapters III.B and III.C.

III.B. The Gephyrin-DYNLL1 interaction

III.B.1. Introduction

III.B.1.1 The dynein motor

Cytoplasmic dyneins are minus-end directed microtubule-based motors (Pfister *et al.*, 2005) and are composed of several proteins of different masses, of which the so-called heavy chains determine their functionality: While cytoplasmic dynein 2 mediates intraflagellar transport (Cole, 2003), cytoplasmic dynein 1 is involved in almost the complete cytosolic minus-end directed traffic (Allan, 2011, Kikkawa, 2013, Pfister *et al.*, 2006, Roberts *et al.*, 2013). The central role of dynein 1 is illustrated by the large variety of cargoes ranging from RNA (Gagnon & Mowry, 2011) over proteins (Harrell *et al.*, 2004) to entire organelles (Akhmanova & Hammer, III, 2010, Hirokawa, 1998, Roberts *et al.*, 2013), thereby regulating fundamental processes such as neuronal migration (Vallee *et al.*, 2009), organelle biogenesis and signalling (Muresan & Muresan, 2012). Notably this transport system can also be hijacked by viruses (Dodding & Way, 2011). Last but not least dynein is crucially involved in spindle positioning and chromosome segregation (McNally, 2013, Roberts *et al.*, 2013).

Cytoplasmic dynein 1 (herein referred to as dynein) forms a dimeric ~1.5 MDa complex, in which the heavy chain (DYNC1H1, ~530 kDa) is the central component. Recent crystal structures of the heavy chain (Carter *et al.*, 2011, Kon *et al.*, 2012, Schmidt *et al.*, 2012) clearly enhanced the understanding of the dynein motor action and, in addition, detailed reviews/studies on the mechanistic implications are available (Allan, 2011, Cho & Vale, 2012, DeWitt *et al.*, 2012, Kikkawa, 2013). The heavy chain is an atypical member of the AAA+ (ATPase associated with various cellular activities) family of ATPases as its six AAA domains are encoded by a single polypeptide. The six AAA domains form a ring-like structure with three prominent protrusions, first, the stalk which mediates microtubule binding, second, the buttress and last, the N-terminal tail together with the subsequent linker (Fig. 57). Linker, stalk and buttress are important for the conversion of ATP hydrolysis into mechanical energy (Kon *et al.*, 2012, Lin *et al.*,

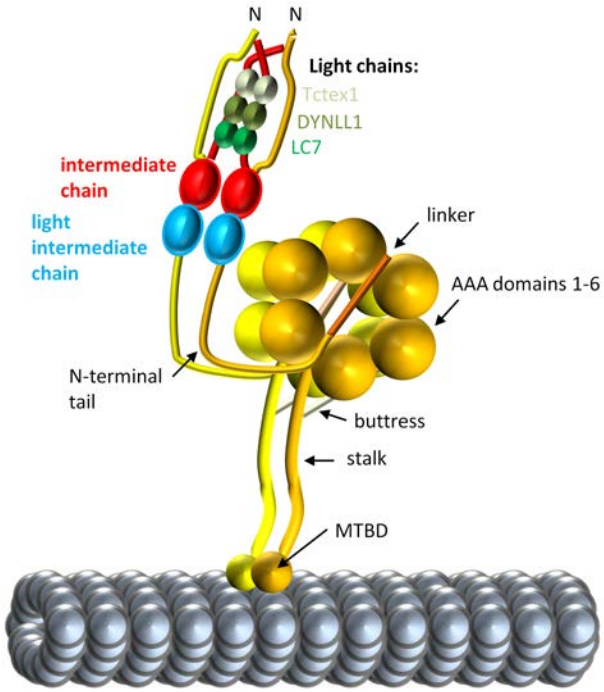

Figure 57 Dynein subunit composition in the style of (Hall *et al.*, 2009). The dynein heavy chains are coloured in yellow/orange and associate with the light intermediate (blue) and intermediate (red) chains. The latter provides binding sites for the dimeric light chains LC7, DYNLL1 and Tctex1. *MTBD* stands for microtubule binding domain.

2014). The N-terminal tail harbours binding sites for two accessory chains, namely the light intermediate chain (DLIC,~50-60 kDa) and the intermediate chain (DIC, 74 kDa) (Tynan *et al.*, 2000), which promote dimerization and enhance the solubility of the N-terminal tail of the heavy chain (Trokter *et al.*, 2012). Beyond that the intermediate chain has been reported to link cargoes to the dynein motor either via direct interactions with the cargo (Dhani *et al.*, 2003, Karki *et al.*, 2002, Ye *et al.*, 2000) or indirectly via its interaction with e.g. dynactin which, in turn, binds the actual cargo (Kardon & Vale, 2009, Rapali *et al.*, 2011b, Vallee *et al.*, 2012).

However, for the complete reconstitution of the dynein motor the heavy chain, DLIC and DIC were not sufficient, and only the addition of the dynein light chains ensured the correct shape of dynein (Trokter *et al.*, 2012). There are three classes of dynein light chains which all bind to the DIC (Nyarko & Barbar, 2011, Williams *et al.*, 2007): LC7 (Roadblock DYNLR, (Sakakibara & Oiwa, 2011)), LC8 (DYNLL, (Rapali *et al.*, 2011b)) and Tctex1 (DYNLT, (Mok *et al.*, 2001)). Structural studies of DIC-Tctex1-DYNLL (Hall *et al.*, 2009, Williams *et al.*, 2007) and IC-LC7 (Hall *et al.*, 2010) suggested that the three dynein light chain dimers are arranged like beads connecting two flexible strings. Especially the functional significance of DYNLL in the context of cytoplasmic dynein could be demonstrated by a combination of structural and single-molecule analysis: In yeast the DYNLL orthologue Dyn2 induced dimerization of the DYNC1HC1 yeast orthologue Dyn1 via Pac11 (orthologue of DIC) which was required for normal processivity of the dynein motor, which means its capability to move along microtubule tracks without detachment (Rao *et al.*, 2013).

III.B.1.2 Dynein light chains of the DYNLL type interact with gephyrin

Gephyrin could be shown to bind to dynein components DYNLL1 and 2 in yeast-two-hybrid screens (Fuhrmann *et al.*, 2002). Pulldown analysis confirmed a direct interaction between the DYNLLs and gephyrin *in vitro*. Fluorescence and electron microscopy suggested that only a small fraction of spinal cord DYNLL localizes (close) to synapses (6% postsynaptic and 6% extrasynaptic), and the deletion of the initially mapped DYNLL binding site (residues 181-243) did not alter the gephyrin targeting to postsynaptic sites (Fuhrmann *et al.*, 2002). In analogy with other synaptic scaffolding protein-receptor complexes (Kneussel, 2005), gephyrin-GlyR complexes could be shown to be associated with the dynein motor (Maas *et al.*, 2006). In this follow-up study mobile, cytoplasmic gephyrin clusters were observed to be 2.3 times smaller than their seemingly static synaptic counterparts (Maas *et al.*, 2006). Co-transport of gephyrin-GlyR complexes was suggested by sedimentation and co-IP experiments and demonstrated by time-lapse video microscopy (Maas *et al.*, 2006). In accordance with the previous finding that DYNLL was localized at the edges of synapses rather than at their centres (Fuhrmann *et al.*, 2002), gephyrin-DYN1HC1 and GlyR-DYN1HC1 colocalization was observed close to but not directly at synapses (Maas *et al.*, 2006). Gephyrin

transport could be altered in primary hippocampal neurons: In the presence of strychnine, a GlyR antagonist, the ratio of anterograde to retrograde gephyrin transport could be shifted to smaller values, whereas $GABA_AR$ blockage with bicculine had no effect (Maas *et al.*, 2006). Second, endogenous gephyrin clusters in primary hippocampal neurons were lost upon overexpression of the dominant-negative variant GephG (actually a construct comprised of residues 2-188 and hence also the very N-terminus of the linker), but could be rescued by the simultaneous overexpression of dynamitin which interferes with dynein function (Burkhardt *et al.*, 1997), or by the presence of nocodazole, which leads to microtubule depolymerization (Samson *et al.*, 1979), thus destroying the dynein track (Maas *et al.*, 2006). Third, interference of interactions between endogenous gephyrin and endogenous DYNLL by the overexpression of RFP (red fluorescent protein) fused to residues 181-243 (harbouring the DYNLL binding site of gephyrin) affected the retrograde transport of gephyrin and the GlyR, for which no mobile particles could be identified anymore rather than the anterograde transport which was affected only after several days of overexpression (Maas *et al.*, 2006). Taken together, these results suggested that DYNLLs are involved in the retrograde transport of gephyrin-GlyR complexes by the dynein motor (Maas *et al.*, 2006).

III.B.1.3 Crystal structure of the DYNLL-Geph complex

The DYNLL binding site in gephyrin could be further refined to an octapeptide (residues 205-212) in the N-terminal quarter of gephyrin's linker region (Navarro-Lérida *et al.*, 2004). A dodecapeptide, derived from the octapeptide by the addition of two residues at either terminus, is referred to as DYNLL binding motif or $Geph_{DB}$ (residues 203-214, Figs. 58 & 59A). A former PhD student in the lab, Eun-Young Lee, succeeded in the cocrystallization of DYNLL1 and DYNLL2 with $Geph_{DB}$ (Lee, 2009). The crystal structures revealed that nine residues (namely Gln204-Cys212) of the gephyrin-derived dodecapeptide bound tightly to DYNLL1/2 (Fig. 58) (Lee, 2009)). The minor differences between DYNLL1 and DYNLL2 could rather be attributed to the resolution than to sequence specific features; DYNLL1 and DYNLL2 differ in only six residues which are distant from the DYNLL binding groove. All in all, DYNLL1/2-gephyrin complexes were highly reminiscent of other DYNLL/LC8 complexes such as nNOS (Liang *et al.*, 1999), the dynein intermediate chain (Benison *et al.*, 2007, Rao *et al.*, 2013), the dynein intermediate chain-Tctex1 complex (Hall *et al.*, 2009, Williams *et al.*, 2007), Swallow (Benison *et al.*, 2007), Pak1 (Lightcap *et al.*, 2008), EML3 (Rapali *et al.*, 2011a), Nup159 (Romes *et al.*, 2012), EML3 (Rapali *et al.*, 2011a), NEK 9 (Gallego *et al.*, 2013) and the NMR structure of the LC8-Bim1 complex (Fan *et al.*, 2001).

DYNLL1 and 2 form dimers in which the central four-stranded β-sheet of one monomer is surrounded by two α-helices and extended by a fifth β-strand provided by the other monomer to yield an intertwinned dimer (Lee, 2009). The β-sheets can be further extended in the presence of the

gephyrin-derived peptides which, in isolation, were found to be intrinsically disordered in CD experiments and adopted the β-strand conformation upon binding into the two hydrophobic binding grooves (Lee, 2009), as is typical for DYNLL ligands, which are also referred to β-MoRE (**Mo**lecular **R**ecognition **E**lement) (Rapali *et al.*, 2011b). Ligand binding induced minor changes, e.g. a slight increase in the average width of the binding cleft from 13.0 Å in apo-DYNLL2 to 13.5 Å in the DYNLL2-$Geph_{DB}$ complex. The structures also revealed the basis for the recognition of the non-canonical $Geph_{DB}$ motif, which neither belongs to the class I ($K_{-3}X_{-2}T_{-1}Q_0T_1X_2$) nor to the class II ligands ($X_{-3}G_{-2}(I/V)_{-1}Q_0V_1D_2$) (Rapali *et al.*, 2011b).

The relevance of the peptide-DYNLL interactions observed in the crystal structures was substantiated by ITC measurements, which suggested that there were two hot spots which mediated binding: Gephyrin residues 207-208 and residues 210-212 around the canonical Gln211. The affinity of DYNLLs to $Geph_{DB}$ (K_D = 3.3 µM) (Lee, 2009) was in the range typical for DYNLL complexes (0.1 µM<K_D<40 µM) (Rapali *et al.*, 2011b).

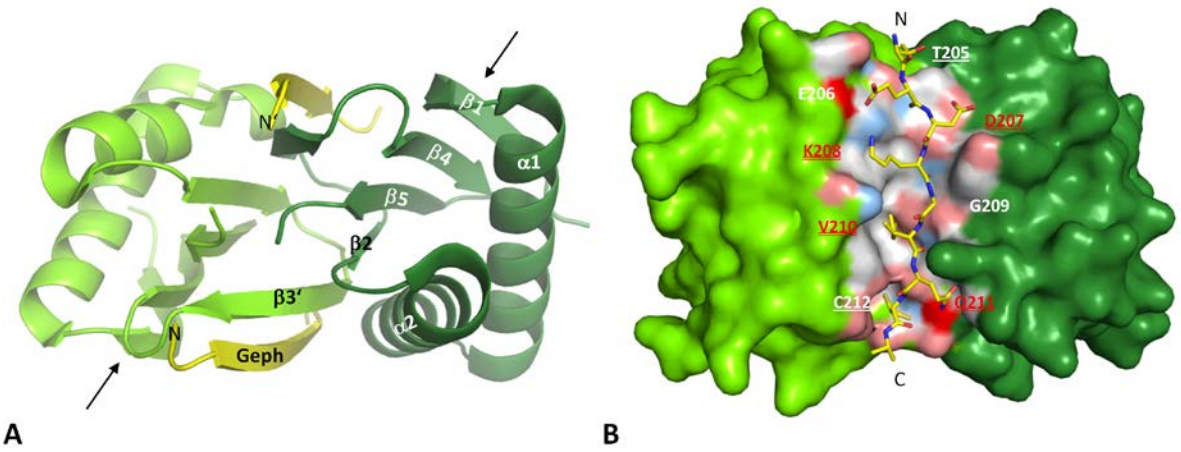

Figure 58 Crystal structure of the DYNLL2-$Geph_{DB}$ complex. (A) The two DYNLL protomers are coloured in light and dark green, respectively. The complex harbours two six-stranded β-sheets in the complex (indicated by the two arrows) in the centre of the assembly. Four strands are contributed by one protomer (β1, β4, β5, β2) and the remaining two by the other protomer (β3') and the gephyrin-derived peptide (Geph). The N-termini of the $Geph_{DB}$ peptides are indicated by N and N'. (B) Side view of the complex. DYNLL2 residues involved in complexation of $Geph_{DB}$ (yellow stick representation) are coloured in white (hydrophobic), salmon (polar oxygen atoms), red (oxygen atoms provided by negatively charged side chains), marine (polar nitrogen atoms) and blue (nitrogen atoms provided by positively charged residues). In the $Geph_{DB}$ peptide yellow, red and blue portions correspond to carbon, oxygen and nitrogen atoms. Note the complementation of polar, charged and hydrophobic residues. Residue numbers 205-212 refer to the bound peptide, where mutation of underlined or residues labelled in red to alanines led to either moderate (3- to 4-fold) or severe attenuation (6-fold or higher) of binding strength, respectively (Lee, 2009).

III.B.1.4 Cargo transport or dimerization hub?

Initially, DYNLL1/2 were considered as cargo adaptors, which simultaneously binds to the dynein motor via the intermediate chain and the cargo (Fig. 59). However, the consideration of DYNLL1 as a cargo adaptor has been challenged: First, crystal structures of DYNLL-IC complexes revealed that IC and cargo (such as gephyrin) compete for the two binding grooves (see Fig. 3B in (Benison *et al.*, 2007, Williams *et al.*, 2007)). Second, plants express LC8 (DYNLL1/2) but lack the dynein heavy chain, which is the integral and catalytically active dynein subunit (Wickstead & Gull, 2007) that mediates the movement along microtubules, and, last but not least, not all DYNLL binding partners are involved in transport processes, but also cover a wide spectrum of functions including apoptosis, PSD organization and regulation of transcription (Rapali *et al.*, 2011b). Hence, the cargo adaptor hypothesis has gone out of fashion, and DYNLL is now rather considered to be a general dimerization hub, i.e. DYNLL binds to two copies of a predominantly monomeric interaction partner which - in

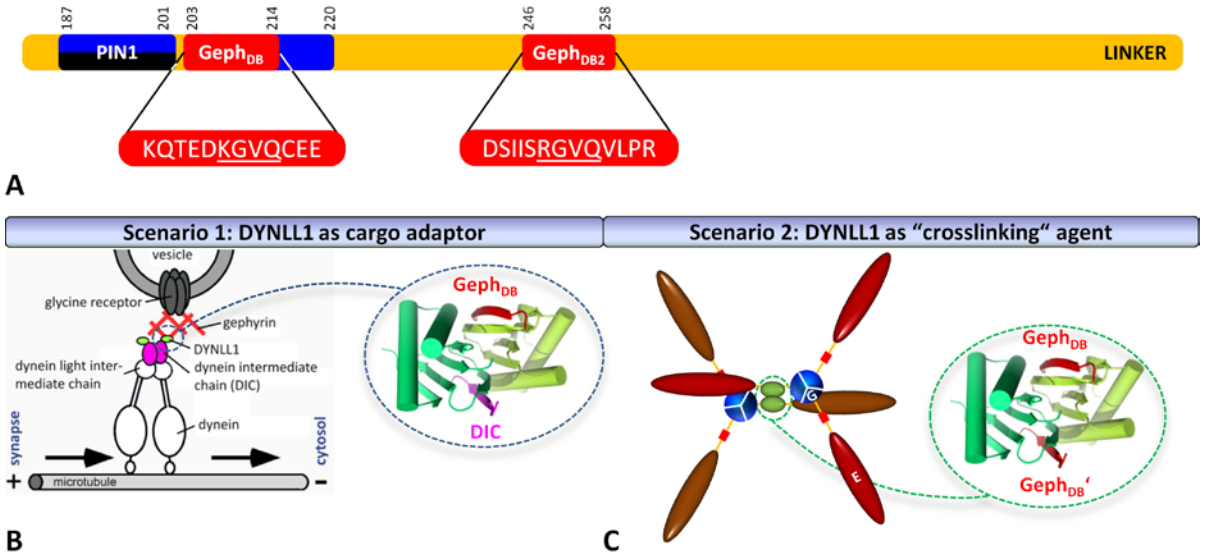

Figure 59 Two hypotheses regarding the function of the Geph-DYNLL complex. (A) A scheme of the linker containing the two confirmed binding motifs for PIN1 and DYNLL (DB or Geph$_{DB}$ in the text). A second putative binding site (Geph$_{DB2}$) identified by Eunyoung Lee is also shown (Lee, 2009). Regions marked in blue potentially contain poly-proline helices. Underlined residues highlight the similarity between the two motifs. (B) The cargo adaptor hypothesis. The scheme on the left-hand side which depicts the dynein motor interacting with gephyrin-glycine receptor complexes via the DYNLL1-DIC complex was taken and modified from Maas et al., 2006 (originally published in Journal of Cell Biology. doi: 10.1083/jcb.200506066). The two binding grooves are occupied by gephyrin on one side and DIC on the other. Note that the depicted microtubule polarity is not valid for the complete dendritic compartment, as mixed microtubule orientations were observed (Baas *et al.*, 1988). (C) The (simplified) dimerization hub scenario: DYNLL1 again depicted in green on the left-hand side binds to two different gephyrin trimers (in one GephE is coloured in dark brown, in the other one in red-brown). For legibility only one pair of the DYNLL binding sites is used in this example, but in principle further Geph$_{DB}$ motifs might be linked (also within the same trimer), potentially triggering GephE-GephE interactions.

addition to its DYNLL binding site - contains a (weak) dimerization motif. As a consequence of DYNLL binding a higher local concentration of this motif shifts the equilibrium of the interaction partner towards the dimer (Barbar & Nyarko, 2014, Barbar, 2008).

In the case of gephyrin, this would be consistent with the linkage of two gephyrin trimers (considered as inter-trimeric dimerization, depicted in Fig. 59C) and/or with DYNLL bridging two linkers within a trimer (referred to as intra-trimeric dimerization. Strictly speaking, the dimerization hub scenario as suggested in (Barbar, 2008) also includes a second criterion, namely the DYNLL-induced association of $Geph_{DB}$-independent segments/portions gephyrin, i.e. the dimerization via GephE, which is otherwise autoinhibited. However, as a distinction between gephyrin bridging via DYNLL (as depicted in Fig. 59) with or without additional GephE dimerization is difficult to analyse, I apply the term dimerization hub with respect to mere gephyrin bridging, which, of course, does not exclude the possibility of GephE dimerization.

III.B.1.5 The aims of this work

Although structural details and the key determinants of the gephyrin-DYNLL complex formation were already elucidated, the stoichiometry of the complex could not be determined unambiguously (Lee, 2009) and became the central issue of this work. In the first part of this chapter a-step-by-step elucidation of the stoichiometry of the gephyrin complex with DYNLL1 is presented, in the second part explanations for the observed stoichiometry are given. Experiments could have been conducted with DYNLL2 as well, however, since gephyrin had been shown to interact with DYNLL2 in the same manner as DYNLL1 (Lee, 2009), and the role of DYNLL2 in the context of the dynein motor has been controversial (Day *et al.*, 2004, Lo *et al.*, 2007) I focused exclusively on DYNLL1.

III.B.2. Results

III.B.2.1 Determination of the gephyrin-DYNLL1 stoichiometry

III.B.2.1.1 Gephyrin and DYNLL each provide a single binding site

The first step towards the determination of the stoichiometry was to confirm the number of binding sites in both binding partners. Based on the crystal structures by my predecessor Eunyoung Lee, there was no doubt that one gephyrin binding site existed per DYNLL monomer (Lee, 2009). For gephyrin the situation also seemed quite clear: The binding site could be narrowed down to a segment containing residues 205 to 212 (Lee, 2009, Navarro-Lérida *et al.*, 2004), and a peptide corresponding to the second putative binding site in gephyrin (residues 246-257, referred to as $Geph_{DB2}$) turned out to be a non-binder in ITC experiments (Lee, 2009), although its sequence displayed six subsequent amino acids (SRGVQV) which are in good agreement with a motif search on the basis of 41 DYNLL ligands (Rapali *et al.*, 2011a).

To confirm previous binding studies and to rule out significant contributions by $Geph_{DB2}$, the mentioned ITC experiments using synthesized peptides comprising the DYNLL motifs were repeated. In the case of $Geph_{DB2}$ arginine 258 was included at the C-terminus of the peptide, since the DYNLL binding motif of neuronal nitric oxide synthase contains an arginine at the corresponding position in the $Geph_{DB2}$ motif and was found to be involved in a cation-π interaction (Liang *et al.*, 1999).

	$Geph_{DB}$	GephWT
n	1.27 ± 0.07	0.99 ± 0.07
$K_{D,app}$ [µM]	3.3 ± 1.1	2.3 ± 0.9
ΔH [kJ/mol]	-30.1 ± 2.9	-54.4 ± 3.0
-TΔS [kJ/mol]	-2.6 ± 2.7	20.8 ± 2.6

Table 37 Full-length gephyrin and the isolated $Geph_{DB}$ motif exhibit similar binding affinities to DYNLL1. Experiments were conducted in SEC-7 buffer at 37°C (like all experiments presented in this chapter). The parameters were obtained from three measurements and were analysed with a 1:1 binding model. A representative fit is shown in Fig. 60.

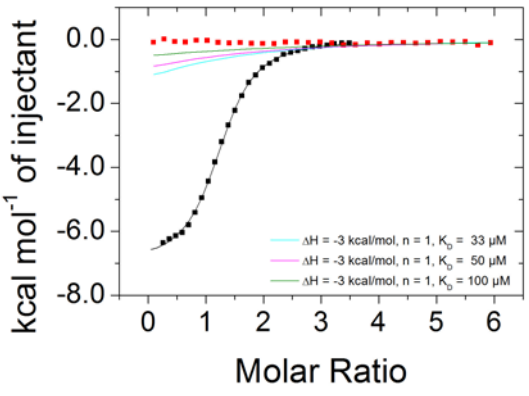

Figure 60 DYNLL1 bound to a single motif in gephyrin's linker. $Geph_{DB}$ and $Geph_{DB2}$ share a very similar core motif (Fig. 59A). However, only the titration of $Geph_{DB}$ (black circles) but not that of $Geph_{DB2}$ (red circles) to DYNLL1 resulted in a nearly-sigmoidal heat signature at cell concentrations of 40 µM ($Geph_{DB}$) and 25 µM ($Geph_{DB2}$), respectively. Cyan, pink and green curves were simulated, assuming the given parameters and the concentrations of the $Geph_{DB2}$ titration to show that K_Ds of a putative $Geph_{DB2}$-DYNLL1 complex below 100 µM were rather unlikely.

In agreement with previous data of Eun-Young Lee (Lee, 2009), robust binding with an apparent K_D ($K_{D,app}$) of 3.3 µM could be detected only for $Geph_{DB}$ and not for $Geph_{DB2}$ (Fig. 60), which was close to the measured $K_{D,app}$ of the full-length gephyrin-DYNLL1 complex (Table 37). The minimal differences in affinity were in striking contrast with differing thermodynamic parameters: Entropic costs occurred under the given conditions only for the GephWT-DYNLL1 complex and had to be compensated for by a twofold increased binding enthalpy compared to the $Geph_{DB}$-DYNLL1 complex, for whose formation the net entropic term did not counteract the binding enthalpy under the given conditions. Regarding the stoichiometry, n, values of 1.27 and 1 were observed for the $Geph_{DB}$-DYNLL1 and the DYNLL1-GephWT complex, respectively. The stoichiometry for the latter complex suggested that either one DYNLL1 monomer bound per gephyrin protomer or that a first DYNLL1 dimer bound to two linkers of a gephyrin trimer, while the third linker interacted with either a DYNLL1 monomer or shared a DYNLL1 dimer with another gephyrin trimer (as displayed in Fig. 59C).

III.B.2.1.2 DYNLL dimers do not act as efficient dimerization hubs for gephyrin trimers

For structural reasons (discussed in III.B.3.1) it appeared plausible to assume that DYNLL bound as a dimer to a still to be defined number of gephyrin molecules. To analyse the stoichiometry, aSEC experiments were conducted to test whether DYNLL acted as dimerization hub. If this assumption was valid, DYNLL1 binding would lead to a pronounced left-shift of the gephyrin peak in the chromatogram, as the molecular mass difference would be at least 276 kDa (one gephyrin trimer + one DYNLL1 dimer). On a Superdex 200 10/300GL column this was expected to translate - according to intrapolations of a protein standard based on the manufacturer's manual - into at a minimum a ~1 mL-shift of the gephyrin peak in the presence of DYNLL1 or, at least, to a visible shoulder towards smaller elution volumes. However, apo-gephyrin and the Gephyrin-DYNLL1 complex differed by just 0.3 mL in elution volume - despite high concentrations of both proteins (Fig. 61A, 500 µL of 100 µM GephWT plus 400 µM DYNLL1). These numbers argued against stable higher gephyrin oligomers and thus against the hypothesis that DYNLL1 acted as an inter-trimeric dimerization hub. However, the inter-trimeric dimerization hub hypothesis was not completely discarded, as the chromatogram could be deconvoluted into five separate Gaussian peaks (mentioned in the order according to the numbering in Fig. 61B): Peaks 1 and 2 with a R_H higher than the R_H of gephyrin, peak 3 at the R_H of apo-gephyrin, peak 4 with an R_H(gephyrin) > R_H(peak 4) > R_H(DYNLL1) (denoted as dissociating DYNLL1) and a last peak with R_H=R_H(unbound DYNLL1). Peak 1 displayed an elution volume of 8.5 mL, clearly below that of apo-gephyrin (10.5 mL). Nevertheless this species would be outnumbered by peak 2 (with an eightfold higher area under the curve), corresponding to trimeric gephyrin in complex with DYNLL1. Of course, these calculations were rather speculative – especially considering the fact that the chromatogram could also be deconvoluted into four peaks with none of the peaks

possessing an elution volume smaller than 10.1 mL, thus indicating the absence of “crosslinked” gephyrin assemblies. However, peak deconvolution also demonstrates that – based on the chromatogram – the inter-dimerization hub theory should not be ignored.

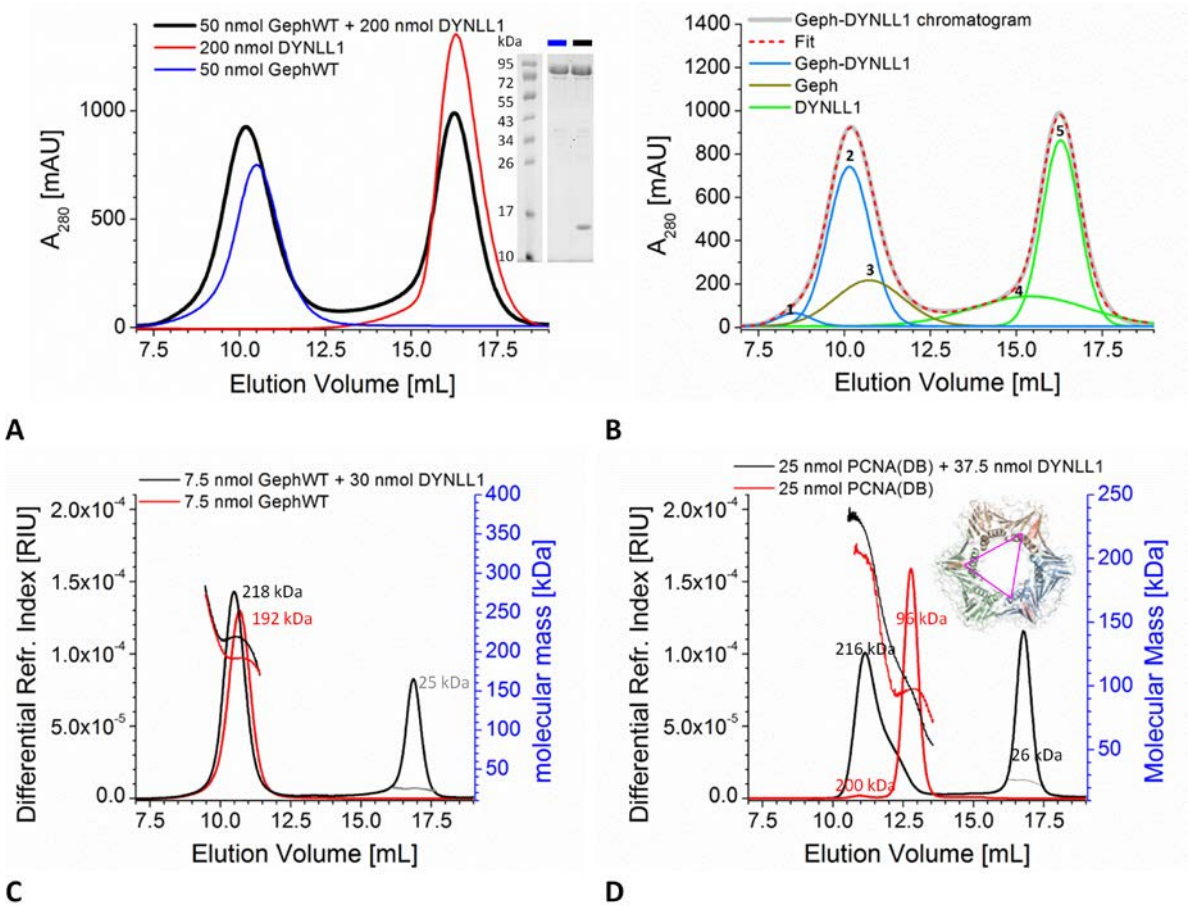

Figure 61 Analytical SEC experiments revealed that GephWT trimers were not stably bridged by DYNLL1. All experiments in this figure were carried out in SEC-1 buffer using a Superdex 200 10/300GL SEC column. (A) Gephyrin formed a complex with DYNLL1 which was indicated by a 0.3 mL shift in the chromatogram and the presence of DYNLL1 in the 10.2 mL fraction, as revealed by the SDS-PAGE gel in the inset. (B) The chromatogram of (A) was used for peak deconvolution, where peak minima were set initially at 9 mL, 10.2 mL, 10.5 mL, 13.5 mL and 16.3 mL and were refined by Origin 8.0. (C) SEC-MALS experiments accounted for binding of a single DYNLL1 dimer per gephyrin trimer. Protein elution is indicated by changes in the differential refractive index (left y-axis). Gephyrin’s molecular mass was increased upon complex formation by 26 kDa, in good agreement with the molecular mass of a DYNLL1 dimer (expected molecular mass: 25.4 kDa). (D) The three C-termini of PCNA(DB) (indicated by the corners of the pink triangle) are too far away from each other to allow for intratrimeric dimerization of DYNLL1. In fact DYNLL1 performed inter-trimeric dimerization of two PCNA(DB) molecules. The 200 kDa species in the apo-PCNA(DB) sample appeared to be of little significance in comparison to the complex at 216 kDa which was in excellent agreement with one DYNLL1 (25 kDa) bridging two PCNA(DB) trimers with 96 kDa each, resulting in a calculated molecular weight of 217 kDa.

While it became clear that under the conditions tested so far the majority of the gephyrin molecules stayed trimeric upon DYNLL1 binding, the number of DYNLL1 remained to be determined. Hence, SEC-MALS experiments were conducted to determine the mass increase in the presence of DYNLL1 (Fig. 61C). Molecular masses of 216 kDa, 192 kDa and 26 kDa were obtained for the Geph-DYNLL1 complex, apo-gephyrin and apo-DYNLL1, respectively, in agreement with a single DYNLL1 dimer binding to a gephyrin, acting as an intra-trimeric (and not as an inter-trimeric) dimerization hub. Mixtures of different species were not supported by the rather constant molecular mass distribution of the gephyrin-DYNLL1 peak (Fig. 61C).

To exclude that DYNLL1 preparations under the given conditions were not capable of crosslinking different molecules, a positive control was designed: A fusion protein of *Chaetomium thermophilum PCNA (*Proliferating-Cell-Nuclear-Antigen, the plasmid encoding for the wildtype protein was kindly provided by Florian Rohleder (AG Kisker)) and the $Geph_{DB}$ motif. In this construct, referred to as PCNA(DB), the $Geph_{DB}$ motif was appended to the C-terminus of PCNA, which was defined as the last residue resolved in the crystal structure (Florian Rohleder, unpublished data). Four additional ctPCNA residues beyond the C-terminus were still included as linker region preceding the $Geph_{DB}$ motif. Intra-trimeric dimerization was rather unlikely, because the distance of 56 Å between two C-termini (residues marked in red in Fig. 61D) could hardly be bridged by the 25 Å gap between the two DYNLL1 binding grooves plus two linker regions of eight residues. Hence, PCNA(DB) was expected to be principally capable of binding to three DYNLL1 dimers. This could result in vacant binding sites at each bound DYNLL1 dimer, which could be theoretically occupied by another PCNA(DB). Indeed, DYNLL1 induced the formation of higher oligomers, as indicated by a 1.6 mL difference in the chromatograms of PCNA(DB) and the PCNA(DB)-DYNLL1 complex (Fig. 61D). The derived molecular mass of the complex (216 kDa) was in excellent agreement with a single DYNLL1 dimer (25 kDa) linking two PCNA(DB) trimers (96 kDa vs. expected molecular mass of 100 kDa). Hence, if the $Geph_{DB}$ motifs within a gephyrin trimer had been freely accessible, the affinity for $Geph_{DB}$ motif should have been sufficient for DYNLL1 to induce higher oligomers in gephyrin as well.

III.B.2.1.3 Gephyrin binds to DYNLL1(S88E) with attenuated affinity

Before testing the cargo hypothesis, binding of monomeric DYNLL1 was assessed. If only DYNLL1 monomers bound to gephyrin, binding of a second ligand (as assumed in the cargo hypothesis) could be excluded, because one monomer offered only a single binding site which, in addition, was even incomplete due to the absence of one β-strand derived from the second monomer which forms part of the binding pocket.

To prevent DYNLL1 dimerization, a phosphomimetic mutation, S88E, was purified, which was previously shown to interfere with the formation of DYNLL1 dimers (Benison *et al.*, 2009). The SEC-

MALS-derived molecular mass of the predominant DYNLL1(S88E) fraction was 12.8 kDa ± 0.3 kDa, just slightly deviating from the expected molecular mass of 12.7 kDa while the DYNLL1 dimer (determined molecular mass: 28.5 kDa ± 3.0 kDa) constituted five percent of the sample or less (data not shown).

Preliminary binding studies by aSEC confirmed that monomeric DYNLL1 exhibited a clearly attenuated affinity to gephyrin (Fig. 62A), as indicated by the small peak increase and the fact that the elution volume of gephyrin in the presence of DYNLL1(S88E) was not significantly different from that of apo-gephyrin. A direct comparison with the chromatogram of a complex containing both proteins in their wild-type form exemplified how strong complex formation was attenuated (Fig. 62B), albeit not completely abrogated, as complex formation could be verified by SDS-PAGE of the peak fractions (inset in Fig. 62A). In light of the already published binding studies of DYNLL1(S88E) it appeared likely that the small amount of DYNLL1 dimers was depleted by gephyrin binding, hence shifting the monomer-dimer equilibrium (slightly) to the dimer side (Radnai *et al.*, 2010). Future SEC-MALS experiments will hopefully elucidate whether DYNLL1(S88E) monomers or dimers bound to gephyrin.

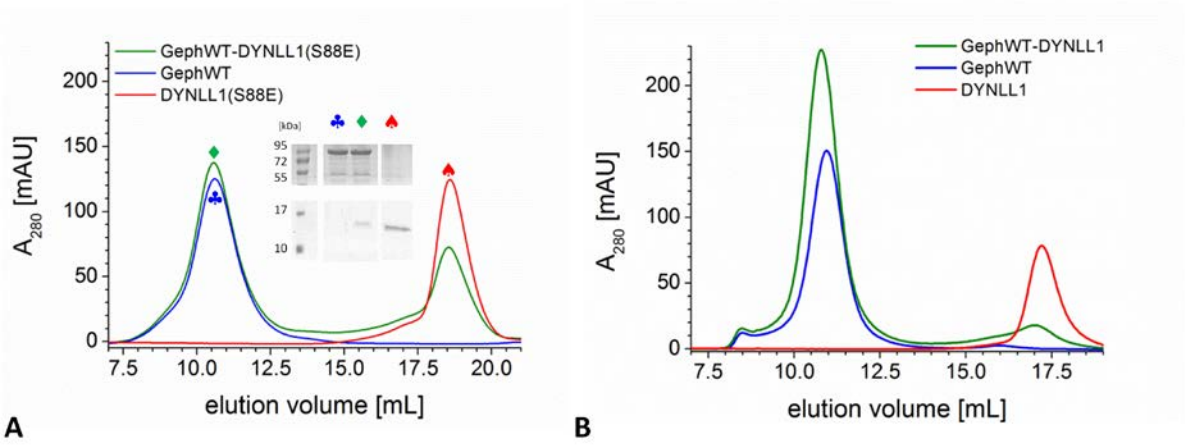

Figure 62 Gephyrin's affinity to monomeric DYNLL1 S88E was significantly attenuated in comparison to dimeric DYNLL1 WT. (A) In aSEC experiments the GephWT peak was not shifted in the presence of DYNLL1(S88E), and the A_{280} gain was only marginal. However, SDS-PAGE gels showed that DYNLL1(S88E) had some residual binding capacity. (B) At concentrations comparable to the experiment displayed in (A) the GephWT peak was shifted, and the peak ratios implied a tighter binding of wildtype DYNLL1 to GephWT than observed for the monomeric DYNLL1(S88E). Please note the position of the DYNLL1(S88E) peak at 18.5 ml compared to the peak of the wild-type at 17.3 mL.

III.B.2.1.4 DYNLL1 does not form a heterotrimeric complex with gephyrin and the dynein intermediate chain

While the inter-trimer dimerization hub theory obviously did not apply to gephyrin, the remaining hypothesis – namely that of the DYNLL-cargo adaptor – was tested. In agreement with a valid cargo adaptor hypothesis DYNLL1 was supposed to simultaneously bind to gephyrin and the dynein intermediate chain (DIC). For this purpose, the DYNLL binding motif of rat DIC1 (DB_{DIC1}) was fused to the maltose binding protein. Between MBP and the DB_{DIC1} a 28-residue linker was introduced to avoid potential sterical hindrance. This protein (referred to as MBP-DIC) could be easily purified using nickel affinity chromatography and SEC and was used for aSEC and native gel experiments with the gephyrin-DYNLL1 complex. The detection of a ternary complex would validate the DYNLL-cargo adaptor hypothesis but would also require a vacant DYNLL1 binding site prior to DIC binding, which was not expected assuming that the GephWT-DYNLL1 stoichiometry of 3:2 obtained so far had been correct.

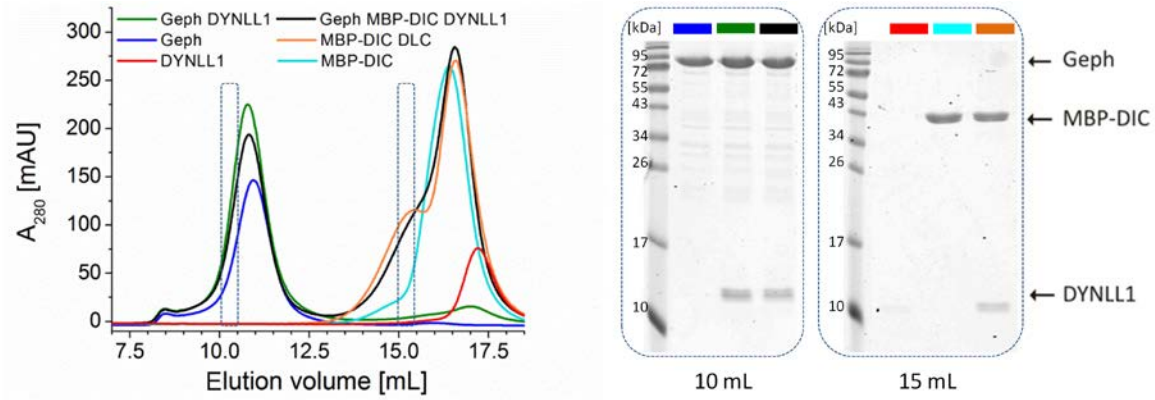

Figure 63 The DYNLL1 binding motif of the dynein intermediate chain did not bind stably to the preformed gephyrin-DYNLL1 complex. (A) As expected, both MBP-DIC and gephyrin formed complexes with DYNLL1, as suggested by the shifts of the corresponding peaks to a higher elution volume. Mixtures contained equimolar concentrations of the (putative) binding partners (8 nmol). Note that the chromatograms of the experiments with GephWT, DYNLL1 and the GephWT-DYNLL1 complex were already displayed in Fig. 62B. (B) SDS-PAGE gel excerpts displaying the fractions in (A), which were labeled with rectangular boxes, confirmed that MBP-DIC was absent from the fraction containing gephyrin and DYNLL1 (marked in black).

In aSEC experiments the expected binary complexes formed, gephyrin-DYNLL1 and MBP-DIC-DYNLL1, as indicated by shifts in the chromatogram of the complex runs in comparison to the single runs (Fig. 63A) while SDS-PAGE gels confirmed the existence of the binary complexes (Fig. 63B). However, ternary complex formation could not be observed: DYNLL1 did not recruit MBP-DIC to gephyrin – at least not in amounts that would have been detectable on an SDS-PAGE gel (left excerpt of Fig. 63B). Native PAGE gels did not reveal ternary complex formation either (data not shown). These results did not only imply that DYNLL in the case of gephyrin does not act as a stable cargo

adaptor, they also support the MALS-derived stoichiometry, according to which a single DYNLL1 dimer bound to gephyrin.

III.B.2.2 Searching for explanations of the gephyrin-DYNLL1 stoichiometry

Given that the formation of a gephyrin$_3$-DYNLL$_2$ complex but not of stable higher oligomers was observed, it seemed plausible to assume that the bound DYNLL1 dimer was captured by two Geph$_{DB}$ motifs, whereas the remaining Geph$_{DB}$ motif did not bind to DYNLL1. This could be explained as follows: In principle all three Geph$_{DB}$ motifs had the same (low) affinity, but the capture of a DYNLL1 dimer by two Geph$_{DB}$ motifs was avidity-mediated. For the remaining Geph$_{DB}$ there was no opportunity to overcome the low affinity by avidity. This inevitably led to the question about the nature of this barrier. Two hypotheses were investigated, which do not necessarily exclude each other:

- First, the third Geph$_{DB}$ motif forms an intramolecular complex with the rest of the molecule.
- Second, the accessibility of the Geph$_{DB}$ motif to DYNLL1 is significantly reduced.

III.B.2.2.1 The attenuated availability of Geph$_{DB}$ in the context of the full-length protein depends in large parts on the first 220 residues

To figure out, whether the C-terminal part of the linker and/or GephE are involved in the apparent "shutdown" of the third DYNLL binding site, DYNLL1 binding to the truncated variant GephGL220 (section II.A.2.7.2) was analysed by aSEC(-MALS) and ITC. This variant contains residues 1-220 and hence lacks GephE and the linker past the poly-glutamate rich region (section II.A.2.7.2, Fig. 40).

	GephGL220	Geph$_{DB}$	GephWT
n	0.65 ± 0.1	1.27 ± 0.07	0.99 ± 0.07
K_D [µM]	1.0±0.2	3.3 ± 1.1	2.3 ± 0.9
ΔH [kJ/mol]	-56.6 ± 4.5	-30.1 ± 2.9	-54.4 ± 3.0
-TΔS [kJ/mol]	16.6 ± 3.4	-2.6 ± 2.7	20.8 ± 2.6

Table 38 Binding parameters of the GephGL220-DYNLL1 complex in comparison with those of full-length gephyrin.

ITC experiments revealed a slightly smaller unfavourable entropic term than that observed for the full-length gephyrin-DYNLL1 complex, which resulted in a twofold reduced apparent dissociation constant (Table 38), accounting for a rather small contribution of residues beyond position 220 in the "shutdown" of the third Geph$_{DB}$ motif. In addition, the apparent stoichiometry of the GephGL220-DYNLL1 complex was significantly reduced in comparison to the GephWT-DYNLL1 complex (0.65 vs. 1). The ITC-derived stoichiometry of the GephGL220-DYNLL1 complex would account for one DYNLL1 dimer binding to one GephGL220 trimer.

Pursuing the differing ITC-derived stoichiometries of the GephWT-DYNLL1 and GephGL220-DYNLL1 complexes (Table 38), a further characterization of the GL220-DYNLL1 complex was carried out by means of SEC-MALS experiments. In the first experiment (Fig. 64) concentrations were similar to those used for GephWT-DYNLL1 (Fig. 61C). The resulting molecular masses of 101 kDa (GephGL220-DYNLL1) and 77 kDa (GephGL220) and the resulting mass increase of GephGL220 by 24 kDa in the presence of DYNLL1 were in good agreement with a single DYNLL1 dimer (expected molecular mass of 25.4 kDa) binding to a GephGL220 trimer (expected molecular mass of 79.4 kDa). Another experiment, in which the amount of DYNLL1 was increased to 74 nmol, neither resulted in a more significant GephGL220 peak shift nor in a mass increase (data not shown), hence arguing against significantly different stoichiometries between the GephGL220-DYNLL1 and GephWT-DYNLL1 complexes. This implied that – under the conditions given – DYNLL1 could not bridge different GephGL220 trimers, like it could not bridge GephWT trimers. It should be noted that the mass distributions of GephGL220 (black in Fig. 64) and especially the complex sample (red in Fig. 64) displayed a decline with increasing elution volume, which was not observed for the GephWT-DYNLL1 complex before. Repetitions of DYNLL1 binding experiments with GephWT and GephGL220 are required to evaluate this feature.

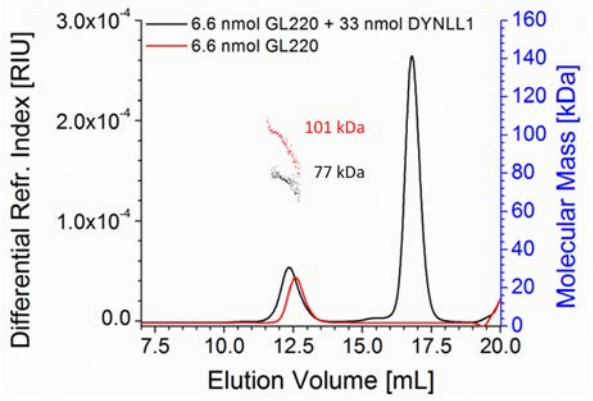

Figure 64 SEC-MALS experiments revealed a mass increase of GephGL220 by 24 kDa upon DYNLL1 binding. The experiment was conducted with a Superdex 200 10/300 GL column equilibrated in SEC-1 buffer.

Considering the similar DYNLL1 binding modes of GephWT and GephGL220, a crystal structure of the GephGL220-DYNLL1 could have provided a good model to study the basis for the stoichiometry, also in the context of the full-length protein. Cocrystallization trials with the GephGL220-DYNLL1 complex in a 96-well-plate resulted in hexagonally shaped crystals with a size of ~20 µm (Fig. 65), which were obtained after four weeks by hanging drop crystallization at 20 °C in 20% PEG3350 and 200 mM magnesium formate at a total protein concentration of 6.2 mg/mL (molar GephGL220/DYNLL1 ratio: 1:2). These crystals could not be reproduced in a follow-up screen in the 24-well format. However, data could be collected for one of the 20 µm crystals. Unfortunately, molecular replacement carried out with GephG (PDB entry 1JLJ) revealed that only GephG had crystallized: Only for segments of this protein a well-defined electron

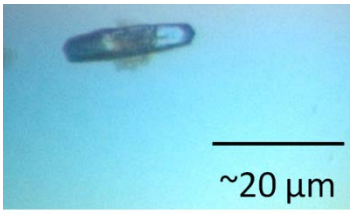

Figure 65 Side view of a crystal obtained after GephGL220-DYNLL1 cocrystallization attempts.

Data collection		Refinement	
Wavelength (Å)	0.91841	No. of molecules/ASU	6
Space group	P 1	Programme	REFMAC
a, b, c (Å)	65.9, 66.0, 77.5	Resolution (Å)	2.4-35.7
α, β, γ (°)	69.5, 71.2, 60.1	No. of reflections	36674
Resolution (Å)	2.3-71.3	R_{cryst} (R_{free})[d]	0.182 (0.238)
Unique reflections[a]	44965 [6559]	Rmsd in bond lengths (Å)	0.0153
$\langle \mathbf{I}/\boldsymbol{\sigma}(\mathbf{I}) \rangle$[a, b]	18.7 [3.0]	Rmsd in bond angles (°)	1.810
Completeness (%)[a]	97.2 [96.5]	Overall average B-factor (Å²)	19.8
Redundancy[a,]	3.9 [4.0]	Av. B-factor solvent	-
R_{merge}[a,c]	0.03 [0.35]	Ramachandran stat.[e] (%)	96.6/3.3/0.1

Table 39 Statistics on the GephG dataset obtained after cocrystallization attempts with the GephGL220-DYNLL1 complex after initial refinement. [a] Numbers in square brackets refer to the respective highest resolution shell in the data set. [b] $\langle I/\sigma(I) \rangle$ stands for the ratio of average intensity and the corresponding standard deviation [c] $R_{merge} = \sum_{hkl} \sum_{i=1} |I_i - \langle I \rangle| / \sum_{hkl} \sum_{i=1} I_i$ [d] $R_{cryst} = \sum_{hkl} ||F_0| - |F_c|| / \sum_{hkl} |F_0|$, R_{free}, same as R_{cryst} for 5% of the data randomly discarded from the refinement (see also II.B.7.1.6) [e] Ramachandran statistics yielded the fraction of residues in the favored, allowed, and disallowed regions of the Ramachandran diagram as defined by RAMPAGE. ASU is the abbreviation for asymmetric unit.

density could be observed, while there was no unaccounted electron density corresponding to even a single DYNLL1 monomer.

GephGL220 offered - due to higher protein yields and due to its high solubility - the additional advantage to explore whether higher concentrations could “mobilize” the “lonely” third linker of GL220 to undergo complex formation with DYNLL1. In fact, higher concentrations induced the

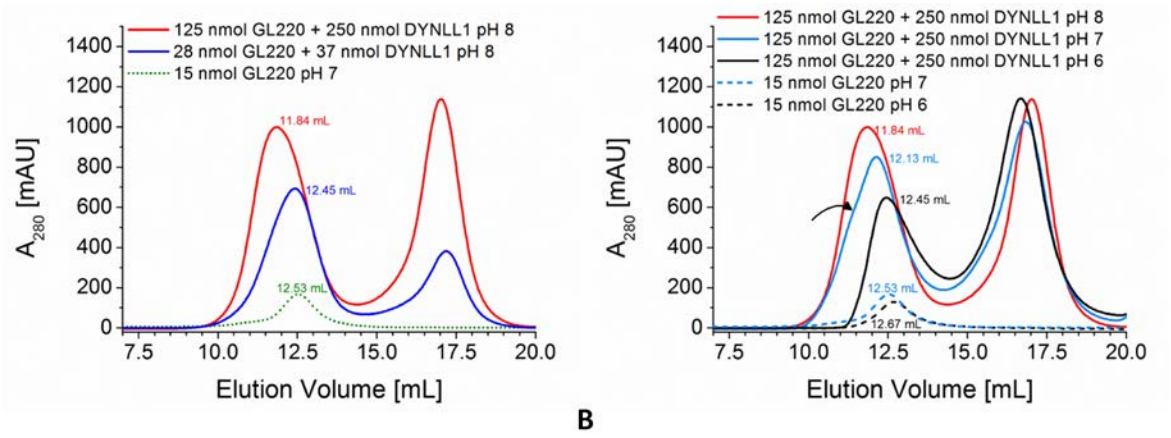

Figure 66 Concentration dependence of GephGL220-DYNLL1 complexes. For both sets of experiments a Superdex 200 10/300GL column was equilibrated in SEC-1 buffer. (A) Higher concentrations of both components led to a more pronounced left-shift of the GL220-DYNLL1 peak. (B) Higher pH values (at least in the tested range) were preferable for the formation of the higher order complex. The pH had no significant influence on the elution volume of apo-GephGL220, as it eluted at ~12.5 mL at pH 8 (see for example Fig. 64). The black arrow pointing to the blue curve indicates a shoulder.

formation of a species with a higher hydrodynamic radius. While a fourfold higher GephGL220 concentration (compared to the MALS experiments) resulted in a mild retention time shift of 0.1-0.2 mL, a more pronounced shift of ~0.6 mL could be observed when the GephGL220 concentration was 18-fold higher than in the MALS experiment (Fig. 66A). In addition, complex formation was pH dependent (Fig. 66B). The most pronounced peak shift was observed at pH 8, followed by pH 7 and pH 6. In line with that, the reversed order applied to the A_{280} between the complex and the DYNLL1 peaks (at an elution volume of ~14 mL) where complex dissociation became apparent (Fig. 66B).

III.B.2.2.2 Assessing potential steric hindrance of $Geph_{DB}$ by GephL

The fact that the impairment of the third DYNLL binding site in gephyrin compared to the two higher affinity binding sites was mediated by segments present within the first 220 residues implied that potential disturbing sterical hindrance(s) or interactions must have taken place either via GephG or the N-terminal linker segment. The latter hypothesis is the subject of this section, while the first possibility is presented in the next section.

If factors hampering the Geph-DYNLL interaction were independent of GephG, they could reside within the linker, more exactly within the segment containing residues 182-220. This stretch was devoid of aromatic residues, and hence, it was fused to MBP, referred to as MBP-L220, to achieve

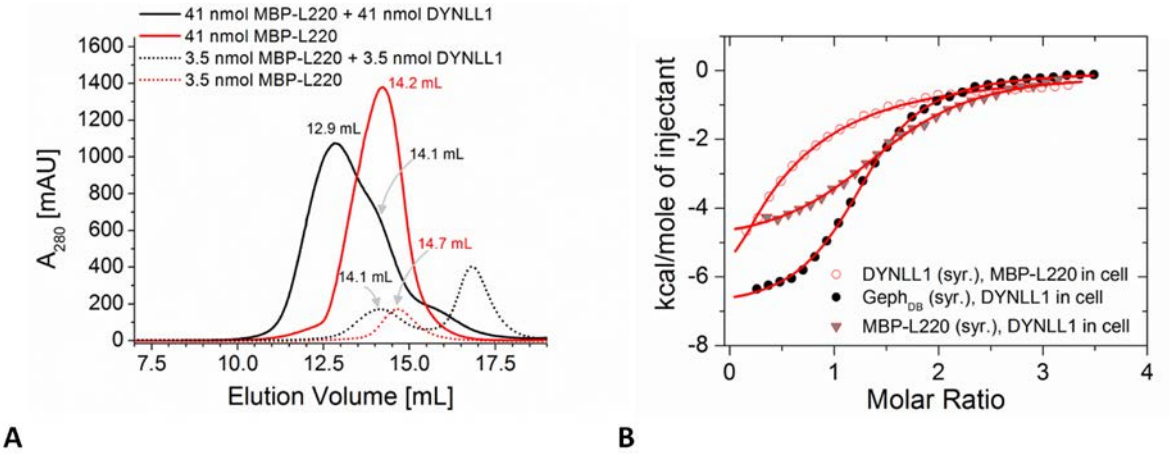

Figure 67 MBP-L220 displays a slightly attenuated affinity for DYNLL1. (A) aSEC experiments (conducted with a Superdex 200 10/300GL column, SEC-2 buffer) revealed a concentration-dependent Stokes radius increase of MBP-L220 upon DYNLL1 binding. Apo-DYNLL1 eluted at ~17 mL. The different elution volumes of 14.2 ml and 14.7 ml for MBP-L220 were presumably the result of two different columns (and/or different tubings). Nevertheless, the MBP-L220-shifts upon complex formation were valid as there was no column change for MBP-L220 samples exhibiting the same concentrations. (B) ITC experiments with the MBP-L220:DYNLL1 complex differed from the $Geph_{DB}$-DYNLL1 complex. These differences appeared more pronounced when DYNLL1 was titrated into the cell containing MBP-L220. Red lines represent the fit to the respective experimental data (circles or triangles).

reliable concentration determination via the absorbance at 280 nm (A_{280}). An impaired affinity of MBP-L220 to DYNLL1 should render this construct a prototype for the third linker in the context of the full-length protein.

In fact, aSEC experiments pointed to the possibility that the affinity of DYNLL1 to MBP-L220 was attenuated as compared to the isolated $Geph_{DB}$ motif (Fig. 67A): Similar to the GephGL220:DYNLL1 complex the degree of the peak shift was concentration dependent. Amounts of 207 nmol of both MBP-L220 and DYNLL1 resulted in a significant shift of MBP-L220 (apo-form: 14.2 mL) by 1.3 mL, in agreement with the values expected for a 2:2-complex of MBP-L220:DYNLL1 (obtained by intrapolation of a standard curve provided by the manufacturer of the column). However, the complex peak also displayed two shoulders, one of which was expected (at 16 mL), presumably representing excessive DYNLL1 that could not be stably bound. The other one at more or less the same position as that observed for apo-MBP-L220 implied that, despite high initial concentrations, complex formation was incomplete. The experiment was repeated using significantly smaller amounts of MBP-L220 (3.5 nmol) and DYNLL1 (35 nmol), to roughly imitate the conditions of the MALS experiments of GephWT-DYNLL1: Assuming a $GephWT_3DYNLL1_2$-stoichiometry in the MALS experiment 2.5 nmol free linker (7.5 nmol gephyrin - 5 nmol complex) and 25 nmol DYNLL1 (30 nmol DYNLL1 - 5 nmol complex) were available. Complex formation could be observed as indicated by the peak shift of 0.6 mL. This value was higher than the peak shift for the GephWT/GL220-DYNLL1 (0.2 mL), presumably because of the mass difference of the DYNLL1 ligands. However, a 0.6 mL peak shift was clearly less than 1.3 mL (when higher concentrations were used, Fig. 67A), pointing to an attenuated affinity of MBP-L220 towards DYNLL1.

	MBP-L220*	MBP-L220**	$Geph_{DB}$
n	0.44 ± 0.09	2.4	1.27 ± 0.07
K_D [µM]	10.9 ± 1.1	6.4	3.3 ±1.1
ΔH [kJ/mol]	-16.3 ± 1.8	-13.6	-30.1 ± 2.9
-TΔS [kJ/mol]	29.7 ± 5.9	-17.2	-2.6 ±2.7

Table 40 Preliminary ITC results suggested a slight attenuation of the DYNLL1 affinity of the $Geph_{DB}$ motif when embedded in the first "quarter" of the linker as in the MBP-L220 fusion protein. "*" and "**" indicate the reversal of ligand and cell content. Different binding parameters were observed. *The parameters were derived from two measurements using DYNLL1 as titrant (black circles in Fig. 67B). **The corresponding ITC measurement is marked with grey triangles in Fig. 67B (DYNLL1 in the cell).

ITC analysis of the complex revealed a slightly attenuated affinity of MBP-L220 to DYNLL1 as indicated by the average K_D of 9.4 µM (Table 40). Further experiments might be required, since K_D values varied between 6.7 µM and 12.8 µM, depending on whether DYNLL1 or MBP-L220 was injected (Fig. 67B). Nevertheless, the data point to a 2 to 3-fold increase in the K_D, which suggested

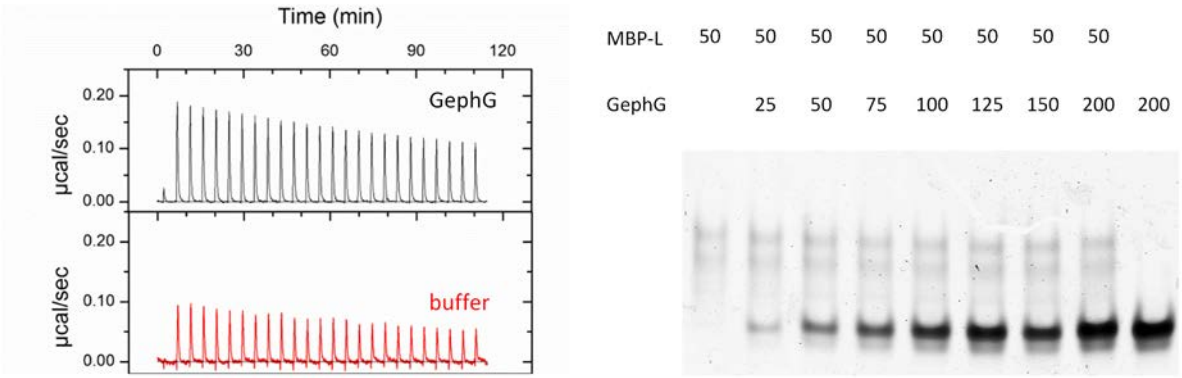

Figure 68 Neither $Geph_{DB}$ nor MBP-L formed a stable complex with GephG. (A) ITC raw data of $Geph_{DB}$ titrations into buffer (red) and GephG (black). Since the $Geph_{DB}$-buffer titration was conducted at lower concentrations, the signals were therefore multiplied by the ratio of the concentrations. (B) Native PAGE experiments did not yield evidence for a GephG-MBP(L) complex despite GephG concentrations of up to 200 µM.

that factors other than the linker are also involved in attenuating the affinity of the third $Geph_{DB}$ within a gephyrin trimer.

III.B.2.2.3 Assessing potential interactions between $Geph_{DB}$ and GephG

To assess whether direct interactions between GephG and $Geph_{DB}$ attenuated the affinity of monomeric $Geph_{DB}$ to DYNLL1 in the context of full-length gephyrin, an ITC experiment was conducted in which $Geph_{DB}$ was titrated to GephG. The heat signature differed from that of the control experiment in which only $Geph_{DB}$ was titrated into buffer, however, the integrated heats were rather reminiscent of straight lines in both experiments, suggesting that there was either no interaction or that the concentrations of 50 µM (GephG in the cell) and 800 µM ($Geph_{DB}$ as a titrant) were not high enough to yield an informative binding isotherm (Fig. 68A).

To assess whether segments surrounding $Geph_{DB}$ bind to GephG and hence induced a sterical hindrance of $Geph_{DB}$, binding experiments with GephG and MBP-L by means of native PAGE were conducted. These experiments did not yield positive results either (Fig. 68B). Thus, the identification of potential interactions between GephG and $Geph_{DB}$ was not straightforward, when both components were present in their isolated form.

III.B.2.2.4 The replacement of the $Geph_{DB}$ motif by a high affinity binding epitope induces higher oligomeric states

Recently, a phage display study was conducted with the goal of directed evolution of the DYNLL binding peptides (Rapali *et al.*, 2011a). The outcome of this study was a high-affinity binding peptide

with the sequence VSRGTQTE which exactly matches residues 82 to 89 of the *Homo sapiens* echinoderm microtubule associated protein like 3 (EML3) isoform X4. The K_D of recombinant EML3 (res. 8-94) was 50 nM, while the K_D of the isolated (acetylated) octapeptide was measured to be 80 nM. Replacement of the central 8 residues of the $Geph_{DB}$ motif by the EML3 motif was therefore expected to stabilize the gephyrin-DYNLL1 interaction and hence potentially also lead to gephyrin-DYNLL1 complexes with a higher oligomeric nature.

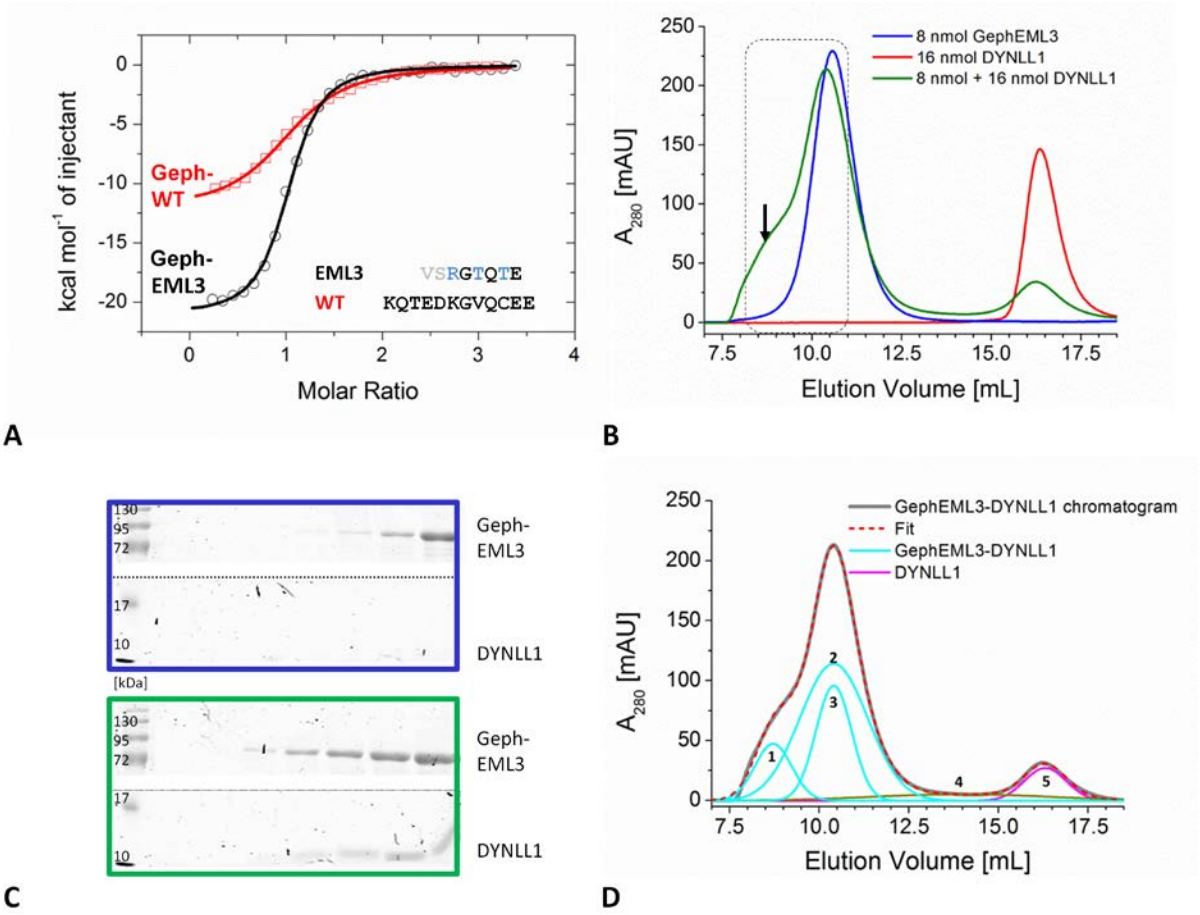

Figure 69 GephEML3 trimers have a higher tendency to be linked by DYNLL1. (A) A gephyrin variant in which the original DB motif was replaced by the high affinity binding motif of the EML3 protein (abbreviated here as EML3) displayed a higher affinity for DYNLL1 than the wildtype protein (Table 41), as can also be deduced from the steeper rise of the GephEML3-DYNLL1 isotherm. The cell contained 11 µM GephWT, the syringe 161 µM DYNLL1. (B) & (C) The higher affinity demonstrated in (A) is presumably the reason why at least to some extent higher gephyrin oligomers were induced (black arrow pointing to the green curve). (D) The chromatogram of the complex could be deconvoluted into five Gaussian peaks.

ITC experiments revealed a 10 to 20-fold lower K_D of ~200 nM for the GephEML-DYNLL1 complex as compared to GephWT-DYNLL1. This was predominantly the result of a more negative ΔH term which even compensated the more positive entropy term (Table 41). The apparent stoichiometry was 1:1 as for the wildtype which is consistent with the same stoichiometry for both protein complexes.

	GephEML3	GephWT
n	0.97 ± 0.03	0.99 ± 0.07
K_D [µM]	0.20 ± 0.08	2.3 ± 0.9
ΔH [kJ/mol]	-85.8 ± 0.7	-54.4 ± 3.0
-TΔS [kJ/mol]	45.8 ± 1.7	20.8 ± 2.6

Table 41 ITC data analysis revealed that GephEML3 exhibited a tenfold higher affinity towards DYNLL when compared to GephWT. Enthalpic effects could compensate the more positive entropy term. The experiments were conducted under the same conditions as all other experiments presented in this chapter.

To analyse the possibility that the observed higher affinity transformed the Geph-EML3 chimera into a protein with an increased tendency to form higher oligomers in the presence of DYNLL1 aSEC experiments were conducted - with $Geph_{EML3}$ chimera in the presence and the absence of a twofold excess of DYNLL1. In the presence of DYNLL1 a pronounced shoulder towards smaller elution volumes in the complex run did indeed indicate the formation of higher oligomers (Figs. 69B & C) which could not be detected with certainty for gephyrin-DYNLL1 at even higher concentrations (Fig. 61A). A peak deconvolution was conducted to exclude that the shoulder was primarily caused by the formation of aggregates. Using five peaks, three peaks with a higher hydrodynamic radius (R_H) than that of apo-GephEML3 (denoted as GephEML3-DYNLL1) were obtained, one peak located at the R_H of apo-DYNLL and another one in between (potentially DYNLL1 dissociating from GephEML3). Although the first peak obtained by deconvolution (presumably indicating the higher oligomeric fraction) could principally represent the sum of the higher oligomer and aggregates, it was not expected that potential aggregates were the only explanation. To obtain a rough measure to what extent the putative higher oligomeric fraction contributed to the sample composition, the absorbance recordings of the three putative Geph-EML3-DYNLL1 peaks were compared (under the simplifying assumption that the extinction coefficients for all forms of GephEML3-DYNLL1 complexes were the same). While this estimate should be taken with caution, it yielded a contribution of ~15% from the higher oligomers.

III.B.2.3 SAXS analysis of the gephyrin-DYNLL1 complex

SAXS measurements were conducted to derive information about conformational changes induced in gephyrin as a consequence of DYNLL1 binding. As presented below, data analysis met several obstacles, which prevented a detailed analysis of the conformational changes and were probably the result of the previously determined characteristics of the gephyrin-DYNLL1 complex, specifically the rather moderate to low affinity associated with the DYNLL1 binding by the third “lonely” gephyrin linker that severely affected sample homogeneity.

Problems were already encountered when the concentration dependence of the scattering data was analysed. Different datasets were recorded in 2011, 2012 and 2013. In the datasets from 2011 GephWT-DYNLL1 and apo-DYNLL1 samples displayed a considerable concentration dependence,

which is given by the slope of a linear fit through the data points of a concentration series (as in Fig. 69A). Values of 0.28 nm·mg/mL and 0.09 nm·mg/mL were obtained for the complex and DYNLL1, respectively, in contrast, this value was significantly smaller in the apo-gephyrin dataset with 0.05 nm·mg/mL. As mentioned in II.B.6.2.3, a concentration dependence is tolerable, if the R_g vs. concentration plot is linear, which allows one to extrapolate to zero concentration. On the contrary, a clearly non-linear R_g concentration dependence for data derived from a dynamic complex is

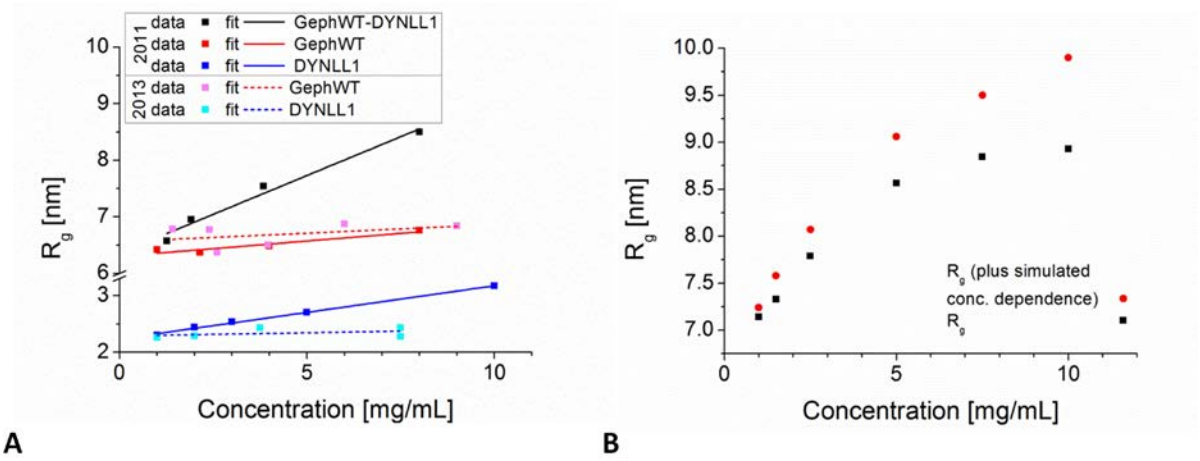

Figure 70 Interparticle effects can disturb SAXS data analysis. (A) DYNLL1 data recorded in 2011 and 2013 (2012 data not shown) displayed concentration dependencies of 0.11 and 0.09 nm·mL/mg, respectively, while data from 2013 exhibited a significantly smaller concentration dependence (0.01 to 0.03 nm·mL/mg). The concentration dependence for the complex in 2013 is shown in a separate figure (Fig. 71). (B) Simulated data for a complex exhibiting moderate affinity. At lower concentrations the complex will dissociate as suggested by the hyperbolic curve for the simulated data (black). Including a concentration dependence of 0.1 nm·mL/mg for this system, however, masks dissociation of the same complex (red). The latter concentration dependence could be misinterpreted as a linear concentration dependence, thus corresponding to stable complex, if only data in the range from 1 to 5 mg/mL had been recorded.

generally considered to be a sign of complex dissociation. Consequently, the increase in concentration dependence for GephWT-DYNLL1 complex (as compared to the single components) was interpreted as an indication of a dissociating complex. However, as shown in Fig. 69 and compounding the analysis of the GephWT-DYNLL1 complex, a considerable concentration dependence could principally mask complex dissociation, if not enough data at different dilutions were recorded and the K_D lies in the same range as the maximum concentration or slightly above.

Given the high concentration dependence for the complex sample, efforts aimed for at least a minimization of concentration dependence for the apo-components. In 2012 a change to a high salt buffer did not reduce the concentration dependence, on the contrary, the values for the apo-components were even increased (Table 42).

	2011	2012	2013
Apo-protein preparation			
DYNLL1 preparation	NiMAC – SEC	NiMAC –SEC	NiMAC – MonoS – SEC
Gephyrin preparation	No HO check	HO check	HO check
Complex formation			
Buffer	20 mM Hepes pH 8	20 mM Hepes pH 7	20 mM Hepes pH 8
	250 mM NaCl	500 mM NaCl	250 mM NaCl
	1 mM EDTA	1 mM EDTA	1 mM EDTA
	5 mM β-ME	5 mM β -ME	5 mM β -ME
Ratio DYNLL1/Geph	2:1	3:1	4:1
T(SEC) [°C]	4°C	RT	4°C
SAXS measurement			
No. of dilutions	4	4	6
R_g/c(GephWT) [nm·mg/mL]	0.05	0.11	0.03
R_g/c(DYNLL1) [nm·mg/mL]	0.09	0.11	0.01
R_g/c(GephWT-DYNLL1) [nm·mg/mL]	0.27	0.28	n.d.

Table 42 Concentration dependence of different SAXS datasets for GephWT-DYNLL1 complexes and their preparation. HO check refers to whether native PAGE of gephyrin samples after anion exchange chromatography was conducted to rule out that higher oligomers (HO) were included in the final sample (III.A.2.2, Fig. 18C). The concentration dependence (R_g/c) of the GephWT-DYNLL1 sample in 2013 is not given, as it was clearly non-linear (see Fig. 71).

While a buffer exchange in 2012 was not successful with regard to minimization of the R_g/c ratio, further changes in 2013 were helpful for the data analysis: First, complex data were recorded at more than the usual four concentrations to achieve a better assessment of complex dissociation. Second, minimized inter-particle effects especially in DYNLL1 (Fig. 70A) reduced the concentration dependence for the complex as well. The reduced concentration dependence for DYNLL1 was presumably the result of an additional cation exchange chromatography step in the purification protocol. These measures led to a hyperbolic R_g vs. concentration relationship, which resembled a binding curve. This was illustrated by the good match between the R_g. vs. conc. plot and the saturation of the DYNLL binding sites in gephyrin – assuming, in addition to a saturated binding site involving a DYNLL1 dimer bridging two linkers of a gephyrin trimer, a single binding site scenario and a K_D of ~20 µM for the third linker interacting with a DYNLL1 dimer. As the curve form suggested, the concentration dependence was presumably not primarily caused by inter-particle effects but rather by complex dissociation: Assuming a concentration dependence of just 0.02 nm·mL/mg for the complex sample and subtracting this contribution from the experimentally derived R_g, led to a corrected R_g value of 8.75 nm at 10 mg/mL. This value was just slightly higher than the corrected R_g

value of 8.7 nm at 7.5 mg/mL, thus pointing to saturation above concentrations of 10 mg/ml. However, even in a scenario, in which a K_D value significantly smaller than 20 µM was assumed, complete saturation would not occur even at the highest concentration. Hence the concentration dependence was presumably smaller than 0.02 nm·mL/mg.

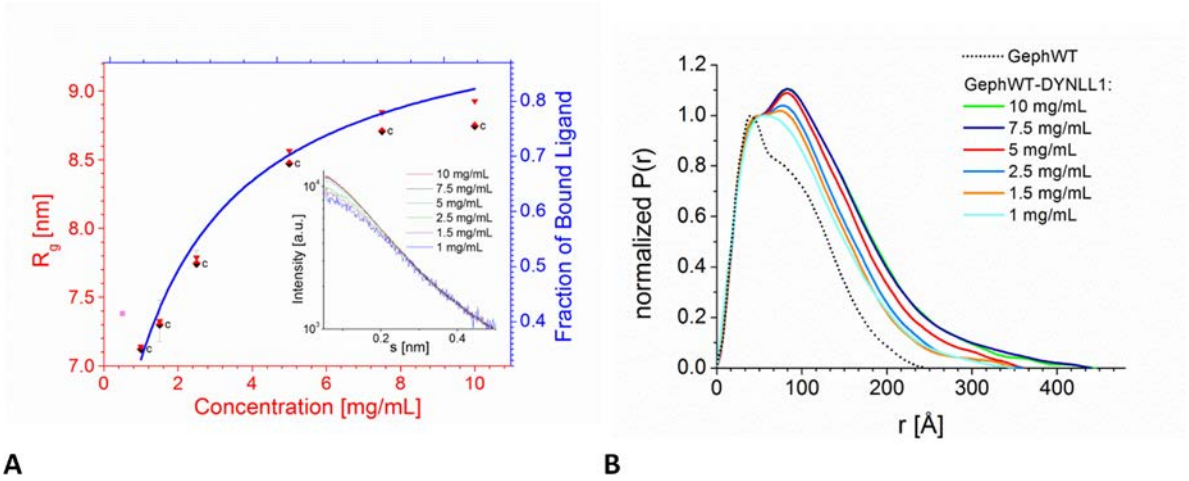

Figure 71 SAXS data of the gephyrin-DYNLL1 complex. (A) The R_g of the gephyrin-DYNLL1 samples varied with the concentration (red triangles) and was reminiscent of a binding curve assuming a 1:1 binding as described by equation 4 (see Material & Methods). Red-black squares (indicated by a "c") correspond to the same set of R_g values, which were corrected by a 0.02 nm·mL/mg concentration dependence (further details in the main text). The inset illustrates the observed concentration dependence in the small-angle region. (B) Normalized pair-distribution functions of apo-gephyrin and the gephyrin-DYNLL1 complex were consistent with a mass increase near the center of the assembly since intermediate distances were significantly increased.

In principle one could proceed with data analysis at this point, since the concentration dependence could be excluded as a significant error source. Instead of a linear extrapolation to zero concentration one could perform an extrapolation using a one site binding equation to infinitely high concentrations to derive the solution structure of a GephWT-DYNLL1 complex with a 6:6 stoichiometry (two GephWT trimers and 3 DYNLL1 dimers). However, this analysis was not pursued for the following reasons:

- This experiment would have to be repeated – maybe with even more data points at different concentrations.
- Even a small concentration dependence could change the K_D. This can be seen in Fig. 71A where a concentration dependence of just 0.02 nm·mL/mg was assumed. These modified R_g values (represented as red-black squares in Fig. 71A) reached the saturation earlier than the original R_g values (red triangles). Likewise even small measuring errors could distort the K_D analysis.
- Finally, the samples were purified by aSEC, meaning that an excess of DYNLL1 ligand was separated from the complex. This separation was performed at concentrations that might

have been even below the K_D, since the chromatograms did not argue for the majority of the GephWT-DYNLL1 complex to possess a 6:6 stoichiometry.

A hyperbolic concentration dependence was observed for the Porod volumes as well (data not shown) and concentration effects were also observed for the normalized P(r) functions of the GephWT-DYNLL1 complex. While gephyrin on its own exhibited a single maximum at 35 Å in the P(r) function with a shoulder at 70 Å (in good agreement with the apo-gephyrin preparation shown in section III.A.2.5.1), a second maximum emerged in the presence of DYNLL1, which was shifted towards 100 Å and became more pronounced at higher concentrations (Fig. 71B).

III.B.3. Discussion

Gephyrin is an unusual DYNLL binding partner in that it is trimeric and in this sense – at least to the best of my knowledge – unique among the plethora of more than 40 DYNLL interaction partners (Barbar & Nyarko, 2014, Rapali *et al.*, 2011b). This uncommon complex between a trimeric and a dimeric protein might give rise to large oligomers, e.g. if DYNLL was an adequate dimerization substitute for GephE being not in a dimeric state in full-length gephyrin. As structural and binding analyses were already available (Lee, 2009), the central issue of this analysis was the determination of the gephyrin-DYNLL1 stoichiometry, which could be connected to the issue whether DYNLL acts as a cargo adaptor as initially proposed (Maas *et al.*, 2006) or whether it functions as a dimerization hub (Barbar, 2008). The latter hypothesis received a lot of support – amongst others by the observation that DIC and putative cargoes (including gephyrin) would compete for a common binding site in DYNLL (Nyarko & Barbar, 2011, Williams *et al.*, 2007). The clarification of the stoichiometry of the gephyrin-DYNLL and gephyrin-DYNLL-DIC complexes was therefore expected to shed light on the (still elusive) mechanism which drives gephyrin coupling to the dynein motor.

III.B.3.1 The gephyrin-DYNLL stoichiometry

It could be shown previously that the dissociation constant for the gephyrin-DYNLL1 complex was in the low micromolar range (Lee, 2009), which facilitated the following analysis. At first glance the affinity of DYNLL1 to both the isolated peptide containing the sole $Geph_{DB}$ motif or the full-length protein was comparable (Lee, 2009). However, during this work it turned out that a single $Geph_{DB}$ motif in the context of the full-length protein exhibited an attenuated affinity (Figs. 61A, 61C, 64 & 66).

One of the first issues was to determine whether the oligomeric states of gephyrin and DYNLL1 changed upon complex formation. As pointed out above, DYNLL1 could have acted as a dimerization hub for gephyrin, inducing the formation of hexamers or even higher oligomers. However, aSEC experiments (at least at first glance) argued against an alteration of gephyrin's trimeric state in the complex with DYNLL1 under the tested conditions, although one cannot completely rule out that higher oligomers also formed (Fig. 61B). These experiments did – due to the huge differences in molecular mass – not allow for similar conclusions for DYNLL1, hence, complex formation with DYNLL1(S88E) was analysed. This variant was previously shown to be primarily monomeric (Benison *et al.*, 2009), and my own SEC-MALS experiments were in line with these former results (data not shown). Complex formation of gephyrin with DYNLL1(S88E) was observed in aSEC experiments, but was not as pronounced as for the wild-type protein, as deduced from the corresponding chromatograms (Fig. 62). Although ITC data on the Geph-DYNLL1(S88E) complex are still missing, the results obtained so far suggested that DYNLL1 monomer binding was weaker than DYNLL1 dimer

binding, breaking the question after the stoichiometry down to how many DYNLL1 dimers bound per gephyrin trimer.

SEC-MALS experiments with full-length gephyrin and DYNLL1 were conducted to find an answer to this question. At the concentrations used in these experiments gephyrin experienced a mass increase by 26 kDa, consistent with one DYNLL1 dimer (expected mass: 25 kDa) binding to gephyrin. As the refractive index was constant during gephyrin elution it was concluded that the complex was rather stable and that DYNLL1 did not induce higher oligomers of gephyrin (in line with previous SEC experiments (Lee, 2009)). In agreement with a gephyrin$_3$-DYNLL1$_2$ complex MBP-DIC could bind to isolated DYNLL1 but not to DYNLL1 in complex with gephyrin (Fig. 63). These results suggested that a single DYNLL1 dimer bound to two Geph$_{DB}$ motifs in GephWT: The binding of two or three DYNLL1 dimers per gephyrin trimer would have resulted in four or six DYNLL binding grooves, of which one or three groves should have been accessible for MBP-DIC in a potential ternary GephWT-DYNLL1- MBP-DIC complex. Likewise, our collaboration partners did not obtain a ternary gephyrin-DYNLL1- MBP-DIC complex in GST pulldown experiments using DICs as bait protein as well (Schwiese, 2011). This is in line with the hypothesis that cargo loading is not mediated by simultaneous binding of DYNLL to gephyrin and the intermediate chain of the dynein motor (Barbar, 2008, Williams *et al.*, 2007).

III.B.3.2 Possible reasons for the attenuated affinity of the Geph$_{DB}$ in the context of full-length gephyrin

The fundamental questions that aroused from these experiments was: Why did a single DYNLL1 dimer bind to presumably two out of three gephyrin linkers and left the third binding site unoccupied? What affected the affinity of Geph$_{DB}$ in the context of gephyrin?

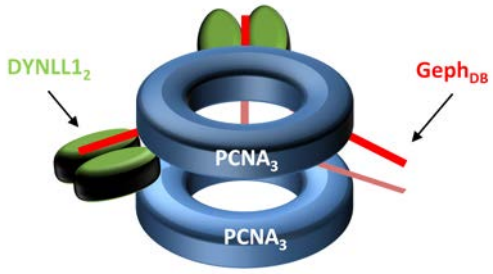

Figure 72 DYNLL1 dimers (DYNLL1$_2$) can theoretically induce a sandwich-like assembly with two PCNA(DB) trimers via Geph$_{DB}$. Two Geph$_{DB}$ sites are unoccupied for clarity. Upon binding of the first DYNLL1$_2$, the number of binding sites, which could make use of avidity effects, is increased, and therefore the sandwich assembly is expected to predominate.

Principally, trimers containing Geph$_{DB}$ can be bridged by DYNLL1 dimers, as demonstrated by SEC-MALS experiments with mixtures of DYNLL1 and PCNA(DB), a fusion protein with the trimeric PCNA core and the C-terminally appended Geph$_{DB}$ motif. DYNLL1 clearly induced the formation of higher oligomers since the mass of PCNA increased from 96 to 216 kDa (Fig. 61D), consistent with a single DYNLL1 dimer bridging the C-termini of two PCNA trimers. This would imply four unoccupied Geph$_{DB}$ motifs per complex, which could in an occupied state principally give rise to higher oligomers or – due to avidity effects

(and the absence of species with masses higher than 300 kDa) even more probable – two PCNA(DB) trimers bridged by thre DYNLL1 dimers (Fig. 72). The reason for the unexpected stoichiometry of one DYNLL1 dimer per two PCNA trimers was unclear. Even if degradation of PCNA(DB) affected the analysis, a scenario in which virtually every PCNA trimer lost two $Geph_{DB}$ motifs appears rather implausible. Hence steric hindrances could serve as an explanation, but also imprecision in mass determination should also be considered. However, the more important information from this experiment was that the affinity of the $Geph_{DB}$-DYNLL1 complex was sufficient to crosslink trimers under the tested conditions, as only a minor fraction of PCNA(DB) did not bind to DYNLL1, which could be due either to the intermediate affinity or due to C-terminal degradation of PCNA(DB).

Hence, gephyrin-specific factors obviously impeded the induction of higher oligomers by DYNLL1, and it turned out that these factors are by and large located within the first 220 residues of gephyrin, encompassing GephG and the first 39 residues of the linker (Fig. 40): The GephGL220 variant exhibited a just slightly higher affinity than full-length gephyrin (apparent K_D of 1 µM instead of 2 µM), and MALS experiments conducted at concentrations comparable to those in the analogous experiments with the full-length protein pointed to a $GephGL220_3$-$DYNLL1_2$ complex (Fig. 64). Surprisingly there was a pronounced concentration dependence of the peak position for the GephGL220-DYNLL1 complex (Fig. 66): At GephGL220 concentrations of ~10 µM and ~50 µM (as determined during the passage in the UV detector) GephGL220 peak shifts of 0.1 and 0.6 mL were observed, respectively, meaning that even a 50-fold higher concentration than the apparent K_D was not sufficient to completely shift the GephGL220 peak (Fig.66).

Taken together, these results suggested that in principle all 3 linkers possessed the same weak affinity, but two linkers could make use of avidity effects to overcome the weak affinity (Fig. 73). This is comparable to a case described in the literature (Radnai *et al.*, 2010): Here DYNLL2 bound with an intermediate affinity to monomeric MyoV (8.8 µM), and avidity effects elevated the affinity by a factor of 200 when *dimerized* MyoV bound to DYNLL2. A similar principle could apply to gephyrin: Monomeric $Geph_{DB}$ in the context of a GephWT monomer displays a weak DYNLL affinity, however, in the context of the GephWT trimer two $Geph_{DB}$ motifs might cooperate to sequester a single DYNLL dimer, while the remaining $Geph_{DB}$ motif is restricted to the originally low affinity as it lacks an intra-assembly "cooperation partner" which would be required for DYNLL binding.

Interestingly, a buffer change resulted in a better stability of the GephGL220-DYNLL1 complex. The pH of the SEC-1 buffer (section II.A.7.1.8) was reduced from 8 to 7, and the salt concentration was increased to 500 mM. Now even at final concentrations of ~30 µM a peak shift of 1.1 mL was observed (data not shown). Therefore one should consider aSEC experiments with full-length gephyrin in this buffer, which might reveal convincingly higher GephWT oligomers in the presence of DYNLL1. This was tried once but failed due to gephyrin-DYNLL1 aggregation already in the reaction

tube (so before aSEC), obviously due to the addition of highly concentrated Hepes buffer at pH 7. Buffer exchange for both proteins before mixing them might help to circumvent aggregation.

The degree of attenuated DYNLL1 affinity of gephyrin in comparison to isolated DYNLL binding motifs was strikingly exemplified by the analysis of the GephEML3 chimera (Fig. 69), in which the original $Geph_{DB}$ motif in full-length gephyrin was replaced by the high affinity DYNLL1 binding motif derived from EML3 (Rapali *et al.*, 2011a). Indeed, this substitution resulted in a higher affinity to DYNLL1, yielding an apparent K_D of 0.2 µM in ITC experiments. However, even this enhanced affinity

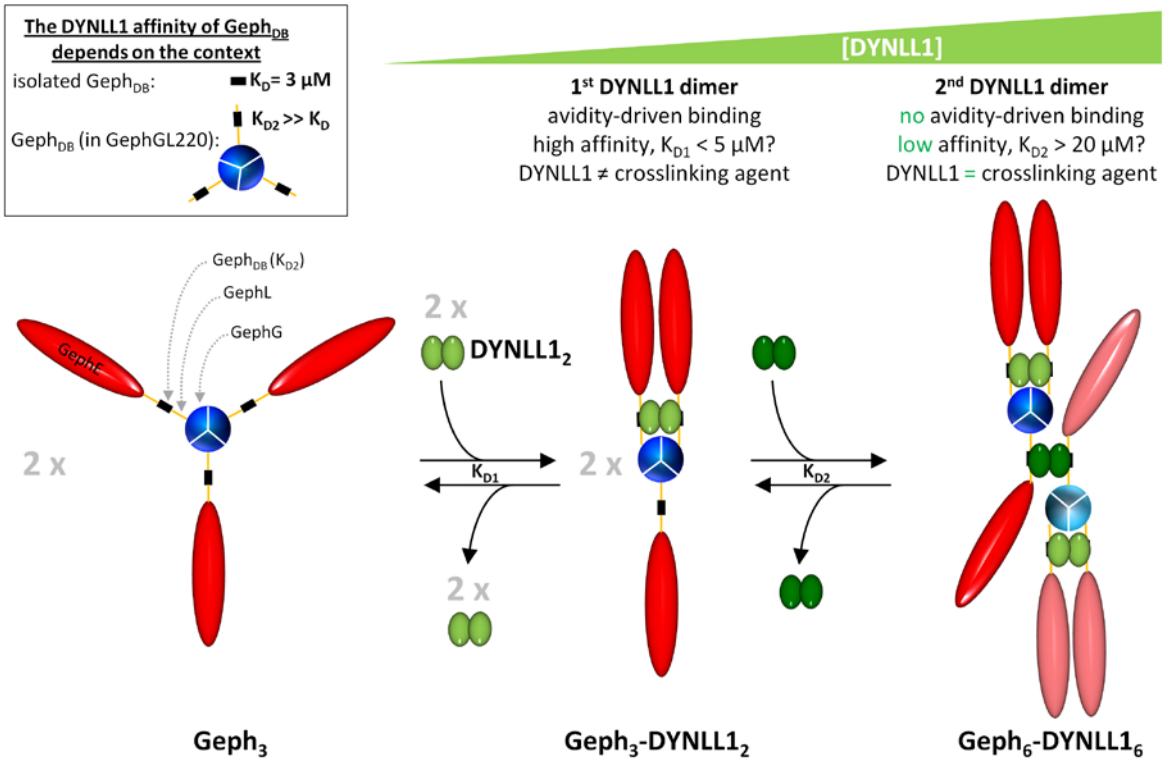

Figure 73 DYNLL1 binds to gephyrin in two steps. As pointed out in the inset in the upper left corner, isolated $Geph_{DB}$ binds DYNLL1 with a significantly higher affinity than in the context of GephGL220 (and GephWT). Avidity effects help to overcome the weak affinity in the first step (resulting in a K_{D1}<<K_{D2}), when just one DYNLL1 dimer (light green) binds to gephyrin ($Geph_3$). The third $Geph_{DB}$ is not occupied at low DYNLL1 concentrations due to the lack of avidity effects. Hence, the third $Geph_{DB}$ motif exhibits a clearly lower affinity (K_{D2}) for the second DYNLL1 dimer bound to the assembly (dark green). The fourth, unoccupied DYNLL binding groove can bind to another gephyrin trimer which is present in the same configuration. Grey numbers indicate the number of equivalents, if different from one. It is unclear whether DYNLL binding results in enhanced GephE-GephE interactions in the $Geph_3$-$DYNLL1_2$ and the $Geph_6$-$DYNLL1_6$ configurations.

was not adequate to recruit the majority of Geph-EML3 chimeras to higher oligomers, as judged by aSEC experiments. Curve deconvolution algorithms yielded a percentage of higher oligomeric gephyrin of only 15%, which is well below a predicted percentage of 88% under the assumption of a 1:1 binding model along with final protein concentrations of ~3 µM and the K_D of the isolated EML3-derived peptide of 80 nM (Rapali *et al.*, 2011a). As a matter of fact curve deconvolution is error-prone and the obtained value should be taken with caution. But even a more conservative higher

oligomer estimate of 33% yielded a K_D of 4 µM for the DYNLL1 affinity to the third $EML3_{DB}$ motif, consistent with a 50-fold reduction in affinity when compared to the isolated peptide. More reliable estimates for the K_D attenuation

$$\frac{K_{D2}(Geph - DYNLL1)}{K_D(Geph_{DB} - DYNLL1)} = attenuation \qquad \text{(equation 18)}$$

might be obtained by the determination of the K_D of the $EML3_{DB}$-DYNLL1 interaction and K_{D2} of the GephEML3-DYNLL1 interaction (Appendix F).

In summary, the experiments pointed to a severely impaired DYNLL1 affinity of the $Geph_{DB}$ motif in the context of the first 220 residues. Several explanations come into question (Fig. 74): (I) $Geph_{DB}$ interacts with the remaining linker. (II) Linker-linker interactions distort the $Geph_{DB}$ motif. (III) GephG and GephG interact with each other. (IV) GephG interacts with the linker surrounding GephDB, resulting in steric hindrance of $Geph_{DB}$.

To test whether the linker on its own possessed the capability to weaken $Geph_{DB}$-DYNLL1 binding (scenarios I & II), a MBP fusion protein was generated, which contained the first 39 residues of the linker (residues 182-220) and was used for DYNLL1 binding assays (Fig. 68). In aSEC experiments final MBP-L220 concentrations of 16 µM were sufficient to detect DYNLL1 induced MBP-L220 dimers, which were more prevalent in the sample than non-bound MBP-L220. For comparison, in the aSEC MBP-L220:DYNLL1 experiments 41 nmol were used, while with even higher concentrations in the gephyrin-DYNLL1 mixture (50/100 nmol, Fig. 61A) no peak shift was obtained, which convincingly accounted for the formation of higher oligomers. ITC experiments with the MBP-L220-DYNLL1 complex were consistent with aSEC experiments: The affinity of MBP-L220 was just 2 to 3-fold lower than for $Geph_{DB}$, which can certainly not account for the high degree of $Geph_{DB}$ autoinhibition (Fig. 67).

Scenario III was also tested: The affinity of the isolated $Geph_{DB}$ motif to GephG was probed by a (single) ITC experiment (Fig. 68). The resulting isotherm was a straight line despite concentrations of 50 µM in the cell and 800 µM in the syringe, arguing against a K_D in the range of 50 µM. In accordance with that, GephG-MBP-L complexes could not be detected in native PAGE experiments, although concentrations as high as 200 µM were used (Fig. 68). This did not rule out the possibility that the affinity of $Geph_{DB}$ to GephG was considerably weaker, which would also make sense: If the K_D was in the range of e.g. 50 µM, non-binding of $Geph_{DB}$ in the context of gephyrin to DYNLL1 would not be a huge surprise, as avidity effects would account for a $Geph_{DB}$ binding preference to GephG rather than to the non-covalently linked ligand DYNLL1. A repetition of the ITC experiment with a higher syringe concentration might reveal slight traces of binding, as the $Geph_{DB}$-GephG and $Geph_{DB}$-buffer titrations differed slightly (Fig. 68), but even then it would not be possible to measure the intramolecular dissociation constant.

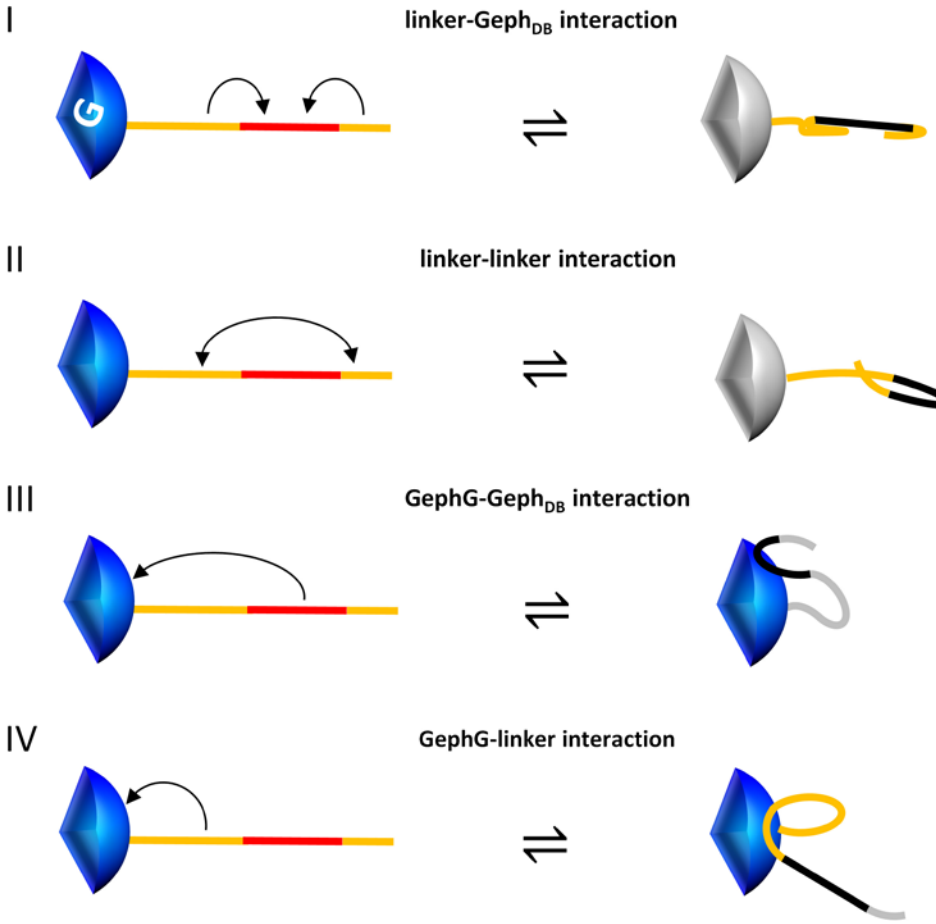

Figure 74 Potential modes of Geph$_{DB}$ autoinhibition. DYNLL1 binding-competent monomeric GephGL220 conformations are shown on the left-hand side with GephG coloured in blue, binding competent Geph$_{DB}$ in red and residual linker segments in yellow. On the right-hand side binding incompetent conformations are displayed, where autoinhibited Geph$_{DB}$ segments are coloured in black and elements not involved in the process in grey. In scenario IV an incoming DYNLL1 dimer would sterically clash with GephG.

The experiments with the GephEML3 chimera (Fig. 69) at first glance suggested that the dynein light chain binding motifs were not the primary determinant of the observed attenuated affinity, rather it seemed the context in which the DYNLL binding motifs were embedded was a critical factor, arguing for a steric hindrance, caused by GephG-linker interactions (scenario IV). Regarding this hypothesis one should also keep in mind that Geph$_{DB}$ and EML3$_{DB}$ possess relatively similar sequences (Fig. 69). Therefore the EML3$_{DB}$ motif may bind to GephG as well. Whether Geph$_{DB}$ and EML3$_{DB}$ adopt comparable conformations in the context of full-length gephyrin remained elusive so far, however, should K_D determinations for Geph$_{DB}$ and EML3$_{DB}$ be possible and yield similar results, the data would point to scenario IV (Fig. 74).

In summary, reliable estimates for the contribution of the pontentially different autoinhibition mechanisms to the attenuated Geph$_{DB}$-DYNLL1 stability in the context of full-length gephyrin, GephGL220 and GephEML3 are difficult to obtain. Nevertheless, one can conclude that an interplay between GephG and the linker renders the Geph$_{DB}$ less accessible for binding.

III.B.3.3 SAXS analysis of the gephyrin-DYNLL1 complex

Before the stoichiometry of the gephyrin-DYNLL1 complex was determined, SAXS measurements were conducted to obtain insights into the conformational changes in gephyrin that were induced by DYNLL1. However, a detailed picture could not be drawn. First, it was already demonstrated that the ensemble optimization methods (EOM) failed to detect asymmetric gephyrin conformers (Fig. 28), as they are presumably induced by DYNLL1. Second, the mass increase of 25 kDa in the 250 kDa gephyrin assembly (per bound DYNLL1 dimer) was presumably too small to derive even a rough localization of DYNLL1 in this still rather flexible assembly at the resolution of the SAXS experiment (Fig. 61). Last, there was a marked concentration dependence of the radius of gyration and the Porod volume, which clearly deviated from the typical linear relationship (Fig. 71A), and therefore presumably reflected different degrees of $Geph_{DB}$ saturation with DYNLL1. As pointed out above, at small concentrations just the first dimer bound to two linkers of a gephyrin trimer (Fig. 73). The remaining linker sites became saturated only at higher concentrations. Hence, it appears plausible that two asymmetric gephyrin trimers both provided a remaining linker for DYNLL1 that now acted as crosslinking component (Fig. 73). This would also explain the second maximum in the P(r) function which emerged with increasing concentrations of DYNLL1 (Fig. 71B). For reasons already given in the Results section (III.B.2.3), further SAXS data analysis was not pursued.

III.B.3.4 Future experiments

While the issue of the gephyrin-DYNLL1 stoichiometry appears to be clarified, a few questions have remained, which should be investigated: The differing GephGL220-DYNLL1 and GephWT-DYNLL1 ITC-derived stoichiometries of 0.66 and 1 (Table38), respectively, are likely the result of imperfect concentration determinations. Less likely, they might be a hint to indeed slightly different stoichiometries. In gephyrin variants with a higher stoichiometry (GephWT and GephEML3) there was an additional putative and so far unconfirmed DYNLL binding site ($Geph_{DB2}$). However, based on the negative results for a potential $Geph_{DB2}$-DYNLL1 complex (Fig. 60 & Lee, 2009) one could not exclude the possibility of avidity driven $Geph_{DB2}$-DYNLL1 complex formation in the context of full-length gephyrin: DYNLL1 binding to $Geph_{DB}$ might increase the local concentration of $Geph_{DB2}$ binding motifs that might then bind to DYNLL1. It might be rewarding to obtain the ITC-derived stoichiometry of the DYNLL1 binding to a full-length gephyrin variant, in which the crucial glutamine residue of $Geph_{DB2}$ is exchanged to an alanine. Such mutations in DYNLL binding motifs have been demonstrated to abrogate DYNLL binding previously (Lee, 2009, Liang *et al.*, 1999). Should this mutant display indeed a significantly smaller stoichiometry, this might point to an involvement of $Geph_{DB2}$.

Even more importantly, further studies are required to obtain reliable estimates of the K_D values for the DYNLL1 binding to the first two gephyrin linkers (K_{D1}) and to the third, “lonely” $Geph_{DB}$ motif

(K_{D2}) in the context of full-length gephyrin (see also Fig. 73), GephGL220 and GephEML3. The derived K_{D2} value compared to the K_D(Geph$_{DB}$-DYNLL1) would indicate the degree of attenuation (determined in analogy to that of GephEML3 in the previous section).

aSEC experiments with equimolar Geph-DYNLL1 mixtures at various concentrations (possibly conducted with a small SD200 5/150 column) appear to be the best choice to obtain the desired estimates for $K_{D2.}$ For this purpose, one might plot the peak shifts as a function of final gephyrin concentrations on the column to derive a binding curve. Fitting might be performed based on an equation provided in Appendix F. Alternatively, DLS experiments could be analysed in an analogous manner by plotting the hydrodynamic radius (R_H) vs. the concentration. Theoretically ITC experiments should also provide information on K_{D1} and K_{D2}, and K_{D1} may be derived if the aSEC/DLS-derived K_{D2} values are already known. The ratio of K_{D1} to K_{D2} would then give the impact of the avidity effect:

$$\frac{K_{D1}(GephWT-DYNLL1)}{K_{D2}(GephWT-DYNLL1)} = avidity \qquad \text{(equation 19)}$$

III.B.3.5 Biological implications

Although the consideration of DYNLL1 as cargo adaptor for gephyrin to the dynein motor was questioned (Barbar, 2008, Lee, 2009, Williams *et al.*, 2007), DYNLLs role in the retrograde transport of gephyrin-GlyR complexes seemed quite clear at the beginning of this project (Maas *et al.*, 2006). However, it should be mentioned that unpublished cell biological data by our collaboration partners challenged this view (Schwarz *et al.*, unpublished data). They found that a non-binder mutant, Geph(Q211A), identified by Eunyoung Lee (Lee, 2009), displayed attenuated synaptic clustering compared to GephWT. In addition overexpression of DYNLL1 in neuronal cells led to an increase in gephyrin cluster size. These and further data suggested that the gephyrin-DYNLL interaction may be involved in enhancing gephyrin clustering (Schwarz *et al.*, unpublished data), potentially utilizing the low-affinity binding of a second DYNLL as a regulatory step (Fig. 73). This hypothesis contradicts the previously published data, in which retrograde DYNLL-dependent dynein-mediated gephyrin-GlyR cotransport was observed, triggering rather synapse disassembly than formation (Maas *et al.*, 2006).

Obviously, the two point mutations in the Geph$_{DB}$ motif (used by our collaboration partner) are expected to exhibit far more specific effects than the complete excision of 63 linker residues in GephΔ(181-243), which exhibited a similar clustering tendency as the wildtype protein (Fuhrmann *et al.*, 2002). Beyond the Geph$_{DB}$ this long stretch might also harbour segments, which might be involved in the binding of (yet unknown) binding partner(s)/complex(es) which drive anterograde or retrograde transport or gephyrin clustering. For instance, the PIN1 binding motif is located close to

the DYNLL1 binding motif. The net effect of opposing driving forces might be zero, if other factors can still drive transport processes (Maas *et al.*, 2009).

In these experimental setups one should consider that there is a mixed microtubule orientation in dendrites (Baas *et al.*, 1988). Hence, the mentioned, attenutated Geph-Q211A clustering is not necessarily in contrast with Maas *et al.*, 2006. Mixed microtubule orientations would also be consistent with the finding that gephyrin clusters werethe subject of short-range transport processes, which were shown to account for the movement of small gephyrin clusters from one active synapse to the next (Maas *et al.*, 2006).

While the results of the gephyrin point mutant clustering (Schwarz et al., unpublished data) will certainly enhance our understanding of the role of DYNLL on gephyrin clustering, the previous results should not be completely questioned (Maas *et al.*, 2006): For example, the combination of time-lapse video microscopy and manipulation of transport processes were convincing (Maas *et al.*, 2006), and these approaches should also be applied in the analysis of the Geph-Q211A mutant, for which transport processes have not been addressed so far. Hence, the following analysis will focus on the gephyrin-DYNLL interaction in the context of transport processes.

What is the functional relevance of the observed gephyrin-DYNLL stoichiometry in the context of transport processes? There is no straightforward answer to this question. First the literature on the gephyrin-DYNLL interaction encompasses only three publications plus two manuscripts in preparation (Sander *et al.* & Schwarz *et al.*, manuscripts in preparation), all of which did not successfully address the mechanism of DYNLL mediated gephyrin loading to the motor. Furthermore this process has been elucidated only for a few examples (Kardon & Vale, 2009, Liu *et al.*, 2013, Vallee *et al.*, 2012). Second also the knowledge about DYNLL, microtubules and the dynein motor at inhibitory synapses is still limited. Last but not least DYNLL binds to a multitude of binding partners, which (at least theoretically) could influence gephyrin clustering as well (Rapali *et al.*, 2011b).

Nevertheless, one can combine the findings on the gephyrin-DYNLL interaction with the knowledge about the dynamics of gephyrin-receptor complexes to get at least a rough idea of the consequences of the gephyrin-DYNLL binding mode. It was shown that gephyrin-receptor interactions were not confined to synaptic sites and that extrasynaptic membrane patches serve as entry/exit sites for the transfer of receptors from the cytosol to the plasma membrane (Bogdanov *et al.*, 2006, Rosenberg *et al.*, 2001). At least for $GABA_A$ receptors endocytosis could be demonstrated to occur exclusively at extrasynaptic sites (Bogdanov *et al.*, 2006). So the extrasynaptic membrane appears to be a transhipment point. Notably, membrane associated DYNLL was observed at equal numbers at extrasynaptic and synaptic sites, and at the latter rather at the border than in the centre of synapses – at least in ventral spinal cord-derived cultures (Fuhrmann *et al.*, 2002) known to contain mixed GABAergic/glycinergic synapses (Todd *et al.*, 1996). It therefore seems plausible to

assume that DYNLL mediated gephyrin loading onto dynein takes place at the synapse border. Maybe DYNLL concentrations act as signals for synapse disassembly. Higher concentrations might lead to higher oligomeric gephyrin-DYNLL1 complexes, which would provide more dynein motor coupling sites (Fig. 75). Higher motor numbers per cargo might enhance cooperative transport (Fig. 75 & (Allan, 2011, Kural *et al.*, 2005)). Vice versa, DYNLL concentrations below a certain threshold (which would depend on K_{D1}) would lead to a less efficient transport and hence a less pronounced loss of gephyrin molecules of the respective cluster. On the other hand it should be mentioned, that several motors were not always found to enhance transport velocity (Shubeita *et al.*, 2008).

The antiparallel orientation of coupling sites A and B in Fig. 75 could principally translate into opposing migration directions of the two dynein motors, unless the latter could compensate for this by e.g. the flexible intermediate chain. Coupling site C (represented as dashed pink line) would not be complete in this orientation (Fig. 75), and linker rearrangements would be required to also complete this coupling site. A parallel arrangement of up to three dynein motors per $Geph_6$-$DYNLL_6$ assembly

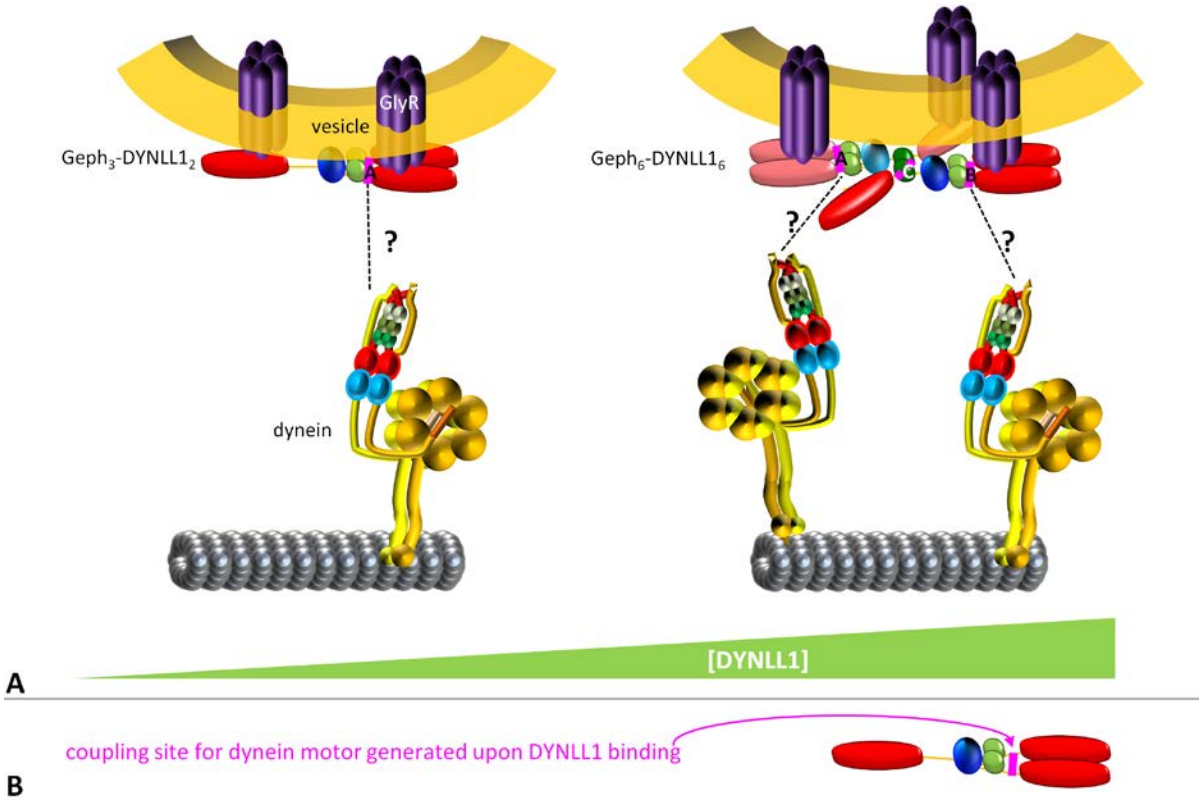

Figure 75 How different gephyrin-DYNLL1 stoichiometries could influence motor processivity and velocity. (A) At low DYNLL concentrations $Geph_3$-$DYNLL1_2$ (Fig. 73) might bind to a single dynein motor via a coupling site that was generated upon DYNLL1 binding (magenta, see also (B)). At high DYNLL concentrations two $Geph_3$-$DYNLL1_2$ complexes could assemble into $Geph_6$-$DYNLL1_6$. Two coupling sites would be provided at high DYNLL1 concentrations. Coupling site C at high concentrations would be incomplete unless conformational changes would reorient the antiparallely arranged linkers. Likewise, the orientation of two dynein motors binding to a $Geph_6$-$DYNLL1_6$ assembly might be changed by additional factors.

might be achieved in the presence of other gephyrin binding partners that modulate the conformation of the flexible gephyrin linkers.

Alternatively, if multiple motors would affect cargo movement, one might envision that high DYNLL concentrations are not desired at the transhipment points, as they could affect efficient gephyrin transport. In this scenario the "shutdown" of the third $Geph_{DB}$ within a gephyrin trimer might therefore be of advantage for transport processes. Further levels of complexity are added by the observations that dynein and kinesin motors can bind to the same cargo (Allan, 2011, Kural *et al.*, 2005) and that the corresponding microtubule tracks are the subject of posttranslational modifications which can regulate transport along microtubules (Maas *et al.*, 2009).

The coupling of gephyrin to the dynein motor is another major issue which has remained elusive so far. Obviously, simultaneous binding of DYNLL to gephyrin and the DIC appears rather unrealistic given the hints from the literature (Barbar & Nyarko, 2014, Barbar, 2008) and the aSEC and native PAGE experiments. How can this be reconciled with the findings, in which dynein-gephyrin-GlyR complexes required DYNLLs (Maas *et al.*, 2006)? It was demonstrated that DYNLL could for example trigger the formation of a coiled coil in the DIC (Benison *et al.*, 2006), and many other DYNLL binding partners contain predicted coiled coil motifs in proximity to the DYNLL binding site (Rapali *et al.*, 2011b). Indeed several examples are now known, in which DYNLL/LC8 induced the formation of coiled coils in the binding partners, such as in DIC, swallow, myosin Va and syntaphilin (Barbar & Nyarko, 2014, Benison & Barbar, 2009, Chen *et al.*, 2009, Kidane *et al.*, 2013, Wagner *et al.*, 2006). Based on several of these and other examples it was proposed that DYNLL1 mediated dimerization stabilizes a conformation that allows for the binding of the actual dynein adaptor (Rapali *et al.*, 2011b). Maybe DYNLL binding induces a gephyrin conformation that harbours a (low- to medium-affinity) recognition site for the dynein intermediate chain or dynein adaptors such as dynactin.

Puzzlingly, one group observed dynein mediated transport of fluorospheres coated with bare DYNLL binding motifs (Parassol *et al.*, 2013), ruling out the scenario of DYNLL induced conformational changes that generate a new binding site for dynein adaptors. To explain this finding the authors referred to other publications in which potential DYNLL tetramers were reported both in solution (Fan *et al.*, 2012) and even higher oligomers in a crystal (Rapali *et al.*, 2011a). However, during my studies I did not observe DYNLL tetramers in aSEC experiments despite concentrations as high as ~100 µM during elution. NMR studies conducted at even higher concentrations did not seem to reveal tetrameric species as well (Barbar *et al.*, 2001). In addition, the reported crystal structure, in which ligand EML3 β-strands of distinct dimers formed crystal contacts (PDB code 3P8M, (Rapali *et al.*, 2011a)), did not reveal a large and hence a rather labile interface of 153 Å² (for comparison the actual DYNLL-EML3 interface covered 733 Å²), as judged by PISA analysis (Krissinel & Henrick, 2007).

Taken together, more information on the role of DYNLL1/2 and the dynein motor at synapses (including the knowledge of the dynein-cargo adaptor(s)) would be required to derive more reliable conclusions on the role of gephyrin-DYNLL interactions in the context of gephyrin transport.

III.C. The gephyrin-neuroligin 2-collybistin complex

III.C.1. Introduction

As mentioned above, at a subset of GABAergic synapses receptor clustering is mediated by the gephyrin-collybistin-neuroligin 2 complex (Poulopoulos *et al.*, 2009). These three proteins were sufficient to generate postsynaptic density-like structures in non-neuronal COS7 cells (Poulopoulos *et al.*, 2009). All three proteins were shown to form binary complexes with each other (Harvey *et al.*, 2004, Kins *et al.*, 2000, Poulopoulos *et al.*, 2009). In this introduction I will provide an overview of what has been known on the interplay between the three proteins.

III.C.1.1 NL2 drives gephyrin clustering at perisomatic synapses

Neuroligin 2 is the only Neuroligin which selectively localizes to inhibitory synapses (Varoqueaux *et al.*, 2004). NL2 knock-out mice do not die shortly after birth as NL1-3 triple knock-out mice, but they exhibit pronounced anxiety-like behaviour and attenuated pain sensitivity as well as a slightly impaired motor coordination (Blundell *et al.*, 2009). In line with these findings in NL2 knock-out mice inhibitory transmission was shown to be affected specifically at perisomatic GABAergic synapses in the somatosensory cortex, more precisely by fast-spiking interneurons, (Chubykin *et al.*, 2007) and in the hippocampus (Jedlicka *et al.*, 2011) as well as in glycinergic and GABAergic synapses in the ventrolateral medulla, which is part of the brainstem and involved in the generation of the respiratory mechanism (Poulopoulos *et al.*, 2009). In hippocampal neurons affected GABAergic transmission coincided with a lack of gephyrin and $GABA_A$ receptor clusters at perisomatic synapses (Jedlicka *et al.*, 2011, Poulopoulos *et al.*, 2009), presumably due to the missing interaction between gephyrin and NL2, which was observed by means of yeast-two-hybrid studies, pulldown experiments and co-IPs in the presence of crosslinker (Poulopoulos *et al.*, 2009).

The relevance of the gephyrin-NL2 interaction was demonstrated in siRNA mediated gephyrin knock-down experiments in dissociated hippocampal neurons (Levinson *et al.*, 2010), which led to NL2 redistribution from inhibitory to excitatory synapses. Vice versa, NL1 was redistributed from excitatory to inhibitory synapses upon PSD95 knock-down. These results suggest that not only NL-Nrx interactions determine the fate of a synapse, but that also scaffolding protein-NL interactions at the post-synaptic density (Levinson *et al.*, 2010) are required for a balanced excitation/inhibition ratio (Levinson & El-Husseini, 2005). Disturbances in this ratio are e.g. considered as potential source of autism (Rubenstein & Merzenich, 2003).

In addition these results raised the possibility that gephyrin and NL2 reciprocally influence their localization. However, it seems that NL2 can localize to inhibitory synapses independent of gephyrin and $GABA_A$ receptors (O'Sullivan *et al.*, 2009, Patrizi *et al.*, 2008). And NL2 on its own is not sufficient to recruit gephyrin to membranous compartments, as coexpression of both proteins in non-neuronal

cells results in the formation of large cytosolic gephyrin aggregates (Poulopoulos, 2008, Poulopoulos *et al.*, 2009). With this experimental approach colocalization of NL2 with intracellular gephyrin "blobs" was only observed in less than 20% of the analysed cells (Poulopoulos, 2008), pointing to a weak interaction between gephyrin and NL2. Taken together these data raise the possibility that an additional factor is required for proper gephyrin localization to membranous compartments harbouring NL2. One such factor is collybistin (Poulopoulos *et al.*, 2009), which will be presented in the following section.

III.C.1.2 Collybistin

III.C.1.2.1 Collybistin's role in diseases

Without doubt, collybistin is one of the best characterized gephyrin interaction partners, whose relevance in terms of gephyrin and $GABA_A$ receptor clustering is well-documented. Not surprisingly, several mutations observed in collybistin are related to neurological disorders such as hyperekplexia, epilepsy, anxiety, aggression, insomnia, and mental retardation (Harvey *et al.*, 2004, Kalscheuer *et al.*, 2009, Shimojima *et al.*, 2011). In collybistin knock-out mice reduced gephyrin and $GABA_A$ receptor clustering resulted in reduced GABAergic transmission and altered synaptic plasticity in the amygdala and in the hippocampus, which coincided with increased anxiety levels and affected spatial learning (Papadopoulos *et al.*, 2007). In contrast to NL2 mice (Poulopoulos *et al.*, 2009) not only perisomatic but also dendritic synapses were affected (Papadopoulos *et al.*, 2007). The analysis of conditional collybistin knockout mice, in which collybistin expression was abolished at different developmental stages, revealed that collybistin is involved in the formation and maintenance of GABAergic synapses (Papadopoulos *et al.*, 2008).

III.C.1.2.2 Collybistin can form a ternary complex with gephyrin and $GABA_A$ receptors

The reduced gephyrin and $GABA_A$ receptor clustering in collybistin knockout mice can be regarded as logical consequence of interactions of collybistin with gephyrin and the $GABA_A$ receptor subunits α1, α2 and α3 (Maric, 2012, Saiepour *et al.*, 2010, Tretter *et al.*, 2008). Notably, collybistin's and gephyrin's binding sites in α2 display an overlap (Maric *et al.*, 2011, Saiepour *et al.*, 2010, Tretter *et al.*, 2008), and indeed gephyrin and collybistin theoretically compete for the same binding site in the α2 subunit of the $GABA_A$ receptor (Maric, 2012). However, *in vitro* data suggest, that the $GABA_A$ receptor subunit α2 can associate with collybistin, while the $GABA_A$ receptor subunits α1 and α3 are expected to bind to gephyrin (Maric, 2012). In the following an overview of the current view on collybistin's role in gephyrin and $GABA_A$ receptor clustering is given with a focus on the domain organization of collybistin and what is known about the functional/mechanistic consequences of this domain arrangement.

III.C.1.2.3 Collybistin's domain architecture

Collybistin belongs to the Dbl family of guanine exchange factors (GEF), and as such it possesses the Dbl family-typical domain arrangement (Zheng, 2001): A Dbl-homology domain, which mediates GDP-GTP exchange to activate the bound GTPase, followed by a Pleckstrin homology domain (Kins *et al.*, 2000), which is responsible for membrane targeting (Kalscheuer *et al.*, 2009). Four isoforms exist in mouse, and they can be distinguished by their C-terminus (CB1, 2 & 3) and the presence/absence of the SH3 domain in CB2 ($CB2_{SH3+}$ and $CB2_{SH3-}$) (Fig. 76). Of these, CB3 is the only variant expressed in human brain and spinal cord and is called hPEM-2 (Harvey *et al.*, 2004). Rodents additionally express the $CB2_{SH3+}$ variant, while expression levels for $CB2_{SH3-}$ and CB1 appear to be rather low (Harvey *et al.*, 2004). Hence, their relevance is still unclear, although one study even suggested that the co-expression of the $CB2_{SH3-}$ variant with gephyrin in hippocampal rodent neurons induced larger gephyrin clusters than the $CB2_{SH3+}$ variant, which, in this study, was found to rather increase the cluster number especially at extrasynaptic sites (Chiou *et al.*, 2011). In the following the functions of the individual domains are presented. The discussion of the SH3 domain is postponed to III.C.1.3.1.

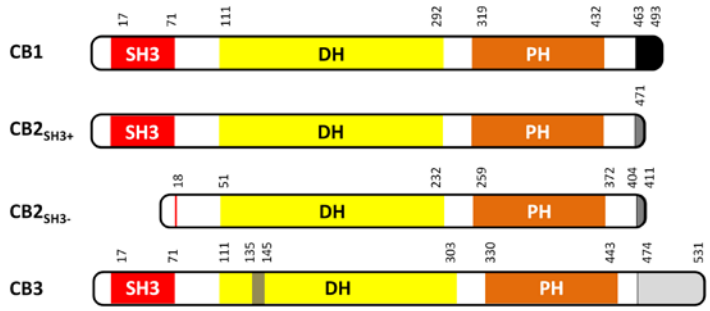

Figure 76 Collybistin splice variants in *Rattus norvegicus*. Collybistin splice variants share a DH-PH tandem and vary in their C-terminus (as indicated by the different grey tones), which determines the classification into CB isoforms 1, 2 or 3. Two variants of CB2 exist, which differ in the presence/absence of a SH3 domain. An 11 amino acid insert is present in CB3 of *Rattus norvegicus*, but is missing in *Mus musculus* or *Homo sapiens*.

III.C.1.2.4 The DH domain mediates collybistin's GEF activity

Collybistin's GEF activity was first documented for the collybistin homologue hPEM-2 which specifically exhibited GEF activity towards the Rho-like GTPase Cdc42 (Reid *et al.*, 1999). Even a crystal structure of $CB2_{SH3-}$ in complex with Cdc42 is available, which revealed two different orientations of the PH domain with respect to the DH domain (Xiang *et al.*, 2006). Despite the obvious flexibility of the DH-PH tandem, in neither conformation was the PH domain involved in interactions with Cdc42 (Fig. 77) or with the DH domain, as observed before in the Dbs-Cdc42 complex (Rossman *et al.*, 2002) or Sos (Soisson *et al.*, 1998), respectively. Collybistin's substrate, Cdc42, is involved in the organization of the neuronal cytoskeleton (Ito *et al.*, 2014, Mackay & Hall, 1998, Negishi & Katoh, 2005). Hence, it was suggested that collybistin and Cdc42 recruit gephyrin to the postsynaptic density (Kneussel & Betz, 2000). This model was further extended after the observation, that gephyrin negatively regulated GEF activity of collybistin (Xiang *et al.*, 2006),

suggesting, that gephyrin might terminate Cdc42 activity in the later stages of synapse formation when Cdc42 activity is dispensible (Xiang *et al.*, 2006) (Fig. 77). However, cell biological experiments of various CB mutants and the analysis of Cdc42 knock-out mouse suggested that collybistin's GEF activity and the action of Cdc42 are not required for synapse formation (Reddy-Alla *et al.*, 2010).

III.C.1.2.5 Collybistin's PH domain is required for membrane targeting

Collybistin's DH domain is connected with the PH domain via a long α-helix. PH domains are poorly conserved domains, which mediate membrane targeting but also protein-protein interactions (Scheffzek & Welti, 2012). The PH domain of collybistin contains two anti-parallel β-sheets, that are capped by an α-helix. Interestingly, the subsequent, second α-helix has not been observed in any other DH-PH-tandem so far (as of December 2013). The PH domain has been shown to be important for gephyrin targeting in many studies (Harvey *et al.*, 2004, Kalscheuer *et al.*, 2009, Reddy-Alla *et al.*, 2010), with a crucial contribution of two solvent-exposed arginines 303 and 304 (Reddy-Alla *et al.*, 2010). A recent study showed, that the GTPase TC10 interacted with the PH domain to trigger membranous gephyrin clustering in non-neuronal cells (Mayer *et al.*, 2013). As in the case of Cdc42, GEF activity of collybistin was not important for the membraneous localization of gephyrin in non-neuronal cells (Mayer *et al.*, 2013). However, constitutively activated TC10 (GTP bound) enhanced gephyrin clustering upon coexpression in neurons, whereas a dominant negative TC10 variant led to attenuated gephyrin clustering (Mayer *et al.*, 2013).

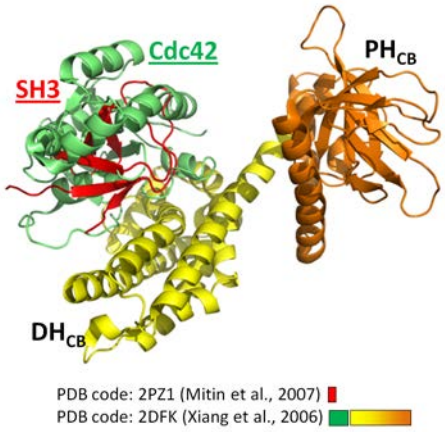

Figure 77 Crystal structures of the CB2$_{SH3-}$-Cdc42 complex and the SH3 domain of ASEF1. The DH domains of collybistin and ASEF1 were superposed, and only the SH3 domain of ASEF1 is shown to illustrate a potential competitive binding of Cdc42 and the SH3 domain of collybsitin as suggested by the finding that CB1 (containing a SH3 domain) exhibits an affected GEF activity in comparison to CB2$_{SH3-}$ (Xiang *et al.*, 2006).

III.C.1.3 The gephyrin-collybistin-NL2 complex at perisomatic GABAergic synapses

III.C.1.3.1 The SH3 domain renders collybistin in an inactive state

Although the PH domain appears to be essential for membrane targeting, it is not sufficient: All splice variants harbor the PH domain, but overexpression of any collybistin isoform in non-neuronal cells reported so far, resulted in a predominantly dispersed collybistin localization all over the cytoplasm (Harvey *et al.*, 2004). The coexpression of gephyrin with SH3-domain containing collybistin isoforms led to a collybistin recruitment to large cytoplasmic gephyrin aggregates ("blobs"), which

were also observed in the absence of CB. On the contrary, upon coexpression of $CB2_{SH3-}$ and gephyrin submembranous microclusters containing both collybistin and gephyrin were observed (Harvey *et al.*, 2004). These results imply, that at least two additional factors beyond the PH domain favour collybistin membrane targeting: First, the activation of CB variants containing the SH3 domain (which are the prevalent isoforms in the cell) and second, gephyrin. While the mechanism for gephyrin-mediated collybistin targeting is not understood on the molecular level, an attractive hypothesis on the role of the SH3 domain in collybistin targeting emerged.

For collybistin's structural homologue ASEF1, which shares the SH3-DH-PH domain core with collybistin (Soykan, 2011), crystal structures revealed an intramolecular interaction between the SH3 domain and the DH-PH tandem (Mitin *et al.*, 2007, Murayama *et al.*, 2007). Many residues involved in this interface are identical in collybistin, and hence mutations could be inferred into the putative collybistin interface of $CB2_{SH3+}$, rendering even SH3 containing collybistin variants constitutively active in terms of gephyrin clustering (Soykan, 2011). Along this line, the crystal structure of collybistin comprising the SH3-DH-PH core revealed a domain arrangement very reminiscent of the ASEF1 structures, and there was indeed a correlation between the mentioned mutants and a decoupling of the SH3 domain from the DH-PH tandem (Drs. Tolgan Soykan and Daniela Schneeberger *et al.*, unpublished data).

III.C.1.3.2 NL2-guided release of SH3-mediated autoinhibition

Neurons have developed several mechanisms to overcome SH3 mediated autoinhibition, as suggested by the observations that membrane targeting of gephyrin and collybistin isoforms containing the SH3 domain in non-neuronal cells was achieved by coexpression of neuron-specific proteins such as the $GABA_AR$ subunit α2, NL2 and NL4 (Hoon *et al.*, 2011, Poulopoulos *et al.*, 2009, Saiepour *et al.*, 2010). In these studies, all three proteins were shown to bind to the SH3 domain of collybistin.

Collybistin's SH3 domain displays the typical SH3 domain fold with five β-strands interconnected by three loops and a 3_{10} helix and provides a flat conserved, hydrophobic binding pocket, well-suited for poly-proline-rich motifs (PRMs) (Fig. 78A) as they are present in all three mentioned activators of collybistin, while residues crucial for PRM binding are conserved in collybistin. While it became clear that the $GABA_AR$ subunit α2 uses an atypical SH3 binding motif (Maric, 2012), there has been no counter-evidence that NL2 and NL4 would not bind via one of their 4 or 2 proline-rich motifs (PRM), respectively (Fig. 78A). Unpublished data on the collybistin-NL2 interaction point to an involvement of the proline-rich stretch beyond residue 798 (Dr. Tolga Soykan, personal communication).

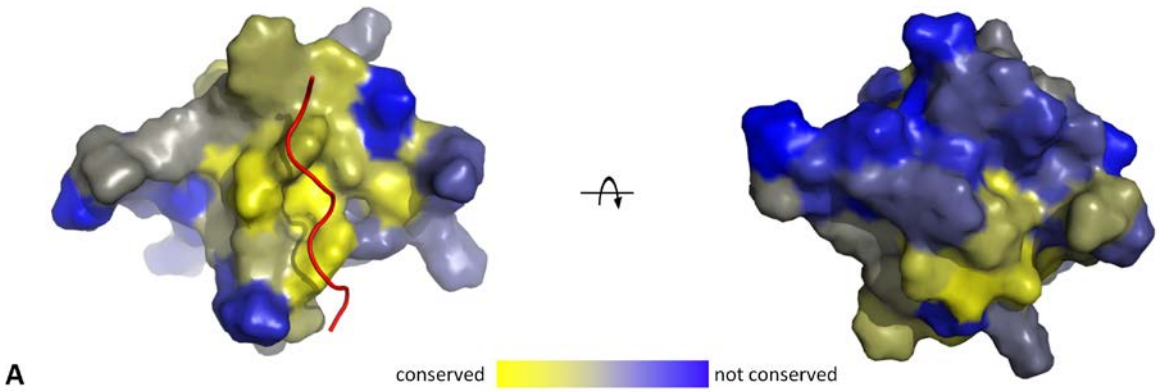

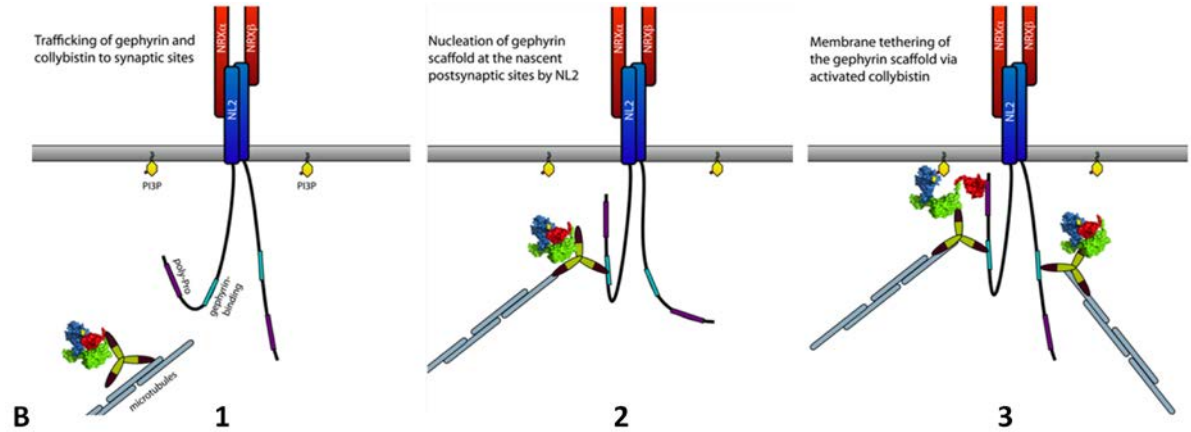

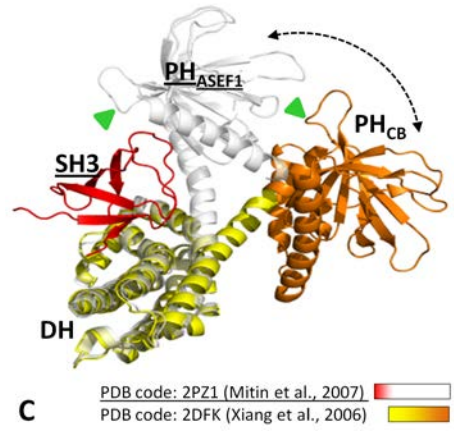

Figure 78 Collybistin activation via the SH3 domain. (A) Conserved residues in 47 arbitrarily chosen SH3 domains as judged by a CONSURF analysis are also conserved in collybistin (not shown) and cluster around the flat hydrophobic binding groove, so that from a structural perspective binding of PRMs (red) is conceivable. The PRM is a synthetic peptide bound to the abl tyrosine kinase SH3 domain (PDB entry 1ABO) which was superposed with collybistin's SH3 domain (PDB code: 2YSQ). (B) Collybistin activation model, adapted from Papadopoulos & Soykan, 2011 (with the permission of the authors). The three-pronged star represents a gephyrin trimer, co-transported with collybistin (in surface representantion). Upon gephyrin binding (2), the SH3 domain (red) gets removed from the DH-PH tandem (green-blue) (3), so that the PH domain can be anchored by PI(3)P (yellow). Further steps proposed in Papadopoulos & Soykan, 2011 are not shown here, but are described in the main text. (C) Structural rationale for SH3 mediated autoinhibition of collybistin. Superposition of two structures, one of the "constitutively" active $CB2_{SH3-}$ variant (yellow/orange), another one of collybistin homologue ASEF1 (SH3 domain in red, rest in white). The green arrows mark the loop which is involved in PI(3)P binding, which in the autoinhibited state is in close proximity to the SH3 domain. Upon activation the full PI(3)P binding capacity might be reached.

Binding of either activator to collybistin is thought to decouple the SH3 domain from the DH-PH tandem (Fig. 78 B&C), giving rise to the activation of collybistin. The functional consequence is not entirely understood, however, in lipid overlay assays inactivated $CB2_{SH3+}$ exhibited a lower affinity to PI(3)P than $CB2_{SH3-}$, and $CB2_{SH3+}$ mutants, in which (at least partial) activation was achieved (e.g. at positions 24 and 262), and the addition of NL2 was shown to endow $CB2_{SH3+}$ with an enhanced PI(3)P affinity (Soykan, 2011). All these data are consistent with the following model originally proposed by Poulopoulos & Soykan (2009), which was extended in Papadopoulos & Soykan (2011):

Gephyrin and collybistin are co-transported to the membrane (Fig. 78B1), where they encounter NL2, which binds to gephyrin (Fig. 78B2). Now NL2 is in close proximity to bind to and hence activate collybistin's SH3 domain (Fig. 78B3). This in turn enhances collybistin binding to PI(3)P (Fig. 78B3) and leads to a stable anchoring of gephyrin-collybistin to the membrane and to the subsequent assembly of the gephyrin scaffold and $GABA_A$Rs. A similar model was proposed for NL4, which was shown to promote the formation of glycinergic synapses in the retina (Hoon *et al.*, 2011) and is expected to apply to $GABA_A$R subunit α2 as well.

III.C.1.3.3 Gephyrin-collybistin

The finding, that gephyrin affects collybistin's GEF activity raised the possibility of allosteric gephyrin-mediated inhibition but also that of a direct interaction between the DH domain and gephyrin (Xiang *et al.*, 2006). The latter received support by colocalization studies in which the

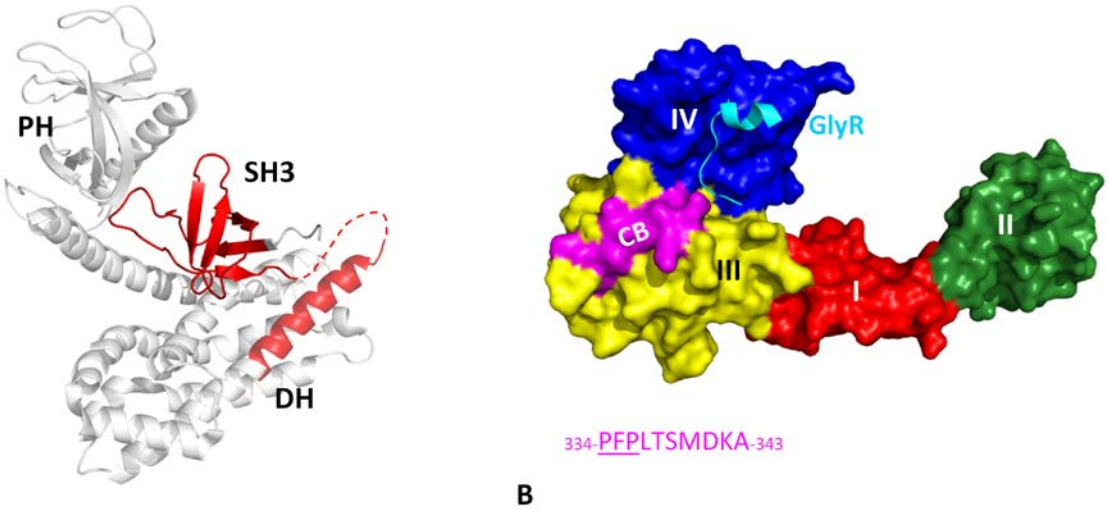

Figure 79 Potential gephyrin-collybistin interfaces. (A) The crystal structure of collybistin's structural homologue ASEF1 (PDB code: 2PZ1). The dashed line indicates residues, which could not be resolved. Segments marked in red comprise candidate residues for the gephyrin binding site. (B) Gephyrin's putative collybistin binding site in GephE's subdomain III is part of the magenta-colored segment and in close proximity of the GlyR/$GABA_A$R binding site. Alanine substitutions in the corresponding GephE sequence displayed below led to an abolishment of gephyrin-CB interactions in a Y2H screen (Harvey *et al.*, 2004). The replacement of the underscored tripeptide prevented gephyrin-collybistin colocalization in COS7 cells (Soykan, 2011).

deletion of the DH domain abolished colocalization with gephyrin (Harvey *et al.*, 2004). However, a more exact mapping of the gephyrin binding site, which is compatible with collybistin's structural integrity has not been published so far (Grosskreutz *et al.*, 2001, Xiang *et al.*, 2006). Nevertheless, in the course of this work binding assays, which assessed gephyrin binding to ASEF1 and collybistin-ASEF1 swap mutants suggested that the region encompassing the SH3 domain and only a few residues of the DH domain harbour the gephyrin binding motif (Fig. 79A) (Soykan, 2011). These findings are taken up in the course of the discussion (section III.D.2.3). Vice versa, the collybistin binding site in gephyrin, narrowed down to the very N-terminal portion of GephE (Harvey *et al.*, 2004) (marked in magenta in Fig. 79B), could also be confirmed by our collaboration partner (Soykan, 2011).

III.C.1.3.4 Gephyrin-NL2

The gephyrin-NL2 interaction presumably involves GephE and possibly parts of the linker (residues 286-768 of gephyrin harbouring the G2 and C4a cassettes, gephyrin P2 contains the C4b cassette instead, see also section I.C.2.1) and a 15 amino-acid long stretch in the center of the cytosolic region of NL2 (Poulopoulos *et al.*, 2009) referred to as GB_{NL2}. GB_{NL2} is conserved among the four rat neuroligins (Fig. 80), and indeed all NLs were shown to bind to gephyrin in Y2H studies. The gephyrin binding motif does not encompass a PDZ binding motif and features a tyrosine (Y770), which is crucial for gephyrin binding, as established by Co-IP and pulldown experiments as well as yeast-two-hybrid screens (Poulopoulos *et al.*, 2009). This tyrosine is a phosphorylation target in NLs 1-3 (phosphosite.org), and in NL1 this phosphorylation was reported to abolish gephyrin binding which resulted in a preferential recruitment of PSD95, one of the key components at excitatory postsynaptic densities (Giannone *et al.*, 2013). As mentioned above, the gephyrin-NL2 interaction is not sufficient to trigger submembranous localization of gephyrin, and the addition of collybistin is

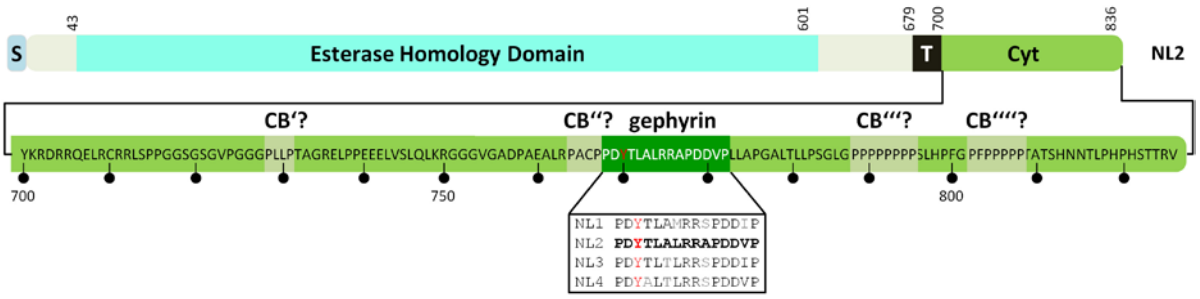

Figure 80 Domain architecture of neuroligin 2. NL2 is a type I membrane protein, containing an extracellular esterase homology domain followed by a glycosylation region before the transmembrane region (T). The cytoplasmic region (Cyt) harbors an identified gephyrin binding motif and four proline-rich, putative collybistin binding regions. The signal peptide (S) is a translocation signal. Note the high degree of conservation among the four gephyrin binding motifs (GB_{NL}) of the NL mouse paralogues. GB_{NL2} starts at Pro768 and terminates at Pro782.

required. As neither NL1, 3 could replace NL2 without preventing membranous localization, but the collybistin interactor NL4 could, collybistin has considered as an indispensible bridge between NL2 & 4 on the one hand and gephyrin on the other.

Taken together, gephyrin, collybistin and NL2 can form a ternary complex, which is kept together via binary interactions between all components. A removal of either component in non-neuronal cells leads to a loss of submembranous aggregates, which have been considered as self-organizing post-synaptic elements (Poulopoulos *et al.*, 2009). However, interaction sites for the three binary complexes have largely been known on the domain level (summarized in Fig. 81), but not even for one of the binary complexes structural data have been available. The aim of the work presented in this chapter aimed to address this gap in knowledge.

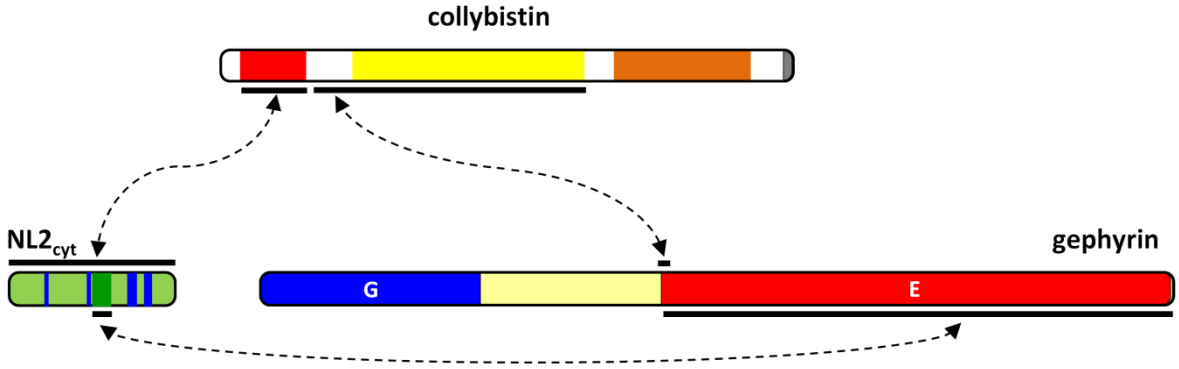

Figure 81 Binary interactions presumably involved in the formation of a ternary gephyrin-collybistin-NL2 complex.

III.C.2. Results

III.C.2.1 Characterization of NL2$_{cyt}$

III.C.2.1.1 Bioinformatics

The cytosolic region of NL3 (NL3$_{cyt}$) was previously identified as an intrinsically disordered region (IDR) (Paz *et al.*, 2008). Hence, secondary structure and disorder prediction algorithms implemented in the PHYRE2 webserver were used to get a first hint whether NL2$_{cyt}$ is also an IDR.

While disorder prediction algorithms yielded conflicting data (suggesting IDR contents between 21% and 100%), secondary structure prediction algorithms consistently accounted for an IDR content of 77%-85% with only two α-helical segments (residues 740-750 and residues 789-792). Interestingly, another group conducted a NMR analysis with NL3$_{cyt}$ and found residual secondary structure only in two segments (Fig. 82), two of which were predicted by JPRED3 (Wood *et al.*, 2012). For this reason, JPRED3 was utilized to predict NL2$_{cyt}$ secondary structure. Indeed, two of the putative NL2$_{cyt}$ and the two putative NL3$_{cyt}$ segment could be partially aligned. One of these helices is part of the gephyrin binding motif of NL2$_{cyt}$.

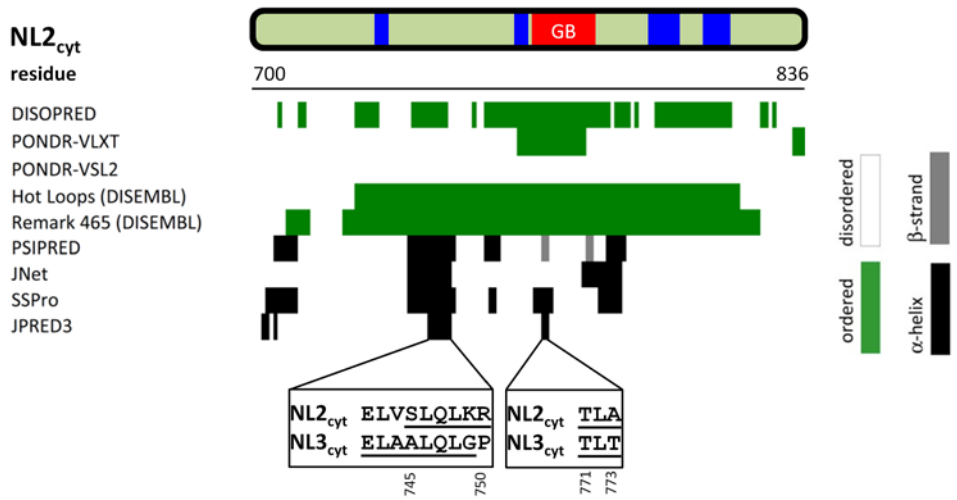

Figure 82 Secondary structure and disorder prediction for the cytosolic region of NL2. The first four algorithms predicted disorder, the remaining four the secondary structure. The secondary structure prediction of NL3$_{cyt}$ by JPRED3 was consistent with an NMR analysis (Wood *et al.*, 2012). Therefore, the corresponding JPRED3 prediction for NL2$_{cyt}$ was compared with that of NL3$_{cyt}$. Underscored residues were predicted to be helical.

In analogy to gephyrin sequence analysis the features of the NL2 sequence were assessed with the composition profiler (Table 43). Several features, such as an enrichment of amino acids that have a high solvation potential and contribute to disorder and flexibility as well as the depletion of aromatic and order-promoting residues suggested that NL2$_{cyt}$ contains a significant fraction of IDRs.

criterion	⇩/⇧	p-value	criterion	⇩/⇧	p-value
Order promoting (Dunker)	⇩	0.002087	Hydrophobic (Eisenberg)	*n. s.*	0.094264
Frequent in beta struc. (N)	⇩	0.002818	Exposed (Janin)	*n. s.*	0.184355
Aromatic content	⇩	0.005298	Negatively charged	*n. s.*	0.214689
High interface prop. (J-T)	⇩	0.007092	Bulky (Zimmerman)	*n. s.*	0.24175
Hydrophobic (K-D)	⇩	0.056138	Frequent in alpha hel. (N)	*n. s.*	0.187427
Disorder promoting (Dunker)	⇧	0.000065	Hydrophobic (F-P)	*n. s.*	0.470402
Frequent in coils (N)	⇧	0.000168	Charged residues	*n. s.*	0.551659
High linker propensity (G-H)	⇧	0.00309	Polar (Zimmerman)	*n. s.*	0.413576
Flexible (Vihinen)	⇧	0.004656	Positively charged	*n. s.*	0.601714
High solvation poten. (J-T)	⇧	0.003856	Large (Dawson)	*n. s.*	0.700952

Table 43 Composition profiler analysis of $NL2_{cyt}$. Residues 700 to 836 of *Rattus norvegicus* NL2 were tested for a depletion (⇩) or enrichment (⇧) of certain amino acid classes with respect to a largely folded reference protein, the extracellular domain of mouse $NL2_{cyt}$ splice variant A (PDB entry: 3BL8 (Koehnke *et al.*, 2008)), which is identical to *Rattus norvegicus* NL2 except for a single mutation. All significant depletions/enrichments were characteristic for IDRs. *n. s*. stands for *not significant (p-values > 0.05)*.

III.C.2.1.2 $NL2_{cyt}$ purification

As no overexpression and purification protocols for $NL2_{cyt}$ had been available, several vectors were screened for overexpression. With vectors from the pTYB series (NEB, provided by Dr. Daniela Schneeberger) $NL2_{cyt}$ could not be expressed satisfyingly, and only one truncation variant could be obtained in very small amounts ($NL2_{cyt}$-C46 comprising residues 752 to 797, data not shown). On the contrary, sufficiently high expression levels were achieved with vectors of the pETM series (EMBL), which carry an N-terminal His-tag that can be removed by a cleavage with the Tobacco Etch Virus (TEV) protease. Initial expressions were carried out with the pETM11 vector, encoding for an N-terminal His-tag followed by $NL2_{cyt}$. With this vector sufficient but still weak expression was achieved, which could hardly be regarded as overexpression, and

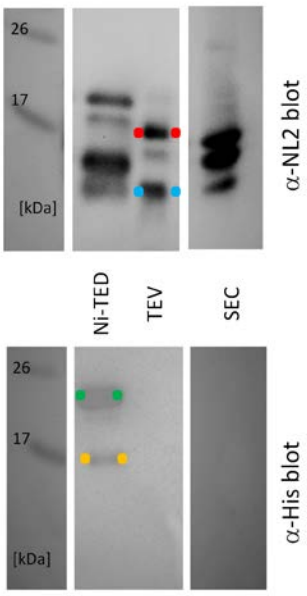

Figure 83 Western blot analysis of $NL2_{cyt}$ obtained after selected purification steps. The protein was expressed by means of the pETM11 vector. Antibodies targeted either $NL2_{cyt}$ (upper panel) or the His-tag (lower panel). The blots confirmed the identity of $NL2_{cyt}$ and that the His-tag was cleaved efficiently by the TEV protease. The marked bands corresponded to $NL2_{cyt}$ (red), $NL2_{cyt,sh}$ (cyan), TEV protease (green), His-$NL2_{cyt}$ (yellow).

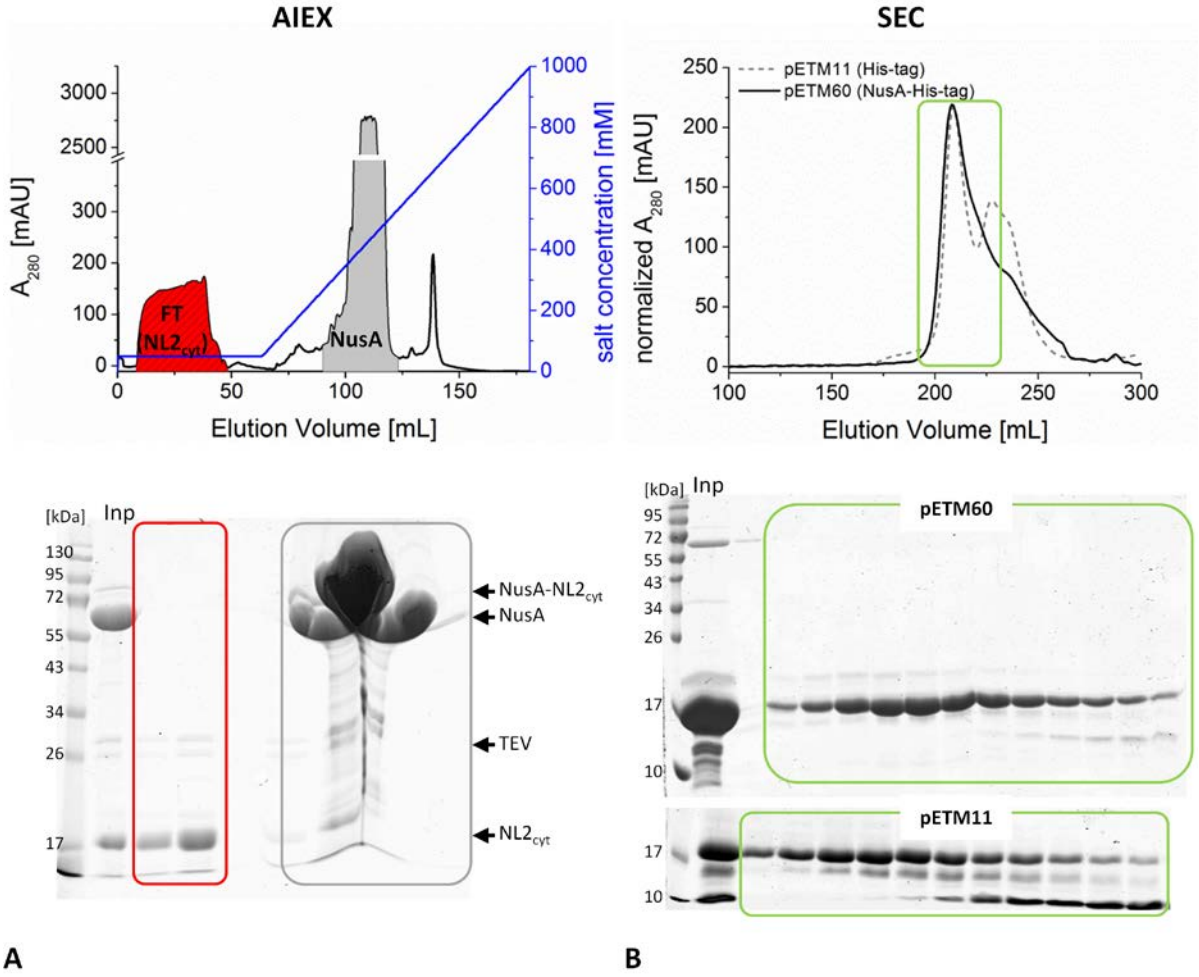

Figure 84 Purification of $NL2_{cyt}$ by means of AIEX and SEC. (A) Representative separation of $NL2_{cyt}$ from NusA via AIEX. The chromatogram displays two dominant peaks. One corresponds to $NL2_{cyt}$ in the flowthrough (red) and one to NusA eluted by the salt gradient (grey). Note the break in the y-axis which was introduced for better legibility. The content of the respective fractions is depicted in the lower panel. A faint band at ~75 kDa in the AIEX input (Inp) could represent non-cleaved NusA-$NL2_{cyt}$ (expected mass: 74.4 kDa). Like $NL2_{cyt}$ (band at 17 kDa) the TEV protease did not bind to the column (bands at ~26 kDa). (B) $NL2_{cyt}$ expression as NusA fusion protein led to a higher degree of purity, as suggested by the chromatogram and the corresponding SDS-gels in the upper and lower panel, respectively.

degradation was a serious problem (Fig. 83, third lane), however, $NL2_{cyt}$ identity could be verified by Western blot analysis. Subsequent trials with pETM60 resulted in overexpression and a higher degree of protein purity. The purification protocol could be applied to both, His-$NL2_{cyt}$ (derived from the pETM11 vector) and NusA-His-$NL2_{cyt}$ (resulting from overexpression with the pETM60 vector): The eluate from a Ni affinity chromatography column was dialysed in the presence of TEV protease for Tag removal (Fig. 83). The pH value of 9 and the low salt concentration of the dialysis buffer were appropriate for subsequent anion exchange chromatography (AIEX): These parameters allowed *E. coli* proteins as well as the His-tag (pI = 6.8) and His-$NL2_{cyt}$ (pI = 8.3) (or NusA and NusA-$NL2_{cyt}$) to bind to the anion exchange chromatography column, while $NL2_{cyt}$ with its rather high predicted pI of

9.4 was obtained in the flow-through (Fig. 84A). The latter was concentrated prior to the final size exclusion chromatography step. Principally, a heating step could be introduced (10 minutes at 60°C and subsequent centrifugation), however, this was actually not required given the satisfying purity of the SEC purified sample (Fig. 84B).

III.C.2.1.3 CD spectroscopy and SAXS revealed that $NL2_{cyt}$ is an IDR

Hints to potential disorder within $NL2_{cyt}$ (section III.C.2.1.1) were verified by means of CD spectroscopy and SAXS experiments. The CD spectrum of $NL2_{cyt}$ displayed a minimum at 200 nm as is typical for intrinsically disordered proteins. Further features for proteins with minor contributions of α-helices and β-strands were the absence of minima at ~210 nm and ~220 nm which were not detectable in the CD spectrum (Fig. 85A), in analogy to $NL3_{cyt}$ (Paz *et al.*, 2008).

In a next step SAXS was used to analyse the intrinsic disorder suggested by CD spectroscopy. The SAXS data obtained for $NL2_{cyt}$ could be used despite 1) a low signal-to-noise ratio throughout the complete curve and 2) a strong increase of the data points beyond the linear Guinier approximation (Fig. 85B), which could be indicative of aggregates. Such an increase could only be observed for the first two to three data points in the very small angle region ($s<0.008$ Å). To exclude that data analysis was affected by potential aggregation, only data with $s>0.01035$ were used. Despite the apparent noise, the R_g could be determined with acceptable certainty, as revealed by the arbitrary distribution of the data points along the linear Guinier fit (Fig. 85B), yielding an R_g of 37 Å. The fact that even the inclusion of the omitted data points does not lead to a change of the R_g (data not shown), indicated that data analysis was presumably not been hampered by potential aggregation.

SAXS data corroborated CD spectroscopy and bioinformatics and suggested that $NL2_{cyt}$ can be considered as an IDR (Table 44): First, the R_g of $NL2_{cyt}$ of 37 Å is higher than that of $NL3_{cyt}$ (with molecular mass of 15.4 kDa comparable to $NL2_{cyt}$) under native conditions (33 Å) and just slightly smaller than that of denatured $NL3_{cyt}$ (40 Å) (Paz *et al.*, 2008). For comparison: For a folded protein of comparable mass such as lysozyme (14 kDa) the R_g is in the range of 15 Å. Second, the P(r)-derived D_{max} value of 145 Å indicates an elongated shape (Fig. 85C). Third, the Kratky plot is typical for an IDR (Fig. 85D), clearly deviating from a bell-shaped curve as is typical for folded proteins.

Three of the four molecular mass estimations yielded values of about 20 kDa, consistent with a mixture of monomers and dimers (Table 44). Only the SAXS MOW server estimate was in agreement with dimers as the predominant oligomeric state. As a MALS measurement was consistent with an $NL2_{cyt}$ monomer with only 3% deviation between the experimentally derived value and the theoretical monomer mass (data not shown), only the ensemble analysis by EOM derived from a pool of monomers is presented here (Fig. 85E & F). Several repetitions of the EOM analysis yielded very similar solutions, for which good fits could be obtained. The comparatively high χ of 1.13 can be

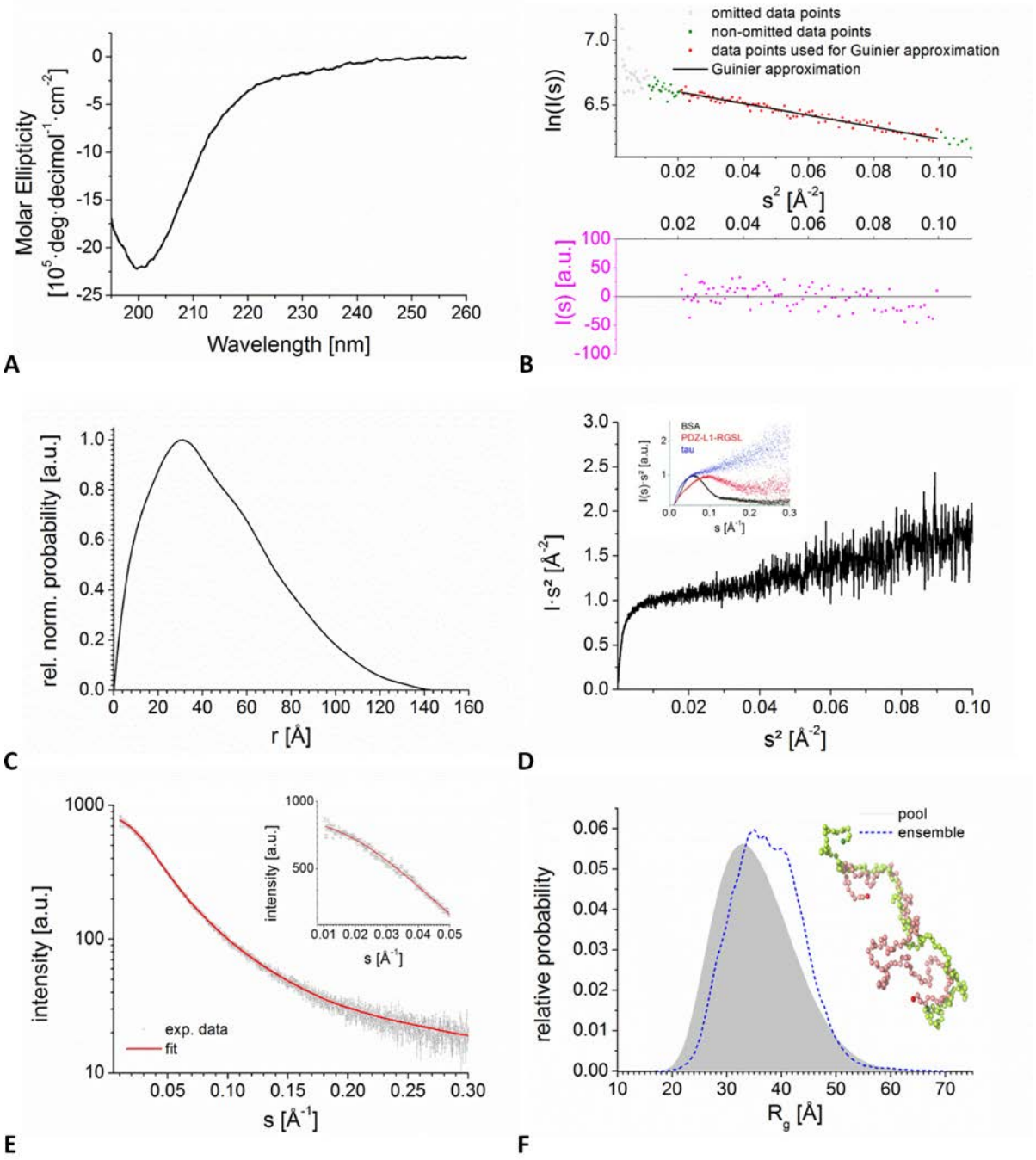

Figure 85 $NL2_{cyt}$ characterization by CD and SAXS. (A) CD spectrum of $NL2_{cyt}$. (B) Guinier plot in the upper panel and the corresponding residuals in the lower panel. Grey data points were omitted from further analyses, as the strong increase for the first three data points indicated potential aggregation. Data points used for further analyses are coloured in green, unless they were used for the Guinier approximation (red data points). (C) Normalized P(r) function of $NL2_{cyt}$. (D) Kratky plot of $NL2_{cyt}$. The curve can roughly be considered as hyperbolic, typical of intrinsically disordered proteins/segments. The inset is the same as in Fig. 23B. (E) The EOM-derived fit to the $NL2_{cyt}$ data. Note the good agreement of the fit to the experimental data in the inset, where non-logarithmic scaling was applied. (F) EOM-derived R_g distribution of the NL2 ensembles. This distribution displays a good match to the R_g distribution of the initial pool. In addition the most compact and the most extended of the 20 conformers of the selected $NL2_{cyt}$ ensemble are displayed in salmon and in green, respectively.

explained by the noise level in the experimental data; a more important criterion than the χ value was the good agreement between the experimental data and the ensemble-derived scattering profile also in the very small angle region (see inset Fig. 85E). The R_g distributions of all ensembles appeared like a slightly right-shifted version of the R_g distributions of the initial pool (Fig. 85F). Not surprisingly, ensembles were made up by of 19-31 conformers. In the selected ensemble the R_g values of the conformers varied considerably between 25 Å and 47 Å (Fig. 85F), reflected by a high NSD of 2.18 ± 0.01. Taken together, CD spectroscopy and SAXS supported the idea that the structure of $NL2_{cyt}$ is dominated by intrinsically disordered segments.

	R_g(Guinier) [Å]	R_g (P(r)) [Å]	D_{max} [Å]	Porod vol. [Å³]	MM_{Porod} [kDa]	MW_{DAMMIN} [kDa]	$MM_{SAXS-MOW}$ [kDa]	MM_{VC} [kDa]	$MM_{monomer}$ [kDa]
$NL2_{cyt}$	37±2	38±2	145±30	33	20.6 (1.4)	20 (1.4)	32.2 (2.2)	22.9 (1.6)	14.4

Table 44 Overall characterization of $NL2_{cyt}$ by SAXS. R_g (Guinier) and R_g (P(r)) refer to the radii of gyration obtained by either the Guinier approximation or the P(r) function, respectively. D_{max} is the maximum interatomic distance obtained by the P(r) function. Molecular masses in kDa (MM) were derived by (1) division of the Porod volume in Å³ by a factor of 1.6 (MM_{Porod}), (2) division of the excluded volumes of DAMMIN models without symmetry (MM_{DAMMIN}) by a factor of 2, (3) by the SAXS-MOW webserver ($MM_{SAXS-MOW}$) and (4) by the volume of correlation invariant (VC), introduced by Rambo and Tainer (MM_{VC}). Values in brackets indicate the oligomeric state, obtained by division of the experimental value by the molecular mass of the monomer

III.C.2.2 The gephyrin-NL2 interaction

III.C.2.2.1 Biochemical analysis

Initial attempts to characterize the gephyrin-NL2$_{cyt}$ interaction focused on pulldown analysis. Several matrices with different baits were tested. The fact that the interaction was disturbed at a salt concentration of 250 mM, suggested that electrostatic interactions play a critical role in complex formation (Fig. 86A). It should be noted that signals of unspecifically bound prey proteins could not be completely eliminated without a significant reduction of the signal for specifically bound prey proteins, so that typically only two washing steps were conducted. Two representative examples are discussed. The most promising results were obtained with NL2$_{cyt}$-coated nickel beads and GephE as a prey, as in these experiments repeatedly a reduction of GephE in the supernatant coupled to an enrichment of GephE in the pellet was observed (Fig. 86A, lane 8, Fig. 86B, lane 4). In line with a

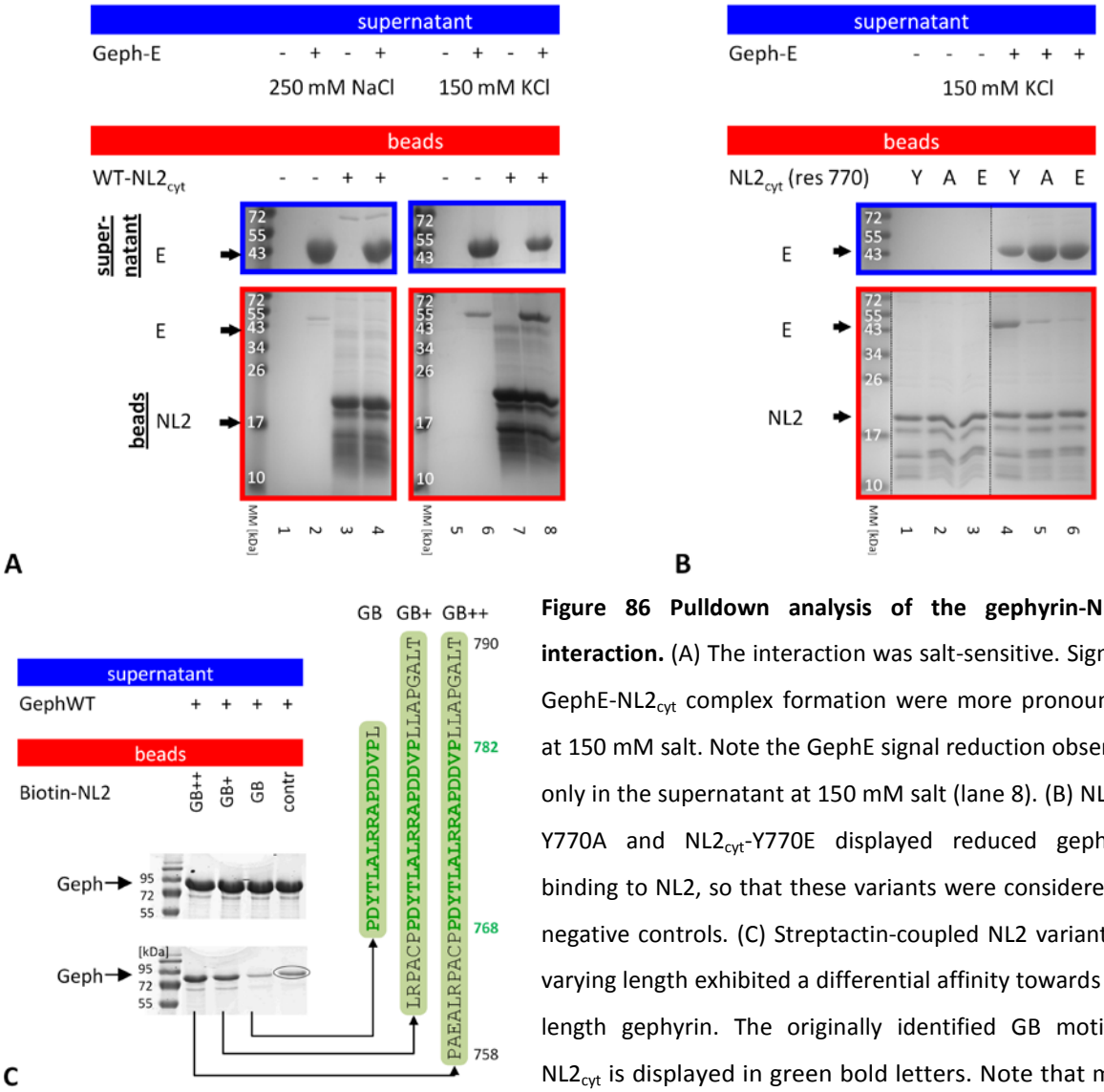

Figure 86 Pulldown analysis of the gephyrin-NL2$_{cyt}$ interaction. (A) The interaction was salt-sensitive. Signs of GephE-NL2$_{cyt}$ complex formation were more pronounced at 150 mM salt. Note the GephE signal reduction observed only in the supernatant at 150 mM salt (lane 8). (B) NL2$_{cyt}$-Y770A and NL2$_{cyt}$-Y770E displayed reduced gephyrin binding to NL2, so that these variants were considered as negative controls. (C) Streptactin-coupled NL2 variants of varying length exhibited a differential affinity towards full-length gephyrin. The originally identified GB motif of NL2$_{cyt}$ is displayed in green bold letters. Note that more gephyrin was pulled down with the control beads (oval selection) than with GB-coated beads.

previous study (Poulopoulos *et al.*, 2009), the replacement of Y770 by alanine or glutamate led to a decreased amount of NL2-GephE complexes (Fig. 86B, lanes 4 to 6). In the second example biotinylated peptides were coupled to streptactin beads, and full-length gephyrin was used as a prey. Not only the original GB_{NL2} motif (comprising residues 768 to 782 plus residue 783, here referred to as GB, see also Fig. 80) was used but also extended versions, referred to as GB+ and GB++. Again only a slight enrichment of gephyrin on the beads was achieved (paralleled by no decrease of the gephyrin signal in the supernatant). With GB++ and GB+ more convincing results were obtained than with GB-coated beads which did not bind significantly better to gephyrin than uncoated beads (Fig. 86C). However, all these results should be taken with caution, as other pulldown analyses did not yield positive results at all: For example, $NL2_{cyt}$ as a prey did not stably bind to either intein-tagged GephE coupled to chitin beads or His-tagged full-length gephyrin coupled to nickel beads as baits, so that no signs of binding could be obtained (data not shown). Taken together, pulldown analysis suggested that gephyrin and NL2 exhibit at best a weak affinity to each other.

Further evidence for a rather weak interaction came from aSEC experiments performed with putative $NL2_{cyt}$ complexes and full-length gephyrin (Fig. 99), GephLE208 (data not shown) or GephE. The most promising experiment is shown in Fig. 87. Here, initial concentrations of 150 µM GephE and 270 µM $NL2_{cyt}$ were not sufficient to provide evidence for a robust complex. At best, the chromatograms and the corresponding gels account for a rather transient interaction. The retention time of GephE on the column is shortened in the presence of $NL2_{cyt}$, as indicated by a gentle left-shift of just 0.1 mL. Accordingly, the corresponding SDS-PAGE gels revealed minimal to no changes (Fig. 87B). To explore additional indications for complex formation, the experimental chromatogram was

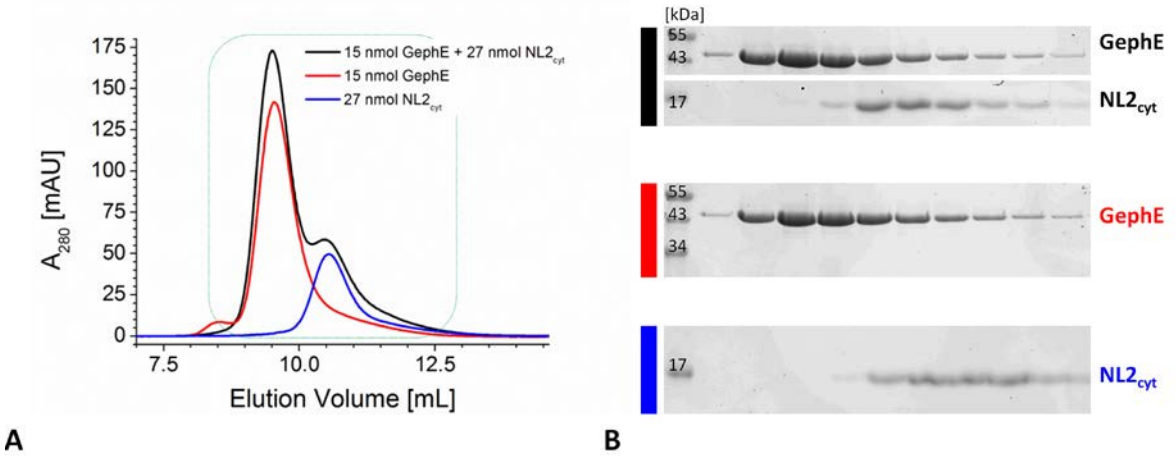

Figure 87 aSEC experiments with the GephE and $NL2_{cyt}$. (A) The chromatogram of the protein mixture (black curve) displays a slight left shift in comparison to the GephE chromatogram and deviates from a simple addition of the chromatograms of the individual components. (B) The gels display the contents of the fractions encircled in green (A), with (at best) hardly detectable changes in the Geph-$NL2_{cyt}$ experiment when compared to the GephE and the $NL2_{cyt}$ experiments.

compared with the sum of the chromatograms of the single control experiments. In fact this analysis accounts for complex formation: The areas under the curves of both chromatograms were virtually equal (266 mAU·mL vs. 267 mAU·mL), so that the gain in absorbance in the GephE fractions (7 ml - 9.7 mL) could be contrasted with the decrease in the NL2 fractions (9.7 mL - 15 mL). In the experimental curve the peak height for $NL2_{cyt}$ was decreased by 22 mAU·mL, whereas the height of the peak containing GephE and potentially $NL2_{cyt}$ was increased by 21 mAU·mL, again pointing to a transient interaction between $NL2_{cyt}$ and gephyrin.

To get at least a rough estimate of the K_D, ITC experiments were conducted. Not surprisingly, the most promising experiment at concentrations of 22 µM GephE in the cell and 690 µM $NL2_{cyt}$ in the syringe turned out to be a low c measurement (Fig. 88), which means that the used concentrations were not high enough to ensure an at least nearly-sigmoidal shape of the isotherm. Hence, the estimation of thermodynamic parameters ΔH and $T\Delta S$ became unreliable. Nevertheless, the experiment revealed binding, as the heat signature of the control experiment ($NL2_{cyt}$ into buffer) was significantly decreased when compared to the $NL2_{cyt}$-GephE titration (Fig. 88). Consistent with the fact, that a saturation could not be achieved even at a molar ratio of 8:1, K_D values of 60 and 40 µM were obtained, depending on whether the negative control ($NL2_{cyt}$ titration into buffer) was subtracted or not.

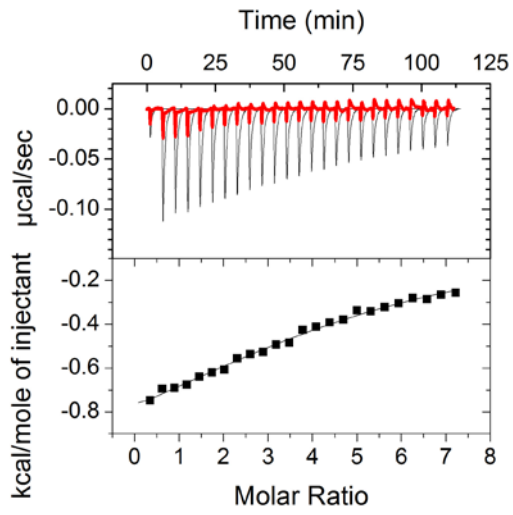

Figure 88 ITC analysis of the GephE-$NL2_{cyt}$ interaction. The upper panel displays the thermograms of both the actual GephE-$NL2_{cyt}$ and the reference titration in black and in red, respectively, while in the lower panel only the integrated heats of the GephE-$NL2_{cyt}$ experiment are shown.

The outcome of the aforementioned experiments was in agreement with the observation that the interaction between gephyrin and NL2 in CoIP experiments with mouse brain homogenates could only be convincingly detected in the presence of the DSP crosslinker (personal communication, Dr. Frederique Varoqueaux, MPI Göttingen). To get hints at the NL2 binding site in GephE, crosslinking experiments with GephE, $NL2_{cyt}$ and the gephyrin-nonbinding mutant $NL2_{cyt}$(Y770A) were conducted with the BS^3 crosslinker, which possesses the same functional groups as DSP (NHS esters) and a very

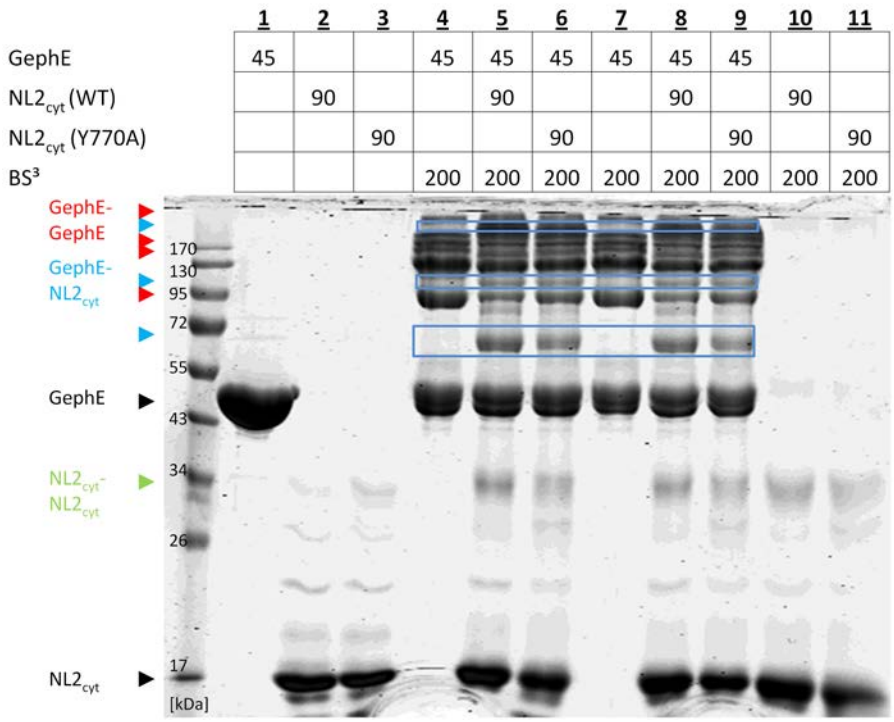

Figure 89 Crosslinking experiments with the GephE-NL2$_{cyt}$ complex. While black arrows mark the apo-components, crosslinking products are indicated by coloured arrows. In addition, GephE-NL2$_{cyt}$ crosslinking products are also highlighted by light blue boxes. Numbers in the table refer to the used concentrations in µM. Note that crosslinking of samples containing GephE was conducted in duplicate (samples 4-9).

similar linker length (11 Å instead of 12 Å as in the case of DSP). Indeed bands at ~60 kDa, ~110 kDa and more than 170 kDa (indicated by the light blue boxes in Fig. 89) could be observed. These bands could not be detected in crosslinking experiments with the individual proteins. Considering the monomer masses of 46 kDa and 14 kDa for GephE and the NL2$_{cyt}$ variants, respectively, the 60 kDa band presumably corresponded to a GephE-NL2$_{cyt}$ 1:1 complex, while the ~110 kDa band might represent a GephE$_2$-NL2$_1$ complex. Unfortunately, these bands were not only discernable for WT-NL2$_{cyt}$ but also for the non-binder mutants NL2$_{cyt}$(Y770A) although at a slightly reduced level (Fig. 89) and NL2$_{cyt}$(GB→CD8α) (data not shown). In the NL2$_{cyt}$(GB→CD8α) variant the gephyrin binding motif (res. 768-782) was replaced by the cytosolic loop of CD8α (Poulopoulos *et al.*, 2009). In addition, NL2$_{cyt}$ (which is monomeric, see section III.C.2.1.3) could also be crosslinked (green arrows in Fig. 89), and this also applied to NL2$_{cyt,sh}$ (a degradation product (Fig. 83), data not shown). Hence further trials to characterize the gephyrin-NL2$_{cyt}$ interation by crosslinking, were put aside.

The next choice for the analysis of the obviously weak gephyrin-NL2$_{cyt}$ interaction was native PAGE, for which only small amounts of protein were required and which ensured relatively high protein concentrations during the experiment. Even with this method gephyrin-NL2 complexes were hardly detectable (Fig. 90). Nevertheless, additional bands that were not observed for gephyrin and NL2$_{cyt}$, were present in gephyrin-NL2$_{cyt}$ mixtures, albeit at tiny amounts despite a NL2$_{cyt}$

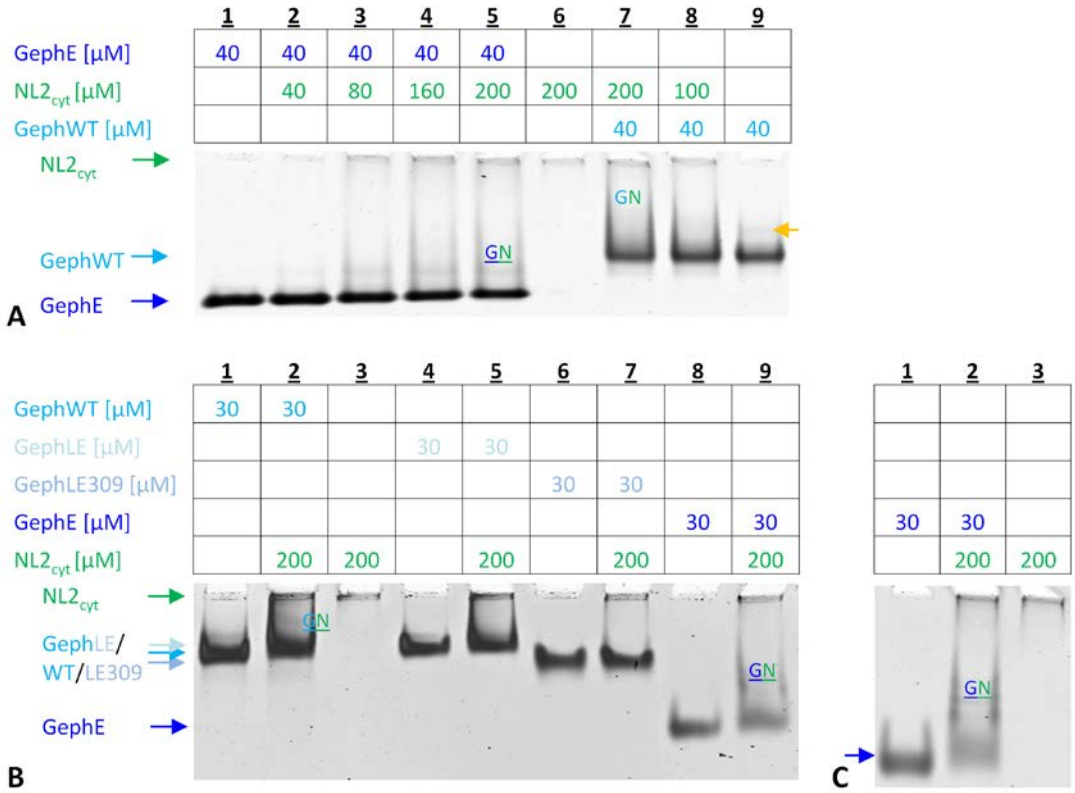

Figure 90 Native PAGE analysis of the gephyrin-NL2$_{cyt}$ complex. (A) Native PAGE analysis with a 4% acrylamide gel at 4°C, pH 8, 55 V for 160 min. Increasing NL2$_{cyt}$ concentrations resulted in additional bands (whose position is indicated by GN), which were not observed for the single components. (B) Native PAGE analysis with a 4.5% acrylamide gel at 4°C, pH 7.6, 55 V for 140 min. (C) Native PAGE with a 4.5% acrylamide gel at 4°C, pH 8, 55 V for 120 min.

concentration of 200 µM. The value of these additional signals, which appeared to be most pronounced for GephWT and GephE, will be evaluated in future experiments by western blot analysis and the inclusion of various NL2$_{cyt}$ truncation and non-binder mutants.

III.C.2.2.2 Cocrystallization

Initial cocrystallization attempts were conducted with GephE and the following NL2 variants in a 96-well-formate: Chemically synthesized peptides NL2GB, NL2GB++ as well as recombinantly produced NL2$_{cyt}$ and NL2$_{cyt,sh}$. Crystals could only be obtained with NL2$_{cyt,sh}$. NL2$_{cyt,sh}$ is an NL2$_{cyt}$ degradation product (Fig. 83) terminating after Thr790 (as judged by mass-spectrometric analysis, performed by Bernd Thiede, Bioteknologisenteret, Oslo), The crystals were hexagonally shaped with a diameter of ~10 µm and a considerably smaller height and appeared in the Qiagen Protein Complex Suite 96-well screen at 1) 0.1 magnesium acetate, 0.1 M MES pH 6.5, 10% (w/v) PEG 10,000 and 2) 0.2 M lithium sulfate, 0.1 M MES pH 6, 20% (w/v) PEG 4,000. While in reproduction attempts only crystalline material was obtained for the second condition (but no crystals comparable to those in the 96-well screen), crystals of the first condition could be reproduced in the 24-well format (in

which the pH and the PEG concentration were varied) – albeit in slightly different conditions: 0.1 M magenisum acetate, 0.1 M MES pH 5.75, 8 & 9.5% (w/v) PEG 10,000. Variation of the drop size, temperature or the magnesium acetate concentration as well as streak seeding did not reduce the number of crystallization nuclei, however, an increase in concentration of both components (from initially 120 µM to 150 µM or higher) led to slightly bigger crystals. One dataset was collected, but a combination of a long cell axis (371 Å), high mosaicity, anisotropy and low resolution prevented further data analysis. Accordingly, molecular replacement attempts with GephE and GephE covering subdomains 1,3 and 4 failed.

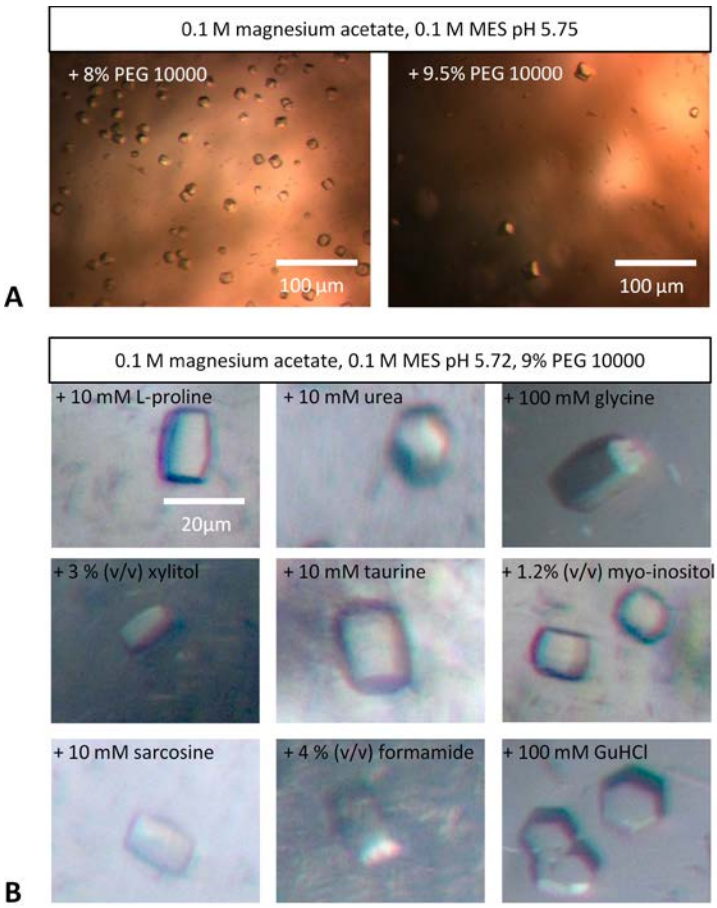

Figure 91 Putative GephE-NL2$_{cyt,sh}$ crystals. (A) Crystals in the 24-well format occurred within three days at room temperature. One of the crystals in the right panel could be used for the data collection summarized in Table 45. (B) Crystals could also be reproduced in 96-well plates with the Hampton research additive screen using various conditions.

Data collection	
wavelength (Å)	0.9795
space group	P 3
a, b, c (Å)	100.1, 100.1, 371.1
α, β, γ (°)	90, 90, 120
resolution (Å)	4.8-39.3
Unique reflections [a]	20295
$\langle I/\sigma(I)\rangle$ [a, b]	7.6 [3.9]
Completeness (%) [a]	99.8 [100]
Redundancy [a,]	5.6 [5.5]
R_{merge} [a,c]	0.18 [0.39]

Table 45 Statistics on the putative GephE-NL2$_{cyt,sh}$ dataset.

[a] Numbers in squared brackets refer to the respective highest resolution data shell in the data set. [b] $\langle I/\sigma(I)\rangle$ stands for the ratio of the average intensity and the correspondig standard deviation. [c] $R_{merge} = \sum_{hkl}\sum_{i=1}|I_i - \langle I\rangle| / \sum_{hkl}\sum_{i=1} I_i$, where I_i is the ith measurement and $\langle I\rangle$ is the weighted mean of all measurements of I.

III.C.2.3 The collybistin-NL2 interaction

Previous results had suggested that gephyrin coexpression with NL2 was not sufficient to trigger gephyrin cluster formation in non-neuronal cells (Poulopoulos *et al.*, 2009). Given the obviously weak stability of the gephyrin-$NL2_{cyt}$ complex, the fact that both proteins can interact with collybistin and that all three proteins were required to induce $GABA_A$ receptor clusters in non-neuronal cells, the original aim was extended to the characterization of the ternary gephyrin-collybistin-NL2 complex. Before the experiments with the ternary complex are presented in section III.C.2.5, this section and section III.C.2.4 deal with the remaining binary complexes.

First attempts aimed at the improvement of the purification of $CB2_{SH3+}$, for which Tolga Soykan provided an established protocol and a GST-$CB2_{SH3+}$ construct. He found that the addition of CHAPS improved the solubility of the protein. To avoid/minimize the usage of detergent, Tolga and I performed a buffer optimization with the Thermofluor method using Tolga's $CB2_{SH3+}$ sample and identified 10% glycerol and 10 mM EDTA as promising buffer ingredients (data not shown). Two difficulties persisted despite the inclusion of glycerol and EDTA: The bad solubility and the fact that collybistin could not be separated from GST and uncleaved GST-collybistin by MonoQ and SEC columns. I then switched the construct and obtained a MBP-$CB2_{SH3+}$ fusion protein. After TEV cleavage, a good separation of $CB2_{SH3+}$ from the MBP tag could be achieved, because MBP at pH 7.5 did not bind to a MonoQ column in contrast to GST at pH 8 (as used in the former protocol). Still, the maximum concentration that could be achieved for this variant, was about 1 mg/mL (data not shown). In the course of this work, my colleague Dr. Daniela Schneeberger generated the $CB2_{SH3+}\Delta C15$ construct in which the C-terminal 15 amino acids have been removed, allowing the protein to be concentrated to more than 10 mg/mL. After that I generated MBP versions of $CB2_{SH3+}\Delta C3$ and $CB2_{SH3+}\Delta C7$ (missing the three and seven C-terminal residues, respectively), but their solubility after cleavage and purification was also limited to about 1 mg/mL (data not shown).

As the $CB2_{SH3+}\Delta C15$ construct was not available in the beginning, the focus shifted to the biochemical characterization of the interaction between $NL2_{cyt}$ and the isolated SH3 domain (a GST-SH3 construct was kindly provided by Tolga Soykan, MPI Göttingen). Another argument was the observation that the typical polyproline binding site of the SH3 domain was partially occluded in the crystal structure of collybistin's close homologue ASEF1.

However, already the first aSEC experiment (using 100 µL 200 µM $NL2_{cyt}$ and 270 µM SH3 domain) argued against a K_D in the low micromolar range (Fig. 92). The only (weak) sign that could be interpreted as a consequence of a binding event, came from a peak shift of the smaller compound, the SH3 domain, which potentially eluted slightly earlier, because it could have been associated with $NL2_{cyt}$ initially, but was separated during the aSEC experiment. However, a peak shift for $NL2_{cyt}$ could not be detected.

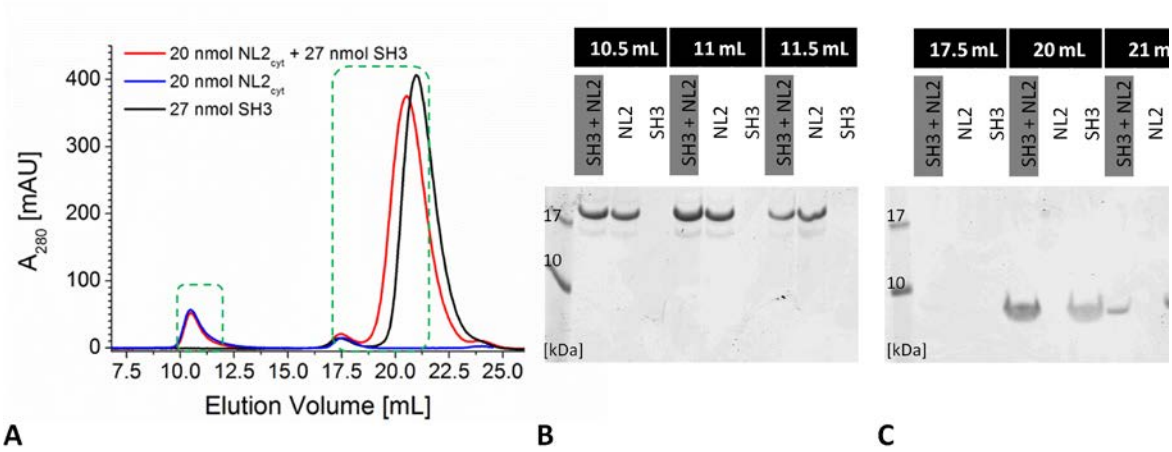

Figure 92 aSEC experiments with the putative NL2cyt-SH3 complex. For this purpose a Superdex 75 column was equilibrated in 20 mM Hepes pH 8, 150 mM NaCl, 1 mM EDTA, 5 mM β-ME. (A) In the corresponding chromatogram the $NL2_{cyt}$ peak at 10.5 mL is not shifted in the presence of the SH3 domain. Note the shift of the SH3 peak at about 20 mL in the presence of $NL2_{cyt}$. (B) & (C) SDS-PAGE analyses of selected fractions marked in green in (A) are in agreement with the chromatogram.

Trials to convincingly visualize an SH3-$NL2_{cyt}$ complex on native PAGE (Fig. 93A) failed, as no third species in addition to the apo-components could be detected. Instead a smearing of the SH3 band was observed in the presence of $NL2_{cyt}$ variants, which did not enter the gel. In native agarose gels, both the $NL2_{cyt}$ band and the SH3 band were shifted towards the gel pocket at concentrations of 50 µM and 30 µM (Fig. 93B). A (single) ITC experiment using 45 µM $NL2_{cyt}$ in the cell and 1.2 mM SH3 domain (Fig. 93C) resulted in a weak heat signature, which could be fitted with an apparent K_D of 39 µM. As no ligand-buffer titration was conducted and the c value was about 1, thermodynamic parameters are not given. All in all the data pointed to a weak stability of the complex under the given conditions.

To obtain a negative control for the binding studies presented above, collybistin's DH-PH tandem was also tested for complex formation with $NL2_{cyt}$, as no binding between these two protein segments has been described so far and as yeast-to-hybrid screens argued against a significant contribution of the tandem to $NL2_{cyt}$ binding. However, on native agarose gels of mixtures of either $CB2_{SH3-}$ or $CB2_{SH3}$-ΔC15 (plasmids were kindly provided by Dr. Daniela Schneeberger) with $NL2_{cyt}$ did not appear as a simple superposition of the single components: The respective CB band was shifted towards the gel pocket and an additional band close to the pocket was observed (Figs. 94A & B).

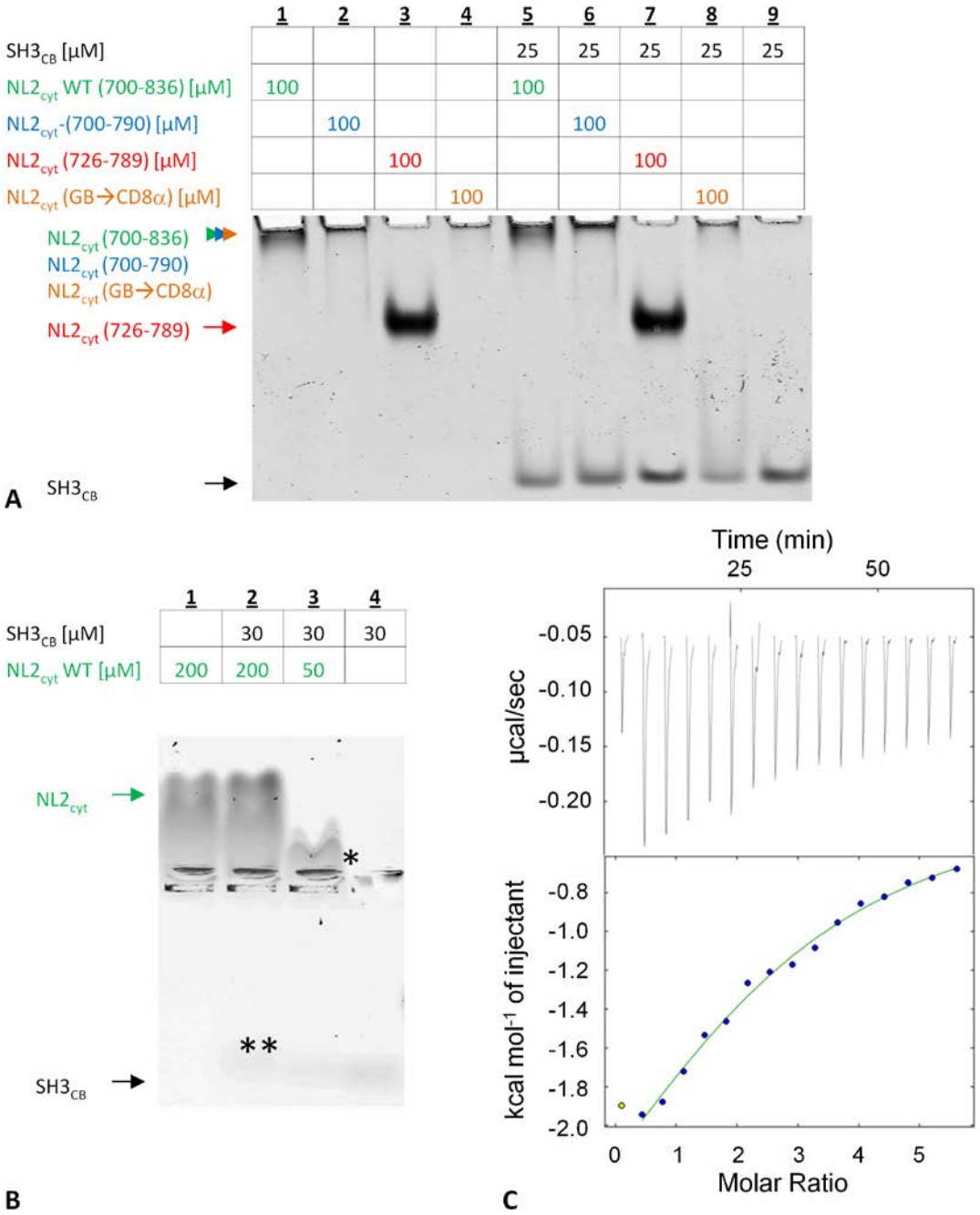

Figure 93 Binding studies of the $SH3_{CB}$-$NL2_{cyt}$ complex. (A) Native PAGE gel (0.4xTBE, 8% acrylamide (acrylamide:bisacrylamide ratio 80:1)), run for 90 minutes at 80 V. Note the smearing of SH3 bands in the presence of non-migrating $NL2_{cyt}$ variants. (B) Native 0.8% agarose gel (0.5x tris/glycine pH 9) run for 170 min at 50 V. Note the clear shift of $NL2_{cyt}$ towards the gel pocket (*) and the gentle shift of the SH3 domain in the presence of $NL2_{cyt}$ (**). (C) ITC experiment conducted in 20 mM Hepes pH 8, 150 mM NaCl, 1 mM EDTA, 1 mM β-ME in an iTC200 calorimeter. The first injection was omitted from the analysis, which was conducted with NITPIC, as with this program a better fit to the experimental data was achieved than with the Origin Software.

As PH-like domains were described to bind to polyproline motifs (Peterson & Volkman, 2009), a construct encompassing the PH domain plus the adjacent part of the stalk (referred to as PH_{stalkC}) was

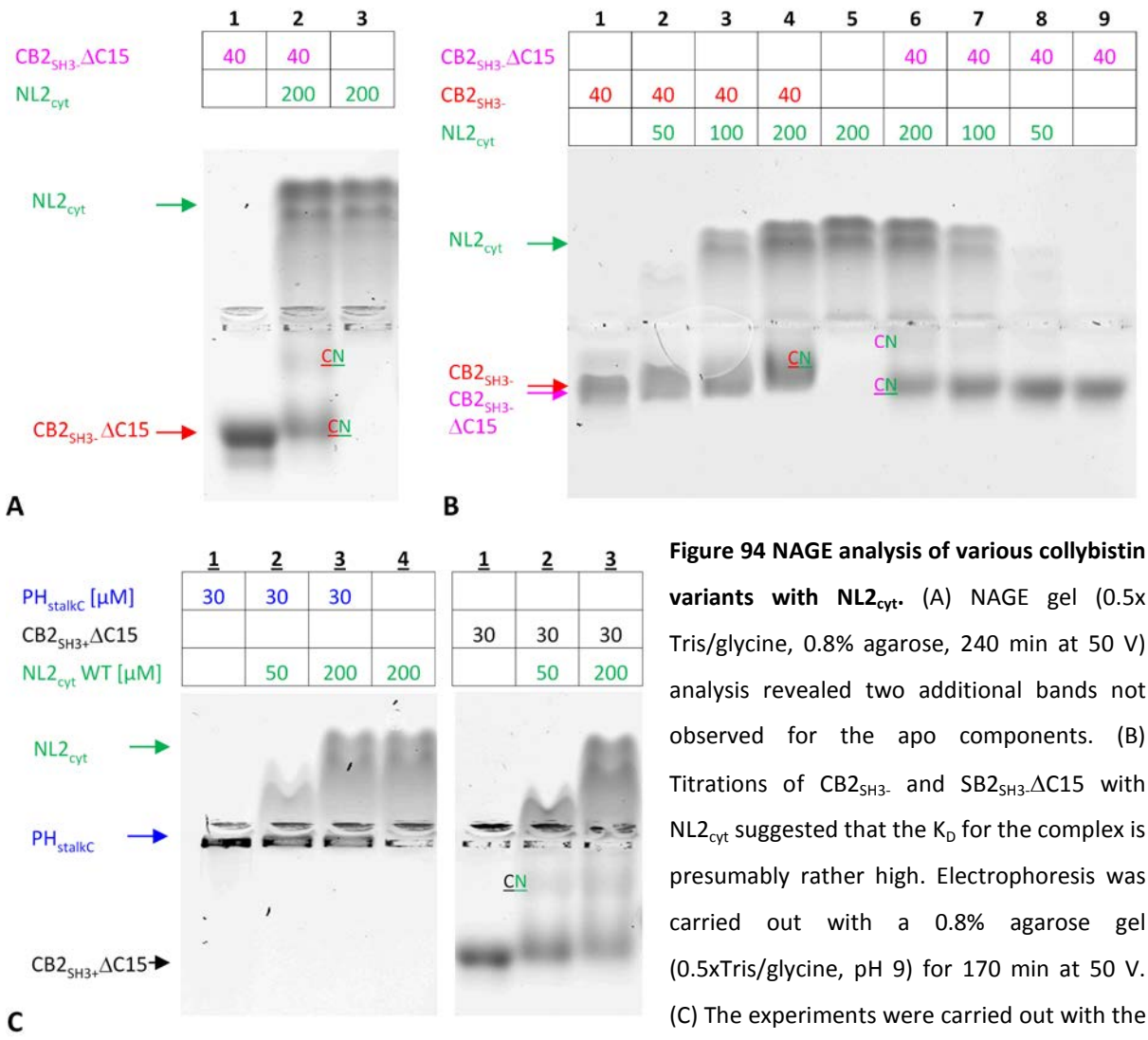

Figure 94 NAGE analysis of various collybistin variants with NL2$_{cyt}$. (A) NAGE gel (0.5x Tris/glycine, 0.8% agarose, 240 min at 50 V) analysis revealed two additional bands not observed for the apo components. (B) Titrations of CB2$_{SH3-}$ and SB2$_{SH3-}$ΔC15 with NL2$_{cyt}$ suggested that the K_D for the complex is presumably rather high. Electrophoresis was carried out with a 0.8% agarose gel (0.5xTris/glycine, pH 9) for 170 min at 50 V. (C) The experiments were carried out with the same NAGE gel as in (A). For PH$_{stalkC}$-NL2$_{cyt}$ mixtures an intensity decrease of PH$_{stalkC}$ was observed, combined with a shift of NL2$_{cyt}$ towards the gel pocket. These two features were also observed for CB2$_{SH3+}$ΔC15, but here an additional band was discernable.

also tested for NL2$_{cyt}$ binding, and this variant behaved similar to the SH3 domain in the presence of NL2$_{cyt}$: The PH$_{stalkC}$ band was slightly shifted out of the pocket, towards the cathode and hence towards NL2$_{cyt}$. In addition, the NL2$_{cyt}$ band in the protein mixture migrated towards the gel pocket (Fig. 94C, lane 2). Similar to what was observed for CB2$_{SH3-}$ΔC15, the mixtures of the SH3-containing variant CB2$_{SH3+}$ΔC15 (the protein was kindly provided by Dr. Daniela Schneeberger) with NL2$_{cyt}$ could not be regarded as a simple superposition of the migration profiles of the individual components, and an additional band formed close to the gel pocket.

In summary, these results argue for a weak interaction of NL2 with collybistin, no matter, whether the isolated SH3 domain, CB2$_{SH3+}$ΔC15 or the DH-PH tandem were tested. Although important controls (especially non-binder mutants) were not included in this work, results at least suggest the possibility of a second NL2 binding site beyond the SH3 domain.

III.C.2.4 The gephyrin-collybistin interaction

In this section the analysis of the third possible binary complex is presented – that of gephyrin and collybistin. The affinity of this complex has remained elusive so far, pointing to the possibility that this complex is not stable as well. Hence, first trials involved native PAGE – initially with gephyrin-$CB2_{SH3+}\Delta C15$ and gephyrin-$CB2_{SH3-}$ mixtures. For gephyrin-$CB2_{SH3+}\Delta C15$ mixtures no complex formation was observed (first three lanes in Fig. 95A). Absent complex formation could have been related to either the presence of the SH3 domain or the lack of the C-terminal 15 amino acids. To explore the former explanation, the experiment was repeated with the $CB2_{SH3-}$ variant. In these experiments, the gephyrin band faded away in the presence of $CB2_{SH3-}$ at the expense of the $CB2_{SH3-}$ band, which became thicker (magenta complex band vs. blue CB band in Fig. 95A). As no additional band became apparent for the Geph-$CB2_{SH3-}$ complex, electrophoresis was prolonged to achieve a better separation. Gephyrin at a concentration of 15 µM was titrated with increasing $CB2_{SH3-}$ concentrations, and the resulting gel displays at least one additional band of the Geph-$CB2_{SH3-}$ complex which was not observed for the individual components (marked in magenta). Between 15 and 30 µM $CB2_{SH3-}$ the gephyrin band intensity became reduced by 50%, pointing to a K_D in this range at least under the given conditions.

To confirm complex formation with a different method, aSEC was conducted, first with the Geph-$CB2_{SH3-}$ complex (Fig. 96). Complex formation could be confirmed by the corresponding SDS-gels (Fig. 96B), however, two signs accounted for a rather modest stability of the complex: First, the gentle shift of the gephyrin peak in the presence of $CB2_{SH3-}$ (only 0.2 mL) and second, the decrease of the

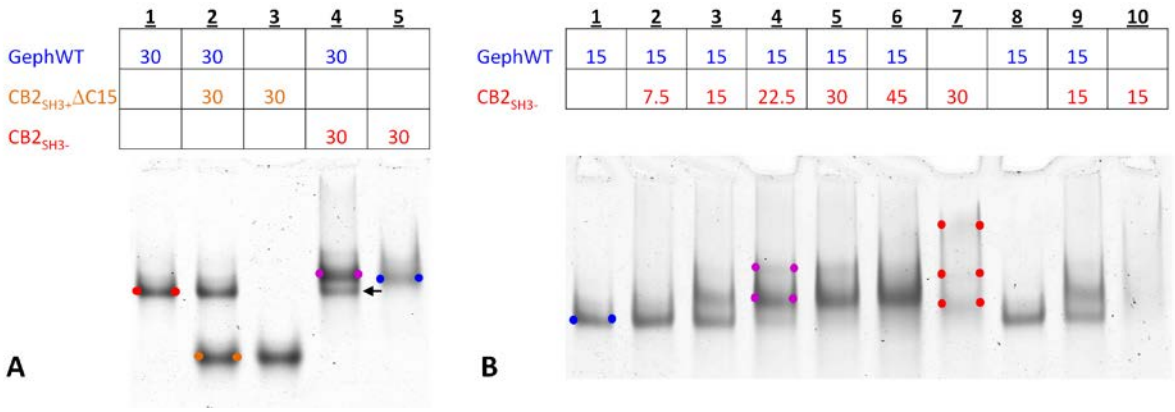

Figure 95 Native PAGE analysis of gephyrin-collybistin complexes. (A) Gephyrin formed a complex with $CB2_{SH3-}$, but not with $CB2_{SH3+}$. Native PAGE with a 3.5% gel (AA/BA=80:1) was conducted in 0.5x Tris/glycine, pH 8.6 for 70 min at 80 V. Dots indicate the apo components and the putative complex (pink). (B) A titration experiment using native PAGE to determine the apparent K_D of the GephWT-$CB2_{SH3-}$ complex was conducted under the same conditions except with a 15 min longer runtime. Note that the apo-gephyrin bands fades away between lanes 3 and 5 (corresponding to 15 µM and 30 µM $CB2_{SH3-}$).

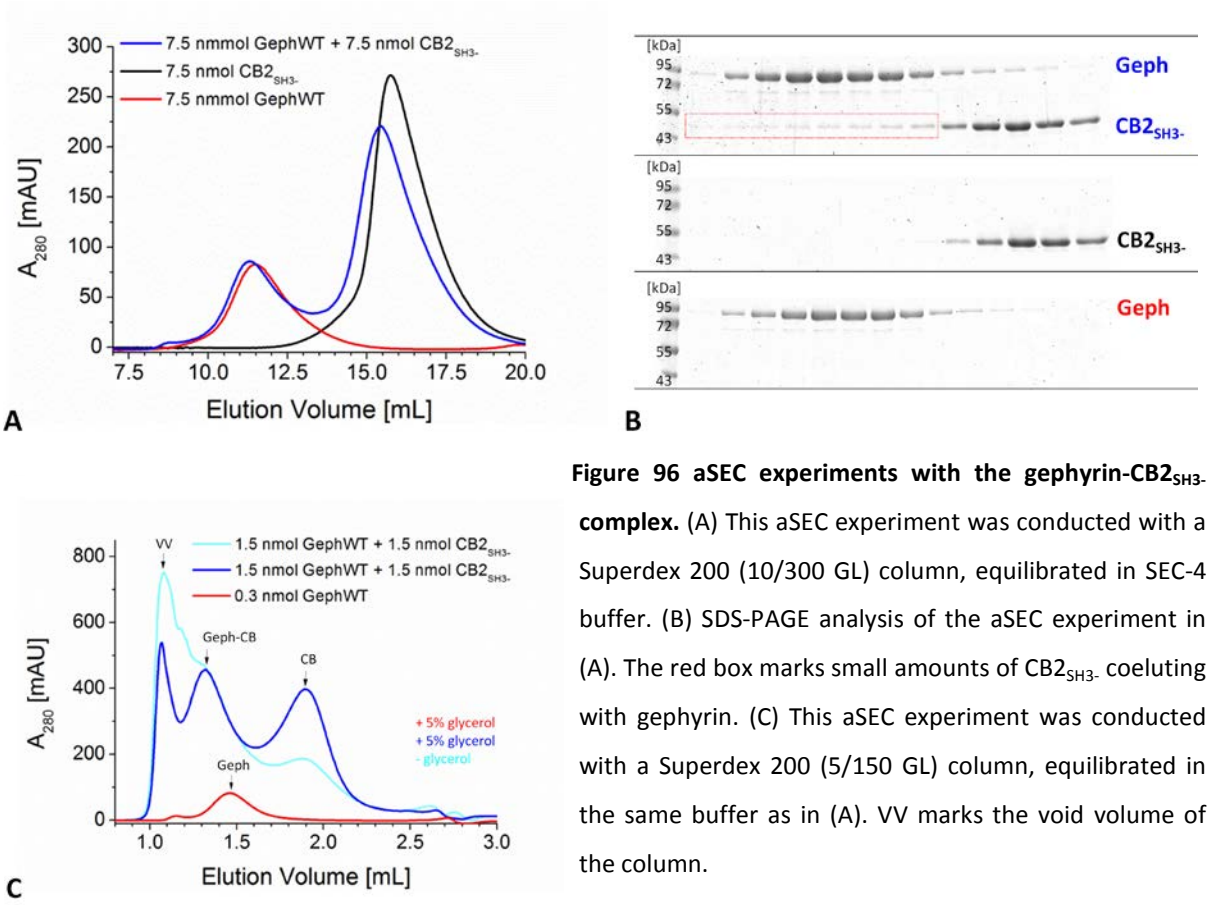

Figure 96 aSEC experiments with the gephyrin-$CB2_{SH3-}$ complex. (A) This aSEC experiment was conducted with a Superdex 200 (10/300 GL) column, equilibrated in SEC-4 buffer. (B) SDS-PAGE analysis of the aSEC experiment in (A). The red box marks small amounts of $CB2_{SH3-}$ coeluting with gephyrin. (C) This aSEC experiment was conducted with a Superdex 200 (5/150 GL) column, equilibrated in the same buffer as in (A). VV marks the void volume of the column.

area under the curve under the $CB2_{SH3-}$ peak, which was in the range of 10-15% (depending on the integration borders). Using the latter value to estimate the degree of complex formation and assuming a simple 1:1 binding model and that the final concentrations of both components were ~3 µM (based on the peak heights), K_D values between 20 and 30 µM appeared quite realistic – in good agreement with the estimation from the native PAGE gels. From these experiments one could conclude that higher concentrations were required to observe stable complex formation. To achieve this aim a smaller aSEC column (Superdex 200 5/150 GL) was used. While initial concentrations of 75 µM were decreased by a factor of ~25 on a Superdex 200 10/300 GL column, for the Superdex 200 5/50 GL only a fivefold dilution was observed. Consequently, complex formation became more apparent than in the case of the Superdex 200 10/300 GL column. The experiments were of preliminary character, because only gephyrin and gephyrin-collybistin-mixtures were investigated and because fractions were not analysed by means of SDS-PAGE gels. Nevertheless, clear peak shifts of 0.15 mL (corresponding to 5% of the column volume) account for complex formation (Fig. 96C). The void volume peak in the gephyrin-collybistin-mixture was more pronounced when the column was not equilibrated in a glycerol-containing buffer. The addition of 5% glycerol attenuated the peak in the void volume, but the putative complex peak was neither shifted nor reduced. Instead the collybistin peak at about 1.9 mL was increased, suggesting that collybistin significantly contributed to

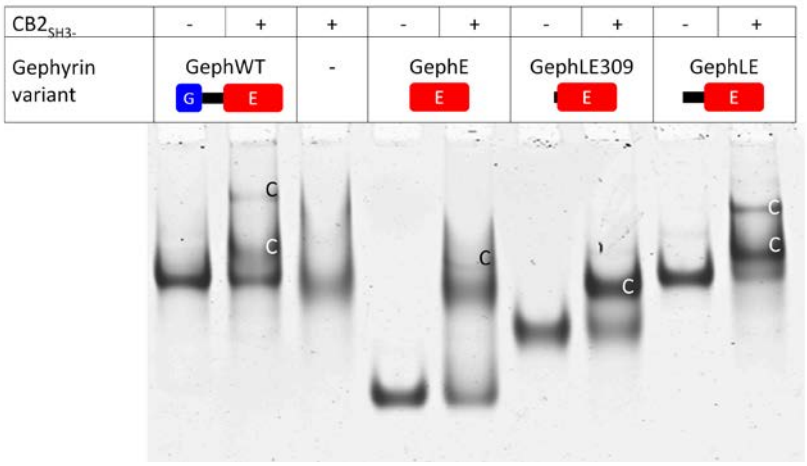

Figure 97 $CB2_{SH3-}$ binding to various GephE containing gephyrin constructs. Note that two putative complex bands were observed only for full-length gephyrin and GephLE. The experiment was conducted with a 4.5% (29:1 AA/BA) polyacrylamide gel in 0.5x Tris/glycine, pH 9 for 90 min at 80 V.

the peak in the void volume in the absence of glycerol. Taken together, although complex formation could be confirmed with aSEC, further analysis was conducted with native PAGE, as the results appeared clearer than those obtained with aSEC.

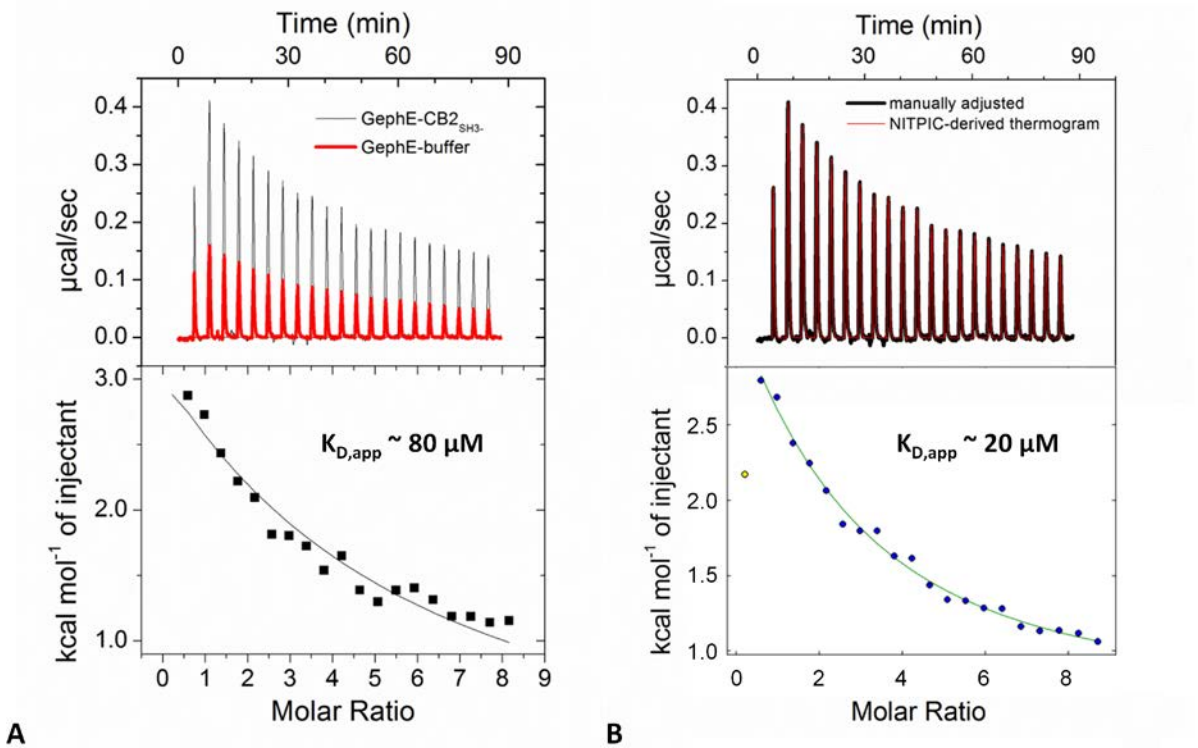

Figure 98 ITC analysis of the gephyrin-collybistin interaction. The shown data correspond to a single ITC experiment, which was conducted in 20 mM Sorensen's buffer pH 8, 200 mM NaCl, 1.25 mM EDTA, 1 mM β-ME, 2.5% glycerol. Isotherms were obtained with Origin (A) or with NITPIC (B). Fits and baseline corrected raw data are displayed in the lower and the upper panels, respectively. The yellow data point in (B) indicates the first injection, which was not considered in the analysis. Note the significant difference between the raw data of GephE-$CB2_{SH3-}$ and GephE-buffer titrations (only displayed in A). The latter titration was subtracted from the protein-protein titration before the fitting procedures. Also note that the thermograms obtained with both programs in the upper panels did not reveal significant differences.

A comparison of various gephyrin variants revealed that GephE was already sufficient to bind to collybistin. For all variants, namely GephWT, GephE, GephLE309 and GephLE, the band faded away in the presence of collybistin, however, only for GephLE and GephWT a second putative complex band was observed. To explore whether the linker is involved in collybistin binding, the K_D of all these gephyrin variants to collybistin should be determined. Hence, an initial ITC experiment was conducted with $CB2_{SH3-}$ and GephE. With a phosphate buffer at 30°C and a collybstin cell concentration as low as 6 µM an endothermic heat signature was obtained, which significantly deviated from the GephE-buffer-titration. Depending on the software used for the isotherm fitting, K_D values of 80 µM (Origin) or 19 µM (NITPIC) were obtained. Due to the low c character of the measurement no thermodynamic parameters are given.

III.C.2.5 The gephyrin-collybistin-NL2 complex

Due to the moderate or weak affinities of the binary complexes, ITC experiments were not a suitable choice to characterize the ternary complex, as the heat signature upon addition of a third component could not be unambiguously assigned to a single process. Hence, the analysis was restricted to aSEC and native gel electrophoresis experiments. aSEC studies were carried out with full-length gephyrin, $CB2_{SH3-}$ and $NL2_{cyt}$. Results from aSEC experiments were in agreement with the results described (Fig. 99). Of all possible binary complexes only the combination of gephyrin-$CB2_{SH3-}$ exhibited signs of complex formation in the chromatogram and on the corresponding SDS-gels. The addition of $NL2_{cyt}$ led to a gentle shift of the gephyrin/gephyrin-$CB2_{SH3-}$ peak but also to an increase of a peak in the void volume. Even if this was a sign of specific complex formation (and not aggregates), the ternary complex of gephyrin, $CB2_{SH3-}$ and $NL2_{cyt}$ was rather unstable at final concentrations of 4 µM collybistin, 4 µM gephyrin and 30 µM $NL2_{cyt}$.

Next, NAGE analyses of potential ternary complexes with the same variants as in the aSEC

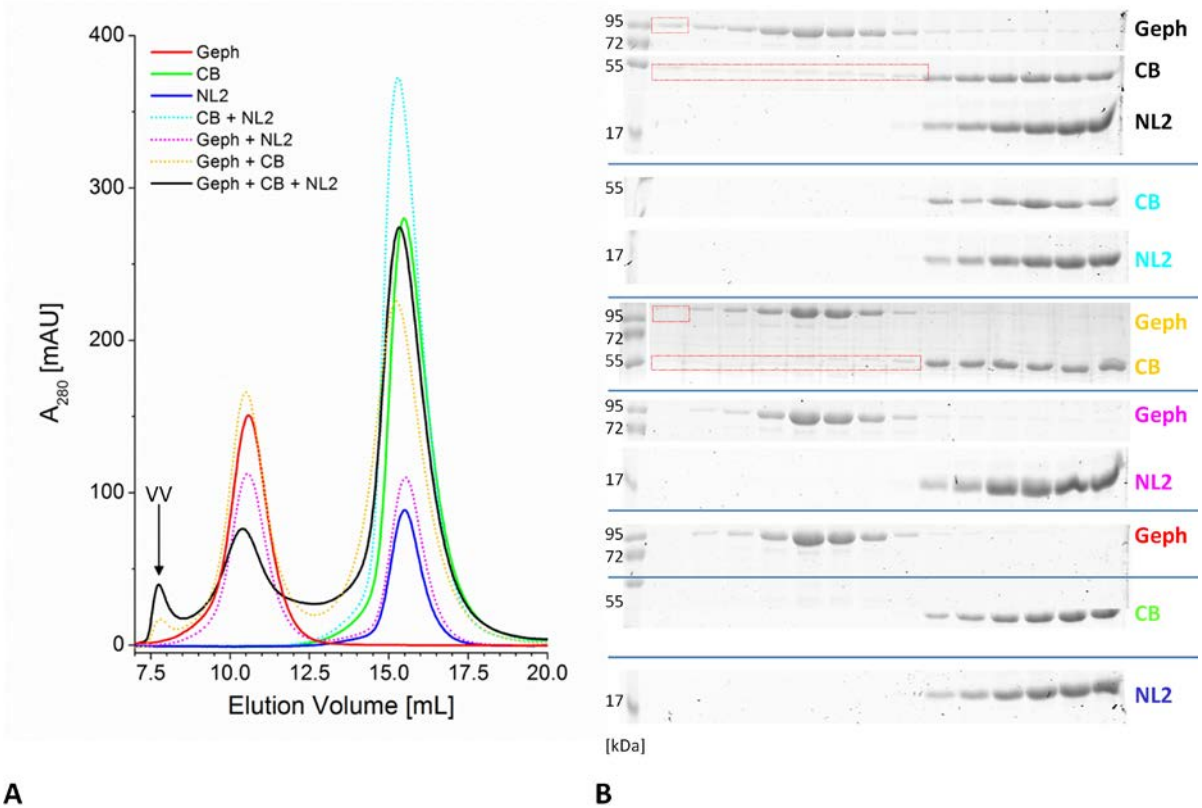

Figure 99 aSEC experiments with the putative gephyrin-$NL2_{cyt}$-$CB2_{SH3-}$ complex. For this purpose a Superdex 200 10/300 GL column was equilibrated with SEC-4 buffer. Mixtures of 100 µL gephyrin, collybistin and $NL2_{cyt}$ were injected at concentrations of 75 µM, 75 µM and 300 µM, respectively. (A) The chromatogram did not reveal significant changes except for minimal alterations in the elution volumes (typically less than 0.1 mL) and a void volume (VV) peak for the putative ternary complex. (B) The corresponding SDS-PAGE gels were in line with the conclusions drawn from the chromatogram. Small deviations for binary and ternary complex experiments in comparison to the single component experiments are highlighted by red boxes.

experiments were carried out (Fig. 100). In addition, $CB2_{SH3-}\Delta C15$ was included. Signs for binary collybistin-$NL2_{cyt}$ complexes could be confirmed, however, gephyrin-collybistin complexes were not mirrored by an additional band, which could be distinguished from the bands of the single components. Rather the collybistin band faded away, and the gephyrin band became thicker. For gephyrin-$NL2_{cyt}$ mixtures a smearing of the gephyrin band towards the gel pocket was observed. A putative ternary complex of GephWT-$CB2_{SH3-}$-$NL2_{cyt}$ exhibited an electrophoretic mobility between those of the $CB2_{SH3-}$-$NL2_{cyt}$ and the putative $CB2_{SH3-}$-gephyrin complexes. If $CB2_{SH3-}$ was replaced by $CB2_{SH3-}\Delta C15$, at least a significant fraction of the putative ternary complex exhibited a migration behavior, which was not observed for the single components and the binary complexes. However, an assay with more significant changes was desirable.

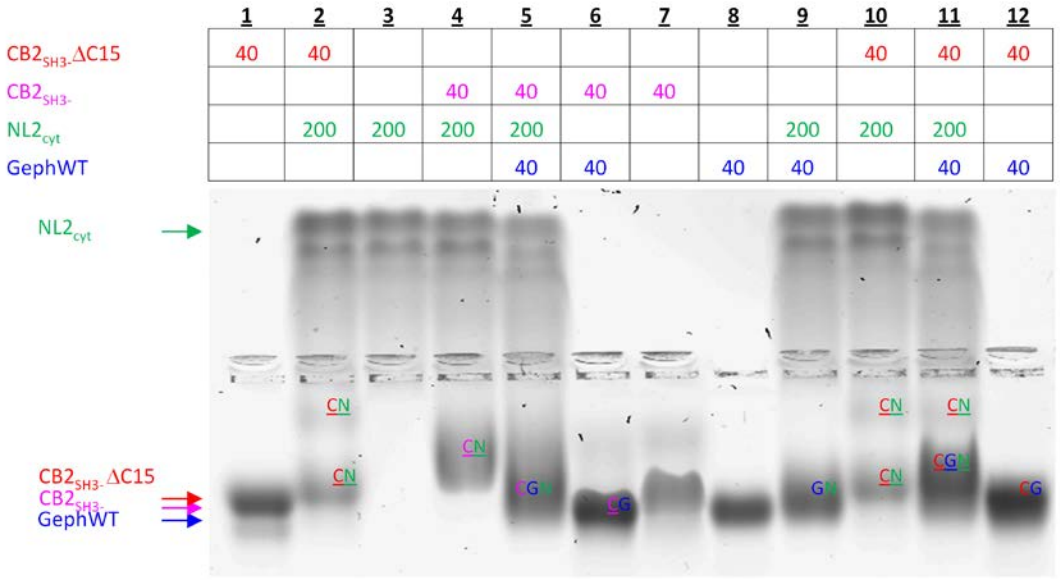

Figure 100 NAGE analysis of gephyrin-collybistin-$NL2_{cyt}$ complexes. The experiment was conducted with a 0.8% agarose gel in 0.5x Tris/glycine buffer, pH 9 for 170 min at 50 V. The first three lanes were already shown in Fig. 94A. Species with migration speeds not observed for the individual components are labeled with the underscored first letters of the corresponding proteins. Additional differences are marked with non-underscored first letters.

Parameters (especially the mesh width) of native PAGE experiments could be improved, so that in contrast to initial experiments now reproducibly additional bands for the putative GephWT-$CB2_{SH3-}$-$NL2_{cyt}$ complex were obtained, which were absent in all other six samples. In these experiments $CB2_{SH3-}$ could also be replaced with the $CB2_{SH3-}\Delta C15$ variant (Fig. 101A). Notably, the complex of GephWT with $CB2_{SH3-}\Delta C15$ migrated slower towards the anode than the complex with $CB2_{SH3-}$ (Fig. 101A, lanes 3 & 9). When wildtype gephyrin was replaced with GephE or when $CB2_{SH3-}\Delta C15$ was replaced with $CB2_{SH3+}\Delta C15$, the amount of the gephyrin-collybistin complex appeared to be reduced, and convincing indications for a ternary complex were not discernable.

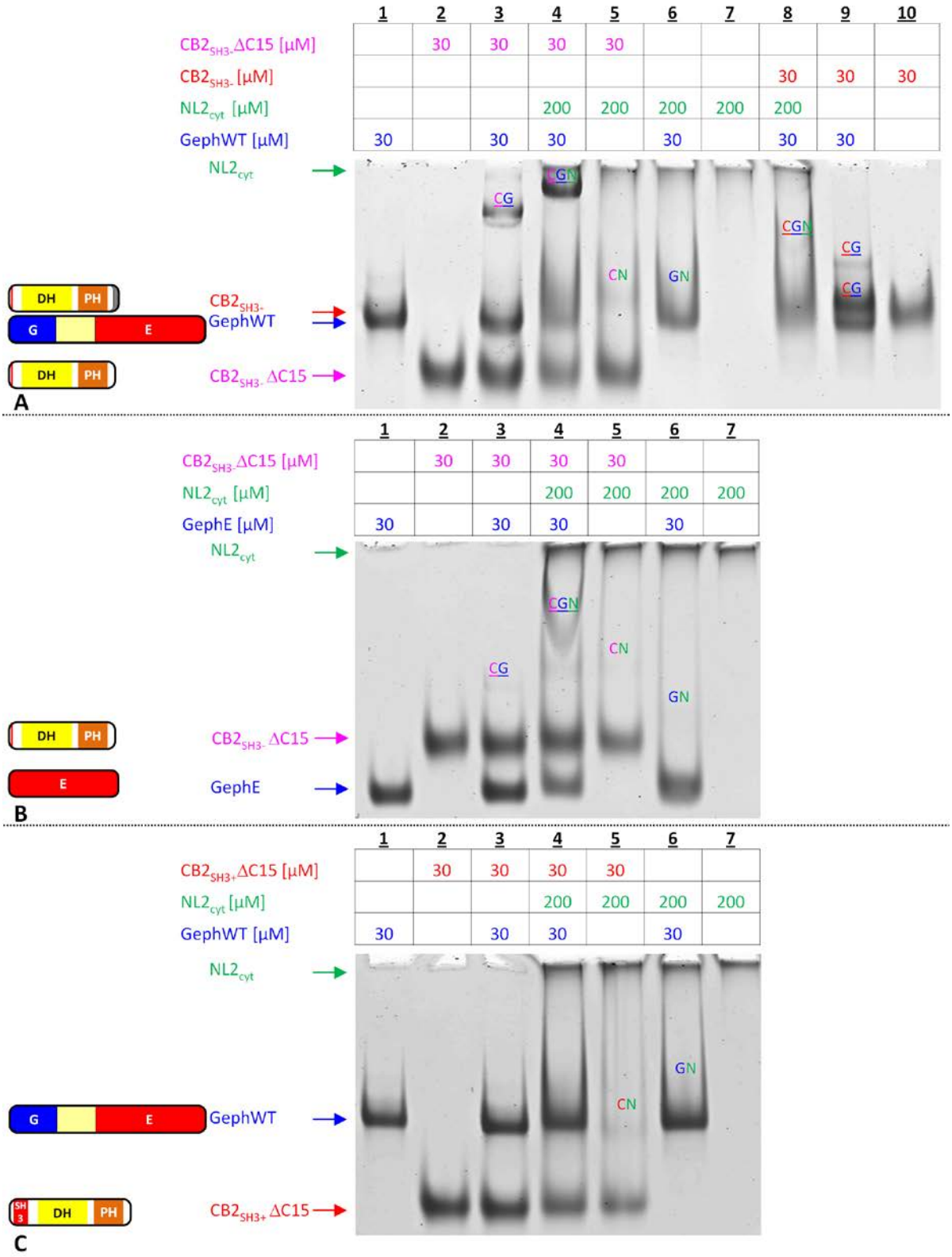

Figure 101 Native PAGE analysis of the putative gephyrin-collybistin-NL2$_{cyt}$ complex at pH 9. Additional bands, absent from the respective controls, are indicated by the initials of the components. Less convincing changes (hardly discernable/smeared bands) are not underscored. Electrophoresis was conducted in 0.5x Tris/glycine with 3.5% PAA gels for 90 minutes at 80 V. (A) The SH3 domain is not required for ternary complex formation. (B) For GephE ternary complex formation is impaired in contrast to GephWT (in A). (C) Under the given conditions the SH3 domain affects complex formation with gephyrin and gephyrin plus NL2$_{cyt}$.

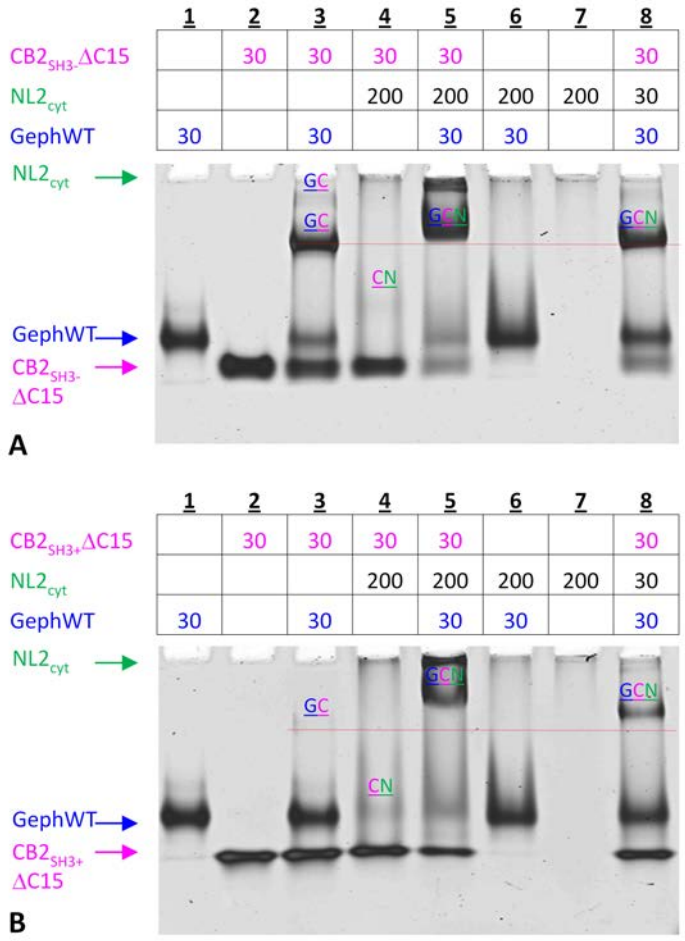

Figure 102 Native PAGE analysis of the putative gephyrin-CB2$_{SH3-}$ΔC15/CB2$_{SH3+}$ΔC15-NL2$_{cyt}$ complex at pH 8. Electrophoresis was conducted in 0.5x Tris/glycine with 3.5% PAA gels for 150 minutes at 55 V. The red lines are adjusted to the center of the predominant gephyrin-collybistin complex band to allow for a distinction with putative ternary complexes in lanes 5 & 8. (A) Binary/ternary complex formation with CB2$_{SH3-}$ΔC15. Note that for the gephyrin-CB2$_{SH3-}$ΔC15 complex at least two putative complex species were observed (lane 3). (B) Despite a rather labile gephyrin-CB2$_{SH3+}$ΔC15 complex (lane 3), the putative ternary complex band is of a thickness comparable to the one obtained in (A). Compare lanes 5 in both gels.

All native PAGE experiments described in this section so far were carried out with 0.5x Tris/glycine, pH 9. The reduction of the pH to a value of 8 changed the situation for the gephyrin-CB2$_{SH3+}$ΔC15 mixture, for which an additional (albeit very thin band) became apparent, and the addition of NL2$_{cyt}$ to this mixture resulted in an additional band, potentially corresponding to the ternary complex. As judged by the thickness of the bands from these initial experiments, also the gephyrin-CB2$_{SH3-}$ΔC15 complex and the gephyrin-CB2$_{SH3-}$ΔC15-NL2$_{cyt}$ complexes appeared to be more stable at pH 8 than at pH 9. Despite the smaller amount of GephWT-collybistin complex in the presence of the SH3 domain, the amount of gephyrin-collybistin-NL2$_{cyt}$ complex was independent of the SH3 domain (judged by the thickness of the band). Putative ternary complexes were obtained in the presence of a huge NL2$_{cyt}$ excess so far (concentration of 200 µM). A decrease to a concentration of 30 µM still led to a shift of the gephyrin-collybistin bands, albeit to a certainly smaller extent than at 200 µM NL2$_{cyt}$, pointing to a moderate stability also of the putative ternary complexes under the given conditions. The bands in or close to the gel pocket (Fig. 102, lanes 5) are not expected to represent aggregates, as the samples were centrifuged before loading. However, it cannot be

excluded that aggregation occurred after loading. Future experiments will be required to clarify this issue.

In summary, a native PAGE assay appeared as the most promising approach to visualize the formation of the postulated gephyrin-collybistin-$NL2_{cyt}$ complexes. Nevertheless, future work should include negative controls and western blot analysis to verify the conclusions presented above.

III.C.3. Discussion

Gephyrin is a central organizer of many glycinergic and GABAergic synapses. The simultaneous utilization of the two oligomerization domains is believed to give rise to higher order oligomers, arranged in a hexagonal scaffold. However, heterologously expressed gephyrin (using *E. coli*) predominantly forms trimers (Herweg & Schwarz, 2012, Sander *et al.*, 2013, Schrader *et al.*, 2004, Sola *et al.*, 2004). The exact triggers for the formation of higher oligomers are not known, but complex formation with interaction partners appeared to be a feasible approach to induce the formation of higher oligomers. Interestingly, most gephyrin binding partners (except for enzymes which presumably interact transiently with gephyrin) do not interact with the long linker, which seems to be predestined for a variety of ligands and has been considered as an autoinhibitory unit for GephE dimerization (Bedet *et al.*, 2006). Rather, most gephyrin binding partners identified so far were shown to bind to GephE. Among these binding partners are the glycine receptor β subunit and various $GABA_A$ receptor subunits, but also the guanine nucleotide exchange factor collybistin (Tretter *et al.*, 2012, Tyagarajan & Fritschy, 2014), which has been regarded as an important gephyrin clustering component for quite some time (Kins *et al.*, 2000).

All collybistin splice variants share the DH-PH tandem, and all except for one, contain an SH3 domain (Harvey *et al.*, 2004). The SH3 domain was shown to mediate autoinhibition of collybistin by intramolecular interactions with the DH-PH tandem (Harvey *et al.*, 2004, Poulopoulos *et al.*, 2009), which were suggested to prevent PI(3)P binding of collybistin and hence its submembraneous localization (Papadopoulos & Soykan, 2011). This hypothesis was substantiated by cell biological and biochemical studies (Drs Tolga Soykan & Daniela Schneeberger *at al.*, unpublished data). Neuron-specific activators, which trigger gephyrin-collybistin membrane targeting, namely NL2 as well as $GABA_AR$ subunit α2 and NL4 (Hoon *et al.*, 2011, Poulopoulos *et al.*, 2009, Saiepour *et al.*, 2010) were identified in cell biological studies. In agreement with the autoinhibition hypothesis, all these activators were shown to bind to the SH3 domain and have been assumed to weaken the SH3-DH/PH interactions. The three activators also interact with gephyrin and were suggested to form ternary complexes that drive the assembly of the postsynatptic density. The ternary complex of gephyrin-collybistin and NL2 is crucially involved in the organization of the postsynaptic clustering of perisomatic $GABA_A$ receptors and was the subject of this chapter. It turned out that the gephyrin-collybistin interaction was the only interaction with at least moderate affinity, while the bipartite binding of $NL2_{cyt}$ with collybistin was considerably weaker, but nevertheless still stronger than the gephyrin-NL2 interaction (Figs. 103, 102B).

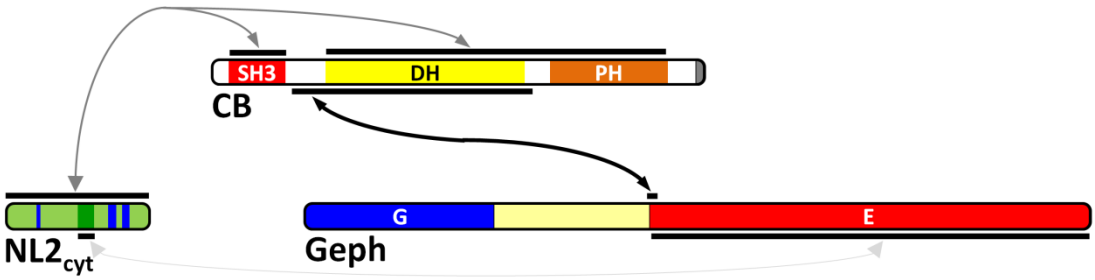

Figure 103 Summary of the relative stabilities of the analysed binary interactions. The grey-to-black gradient and the thickness of the arrows indicate the binding strengths. Gephyrin and collybistin clearly exhibited the highest affinity for each other.

III.C.3.1 Gephyrin-NL2$_{cyt}$

Initially the focus of this project was set on the GephE-NL2 interaction, as it appeared conceivable that a membrane tethering component exhibits an affinity comparable to those obtained for the gephyrin-GlyR (Schrader *et al.*, 2004) and the NL1-PSD95 (Saro *et al.*, 2007) interactions with affinities in the submicro- to low micromolar range. However, such expectations were disappointed. None of the employed methods suggested even a moderate affinity under the tested conditions. For example, pulldown analysis of the gephyrin-NL2$_{cyt}$ complex suffered from conflicting data (Fig. 86). When NL2$_{cyt}$ was coupled to nickel matrices GephE could be pelletted. Vice, versa coupling of GephE to the chitin matrix did not lead to a pulldown of NL2$_{cyt}$, and in pulldown assays with biotinylated NL2-derived peptides the gephyrin signals vanished after more than two wash steps, presumably due to the high K_D.

aSEC experiments also accounted for a low stability of the gephyrin-NL2 complex: Final concentrations of the interaction partners were in the range of 10 to 15 µM at the time of elution, nevertheless, only slight hints at complex formation were obtained (Fig. 87). Attempts to improve the detectability of the complex by using the NusA-NL2$_{cyt}$ fusion protein instead of NL2$_{cyt}$ (with a small extinction coefficient and a small molecular mass) in an aSEC experiment were not successful (data not shown).

Even in native gels (either agarose- or acrylamide-based), in which high protein concentrations (200 µM NL2) were maintained, complex detection was not straightforward (Fig. 90). It should be noted, however, that the typically observed smears of the gephyrin bands in the presence of NL2$_{cyt}$ might well be a, certainly not convincing, hint at complex formation: Compare for example lanes 4 and 8 in Fig. 101. Given that the experiments presented in this thesis suggest that the C-terminal 15 residues of collybistin are presumably not involved in interactions with gephyrin or NL, a less pronounced band need not mean that less complex formation occurred.

In the case of the gephyrin-NL2 interaction one could try to remove segments which do not contribute to binding but affect the migration behaviour of the proteins in the gel. For example, it seems that the removal of residues 700-725 is sufficient to endow NL2 with an overall negative charge so that it can migrate towards the anode like the other proteins (Fig. 93A). Initial binding experiments with gephyrin and the $NL2_{cyt}$-Δ(700-725) variant did not yield positive results (data not shown), however, these experiments were carried out under slightly different conditions, and an extensive improvement of the gel conditions (as it was carried out for the gels showing the putative ternary complexes) has not been performed with this variant yet.

To get a rough estimate of the affinity, several ITC experiments with GephE and $NL2_{cyt}$ were carried out, of which only one yielded an interpretable curve (the measurement using the highest concentrations). The resulting K_D of about 80 µM implies a weak affinity of $NL2_{cyt}$ to gephyrin and might be explained by its predominantly disordered character, which was experimentally verified by means of CD spectroscopy and SAXS analysis. IDRs were often found to bind with low affinity to their binding partners due to entropic costs, which result from disorder-order transitions of the flexible IDRs (London *et al.*, 2010, Uversky *et al.*, 2008). However, there are also examples in which IDRs retain their disorder (Tompa & Fuxreiter, 2008).

Short linear motifs as obviously used in NL2 offer – in analogy with gephyrin's linker – the advantage of potentially harbouring a high number of binding partners in a relatively short sequence. The accessibility of the binding site allows for the regulation of complex formation depending on the posttranslational modification status (Uversky *et al.*, 2008). The likely absence of posttranslational modifications might have provided one explanation for the low affinity. However, cell biological studies of gephyrin and NL2 in HEK293T cells argue against this possibility: In only less than 20% of the analysed cells colocalization was observed (Poulopoulos, 2008). These observations are in line with CoIP experiments of our collaboration partner, for which a crosslinker was required to achieve a convincing confirmation of the interaction which was identified in yeast two-hybrid screens (Poulopoulos *et al.*, 2009).

To identify possible interaction sites, crosslinking experiments were conducted with gephyrin (preferentially GephE) and $NL2_{cyt}$, also including the non-binder variants Y770A (Fig. 89) and NL2(GB→CD8α). However, there were only slight differences between GephE-$NL2_{cyt}$ wildtype and GephE-$NL2_{cyt}$ non-binder mutant mixtures. In the course of this work a publication described that crosslinking experiments with low affinity complexes (K_D > 25 µM) can lead to unspecific adduct formation, rendering crosslinking at least questionable in terms of K_D estimation (Madler *et al.*, 2010). As MS analysis did not lead to the identification of the gephyrin-$NL2_{cyt}$ interface (despite the use of equimolar mixtures of deuterated and non-deuterated crosslinker), the crosslinking method was abandoned.

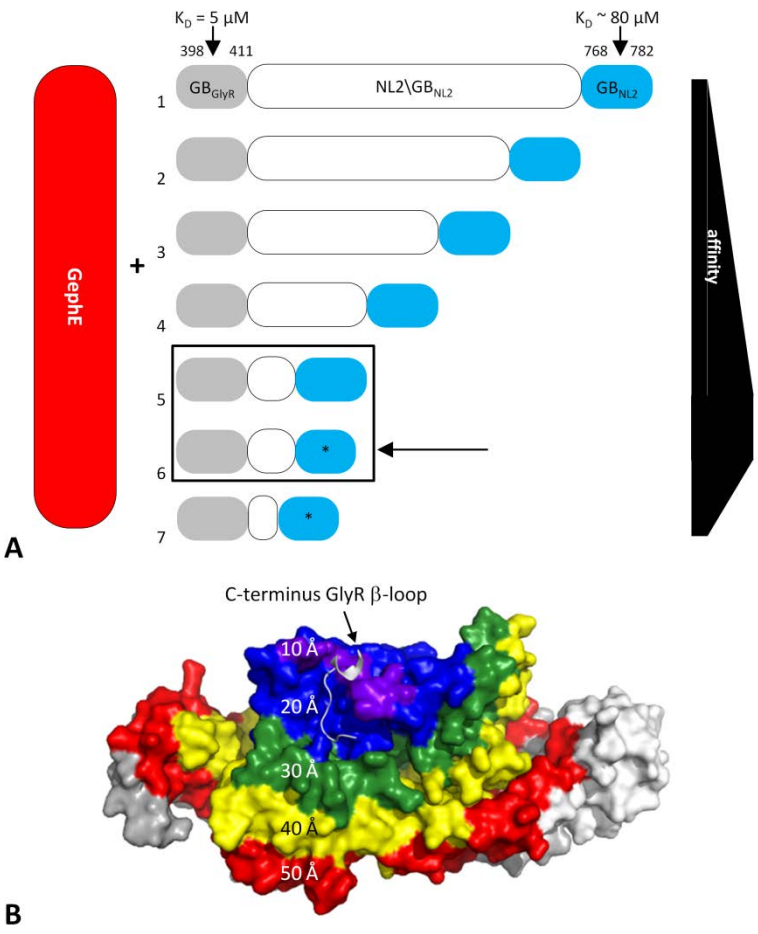

Figure 104 How a GB$_{GlyR}$-GB$_{NL2}$ fusion protein might help to identify the NL2 binding site in GephE. (A) Fusion proteins 1-7 encompass the GB$_{GlyR}$ sequence extended by NL2$_{cyt}$, where only the NL2$_{cyt}$ segment (GB$_{NL2}$, coloured in cyan) is expected to bind to gephyrin. The preceding NL2$_{cyt}$ segment (NL2\GB$_{NL2}$) can be considered as a (non-binding) ruler. Too long or too short rulers might still exhibit an increased affinity in comparison with GB$_{GlyR}$, but in this example constructs 5&6 would have the optimal affinity. The shorter GB$_{NL2}$ motif (*) still exhibits the same affinity as GB$_{NL2}$. (B) The length of the NL2\GB$_{NL2}$ segment yields a rough estimate of the distance between the C-terminus of the GlyR β-loop and the N-terminus of GB$_{NL2}$.

To pinpoint the NL2 binding site in gephyrin, one might use the GephEΔSD2 construct (missing subdomain 2, as suggested in section III.A.3.8. Alternatively one could try to identify the NL2 binding site in GephE via ITC analysis of the GephE binding to a GlyR-β-loop-NL2cyt fusion protein (Fig. 104). Residues 398-411 of the GlyR (referred to as GB$_{GlyR}$) bind to GephE with a K$_D$ of 5 µM (Maric, 2012). The addition of the a second gephyrin binding site, namely that of NL2 (GB$_{NL2}$), is expected to increase the affinity due to avidity effects, if the linker between both motifs possesses an appropriate length. Hence, one could append NL2$_{cyt}$ (residues 700-782 encompassing the gephyrin binding motif (residues 768-782)) to GB$_{GlyR}$ and shorten the linker, until its length is not sufficient anymore to bridge the distance between the C-terminus of the GlyR β-loop and the N-terminus of the gephyrin binding motif (referred to as d$_{GlyR-NL2}$) and the affinity drops to the level of the sole GlyR β-loop. These data can be used to deduce a rough estimate of d$_{GlyR-NL2}$ (Fig. 104) because the N-terminus of GB$_{NL2}$ could be pinpointed quite precisely: In yeast two-hybrid screens the P768A mutation did not abolish binding to gephyrin, whereas an replacement of Tyr770 with alanine was sufficient to abrogate the interaction with gephyrin (Poulopoulos, 2008). The knowledge of d$_{GlyR-NL2}$ in turn might help to narrow down the NL2 binding site in gephyrin. Site-directed mutagenesis of candidate amino acids in GephE matching to the distance restraints might yield residues involved in the interaction. Beyond

that the GlyR-NL2 fusion protein with the highest affinity could be used for crystallization experiments.

III.C.3.2 Collybistin-NL2$_{cyt}$

As NL2 is an activator of collybistin, the assumption of a reasonable affinity appeared to be feasible. First the focus was set on the SH3 domain, as the disturbance of the intramolecular SH3 interface with the DH-PH tandem is thought to be responsible for collybistin activation (Drs. Soykan & Schneeberger *et al.*, unpublished data) and as NL2$_{cyt}$ harbours several SH3 binding motifs (Fig. 80). However, also this interaction is of transient character: aSEC experiments, in which final concentrations of ~15 µM were reached, did not show signs of stable complex formation, and other binding experiments such as native gels and ITC likewise pointed to a weak interaction (Fig. 93). Also for the CB2$_{SH3+}$ΔC15 variant only signs of weak binding were obtained in native gels (e.g. Fig. 102B). Surprisingly, the DH-PH tandem (either containing the C-terminus or not) appeared to exhibit an affinity for NL2$_{cyt}$ as well (Fig. 94) in contrast to Yeast two-hybrid screens with CB2$_{SH3-}$ and NL2, which argued against this interaction (Soykan, 2011).

Although it remains to be determined whether the DH or the PH domain binds to NL2, NL2 binding to the PH domain appears feasible, as this domain is an interaction module like the SH3 domain (Scheffzek & Welti, 2012), and proline-rich motifs (PRMs) can bind to domains of the PH-superfamily members EVH1, WASP and Homer (Peterson & Volkman, 2009). However, there is no obvious PRM binding site in the PH domain, which resembles those of previously determined proline binding pockets (Ball *et al.*, 2005, Peterson & Volkman, 2009). Of course, this does not exclude that an unusual binding pocket in the PH domain is used or other non-proline-rich motifs mediate this interaction.

The identification of the DH-PH tandem as a second NL2 binding site mirrored the observation that the large intracellular GABA$_A$ receptor M3-M4 loops did not bind to CB2$_{SH3-}$ΔC15 but CB2$_{SH3-}$ (Dr. Daniela Schneeberger, personal communication), thus implying an involvement of either the C-terminus of collybistin and/or the PH domain in GABA$_A$ receptor clustering and hence a binding mode different from that of NL2. This also suggested that both activators, GABA$_A$ receptors and NL2, would make use of two recognition sites in collybistin. Hence it appears feasible that the second, SH3 domain independent binding site also contributes to the activation of collybistin.

For example our collaboration partner Dr. Tolga Soykan observed an enhanced PI(3)P affinity of CB2$_{SH3+}$ in the presence of recombinant NL2$_{cyt}$ (purified according to the protocol presented in section III.C.2.1.2) in lipid overlay assays (Soykan, 2011). Maybe NL2 binding to the PH domain resulted in rearrangements in the proximity of the PI(3)P binding site: In line with this assumption the CB2$_{SH3+}$(W24A/E262A) variant, in which the SH3 domain is by and large decoupled from the rest of collybistin, displayed a better binding than the wildtype but still a worse binding than CB2$_{SH3-}$. This

might be result of an incomplete decoupling of the SH3 domain from the DH-PH tandem (Drs. Soykan & Schneeberger *et al.*, unpublished data) or point to the possibility that factor other than SH3 interactions with the DH-PH tandem play a role – for example a potential NL2 interaction with collybistin's PH domain.

In another scenario the two NL2 binding sites are in such close proximity that the SH3 domain and the PH domain are arranged like two beads on a short string (Fig. 105). Depending on where the NL2 binding site resides in the PH domain, the SH3 domain could be torn apart from the DH-PH tandem, thereby releasing the PI(3)P binding site in the PH domain.

Unpublished data of our collaboration partner suggested that collybistin binding occurs via the proline-rich tail of $NL2_{cyt}$: The removal of residues beyond P798 prevented NL2 from binding to $CB2_{SH3+}$ in Yeast two-hybrid assays (Soykan, 2011). However, based on the observation of the second NL2 binding site in collybistin, one cannot necessarily exclude that there is no second collybistin binding site in NL2 upstream of residue 798 (compare with Fig. 80). Nevertheless, abolished binding to NL2(798term) is interesting with respect to two mutations: First, in one of the two proline clusters beyond residue 797 the P800L mutant was reported in a patient with schizophrenia (Sun *et al.*, 2011a); a second mutation in NL2 also related to schizophrenia (A819S) occurred in close proximity to the second proline-rich cluster (Sun *et al.*, 2011a). These issues underscore the need to unveil which domain/segments of collybistin and NL2 are exactly involved in this interaction.

III.C.3.3 The gephyrin-collybistin binding is stronger than that of the other binary complexes and appears to be regulated by the SH3 domain

Although the gephyrin-collybistin interaction was the only binary interaction for which aSEC results (at even lower concentrations than the other binary complexes) displayed signs of complex formation (section III.C.2.4), this interaction cannot be considered as strong as well. This view receives support from an ITC experiment, which pointed to a moderate affinity of GephE to $CB2_{SH3-}$ (K_D ~20 µM) but needs to be repeated at higher concentrations (Fig. 98). Along this line, a K_D estimate based on a native PAGE gel, also accounts for a K_D in the same range (Fig. 95B).

As for the gephyrin-collybistin interface, native PAGE assays argued against a direct involvement of collybistin's C-terminus, since $CB2_{SH3-}$ and $CB2_{SH3-}\Delta C15$ both exhibited gephyrin binding with non-detectable differences. However, the gephyrin-collybistin interaction appeared to be more stable in the absence of the SH3 domain (Fig. 95A). This observation certainly requires further support, e.g. by using alternative binding assays such as aSEC, ITC or the analysis of potential gephyrin-$CB2_{SH3+}\Delta C15$(E262A/W24A) complexes. SH3 domain mediated autoinhibition is affected in the E262A mutant (Drs. Tolga Soykan and Daniela Schneeberger *et al.*, unpublished data), and therefore also the potential gephyrin binding site could be unlocked. A change in pH from 9 to 8 resulted in an at least

detectable binding signal for the $CB2_{SH3+}\Delta C15$-gephyrin complex, but still not as convincing as for the $SH3^-$ variant (Fig. 102). This was not expected, as in non-neuronal cells SH3-containing collybistin variants are typically recruited to cytosolic gephyrin aggregates (Harvey *et al.*, 2004), suggesting that the gephyrin-collybistin interaction is – at least in a cellular context – not affected by the SH3 domain. The conflicting results on the role of the SH3 domain in gephyrin binding can be reconciled with posttranslational modifications, which can be conducted in mammalian cells but are untypical for proteins heterologously expressed in *E. coli*.

Such a post-translational modification would not be the only hint at a role of gephyrin's linker in collybistin binding: First, only for full-length gephyrin and GephLE two putative complex bands could be observed but not for GephE and GephE with 23 residues of the linker (GephLE309) (Fig. 97); second, in preliminary native PAGE experiments Geph-MLH2 exhibited an apparently lower affinity to $CB2_{SH3-}$, although complex formation was clearly detected for full-length gephyrin on the same gels (preliminary data in Appendix G).

Although preliminary experiments on the phosphomimetic gephyrin mutants presented in section III.A.2.6 did not exhibit differential collybistin binding (data not shown), there is still the chance, that one (or more) of the more than 20 remaining phosphorylation sites is involved in collybistin binding, among them Thr276 and Ser277. In hippocampal neurons expression of gephyrin variants, in which both residues were mutated to alanine, led to a reduced number of gephyrin puncta and large (presumably cytosolic) aggregates (Kuhse *et al.*, 2012), whose distribution was reminiscent of that obtained upon coexpression with collybistin lacking the PH domain (Tyagarajan *et al.*, 2011a). Although the corresponding collybistin localization was not provided in this study, residues 276 and 277 might be involved in the interaction with collybistin (Kuhse *et al.*, 2012). In the same publication it was also shown that collybistin triggers gephyrin phosphorylation in the second half of the linker at residue 270 (Kuhse *et al.*, 2012). A further hint for an involvement of gephyrin's linker in collybistin binding came from a pulldown analysis with gephyrin and GephE as baits and collybistin expressed in HEK293 cells as prey (Tyagarajan *et al.*, 2011a).

As for the gephyrin binding site in collybistin, the literature argues for a crucial role of the DH domain, as only the removal of the DH domain, but not of the PH or the SH3 domain, prevented collybistin's colocalization with gephyrin in neurons and HEK293 cells, respectively (Harvey *et al.*, 2004). In line with that, in initial native PAGE experiments no binding between full-length gephyrin and the SH3 domain was observed (data not shown), whereas gephyrin bound to the DH-PH tandem. Other, unpublished results should be considered for the identification of the gephyrin-collybistin interface as well: Our collaborators found that ASEF1 cannot bind to gephyrin despite the fact that collybistin and ASEF share 60% identity on the protein level (Soykan, 2011). Hence, they created chimeric constructs of which only domain swap 1, in which residues 30-130 of collybistin were

replaced with the corresponding ASEF1 residues, resulted in an abolished binding of gephyrin (Soykan, 2011) (Fig. 105). The majority of differences between ASEF and collybistin occur in the SH3 domain (which presumably does not provide a binding site for gephyrin, see above) and the linker connecting the SH3 and the DH domain (where 25 of 37 residues are different to that of ASEF1). Hence, this linker was suggested to be involved in gephyrin binding (Soykan, 2011).

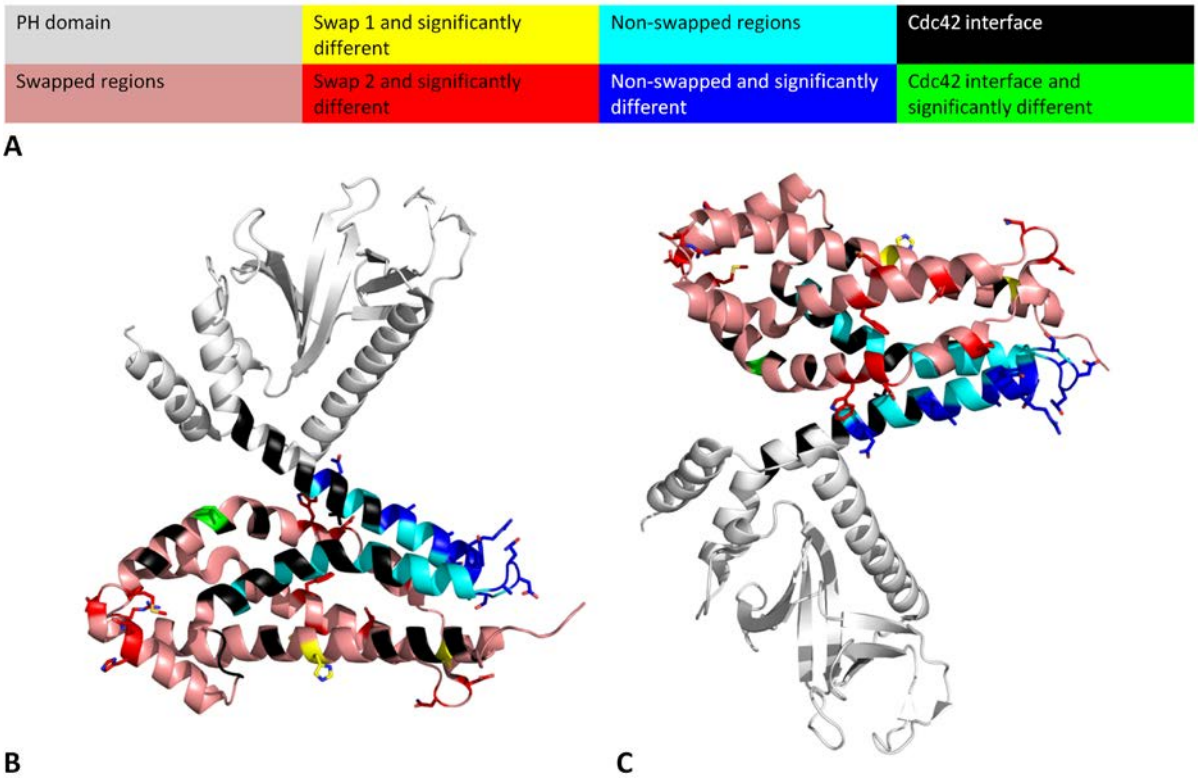

Figure 105 Analysis of collybistin-ASEF1 domain swap experiments, carried out by Dr. Tolga Soykan. (A) Color code which applies to the ribbon diagrams in (B) and (C). (B) $CB2_{SH3-}$ model (PDB entry: 2DFK), in which swapped and non-swapped regions are marked together with the Cdc42 interface. Residues significantly differing from those in ASEF1 are highlighted according to the colour code presented in (A).

Beyond the aforementioned differences between collybistin and ASEF1 in the swap 1 mutant, also two residues of the DH domain were exchanged for their ASEF counterparts (A112 & H124) in the non-binder swap mutant. Therefore, binding could be mediated exclusively by the DH domain. However, a look at the localization of these residues in the collybistin structure (PDB entry 2DFK) reveals that these two residues are surrounded by residues which are either similar in both proteins (salmon in Fig. 105) or whose replacement with the ASEF counterparts did not affect gephyrin binding capacity (red), arguing rather for an important role of the SH3-DH linker. On the other hand, the assumption that the linker contains the complete gephyrin binding motif would intuitively fail to explain reduced GEF activity of $CB2_{SH3-}$ in the presence of gephyrin (Xiang *et al.*, 2006), unless the obviously flexible apo-SH3-DH loop would be constricted in its flexibility, so that gephyrin would exhibit a higher tendency to overlap with an incoming Cdc42. In addition, not the complete DH

domain was analysed in the mentioned swap experiments (Soykan, 2011). Residues which were not swapped and not similar to ASEF counterparts cluster in the stalk (α6) and the preceding α5- α6 linker (Fig. 105).

To identify the gephyrin binding site in collybistin, collybistin variants that either (1) miss the linker between the SH3 domain and the DH domain, or (2) are mutated at positions A112 and H124, or (3) miss the stalk which connects the DH and the PH domains should be tested for gephyrin binding in native PAGE and ITC experiments. With either collybistin variant hopefully higher protein concentrations will be obtained than achieved so far with $CB2_{SH3-}$, which was so far prone to aggregation in dialysis units. For the reproduction of the positive control, the GephE(+linker)-$CB2_{SH3-}$ experiment, SEC instead of dialysis (to achieve buffer exchange) is a valid alternative.

ITC experiments might also allow for a further refinement of the binding buffer, which might in turn allow for a characterization with at least a Superdex 200 5/150 GL column, paving the way for an alternative to native gel analysis, which would also be useful for higher order complexes containing the gephyrin-collybistin complex. The use of $CB2_{SH3-}$ΔC15 or even shorter variants terminating after the DH domain is expected to reduce the amount of aggregated collybistin.

III.C.3.4 The first steps towards the characterization of the moderately stable ternary gephyrin-collybistin-NL2 complex

Weak binary interactions might be potentiated in the context of a higher order protein complex. Attempts to obtain a ternary complex involved full-length gephyrin, $CB2_{SH3-}$(ΔC15) and $NL2_{cyt}$, for the following reasons:

- $NL2_{cyt}$ bound to collybistin in the absence of the SH3 domain (Fig. 94). As $CB2_{SH3-}$ was not preferred over $CB2_{SH3-}$ΔC15, in subsequent experiments the latter collybistin variant was used.
- GephE and Geph-MLH2 appeared to have a weaker affinity to $CB2_{SH3-}$ than full-length gephyrin (Fig. 97 and Appendix G).
- Full-length gephyrin did not bind to $CB2_{SH3+}$ΔC15.

The choice of these proteins appeared to be additionally justified by the observations that the replacements of full-length gephyrin with GephE and of $CB2_{SH3-}$ΔC15 with $CB2_{SH3+}$ΔC15 led to lower detectable levels of a band, which was not observed in the other six samples (containing the individual components or binary complexes) and was therefore considered to represent the ternary complex (Fig. 101). The exact composition of this species, however, should be verified by Western blot analysis.

Notably, a pH decrease from 9 to 8 presumably increased the fraction of ternary complex made up of full-length gephyrin, $CB2_{SH3+}$ΔC15 and $NL2_{cyt}$. (Fig. 101 & Fig. 102). It appears rather unlikely,

that this is just due to the slightly higher affinity of gephyrin for $CB2_{SH3+}\Delta C15$ at pH 8 or a (potentially) better stability of the gephyrin-NL2 complex: $CB2_{SH3-}\Delta C15$ could contribute to a ternary complex even at pH 9 (Fig. 101), and there were no signs for a dramatically altered gephyrin-NL2 stability. The most likely explanation is that the SH3 domain provides an additional NL2 binding site in $CB2_{SH3+}\Delta C15$ (when compared with $CB2_{SH3-}\Delta C15$). Bipartite binding might facilitate $NL2_{cyt}$ association in the SH3 containing variant and might (partially) compensate for the SH3 domain inferred attenuation of gephyrin binding capacity. As a consequence of NL2 binding the orientation of the SH3 domain might be altered, so that the addition of gephyrin to the complex is possible (Fig. 106B). Vice versa, in ternary complex formation involving $CB2_{SH3-}$ presumably the gephyrin-collybistin association could be the crucial first step. The gephyrin-collybistin complex now offers two binding sites for NL2 instead of one, so that avidity effects favour NL2 binding (Fig. 106A).

Beyond a potential contribution of a second NL2 binding site in gephyrin there is a second aspect of the aforementioned collybistin activation model that might be worth considering: Should the SH3

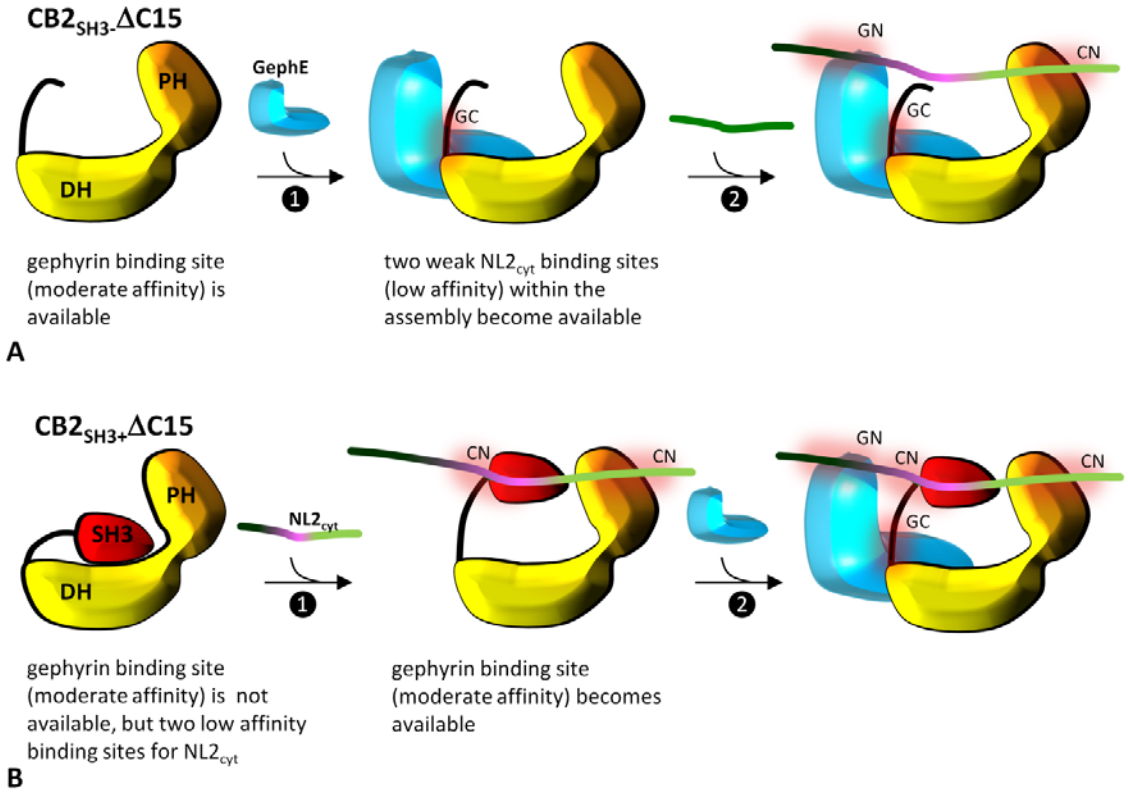

Figure 106 Hypotheses for ternary complex formation involving $CB2_{SH3-}\Delta C15$ and $CB2_{SH3+}\Delta C15$. This model is speculative, as the order of the three NL2 binding sites remains to be deciphered as well as the exact interfaces of the binary complexes. (A) For $CB2_{SH3-}$ gephyrin binding is presumably the first step in ternary complex formation, as this process is driven by a higher affinity than the $CB2_{SH3-}$-NL2 association. (B) For $CB2_{SH3+}$ presumably $NL2_{cyt}$ binding precedes gephyrin association. If the two collybistin-NL2 interfaces are in close proximity, this might drive the exposure of the gephyrin binding site.

domain interference with gephyrin binding be substantiated, the current model of the gephyrin-collybistin complex in $GABA_A$ receptor clustering might require a slight refinement: So far it has been assumed that gephyrin and collybistin are associated with each other during transport (Papadopoulos & Soykan, 2011). As collybistin predominantly contains an SH3 domain *in vivo* (Harvey *et al.*, 2004) and as activation has been suggested to occur at nucleation sites containing activators like NL2 (Papadopoulos & Soykan, 2011), an incoming gephyrin-collybistin complex (if it exists at all) would either require an additional trigger (which e.g. could unlock the gephyrin binding site in collybistin, see also III.C.2.4) before NL2 mediates membrane anchoring activates collybistin in terms of membrane targeting, or NL2 activates collybistin prior to the arrival at the membrane. The latter scenario appears rather unlikely, as NL2 localization to the membrane is independent of gephyrin and collybistin and is therefore expected to occur before the arrival of gephyrin and collybistin (O'Sullivan *et al.*, 2009, Patrizi *et al.*, 2008, Poulopoulos *et al.*, 2009).

The experiments presented in this thesis are starting points to hopefully extend our understanding of NL/collybistin triggered gephyrin clustering. The improvement of binding conditions of the binary complexes is one of the major goals to achieve crystallization of the ternary complex. With the gephyrin-collybistin complex there is at least one such complex, whose characterization is within reach. NL2 certainly offers opportunities for optimization as well: An N- and C-terminally truncated NL2 peptide could potentially facilitate crystallization. Native PAGE assays will help to narrow down the segment essential for ternary complex formation. Should crystallization of both ternary complexes (involving either collybistin with or without SH3 domain) fail, structural characterization of binary complexes would still be rewarding. The low affinity binding of NL2 binding to collybistin and gephyrin could be overcome by the fusion of the (to be defined) corresponding binding stretch(es) to the SH3, DH or PH domain or GephE. A fusion protein of $NL2_{cyt}$ added to the C-terminus of $CB2_{SH3-}$ was hardly soluble (~1 mg/mL) and tended to form aggregates (data not shown). This might be the result of an unfortunate combination of the hydrophobic stretches enriched in the terminal quarter of $NL2_{cyt}$ and the C-terminus of CB2. However, with more defined interaction sites this apporach might be useful for the structural characterization of low affinity complexes (Chichili *et al.*, 2013).

III.C.3.5 Other gephyrin-collybistin complexes

The gephyrin-collybistin complex is not only engaged in assemblies with NL2. In fact this assembly plays a role at only a subset of synapses (Poulopoulos *et al.*, 2009). For example, the analysis of the collybistin knock-out mice revealed that gephyrin and $GABA_A$ receptor clustering were compromised not only at perisomatic but also at dendritic synapses (Jedlicka *et al.*, 2009, Papadopoulos *et al.*, 2007). There are several gephyrin and collybistin binding partners, which could dock to the gephyrin-

Ternary complex	Literature
Geph-CB-NL2	(Poulopoulos *et al.*, 2009)
Geph-CB-NL4	(Hoon *et al.*, 2011)
Geph-CB-GABA$_A$R α2	(Saiepour *et al.*, 2010)
Geph-CB-Cdc42	(Tyagarajan *et al.*, 2011a)
Geph-CB-TC10	(Mayer *et al.*, 2013)
Geph-Mena-Pfn2	(Giesemann *et al.*, 2003)

Table 46 Ternary complexes involving gephyrin at postsynaptic densities. Note that the binding sites of Mena and Pfn 2 in gephyrin might overlap. Collybistin (CB) containing complexes are expected to bind to PI(3)P.

collybistin complex at dendritic synapses (but also on perisomatic synapses as well). A second reason to watch out for additional binding partner is the presumably moderate stability of the gephyrin-collybistin complex. This is indicated by the less pronounced gephyrin-collybistin band shifts in the presence of 30 µM NL2$_{cyt}$ (when compared to 200 µM NL2$_{cyt}$, Fig. 102) and the observation that aSEC experiments did not convincingly argue for ternary complex formation (presumably due to the low final concentrations, Fig. 99). Hence, a short overview of binding partners that might couple to the gephyrin-CB complex is given, which is summarised in Table 46.

III.C.3.5.1 GABA$_A$ receptor subunits

As for NL2 also for the GABA$_A$R subunit α2 a release of SH3 mediated autoinhibition was observed. In principle, GABA$_A$ receptor subunits α1-α3 can interact with both gephyrin and collybistin. In practice, the α2 subunit presumably binds to collybistin (K_D of 1 µM), while the α3 and α1 subunits are expected to bind to gephyrin (K_Ds of 5 µM and 17 µM, respectively). This is due to weak affinities of α1 and α3 to collybistin (K_D~500 µM) and the weak affinity of the GABA$_A$R subunit α2 to gephyrin (Maric, 2012). As there is a consensus that most GABA$_A$ receptors occur in a 2α/2β/γ configuration (Tretter *et al.*, 1997), where the two α subunits might differ, it is conceivable that e.g. the α2 subunit associates with collybistin, whereas the other α-subunit, e.g. α3, binds to gephyrin, so that a single receptor is tethered to both gephyrin and collybistin. As β2 and β3 can also bind to gephyrin (Kowalczyk *et al.*, 2013), even a receptor using just the α2 subunit could bind to collybistin. Therefore, it might make sense to fuse intracellular TM3-TM4 loops of two different GABA$_A$R α subunits or GABA$_A$R subunits α2 with β2 or β3.

As for a possible quarternery complex, in which NL2 is included, the GABA$_A$R subunit α2 and NL2 might compete for a single binding site in the SH3 domain, as the disease-relevant G55A mutation into the SH3 domain abolished the interactions with NL2 and α2 (Poulopoulos *et al.*, 2009, Saiepour *et al.*, 2010). Whether the overall architecture of the SH3 domain in this mutant is affected, remains to be determined. If the overall structure was not disturbed, this would be a hint at a common binding site. However, not even an overlap of their second binding sites in the DH-PH tandem is expected, as NL2$_{cyt}$ bound to CB2$_{SH3}$-ΔC15, whereas GABA$_A$R subunit α2 binding to this collybistin variant was affected (Dr. Daniela Schneeberger, personal communication). Hence, analyses of the

complexes between gephyrin-collybistin and the $GABA_A$ receptor α2 subunit will be rewarding as well, especially in the light of yeast (two-/three-)hybrid data suggesting that binary interactions of $GABA_AR$ subunit α2 with gephyrin and $CB3_{SH3+}$ were significantly strengthened in the presence of the respective remaining binding partner (Saiepour *et al.*, 2010), which is reminiscent of the gephyrin-$CB2_{SH3+}\Delta C15$-NL2 complex (Fig. 102), raising the possibility that NL2 and the $GABA_AR$ subunit α2 activate collybistin in a similar manner.

Similar activation modes for NL2 and $GABA_AR$ subunit α2 could be a sign of a competition between both proteins for the SH3 domain and should be addressed in competition assays. If there was competition, one could use e.g. the α1 subunit for the quarternery complex, as α1 is expected to bind to gephyrin and the C-terminus of collybistin without competing with NL2 for the SH3 domain. Alternatively, one could use a chimeric construct, in which the SH3 domain binding segment of $GABA_AR$ subunit α2 precedes the DH/PH binding motif of NL2. It will also make sense to include a $CB2_{SH3+}$ variant which is longer than $CB2_{SH3+}\Delta C15$, and might be capable of binding to $GABA_AR$ α loops but at the same time is not compromised in its solubility. For example, there are five residues missing in the $CB2_{SH3+}\Delta C15$ construct, which could be shown to extend the C-terminal helix in $CB2_{SH3-}$ (PDB entry: 2DFK, chain A) (Xiang *et al.*, 2006). Hence, a $CB2_{SH3+}\Delta C10$ construct should be considered. In principle, one can proceed analogously to the presented procedures for the gephyrin-collybistin-NL2 complex, taking into account potential direct interactions between NL2 and $GABA_AR$ subunit α2 (Dong *et al.*, 2007), which could strengthen the complex.

III.C.3.5.2 Cdc42

Cdc42 binding to the described ternary complex might not only be mediated via collybistin-Cdc42 interactions since direct interactions of Cdc42 with GephG and GephE were detected in pull-down experiments, respectively. Even a ternary gephyrin-collybistin-Cdc42 complex was suggested based on GST-pulldown experiments with HEK293 cell lysates, but only for $CB2_{SH3-}$ and not for the $CB2_{SH3+}$ variant (Tyagarajan *et al.*, 2011a). Several issues of this study remain to be clarified, e.g. the role of the SH3 domain in differential ternary complex formation or the observed functional redundancy of collybsitin's PH domain and constitutively active Cdc42, which can restore gephyrin membrane targeting upon coexpression with PH-deficient collybistin (Tyagarajan *et al.*, 2011a). The observation that also Cdc42, which does not bind to the SH3 domain, induced the gephyrin-$CB2_{SH3+}$ complex to redistribute from the cytosol to the membrane of non-neuronal cells (Mayer *et al.*, 2013), as it was observed for NL2, NL4 and α2 before ((Hoon *et al.*, 2011, Poulopoulos *et al.*, 2009, Saiepour *et al.*, 2010), see also section III.C.1.3.1)) also raised the possibility of a ternary complex comprising gephyrin-collybistin-Cdc42.

Also related to this would be the question whether the binding of the SH3 domain, gephyrin and Cdc42 would lead to steric clashes as suggested by Xiang et al. (2006), who observed that $CB1_{SH3+}$ and $CB2_{SH3-}$-gephyrin complexes exhibited a lower GDP-GTP exchange rate than apo-$CB2_{SH3-}$ alone. As discussed above, reduced gephyrin binding in $CB2_{SH3+}\Delta C15$ would be consistent with this hypothesis. On the other hand, gephyrin binding to $CB2_{SH3+}\Delta C15$ was not completely abolished (at least at pH 8, Fig. 102), and hence, it seems as if the SH3 domain is not completely fixed to the DH-PH tandem, which would be in agreement with recent studies, which did not reveal significant differences in the GEF activities of $CB2_{SH3+}$ and $CB2_{SH3-}$ (Mayer *et al.*, 2013). It was more important whether the nucleotide exchange was measured in (non-neuronal) cells or *in vitro*, raising the possibility that there are additional, so far unidentified factors, which regulate collybistin's GEF activity (Mayer *et al.*, 2013).

III.C.3.5.3 TC10

A recent study identified TC10 as a novel collybistin binding partner (Mayer *et al.*, 2013). TC10 is a Rho family GTPase and a close homologue to Cdc42. Like the α2 subunit, NL2, NL4 and Cdc42 (Hoon *et al.*, 2011, Poulopoulos *et al.*, 2009, Saiepour *et al.*, 2010), TC10 could also trigger gephyrin-$CB2_{SH3+}$ redistribution from the cytosol to the membrane of non-neuronal cells, but, in contrast to the $GABA_AR$ subunit α2, NL2 and NL4, TC10 is not expected to be a SH3 domain ligand and could be shown to bind to the PH domain in its GTP bound state, and hence, the activation process must operate in a different way. Based on their binding assays, the authors suggested that collybistin complexes with TC10 but also with Cdc42 are not transient but rather stable, reminiscent of GTPase-effector complexes. As observed for Cdc42, collybistin's GEF activity was enhanced in a cellular context. In contrast to Cdc42, TC10 could not be activated in cells upon coexpression of $CB2_{SH3+}$, and the addition of gephyrin was required to endow collybistin with GEF activity toward TC10 (Mayer *et al.*, 2013). Taken together, these results raise the possibility of a ternary gephyrin-collybistin-TC10 complex. As TC10 appears to bind predominantly to the PH domain and Cdc42 to the DH domain of collybistin, and as the DH-PH tandem exhibits an unexpected flexibility (Xiang *et al.*, 2006), simultaneous binding of collybistin, TC10 and Cdc42 to gephyrin should be considered as well.

III.C.3.5.4 PI(3)P

The collybistin-PI(3)P binding appears to be rather weak, and no dissociation constant is available for this complex (Dr. Daniela Schneeberger, personal communication). This might be different in the presence of gephyrin and NL2. For the $CB2_{SH3+}$ variant the addition of $NL2_{cyt}$ was required to trigger PI(3)P binding (Soykan, 2011). Likewise $GABA_A$ receptor binding might enhance PI(3)P binding to collybistin. In $CB2_{SH3-}$ the PI(3)P binding should not be affected by sterical hindrance, as the DH-PH tandem exhibits a high level of structural plasticity. Nevertheless, one should also test whether the

presence of gephyrin enhances the $CB2_{SH3-}$-PI(3)P stability, especially considering the predominantly cytosolic localization of $CB2_{SH3-}$ (Harvey *et al.*, 2004): Gephyrin's contribution to collybistin membrane localization might be related to its palmitoylation (Kang *et al.*, 2008), but on the other hand gephyrin could theoretically induce a higher PI(3)P affinity of collybistin or serve as a scaffold for enzymes that acylate Cdc42 (Wirth *et al.*, 2013). Maybe the addition of PI(3)P to a preformed ternary gephyrin-collybistin-NL2 complex could help to decipher the structural details of PI(3)P binding.

III.C.3.5.5 Profilin and Mena

Mena and profilin, two proteins involved in the organization of the actin cytoskeleton, were identified as binding partners of NL2 (Poulopoulos *et al.*, 2009) and gephyrin (Giesemann *et al.*, 2003, Mammoto *et al.*, 1998, Murk *et al.*, 2012). Interestingly, NL2 harbours a Mena binding motif (FPPPP). This motif is present in several Mena binding membrane proteins as well: Zyxin (Reinhard *et al.*, 1995), vinculin (Reinhard *et al.*, 1996), lammelipodin (Krause *et al.*, 2004), migfilin (Zhang *et al.*, 2006) and palladin (Boukhelifa *et al.*, 2004). Residues flanking this FPPPP motif have been reported to influence EVH1 binding (Prehoda *et al.*, 1999), and based on these binding studies, the PFPPPPTATS motif of NL2, lacking acidic residues at its C-terminus, is expected to bind with weak affinity with a K_D of 100 µM or even higher (Prehoda *et al.*, 1999). However, multiple phosphorylations in the TATS motif might convert NL2 to a strong Mena binder. As Mena is present at synapses, and as it binds to gephyrin, NL2, gephyrin and Mena could form a ternary complex, which could theoretically form a link to the cytoskeleton, as Mena was reported to be an adaptor for gephyrin to the barbed ends of filamentous actin. Mena could exert its actin uncapping function, recruit profilin to barbed ends of F-actin, possibly supported by NL2 and gephyrin.

However, gephyrin might compete with NL2 for the same binding site in Mena, as it is quite likely that gephyrin binds to Mena also via a proline-rich motif (Bausen *et al.*, 2006). In addition, gephyrin and G-actin compete for the same binding site in profilin (Giesemann *et al.*, 2003). Profilin-G-actin complexes bind to Mena, which then adds G-actin to the preexisting F-actin filament. Hence, gephyrin is expected to attenuate the actin incorporation into F-actin (Fig. 107). One can speculate, whether in the early stages NL2 recruits Mena and/or profilin to postsynaptic densities to induce F-actin extension and whether gephyrin - in response to so far unknown binding/signalling events (maybe phosphorylations in gephyrin's N-terminal poly-proline stretch) – exhibits a higher profilin affinity, which leads to the termination of actin remodelling (Fig. 107). However, in the initial stages actin remodelling is required (Bausen *et al.*, 2010), so that termination via gephyrin would be required only in the later stages of synapse maturation. The findings concerning gephyrin clustering raise many questions and therefore – although the linkage of gephyrin and NL2 to profilin and Mena

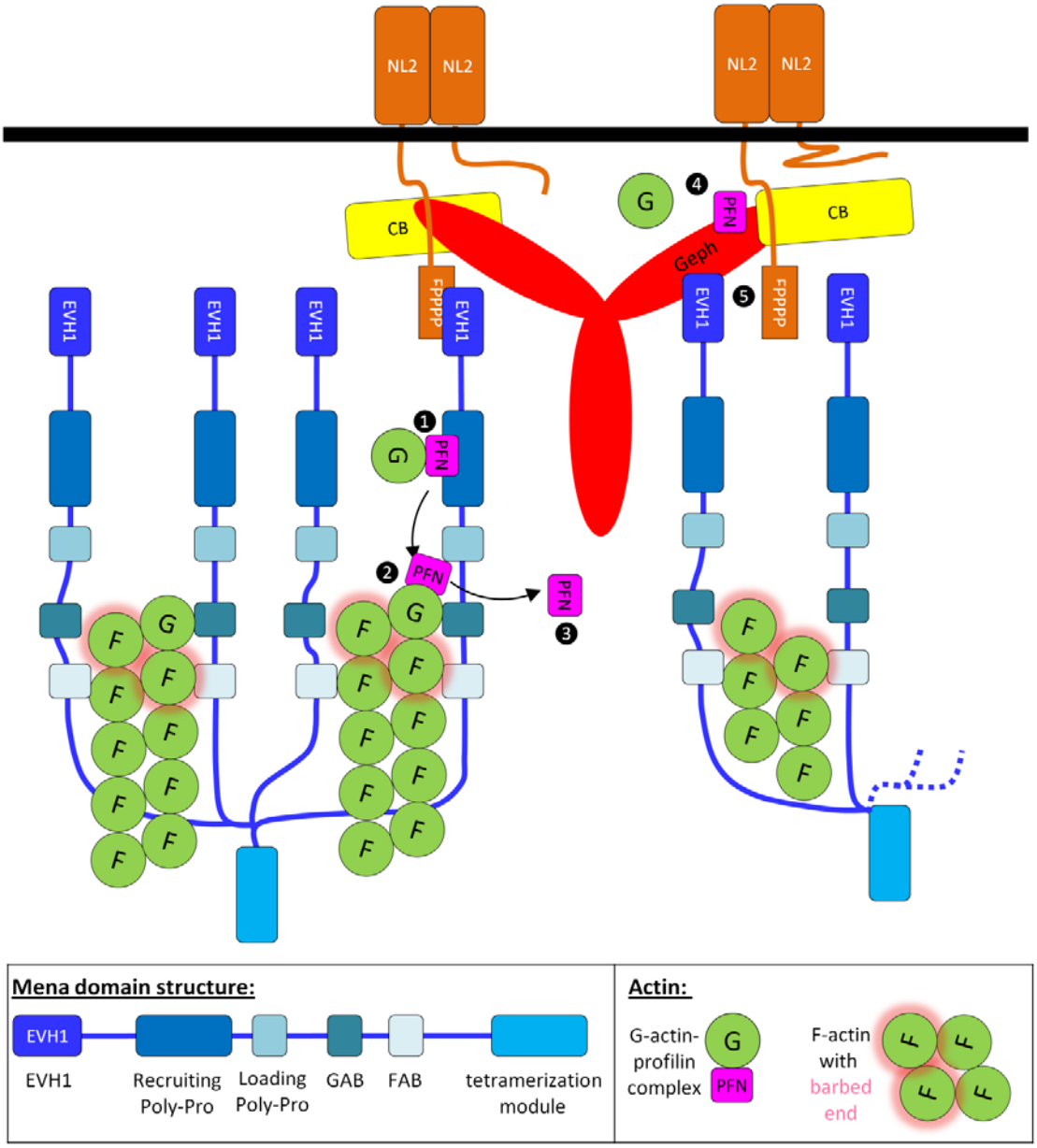

Figure 107 The roles of Mena and profilin in the elongation of actin filaments and how gephyrin, collybistin and NL2 could participate. The general concept of the figure was adapted from (Ferron *et al.*, 2007). ❶ G-actin complexed with profilin (PFN) is recruited by the "Recruiting Poly-Pro" motif of Mena. ❷ Subsequently, this complex is transferred to the "Loading Poly-Pro" motif (which interacts with profilin) and the G-actin binding site (abbreviated as GAB, which interacts with G-actin), and profilin is released. ❸ Then G-actin is incorporated into filamentous actin, which interacts with the FAB domain (F-actin binding site). NL2 could theoretically tether Mena to the membrane, allowing for actin extension. Gephyrin might ❹ sequester profilin and thereby displace G-actin, so that F-actin extension could be at least attenuated. ❺ In addition, gephyrin might compete with NL2 for Mena.

might not appear as promising in terms of a quarternery complex – the deciphering of this intricate interplay might be of high interest.

A look at Table 47, which summarizes verified binary interactions, reveals that gephyrin binds to all of the selected proteins except for TC10, for which a potential interaction has not been assessed. $NL2_{cyt}$ and $NL4_{cyt}$ are not expected to bind simultaneously, but based on published results so far a gephyrin-collybistin-NL2-$GABA_AR$-TC10-Cdc42-PI(3)P complex appears conceivable. Such a huge complex, in which the orientation of TC10, Cdc42 and gephyrin (which were reported to be lipidated (Kang *et al.*, 2008, Roberts *et al.*, 2008)) and $GABA_AR$ and NL2 (membrane proteins) would be restrained, could favour the assembly of gephyrin into a hexagonal scaffold.

	Geph	CB	$NL2_{cyt}$	$NL4_{cyt}$	α_1	α_2	α_3	Cdc42	TC10	Mena	Pfn2a
Geph		(o)	(-)	x	(o)	(-)	(+)	x	?	x	x
CB			(o)	x	(-)	+	(-)	x	x	?	?
NL2				?	?	?	?	?	?	(-)*	x
Mena											x
NL4					?	?	?	?	?	?	?
α1/α2/α3								?	?	?	?
Cdc42									?	?	?
TC10										?	?

Table 47 Summary of binary interactions involving important gephyrin and collybistin binding partners. Bold letters indicate that biochemical data argue for a strong ((+), K_D <10 µM), medium affinity ((o), 10 µM < K_D < 50 µM) or weak affinity ((-), K_D > 50 µM). An "x" marks interactions, which were observed in the context of cell biological studies, whereas an question mark indicates that data on a (potential) respective interaction have not been published so far.

IV. CONCLUDING DISCUSSION

Disturbed inhibitory neurotransmission can impair the functionality of neuronal networks and consequently the procession and integration of information. Hence, altered inhibitory neurotransmission can lead to a variety of neurological disorders (Harvey *et al.*, 2008, Marin, 2012, Wang *et al.*, 2009), which justify extensive efforts to decipher the molecular basis of inhibitory synapses. Recent years brought considerable progress in this research area: For instance, the basis and the functional implications of the heterogeneity on the cellular (Kepecs & Fishell, 2014) and the receptor level (Rudolph & Knoflach, 2011) have become more and more understood and many components of synapses and their functional roles have been revealed just in the last few years. Also the view of synapses as rather static structures has changed considerably (Choquet & Triller, 2013). Rigid synapse architectures are presumably not the rule since entire synapses have been shown to migrate (Dobie & Craig, 2011) and even synaptic receptors can exhibit a high degree of dynamics (Choquet & Triller, 2013). These findings are related to synaptic plasticity, which is required for the proper functioning of neurotransmission and which comprises among other factors spatio-temporal changes in the composition of the postsynaptic densities. Hence, one can conceive that proteins underlying these networks are endowed with dynamic properties that allow for a fast adaptation of these processes. The scaffolding protein gephyrin is such a dynamic protein and is well-suited to play a key role in the regulation of the PSD composition. Basically gephyrin has to fulfil three tasks (Tretter *et al.*, 2012, Tyagarajan & Fritschy, 2014): First it binds to inhibitory neurotransmitter receptors linking them to other PSD components which also regulate neurotransmitter receptor clustering. Second, receptor clustering appears to require the formation of higher gephyrin oligomers. Third, gephyrin provides binding sites for other PSD proteins which help to regulate receptor density.

The self-oligomerization of gephyrin is still poorly understood for the holo-protein. Crystallization trials have not been successful so far, and presumably this is related to the dynamic character of gephyrin. Therefore, other techniques were chosen to assess the structure of gephyrin and its dynamic character on the nm-scale. The complementary approaches of SAXS (section III.A.2.5) and AFM (section III.A.2.4) yielded consistent results, namely a highly heterogeneous mixture containing predominantly compact conformers but also extended assemblies. In agreement with secondary structure predictions (section III.A.2.1), the linker was found to mediate the heterogeneity (section III.A.2.4) (Sander *et al.*, 2013).

The linker has also been regarded as the key to a better understanding of gephyrin oligomerization. Furthermore, it was suggested that it is the linker which interferes with GephE dimerization in the context of the full-length protein (Bedet *et al.*, 2006) that – under the used conditions – only utilized its GephG trimer interface. This idea was based on the finding that GephLE displayed a significantly smaller hydrodynamic radius than GephE, which suggested that GephLE

formed monomers (Bedet *et al.*, 2006). Following up on this finding I attempted to convert GephLE monomers to dimers (section III.A.2.7.4). The knowledge of the corresponding mutations could have potentially yielded determinants of linker-GephE interactions, yet, surprisingly, even unmutated GephLE still formed dimers (Fig. 46). This was not the first observation of GephLE dimers since Eunyoung Lee, a former graduate student in the Schindelin group, observed that GephLE variants, which started either at residue 167, 188, 208, 260 or 309 (Lee, 2009) instead of residue 182 (Fig. 3), exhibited larger hydrodynamic radii than GephE dimers, whereas the order was reversed in Bedet et al. (2006). Taken together, the data obtained in the Schindelin lab suggested that the linker on its own cannot prevent GephE dimerization, pointing to an even more complicated mode of autoinhibition than assumed so far. One should therefore consider that GephG, the only difference between GephLE and GephWT, does not only confer a trimer interface to full-length gephyrin but might also interfere with GephE dimerization by interactions with the linker or with GephE. The latter of the two options appears to be more valid, as the linker is not required for GephE dimerization, and GephG-GephE interactions are the subject of previous speculations (Fritschy *et al.*, 2008). Indeed, preliminary experimental findings obtained during the course of this project support this notion. A model, which integrates the results in this work, is presented in section III.A.3.9. In this model, GephG is considered as a platform that drives compaction via direct interactions with GephE but also regenerates extended states by acting as a chaperone for the linker segment which associates with the GephE dimerization interface (Fig. 56). This model explains the coexistence of compact and extended states as observed in AFM and SAXS studies (Sander *et al.*, 2013), the independence of the trimeric state of the linker deletion mutants, the linker association with the terminal domains (section III.A.2.6.2) and also the small amounts of higher oligomers (section III.A.2.2).

The results obtained so far, however, show that the verification of the herein proposed model will be connected to experimental obstacles which need to be overcome. There are techniques, which were not used in this study and which can theoretically yield information beyond the level presented here. Crosslinking studies could help to derive restraints on interatomic distances, and, if several such pairs were identified, one could use these restraints for SAXS modelling. Even more detailed information could theoretically be derived by hydrogen/deuterium exchange mass spectrometry experiments (HDX-MS) experiments, in which deuteration levels correlate with solvent-exposure of the analysed protein segments (Konermann *et al.*, 2011, Serpa *et al.*, 2012). However, one would have to ensure that both crosslinking and HDX-MS experiments are not conducted with mixtures of compact and extended states. Otherwise these approaches might yield results of limited use, as one could not distinguish whether certain restraints correspond to the compact, extended or intermediate states identified by SAXS in the course of this work. Therefore, the enrichment of rather compact or rather extended states (e.g. by the use of different buffers) might be helpful. One could

check the sample heterogeneity in AFM (and/or SAXS) and then – after confirmation of a relative depletion of a certain species – proceed with HDX-MS or crosslinking studies and derive at least certain trends, which could be milestones in our understanding of gephyrin's structural and functional properties.

During the purification of even wild-type gephyrin also higher oligomers were observed (section III.A.2.2). The characterization of higher oligomers, however, might be connected to even more obstacles than the analysis of trimeric gephyrin, as more degrees of freedom exist for higher oligomers. Furthermore, GephE-GephE interactions within an assembly are expected to be favoured over inter-assembly GephE interactions, be it in a trimer or a higher oligomer (Fig. 108). Hence, it is conceivable that disinhibited gephyrin predominantly terminates at the hexameric state. An additional layer of complexity arises from the observed higher tendency of gephyrin to aggregate in relation to an increase in the hydrodynamic radius; this might be a consequence of a dimerization-induced release of autoinhibitory linker segments, e.g. in the case of the higher oligomers, which could decrease the solubility. Such a decrease in solubility was observed for the solubility tag MBP, when the gephyrin linker was attached at the MBP C-terminus (section III.A.2.7.1). The used buffer allowed for higher gephyrin concentrations (>200 µM) than MBP-L concentrations (~100 µM). Exceeding MBP-L concentrations of ~100 µM led to phase separation upon centrifguation. This phenomenon has been described for several other proteins before (Forman-Kay & Mittag, 2013) and might be prevented *in vivo* by the presence of a sufficient number of binding partners.

The dynamic character of synapses questioned whether the postulated hexagonal scaffold does exist at all (Tyagarajan & Fritschy, 2010). For instance, gephyrin clusters were found to be rather mobile (Ehrensperger *et al.*, 2007, Maas *et al.*, 2006, Vlachos *et al.*, 2013), allowing for a fast adaptation of synaptic strength. A rigid scaffold with possibilities for a fast down-regulation of its size only at its borders might not offer a sufficiently high degree of plasticity. In addition, GephE dimerization in the context of a hexagonal scaffold is not required for GlyR binding as indicated by preliminary ITC experiments, in which the affinity of dimerization-deficient GephΔL did not significantly differ from that of full-length gephyrin (data not shown). This was in line with the finding that trimeric full-length gephyrin did not change its oligomeric state upon GlyR binding (Schrader *et al.*, 2004).

In agreement with the hypothesis that the hexagonal lattice might not be required for gephyrin clustering, an EM tomography study of inhibitory postsynaptic densities of GABAergic synapses was not consistent with a planar gephyrin scaffold and revealed rather disrupted patches of potential subclusters (Linsalata *et al.*, 2014). Principally, this finding could be related to a less dense gephyrin packing at GABAergic synapses and need not necessarily mean that a hexagonal scaffold does not exist as unoccupied, solvent exposed linker segments, as observed in the AFM micrographs in this

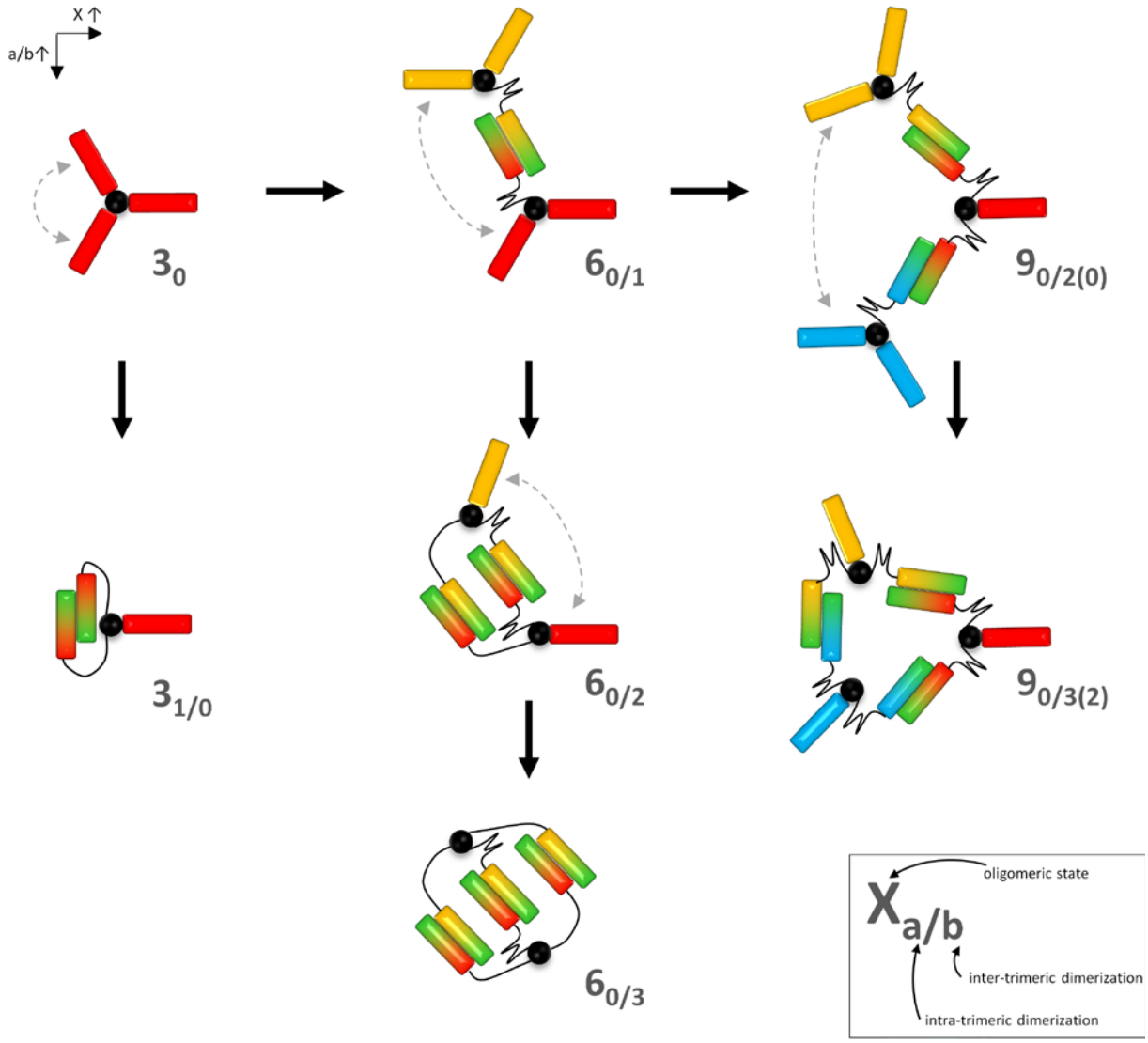

Figure 108 Potential difficulties in the analysis of higher gephyrin oligomers. In the first row gephyrin trimers are added step by step. The conformers in each column possess the same oligomeric state. Gephyrin assemblies are so flexible that inter-trimeric dimerization (increasing b values) is not only used to incorporate other trimers into an assembly (increasing X values in the first row) but also to circularize gephyrin assemblies (indicated by the grey double-headed arrows), as exemplified for hexamers (X=6) and nonamers (X=9). With each circularization step opportunities to connect to a different trimer are lost. Intratrimeric dimerization is only depicted for the trimer. For the sake of simplicity only a small selection of possible conformers per oligomeric state is shown.

work (Fig. 20), are presumably too small to be resolved in EM experiments. On the other hand, a recent single-molecule study of gephyrin clusters in neurons accounted for rather high gephyrin densities, ranging from 5,000 to 10,000 gephyrin molecules per µm², depending on synapse type or developmental stage (Specht *et al.*, 2013). So planar gephyrin scaffolds might exist at least in a subset of synapses. In comparison, the hexagonal scaffold displayed in Fig. 3C would display a density of ~4500 gephyrin molecules per µm². Given that the distances between GephG and GephE are

rather small in this model, 10,000 gephyrin molecules appear a bit too high, but 5,000 gephyrin molecules/µm³ are easily within reach.

Gephyrin-ligand interactions could trigger the assembly of the proposed hexagonal lattice. To be instructive for such a scaffold, a linker or GephE binding partner should possess a sufficiently high affinity and should (ideally) avoid intra-trimeric dimerization (Fig. 108, conformer $3_{1/0}$), while at the same time specifically favouring inter-trimeric dimerization. As single gephyrin ligands with these properties have not been identified yet, after a period of more than 20 years, the chances to obtain the postulated hexagonal scaffold *in vitro* are expected to be rather small, but one can proceed with the characterization of gephyrin-ligand complexes.

Many GephL ligands are enzymes including various kinases, which typically associate with their substrates in a "kiss-and-run-manner". The same mechanism presumably also applies to PIN1 (Keller, 2010), as indicated by the absence of stable gephyrin-PIN1 complexes. In addition, PIN1 did not induce higher gephyrin oligomers in aSEC experiments by Kristina Keller, a former Diploma student (Keller, 2010). GABARAP-gephyrin interactions have not been characterized so far, but as GABARAP is not a component of the PSD, the analysis of its complex with gephyrin might be of questionable value.

DYNLL1, whose interaction with GephL was one topic of this work, seems to bind with sufficient affinity but might induce an asymmetry into gephyrin. Even more importantly, DYNLL1 was reported to trigger a retrograde transport of gephyrin-GlyR complexes (Maas *et al.*, 2006), hence favouring a non-synaptic localization (section III.B.1). Initial hints that DYNLL1 induces the formation of gephyrin clusters (Schwarz *et al.*, unpublished data, briefly described in section III.B.3.5) require further support, but should these findings be substantiated, the observed binding mode might represent an unusual way of concentration-dependent clustering. Further investigations into the originally proposed role of DYNLL1 in the gephyrin-dynein loading (Maas *et al.*, 2006) could include time-lapse total internal reflection fluorescence (TIRF) microscopy assays which are available for the dynein motor (Reck-Peterson *et al.*, 2010, Trokter *et al.*, 2012). With this method one could test whether a dynein motor composed of its heavy chain, DLICs, LICs and LCs is sufficient to bind to gephyrin or whether additional proteins are required and, if that is the case, one could identify them. Furthermore, one could compare various fluorescence-tagged gephyrin forms – including the bare $Geph_{DB}$ motif but also higher gephyrin oligomers – with respect to the speed and the processivity of the dynein motor. These studies would probably be the best choice to assess the function of the gephyrin-DYNLL1 complex – at least in the context of the dynein motor.

This leaves microtubules (Ramming *et al.*, 2000) and collybistin (Tyagarajan *et al.*, 2011a) as putative GephL interaction partners, both of which have been reported to bind to GephE as well (Harvey *et al.*, 2004, Sauer, 2007). Mechanistic details of microtubule mediated gephyrin-receptor

clustering have remained elusive so far, but a deeper understanding of this interaction could be an important piece in the puzzle. Likewise a detailed biochemical and structural characterization of the gephyrin-collybistin complex is desirable. Whether collybistin really binds to GephL remains to be deciphered (Appendix G), but its binding site at the very N-terminus of GephE and the fact that it is involved in the synaptic targeting of gephyrin, render collybistin an interesting target, irrespective of the location of its binding site. Intriguingly, even for this gephyrin ligand which is directly involved in gephyrin clustering (Papadopoulos & Soykan, 2011), only an intermediate affinity to gephyrin with K_D of ~20 µM was observed in this work (Figs. 95 & 98), underscoring that clustering at synapses is subject to dynamic processes in space and time. Along the same line, NL2 binds to collybistin and gephyrin with (at best) moderate and low affinity, respectively (sections III.C.2.3 & III.C.2.2). The assembly of all three proteins seems to be more stable than the three binary complexes, but still it appears to be less stable (Fig. 102) than the gephyrin-GlyR complex (Kim *et al.*, 2006, Schrader *et al.*, 2004, Tretter *et al.*, 2012) – at least *in vitro*. In living cells the stability of the binary and ternary complexes might be altered: NL2 is embedded in the membrane and collybistin-gephyrin complexes are membrane associated via binding to phospholipids in the case of collybistin (Kalscheuer *et al.*, 2009) or palmitoylated residues for gephyrin (Kang *et al.*, 2008). In such an environment entropic costs for complex formation are considerably smaller, as rotational and translational degrees of freedom are reduced in comparison with the conditions of the *in vitro* analyses in this work, when complex formation was observed in a non-membraneous environment (Jackson, 2006). In addition, the protein enrichment at membranes could give rise to avidity effects which could help to overcome high dissociation rate constants (Kane, 2010). Similar effects were also suggested to play a role in $GABA_AR$ clustering (Maric, 2012). Even if *in vitro* experiments underestimate the stability of the complex, one can assume that multiprotein complexes offer more possibilities for regulation and fine-tuning of complex stability and consequently of synaptic strength than do stable binary complexes, or phrased differently: Structural plasticity and transient interactions might render a synapse more reactive in terms of its ability to undergo structural reorganizations.

Among the projects investigated herein, the gephyrin-collybistin-NL2 project is certainly the most promising in terms of future structural studies. Given the still moderate *in vitro* stability of this complex, it is worth to analyse whether the underlying interactions can be enhanced by other buffer conditions than those used in this work or by the addition of $GABA_AR$ subunit α1 (or further interaction partners). Likewise, the collybistin-gephyrin-$GABA_AR$ α2 complex could be a promising crystallization target as well (discussed in section III.C.3.5.1). One could also proceed with the identification of new, so far unidentified triggers of gephyrin clustering. These might comprise additional binding partners but also posttranslational modifications and could be the same that redistribute gephyrin from the so-called gephyrin “blobs” to the postsynaptic membrane (section

III.A.1.5). In dissociated hippocampal neurons most gephyrin molecules reside initially in these blobs, but upon development gephyrin increasingly localizes to postsynaptic specializations (Poulopoulos *et al.*, 2009). Therefore, one could perform a mass spectrometry based time course analysis of gephyrin's post-translational modifications and binding partners.

Taken together, the assessment/characterization of the (still putative) gephyrin hexagonal scaffold does not appear to be straightforward in intact cells as well. Rather, the biochemical and structural characterization of selected gephyrin and collybistin-ligand complexes are within reach. Hence, the focus will shift from the hexagonal scaffold to interdisciplinary approaches in which biochemical and structural data of synaptic subcomplexes are integrated into the framework of cell biological studies and *vice versa*.

V. REFERENCES

1. Agarwal, S., Tannenberg, R. K., & Dodd, P. R. (2008). Reduced expression of the inhibitory synapse scaffolding protein gephyrin in Alzheimer's disease. J Alzheimers. Dis. 14, 313-321.

2. Akhmanova, A. & Hammer, J. A., III (2010). Linking molecular motors to membrane cargo. Curr Opin. Cell Biol 22, 479-487.

3. Allan, V. J. (2011). Cytoplasmic dynein. Biochem Soc Trans. 39, 1169-1178.

4. Allison, D. W., Chervin, A. S., Gelfand, V. I., & Craig, A. M. (2000). Postsynaptic scaffolds of excitatory and inhibitory synapses in hippocampal neurons: maintenance of core components independent of actin filaments and microtubules. J Neurosci 20, 4545-4554.

5. Alnemri, E. S., Fernandes-Alnemri, T., Pomerenke, K., Robertson, N. M., Dudley, K., DuBois, G. C., & Litwack, G. (1994). FKBP46, a novel Sf9 insect cell nuclear immunophilin that forms a protein-kinase complex. J Biol Chem 269, 30828-30834.

6. Arac, D., Boucard, A. A., Ozkan, E., Strop, P., Newell, E., Sudhof, T. C., & Brunger, A. T. (2007). Structures of neuroligin-1 and the neuroligin-1/neurexin-1 beta complex reveal specific protein-protein and protein-Ca2+ interactions. Neuron 56, 992-1003.

7. Ashkenazy, H., Erez, E., Martz, E., Pupko, T., & Ben-Tal, N. (2010). ConSurf 2010: calculating evolutionary conservation in sequence and structure of proteins and nucleic acids. Nucleic Acids Res 38, W529-W533.

8. Atkins, P. & De Paula, J. (2011). Physical Chemistry For The Life Sciences, second edition ed Oxford University Press.

9. Baas, P. W., Deitch, J. S., Black, M. M., & Banker, G. A. (1988). Polarity orientation of microtubules in hippocampal neurons: uniformity in the axon and nonuniformity in the dendrite. Proc Natl Acad Sci U S A 85, 8335-8339.

10. Baer, K., Waldvogel, H. J., Faull, R. L., & Rees, M. I. (2009). Localization of glycine receptors in the human forebrain, brainstem, and cervical spinal cord: an immunohistochemical review. Front Mol. Neurosci 2, 25.

11. Bagnall, M. W., Zingg, B., Sakatos, A., Moghadam, S. H., Zeilhofer, H. U., & du, L. S. (2009). Glycinergic projection neurons of the cerebellum. J Neurosci 29, 10104-10110.

12. Balic, E., Rudolph, U., Fritschy, J. M., Mohler, H., & Benke, D. (2009). The alpha5(H105R) mutation impairs alpha5 selective binding properties by altered positioning of the alpha5 subunit in GABAA receptors containing two distinct types of alpha subunits. J Neurochem 110, 244-254.

13. Ball, L. J., Kuhne, R., Schneider-Mergener, J., & Oschkinat, H. (2005). Recognition of proline-rich motifs by protein-protein-interaction domains. Angew Chem Int Ed Engl 44, 2852-2869.

14. Bang, M. L. & Owczarek, S. (2013). A matter of balance: role of neurexin and neuroligin at the synapse. Neurochem Res 38, 1174-1189.

15. Barbar, E., Kleinman, B., Imhoff, D., Li, M., Hays, T. S., & Hare, M. (2001). Dimerization and folding of LC8, a highly conserved light chain of cytoplasmic dynein. Biochemistry 40, 1596-1605.

16. Barbar, E. & Nyarko, A. (2014). NMR Characterization of Self-Association Domains Promoted by Interactions with LC8 Hub Protein. Comput. Struct Biotechnol. J 9, e201402003.

17. Barbar, E. (2008). Dynein light chain LC8 is a dimerization hub essential in diverse protein networks. Biochemistry 47, 503-508.

18. Baroncelli, L., Braschi, C., Spolidoro, M., Begenisic, T., Maffei, L., & Sale, A. (2011). Brain plasticity and disease: a matter of inhibition. Neural Plast. 2011, 286073.

19. Bas, D. C., Rogers, D. M., & Jensen, J. H. (2008). Very fast prediction and rationalization of pKa values for protein-ligand complexes. Proteins 73, 765-783.

20. Battye, T. G., Kontogiannis, L., Johnson, O., Powell, H. R., & Leslie, A. G. (2011). iMOSFLM: a new graphical interface for diffraction-image processing with MOSFLM. Acta Crystallogr D. Biol Crystallogr 67, 271-281.

21. Bausen, M., Fuhrmann, J. C., Betz, H., & O'Sullivan, G. A. (2006). The state of the actin cytoskeleton determines its association with gephyrin: role of ena/VASP family members. Mol. Cell Neurosci 31, 376-386.

22. Bausen, M., Weltzien, F., Betz, H., & O'Sullivan, G. A. (2010). Regulation of postsynaptic gephyrin cluster size by protein phosphatase 1. Mol. Cell Neurosci 44, 201-209.

23. Bedet, C., Bruusgaard, J. C., Vergo, S., Groth-Pedersen, L., Eimer, S., Triller, A., & Vannier, C. (2006). Regulation of gephyrin assembly and glycine receptor synaptic stability. J Biol Chem 281, 30046-30056.

24. Belaidi, A. A. & Schwarz, G. (2012). Metal insertion into the molybdenum cofactor: Product-substrate-channeling demonstrates the functional origin of domain fusion in gephyrin. Biochem J.

25. Ben-Ari, Y. (2002). Excitatory actions of gaba during development: the nature of the nurture. Nat Rev Neurosci 3, 728-739.

26. Benison, G. & Barbar, E. (2009). NMR analysis of dynein light chain dimerization and interactions with diverse ligands. Methods Enzymol 455, 237-258.

27. Benison, G., Chiodo, M., Karplus, P. A., & Barbar, E. (2009). Structural, thermodynamic, and kinetic effects of a phosphomimetic mutation in dynein light chain LC8. Biochemistry 48, 11381-11389.

28. Benison, G., Karplus, P. A., & Barbar, E. (2007). Structure and dynamics of LC8 complexes with KXTQT-motif peptides: swallow and dynein intermediate chain compete for a common site. J Mol. Biol 371, 457-468.

29. Benison, G., Nyarko, A., & Barbar, E. (2006). Heteronuclear NMR identifies a nascent helix in intrinsically disordered dynein intermediate chain: implications for folding and dimerization. J Mol. Biol 362, 1082-1093.

30. Bernado, P. (2010). Effect of interdomain dynamics on the structure determination of modular proteins by small-angle scattering. Eur Biophys J 39, 769-780.

31. Bernado, P., Mylonas, E., Petoukhov, M. V., Blackledge, M., & Svergun, D. I. (2007). Structural characterization of flexible proteins using small-angle X-ray scattering. J Am. Chem Soc 129, 5656-5664.

32. Bernado, P. & Svergun, D. I. (2012). Analysis of intrinsically disordered proteins by small-angle X-ray scattering. Methods Mol. Biol 896, 107-122.

33. Berninghausen, O., Rahman, M. A., Silva, J. P., Davletov, B., Hopkins, C., & Ushkaryov, Y. A. (2007). Neurexin Ibeta and neuroligin are localized on opposite membranes in mature central synapses. J Neurochem 103, 1855-1863.

34. Bertaccini, E. J., Wallner, B., Trudell, J. R., & Lindahl, E. (2010). Modeling anesthetic binding sites within the glycine alpha one receptor based on prokaryotic ion channel templates: the problem with TM4. J Chem Inf. Model. 50, 2248-2255.

35. Betz, H., Kuhse, J., Schmieden, V., Malosio, M. L., Langosch, D., Prior, P., Schmitt, B., & Kirsch, J. (1991). How to build a glycinergic postsynaptic membrane. J Cell Sci Suppl 15, 23-25.

36. Betz, H. & Laube, B. (2006). Glycine receptors: recent insights into their structural organization and functional diversity. J Neurochem 97, 1600-1610.

37. Biederer, T. & Sudhof, T. C. (2001). CASK and protein 4.1 support F-actin nucleation on neurexins. J Biol Chem 276, 47869-47876.

38. Birke, G. & Draguhn, A. (2010). No simple brake--the complex functions of inhibitory synapses. Pharmacopsychiatry 43 Suppl 1, S21-S31.

39. Blaesse, P., Airaksinen, M. S., Rivera, C., & Kaila, K. (2009). Cation-chloride cotransporters and neuronal function. Neuron 61, 820-838.

40. Bloodgood, B. L. & Sabatini, B. L. (2005). Neuronal activity regulates diffusion across the neck of dendritic spines. Science 310, 866-869.

41. Blow, D. (2002). Outline Of Crystallography For Biologists Oxford University Press.

42. Blundell, J., Tabuchi, K., Bolliger, M. F., Blaiss, C. A., Brose, N., Liu, X., Sudhof, T. C., & Powell, C. M. (2009). Increased anxiety-like behavior in mice lacking the inhibitory synapse cell adhesion molecule neuroligin 2. Genes Brain Behav. 8, 114-126.

43. Bocquet, N., Nury, H., Baaden, M., Le, P. C., Changeux, J. P., Delarue, M., & Corringer, P. J. (2009). X-ray structure of a pentameric ligand-gated ion channel in an apparently open conformation. Nature 457, 111-114.

44. Bocquet, N., Prado de, C. L., Cartaud, J., Neyton, J., Le, P. C., Taly, A., Grutter, T., Changeux, J. P., & Corringer, P. J. (2007). A prokaryotic proton-gated ion channel from the nicotinic acetylcholine receptor family. Nature 445, 116-119.

45. Bogdanov, Y., Michels, G., Armstrong-Gold, C., Haydon, P. G., Lindstrom, J., Pangalos, M., & Moss, S. J. (2006). Synaptic GABAA receptors are directly recruited from their extrasynaptic counterparts. EMBO J 25, 4381-4389.

46. Boucard, A. A., Chubykin, A. A., Comoletti, D., Taylor, P., & Sudhof, T. C. (2005). A splice code for trans-synaptic cell adhesion mediated by binding of neuroligin 1 to alpha- and beta-neurexins. Neuron 48, 229-236.

47. Boukhelifa, M., Parast, M. M., Bear, J. E., Gertler, F. B., & Otey, C. A. (2004). Palladin is a novel binding partner for Ena/VASP family members. Cell Motil. Cytoskeleton 58, 17-29.

48. Boze, H., Marlin, T., Durand, D., Perez, J., Vernhet, A., Canon, F., Sarni-Manchado, P., Cheynier, V., & Cabane, B. (2010). Proline-rich salivary proteins have extended conformations. Biophys J 99, 656-665.

49. Brejc, K., van Dijk, W. J., Klaassen, R. V., Schuurmans, M., van Der, O. J., Smit, A. B., & Sixma, T. K. (2001). Crystal structure of an ACh-binding protein reveals the ligand-binding domain of nicotinic receptors. Nature 411, 269-276.

50. Brickley, S. G. & Mody, I. (2012). Extrasynaptic GABA(A) receptors: their function in the CNS and implications for disease. Neuron 73, 23-34.

51. Budreck, E. C. & Scheiffele, P. (2007). Neuroligin-3 is a neuronal adhesion protein at GABAergic and glutamatergic synapses. Eur J Neurosci 26, 1738-1748.

52. Burkarth, N., Kriebel, M., Kranz, E. U., & Volkmer, H. (2007). Neurofascin regulates the formation of gephyrin clusters and their subsequent translocation to the axon hillock of hippocampal neurons. Mol. Cell Neurosci 36, 59-70.

53. Burkhardt, J. K., Echeverri, C. J., Nilsson, T., & Vallee, R. B. (1997). Overexpression of the dynamitin (p50) subunit of the dynactin complex disrupts dynein-dependent maintenance of membrane organelle distribution. J Cell Biol 139, 469-484.

54. Butler, M. H., Hayashi, A., Ohkoshi, N., Villmann, C., Becker, C. M., Feng, G., De, C. P., & Solimena, M. (2000). Autoimmunity to gephyrin in Stiff-Man syndrome. Neuron 26, 307-312.

55. Calamai, M., Specht, C. G., Heller, J., Alcor, D., Machado, P., Vannier, C., & Triller, A. (2009). Gephyrin oligomerization controls GlyR mobility and synaptic clustering. J Neurosci 29, 7639-7648.

56. Calimet, N., Simoes, M., Changeux, J. P., Karplus, M., Taly, A., & Cecchini, M. (2013). A gating mechanism of pentameric ligand-gated ion channels. Proc Natl Acad Sci U S A 110, E3987-E3996.

57. Carter, A. P., Cho, C., Jin, L., & Vale, R. D. (2011). Crystal structure of the dynein motor domain. Science 331, 1159-1165.

58. Carver, C. M. & Reddy, D. S. (2013). Neurosteroid interactions with synaptic and extrasynaptic GABA(A) receptors: regulation of subunit plasticity, phasic and tonic inhibition, and neuronal network excitability. Psychopharmacology (Berl) 230, 151-188.

59. Cavelier, P., Hamann, M., Rossi, D., Mobbs, P., & Attwell, D. (2005). Tonic excitation and inhibition of neurons: ambient transmitter sources and computational consequences. Prog. Biophys Mol. Biol 87, 3-16.

60. Celie, P. H., van Rossum-Fikkert, S. E., van Dijk, W. J., Brejc, K., Smit, A. B., & Sixma, T. K. (2004). Nicotine and carbamylcholine binding to nicotinic acetylcholine receptors as studied in AChBP crystal structures. Neuron 41, 907-914.

61. Charrier, C., Ehrensperger, M. V., Dahan, M., Levi, S., & Triller, A. (2006). Cytoskeleton regulation of glycine receptor number at synapses and diffusion in the plasma membrane. J Neurosci 26, 8502-8511.

62. Charrier, C., Machado, P., Tweedie-Cullen, R. Y., Rutishauser, D., Mansuy, I. M., & Triller, A. (2010). A crosstalk between beta1 and beta3 integrins controls glycine receptor and gephyrin trafficking at synapses. Nat Neurosci 13, 1388-1395.

63. Chau, P. L. (2010). New insights into the molecular mechanisms of general anaesthetics. Br. J Pharmacol 161, 288-307.

64. Chen, C., Wirth, A., & Ponimaskin, E. (2012). Cdc42: an important regulator of neuronal morphology. Int J Biochem Cell Biol 44, 447-451.

65. Chen, J. L. & Nedivi, E. (2013). Highly specific structural plasticity of inhibitory circuits in the adult neocortex. Neuroscientist. 19, 384-393.

66. Chen, S. X., Tari, P. K., She, K., & Haas, K. (2010). Neurexin-neuroligin cell adhesion complexes contribute to synaptotropic dendritogenesis via growth stabilization mechanisms in vivo. Neuron 67, 967-983.

67. Chen, X., Liu, H., Shim, A. H., Focia, P. J., & He, X. (2008). Structural basis for synaptic adhesion mediated by neuroligin-neurexin interactions. Nat Struct Mol. Biol 15, 50-56.

68. Chen, Y. M., Gerwin, C., & Sheng, Z. H. (2009). Dynein light chain LC8 regulates syntaphilin-mediated mitochondrial docking in axons. J Neurosci 29, 9429-9438.

69. Chichili, V. P., Kumar, V., & Sivaraman, J. (2013). Linkers in the structural biology of protein–protein interactions. Protein Sci 22, 153-167.

70. Chih, B., Gollan, L., & Scheiffele, P. (2006). Alternative splicing controls selective trans-synaptic interactions of the neuroligin-neurexin complex. Neuron 51, 171-178.

71. Chiou, T. T., Bonhomme, B., Jin, H., Miralles, C. P., Xiao, H., Fu, Z., Harvey, R. J., Harvey, K., Vicini, S., & De Blas, A. L. (2011). Differential regulation of the postsynaptic clustering of gamma-aminobutyric acid type A (GABAA) receptors by collybistin isoforms. J Biol Chem 286, 22456-22468.

72. Cho, C. & Vale, R. D. (2012). The mechanism of dynein motility: insight from crystal structures of the motor domain. Biochim. Biophys Acta 1823, 182-191.

73. Choquet, D. & Triller, A. (2003). The role of receptor diffusion in the organization of the postsynaptic membrane. Nat Rev Neurosci 4, 251-265.

74. Choquet, D. & Triller, A. (2013). The dynamic synapse. Neuron 80, 691-703.

75. Christian, C. A., Herbert, A. G., Holt, R. L., Peng, K., Sherwood, K. D., Pangratz-Fuehrer, S., Rudolph, U., & Huguenard, J. R. (2013). Endogenous positive allosteric modulation of GABA(A) receptors by diazepam binding inhibitor. Neuron 78, 1063-1074.

76. Chubykin, A. A., Atasoy, D., Etherton, M. R., Brose, N., Kavalali, E. T., Gibson, J. R., & Sudhof, T. C. (2007). Activity-dependent validation of excitatory versus inhibitory synapses by neuroligin-1 versus neuroligin-2. Neuron 54, 919-931.

77. Cohen, S. N., Chang, A. C., Boyer, H. W., & Helling, R. B. (1973). Construction of biologically functional bacterial plasmids in vitro. Proc Natl Acad Sci U S A 70, 3240-3244.

78. Cole, C., Barber, J. D., & Barton, G. J. (2008). The Jpred 3 secondary structure prediction server. Nucleic Acids Res 36, W197-W201.

79. Cole, D. G. (2003). The intraflagellar transport machinery of Chlamydomonas reinhardtii. Traffic 4, 435-442.

80. Colin, I., Rostaing, P., Augustin, A., & Triller, A. (1998). Localization of components of glycinergic synapses during rat spinal cord development. J Comp Neurol 398, 359-372.

81. Colin, I., Rostaing, P., & Triller, A. (1996). Gephyrin accumulates at specific plasmalemma loci during neuronal maturation in vitro. J Comp Neurol 374, 467-479.

82. Colledge, M. & Froehner, S. C. (1998). To muster a cluster: anchoring neurotransmitter receptors at synapses. Proc Natl Acad Sci U S A 95, 3341-3343.

83. Comoletti, D., Flynn, R., Jennings, L. L., Chubykin, A., Matsumura, T., Hasegawa, H., Sudhof, T. C., & Taylor, P. (2003). Characterization of the interaction of a recombinant soluble neuroligin-1 with neurexin-1beta. J Biol Chem 278, 50497-50505.

84. Copley, S. D. (2003). Enzymes with extra talents: moonlighting functions and catalytic promiscuity. Curr Opin. Chem Biol 7, 265-272.

85. Craig, A. M., Blackstone, C. D., Huganir, R. L., & Banker, G. (1994). Selective clustering of glutamate and gamma-aminobutyric acid receptors opposite terminals releasing the corresponding neurotransmitters. Proc Natl Acad Sci U S A 91, 12373-12377.

86. Cummings, M. D., Farnum, M. A., & Nelen, M. I. (2006). Universal screening methods and applications of ThermoFluor. J Biomol. Screen. 11, 854-863.

87. Dahan, M., Levi, S., Luccardini, C., Rostaing, P., Riveau, B., & Triller, A. (2003). Diffusion dynamics of glycine receptors revealed by single-quantum dot tracking. Science 302, 442-445.

88. Dalva, M. B., McClelland, A. C., & Kayser, M. S. (2007). Cell adhesion molecules: signalling functions at the synapse. Nat Rev Neurosci 8, 206-220.

89. Davies, J. S., Chung, S. K., Thomas, R. H., Robinson, A., Hammond, C. L., Mullins, J. G., Carta, E., Pearce, B. R., Harvey, K., Harvey, R. J., & Rees, M. I. (2010). The glycinergic system in human startle disease: a genetic screening approach. Front Mol. Neurosci 3, 8.

90. Davies, P. A., Wang, W., Hales, T. G., & Kirkness, E. F. (2003). A novel class of ligand-gated ion channel is activated by Zn2+. J Biol Chem 278, 712-717.

91. Day, C. L., Puthalakath, H., Skea, G., Strasser, A., Barsukov, I., Lian, L. Y., Huang, D. C., & Hinds, M. G. (2004). Localization of dynein light chains 1 and 2 and their pro-apoptotic ligands. Biochem J 377, 597-605.

92. Dean, C. & Dresbach, T. (2006). Neuroligins and neurexins: linking cell adhesion, synapse formation and cognitive function. Trends Neurosci 29, 21-29.

93. Dejanovic, B., Lal, D., Catarino, C. B., Arjune, S., Belaidi, A. A., Trucks, H., Vollmar, C., Surges, R., Kunz, W. S., Motameny, S., Altmuller, J., Kohler, A., Neubauer, B. A., Epicure Consortium, Nurnberg, P., Noachtar, S., Schwarz, G., & Sander, T. (2014). Exonic microdeletions of the gephyrin gene impair GABAergic synaptic inhibition in patients with idiopathic generalized epilepsy. Neurobiol Dis.

94. del Pino, I., Koch, D., Schemm, R., Qualmann, B., Betz, H., & Paarmann, I. (2014). Proteomic Analysis of Glycine Receptor beta Subunit (GlyRbeta)-interacting Proteins: EVIDENCE FOR SYNDAPIN I REGULATING SYNAPTIC GLYCINE RECEPTORS. J Biol Chem 289, 11396-11409.

95. del Pino, I., Paarmann, I., Karas, M., Kilimann, M. W., & Betz, H. (2011). The trafficking proteins Vacuolar Protein Sorting 35 and Neurobeachin interact with the glycine receptor beta-subunit. Biochem Biophys Res Commun 412, 435-440.

96. Dellisanti, C. D., Yao, Y., Stroud, J. C., Wang, Z. Z., & Chen, L. (2007). Crystal structure of the extracellular domain of nAChR alpha1 bound to alpha-bungarotoxin at 1.94 A resolution. Nat Neurosci 10, 953-962.

97. Demirkan, G., Yu, K., Boylan, J. M., Salomon, A. R., & Gruppuso, P. A. (2011). Phosphoproteomic profiling of in vivo signaling in liver by the mammalian target of rapamycin complex 1 (mTORC1). PloS One 6, e21729.

98. Dephoure, N., Gould, K. L., Gygi, S. P., & Kellogg, D. R. (2013). Mapping and analysis of phosphorylation sites: a quick guide for cell biologists. Mol. Biol Cell 24, 535-542.

99. DeWitt, M. A., Chang, A. Y., Combs, P. A., & Yildiz, A. (2012). Cytoplasmic dynein moves through uncoordinated stepping of the AAA+ ring domains. Science 335, 221-225.

100. Dhani, S. U., Mohammad-Panah, R., Ahmed, N., Ackerley, C., Ramjeesingh, M., & Bear, C. E. (2003). Evidence for a functional interaction between the ClC-2 chloride channel and the retrograde motor dynein complex. J Biol Chem 278, 16262-16270.

101. Diederichs, K. & Karplus, P. A. (1997). Improved R-factors for diffraction data analysis in macromolecular crystallography. Nat Struct Biol 4, 269-275.

102. Dobie, F. A. & Craig, A. M. (2011). Inhibitory synapse dynamics: coordinated presynaptic and postsynaptic mobility and the major contribution of recycled vesicles to new synapse formation. J Neurosci 31, 10481-10493.

103. Dodding, M. P. & Way, M. (2011). Coupling viruses to dynein and kinesin-1. EMBO J 30, 3527-3539.

104. Dong, N., Qi, J., & Chen, G. (2007). Molecular reconstitution of functional GABAergic synapses with expression of neuroligin-2 and GABAA receptors. Mol. Cell Neurosci 35, 14-23.

105. Draguhn, A., Axmacher, N., & Kolbaev, S. (2008). Presynaptic ionotropic GABA receptors. Results Probl. Cell Differ 44, 69-85.

106. Dumoulin, A., Levi, S., Riveau, B., Gasnier, B., & Triller, A. (2000). Formation of mixed glycine and GABAergic synapses in cultured spinal cord neurons. Eur J Neurosci 12, 3883-3892.

107. Dumoulin, A., Triller, A., & Kneussel, M. (2009). Cellular transport and membrane dynamics of the glycine receptor. Front Mol. Neurosci 2, 28.

108. Dunker, A. K., Brown, C. J., Lawson, J. D., Iakoucheva, L. M., & Obradovic, Z. (2002). Intrinsic disorder and protein function. Biochemistry 41, 6573-6582.

109. Dutertre, S., Becker, C. M., & Betz, H. (2012). Inhibitory glycine receptors: an update. J Biol Chem 287, 40216-40223.

110. Edwards, K. J., Ollis, D. L., & Dixon, N. E. (1997). Crystal structure of cytoplasmic Escherichia coli peptidyl-prolyl isomerase: evidence for decreased mobility of loops upon complexation. J Mol. Biol 271, 258-265.

111. Eguchi, M., Eguchi-Ishimae, M., & Greaves, M. (2004). The small oligomerization domain of gephyrin converts MLL to an oncogene. Blood 103, 3876-3882.

112. Ehrensperger, M. V., Hanus, C., Vannier, C., Triller, A., & Dahan, M. (2007). Multiple association states between glycine receptors and gephyrin identified by SPT analysis. Biophys J 92, 3706-3718.

113. Emsley, P. & Cowtan, K. (2004). Coot: model-building tools for molecular graphics. Acta Crystallogr D. Biol Crystallogr 60, 2126-2132.

114. Essrich, C., Lorez, M., Benson, J. A., Fritschy, J. M., & Luscher, B. (1998). Postsynaptic clustering of major GABAA receptor subtypes requires the gamma 2 subunit and gephyrin. Nat Neurosci 1, 563-571.

115. Evans, P. R. (2011). An introduction to data reduction: space-group determination, scaling and intensity statistics. Acta Crystallogr D. Biol Crystallogr 67, 282-292.

116. Fabrichny, I. P., Leone, P., Sulzenbacher, G., Comoletti, D., Miller, M. T., Taylor, P., Bourne, Y., & Marchot, P. (2007). Structural analysis of the synaptic protein neuroligin and its beta-neurexin complex: determinants for folding and cell adhesion. Neuron 56, 979-991.

117. Fan, J., Zhang, Q., Tochio, H., Li, M., & Zhang, M. (2001). Structural basis of diverse sequence-dependent target recognition by the 8 kDa dynein light chain. J. Mol. Biol 306, 97-108.

118. Fan, K. Y., Baufreton, J., Surmeier, D. J., Chan, C. S., & Bevan, M. D. (2012). Proliferation of external globus pallidus-subthalamic nucleus synapses following degeneration of midbrain dopamine neurons. J Neurosci 32, 13718-13728.

119. Fang, M., Shen, L., Yin, H., Pan, Y. M., Wang, L., Chen, D., Xi, Z. Q., Xiao, Z., Wang, X. F., & Zhou, S. N. (2011). Downregulation of gephyrin in temporal lobe epilepsy neurons in humans and a rat model. Synapse 65, 1006-1014.

120. Feng, G., Tintrup, H., Kirsch, J., Nichol, M. C., Kuhse, J., Betz, H., & Sanes, J. R. (1998). Dual requirement for gephyrin in glycine receptor clustering and molybdoenzyme activity. Science 282, 1321-1324.

121. Ferron, F., Rebowski, G., Lee, S. H., & Dominguez, R. (2007). Structural basis for the recruitment of profilin-actin complexes during filament elongation by Ena/VASP. EMBO J 26, 4597-4606.

122. Fischer, H., de Oliveira Neto, M., Napolitano, H. B., Polikarpov, I., & Craievich, A. F. (2009). Determination of the molecular weight of proteins in solution from a single small-angle X-ray scattering measurement on a relative scale. J Appl Crystallogr 43, 101-109.

123. Forman-Kay, J. D. & Mittag, T. (2013). From sequence and forces to structure, function, and evolution of intrinsically disordered proteins. Structure 21, 1492-1499.

124. Forstera, B., Belaidi, A. A., Juttner, R., Bernert, C., Tsokos, M., Lehmann, T. N., Horn, P., Dehnicke, C., Schwarz, G., & Meier, J. C. (2010). Irregular RNA splicing curtails postsynaptic gephyrin in the cornu ammonis of patients with epilepsy. Brain 133, 3778-3794.

125. Fotiadis, D., Scheuring, S., Muller, S. A., Engel, A., & Muller, D. J. (2002). Imaging and manipulation of biological structures with the AFM. Micron. 33, 385-397.

126. Franke, D., Kikhney, A. G., & Svergun, D. I. (2012). Automated acquisition and analysis of small angle X-ray scattering data. Nucl Instrum Meth A 689, 52-59.

127. Franke, D. & Svergun, D. I. (2009). DAMMIF , a program for rapid ab-initio shape determination in small-angle scattering. J Appl Crystallogr 42, 342-346.

128. Freund, T. F. & Katona, I. (2007). Perisomatic inhibition. Neuron 56, 33-42.

129. Frisken, B. J. (2001). Revisiting the method of cumulants for the analysis of dynamic light-scattering data. Appl Opt. 40, 4087-4091.

130. Fritschy, J. M., Harvey, R. J., & Schwarz, G. (2008). Gephyrin: where do we stand, where do we go? Trends Neurosci 31, 257-264.

131. Fu, Y. & Huang, Z. J. (2010). Differential dynamics and activity-dependent regulation of alpha- and beta-neurexins at developing GABAergic synapses. Proc Natl Acad Sci U S A 107, 22699-22704.

132. Fuhrmann, J. C., Kins, S., Rostaing, P., El, F. O., Kirsch, J., Sheng, M., Triller, A., Betz, H., & Kneussel, M. (2002). Gephyrin interacts with Dynein light chains 1 and 2, components of motor protein complexes. J Neurosci 22, 5393-5402.

133. Fukaya, M., Kamata, A., Hara, Y., Tamaki, H., Katsumata, O., Ito, N., Takeda, S., Hata, Y., Suzuki, T., Watanabe, M., Harvey, R. J., & Sakagami, H. (2011). SynArfGEF is a guanine nucleotide exchange factor for Arf6 and localizes preferentially at post-synaptic specializations of inhibitory synapses. J Neurochem 116, 1122-1137.

134. Gagnon, J. A. & Mowry, K. L. (2011). Molecular motors: directing traffic during RNA localization. Crit Rev Biochem Mol. Biol 46, 229-239.

135. Gallego, P., Velazquez-Campoy, A., Regue, L., Roig, J., & Reverter, D. (2013). Structural analysis of the regulation of the DYNLL/LC8 binding to Nek9 by phosphorylation. J Biol Chem 288, 12283-12294.

136. Gasteiger, E., Gattiker, A., Hoogland, C., Ivanyi, I., Appel, R. D., & Bairoch, A. (2003). ExPASy: The proteomics server for in-depth protein knowledge and analysis. Nucleic Acids Res 31, 3784-3788.

137. Giannone, G., Mondin, M., Grillo-Bosch, D., Tessier, B., Saint-Michel, E., Czondor, K., Sainlos, M., Choquet, D., & Thoumine, O. (2013). Neurexin-1beta binding to neuroligin-1 triggers the preferential recruitment of PSD-95 versus gephyrin through tyrosine phosphorylation of neuroligin-1. Cell Rep 3, 1996-2007.

138. Giesemann, T., Schwarz, G., Nawrotzki, R., Berhorster, K., Rothkegel, M., Schluter, K., Schrader, N., Schindelin, H., Mendel, R. R., Kirsch, J., & Jockusch, B. M. (2003). Complex formation between the postsynaptic scaffolding protein gephyrin, profilin, and Mena: a possible link to the microfilament system. J Neurosci 23, 8330-8339.

139. Gkogkas, C. G., Khoutorsky, A., Ran, I., Rampakakis, E., Nevarko, T., Weatherill, D. B., Vasuta, C., Yee, S., Truitt, M., Dallaire, P., Major, F., Lasko, P., Ruggero, D., Nader, K., Lacaille, J. C., & Sonenberg, N. (2013). Autism-related deficits via dysregulated eIF4E-dependent translational control. Nature 493, 371-377.

140. Grosskreutz, Y., Betz, H., & Kneussel, M. (2003). Rescue of molybdenum cofactor biosynthesis in gephyrin-deficient mice by a Cnx1 transgene. Biochem Biophys Res Commun 301, 450-455.

141. Grosskreutz, Y., Hermann, A., Kins, S., Fuhrmann, J. C., Betz, H., & Kneussel, M. (2001). Identification of a gephyrin-binding motif in the GDP/GTP exchange factor collybistin. Biol Chem 382, 1455-1462.

142. Grudzinska, J., Schemm, R., Haeger, S., Nicke, A., Schmalzing, G., Betz, H., & Laube, B. (2005). The beta subunit determines the ligand binding properties of synaptic glycine receptors. Neuron 45, 727-739.

143. Haenggi, T. & Fritschy, J. M. (2006). Role of dystrophin and utrophin for assembly and function of the dystrophin glycoprotein complex in non-muscle tissue. Cell Mol. Life Sci 63, 1614-1631.

144. Hales, C. M., Rees, H., Seyfried, N. T., Dammer, E. B., Duong, D. M., Gearing, M., Montine, T. J., Troncoso, J. C., Thambisetty, M., Levey, A. I., Lah, J. J., & Wingo, T. S. (2013). Abnormal gephyrin immunoreactivity associated with Alzheimer disease pathologic changes. J Neuropathol Exp. Neurol 72, 1009-1015.

145. Hall, J., Karplus, P. A., & Barbar, E. (2009). Multivalency in the assembly of intrinsically disordered Dynein intermediate chain. J Biol Chem 284, 33115-33121.

146. Hall, J., Song, Y., Karplus, P. A., & Barbar, E. (2010). The crystal structure of dynein intermediate chain-light chain roadblock complex gives new insights into dynein assembly. J Biol Chem 285, 22566-22575.

147. Hanus, C., Vannier, C., & Triller, A. (2004). Intracellular association of glycine receptor with gephyrin increases its plasma membrane accumulation rate. J Neurosci 24, 1119-1128.

148. Harrell, J. M., Murphy, P. J., Morishima, Y., Chen, H., Mansfield, J. F., Galigniana, M. D., & Pratt, W. B. (2004). Evidence for glucocorticoid receptor transport on microtubules by dynein. J Biol Chem 279, 54647-54654.

149. Harris, K. M. & Kater, S. B. (1994). Dendritic spines: cellular specializations imparting both stability and flexibility to synaptic function. Annu Rev Neurosci 17, 341-371.

150. Harvey, K., Duguid, I. C., Alldred, M. J., Beatty, S. E., Ward, H., Keep, N. H., Lingenfelter, S. E., Pearce, B. R., Lundgren, J., Owen, M. J., Smart, T. G., Luscher, B., Rees, M. I., & Harvey, R. J. (2004). The GDP-GTP exchange factor collybistin: an essential determinant of neuronal gephyrin clustering. J Neurosci 24, 5816-5826.

151. Harvey, R. J., Topf, M., Harvey, K., & Rees, M. I. (2008). The genetics of hyperekplexia: more than startle! Trends Genet 24, 439-447.

152. Heisler, F. F., Loebrich, S., Pechmann, Y., Maier, N., Zivkovic, A. R., Tokito, M., Hausrat, T. J., Schweizer, M., Bahring, R., Holzbaur, E. L., Schmitz, D., & Kneussel, M. (2011). Muskelin regulates actin filament- and microtubule-based GABA(A) receptor transport in neurons. Neuron 70, 66-81.

153. Heller, E. A., Zhang, W., Selimi, F., Earnheart, J. C., Slimak, M. A., Santos-Torres, J., Ibanez-Tallon, I., Aoki, C., Chait, B. T., & Heintz, N. (2012). The biochemical anatomy of cortical inhibitory synapses. PloS One 7, e39572.

154. Herrera-Molina, R., Sarto-Jackson, I., Montenegro-Venegas, C., Heine, M., Smalla, K. H., Seidenbecher, C. I., Beesley, P. W., Gundelfinger, E. D., & Montag, D. (2014). Structure of Excitatory Synapses and GABAA Receptor Localization at Inhibitory Synapses Are Regulated by Neuroplastin-65. J Biol Chem 289, 8973-8988.

155. Herweg, J. & Schwarz, G. (2012). Splice-specific glycine receptor binding, folding, and phosphorylation of the scaffolding protein gephyrin. J Biol Chem 287, 12645-12656.

156. Hibbs, R. E. & Gouaux, E. (2011). Principles of activation and permeation in an anion-selective Cys-loop receptor. Nature 474, 54-60.

157. Hilf, R. J. & Dutzler, R. (2008). X-ray structure of a prokaryotic pentameric ligand-gated ion channel. Nature 452, 375-379.

158. Hirokawa, N. (1998). Kinesin and dynein superfamily proteins and the mechanism of organelle transport. Science 279, 519-526.

159. Hirokawa, N. & Takemura, R. (2005). Molecular motors and mechanisms of directional transport in neurons. Nat Rev Neurosci 6, 201-214.

160. Holliday, G. L., Thornton, J. M., Marquet, A., Smith, A. G., Rebeille, F., Mendel, R., Schubert, H. L., Lawrence, A. D., & Warren, M. J. (2007). Evolution of enzymes and pathways for the biosynthesis of cofactors. Nat Prod. Rep 24, 972-987.

161. Hollup, S. M., Salensminde, G., & Reuter, N. (2005). WEBnm@: a web application for normal mode analyses of proteins. BMC Bioinformatics. 6, 52.

162. Holm, L., Kaariainen, S., Rosenstrom, P., & Schenkel, A. (2008). Searching protein structure databases with DaliLite v.3. Bioinformatics. 24, 2780-2781.

163. Holz, M. K., Ballif, B. A., Gygi, S. P., & Blenis, J. (2005). mTOR and S6K1 mediate assembly of the translation preinitiation complex through dynamic protein interchange and ordered phosphorylation events. Cell 123, 569-580.

164. Hoon, M., Bauer, G., Fritschy, J. M., Moser, T., Falkenburger, B. H., & Varoqueaux, F. (2009). Neuroligin 2 controls the maturation of GABAergic synapses and information processing in the retina. J Neurosci 29, 8039-8050.

165. Hoon, M., Soykan, T., Falkenburger, B., Hammer, M., Patrizi, A., Schmidt, K. F., Sassoe-Pognetto, M., Lowel, S., Moser, T., Taschenberger, H., Brose, N., & Varoqueaux, F. (2011). Neuroligin-4 is localized to glycinergic postsynapses and regulates inhibition in the retina. Proc Natl Acad Sci U S A 108, 3053-3058.

166. Hosie, A. M., Dunne, E. L., Harvey, R. J., & Smart, T. G. (2003). Zinc-mediated inhibition of GABA(A) receptors: discrete binding sites underlie subtype specificity. Nat Neurosci 6, 362-369.

167. Hubbard, S. J. (1998). The structural aspects of limited proteolysis of native proteins. Biochim. Biophys Acta 1382, 191-206.

168. Huttlin, E. L., Jedrychowski, M. P., Elias, J. E., Goswami, T., Rad, R., Beausoleil, S. A., Villen, J., Haas, W., Sowa, M. E., & Gygi, S. P. (2010). A tissue-specific atlas of mouse protein phosphorylation and expression. Cell 143, 1174-1189.

169. Ibanez, C. F. (2007). Message in a bottle: long-range retrograde signaling in the nervous system. Trends Cell Biol 17, 519-528.

170. Ichtchenko, K., Hata, Y., Nguyen, T., Ullrich, B., Missler, M., Moomaw, C., & Sudhof, T. C. (1995). Neuroligin 1: a splice site-specific ligand for beta-neurexins. Cell 81, 435-443.

171. Ichtchenko, K., Nguyen, T., & Sudhof, T. C. (1996). Structures, alternative splicing, and neurexin binding of multiple neuroligins. J Biol Chem 271, 2676-2682.

172. Irie, F. & Yamaguchi, Y. (2002). EphB receptors regulate dendritic spine development via intersectin, Cdc42 and N-WASP. Nat Neurosci 5, 1117-1118.

173. Ito, H., Morishita, R., Tabata, H., & Nagata, K. I. (2014). Roles of Rho small GTPases in the tangentially migrating neurons. Histol. Histopathol.

174. Jackson, M. B. (2006). Protein association in membranes - reduction of dimensionality, Molecular and Cellular Biophysics, pp. 107-108. Cambridge University Press.

175. Jamain, S., Quach, H., Betancur, C., Rastam, M., Colineaux, C., Gillberg, I. C., Soderstrom, H., Giros, B., Leboyer, M., Gillberg, C., & Bourgeron, T. (2003). Mutations of the X-linked genes encoding neuroligins NLGN3 and NLGN4 are associated with autism. Nat Genet 34, 27-29.

176. Jedlicka, P., Hoon, M., Papadopoulos, T., Vlachos, A., Winkels, R., Poulopoulos, A., Betz, H., Deller, T., Brose, N., Varoqueaux, F., & Schwarzacher, S. W. (2011). Increased dentate gyrus excitability in neuroligin-2-deficient mice in vivo. Cereb. Cortex 21, 357-367.

177. Jedlicka, P., Papadopoulos, T., Deller, T., Betz, H., & Schwarzacher, S. W. (2009). Increased network excitability and impaired induction of long-term potentiation in the dentate gyrus of collybistin-deficient mice in vivo. Mol. Cell Neurosci 41, 94-100.

178. Jinno, S., Klausberger, T., Marton, L. F., Dalezios, Y., Roberts, J. D., Fuentealba, P., Bushong, E. A., Henze, D., Buzsaki, G., & Somogyi, P. (2007). Neuronal diversity in GABAergic long-range projections from the hippocampus. J Neurosci 27, 8790-8804.

179. Jones, B. L. & Henderson, L. P. (2007). Trafficking and potential assembly patterns of epsilon-containing GABAA receptors. J Neurochem 103, 1258-1271.

180. Jungbauer, A. & Hahn, R. (2009). Ion-exchange chromatography. Methods Enzymol 463, 349-371.

181. Kalscheuer, V. M., Musante, L., Fang, C., Hoffmann, K., Fuchs, C., Carta, E., Deas, E., Venkateswarlu, K., Menzel, C., Ullmann, R., Tommerup, N., Dalpra, L., Tzschach, A., Selicorni, A., Luscher, B., Ropers, H. H., Harvey, K., & Harvey, R. J. (2009). A balanced chromosomal translocation disrupting ARHGEF9 is associated with epilepsy, anxiety, aggression, and mental retardation. Hum. Mutat 30, 61-68.

182. Kane, R. S. (2010). Thermodynamics of multivalent interactions: influence of the linker. Langmuir 26, 8636-8640.

183. Kang, R., Wan, J., Arstikaitis, P., Takahashi, H., Huang, K., Bailey, A. O., Thompson, J. X., Roth, A. F., Drisdel, R. C., Mastro, R., Green, W. N., Yates, J. R., III, Davis, N. G., & El-Husseini, A. (2008). Neural palmitoyl-proteomics reveals dynamic synaptic palmitoylation. Nature 456, 904-909.

184. Kardon, J. R. & Vale, R. D. (2009). Regulators of the cytoplasmic dynein motor. Nat Rev Mol. Cell Biol 10, 854-865.

185. Karki, S., Ligon, L. A., DeSantis, J., Tokito, M., & Holzbaur, E. L. (2002). PLAC-24 is a cytoplasmic dynein-binding protein that is recruited to sites of cell-cell contact. Mol. Biol Cell 13, 1722-1734.

186. Kaufholdt, D., Gehl, C., Geisler, M., Jeske, O., Voedisch, S., Ratke, C., Bollhoner, B., Mendel, R. R., & Hansch, R. (2013). Visualization and quantification of protein interactions in the biosynthetic pathway of molybdenum cofactor in Arabidopsis thaliana. J Exp. Bot. 64, 2005-2016.

187. Keller, K. (2010). Charakterisierung der Interaktionen von Gephyrin mit Neuroligin 2, PIN1 und DLC1, Julius-Maximilians-Universität Würzburg, Fakultät für Chemie und Pharmazie.

188. Keller, S., Vargas, C., Zhao, H., Piszczek, G., Brautigam, C. A., & Schuck, P. (2012). High-precision isothermal titration calorimetry with automated peak-shape analysis. Anal. Chem 84, 5066-5073.

189. Kelley, L. A. & Sternberg, M. J. (2009). Protein structure prediction on the Web: a case study using the Phyre server. Nat. Protoc. 4, 363-371.

190. Kelly, S. M., Jess, T. J., & Price, N. C. (2005). How to study proteins by circular dichroism. Biochim. Biophys Acta 1751, 119-139.

191. Kepecs, A. & Fishell, G. (2014). Interneuron cell types are fit to function. Nature 505, 318-326.

192. Kesters, D., Thompson, A. J., Brams, M., van, E. R., Spurny, R., Geitmann, M., Villalgordo, J. M., Guskov, A., Danielson, U. H., Lummis, S. C., Smit, A. B., & Ulens, C. (2013). Structural basis of ligand recognition in 5-HT3 receptors. EMBO Rep 14, 49-56.

193. Kidane, A. I., Song, Y., Nyarko, A., Hall, J., Hare, M., Lohr, F., & Barbar, E. (2013). Structural features of LC8-induced self-association of swallow. Biochemistry 52, 6011-6020.

194. Kikkawa, M. (2013). Big steps toward understanding dynein. J Cell Biol 202, 15-23.

195. Kim, E. Y., Schrader, N., Smolinsky, B., Bedet, C., Vannier, C., Schwarz, G., & Schindelin, H. (2006). Deciphering the structural framework of glycine receptor anchoring by gephyrin. EMBO J 25, 1385-1395.

196. Kinoshita, E., Kinoshita-Kikuta, E., Takiyama, K., & Koike, T. (2006). Phosphate-binding tag, a new tool to visualize phosphorylated proteins. Mol. Cell Proteomics 5, 749-757.

197. Kins, S., Betz, H., & Kirsch, J. (2000). Collybistin, a newly identified brain-specific GEF, induces submembrane clustering of gephyrin. Nat Neurosci 3, 22-29.

198. Kirsch, J. & Betz, H. (1995). The postsynaptic localization of the glycine receptor-associated protein gephyrin is regulated by the cytoskeleton. J Neurosci 15, 4148-4156.

199. Kirsch, J., Kuhse, J., & Betz, H. (1995). Targeting of glycine receptor subunits to gephyrin-rich domains in transfected human embryonic kidney cells. Mol. Cell Neurosci 6, 450-461.

200. Kirsch, J., Langosch, D., Prior, P., Littauer, U. Z., Schmitt, B., & Betz, H. (1991). The 93-kDa glycine receptor-associated protein binds to tubulin. 266, 22242-22245.

201. Kirsch, J., Wolters, I., Triller, A., & Betz, H. (1993). Gephyrin antisense oligonucleotides prevent glycine receptor clustering in spinal neurons. Nature 366, 745-748.

202. Kneussel, M. (2005). Postsynaptic scaffold proteins at non-synaptic sites. The role of postsynaptic scaffold proteins in motor-protein-receptor complexes. EMBO Rep 6, 22-27.

203. Kneussel, M. & Betz, H. (2000). Clustering of inhibitory neurotransmitter receptors at developing postsynaptic sites: the membrane activation model. Trends Neurosci 23, 429-435.

204. Kneussel, M., Brandstatter, J. H., Gasnier, B., Feng, G., Sanes, J. R., & Betz, H. (2001). Gephyrin-independent clustering of postsynaptic GABA(A) receptor subtypes. Mol. Cell Neurosci 17, 973-982.

205. Kneussel, M., Brandstatter, J. H., Laube, B., Stahl, S., Muller, U., & Betz, H. (1999a). Loss of postsynaptic GABA(A) receptor clustering in gephyrin-deficient mice. J Neurosci 19, 9289-9297.

206. Kneussel, M., Haverkamp, S., Fuhrmann, J. C., Wang, H., Wassle, H., Olsen, R. W., & Betz, H. (2000). The gamma-aminobutyric acid type A receptor (GABAAR)-associated protein GABARAP interacts with gephyrin but is not involved in receptor anchoring at the synapse. Proc Natl Acad Sci U S A 97, 8594-8599.

207. Kneussel, M., Hermann, A., Kirsch, J., & Betz, H. (1999b). Hydrophobic interactions mediate binding of the glycine receptor beta-subunit to gephyrin. J Neurochem 72, 1323-1326.

208. Kneussel, M. & Loebrich, S. (2007). Trafficking and synaptic anchoring of ionotropic inhibitory neurotransmitter receptors. Biol Cell 99, 297-309.

209. Knuesel, I., Mastrocola, M., Zuellig, R. A., Bornhauser, B., Schaub, M. C., & Fritschy, J. M. (1999). Short communication: altered synaptic clustering of GABAA receptors in mice lacking dystrophin (mdx mice). Eur J Neurosci 11, 4457-4462.

210. Koch, M. H., Vachette, P., & Svergun, D. I. (2003). Small-angle scattering: a view on the properties, structures and structural changes of biological macromolecules in solution. Q. Rev Biophys 36, 147-227.

211. Koehnke, J., Jin, X., Budreck, E. C., Posy, S., Scheiffele, P., Honig, B., & Shapiro, L. (2008). Crystal structure of the extracellular cholinesterase-like domain from neuroligin-2. Proc Natl Acad Sci U S A 105, 1873-1878.

212. Koehnke, J., Katsamba, P. S., Ahlsen, G., Bahna, F., Vendome, J., Honig, B., Shapiro, L., & Jin, X. (2010). Splice form dependence of beta-neurexin/neuroligin binding interactions. Neuron 67, 61-74.

213. Kon, T., Oyama, T., Shimo-Kon, R., Imamula, K., Shima, T., Sutoh, K., & Kurisu, G. (2012). The 2.8 A crystal structure of the dynein motor domain. Nature 484, 345-350.

214. Konarev, P. V., Petoukhov, M. V., Volkov, V. V., & Svergun, D. I. (2006). ATSAS 2.1, a program package for small-angle scattering data analysis. J. Appl. Cryst. 39, 277-286.

215. Konarev, P. V., Volkov, V. V., Sokolova, A. V., Koch, M. H. J., & Svergun, D. I. (2003). PRIMUS: a Windows PC-based system for small-angle scattering data analysis. J Appl Crystallogr 36, 1277-1282.

216. Konermann, L., Pan, J., & Liu, Y. H. (2011). Hydrogen exchange mass spectrometry for studying protein structure and dynamics. Chem Soc Rev 40, 1224-1234.

217. Korpi, E. R., Grunder, G., & Luddens, H. (2002). Drug interactions at GABA(A) receptors. Prog. Neurobiol 67, 113-159.

218. Kowalczyk, S., Winkelmann, A., Smolinsky, B., Forstera, B., Neundorf, I., Schwarz, G., & Meier, J. C. (2013). Direct binding of GABAA receptor beta2 and beta3 subunits to gephyrin. Eur J Neurosci 37, 544-554.

219. Kralic, J. E., Sidler, C., Parpan, F., Homanics, G. E., Morrow, A. L., & Fritschy, J. M. (2006). Compensatory alteration of inhibitory synaptic circuits in cerebellum and thalamus of gamma-aminobutyric acid type A receptor alpha1 subunit knockout mice. J Comp Neurol 495, 408-421.

220. Kramer, S., Hageman, R. V., & Rajagopalan, K. V. (1984). In vitro reconstitution of nitrate reductase activity of the Neurospora crassa mutant nit-1: specific incorporation of molybdopterin. Arch. Biochem Biophys 233, 821-829.

221. Krause, M., Leslie, J. D., Stewart, M., Lafuente, E. M., Valderrama, F., Jagannathan, R., Strasser, G. A., Rubinson, D. A., Liu, H., Way, M., Yaffe, M. B., Boussiotis, V. A., & Gertler, F. B. (2004). Lamellipodin, an Ena/VASP ligand, is implicated in the regulation of lamellipodial dynamics. Dev Cell 7, 571-583.

222. Kriebel, M., Metzger, J., Trinks, S., Chugh, D., Harvey, R. J., Harvey, K., & Volkmer, H. (2011). The cell adhesion molecule neurofascin stabilizes axo-axonic GABAergic terminals at the axon initial segment. J Biol Chem 286, 24385-24393.

223. Kriebel, M., Wuchter, J., Trinks, S., & Volkmer, H. (2012). Neurofascin: a switch between neuronal plasticity and stability. Int J Biochem Cell Biol 44, 694-697.

224. Krissinel, E. & Henrick, K. (2007). Inference of macromolecular assemblies from crystalline state. J Mol. Biol 372, 774-797.

225. Krueger, D. D., Tuffy, L. P., Papadopoulos, T., & Brose, N. (2012). The role of neurexins and neuroligins in the formation, maturation, and function of vertebrate synapses. Curr Opin. Neurobiol 22, 412-422.

226. Kuhse, J., Kalbouneh, H., Schlicksupp, A., Mukusch, S., Nawrotzki, R., & Kirsch, J. (2012). Phosphorylation of Gephyrin in Hippocampal Neurons by Cyclin-dependent Kinase CDK5 at Ser-270 Is Dependent on Collybistin. J Biol Chem 287, 30952-30966.

227. Kulkarni, V. A. & Firestein, B. L. (2012). The dendritic tree and brain disorders. Mol. Cell Neurosci 50, 10-20.

228. Kullmann, D. M., Ruiz, A., Rusakov, D. M., Scott, R., Semyanov, A., & Walker, M. C. (2005). Presynaptic, extrasynaptic and axonal GABAA receptors in the CNS: where and why? Prog. Biophys Mol. Biol 87, 33-46.

229. Kumar, S., Porcu, P., Werner, D. F., Matthews, D. B., az-Granados, J. L., Helfand, R. S., & Morrow, A. L. (2009). The role of GABA(A) receptors in the acute and chronic effects of ethanol: a decade of progress. Psychopharmacology (Berl) 205, 529-564.

230. Kuper, J., Palmer, T., Mendel, R. R., & Schwarz, G. (2000). Mutations in the molybdenum cofactor biosynthetic protein Cnx1G from Arabidopsis thaliana define functions for molybdopterin binding, molybdenum insertion, and molybdenum cofactor stabilization. Proc Natl Acad Sci U S A 97, 6475-6480.

231. Kural, C., Kim, H., Syed, S., Goshima, G., Gelfand, V. I., & Selvin, P. R. (2005). Kinesin and dynein move a peroxisome in vivo: a tug-of-war or coordinated movement? Science 308, 1469-1472.

232. Kuzirian, M. S., Moore, A. R., Staudenmaier, E. K., Friedel, R. H., & Paradis, S. (2013). The class 4 semaphorin Sema4D promotes the rapid assembly of GABAergic synapses in rodent hippocampus. J Neurosci 33, 8961-8973.

233. Lamla, T. & Erdmann, V. A. (2004). The Nano-tag, a streptavidin-binding peptide for the purification and detection of recombinant proteins. Protein Expr Purif. 33, 39-47.

234. Langosch, D., Hoch, W., & Betz, H. (1992). The 93 kDa protein gephyrin and tubulin associated with the inhibitory glycine receptor are phosphorylated by an endogenous protein kinase. FEBS Lett 298, 113-117.

235. Laplante, M. & Sabatini, D. M. (2012). mTOR signaling in growth control and disease. Cell 149, 274-293.

236. Lardi-Studler, B., Smolinsky, B., Petitjean, C. M., Koenig, F., Sidler, C., Meier, J. C., Fritschy, J. M., & Schwarz, G. (2007). Vertebrate-specific sequences in the gephyrin E-domain regulate cytosolic aggregation and postsynaptic clustering. J Cell Sci 120, 1371-1382.

237. Laumonnier, F., Bonnet-Brilhault, F., Gomot, M., Blanc, R., David, A., Moizard, M. P., Raynaud, M., Ronce, N., Lemonnier, E., Calvas, P., Laudier, B., Chelly, J., Fryns, J. P., Ropers, H. H., Hamel, B. C., Andres, C., Barthelemy, C., Moraine, C., & Briault, S. (2004). X-linked mental retardation and autism are associated with a mutation in the NLGN4 gene, a member of the neuroligin family. Am. J Hum. Genet 74, 552-557.

238. Lawson-Yuen, A., Saldivar, J. S., Sommer, S., & Picker, J. (2008). Familial deletion within NLGN4 associated with autism and Tourette syndrome. Eur J Hum. Genet 16, 614-618.

239. Lee, E.-Y. (2009). Structural and Biochemical Characterization of Interaction between Gephyrin and Dynein Light Chains, Stony Brook University.

240. Lee, H. J., Adham, I. M., Schwarz, G., Kneussel, M., Sass, J. O., Engel, W., & Reiss, J. (2002). Molybdenum cofactor-deficient mice resemble the phenotype of human patients. Hum. Mol. Genet 11, 3309-3317.

241. Lee, K., Kim, Y., Lee, S. J., Qiang, Y., Lee, D., Lee, H. W., Kim, H., Je, H. S., Sudhof, T. C., & Ko, J. (2013). MDGAs interact selectively with neuroligin-2 but not other neuroligins to regulate inhibitory synapse development. Proc Natl Acad Sci U S A 110, 336-341.

242. Lee, S., Yoon, B. E., Berglund, K., Oh, S. J., Park, H., Shin, H. S., Augustine, G. J., & Lee, C. J. (2010). Channel-mediated tonic GABA release from glia. Science 330, 790-796.

243. Legendre, P. (2001). The glycinergic inhibitory synapse. Cell Mol. Life Sci 58, 760-793.

244. Lemaire, P. A., Tessmer, I., Craig, R., Erie, D. A., & Cole, J. L. (2006). Unactivated PKR exists in an open conformation capable of binding nucleotides. Biochemistry 45, 9074-9084.

245. Leone, P., Comoletti, D., Ferracci, G., Conrod, S., Garcia, S. U., Taylor, P., Bourne, Y., & Marchot, P. (2010). Structural insights into the exquisite selectivity of neurexin/neuroligin synaptic interactions. EMBO J 29, 2461-2471.

246. Levi, S., Logan, S. M., Tovar, K. R., & Craig, A. M. (2004). Gephyrin is critical for glycine receptor clustering but not for the formation of functional GABAergic synapses in hippocampal neurons. J Neurosci 24, 207-217.

247. Levinson, J. N. & El-Husseini, A. (2005). Building excitatory and inhibitory synapses: balancing neuroligin partnerships. Neuron 48, 171-174.

248. Levinson, J. N., Li, R., Kang, R., Moukhles, H., El-Husseini, A., & Bamji, S. X. (2010). Postsynaptic scaffolding molecules modulate the localization of neuroligins. Neuroscience 165, 782-793.

249. Li, X., Romero, P., Rani, M., Dunker, A. K., & Obradovic, Z. (1999). Predicting Protein Disorder for N-, C-, and Internal Regions. Genome Inform. Ser. Workshop Genome Inform. 10, 30-40.

250. Liang, J., Jaffrey, S. R., Guo, W., Snyder, S. H., & Clardy, J. (1999). Structure of the PIN/LC8 dimer with a bound peptide. Nat Struct Biol 6, 735-740.

251. Lightcap, C. M., Sun, S., Lear, J. D., Rodeck, U., Polenova, T., & Williams, J. C. (2008). Biochemical and structural characterization of the Pak1-LC8 interaction. J. Biol. Chem 283, 27314-27324.

252. Lin, J., Okada, K., Raytchev, M., Smith, M. C., & Nicastro, D. (2014). Structural mechanism of the dynein power stroke. Nat Cell Biol.

253. Linding, R., Jensen, L. J., Diella, F., Bork, P., Gibson, T. J., & Russell, R. B. (2003). Protein disorder prediction: implications for structural proteomics. Structure 11, 1453-1459.

254. Linsalata, A. E., Chen, X., Winters, C. A., & Reese, T. S. (2014). Electron tomography on gamma-aminobutyric acid-ergic synapses reveals a discontinuous postsynaptic network of filaments. J Comp Neurol 522, 921-936.

255. Liou, Y. C., Zhou, X. Z., & Lu, K. P. (2011). Prolyl isomerase Pin1 as a molecular switch to determine the fate of phosphoproteins. Trends Biochem Sci 36, 501-514.

256. Liu, J., Wu, D. C., & Wang, Y. T. (2010). Allosteric potentiation of glycine receptor chloride currents by glutamate. Nat Neurosci 13, 1225-1232.

257. Liu, Y., Salter, H. K., Holding, A. N., Johnson, C. M., Stephens, E., Lukavsky, P. J., Walshaw, J., & Bullock, S. L. (2013). Bicaudal-D uses a parallel, homodimeric coiled coil with heterotypic registry to coordinate recruitment of cargos to dynein. Genes Dev 27, 1233-1246.

258. Lo, K. W., Kogoy, J. M., Rasoul, B. A., King, S. M., & Pfister, K. K. (2007). Interaction of the DYNLT (TCTEX1/RP3) light chains and the intermediate chains reveals novel intersubunit regulation during assembly of the dynein complex. J Biol Chem 282, 36871-36878.

259. Loebrich, S., Bahring, R., Katsuno, T., Tsukita, S., & Kneussel, M. (2006). Activated radixin is essential for GABAA receptor alpha5 subunit anchoring at the actin cytoskeleton. EMBO J 25, 987-999.

260. London, N., Movshovitz-Attias, D., & Schueler-Furman, O. (2010). The structural basis of peptide-protein binding strategies. Structure 18, 188-199.

261. Lottspeich, F. & Zorbas, H. (1998). Bioanalytik Spektrum.

262. Lozovaya, N., Mukhtarov, M., Tsintsadze, T., Ledent, C., Burnashev, N., & Bregestovski, P. (2011). Frequency-Dependent Cannabinoid Receptor-Independent Modulation of Glycine Receptors by Endocannabinoid 2-AG. Front Mol. Neurosci 4, 13.

263. Luscher, B., Fuchs, T., & Kilpatrick, C. L. (2011). GABAA receptor trafficking-mediated plasticity of inhibitory synapses. Neuron 70, 385-409.

264. Maas, C., Belgardt, D., Lee, H. K., Heisler, F. F., Lappe-Siefke, C., Magiera, M. M., van, D. J., Hausrat, T. J., Janke, C., & Kneussel, M. (2009). Synaptic activation modifies microtubules underlying transport of postsynaptic cargo. Proc Natl Acad Sci U S A 106, 8731-8736.

265. Maas, C., Tagnaouti, N., Loebrich, S., Behrend, B., Lappe-Siefke, C., & Kneussel, M. (2006). Neuronal cotransport of glycine receptor and the scaffold protein gephyrin. J Cell Biol 172, 441-451.

266. Macarov, M., Zeigler, M., Newman, J. P., Strich, D., Sury, V., Tennenbaum, A., & Meiner, V. (2007). Deletions of VCX-A and NLGN4: a variable phenotype including normal intellect. J Intellect. Disabil. Res 51, 329-333.

267. Machado, P., Rostaing, P., Guigonis, J. M., Renner, M., Dumoulin, A., Samson, M., Vannier, C., & Triller, A. (2011). Heat shock cognate protein 70 regulates gephyrin clustering. J Neurosci 31, 3-14.

268. Mackay, D. J. & Hall, A. (1998). Rho GTPases. J Biol Chem 273, 20685-20688.

269. Madler, S., Seitz, M., Robinson, J., & Zenobi, R. (2010). Does chemical cross-linking with NHS esters reflect the chemical equilibrium of protein-protein noncovalent interactions in solution? J Am. Soc Mass Spectrom. 21, 1775-1783.

270. Maedler, S., Bich, C., Touboul, D., & Zenobi, R. (2009). Chemical cross-linking with NHS esters: a systematic study on amino acid reactivities. J Mass Spectrom. 44, 694-706.

271. Magalon, A., Frixon, C., Pommier, J., Giordano, G., & Blasco, F. (2002). In vivo interactions between gene products involved in the final stages of molybdenum cofactor biosynthesis in Escherichia coli. J Biol Chem 277, 48199-48204.

272. Maksay, G., Laube, B., & Betz, H. (2001). Subunit-specific modulation of glycine receptors by neurosteroids. Neuropharmacology 41, 369-376.

273. Maksay, G., Nemes, P., Vincze, Z., & Biro, T. (2008). Synthesis of (nor)tropeine (di)esters and allosteric modulation of glycine receptor binding. Bioorg. Med Chem 16, 2086-2092.

274. Mammoto, A., Sasaki, T., Asakura, T., Hotta, I., Imamura, H., Takahashi, K., Matsuura, Y., Shirao, T., & Takai, Y. (1998). Interactions of drebrin and gephyrin with profilin. Biochem Biophys Res Commun 243, 86-89.

275. Maric, H. M. (2012). Molecular Basis of the Multivalent Glycine and ã-Aminobutyric Acid Type A Receptor Anchoring, Graduate School of Life Sciences, Universität Würzburg.

276. Maric, H. M., Mukherjee, J., Tretter, V., Moss, S. J., & Schindelin, H. (2011). Gephyrin-mediated gamma-aminobutyric acid type A and glycine receptor clustering relies on a common binding site. J Biol Chem 286, 42105-42114.

277. Marin, O. (2012). Interneuron dysfunction in psychiatric disorders. Nat Rev Neurosci 13, 107-120.

278. Masson, J. B., Dionne, P., Salvatico, C., Renner, M., Specht, C. G., Triller, A., & Dahan, M. (2014). Mapping the energy and diffusion landscapes of membrane proteins at the cell surface using high-density single-molecule imaging and Bayesian inference: application to the multiscale dynamics of glycine receptors in the neuronal membrane. Biophys J 106, 74-83.

279. Mayer, S., Kumar, R., Jaiswal, M., Soykan, T., Ahmadian, M. R., Brose, N., Betz, H., Rhee, J. S., & Papadopoulos, T. (2013). Collybistin activation by GTP-TC10 enhances postsynaptic gephyrin clustering and hippocampal GABAergic neurotransmission. Proc Natl Acad Sci U S A 110, 20795-20800.

280. McCoy, A. J., Grosse-Kunstleve, R. W., Adams, P. D., Winn, M. D., Storoni, L. C., & Read, R. J. (2007). Phaser crystallographic software. J Appl Crystallogr 40, 658-674.

281. McCracken, L. M., Trudell, J. R., Goldstein, B. E., Harris, R. A., & Mihic, S. J. (2010). Zinc enhances ethanol modulation of the alpha1 glycine receptor. Neuropharmacology 58, 676-681.

282. McCracken, L. M., Trudell, J. R., McCracken, M. L., & Harris, R. A. (2013). Zinc-dependent modulation of alpha2- and alpha3-glycine receptor subunits by ethanol. Alcohol Clin. Exp. Res 37, 2002-2010.

283. McGuffin, L. J., Bryson, K., & Jones, D. T. (2000). The PSIPRED protein structure prediction server. Bioinformatics. 16, 404-405.

284. McNally, F. J. (2013). Mechanisms of spindle positioning. J Cell Biol 200, 131-140.

285. Mehta, A. K. & Ticku, M. K. (1999). An update on GABAA receptors. Brain Res Brain Res Rev 29, 196-217.

286. Meier, J., Vannier, C., Serge, A., Triller, A., & Choquet, D. (2001). Fast and reversible trapping of surface glycine receptors by gephyrin. Nat Neurosci 4, 253-260.

287. Meier, J. C., Henneberger, C., Melnick, I., Racca, C., Harvey, R. J., Heinemann, U., Schmieden, V., & Grantyn, R. (2005). RNA editing produces glycine receptor alpha3(P185L), resulting in high agonist potency. Nat Neurosci 8, 736-744.

288. Melzer, N., Villmann, C., Becker, K., Harvey, K., Harvey, R. J., Vogel, N., Kluck, C. J., Kneussel, M., & Becker, C. M. (2010). Multifunctional basic motif in the glycine receptor intracellular domain induces subunit-specific sorting. J Biol Chem 285, 3730-3739.

289. Mendel, R. R. (2013). The molybdenum cofactor. J Biol Chem 288, 13165-13172.

290. Mertens, H. D. & Svergun, D. I. (2010). Structural characterization of proteins and complexes using small-angle X-ray solution scattering. J Struct Biol 172, 128-141.

291. Meyer, G., Kirsch, J., Betz, H., & Langosch, D. (1995). Identification of a gephyrin binding motif on the glycine receptor beta subunit. Neuron 15, 563-572.

292. Miller, P. S., Topf, M., & Smart, T. G. (2008). Mapping a molecular link between allosteric inhibition and activation of the glycine receptor. Nat Struct Mol. Biol 15, 1084-1093.

293. Missler, M., Sudhof, T. C., & Biederer, T. (2012). Synaptic cell adhesion. Cold Spring Harb. Perspect. Biol 4, a005694.

294. Missler, M., Zhang, W., Rohlmann, A., Kattenstroth, G., Hammer, R. E., Gottmann, K., & Sudhof, T. C. (2003). Alpha-neurexins couple Ca2+ channels to synaptic vesicle exocytosis. Nature 423, 939-948.

295. Mitin, N., Betts, L., Yohe, M. E., Der, C. J., Sondek, J., & Rossman, K. L. (2007). Release of autoinhibition of ASEF by APC leads to CDC42 activation and tumor suppression. Nat Struct Mol. Biol 14, 814-823.

296. Mohler, H. (2009). Role of GABAA receptors in cognition. Biochem Soc Trans. 37, 1328-1333.

297. Mohrluder, J., Schwarten, M., & Willbold, D. (2009). Structure and potential function of gamma-aminobutyrate type A receptor-associated protein. FEBS J 276, 4989-5005.

298. Mok, Y. K., Lo, K. W., & Zhang, M. (2001). Structure of Tctex-1 and its interaction with cytoplasmic dynein intermediate chain. J Biol Chem 276, 14067-14074.

299. Mou, L., Dias, B. G., Gosnell, H., & Ressler, K. J. (2013). Gephyrin plays a key role in BDNF-dependent regulation of amygdala surface GABAARs. Neuroscience 255, 33-44.

300. Mukherjee, J., Kretschmannova, K., Gouzer, G., Maric, H. M., Ramsden, S., Tretter, V., Harvey, K., Davies, P. A., Triller, A., Schindelin, H., & Moss, S. J. (2011). The residence time

of GABA(A)Rs at inhibitory synapses is determined by direct binding of the receptor alpha1 subunit to gephyrin. J Neurosci 31, 14677-14687.

301. Murayama, K., Shirouzu, M., Kawasaki, Y., Kato-Murayama, M., Hanawa-Suetsugu, K., Sakamoto, A., Katsura, Y., Suenaga, A., Toyama, M., Terada, T., Taiji, M., Akiyama, T., & Yokoyama, S. (2007). Crystal structure of the rac activator, Asef, reveals its autoinhibitory mechanism. J Biol Chem 282, 4238-4242.

302. Muresan, V. & Muresan, Z. (2012). Unconventional functions of microtubule motors. Arch. Biochem Biophys 520, 17-29.

303. Murk, K., Wittenmayer, N., Michaelsen-Preusse, K., Dresbach, T., Schoenenberger, C. A., Korte, M., Jockusch, B. M., & Rothkegel, M. (2012). Neuronal profilin isoforms are addressed by different signalling pathways. PloS One 7, e34167.

304. Murshudov, G. N., Vagin, A. A., & Dodson, E. J. (1997). Refinement of macromolecular structures by the maximum-likelihood method. Acta Crystallogr D. Biol Crystallogr 53, 240-255.

305. Mylonas, E. & Svergun, D. I. (2007). Accuracy of molecular mass determination of proteins in solution by small-angle X-ray scattering. J Appl Crystallogr 40, s245-s249.

306. Nair, R., Lauks, J., Jung, S., Cooke, N. E., de, W. H., Brose, N., Kilimann, M. W., Verhage, M., & Rhee, J. (2013). Neurobeachin regulates neurotransmitter receptor trafficking to synapses. J Cell Biol 200, 61-80.

307. Nam, C. I. & Chen, L. (2005). Postsynaptic assembly induced by neurexin-neuroligin interaction and neurotransmitter. Proc Natl Acad Sci U S A 102, 6137-6142.

308. Navarro-Lérida, I., Martínez Moreno, M., Roncal, F., Gavilanes, F., Albar, J. P., & Rodríguez-Crespo, I. (2004). Proteomic identification of brain proteins that interact with dynein light chain LC8. PROTEOMICS 4, 339-346.

309. Nawrotzki, R., Islinger, M., Vogel, I., Volkl, A., & Kirsch, J. (2012). Expression and subcellular distribution of gephyrin in non-neuronal tissues and cells. Histochem. Cell Biol 137, 471-482.

310. Negishi, M. & Katoh, H. (2005). Rho family GTPases and dendrite plasticity. Neuroscientist. 11, 187-191.

311. Nichols, J. D., Xiang, S., Schindelin, H., & Rajagopalan, K. V. (2007). Mutational analysis of Escherichia coli MoeA: two functional activities map to the active site cleft. Biochemistry 46, 78-86.

312. Niwa, F., Bannai, H., Arizono, M., Fukatsu, K., Triller, A., & Mikoshiba, K. (2012). Gephyrin-independent GABA(A)R mobility and clustering during plasticity. PloS One 7, e36148.

313. Nyarko, A. & Barbar, E. (2011). Light chain-dependent self-association of dynein intermediate chain. J Biol Chem 286, 1556-1566.

314. O'Connor, T. P., Cockburn, K., Wang, W., Tapia, L., Currie, E., & Bamji, S. X. (2009). Semaphorin 5B mediates synapse elimination in hippocampal neurons. Neural Dev 4, 18.

315. O'Neil, R. H., Lilien, R. H., Donald, B. R., Stroud, R. M., & Anderson, A. C. (2003). Phylogenetic classification of protozoa based on the structure of the linker domain in the bifunctional enzyme, dihydrofolate reductase-thymidylate synthase. J Biol Chem 278, 52980-52987.

316. O'Sullivan, G. A., Hofer, W., & Betz, H. (2009). Inhibitory postsynaptic membrane specializations are formed in gephyrin-deficient mice. Neurosci Lett 458, 106-110.

317. O'Sullivan, G. A., Kneussel, M., Elazar, Z., & Betz, H. (2005). GABARAP is not essential for GABA receptor targeting to the synapse. Eur J Neurosci 22, 2644-2648.

318. Oertel, J., Villmann, C., Kettenmann, H., Kirchhoff, F., & Becker, C. M. (2007). A novel glycine receptor beta subunit splice variant predicts an unorthodox transmembrane topology. Assembly into heteromeric receptor complexes. J Biol Chem 282, 2798-2807.

319. Okada, H., Uezu, A., Mason, F. M., Soderblom, E. J., Moseley, M. A., III, & Soderling, S. H. (2011). SH3 domain-based phototrapping in living cells reveals Rho family GAP signaling complexes. Sci Signal. 4, rs13.

320. Olsen, R. W. & Sieghart, W. (2008). International Union of Pharmacology. LXX. Subtypes of gamma-aminobutyric acid(A) receptors: classification on the basis of subunit composition, pharmacology, and function. Update. Pharmacol Rev 60, 243-260.

321. Ozawa, S., Kamiya, H., & Tsuzuki, K. (1998). Glutamate receptors in the mammalian central nervous system. Prog. Neurobiol 54, 581-618.

322. Paarmann, I., Schmitt, B., Meyer, B., Karas, M., & Betz, H. (2006). Mass spectrometric analysis of glycine receptor-associated gephyrin splice variants. J Biol Chem 281, 34918-34925.

323. Painter, J. & Merritt, E. A. (2006). Optimal description of a protein structure in terms of multiple groups undergoing TLS motion. Acta Crystallogr D. Biol Crystallogr 62, 439-450.

324. Panzanelli, P., Gunn, B. G., Schlatter, M. C., Benke, D., Tyagarajan, S. K., Scheiffele, P., Belelli, D., Lambert, J. J., Rudolph, U., & Fritschy, J. M. (2011). Distinct mechanisms regulate GABAA receptor and gephyrin clustering at perisomatic and axo-axonic synapses on CA1 pyramidal cells. J Physiol 589, 4959-4980.

325. Panzanelli, P., Perazzini, A. Z., Fritschy, J. M., & Sassoe-Pognetto, M. (2005). Heterogeneity of gamma-aminobutyric acid type A receptors in mitral and tufted cells of the rat main olfactory bulb. J Comp Neurol 484, 121-131.

326. Papadopoulos, T., Eulenburg, V., Reddy-Alla, S., Mansuy, I. M., Li, Y., & Betz, H. (2008). Collybistin is required for both the formation and maintenance of GABAergic postsynapses in the hippocampus. Mol. Cell Neurosci 39, 161-169.

327. Papadopoulos, T., Korte, M., Eulenburg, V., Kubota, H., Retiounskaia, M., Harvey, R. J., Harvey, K., O'Sullivan, G. A., Laube, B., Hulsmann, S., Geiger, J. R., & Betz, H. (2007). Impaired GABAergic transmission and altered hippocampal synaptic plasticity in collybistin-deficient mice. EMBO J 26, 3888-3899.

328. Papadopoulos, T. & Soykan, T. (2011). The role of collybistin in gephyrin clustering at inhibitory synapses: facts and open questions. Front Cell Neurosci 5, 11.

329. Paradis, S., Harrar, D. B., Lin, Y., Koon, A. C., Hauser, J. L., Griffith, E. C., Zhu, L., Brass, L. F., Chen, C., & Greenberg, M. E. (2007). An RNAi-based approach identifies molecules required for glutamatergic and GABAergic synapse development. Neuron 53, 217-232.

330. Parassol, N., Bienvenu, C., Boglio, C., Fiorucci, S., Cerezo, D., Yu, X. M., Godeau, G., Greiner, J., Vierling, P., Noselli, S., Di, G. C., & Van, D. B., V (2013). In vivo characterization of dynein-driven nanovectors using Drosophila oocytes. PloS One 8, e82908.

331. Park, H. S., Hohn, M. J., Umehara, T., Guo, L. T., Osborne, E. M., Benner, J., Noren, C. J., Rinehart, J., & Soll, D. (2011). Expanding the genetic code of Escherichia coli with phosphoserine. Science 333, 1151-1154.

332. Patrizi, A., Scelfo, B., Viltono, L., Briatore, F., Fukaya, M., Watanabe, M., Strata, P., Varoqueaux, F., Brose, N., Fritschy, J. M., & Sassoe-Pognetto, M. (2008). Synapse formation and clustering of neuroligin-2 in the absence of GABAA receptors. Proc Natl Acad Sci U S A 105, 13151-13156.

333. Paz, A., Zeev-Ben-Mordehai, T., Lundqvist, M., Sherman, E., Mylonas, E., Weiner, L., Haran, G., Svergun, D. I., Mulder, F. A., Sussman, J. L., & Silman, I. (2008). Biophysical characterization of the unstructured cytoplasmic domain of the human neuronal adhesion protein neuroligin 3. Biophys J 95, 1928-1944.

334. Peixoto, R. T., Kunz, P. A., Kwon, H., Mabb, A. M., Sabatini, B. L., Philpot, B. D., & Ehlers, M. D. (2012). Transsynaptic signaling by activity-dependent cleavage of neuroligin-1. Neuron 76, 396-409.

335. Peterson, F. C. & Volkman, B. F. (2009). Diversity of polyproline recognition by EVH1 domains. Front Biosci (Landmark. Ed) 14, 833-846.

336. Petoukhov, M. V. & Svergun, D. I. (2005). Global rigid body modeling of macromolecular complexes against small-angle scattering data. Biophys J 89, 1237-1250.

337. Petoukhov, M. V., Franke, D., Shkumatov, A. V., Tria, G., Kikhney, A. G., Gajda, M., Gorba, C., Mertens, H. D. T., Konarev, P. V., & Svergun, D. I. (2012). New developments in the ATSAS program package for small-angle scattering data analysis. J Appl Crystallogr 45, 342-350.

338. Pettem, K. L., Yokomaku, D., Takahashi, H., Ge, Y., & Craig, A. M. (2013). Interaction between autism-linked MDGAs and neuroligins suppresses inhibitory synapse development. J Cell Biol 200, 321-336.

339. Pfister, K. K., Fisher, E. M., Gibbons, I. R., Hays, T. S., Holzbaur, E. L., McIntosh, J. R., Porter, M. E., Schroer, T. A., Vaughan, K. T., Witman, G. B., King, S. M., & Vallee, R. B. (2005). Cytoplasmic dynein nomenclature. J Cell Biol 171, 411-413.

340. Pfister, K. K., Shah, P. R., Hummerich, H., Russ, A., Cotton, J., Annuar, A. A., King, S. M., & Fisher, E. M. (2006). Genetic analysis of the cytoplasmic dynein subunit families. PLoS Genet 2, e1.

341. Pierce, M. M., Raman, C. S., & Nall, B. T. (1999). Isothermal titration calorimetry of protein-protein interactions. Methods 19, 213-221.

342. Pollastri, G., Przybylski, D., Rost, B., & Baldi, P. (2002). Improving the prediction of protein secondary structure in three and eight classes using recurrent neural networks and profiles. Proteins 47, 228-235.

343. Porod, G. (1982). Small-Angle X-ray Scattering London: Academic Press.

344. Poulopoulos, A. (2008). Mechanisms of Neuroligin Function in Inhibitory Postsynaptic Differentiation, Biologische Fakultät, Georg-August-Universität Göttingen.

345. Poulopoulos, A., Aramuni, G., Meyer, G., Soykan, T., Hoon, M., Papadopoulos, T., Zhang, M., Paarmann, I., Fuchs, C., Harvey, K., Jedlicka, P., Schwarzacher, S. W., Betz, H., Harvey, R. J., Brose, N., Zhang, W., & Varoqueaux, F. (2009). Neuroligin 2 drives postsynaptic assembly at perisomatic inhibitory synapses through gephyrin and collybistin. Neuron 63, 628-642.

346. Poulopoulos, A., Soykan, T., Tuffy, L. P., Hammer, M., Varoqueaux, F., & Brose, N. (2012). Homodimerization and isoform-specific heterodimerization of neuroligins. Biochem J 446, 321-330.

347. Prehoda, K. E., Lee, D. J., & Lim, W. A. (1999). Structure of the enabled/VASP homology 1 domain-peptide complex: a key component in the spatial control of actin assembly. Cell 97, 471-480.

348. Purves, D., Augustine, G. J., Fitzpatrick, D., Hall, W. C., LaMantia, A.-S., McNamara, J. O., & Williams, M. S. (2004). Neuroscience.

349. Radnai, L., Rapali, P., Hodi, Z., Suveges, D., Molnar, T., Kiss, B., Becsi, B., Erdodi, F., Buday, L., Kardos, J., Kovacs, M., & Nyitray, L. (2010). Affinity, avidity, and kinetics of target sequence binding to LC8 dynein light chain isoforms. J Biol Chem 285, 38649-38657.

350. Raissi, A. J., Staudenmaier, E. K., David, S., Hu, L., & Paradis, S. (2013). Sema4D localizes to synapses and regulates GABAergic synapse development as a membrane-bound molecule in the mammalian hippocampus. Mol. Cell Neurosci 57, 23-32.

351. Rambo, R. P. & Tainer, J. A. (2013). Accurate assessment of mass, models and resolution by small-angle scattering. Nature 496, 477-481.

352. Ramming, M., Kins, S., Werner, N., Hermann, A., Betz, H., & Kirsch, J. (2000). Diversity and phylogeny of gephyrin: tissue-specific splice variants, gene structure, and sequence similarities to molybdenum cofactor-synthesizing and cytoskeleton-associated proteins. Proc Natl Acad Sci U S A 97, 10266-10271.

353. Rao, L., Romes, E. M., Nicholas, M. P., Brenner, S., Tripathy, A., Gennerich, A., & Slep, K. C. (2013). The yeast dynein Dyn2-Pac11 complex is a dynein dimerization/processivity factor: structural and single-molecule characterization. Mol. Biol Cell 24, 2362-2377.

354. Rapali, P., Radnai, L., Süveges, D., Harmat, V., Tölgyesi, F., Wahlgren, W. Y., Katona, G., Nyitray, L., & Pál, G. (2011a). Directed evolution reveals the binding motif preference of the LC8/DYNLL hub protein and predicts large numbers of novel binders in the human proteome. PloS One 6, e18818.

355. Rapali, P., Szenes, A., Radnai, L., Bakos, A., Pal, G., & Nyitray, L. (2011b). DYNLL/LC8: a light chain subunit of the dynein motor complex and beyond. FEBS J 278, 2980-2996.

356. Reck-Peterson, S. L., Derr, N. D., & Stuurman, N. (2010). Imaging single molecular motor motility with total internal reflection fluorescence microscopy (TIRFM). Cold Spring Harb. Protoc. 2010, db.

357. Reddy-Alla, S., Schmitt, B., Birkenfeld, J., Eulenburg, V., Dutertre, S., Bohringer, C., Gotz, M., Betz, H., & Papadopoulos, T. (2010). PH-domain-driven targeting of collybistin but not Cdc42 activation is required for synaptic gephyrin clustering. Eur J Neurosci 31, 1173-1184.

358. Reid, T., Bathoorn, A., Ahmadian, M. R., & Collard, J. G. (1999). Identification and characterization of hPEM-2, a guanine nucleotide exchange factor specific for Cdc42. J Biol Chem 274, 33587-33593.

359. Reinhard, M., Jouvenal, K., Tripier, D., & Walter, U. (1995). Identification, purification, and characterization of a zyxin-related protein that binds the focal adhesion and microfilament protein VASP (vasodilator-stimulated phosphoprotein). Proc Natl Acad Sci U S A 92, 7956-7960.

360. Reinhard, M., Rudiger, M., Jockusch, B. M., & Walter, U. (1996). VASP interaction with vinculin: a recurring theme of interactions with proline-rich motifs. FEBS Lett 399, 103-107.

361. Reiss, J. & Hahnewald, R. (2011). Molybdenum cofactor deficiency: Mutations in GPHN, MOCS1, and MOCS2. Hum. Mutat 32, 10-18.

362. Renner, M., Schweizer, C., Bannai, H., Triller, A., & Levi, S. (2012). Diffusion barriers constrain receptors at synapses. PLoS One 7, e43032.

363. Roberts, A. J., Kon, T., Knight, P. J., Sutoh, K., & Burgess, S. A. (2013). Functions and mechanics of dynein motor proteins. Nat Rev Mol. Cell Biol 14, 713-726.

364. Roberts, P. J., Mitin, N., Keller, P. J., Chenette, E. J., Madigan, J. P., Currin, R. O., Cox, A. D., Wilson, O., Kirschmeier, P., & Der, C. J. (2008). Rho Family GTPase modification and dependence on CAAX motif-signaled posttranslational modification. J Biol Chem 283, 25150-25163.

365. Roessle, M. W., Klaering, R., Ristau, U., Robrahn, B., Jahn, D., Gehrmann, T., Konarev, P., Round, A., Fiedler, S., Hermes, C., & Svergun, D. (2007). Upgrade of the small-angle X-ray scattering beamline X33 at the European Molecular Biology Laboratory, Hamburg. J Appl Crystallogr 40, s190-s194.

366. Romes, E. M., Tripathy, A., & Slep, K. C. (2012). Structure of a yeast Dyn2-Nup159 complex and molecular basis for dynein light chain-nuclear pore interaction. J Biol Chem 287, 15862-15873.

367. Rosenberg, M., Meier, J., Triller, A., & Vannier, C. (2001). Dynamics of glycine receptor insertion in the neuronal plasma membrane. J Neurosci 21, 5036-5044.

368. Rossman, K. L., Worthylake, D. K., Snyder, J. T., Siderovski, D. P., Campbell, S. L., & Sondek, J. (2002). A crystallographic view of interactions between Dbs and Cdc42: PH domain-assisted guanine nucleotide exchange. EMBO J 21, 1315-1326.

369. Round, A. R., Franke, D., Moritz, S., Huchler, R., Fritsche, M., Malthan, D., Klaering, R., Svergun, D. I., & Roessle, M. (2008). Automated sample-changing robot for solution scattering experiments at the EMBL Hamburg SAXS station X33. J Appl Crystallogr 41, 913-917.

370. Rubenstein, J. L. & Merzenich, M. M. (2003). Model of autism: increased ratio of excitation/inhibition in key neural systems. Genes Brain Behav. 2, 255-267.

371. Rubinstein, M. & Colby, R. H. (2003). Polymer Physics CUP Oxford.

372. Rudolph, U. & Knoflach, F. (2011). Beyond classical benzodiazepines: novel therapeutic potential of GABAA receptor subtypes. Nat Rev Drug Discov. 10, 685-697.

373. Rui, Y., Myers, K. R., Yu, K., Wise, A., De Blas, A. L., Hartzell, H. C., & Zheng, J. Q. (2013). Activity-dependent regulation of dendritic growth and maintenance by glycogen synthase kinase 3beta. Nat Commun 4, 2628.

374. Rupp, B. (2009). Biomoelcular Crystallography Garland Science.

375. Sabatini, D. M., Barrow, R. K., Blackshaw, S., Burnett, P. E., Lai, M. M., Field, M. E., Bahr, B. A., Kirsch, J., Betz, H., & Snyder, S. H. (1999). Interaction of RAFT1 with gephyrin required for rapamycin-sensitive signaling. Science 284, 1161-1164.

376. Sacho, E. J., Kadyrov, F. A., Modrich, P., Kunkel, T. A., & Erie, D. A. (2008). Direct visualization of asymmetric adenine-nucleotide-induced conformational changes in MutL alpha. Mol. Cell 29, 112-121.

377. Saiepour, L., Fuchs, C., Patrizi, A., Sassoe-Pognetto, M., Harvey, R. J., & Harvey, K. (2010). Complex role of collybistin and gephyrin in GABAA receptor clustering. J Biol Chem 285, 29623-29631.

378. Saiki, R. K., Scharf, S., Faloona, F., Mullis, K. B., Horn, G. T., Erlich, H. A., & Arnheim, N. (1985). Enzymatic amplification of beta-globin genomic sequences and restriction site analysis for diagnosis of sickle cell anemia. Science 230, 1350-1354.

379. Saiyed, T., Paarmann, I., Schmitt, B., Haeger, S., Sola, M., Schmalzing, G., Weissenhorn, W., & Betz, H. (2007). Molecular basis of gephyrin clustering at inhibitory synapses: role of G- and E-domain interactions. J Biol Chem 282, 5625-5632.

380. Sakakibara, H. & Oiwa, K. (2011). Molecular organization and force-generating mechanism of dynein. FEBS J 278, 2964-2979.

381. Samson, F., Donoso, J. A., Heller-Bettinger, I., Watson, D., & Himes, R. H. (1979). Nocodazole action on tubulin assembly, axonal ultrastructure and fast axoplasmic transport. J Pharmacol Exp. Ther 208, 411-417.

382. Sander, B., Tria, G., Shkumatov, A. V., Kim, E. Y., Grossmann, J. G., Tessmer, I., Svergun, D. I., & Schindelin, H. (2013). Structural characterization of gephyrin by AFM and SAXS reveals a mixture of compact and extended states. Acta Crystallogr D. Biol Crystallogr 69, 2050-2060.

383. Santos, A. R., Comprido, D., & Duarte, C. B. (2010). Regulation of local translation at the synapse by BDNF. Prog. Neurobiol 92, 505-516.

384. Saro, D., Li, T., Rupasinghe, C., Paredes, A., Caspers, N., & Spaller, M. R. (2007). A thermodynamic ligand binding study of the third PDZ domain (PDZ3) from the mammalian neuronal protein PSD-95. Biochemistry 46, 6340-6352.

385. Sarto-Jackson, I., Milenkovic, I., Smalla, K. H., Gundelfinger, E. D., Kaehne, T., Herrera-Molina, R., Thomas, S., Kiebler, M. A., & Sieghart, W. (2012). The cell adhesion molecule neuroplastin-65 is a novel interaction partner of gamma-aminobutyric acid type A receptors. J Biol Chem 287, 14201-14214.

386. Sassoe-Pognetto, M., Kirsch, J., Grunert, U., Greferath, U., Fritschy, J. M., Mohler, H., Betz, H., & Wassle, H. (1995). Colocalization of gephyrin and GABAA-receptor subunits in the rat retina. J Comp Neurol 357, 1-14.

387. Sassoe-Pognetto, M. & Wassle, H. (1997). Synaptogenesis in the rat retina: subcellular localization of glycine receptors, GABA(A) receptors, and the anchoring protein gephyrin. J Comp Neurol 381, 158-174.

388. Sauer, F. (2007). Strukturelle Charakterisierung von Gephyrin, Fakulät für Biologie, Julius-Maximilians-Universität Würzburg.

389. Scheffzek, K. & Welti, S. (2012). Pleckstrin homology (PH) like domains - versatile modules in protein-protein interaction platforms. FEBS Lett 586, 2662-2673.

390. Scheiffele, P., Fan, J., Choih, J., Fetter, R., & Serafini, T. (2000). Neuroligin expressed in nonneuronal cells triggers presynaptic development in contacting axons. Cell 101, 657-669.

391. Schmidt, H., Gleave, E. S., & Carter, A. P. (2012). Insights into dynein motor domain function from a 3.3-A crystal structure. Nat Struct Mol. Biol 19, 492-7, S1.

392. Schrader, N., Kim, E. Y., Winking, J., Paulukat, J., Schindelin, H., & Schwarz, G. (2004). Biochemical characterization of the high affinity binding between the glycine receptor and gephyrin. J Biol Chem 279, 18733-18741.

393. Schwarz, G. & Mendel, R. R. (2006). Molybdenum cofactor biosynthesis and molybdenum enzymes. Annu Rev Plant Biol 57, 623-647.

394. Schwarz, G., Mendel, R. R., & Ribbe, M. W. (2009). Molybdenum cofactors, enzymes and pathways. Nature 460, 839-847.

395. Schwarz, G., Schrader, N., Mendel, R. R., Hecht, H. J., & Schindelin, H. (2001). Crystal structures of human gephyrin and plant Cnx1 G domains: comparative analysis and functional implications. J Mol. Biol 312, 405-418.

396. Schwiese, O. (2011). Biochemische und funktionelle Charakterisierung der Interaktion von Gephyrin und Dynein Light Chain, Institut für Biochemie, Universität zu Köln.

397. Serdyuk, I. N., Zacchai, N. R., & Zacchai, J. (2007). Methods in Molecular Biophysics, first edition ed Cambridge University Press.

398. Serpa, J. J., Parker, C. E., Petrotchenko, E. V., Han, J., Pan, J., & Borchers, C. H. (2012). Mass spectrometry-based structural proteomics. Eur J Mass Spectrom. (Chichester, Eng) 18, 251-267.

399. Sertie, A. L., de, A. G., De, P., V, & Passos-Bueno, M. R. (2010). Collybistin and gephyrin are novel components of the eukaryotic translation initiation factor 3 complex. BMC Res Notes 3, 242.

400. Sharma, H., Landau, M. J., Vargo, M. A., Spasov, K. A., & Anderson, K. S. (2013). First three-dimensional structure of Toxoplasma gondii thymidylate synthase-dihydrofolate reductase: insights for catalysis, interdomain interactions, and substrate channeling. Biochemistry 52, 7305-7317.

401. Shen, K. & Scheiffele, P. (2010). Genetics and cell biology of building specific synaptic connectivity. Annu Rev Neurosci 33, 473-507.

402. Sheng, M. & Hoogenraad, C. C. (2007). The postsynaptic architecture of excitatory synapses: a more quantitative view. Annu Rev Biochem 76, 823-847.

403. Sherwood, D. & Cooper, J. (2011). Crystals, X-rays and Proteins Oxford University Press.

404. Shimojima, K., Sugawara, M., Shichiji, M., Mukaida, S., Takayama, R., Imai, K., & Yamamoto, T. (2011). Loss-of-function mutation of collybistin is responsible for X-linked mental retardation associated with epilepsy. J Hum. Genet 56, 561-565.

405. Shirao, T. & Gonzalez-Billault, C. (2013). Actin filaments and microtubules in dendritic spines. J Neurochem 126, 155-164.

406. Shiryev, S. A., Papadopoulos, J. S., Schaffer, A. A., & Agarwala, R. (2007). Improved BLAST searches using longer words for protein seeding. Bioinformatics. 23, 2949-2951.

407. Shrivastava, A. N., Triller, A., & Sieghart, W. (2011). GABA(A) Receptors: Post-Synaptic Co-Localization and Cross-Talk with Other Receptors. Front Cell Neurosci 5, 7.

408. Shubeita, G. T., Tran, S. L., Xu, J., Vershinin, M., Cermelli, S., Cotton, S. L., Welte, M. A., & Gross, S. P. (2008). Consequences of motor copy number on the intracellular transport of kinesin-1-driven lipid droplets. Cell 135, 1098-1107.

409. Sindi, I. A., Tannenberg, R. K., & Dodd, P. R. (2014). A role for the neurexin-neuroligin complex in Alzheimer's disease. Neurobiol Aging 35, 746-756.

410. Smart, T. G. & Paoletti, P. (2012). Synaptic neurotransmitter-gated receptors. Cold Spring Harb. Perspect. Biol 4.

411. Smolinsky, B., Eichler, S. A., Buchmeier, S., Meier, J. C., & Schwarz, G. (2008). Splice-specific functions of gephyrin in molybdenum cofactor biosynthesis. J Biol Chem 283, 17370-17379.

412. Soisson, S. M., Nimnual, A. S., Uy, M., Bar-Sagi, D., & Kuriyan, J. (1998). Crystal structure of the Dbl and pleckstrin homology domains from the human Son of sevenless protein. Cell 95, 259-268.

413. Sola, M., Bavro, V. N., Timmins, J., Franz, T., Ricard-Blum, S., Schoehn, G., Ruigrok, R. W., Paarmann, I., Saiyed, T., O'Sullivan, G. A., Schmitt, B., Betz, H., & Weissenhorn, W. (2004). Structural basis of dynamic glycine receptor clustering by gephyrin. EMBO J 23, 2510-2519.

414. Sola, M., Kneussel, M., Heck, I. S., Betz, H., & Weissenhorn, W. (2001). X-ray crystal structure of the trimeric N-terminal domain of gephyrin. J Biol Chem 276, 25294-25301.

415. Song, J. Y., Ichtchenko, K., Sudhof, T. C., & Brose, N. (1999). Neuroligin 1 is a postsynaptic cell-adhesion molecule of excitatory synapses. Proc Natl Acad Sci U S A 96, 1100-1105.

416. Soykan, T. (2011). Neuroligin 2 Induced Allosteric Transition of Collybistin Underlies Inhibitory Postsynaptic Differentiation, Biologische Fakultät, Georg August Universität Göttingen.

417. Specht, C. G., Izeddin, I., Rodriguez, P. C., El, B. M., Rostaing, P., Darzacq, X., Dahan, M., & Triller, A. (2013). Quantitative nanoscopy of inhibitory synapses: counting gephyrin molecules and receptor binding sites. Neuron 79, 308-321.

418. Stallmeyer, B., Schwarz, G., Schulze, J., Nerlich, A., Reiss, J., Kirsch, J., & Mendel, R. R. (1999). The neurotransmitter receptor-anchoring protein gephyrin reconstitutes molybdenum cofactor biosynthesis in bacteria, plants, and mammalian cells. Proc Natl Acad Sci U S A 96, 1333-1338.

419. Studer, R., von, B. L., Haenggi, T., Schweizer, C., Benke, D., Rudolph, U., & Fritschy, J. M. (2006). Alteration of GABAergic synapses and gephyrin clusters in the thalamic reticular nucleus of GABAA receptor alpha3 subunit-null mice. Eur J Neurosci 24, 1307-1315.

420. Stukenberg, P. T. & Kirschner, M. W. (2001). Pin1 acts catalytically to promote a conformational change in Cdc25. Mol. Cell 7, 1071-1083.

421. Sudhof, T. C. (2008). Neuroligins and neurexins link synaptic function to cognitive disease. Nature 455, 903-911.

422. Sudhof, T. C. (2013). Neurotransmitter release: the last millisecond in the life of a synaptic vesicle. Neuron 80, 675-690.

423. Sumita, K., Sato, Y., Iida, J., Kawata, A., Hamano, M., Hirabayashi, S., Ohno, K., Peles, E., & Hata, Y. (2007). Synaptic scaffolding molecule (S-SCAM) membrane-associated guanylate kinase with inverted organization (MAGI)-2 is associated with cell adhesion molecules at inhibitory synapses in rat hippocampal neurons. J Neurochem 100, 154-166.

424. Sun, C., Cheng, M. C., Qin, R., Liao, D. L., Chen, T. T., Koong, F. J., Chen, G., & Chen, C. H. (2011a). Identification and functional characterization of rare mutations of the neuroligin-2 gene (NLGN2) associated with schizophrenia. Hum. Mol. Genet 20, 3042-3051.

425. Sun, C., Zhang, L., & Chen, G. (2013). An unexpected role of neuroligin-2 in regulating KCC2 and GABA functional switch. Mol. Brain 6, 23.

426. Sun, P., Tropea, J. E., & Waugh, D. S. (2011b). Enhancing the solubility of recombinant proteins in Escherichia coli by using hexahistidine-tagged maltose-binding protein as a fusion partner. Methods Mol. Biol 705, 259-274.

427. Suzuki, K., Hayashi, Y., Nakahara, S., Kumazaki, H., Prox, J., Horiuchi, K., Zeng, M., Tanimura, S., Nishiyama, Y., Osawa, S., Sehara-Fujisawa, A., Saftig, P., Yokoshima, S., Fukuyama, T., Matsuki, N., Koyama, R., Tomita, T., & Iwatsubo, T. (2012). Activity-dependent proteolytic cleavage of neuroligin-1. Neuron 76, 410-422.

428. Svergun, D., Barberato, C., & Koch, M. H. J. (1995). CRYSOL - a Program to Evaluate X-ray Solution Scattering of Biological Macromolecules from Atomic Coordinates. J Appl Crystallogr 28, 768-773.

429. Svergun, D. I. (1992). Determination of the regularization parameter in indirect-transform methods using perceptual criteria. J Appl Crystallogr 25, 495-503.

430. Svergun, D. I. (1999). Restoring Low Resolution Structure of Biological Macromolecules from Solution Scattering Using Simulated Annealing. Biophys J 76, 2879-2886.

431. Svergun, D. I., Petoukhov, M. V., & Koch, M. H. (2001). Determination of domain structure of proteins from X-ray solution scattering. Biophys J 80, 2946-2953.

432. Tabuchi, K. & Sudhof, T. C. (2002). Structure and evolution of neurexin genes: insight into the mechanism of alternative splicing. Genomics 79, 849-859.

433. Takahashi, H., Katayama, K., Sohya, K., Miyamoto, H., Prasad, T., Matsumoto, Y., Ota, M., Yasuda, H., Tsumoto, T., Aruga, J., & Craig, A. M. (2012). Selective control of inhibitory synapse development by Slitrk3-PTPdelta trans-synaptic interaction. Nat Neurosci 15, 389-2.

434. Takazawa, T. & MacDermott, A. B. (2010). Glycinergic and GABAergic tonic inhibition fine tune inhibitory control in regionally distinct subpopulations of dorsal horn neurons. J Physiol 588, 2571-2587.

435. Tanaka, H., Miyazaki, N., Matoba, K., Nogi, T., Iwasaki, K., & Takagi, J. (2012). Higher-order architecture of cell adhesion mediated by polymorphic synaptic adhesion molecules neurexin and neuroligin. Cell Rep 2, 101-110.

436. Taniguchi, H., Gollan, L., Scholl, F. G., Mahadomrongkul, V., Dobler, E., Limthong, N., Peck, M., Aoki, C., & Scheiffele, P. (2007). Silencing of neuroligin function by postsynaptic neurexins. J Neurosci 27, 2815-2824.

437. Thind, K. K., Yamawaki, R., Phanwar, I., Zhang, G., Wen, X., & Buckmaster, P. S. (2010). Initial loss but later excess of GABAergic synapses with dentate granule cells in a rat model of temporal lobe epilepsy. J Comp Neurol 518, 647-667.

438. Thompson, A. J., Lester, H. A., & Lummis, S. C. (2010). The structural basis of function in Cys-loop receptors. Q. Rev Biophys 43, 449-499.

439. Thompson, A. J. & Lummis, S. C. (2003). A single ring of charged amino acids at one end of the pore can control ion selectivity in the 5-HT3 receptor. Br. J Pharmacol 140, 359-365.

440. Tiffany, M. L. & Krimm, S. (1968). New chain conformations of poly(glutamic acid) and polylysine. Biopolymers 6, 1379-1382.

441. Todd, A. J., Watt, C., Spike, R. C., & Sieghart, W. (1996). Colocalization of GABA, glycine, and their receptors at synapses in the rat spinal cord. J Neurosci 16, 974-982.

442. Tompa, P. & Fuxreiter, M. (2008). Fuzzy complexes: polymorphism and structural disorder in protein-protein interactions. Trends Biochem Sci 33, 2-8.

443. Towbin, H., Staehelin, T., & Gordon, J. (1979). Electrophoretic transfer of proteins from polyacrylamide gels to nitrocellulose sheets: procedure and some applications. Proc Natl Acad Sci U S A 76, 4350-4354.

444. Tretter, V., Ehya, N., Fuchs, K., & Sieghart, W. (1997). Stoichiometry and assembly of a recombinant GABAA receptor subtype. J Neurosci 17, 2728-2737.

445. Tretter, V., Jacob, T. C., Mukherjee, J., Fritschy, J. M., Pangalos, M. N., & Moss, S. J. (2008). The clustering of GABA(A) receptor subtypes at inhibitory synapses is facilitated via the direct binding of receptor alpha 2 subunits to gephyrin. J Neurosci 28, 1356-1365.

446. Tretter, V., Kerschner, B., Milenkovic, I., Ramsden, S. L., Ramerstorfer, J., Saiepour, L., Maric, H. M., Moss, S. J., Schindelin, H., Harvey, R. J., Sieghart, W., & Harvey, K. (2011). Molecular basis of the gamma-aminobutyric acid A receptor alpha3 subunit interaction with the clustering protein gephyrin. J Biol Chem 286, 37702-37711.

447. Tretter, V., Mukherjee, J., Maric, H. M., Schindelin, H., Sieghart, W., & Moss, S. J. (2012). Gephyrin, the enigmatic organizer at GABAergic synapses. Front Cell Neurosci 6, 23.

448. Treutlein, B., Gokce, O., Quake, S. R., & Sudhof, T. C. (2014). Cartography of neurexin alternative splicing mapped by single-molecule long-read mRNA sequencing. Proc Natl Acad Sci U S A.

449. Trokter, M., Mucke, N., & Surrey, T. (2012). Reconstitution of the human cytoplasmic dynein complex. Proc Natl Acad Sci U S A 109, 20895-20900.

450. Tyagarajan, S. K. & Fritschy, J. M. (2010). GABA(A) receptors, gephyrin and homeostatic synaptic plasticity. J Physiol 588, 101-106.

451. Tyagarajan, S. K. & Fritschy, J. M. (2014). Gephyrin: a master regulator of neuronal function? Nat Rev Neurosci 15, 141-156.

452. Tyagarajan, S. K., Ghosh, A., Messner, S., Yevenes, G. E., Zeilhofer, H. U., Hottiger, M., & Fritschy, J. M. Proteins involved in the SUMO pathway modulate gephyrin scaffolding and GABAergic transmission, Society of Neuroscience.

453. Tyagarajan, S. K., Ghosh, H., Harvey, K., & Fritschy, J. M. (2011a). Collybistin splice variants differentially interact with gephyrin and Cdc42 to regulate gephyrin clustering at GABAergic synapses. J Cell Sci 124, 2786-2796.

454. Tyagarajan, S. K., Ghosh, H., Yevenes, G. E., Imanishi, S. Y., Zeilhofer, H. U., Gerrits, B., & Fritschy, J. M. (2013). Extracellular signal-regulated kinase and glycogen synthase kinase 3beta regulate gephyrin postsynaptic aggregation and GABAergic synaptic function in a calpain-dependent mechanism. J Biol Chem 288, 9634-9647.

455. Tyagarajan, S. K., Ghosh, H., Yevenes, G. E., Nikonenko, I., Ebeling, C., Schwerdel, C., Sidler, C., Zeilhofer, H. U., Gerrits, B., Muller, D., & Fritschy, J. M. (2011b). Regulation of GABAergic synapse formation and plasticity by GSK3beta-dependent phosphorylation of gephyrin. Proc. Natl. Acad. Sci U. S. A 108, 379-384.

456. Tynan, S. H., Gee, M. A., & Vallee, R. B. (2000). Distinct but overlapping sites within the cytoplasmic dynein heavy chain for dimerization and for intermediate chain and light intermediate chain binding. J Biol Chem 275, 32769-32774.

457. Ule, J., Jensen, K. B., Ruggiu, M., Mele, A., Ule, A., & Darnell, R. B. (2003). CLIP identifies Nova-regulated RNA networks in the brain. Science 302, 1212-1215.

458. Ulrich, D. & Bettler, B. (2007). GABA(B) receptors: synaptic functions and mechanisms of diversity. Curr Opin. Neurobiol 17, 298-303.

459. Um, J. W., Pramanik, G., Ko, J. S., Song, M. Y., Lee, D., Kim, H., Park, K. S., Sudhof, T. C., Tabuchi, K., & Ko, J. (2014). Calsyntenins function as synaptogenic adhesion molecules in concert with neurexins. Cell Rep 6, 1096-1109.

460. Unwin, N. (2005). Refined structure of the nicotinic acetylcholine receptor at 4A resolution. J Mol. Biol 346, 967-989.

461. Ushkaryov, Y. A. & Sudhof, T. C. (1993). Neurexin III alpha: extensive alternative splicing generates membrane-bound and soluble forms. Proc Natl Acad Sci U S A 90, 6410-6414.

462. Uversky, V. N., Oldfield, C. J., & Dunker, A. K. (2008). Intrinsically disordered proteins in human diseases: introducing the D2 concept. Annu Rev Biophys 37, 215-246.

463. Vacic, V., Uversky, V. N., Dunker, A. K., & Lonardi, S. (2007). Composition Profiler: a tool for discovery and visualization of amino acid composition differences. BMC Bioinformatics. 8, 211.

464. Vagin, A. & Teplyakov, A. (2010). Molecular replacement with MOLREP. Acta Crystallogr D. Biol Crystallogr 66, 22-25.

465. Vallee, R. B., McKenney, R. J., & Ori-McKenney, K. M. (2012). Multiple modes of cytoplasmic dynein regulation. Nat Cell Biol 14, 224-230.

466. Vallee, R. B., Seale, G. E., & Tsai, J. W. (2009). Emerging roles for myosin II and cytoplasmic dynein in migrating neurons and growth cones. Trends Cell Biol 19, 347-355.

467. van Zundert, B., Alvarez, F. J., Tapia, J. C., Yeh, H. H., Diaz, E., & Aguayo, L. G. (2004). Developmental-dependent action of microtubule depolymerization on the function and structure of synaptic glycine receptor clusters in spinal neurons. J Neurophysiol. 91, 1036-1049.

468. Varoqueaux, F., Aramuni, G., Rawson, R. L., Mohrmann, R., Missler, M., Gottmann, K., Zhang, W., Sudhof, T. C., & Brose, N. (2006). Neuroligins determine synapse maturation and function. Neuron 51, 741-754.

469. Varoqueaux, F., Jamain, S., & Brose, N. (2004). Neuroligin 2 is exclusively localized to inhibitory synapses. Eur J Cell Biol 83, 449-456.

470. Vithlani, M., Terunuma, M., & Moss, S. J. (2011). The dynamic modulation of GABA(A) receptor trafficking and its role in regulating the plasticity of inhibitory synapses. Physiol Rev 91, 1009-1022.

471. Vlachos, A., Reddy-Alla, S., Papadopoulos, T., Deller, T., & Betz, H. (2013). Homeostatic regulation of gephyrin scaffolds and synaptic strength at mature hippocampal GABAergic postsynapses. Cereb. Cortex 23, 2700-2711.

472. Volkov, V. V., Lapuk, V. A., Kayushina, R. L., Shtykova, E. V., Varlamova, E. Y., Malfois, M., & Svergun, D. I. (2003). Low-resolution structure of immunoglobulins IgG1, IgM and rheumatoid factor IgM-RF from solution X-ray scattering data. J Appl Crystallogr 36, 503-508.

473. Volkov, V. V. & Svergun, D. I. (2003). Uniqueness of ab initio shape determination in small-angle scattering. J. Appl. Cryst. 36, 860-864.

474. Wagner, W., Fodor, E., Ginsburg, A., & Hammer, J. A., III (2006). The binding of DYNLL2 to myosin Va requires alternatively spliced exon B and stabilizes a portion of the myosin's coiled-coil domain. Biochemistry 45, 11564-11577.

475. Walsh, T., McClellan, J. M., McCarthy, S. E., Addington, A. M., Pierce, S. B., Cooper, G. M., Nord, A. S., Kusenda, M., Malhotra, D., Bhandari, A., Stray, S. M., Rippey, C. F., Roccanova, P., Makarov, V., Lakshmi, B., Findling, R. L., Sikich, L., Stromberg, T., Merriman, B., Gogtay, N., Butler, P., Eckstrand, K., Noory, L., Gochman, P., Long, R., Chen, Z., Davis, S., Baker, C., Eichler, E. E., Meltzer, P. S., Nelson, S. F., Singleton, A. B., Lee, M. K., Rapoport, J. L., King, M. C., & Sebat, J. (2008). Rare structural variants disrupt multiple genes in neurodevelopmental pathways in schizophrenia. Science 320, 539-543.

476. Wang, H., Bedford, F. K., Brandon, N. J., Moss, S. J., & Olsen, R. W. (1999). GABA(A)-receptor-associated protein links GABA(A) receptors and the cytoskeleton. Nature 397, 69-72.

477. Wang, H., Brozoski, T. J., & Caspary, D. M. (2011). Inhibitory neurotransmission in animal models of tinnitus: maladaptive plasticity. Hear. Res 279, 111-117.

478. Wang, H., Brozoski, T. J., Turner, J. G., Ling, L., Parrish, J. L., Hughes, L. F., & Caspary, D. M. (2009). Plasticity at glycinergic synapses in dorsal cochlear nucleus of rats with behavioral evidence of tinnitus. Neuroscience 164, 747-759.

479. Ward, J. J., McGuffin, L. J., Bryson, K., Buxton, B. F., & Jones, D. T. (2004). The DISOPRED server for the prediction of protein disorder. Bioinformatics. 20, 2138-2139.

480. Welsh, B. T., Goldstein, B. E., & Mihic, S. J. (2009). Single-channel analysis of ethanol enhancement of glycine receptor function. J Pharmacol Exp. Ther 330, 198-205.

481. Wickstead, B. & Gull, K. (2007). Dyneins across eukaryotes: a comparative genomic analysis. Traffic 8, 1708-1721.

482. Williams, J. C., Roulhac, P. L., Roy, A. G., Vallee, R. B., Fitzgerald, M. C., & Hendrickson, W. A. (2007). Structural and thermodynamic characterization of a cytoplasmic dynein light chain-intermediate chain complex. Proc Natl Acad Sci U S A 104, 10028-10033.

483. Williams, R. W. & Herrup, K. (1988). The control of neuron number. Annu Rev Neurosci 11, 423-453.

484. Wirth, A., Chen-Wacker, C., Wu, Y. W., Gorinski, N., Filippov, M. A., Pandey, G., & Ponimaskin, E. (2013). Dual lipidation of the brain-specific Cdc42 isoform regulates its functional properties. Biochem J 456, 311-322.

485. Wittenmayer, N., Korber, C., Liu, H., Kremer, T., Varoqueaux, F., Chapman, E. R., Brose, N., Kuner, T., & Dresbach, T. (2009). Postsynaptic Neuroligin1 regulates presynaptic maturation. Proc Natl Acad Sci U S A 106, 13564-13569.

486. Woo, J., Kwon, S. K., Nam, J., Choi, S., Takahashi, H., Krueger, D., Park, J., Lee, Y., Bae, J. Y., Lee, D., Ko, J., Kim, H., Kim, M. H., Bae, Y. C., Chang, S., Craig, A. M., & Kim, E. (2013). The adhesion protein IgSF9b is coupled to neuroligin 2 via S-SCAM to promote inhibitory synapse development. J Cell Biol 201, 929-944.

487. Wood, K., Paz, A., Dijkstra, K., Scheek, R. M., Otten, R., Silman, I., Sussman, J. L., & Mulder, F. A. (2012). Backbone and side chain NMR assignments for the intrinsically disordered cytoplasmic domain of human neuroligin-3. Biomol. NMR Assign. 6, 15-18.

488. Wuchter, J., Beuter, S., Treindl, F., Herrmann, T., Zeck, G., Templin, M. F., & Volkmer, H. (2012). A comprehensive small interfering RNA screen identifies signaling pathways required for gephyrin clustering. J Neurosci 32, 14821-14834.

489. Wuebbens, M. M. & Rajagopalan, K. V. (1993). Structural characterization of a molybdopterin precursor. J Biol Chem 268, 13493-13498.

490. Wullschleger, S., Loewith, R., & Hall, M. N. (2006). TOR signaling in growth and metabolism. Cell 124, 471-484.

491. Xiang, S., Kim, E. Y., Connelly, J. J., Nassar, N., Kirsch, J., Winking, J., Schwarz, G., & Schindelin, H. (2006). The crystal structure of Cdc42 in complex with collybistin II, a gephyrin-interacting guanine nucleotide exchange factor. J Mol. Biol 359, 35-46.

492. Xiang, S., Nichols, J., Rajagopalan, K. V., & Schindelin, H. (2001). The crystal structure of Escherichia coli MoeA and its relationship to the multifunctional protein gephyrin. Structure 9, 299-310.

493. Yamagata, M., Sanes, J. R., & Weiner, J. A. (2003). Synaptic adhesion molecules. Curr Opin. Cell Biol 15, 621-632.

494. Ye, G. J., Vaughan, K. T., Vallee, R. B., & Roizman, B. (2000). The herpes simplex virus 1 U(L)34 protein interacts with a cytoplasmic dynein intermediate chain and targets nuclear membrane. J Virol 74, 1355-1363.

495. Yu, W., Charych, E. I., Serwanski, D. R., Li, R. W., Ali, R., Bahr, B. A., & De Blas, A. L. (2008). Gephyrin interacts with the glutamate receptor interacting protein 1 isoforms at GABAergic synapses. J Neurochem 105, 2300-2314.

496. Zacchi, P., Antonelli, R., & Cherubini, E. (2014). Gephyrin phosphorylation in the functional organization and plasticity of GABAergic synapses. Front Cell Neurosci 8, 103.

497. Zhang, C., Atasoy, D., Arac, D., Yang, X., Fucillo, M. V., Robison, A. J., Ko, J., Brunger, A. T., & Sudhof, T. C. (2010). Neurexins physically and functionally interact with GABA(A) receptors. Neuron 66, 403-416.

498. Zhang, L. H., Gong, N., Fei, D., Xu, L., & Xu, T. L. (2008). Glycine uptake regulates hippocampal network activity via glycine receptor-mediated tonic inhibition. Neuropsychopharmacology 33, 701-711.

499. Zhang, Y., Tu, Y., Gkretsi, V., & Wu, C. (2006). Migfilin interacts with vasodilator-stimulated phosphoprotein (VASP) and regulates VASP localization to cell-matrix adhesions and migration. J Biol Chem 281, 12397-12407.

500. Zhao, H., Brown, P. H., & Schuck, P. (2011). On the distribution of protein refractive index increments. Biophys J 100, 2309-2317.

501. Zheng, Y. (2001). Dbl family guanine nucleotide exchange factors. Trends Biochem Sci 26, 724-732.

502. Zita, M. M., Marchionni, I., Bottos, E., Righi, M., Del, S. G., Cherubini, E., & Zacchi, P. (2007). Post-phosphorylation prolyl isomerisation of gephyrin represents a mechanism to modulate glycine receptors function. EMBO J 26, 1761-1771.

VI. SUPPORTING MATERIAL

VI.A. Appendices

VI.A.1. Appendix A: Sequences

Gephyrin splice variant P2 (Rattus norvegicus)

MATEGMILTNHDHQIRVGVLTVSDSCFRNLAEDRSGINLKDLVQDPSLLGGTISAYKIVPDEIEEIKETLIDWCDEKEL
NLILTTGGTGFAPRDVTPEATKEVIEREAPGMALAMLMGSLNVTPLGMLSRPVCGIRGKTLIINLPGSKKGSQECFQ
FILPALPHAIDLLRDAIVKVKEVHDELEDLPSPPPPLSPPPTTSPHKQTEDKGVQCEEEEEEKKDSGVASTEDSSSSHIT
AAALAAKIPDSIISRGVQVLPRDTASLSTTPSESPRAQATSRLSTASCPTPKARLPSCSSTYSVSEVQSRCSSKENILRAS
HSAVDITKVARRHRMSPFPLTSMDKAFITVLEMTPVLGTEIINYRDGMGRVLAQDVYAKDNLPPFPASVKDGYAVR
AADGPGDRFIIGESQAGEQPTQTVMPGQVMRVTTGAPIPCGADAVVQVEDTELIRESDDGTEELEVRILVQARPG
QDIRPIGHDIKRGECVLAKGTHMGPSEIGLLATVGVTEVEVNKFPVVAVMSTGNELLNPEDDLLPGKIRDSNRSTLL
ATIQEHGYPTINLGIVGDNPDDLLNALNEGISRADVIITSGGVSMGEKDYLKQVLDIDLHAQIHFGRVFMKPGLPTTF
ATLDIDGVRKIIFALPGNPVSAVVTCNLFVVPALRKMQGILDPRPTIIKARLSCDVKLDPRPEYHRCILTWHHQEPLP
WAQSTGNQMSSRLMSMRSANGLLMLPPKTEQYVELHKGEVVDVMVIGRL

GephG DYNLL1 binding motif ($Geph_{DB}$) Splice cassette C4c GephE Collybistin binding site in GephE

Neuroligin 2 (Rattus norvegicus)

MWLLALCLVGLAGAQRGGGGPGGGAPGGPGLGLGSLGEERFPVVNTAYGRVRGVRRELNNEILGPVVQFLGVPY
ATPPLGARRFQPPEAPASWPGVRNATTLPPACPQNLHGALPAIMLPVWFTDNLEAAATYVQNQSEDCLYLNLYVP
TEDGPLTKKRDEATLNPPDTDIRDSGKKPVMLFLHGGSYMEGTGNMFDGSVLAAYGNVIVATLNYRLGVLGFLSTG
DQAAKGNYGLLDQIQALRWLSENIAHFGGDPERITIFGSGAGASCVNLLILSHHSEGLFQKAIAQSGTAISSWSVNY
QPLKYTRLLAAKVGCDREDSTEAVECLRRKSSRELVDQDVQPARYHIAFGPVVDGDVVPDDPEILMQQGEFLNYD
MLIGVNQGEGLKFVEDSAESEDGVSASAFDFTVSNFVDNLYGYPEGKDVLRETIKFMYTDWADRDNGEMRRKTLL
ALFTDHQWVAPAVATAKLHADYQSPVYFYTFYHHCQAEGRPEWADAAHGDELPYVFGVPMVGATDLFPCNFSK
NDVMLSAVVMTYWTNFAKTGDPNQPVPQDTKFIHTKPNRFEEVVWSKFNSKEKQYLHIGLKPRVRDNYRANKVA
FWLELVPHLHNLHTELFTTTTRLPPYATRWPPRTPGPGTSGTRRPPPPATLPPESDIDLGPRAYDRFPGDSRDYSTEL
SVTVAVGASLLFLNILAFAALYYKRDRRQELRCRRLSPPGGSGSGVPGGGPLLPTAGRELPPEEELVSLQLKRGGGVG
ADPAEALRPACPPDYTLALRRAPDDVPLLAPGALTLLPSGLGPPPPPPPPSLHPFGPFPPPPPTATSHNNTLPHPHST
TRV

Signal peptide *Extracellular domain* Transmembrane region Cytoplasmic loop Gephyrin binding motif

Collybistin CB2$_{SH3+}$ (Rattus norvegicus)

MQWIRGGSGMLITGDSIVSAEAVWDHVTMANRELAFKAGDVIKVLDASNKDWWWGQIDDEEGWFPASFVRL
WVNQEDGVEEGPSDVQNGHLDPNSDCLCLGRPLQNRDQMRANVINEIMSTERHYIKHLKDICEGYLKQCRKRRD
MFSDEQLKVIFGNIEDIYRFQMGFVRDLEKQYNNDDPHLSEIGPCFLEHQDGFWIYSEYCNNHLDACMELSKLMKD
SRYQHFFEACRLLQQMIDIAIDGFLLTPVQKICKYPLQLAELLKYTAQDHSDYRYVAAALAVMRNVTQQINERKRRLE
NIDKIAQWQASVLDWEGDDILDRSSELIYTGEMAWIYQPYGRNQQRVFFLFDHQMVLCKKDLIRRDILYYKGRIDM
DKYEVIDIEDGRDDDFNVSMKNAFKLHNKETEEVHLFFAKKLEEKIRWLRAFREERKMVQEDEKIGFEISENQKRQA
AMTVRKASKQKVTQRKWHY

CB2$_{SH3-}$ = CB2$_{SH3+}$ – magenta segment – SH3 domain

DH domain PH domain Atypical additional C-terminal PH domain helix Missing in CB2ΔC15 variants

Dynein light chain 1 (Rattus norvegicus)

MCDRKAVIKNADMSEEMQQDSVECATQALEKYNIEKDIAAHIKKEFDKKYNPTWHCIVGRNFGSYVTHETKHFIYF
YLGQVAILLFKSG

Dynein intermediate chain 1 (*Rattus norvegicus*)

MSDKSDLKAELERKKQRLAQIREEKKRKEEERKKKEADMQQKKEPVPDDSDLDRKRRETEALLQSIGISPEPPLVQPL
HFLTWDTCYFHYLVPTPMSPSSKSVSTPSEAGSQDDLGPLTRTLQWDTDPSVLQLQSDSELGRRLNKLGVSKVTQV
DFLPREVVSYSKETQTPLATHQSEEDEEDEEMVEPKVGHDSELENQDKKQETKEAPPRELTEEEKQQILHSEEFLIFF
DRTIRVIERALAEDSDIFFDYSGRELEEKDGDVQAGANLSFNRQFYDEHWSKHRVVTCMDWSLQYPELMVASYSN
NEDAPHEPDGVALVWNMKFKKTTPEYVFHCQSSVMSVCFARFHPNLVVGGTYSGQIVLWDNRSHRRTPVQRTPL
SAAAHTHPVYCVNVVGTQNAHNLITVSTDGKMCSWSLDMLSTPQESMELVYNKSKPVAVTGMAFPTGDVNNFV
VGSEEGTVYTACRHGSKAGIGEVFEGHQGPVTGINCHMAVGPIDFSHLFVTSSFDWTVKLWTTKHNKPLYSFEDN
ADYVYDVMWSPVHPALFACVDGMGRLDLWNLNSDTEVPTASVAIEGAYALNRVRWAQGGKEVAVGDSEGRIW
IYDVGELAVPHNDEWTRFARTLVEIRANRADSEEEGAVELAA

DYNLL binding motif

Proliferating-Cell-Nuclear-Antigen (Chaetomium thermophilum) – referred to as ctPCNA

MLEARLEQASILKKVVDAIKDLVQDCNFDCNDSGIALQAMDNSHVALVSMMLKAEGFSPYRCDRNIALGVNLTSLT
KVLRAAQNEDILTLKAEDAPDVLNLVFESSETDRISEYDLKLMDIDQEHLGIPETEYAATITMPSNEFKRITTDLMAMS
ESVTIEANKDGVKFSCQGDIGNGSVTLRQHTNVEKPNESIEIELSEPVSLTFSLKYLVNFCKASALSNTVKICLSNEVPLL
VEYSLGGSSYLRFYLAPKI|GDDE

Insertion site for extended Geph$_{DB}$ GGGKQTEDKGVQCEE

Glycine receptor β subunit (Rattus norvegicus)

MKFSLAVSFFILMSLLFEDACAKEKSSKKGKGKKKQYLCPSQQSPEDLARVPPNSTSNILNRLLVSYDPRIRPNFKGIP
VDVVVNIFINSFGSIQETTMDYRVNIFLRQKWNDPRLKLPSDFRGSDALTVDPTMYKCLWKPDLFFANEKSANFHD
VTQENILLFIFRDGDVLVSMRLSITLSCPLDLTLFPMDTQRCKMQLESFGYTTDDLRFIWQSGDPVQLEKIALPQFDIK
KEDIEYGNCTKYYKGTGYYTCVEVIFTLRRQVGFYMMGVYAPTLLIVVLSWLSFWINPDASAARVPLGIFSVLSLASE
CTTLAAELPKVSYVKALDVWLIACLLFGFASLVEYAVVQVMLNNPKRVEAEKARIAKAEQADGKGGNAAKKNTVN
GTGTPVHISTLQVGETRCKKVCTSKSDLRSNDFSIVGSLPRDFELSNYDCYGKPIEVNNGLGKPQAKNKKPPPAKPVI
PTAAKRIDLYARALFPFCFLFFNVIYWSIYL

GlyR β-loop in TM3-4 cytoplasmic region Gephyrin binding motif

VI.A.2. Appendix B: PYTHON script for the determination of gephyrin linker R_g values in various environments

```
import sys, os
import glob

dateiliste = glob.glob("*X*.pdb")
datei = "*X*.pdb"

for datei in dateiliste:

    try:
        d = open(datei, "r+")
    except:
        print "Hat nicht geklappt"
        sys.exit(0)

    data = d.readlines()

#delete everything except first linker
    try:
          for i in range(a,b):
                data[i] = ""

          for i in range(c,d):
                data[i] = ""

    except:
        print "Hat nicht geklappt"
        sys.exit(0)

    with open(datei + "_L1.pdb", "w") as file:
          file.writelines( data )

    d.close
```

The script ensured the deletion of all atoms which did not belong to the linker of protomer A of GephGL conformers. This procedure was repeated with additional scripts on protomers B and C, yielding *_L1.pdb, *_L2.pdb and *_L3.pdb.

X: common part of the EOM ensemble PDB files

a, b, c, d: the first and the last line numbers of segments which were deleted.

VI.A.3. Appendix C: Parameter optimization for EOM analysis of holo-gephyrin (section III.A.2.5.3.1)

In the following the optimization of two parameters for the EOM analysis of gephyrin is described: First, the degree of average compaction of the models of the initial pool and second its number of conformers. In EOM linkers and His-tags were modelled as chains of dummy atoms. The program RANCH with which the models of the initial pools were generated, offered an option to influence the compactness of the linkers/tags: With one scenario, “random coil”, models were generated, in which the dummy atoms oriented to each other like in random coils. In the “native-like” models the distribution of the dummy atoms resembled that of a reference set of folded proteins. The latter models were on average less extended than “random coil” models.

For GephWT two pools containing 950,000 (“native-like”) and 1,000,000 (“random coil”) conformers were compared. For s>0.03 $Å^{-1}$ there were hardly any differences between the two scenarios. However, for s<0.03 $Å^{-1}$ the “native like“ scenario displayed the clearly better fit, and – in contrast to the “random coil” scenario – with attenuated deviations that hardly exceed the experimental error range (A). Possible explanations for the failure of the “random coil” pool to explain the data over the complete resolution range could be: (1) The partial compaction of the protein which might necessitate at least some parts of the linker to adopt more compact states. (2) A 150 amino-acid-linker – even if modeled with native-like dihedral angles – could nevertheless adopt “random-coil-like” conformations, as exemplified in Fig. 26C. The most extended states of the “native-like” R_g distribution were not as extended as the ones of the “random-coil” R_g distribution, but both distributions covered similar R_g ranges.

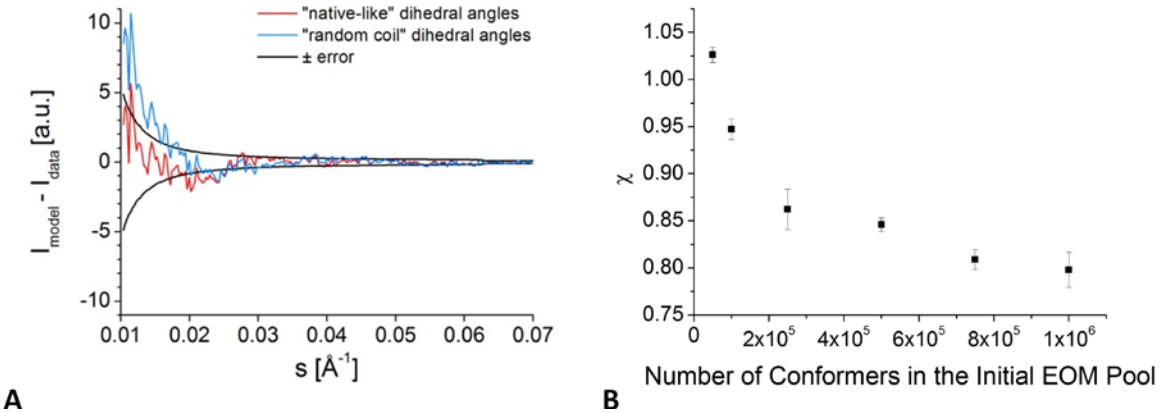

Usually less than 20,000 models in the initial pool are sufficient, however, in the case of gephyrin significantly better fits could be obtained with pools containing 950,000 conformers (B). Especially the fits in the small-angle regions benefitted from larger pools.

VI.A.4. Appendix D: EOM analysis of GephΔL, Geph-MLH1 and Geph-MLH2

The EOM analysis of GephΔL, Geph-MLH1 and Geph-MLH2 data was conducted in the same way as for GephWT, with the exception that the initial pools in Geph-MLH1/2 analysis contained only 500,000 instead of 1,000,000 conformers (GephWT and GephΔL). Further conclusions were not drawn, because the obtained fits (differently coloured in A) to the data (black points, grey error bars) were not satisfying – especially in the small-angle region, as exemplified in (B): The residuals (coloured curves) significantly exceeded the experimental errors. The χ values for the fits were 1.84, 1.91 and 1.15 for GephΔL, Geph-MLH1 and Geph-MLH2, respectively.

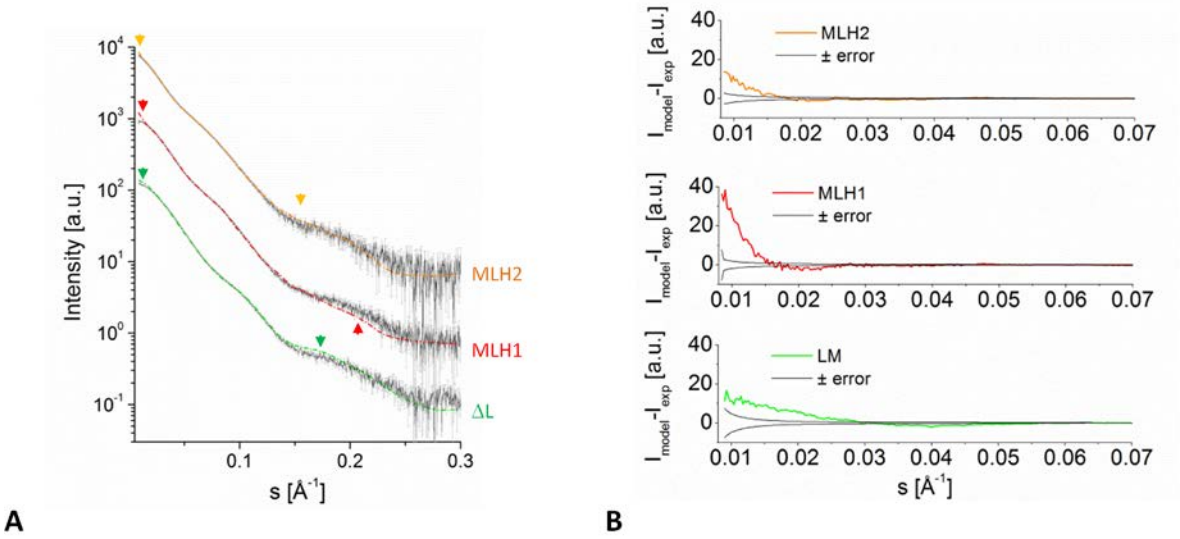

A B

VI.A.5. Appendix E: EOM analysis of MBP-L

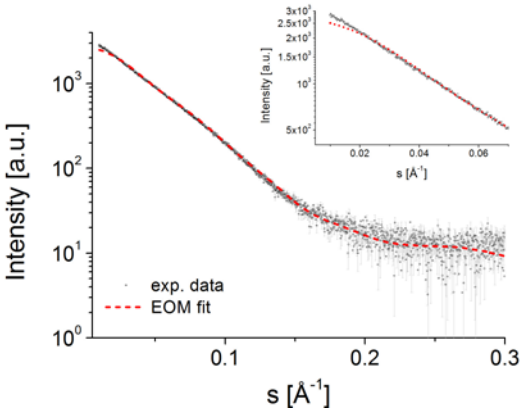

SAXS data of the MBP-L fusion (III.A.2.7.1) protein could not be fitted over the complete data range despite an initial 500,000 conformer pool. To circumvent that potential aggregates affected data quality, data points in the small-angle region (0.01 Å^{-1} < s < 0.016 Å^{-1}) were discarded. This led to an improved χ value of 1.53 instead of 2.6. Nevertheless, significant differences in the small-angle region remained (inset). Please note the comments on data quality in section III.A.2.7.1.

VI.A.6. Appendix F: Derivation of a simplified binding equation for the two-step binding of DYNLL to gephyrin

The described gephyrin-DYNLL binding mode can be considered as two-step binding:

$2\ G_3 + 3\ D_2 \rightleftarrows 2\ G_3D_2 + D_2 \rightleftarrows G_6D_6$

In the first step two linkers within a gephyrin trimer (G_3) exert avidity effects to bind a single DYNLL1 dimer (D_2) to form a G_3D_2 complex, characterized by dissociation constant K_{D1}. In the second step two G_3D_2 complexes are linked via a third D_2, yielding G_6D_6, characterized by a clearly higher dissociation constant K_{D2} (Fig. 73). For the sake of simplicity the presence of even higher oligomers than G_6D_6 is not considered.

For the total complex concentration [GD] both complexes are considered. Edged brackets indicate the concentration of the respective species:

(1) $[GD] = [G_3D_2] + [G_6D_6]$

Concentrations $[G_3D_2]$ and $[G_6D_6]$ are calculated using equations which are based on the previously introduced formula in which P and L form a stoichiometric PL complexes (section II.B.5), characterized by the dissociation constant K_D:

(2) $[PL] = \frac{[P]_T+[L]_T+K_D}{2} + \sqrt{\frac{([P]_T+[L]_T+K_D)^2}{4} - [P]_T \cdot [L]_T}$

Replacing $[P]_T$, $[L]_T$, [PL] and K_D by $2/3 \cdot [G]_T$, $[D]_T$, $[G_3D_2]$ and K_{D1}, respectively, yields:

(3) $[G_3D_2] = \frac{\frac{2}{3}[G]_T+[D]_T+K_{D1}}{2} + \sqrt{\frac{\frac{2}{3}[G]_T+[D]_T+K_{D1})^2}{4} - \frac{2}{3}[G]_T \cdot [D]_T}$

As the third gephyrin linker within a trimer is not used for the formation of the G_3D_2, it can be assumed, that for the first binding process the active gephyrin concentration is only two thirds of the $[G]_T$.

To obtain $[G_6D_6]$, $[P]_T$, $[L]_T$, [PL] and K_D in equation (2) are replaced with $[G]_T$-$[G_3D_2]$, $[D]_T$-$[G_3D_2]$, $[G_6D_6]$ and K_{D2}:

(4) $[G_6D_6] = \frac{[G]_T+[D]_T+K_{D2}-2\cdot[G_3D_2]}{2} + \sqrt{\frac{([G]_T+[D]_T+K_{D2}-2\cdot[G_3D_2])^2}{4} - ([G]_T - [G_3D_2]) \cdot ([D]_T - [G_3D_2])}$

where it is assumed that for second step the total concentrations of gephyrin and DYNLL1 were reduced by $[G_3D_2]$.

VI.A.7. Appendix G: For Geph-MLH2 collybistin binding is impaired when compared to GephWT

Native PAGE with a 3.5% gel (acrylamide/bisacrylamide=80:1) was conducted in 0.5x Tris/glycine, pH 8.6 for 90 min at 80 V. Complexes were pre-incubated for one hour on ice. Based on the thickness of the bands at the positions of the apo-proteins, wild-type gephyrin bound with higher affinity than gephyrin missing the second half of the linker.

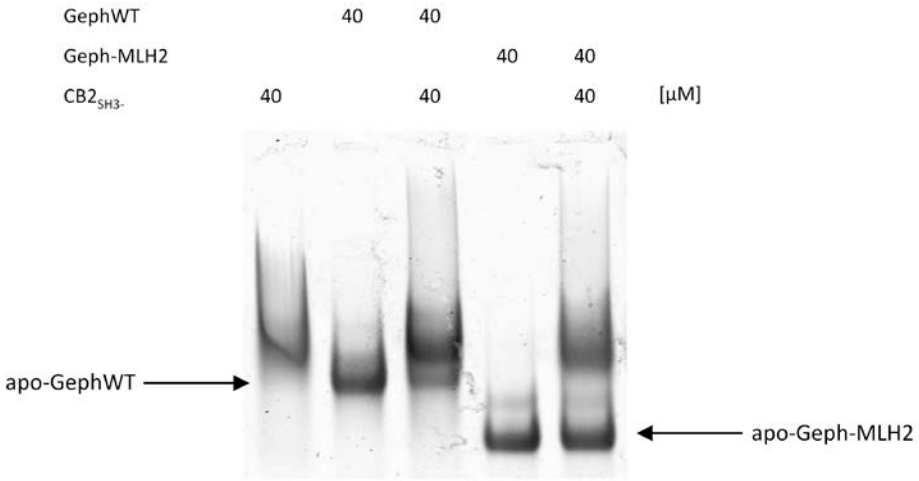

VI.B. List of figures

VI.C. List of tables

VI.D. List of abbreviations

Å	Ångström
A280	Absorbance at 280 nm
AA	Acrylamide
AFM	Atomic Force Microscopy
Amp	Ampicillin
APBS	Adpative Poisson-Boltzmann Solver
APS	Ammonium peroxydisulfate
aSEC	Analytical size-exclusion chromatography
BAA	Bisacrylamide
BLAST	Basic Local Alignment Search Tool
BSA	Bovine serum albumin
c	Concentration
cal	Calorie
Cam	Chloramphenicol
CB	Collybistin
CL	Cluster
Ct	Chaetomium thermophilum
CV	Column volume
d	path length
Da	Dalton
ΔH	Change in enthalpy
DIC	dynein intermediate chain
DLS	Dynamic light scattering
DNA	Deoxyribonucleic acid
DNase	desoxyribonuclease
dRI	Differential Refractive Index
ΔS	Change in entropy
DTT	Dithiothreitol
DYNLL	Dynein light chain
E. coli	Escherichia coli
EDTA	Ethylenediaminetetraacetate
EML3	Echinoderm microtubule associated protein like 3
engl.	Englisch
EOM	Ensemble Optimization Method
ε	Extinction coefficient
Fig.	Figure
ΔG	Change of free enthalpy
GABA	γ-aminobutyric acid
$GABA_AR$	$GABA_A$ receptor
GlyR	Glycine receptor
GST	Glutathione S-transferase
h	Hour
HDX-MS	Hydrogen/deuterium exchange mass spectrometry
HEPES	4-(2-hydroxyethyl)-1-piperazineethanesulfonic acid
IPTG	Isopropyl-β-thiogalactoside
ITC	Isothermal titration calorimetry
J	Joule
K_D	Dissociation constant
LB	Lysogen broth
M	Molar
MALS	multi angle light scattering
MBP	Maltose binding protein
µL	Microliter
µM	Micromolar
min	Minute
mL	Milliliter
MLH	Missing linker half
MR	Molecular Replacement
MWCO	Molecular weight cut off
n. a.	Not available
n.d.	Not determined
NAGE	Native agarose gel electrophoresis
NL	Neuroligin
nm	Nanometer
nM	Nanomolar
P(r)	Pair-distribution function
PAGE	Polyacrylamide gel electophoresis
PCR	Polymerase chain reaction
PDB	Protein Data Bank
PEG	Polyethyleneglycol
PH	Pleckstrin homology

pI	Isoelectric point
PISA	Protein Interfaces, Surfaces and Assemblies
PMSF	Phenylmethylsulfonylfluorid
r	Distance
rmsd	Root mean square deviation
R_g	Radius of gyration
R_H	Radius of hydration
Rn	*Rattus norvegicus*
RT	Room temperature
SAXS	Small-angle X-ray scattering
SDS	Sodium dodecyl sulfate
SF9	Spodoptera frugiperda 9
SH3	Src Homology 3 Domain
src	Acronym for sarcoma
T	Temparature
TCEP	Tris-(2-carboxyethyl)-phosphin
TEMED	N,N,N',N'-Tetramethylethylenediamine
TIRF	Total internal reflection fluorescence
TLS	Translation, libration, screw
TRIS	Trishydroxymethylaminomethane
UV	Ultraviolet
v/v	volume per volume
VV	Void volume
w/v	Weight per volume
WT	Wild-type

The one-letter and three-letter codes for amino acids were used as given in "IUPAC-IUB Joint Commission on Biochemical Nomenclature (JCBN). Nomenclature and symbolism for amino acids and peptides. Recommendations 1983.", published in Eur J Biochem Volume 138, Issue 1, pages 9-37.

VI.E. Copyrights

I adapted several figures from other manuscripts. Beforehand I usually asked for the permission to do (mostly by filling in an electronic form). The (partially automatically generated) answers of the publishers for the respective figures are given in the following sections. When sufficient, I asked the authors directly. As for the characterization of apo-gephyrin by SAXS and AFM as well as the CD melting curves of holo-gephyrin, GephG and GephE have already been published (Sander *et al.*, 2013). These data are found in sections III.A.2.1, III.A.2.2, III.A.2.4, III.A.2.5 and III.A.6.2, and these chapters also contain published text as do sections II.B4.6, II.B.6.1, II.B.6.2, III.A.3.

VI.E.1.1 Acta Crystallographica Section D

As mentioned above, substantial parts the manuscript (Sander *et al.*, 2013) were reused, which was in accordance with the policy of Acta crystallographica Section D:

Author rights after acceptance

Transfer of copyright

Note that for a multi-author article, only one author need sign the Transfer of Copyright Agreement, but that signature is on behalf of all named authors. It is the responsibility of the signing author to obtain the consent of fellow authors to act as their agent in this respect. The rights reserved to authors, listed below, apply equally to *all* the authors of the paper.

Authors retain the following rights to re-use the article, as long as it is not sold or reproduced, in whole or in part, for commercial purposes, *i.e.* for monetary gain on the authors' account or on that of a third party, or for indirect financial gain by a commercial entity. These rights apply **without needing to seek permission** from the IUCr.

Provided that a full bibliographic reference to the article as published in an IUCr journal is made, authors may:

- share print or electronic copies of the article with colleagues;
- use all or part of the article and abstract, without revision or modification, in theses and/or dissertations, in personal compilations or other publications of their own work (and may receive a royalty or other payment for such work);
- use the article within their employer's institution or company for educational or research purposes, including use in course packs;
- post an **authorised electronic reprint** of the article on their own personal website, on their employer's website/repository and on free public servers in their subject area. This includes posting on PubMedCentral and related servers.

The **authorised electronic reprint** stipulated above is automatically made available to authors upon publication of their article, or may subsequently be requested from the IUCr. It includes a cover sheet displaying the full bibliographic reference of the published article and conditions of re-use, and is overstamped with an 'electronic reprint' watermark, but is otherwise identical to the final published version of the article as it appears in the journal. Authors are requested to provide a link from their posting to the original article on the IUCr server.

VI.E.1.2 Figure 1 (Sheng & Hoogenraad, 2007)

Title:	The Postsynaptic Architecture of Excitatory Synapses: A More Quantitative View
Author:	Morgan Sheng, Casper C. Hoogenraad
Publication:	Annual Review of Biochemistry
Publisher:	Annual Reviews
Date:	Jun 7, 2007

Copyright © 2007, Annual Reviews

Permission Not Required

Material may be republished in a thesis / dissertation without obtaining additional permission from Annual Reviews, providing that the author and the original source of publication are fully acknowledged.

VI.E.1.3 Figure 2 (Smart & Paoletti, 2012)

Permission is granted for the use of Figs 1 & 2 as detailed below in your PhD thesis. Please cite this article as Cold Spring Harb Perspect Biol 2012;4:a009662, with copyright held by Cold Spring Harbor Laboratory Press.

Best wishes,

Carol C. Brown
Books Development, Marketing and Sales
Cold Spring Harbor Laboratory Press
500 Sunnyside Blvd.
Woodbury, NY 11797-2924
Tel: 516-422-4038
Fax: 516-422-4095
E-mail: brown@cshl.edu

-----Original Message-----
From: reprint@cshl.edu [mailto:reprint@cshl.edu]
Sent: Friday, May 16, 2014 11:19 AM
To: Reprint
Subject: CSHL Press Reprint Permission Request Form

Default Intro
Default Intro - line2

Name: Bodo Sander
CompanyInstitution: Rudolf Virchow Center/University of Wuerzburg
Library Address: Josef-Schneider-Stra  e 2
Library Address (line 2): Building D15
City: Wuerzburg
State (US and Canada): Bavaria
Country: Germany
Zip: 97080
Title:
Lab/Department: Structural Biology
Phone: +49 179 4677746
Fax: +49 931 31-87320
Email: bodo.sander@virchow.uni-wuerzburg.de
Title of Publication: Structural and biochemical characterization of gephyrin and various gephyrin-ligand complexes
Authors/Editors: Bodo Sander
Date of Publication: May 2014
Publisher:
Title of CSHLP Journal/Book: Cold Spring Harb Perspect Biol
Title of Article/Chapter: Synaptic Neurotransmitter-Gated Receptors
CSHL Authors/Editors: Smart TG, Paoletti P.
Page Numbers: 4, 5
Figure Numbers: 1, 2
Figure Page Numbers: 4, 5
Copyright Date: 2012
Language:
Territory:
Format: usage of Fig. 1, 2 for a PhD thesis
Additional comments:

ipaddress: 132.187.246.167
view here: http://www.cshlpress.com/subs_admin.tpl

Default Footer
Default Footer - line2

VI.E.1.4 Figures 6 (Mendel, 2013) & 51 (Herweg & Schwarz, 2012)

Please note that authors must include the following citation when using material that appeared in an ASBMB journal:

"This research was originally published in Journal Name. Author(s). Title. *Journal Name*. Year; Vol:pp-pp. © the American Society for Biochemistry and Molecular Biology."

For other parties using material for noncommercial use:

Other parties are welcome to copy, distribute, transmit and adapt the work — at no cost and without permission — for noncommercial use as long as they attribute the work to the original source using the citation above.

Examples of noncommercial use include:

- Reproducing a figure for educational purposes, such as schoolwork or lecture presentations, with attribution.
- Appending a reprinted article to a Ph.D. dissertation, with attribution.

VI.E.1.5 Figure 59 (Maas et al., 2006)

Requesting Permission Licensing

Please read below to determine if you must obtain permission for your specific reuse.

Original author reuse (commercial and noncommercial)

Ownership of copyright remains with RUP authors, who may reuse their own material forany purpose, including commercial profit, as long as they provide proper attribution. The permission does not extend to the institution.

- Note that our preferred citation style is as follows:
- ©AUTHOR et al., YEAR. Originally published in *JOURNAL NAME*. doi:########.
- If an article does not carry a doi, our preferred citation style is as follows:
- ©AUTHOR et al., YEAR. Originally published in *JOURNAL NAME*. VOL:PP–PP.

Noncommercial third-party reuse

Third parties may reuse our content for noncommercial purposes without specific permission as long as they provide proper attribution (see citation preferences provided above). Within the first 6 months after publication, the creation of mirror sites is prohibited.

VI.E.1.6 Figure 78 (Papadopoulos & Soykan, 2011)

In this case the authors hold the copyright. I therefore contacted them as follows:

```
On May 19, 2014, at 3:50 PM, Bodo Sander wrote:

Hi Tolga,

if I got it correctly, you still retain the copyright of your 2011 paper in
Frontiers in Neuroscience ("The role of collybistin in gephyrin clustering at
inhibitory synapses: facts and open questions"). I would like to include a
minimally modified version of Fig. 6 (Collybistin activation model). As a matter of
fact I would include a reference. Is this fine for you?

All the best,

Bodo
```

I received the following answer:

```
Hi Bodo,

This is absolutely OK for us. Let me know if you are interested in having the
original TIFF file of the figure.

Best wishes,

Tolga
```

VI.F. Curriculum Vitae

Place, Date

Signature

VI.G. List of publications

Sander, B., Tria, G., Shkumatov, A. V., Kim, E. Y., Grossmann, J. G., Tessmer, I., Svergun, D. I., & Schindelin, H. (2013). Structural characterization of gephyrin by AFM and SAXS reveals a mixture of compact and extended states. Acta Crystallogr D. Biol Crystallogr 69, 2050-2060.

Sander, B., Lee E.-Y., Schwiese, O., Schwarz, G., Schindelin, H. (*in preparation*). The Structural Basis of the Gephyrin-DYNLL1 interaction